Tracking Localized Cracks in the Computational Analysis of Masonry Structures

Doctoral Thesis by:
Savvas Saloustros

TESIS DOCTORAL

Supervised by:
Luca Pelà
Miguel Cervera

Barcelona, September 2017

Thesis by compendium of publications

Universitat Politècnica de Catalunya
Departament d'Enginyeria Civil i Ambiental
Programa de Doctorat en Enginyeria de la Construcció

This page is intentionally left blank.

Tracking Localized Cracks in the Computational Analysis of Masonry Structures

Doctoral Thesis submitted in fulfilment of the requirements for the
Degree of Doctor of Philosophy in Construction Engineering
by

SAVVAS SALOUSTROS

Barcelona, September 2017

Thesis by compendium of publications

Universitat Politècnica de Catalunya
Departament d'Enginyeria Civil i Ambiental
Programa de Doctorat en Enginyeria de la Construcció

Thesis Supervisors:
Assoc. Prof. Luca Pelà
Prof. Miguel Cervera

Board of Examiners:
Prof. Sergio Oller - Universitat Politècnica de Catalunya
Prof. Jaime C. Gálvez - Universidad Politécnica de Madrid
Assoc. Prof. Guido Camata - Università degli Studi "G. d'Annunzio" Chieti - Pescara

External Reviewers:
Prof. Paulo B. Lourenço - Universidade do Minho
Assoc. Prof. Guido Camata - Università degli Studi "G. d'Annunzio" Chieti - Pescara

Acknowledgements

The main core of the research presented in this thesis was carried-out at the Department of Civil and Environmental Engineering of the Technical University of Catalonia (UPC). A complementary part of it was performed at the Department of Civil, Environmental and Geomatic Engineering of the University College of London (UCL).

This research has been possible thanks to the scholarship made available by the UPC. Additional financial support from the MINECO (Ministerio de Economia y Competitividad of the Spanish Government) and the European Regional Development Fund through the research projects MICROPAR (BIA2012-32234), MULTIMAS (BIA2015-63882-P) and EACY (MAT2013-48624-C2-1-P) is gratefully acknowledged.

I am deeply grateful to my supervisors Dr. Luca Pelà and Prof. Miguel Cervera for their continuous support, fruitful meetings and for sharing with me their knowledge on numerical methods, constitutive modelling and structural analysis of masonry structures. Their optimistic and enthusiastic approach towards research have been a great source of motivation during these years.

I would like to express my deep gratitude to Prof. Pere Roca for giving me the opportunity to pursue a PhD degree at UPC and for his permanent interest on this work, useful suggestions and meticulous feedback.

I gratefully acknowledge Prof. Dina D'Ayala for making possible my research stay in UCL and for giving me the opportunity to work under her supervision.

It is a pleasure to thank the Master and PhD students who applied the developed numerical model in their research. Their comments have been really useful for the development of the presented numerical model.

I am grateful to all my new friends and colleagues in Barcelona and London. Thanks for making my stay in these two cities a memorable experience. I also owe a great debt of gratitude to my friends in Greece. The breaks I had with their company were the necessary fuel to continue this journey.

I owe my deepest gratitude to my family, my sister Elena and my parents Hara and Panayiotis. I am grateful for their love, patience and for supporting every choice I have made in my life. All the credit is theirs.

Finally, a special thanks goes to Jenny. I am indebted to her for the support, love and care and for her courage to join me on this trip to Barcelona. Thank you for all the memories we have shared together these years.

Savvas Saloustros

Barcelona, September 29, 2017

This page is intentionally left blank.

Abstract

Numerical methods aid significantly the engineering efforts towards the conservation of existing masonry structures and the design of new ones. Among them, macro-mechanical finite element methods based on the smeared crack approach are commonly preferred as an affordable choice for the analysis of large masonry structures. Nevertheless, they usually result in a non-realistic representation of damage as smeared over large areas of the structure, which hampers the correct interpretation of the damage pattern. Additionally, a more critical pathology of this approach is the mesh-dependency, which influences notably the safety and stability predictions.

To overcome these limitations, this thesis proposes a novel computational tool based on the enrichment of the classical smeared crack approach with a local tracking algorithm. The objective of this *localized damage model* is the realistic and efficient non-linear analysis of masonry structures with an enhanced representation of cracking.

The non-linear behaviour of masonry is simulated through the adoption of a continuum damage mechanics model with two damage indices, allowing the differentiation between the tensile and compressive mechanical responses of masonry. In this context, a novel explicit formulation for the evolution of irreversible strains is proposed and implemented. Two new expressions are derived for the regularization of the tensile and compressive softening responses according to the crack-band approach, ensuring the mesh-size objectivity of the damage model.

The simulation of the structural behaviour of masonry structures under versatile loading and boundary conditions necessitates some developments in the context of local tracking algorithms. To this end, this thesis presents the enhancement of local tracking algorithms with novel procedures that make possible the simulation of multiple, arbitrary and intersecting cracking under monotonic and cyclic loading. Additionally, the effect of different crack propagation criteria is investigated and the selection among more than one potential failure planes is tackled.

The proposed localized damage model is validated through the simulation of a series of structural examples. These vary from small-scale tests on concrete specimens with few dominant cracks, to medium and large-scale masonry structures with multiple tensile, shear and flexural cracking. The analyses are compared with analytical, experimental and numerical results obtained with alternative methods available in the literature. Overall, the localized damage model developed in this thesis largely improves the mesh-independency of the classical smeared crack approach and reproduces crack patterns and collapse mechanisms in an efficient and realistic way.

Keywords: Masonry · Quasi-brittle materials · Finite Element Method · Strain-localization · Tracking · Continuum Damage Mechanics · Irreversible Strains · Tensile/shear/flexural cracks · Intersecting cracks · Mesh-dependence · Cyclic shear loading

This page is intentionally left blank.

Resumen

Trazado de Fisuras Localizadas en el Análisis Computacional de Mampostería

Los métodos numéricos son decisivos en la ingeniería para la conservación de estructuras de mampostería existentes y el diseño de estructuras nuevas. Entre ellos, los métodos macro-mecánicos de elementos finitos, basados en el concepto de fisuras distribuidas, son habitualmente los preferidos como opción asequible para el análisis de grandes estructuras de mampostería. Sin embargo, suelen resultar en a una representación poco realista del daño, distribuido en grandes áreas de la estructura, lo que impide la correcta interpretación del patrón de daño. Además, esta metodología presenta una patología más crítica, la dependencia de la malla, que influye notablemente en las predicciones de seguridad y estabilidad.

Para superar estas limitaciones, esta tesis propone una nueva herramienta numérica basada en el enriquecimiento del clásico enfoque de fisuras distribuidas con un algoritmo de trazado local. El objetivo de este modelo de daño localizado es el análisis no-lineal de las estructuras de mampostería de manera realista y eficiente con una representación mejorada de fisuras.

El comportamiento no-lineal de la mampostería se simula a través de la adopción de un modelo de mecánica de daño continuo con dos índices de daño, permitiendo la diferenciación entre las respuestas mecánicas de tensión y compresión de la mampostería. En este contexto, se propone e implementa una nueva formulación explícita para la evolución de deformaciones irreversibles. Se derivan dos nuevas expresiones para la regularización del ablandamiento de tracción y compresión según el ancho de banda de la fisura, garantizando la objetividad del modelo de daño al respecto del tamaño de la malla.

La simulación del comportamiento estructural de las estructuras de mampostería en condiciones de carga y contorno generales precisa de algunos desarrollos en el contexto de los algoritmos locales de trazado. Con este objetivo, se presenta la mejora de los algoritmos locales de trazado con nuevos procedimientos que posibilitan la simulación de fisuración múltiple, arbitraria e secante bajo cargas monótonas y cíclicas. Además, se investiga el efecto de diferentes criterios de propagación de fisuras y se aborda la selección entre más de un plano de falla posible.

El modelo de daño localizado propuesto se valida mediante la simulación de una serie de ejemplos estructurales. Éstos van desde pruebas a pequeña escala en probetas de hormigón, con pocas fisuras dominantes, hasta estructuras de mampostería de mediana y gran escala con fisuración múltiple de tracción, de cortante y de flexión. Los análisis se comparan con los resultados analíticos, experimentales y numéricos obtenidos con métodos alternativos disponibles en la literatura. El modelo de daño localizado mejora en gran medida la independencia de la malla del clásico método de fisuras distribuidas y reproduce patrones de daño y mecanismos de colapso de una manera eficiente y realista.

Palabras clave: Mampostería, Materiales cuasi-frágiles, Método de elementos finitos, Localización de deformaciones, Algoritmo de trazado, mecánica de daño continuo, Deformaciones irreversibles, Fisuración de tracción/cortante/flexión, Fisuras secantes, Dependencia de la malla, Carga cíclica de cortante

This page is intentionally left blank.

Contents

List of Figures

This page is intentionally left blank.

List of Tables

This page is intentionally left blank.

Part I - Research Summary

This page is intentionally left blank.

Notation, Abbreviations & Terminology

Notation used in this thesis. (+) and (−) superscripts represent tensile and compressive entities respectively. Lowercase bold letters in italics refer to second order tensors (e.g. $\boldsymbol{\sigma}$), Uppercase bold letters in italics to forth order tensors (e.g. $\boldsymbol{C_0}$), lowercase bold letters to vectors (e.g. $\mathbf{n_j}$) and lowercase or uppercase letters (no bold) in italics to scalars (e.g. f^+, A_d).

Latin Characters

Symbol	Name	Place of definition or first occurrence
a	Scalar variable used in the definition of the equivalent stresses	Eq. (3.12)
b	Scalar variable used in the definition of the equivalent stresses	Eq. (3.13)
c	Cohesion	Eq. (6.2)
$d^{\pm}$	Tensile and compressive damage indices	Eqs. (3.32, 3.33, 3.35)
$f^{\pm}$	Uniaxial tensile and compressive strength	Eq. (3.10)
f_p	Compressive strength before exponential softening	Eq. (3.33)
f_0^+	Tensile uniaxial strength	Fig. (3.4)
f_0^-	Compressive strength before parabolic hardening	Fig. (3.6)
f_b^-	Biaxial compressive strength	Eq. (3.12)
l_{dis}	Finite element characteristic length	Eq. (3.36)
$l_{mat}^{\pm}$	Tensile and compressive material characteristic length	Eq. 3.41
$\mathbf{n_j}$	Eigenvector of the effective stress tensor	Eq. (3.5)
p_{ij}	Symmetric tensor used for the computation of the $\boldsymbol{P}^{\pm}$ projection tensors	Eq. (3.5)
$r^{\pm}$	Tensile and compressive stress threshold	Eq. (3.15)
$r_0^{\pm}$	Tensile and compressive initial stress threshold	Eqs. (3.32, 3.33)
r_p	Compressive stress threshold denoting the initiation of exponential softening	Eq. (3.33)
r_e	Compressive stress threshold equal to the uniaxial compresssive strength	Eq. (3.33)
$r(\tilde{\bar{\boldsymbol{\sigma}}}_{n+1})$	Stress threshold in the absence of irreversible strains	Eq. (3.22)
A_{fe}	Area of a finite element	Sec. 3.3
A_d	Scaler used in the definition of the parabolic hardening function	Eq. (3.34)
$\tilde{A}_d$	Scalar used for the regularization of the exponential softening in the compressive damage law	Eq. (3.38)

B_d	Scalar used for the regularization of the exponential softening in the compressive damage law	Eq. (3.39)
$\boldsymbol{C_0}$	Isotropic linear-elastic constitutive tensor	Eq. (3.1)
$\boldsymbol{C}_s$	Secant stiffness matrix	Eq. (3.9)
$\boldsymbol{D}$	Tensor used for the definition of the secant matrix	Eq. (3.8)
E	Young's modulus	Eq. (3.17)
$G_f^{\pm}$	Tensile and compressive fracture energy	Eqs. (3.32, 3.35)
$H_d^{\pm}$	Tensile and compressive discrete softening parameter	Eqs. (3.36, 3.37)
$\boldsymbol{I}$	Identity tensor	Eq. (3.5)
$\bar{I}_1$	First invariant of the effective stress tensor	Eqs. (3.10, 3.11)
$\bar{J}_2$	Second invariant of the deviatoric effective stress tensor	Eqs. (3.10, 3.11)
$\boldsymbol{P}^{\pm}$	Tensile and Compressive projection tensors	Eq. (3.4)

Greek Characters

Symbol	Name	Place of definition or first occurrence
β	Material parameter characterizing the rate intensity of the irreversible strains	Eqs. (3.17, 3.56)
γ	Total dissipated energy	Eq. (3.42)
γ^d	Dissipated energy due to the evolution of damage	Eq. (3.46a)
γ^i	Dissipated energy due to the evolution of irreversible strains	Eq. (3.46b)
$\boldsymbol{\varepsilon}$	Total strain tensor	Eq. (3.2)
$\boldsymbol{\varepsilon}^e$	Elastic strain tensor	Eq. (3.1)
$\boldsymbol{\varepsilon}^i$	Irreversible strain tensor	Eq. (3.2)
ε_p	Total strain before exponential softening for damage under compression	Fig. (3.6)
η	Angle between a fracture plane and the plane of the major principal stress	Fig. (6.1)
κ_1	Scalar parameter for controlling the shape of the compressive damage surface under shear stress states	Eq. (3.11)
λ	Scaling factor of $\tilde{\bar{\boldsymbol{\sigma}}}$ for the calculation of $\bar{\boldsymbol{\sigma}}$	Eq. (3.26)
ν	Poisson's ratio	Eq. (3.4.1)
σ_j	principal stress	Eq. (3.4)
$\bar{\sigma}_{max}$	maximum effective principal stress	Eq. (3.10)
$\bar{\sigma}_{min}$	minimum effective principal stress	Eq. (3.11)
$\boldsymbol{\sigma}$	Cauchy stress tensor	Eq. (3.6)
$\bar{\boldsymbol{\sigma}}$	Effective stress tensor	Eq. (3.1)

$\bar{\boldsymbol{\sigma}}^{\pm}$	Tensile and compressive parts of the effective stress tensor	Eq. (3.3)
$\tilde{\bar{\boldsymbol{\sigma}}}$	Effective stress tensor in the absence of irreversible deformations	Eq. (3.21)
$\tau^{\pm}$	Tensile and compressive equivalent stresses	Eqs. (3.10, 3.11)
τ	Shear stress	Eq. (6.1)
$\theta_{1,2}$	The two angles defining the crack propagation direction with respect to the horizontal axis according to the Mohr-Coulomb failure criterion	Eq. (6.7)
φ	Friction angle	Eq. (6.2)
ψ	Helmholtz free energy	Eq. (3.43)
$\psi_0^{\pm}$	Elastic free energies	Eqs. (3.44, 3.45)
Δr	Increment of the stress threshold between two consecutive time steps of the numerical analysis	Eq. (3.24)
Δr^{max}	Maximum increment of the stress threshold in the absence of irreversible strains between two consecutive time steps of the numerical analysis	Eq. (3.23)
$\Phi^{\pm}$	Tensile and compressive damage criteria	Eq. (3.16)

Symbols

Symbol	Name	Place of definition or first occurrence
:	Double contraction	Eq. (3.1)
$\otimes$	Tensor product	Eq. (3.4a)
$\dot{x}$	Variation of variable "x" with respect to the time	Eq. (3.17)
$H[\cdot]$	Heaviside step function	Eq. (3.4a)
$H_0[\cdot]$	Specific Heaviside step function	Eq. (3.10)

General superscripts

Symbol	Name	Place of definition or first occurrence
$+$	Tensile entity	Eq. (3.6)
$-$	Compressive entity	Eq. (3.6)
i	Irreversible	Eq. (3.17)
e	Elastic	Eq. (3.1)
d	Damage	Eq. (3.46a)

General subscripts

Symbol	Name	Place of definition or first occurrence
fe	Finite element	Sec. 3.5
dis	Discrete	Eq. (3.36)
mat	Material	Eq. (3.36)
0	Initial	Eq. (3.1)

Terminology in tracking algorithm

Crack-root element	The first element of a crack.
Boundary crack-root element	A crack-root element with one or more sides on the boundary of the mesh.
Internal crack-root element	A crack-root element with no sides on the boundary of the mesh.
Crack-tip element	The first element at the propagation front of a crack.
Crack-origin	The coordinates of the origin of the crack at the crack-root element.
Stress threshold criterion	Condition for ending the crack propagation depending on the stress state of the crack-tip.
Boundary criterion	Condition for ending the crack propagation depending on the crack position with regards to the mesh.
r_{excl}	Distance between new and existing active cracks.
r_{neigh}	Radius used for the estimation of the vector sum of the crack propagation directions in the maximum curvature criterion.
r_{crit}	Radius used for the computation of the strain energy fields ahead of a crack-tip in the energy-based criterion for crack propagation according to the Mohr-Coulomb theory of rupture.
a_{max}	Maximum allowed curvature angle
a_{lim}	Threshold angle used for the definition of "active" and "inactive" cracks.

Acronyms

2D	Two-dimensional
3D	Three-dimensional
CDM	Continuum Damage Mechanics
DCA	Discrete Crack Approach
E-FEM	Embedded Finite Element Method
FEM	Finite Element Method
FE	Finite Element
LEFM	Linear Elastic Fracture Mechanics
MC	Mohr-Coulomb
MPS	Maximum Principal Stress
SCA	Smeared Crack Approach
X-FEM	Extended Finite Element Method

This page is intentionally left blank.

1

Introduction

1.1 Background and Motivation

Masonry is characterized by the repeated arrangement of units bound together with mortar or laid dry upon each other. Its intrinsic simplicity, along with the wide availability and diversity of possible components, has established it as one of the most widely used construction techniques from antiquity until today.

Research on masonry structures is important today mainly for two reasons. Firstly, masonry is still the primary construction technique for many countries worldwide. In order to safe-guard people's lives and increase the serviceability levels, it is necessary to validate the design of new masonry structures under complex loading conditions, such as those induced by seismic loads or soil settlements. Secondly, the astonishing durability of many masonry typologies has resulted in long-lasting structures, which constitute a significant part of today's infrastructure and built cultural heritage. The purpose of modern communities is to preserve them, guaranteeing the security of the inhabitants and the conservation of their artistic and cultural value. This procedure necessitates the accurate assessment of the structural pathology and capacity of existing masonry structures, and the consequent design and validation of any necessary strengthening measurements.

The fundamental step towards the accomplishment of the above objectives is the development of accurate tools for the structural analysis. This is not an easy task due to the inherent complex structural response of masonry and its diversity, which is closely connected to the local economy, technology and material resources. Notwithstanding, a great majority of masonry typologies share a common characteristic, which is a striking difference between their tensile and compressive strengths. The relative low, or negligible, tensile strength, compared to the much higher compressive strength, makes cracking of the material the critical reason for its local failure. The development and propagation of these cracks within the structure are responsible for the evolution of local and global collapse mechanisms.

It becomes clear from the above that the accurate modelling of cracking phenomena is a key point for the proper assessment of masonry structures. In fact, classical approaches, such as limit analysis [156], are based on the correct locations of cracks for estimating the stability and strength of a masonry structure. When the load and boundary conditions are well-defined, they can give very accurate predictions regarding the most critical collapse mechanism and the load-carrying capacity. Nevertheless, the classical approaches can hardly be applied for estimating the displacements experienced by the damaging structure, for predicting damage for load levels that do not lead to a limit condition, or for simulating loading scenarios causing progressively accumulated damage, such as in the case of earthquakes. Consequently, it is necessary to develop new structural analysis techniques that overcome the limitations of existing ones.

The pursuit of a methodology that can effectively be used for the analysis of masonry structures is an on-going challenge. Advances in computational methods during the last decades have significantly contributed to this direction. As a matter of fact, today there exists a plethora of numerical tools based on different theories and coming with varying level of complexity and cost. However, a unified approach for the simulation of masonry is still missing, and it can be argued if it will ever exist, judging from the diversity of the involved materials, geometries and scales.

Nowadays, two trends can be identified for the analysis of masonry structures, which are closely connected to the geometrical scale of the problem under investigation. Simulations of single structural elements, such as walls or frames, consider detailed micro-mechanical models, in which all the parameters of masonry components are explicitly considered. These approaches can usually account for a very precise simulation of cracking and the evolution of a collapse mechanism. Moving to a larger scale, the cost for preparing and computing a micro-mechanical model increases dramatically, making them unaffordable in practice. The common procedure for these cases is the use of macro-mechanical approaches, in which masonry is simplified as a homogeneous material with average properties. The advantages of computationally efficient numerical simulations come at the cost of a coarse and, in many cases, non-realistic simulation of damage. Another important difference between the two approaches regards their applicability in industry and academia. The costs associated to the model preparation, computing time and acquisition of material properties required by micro-mechanical approaches, make them still a privilege of advanced research works in academia. Contrary to that, the cost-efficiency and the limited information regarding the material and geometry in macro-mechanical approaches have established them as the most utilized by practitioners in structural engineering.

The Finite Element Method (FEM) is a versatile tool that allows the analysis of whole structures with complex geometries under variable loading and boundary conditions. For this reason, FEM is the most widespread numerical tool and commercial finite element (FE) codes oriented to the micro/macro-mechanical analysis of structures are widely available for practitioners.

One major problem of simulating failure, localized deformation and damage phenomena in the framework of irreducible FE formulations, is the dependency of the numerical solution on the used mesh, which is present in two ways. The first is known as *mesh-size dependency* and concerns the dependency of the energy dissipation on the size of the finite element mesh. The second is the *directional mesh-bias dependency*, referring to the dependency of the cracking pattern on the finite element mesh orientation. These flaws of the numerical method can have a dramatic effect on the capacity, energy dissipation and collapse mechanism predicted by the numerical solution.

An other effect closely connected to the above pathologies is the non-realistic representation of damage by the *smeared crack approach (SCA)*. The smeared crack approach is one of the two possible crack simulations with FEM, with the alternative being the *discrete crack approach (DCA)*. It is described as the smeared representation of cracks over a definite width, which is at least equal to the width of one finite element. The smeared crack approach is commonly used for macro-mechanical simulations of masonry structures due to its straightforward implementation in FEM codes and its lower computational-cost compared to the discrete crack approach. Nevertheless, the wrong localization of cracking induced by the aforementioned pathologies of FEM results many times in the non-realistic spreading of the damage over large areas of the structure. This representation contradicts the localized nature of cracking exhibited by masonry and hampers the correct interpretation of the damage pattern and collapse mechanisms.

Considering the above, we can identify two challenges in the FE analysis of masonry structures. The first one is to bridge the gap between very detailed but costly finite element tools, restricted to the analysis of structural elements, and cost-efficient but simplified methods, used for the assessment of large-scale structures. The second one is to overcome the intrinsic limitations of irreducible FE formulations and classical smeared crack approaches concerning the realistic and mesh-objective simulation of damage. It is the motivation of this work to address these challenges and investigate how to simulate cracking in a realistic, accurate and cost-efficient way such that finite element simulations can capture local and global collapse mechanisms of masonry structures.

1.2 Scope and Objectives

The primary objective of this study is to develop and validate a computational tool for the realistic and efficient non-linear analysis of masonry structures with enhanced representation of localized cracks. This tool is oriented to masonry structures that can be simulated as being in a state of plane-stress or plane-strain.

The research is performed within the scope of strain localization techniques in quasi-brittle materials and non-linear analysis of masonry structures. As a matter of fact, a set of specific objectives have been defined towards the accomplishment of the primary objective that extend to both of these fields. These are:

- To compile comprehensive state-of-the-art information concerning numerical methods developed for the representation of localized cracking and their application to masonry structures.

- To develop a strain localization technique for the numerical simulation of cracking in quasi-brittle materials. Desirable properties of this technique are:

  - Mesh-size and directional mesh-bias independency of the numerical solution.
  - Realistic simulation of linear and curved cracking under tensile, flexural and shear stress states.
  - Modelling of arbitrary cracking initiating at any location of the structure without their a-priori definition.
  - Simulation of multiple-crack problems accounting for crack intersection.
  - Versatility regarding the loading scenarios and boundary conditions, e.g. proportional & non-proportional, horizontal & vertical, monotonic & cyclic loading.
  - Correct representation of local and global collapse mechanisms and description of the post-failure behaviour for assessing the structural safety.
  - Limited computational overhead compared to classical smeared crack approaches.

- To validate the developed technique. This should be done on the basis of comparison with experimental and analytical results available in the literature, as well as different numerical approaches adopted in the analysis of masonry structures.

- To apply the proposed technique to a real-scale and complex case study of an existing masonry building.

- To extend the technique to the analysis of cyclic loads. This includes three sub-objectives:

  - To adopt or develop a constitutive model for the simulation of irreversible strains. Calibrate the selected model with available experimental data.
  - To extend the strain localization technique for the simulation of crack-opening/closing and multi-directional cracking.
  - To validate the proposed technique through the comparison with experimental results under cyclic actions.

Even though particular emphasis is set on masonry structures, it is expected that the developed approach can be applied to other quasi-brittle materials characterized by localized cracking, such as concrete or rocks. Indeed, many examples included in this study concern the analysis of concrete specimens.

1.3 Outline

The document is composed by two parts. The first part is a collection of the main developments and results presented in the accompanying publications, which are included in the second part of the document. It is organised in seven chapters in the following way.

Chapter 2 introduces and motivates the performed research by presenting a literature review on the two underlying fields of this dissertation. The first field concerns the methodology and numerical approaches used for the modelling of cracking in solids, particularly in quasi-brittle materials. Discussion includes early fracture research preceding the advance of computational methods and diverse approaches within the FEM. Particular focus is given on the different versions of tracking algorithms. The second field investigates the application of these techniques to the non-linear analysis of masonry structures. The inventory of available approaches is presented using a categorization according to the level of detail on the material representation.

Chapter 3 details the constitutive model used for the numerical representation of masonry. It is a continuum damage model with two damage indices for distinguishing between damage under tension and compression. An existing formulation used for the simulation of irreversible strains under load-reversal is revisited and its limitations are detailed. To overcome them, a new formulation is proposed and validated against experimental results on concrete and masonry specimens. Discussion includes implementation issues.

Chapter 4 proposes two novel tracking algorithms for the simulation of localized cracking in quasi-brittle materials. The algorithms are designed to allow arbitrary cracking from any location of the structure, as well as multiple and intersecting cracks. Two alternatives are presented concerning the conditions for crack initiation, one oriented to monotonic loading and the second to cyclic loading.

Chapter 5 includes structural applications of the proposed numerical method. These include analysis of small-scale concrete specimens, unreinforced masonry walls and frames, as well as large-scale façades. The proposed computational tool is validated through a three-level comparison with analytical, experimental and numerical results with alternative computational tools of the available literature. Cost and computational issues, as for instance mesh-dependency, are detailed and discussed.

Chapter 6 presents a discussion regarding the definition of the crack propagation direction in tracking algorithms. A new approach is presented, in which the crack propagation is associated with the Mohr-Coulomb failure criterion. This choice entails a dilemma concerning the selection of one among the two potential failure planes proposed by the Mohr-Coulomb theory of rupture. To this aim, a novel tracking algorithm enhanced with an energy-based criterion is proposed. The theoretical and numerical implications of this choice are investigated through the simulation of mixed-mode loading experiments on concrete specimens.

Chapter 7 is the closing chapter of the first part of the thesis. It recapitulates the

performed research, summarizes the conclusions and presents suggestions for future work.

The second part of this document includes the accepted manuscripts of the peer-reviewed international journal articles prepared during the course of this research, which are presented in the following section.

1.4 Research Dissemination

The work included in this thesis has resulted in the following scientific publications:

Peer-reviewed International Journals

- Saloustros S, Pelà L, Cervera M. (2015) A tracking technique for localized cohesive-frictional damage. *Engineering Fracture Mechanics*; Vol. 150: p. 96-114. doi:10.1016/j.engfracmech.2015.10.039.

- Saloustros S, Pelà L, Cervera M, Roca P. (2016) Finite element modelling of internal and multiple localized cracks. *Computational Mechanics*; Vol. 59: p. 299-316. doi:10.1007/s00466-016-1351-6.

- Saloustros S, Cervera M, Pelà L. (2017) Tracking multi-directional intersecting cracks in numerical modelling of masonry shear walls under cyclic loading. *Meccanica*. Special issue of "New Trends in Mechanics of Masonry". doi:10.1007/s11012-017-0712-3, (*in press*).

- Saloustros S, Pelà L, Cervera M, Roca P. (2017) An Enhanced Finite Element Macro-Model for the Realistic Simulation of Localized Cracks in Masonry Structures: A Large-Scale Application. *International Journal of Architectural Heritage*. doi:10.1080/15583058.2017.1323245, (*in press*).

Peer-Review Conference Papers with Presentations in International Conferences

- Saloustros S, Pelà L, Cervera M, Roca P. (2016) A macro-modelling finite element technique for the realistic simulation of cracking in masonry structures. In Van Balen K, Verstrynge E, editors. *10th International Conference on Structural Analysis of Historical Constructions, Leuven, Belgium, 13-15 September*, CRC Press LLC.: p. 284-90.

- Saloustros S, Pelà L, Cervera M, Roca P, D'Ayala DF. (2016) Effect of pier-spandrel geometry on the in-plane response of masonry structures. In: Modena C, da Porto F, Valluzzi MR, editors. *16th International Brick & Block Masonry Conference, Padova, Italy, 26-30 June*, CRC Press LLC.; p. 339-46. doi:10.1201/b21889-43.

Presentations in International Conferences

- Saloustros S, Pelà L, Cervera M, Roca P. (2016) An extension of tracking algorithms for the simulation of multiple and intersecting cracking. *European Congress on Computational Methods in Applied Sciences and Engineering, Crete, Greece 5-10 June.*

This page is intentionally left blank.

2

Literature Review

This chapter presents a literature review of finite element methods used for representing crack propagation in solids, and their application in the computational analysis of unreinforced masonry structures. After a short introduction (Section 2.1), a historical perspective is presented to the early theoretical research devoted to crack propagation, when the foundations for the later developed computational methods for cracking were established (Section 2.2). Following that, Section 2.3 presents an overview of the various finite element methods developed for addressing the problem of crack propagation simulation in solids. Among them, particular emphasis is given in Section 2.4 on the developed tracking algorithms, which are the basis of many discrete and few smeared crack approaches, as well as on the used crack propagation criteria. The last part of the chapter (Section 2.5), preceding the summary (Section 2.6), focuses on finite element methods employed on the simulation of cracking in unreinforced masonry structures.

2.1 Introduction

Strain localization refers to the phenomenon of the development of narrow bands within a loaded structure where material degradation and deformation concentrates, while the material in areas outside these bands tends to unload elastically. In structures made of quasi-brittle materials, the evolution of these bands of localized strains, called hereafter as cracks, can have a detrimental effect on the global structural behaviour. Especially when reinforcement is lacking, as is the case of unreinforced masonry structures, the development of the collapse mechanism depends on the relative location and propagation of dominant cracks within the structure. Due to the high importance of cracking phenomena in the structural capacity and response, the engineering community has shown

an earnest interest during the last century in their understanding and realistic prediction, to such an extent that two new engineering fields have emerged: Fracture Mechanics and Computational Failure Mechanics.

This chapter aims to contextualize the topic of this thesis, which is the efficient and realistic simulation of crack propagation in masonry structures. To this aim, an outline is presented of the progress made in the prediction of cracking starting from early fracture mechanics research to modern finite element methods applied to cracking. This includes a discussion over the unexpected difficulties encountered for the numerical simulation of cracking and the developed solutions. Following this, the chapter closes with a survey on the finite element methods applied to the structural assessment of unreinforced masonry structures presenting their advantages and limitations.

2.2 Early research in Fracture Mechanics

The theory of Linear Elastic Fracture Mechanics (LEFM) was the most important tool in fracture research, prior to the introduction of numerical methods. The main interest of engineers was to estimate the limit value of the applied load leading to crack propagation from material discontinuities, which were intentionally incorporated in the material design (such as windows in aircrafts or hatches in ships), or occurred as imperfections of the fabrication process and damage during service life. The mathematical bases to this aim were set between the dusk of the 19th century and the dawn of the 20th.

The first endeavours for the definition of the moment of fracture initiation relied on a stress-based approach. Kirsch presented in 1898 [185] the solution for the stress-field in an infinite plate with a circular hole subjected to uniaxial tension. His solution could provide a safety factor through a direct comparison of the maximum stress with the yield stress of the material, while different loading conditions could be easily obtained by superposition principles. An immediate application of Kirsch's solution was in rock mechanics, where drilling results in circular holes in the mass of the rock.

Circular holes, however, are a special case of material discontinuity. Inglis tried to overcome this limitation of Kirsch's theory and presented the solution for a stress field surrounding elliptical holes, or sharp cracks with rounded notches in his seminal paper of 1913 [164]. The analytical solution of Inglis gave a completely new insight on the understanding of the stress field around discontinuities. The stress-distribution could be now associated with the crack size and shape, something that is irrelevant for circular perturbations. Interestingly, Inglis' presentation in the Institute of Naval Architecture coincided with that of Coker's [88], who presented the stress distribution around perturbations in xylonite panels using the newly developed photo-elasticity method [87]. This fortunate coincidence allowed for a direct comparison between analytical and experimental results, and the agreement among them bolstered the validity of both methods.

Despite of its great importance, Inglis' work was accepted with scepticism within the

engineering community. In the limit case of a crack with sharp corners, the equation given by Inglis led to an infinite stress at the crack-tip. This singularity condition would become in the years to come a fundamental assumption of the LEFM theory. Nevertheless, it hampered at that moment a direct comparison of the maximum stress with the material strength, which was the main interest of the material-design industry.

To circumvent the stress singularity problem, Griffith looked at the fracture propagation from a different perspective to that of his predecessors. Griffith recognised that even if the stress exceeds locally the strength of the material, this does not necessarily provoke a global failure of the solid. Therefore, he sought for the limit condition in which the applied load would lead to the unstable and catastrophic propagation of an existing crack and in 1921 he proposed a rational approach using thermodynamic principles [151]. Griffith's criterion is based on the concept that at the moment of unstable crack growth, the released elastic energy should be equal to the requisite energy for forming the new crack surfaces. This condition allowed him to find a relationship between the critical stress and the length of a sharp crack. Griffith reached this relationship considering the aforementioned mathematical work of Inglis [164]. His theoretical results were in agreement with experiments on pre-cracked glass tubes and bulbs (see [151]).

Unlike brittle materials, Griffith's approach seemed inapplicable for structural solids undergoing plastic deformations, as it provided very conservative predictions compared to their actual fracture resistance. The reason for the erroneous estimation of the fracture resistance was that the mathematical solution given by Inglis, and also Griffith, based on linear elasticity and thus could address fracture solely of perfectly-brittle materials. Nevertheless, most of the interest during and after World War II was on fracture propagation in metals, as this was the material used in the naval and aircraft industry, which had experienced by then already important failures (e.g. [390, 394]). The above limitation of Griffith's theory was overcome by Irwin [168] and Orowan [274]. The remedy was to consider in the energy balance the dissipated energy due to the plastic deformation near the crack-tip of ductile materials .

In the meanwhile of these developments, research on the mathematical description of the stress-field around sharp cracks was advancing. Westergaard developed a methodology, based on a semi-inverse method, to analyse the stresses and displacements along the plane ahead of a sharp crack [393]. Irwin further elaborated Westergaard's work and showed that the stress and displacement fields around the crack-tip could be described with a single constant, which he called stress-intensity factor [169]. The stress-intensity factor would become one of the fundamental concepts in LEFM with important use until today in numerical methods for crack propagation, discussed in Section 2.3. The most important of Irwin's contribution is the proof that the energy approach of Griffith and the strength approach are equivalent [401]. Shortly later, Irwin classified fracture in the three different well-known today families of Mode-I (in-plane opening), Mode-II (in-plane shear) and Mode-III (out-of-plane shear) [170] and associated a stress-intensity factor

with each one.

The research in the field up to the 1960s focused on the conditions that would result in the extension of a crack. In all cases, the crack was assumed to propagate along its plane. In 1963, Erdogan and Sih [119] questioned the problem of the crack propagation direction. Through a set of experiments on glass plates with straight cracks under different loading conditions, they concluded that the crack was propagating in a direction orthogonal to that of the maximum tension. The so-called *maximum circumferential stress* (or *maximum tensile/hoop stress*) criterion became one of the most important propagation criterion both in LEFM and in the later developed numerical approaches to fracture. One decade later, Sih proposed another famous propagation criterion, the *minimum strain energy density* criterion [346–348]. According to Sih, a crack will propagate in the direction in which the minimum strain energy density at a certain distance around the crack tip reaches a value which is a material characteristic. Griffith's concepts were revived once again by Nuismer in 1975 [247] and Wu in 1978 [395] with the aim this time to define the crack propagation direction. The criterion, became known as the *maximum energy release rate* criterion, and predicts that the crack-path direction is the one resulting in the maximum energy release in the solid. A common characteristic of the above criteria is that the crack direction is based on the elastic field ahead of the crack, and thus material characteristics such as the friction angle are ignored. Nevertheless, all these criteria have played an important role in the definition of the crack propagation direction in the computational era of fracture mechanics and for this reason they are detailed in Section 2.4.5.

2.3 Finite element approaches to cracking

2.3.1 Classical crack representations

The advance of digital computers and the development of the Finite Element Method (FEM) between the 1950s and 1960s offered to engineers a powerful tool for applying and testing the developed fracture theories (for a historical synopsis see Felippa [131]). During the course of the following years, a plethora of methods have been developed focusing on the simulation of propagating cracks in solids. The following of this section presents an outline of the most important of them making a categorization on the basis of the crack representation at discrete level into: the *Discrete/Discontinuous Crack Approach* and the *Smeared/Continuous Crack Approach*.

In the Discrete Crack Approach (DCA), a crack is simulated as an actual displacement discontinuity (called hereafter as a *strong discontinuity*) within a single element or along the boundary of adjacent elements (see Fig. 2.1a). Upon crack initiation, the displacement field across a crack shows a *discrete* jump w and the associated, fictitious, strain field becomes unbounded, shown in Fig. 2.1c. This is achieved through the proper enrichment

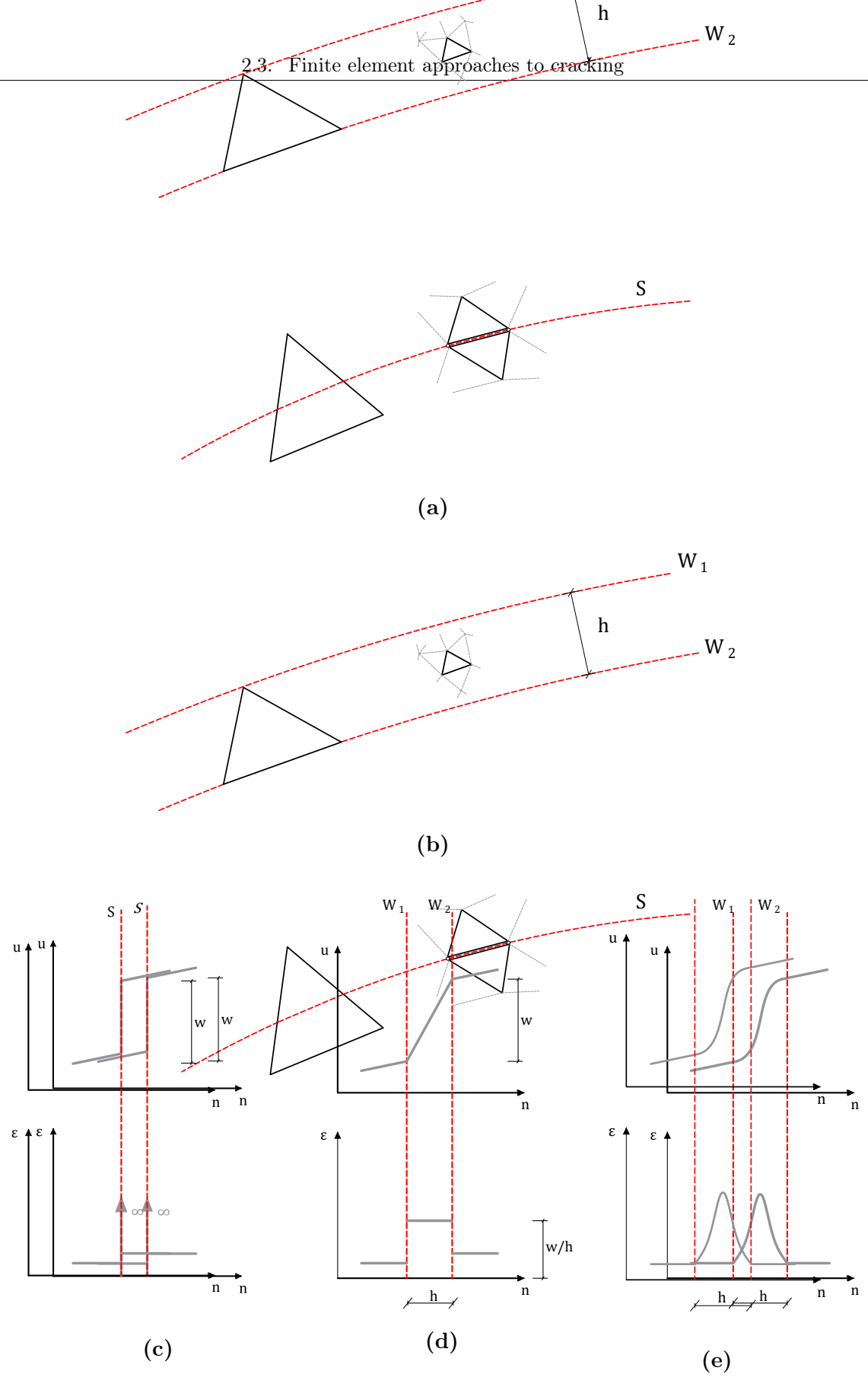

Figure 2.1 (a) Discrete and (b) and smeared crack approaches in triangular finite element meshes. Displacements and strains within the localization band of a (c) discrete crack approach, (d) local smeared crack approach and (e) regularised smeared crack approach .

of the displacement field with discontinuous functions. Alternatively, in the Smeared Crack Approach (SCA), cracks are represented in a continuous setting, and their effect (in the displacement and strains) is *smeared* over a certain region of the discretized domain, called the localization-band, with width h including one or more elements, as illustrated in Fig. 2.1b. The first case corresponds to the *local* smeared crack approaches, in which the displacement jump presents two weak discontinuities between the element within the localization-band and the adjacent ones, and the associated strains show a definite jump (Fig. 2.1d). The second case refers to the *regularised* smeared crack approaches. In this approach, the use of more elements for representing the effect of the crack results in a smoother variation of the displacement and strain fields over the selected localization band h (Fig. 2.1e). It is notable that a discrete crack can be interpreted as the limit case of a smeared one having a localization-band with vanishing width h, and conversely, a smeared crack as the regularization of a discrete crack over a certain width h (cf. Figs. 2.1c, 2.1d).

Despite their substantial differences, discrete and smeared crack approaches define the relationship between stress and deformation embarking from the same starting point; the *cohesive-zone model*. The cohesive-zone model, introduced by Barenblatt [22] for brittle fracture and Dugdale [112] for ductile one, defines the relationship between traction forces and displacements at the surface of the crack. In 1976, Hillerborg et al. [159] adopted the cohesive-zone concept in their *ficticious crack model* for representing discontinuous cracking in quasi-brittle materials within the finite element method. In this fictitious crack model, Hillerborg et al. demonstrated that the loss of cohesion in the forming crack should be directly related to the experimentally measured fracture energy of the material. The same concept was formulated later in 1983 in the context of the smeared crack approach by Bažant and Oh [28]. Today, the bibliography riddles with constitutive models based on these predecessors, which have been developed under the context of plasticity [79, 126, 351], damage [76, 123, 221, 222, 258], a combination of plasticity and damage [13, 190, 209, 397, 399] and smeared cracking [98, 321].

2.3.2 The problem of directional mesh-bias dependency

Discrete and smeared crack approaches have seen many variations since their first applications during the 1960s, the former by Clough [86] and Ngo and Skordelis [242] and the latter by Rashid [311]. The main motivation has been the wide range of engineering applications concerned with fracture simulation, varying from large-scale structures with arbitrary and multiple cracking to small-scale ones with few dominating cracks. In the first cases, numerical tools are developed offering the necessary balance between computational efficiency and correct crack localization. In the latter cases, the increasing importance of the accurate crack representation necessitates the elaboration of numerical approaches that can accurately capture the crack propagation and the associated opening/closing

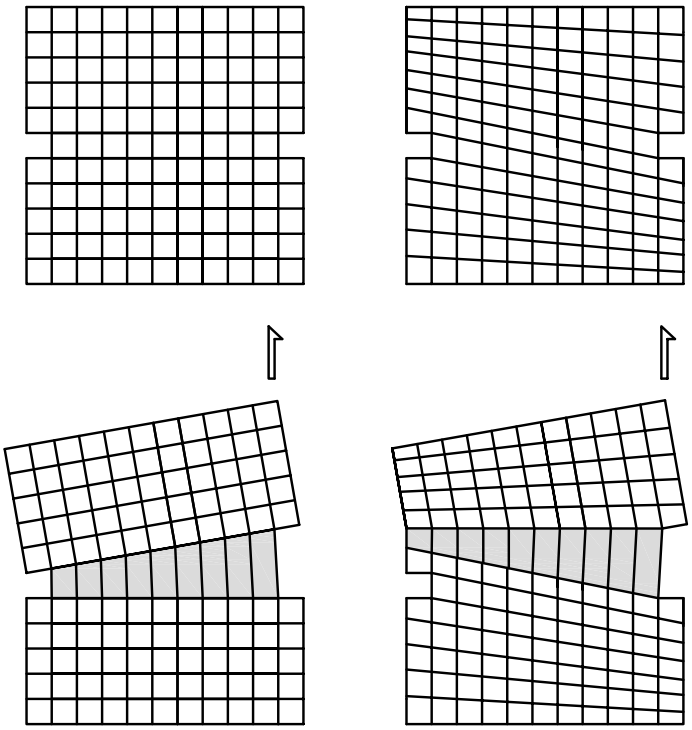

Figure 2.2 Illustration of directional mesh-bias dependency in a mode I crack opening. Top: two meshes with different orientation of the finite elements' sides. Bottom: deformation and strain localization band (in grey) induced by a traction force applied at the top right end. The dependency of the localization band to the structure of the mesh is known as directional mesh-bias dependency.

kinematics.

Another equally important driving force for the development of different numerical methods has been the unexpected numerical difficulties encountered in the simulation of cracking. The most significant of them is, probably, the observation that simulated cracks have the tendency to propagate following the orientation of the finite elements' sides (see Fig. 2.2). This phenomenon became known as *directional mesh-bias dependency* and its underlying cause has been historically a matter of controversy. The origin of this pathology has been naturally thought to be in the main ingredients of a computational failure model, being: (i) an underlying continuum theory, (ii) a constitutive model setting the linear and non-linear response of the material, and (iii) a spatial discretization procedure turning the continuum problem to a discrete one.

Early interpretations of the problem considered directional mesh-bias dependency as a result of mathematical problems associated with the continuum model (e.g. [95, 99, 241]) and the concept is as follows. Strain softening involves negative slope on the local stress-strain (or traction-displacement) relationship, usually represented by the use of a negative material tangent modulus. Due to the latter, the rate Boundary Value Problem (BVP) ceases to be well-posed and the incremental equations lose ellipticity in quasi-static problems or hyperbolicity in dynamic ones. The alteration of the elliptic/hyperbolic character of the BVP results in the loss of uniqueness of the solution, and the final chosen is the one involving the lowest number of finite elements following the continuous mesh

lines. As we will present later, efforts to recover the well-posedness of the BVP have been possible through modifications on the continuum or the constitutive model.

On a different line, mesh-bias dependency has been considered to be the consequence of the approximation error involved in the discrete representation of the continuum differential equations [69, 71, 74]. This argument is briefly described in the following. The finite element method aims to approximate the solution of a continuum problem through its discretization into finite parts, i.e. the finite elements. The discretization procedure induces approximation errors in the pre- and post-peak range of the localization process. In the linear range, the discretization error originates from the differentiation process for obtaining the strains (and equivalently the stresses) from the known displacements. In the post-peak range, the discretization error is induced by the limited capacity of standard finite elements to reproduce in an adequate manner separation modes [77, 262]. Evidently, efforts to overcome these problems have aimed on the enhancement of the finite element method accuracy in the pre- and post-localization regiments.

Finally, a third apprehension of the problem considers the constitutive model as the possible flaw to the mesh-bias dependency of the numerical solution [178]. In this sense, the mesh-bias independency of the numerical solution can be alleviated through the proper definition of the constitutive model and the failure condition.

In the following we present an overview, without claiming completeness, of discrete and smeared crack approaches aiming to the mesh independent simulation of cracking within the context of the Finite Element Method (FEM), which has been the basis of this thesis. Other methodologies outside the FEM field, such as meshfree approaches, boundary element methods or discrete element methods are important alternatives that will not be covered here. For a general review the reader is referred to Rabczuk et al. [306].

2.3.3 Discrete crack approaches

The Discrete Crack Approach (DCA) represents most closely the condition induced by an open crack, resulting to displacement discontinuities within the fractured solid. The concept is based on the long tradition of Fracture Mechanics, which, naturally, have defined the criteria for crack initiation and propagation in discrete crack approaches.

The DCA was preferred in the first endeavours for crack simulation with the finite element method [86, 242, 244]. In these applications, cracks were modelled by means of separating elements, upon satisfying a failure condition. The crack geometry was represented by the element edges and an additional set of nodes was introduced so that the interpolation across the element edges becomes discontinuous. This became known as the *nodal relaxation* technique. An alternative was the use of discrete interface elements along the crack boundaries [146, 159, 338], usually referred as the *discrete-interface approach*. The latter, as will be presented in Section 2.5, is one of the most utilized approaches for the simulation of cracking in masonry structures.

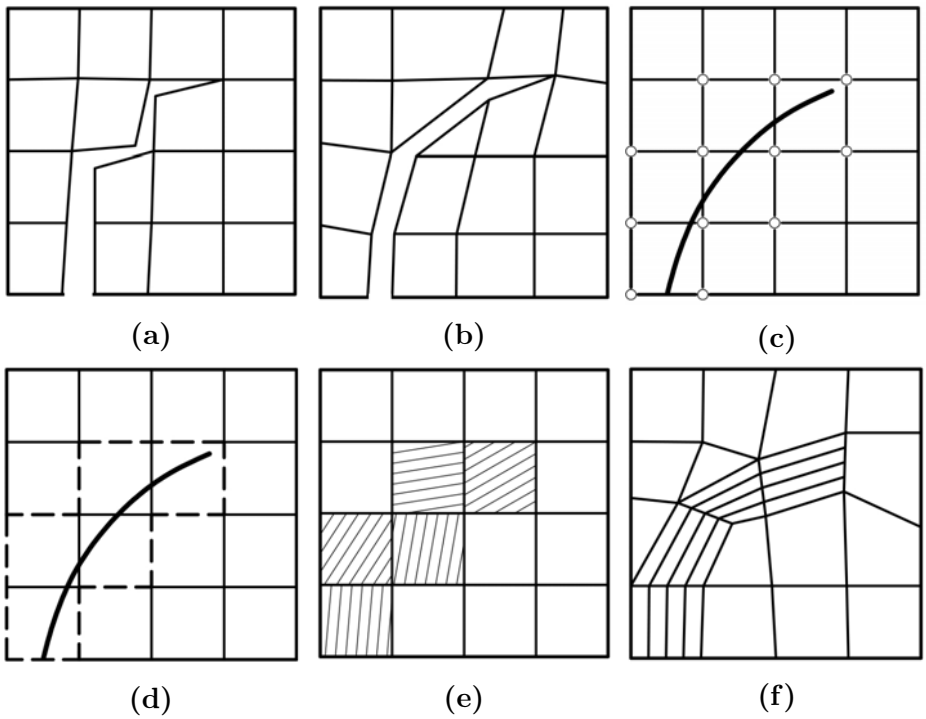

Figure 2.3 Discrete (DCA) and Smeared (SCA) crack approaches for the representation of a curved crack. (a) DCA: Nodal relaxation or introduction of cohesive interface elements at the sides of the elements, (b) DCA: Remeshing, (c) DCA: Nodal enrichment in partition of unity methods, (d) DCA-SCA: elements with embedded discontinuities. (e) SCA: local weak discontinuities, (f) Remeshing and local SCA, (Image adapted from Cervera and Chiumenti [70]).

These approaches had an obvious limitation; cracks could develop only across inter-element boundaries and therefore the crack geometry depended on the mesh orientation (Fig. 2.3a). To overcome this problem, two solutions were proposed. The first one was to use a mesh with predefined element orientations aligned with the a priori known or estimated (through preliminary analyses) crack-paths [65, 137, 320] (Fig. 2.4) or weak zones of the structure [206, 280]. The second choice was the use of a crack propagation criterion and the continuous adaptation of the mesh topology along the crack, so that the crack direction coincides with the element sides (Fig. 2.3b). The crack could be then simulated either by introducing a discrete interface [48, 167, 387] or an additional set of nodes [219, 337, 342, 371] (see Fig. 2.5). These approaches based on graphic-aided design algorithms and became known as *remeshing techniques*.

The increased computational cost due to the addition of nodes and increase of the bandedness of the stiffness matrix, as well as the intrinsic errors due to the projections of the variable fields from the old to the new mesh, made remeshing methods cumbersome for the simulation of evolving cracks. The answer to this was to simulate the effect of a crack within an element so that remeshing and nodal addition are not necessary. This concept led to the development of the *Embedded Finite Element Method (E-FEM)* in which crack discontinuities are embedded within a finite element. An early effort towards this direction can be traced in the work of Johnson and Scott [180]. Some years later, Dvorkin et al. [114] set the basis for the introduction of a strong discontinuity within a finite element. The

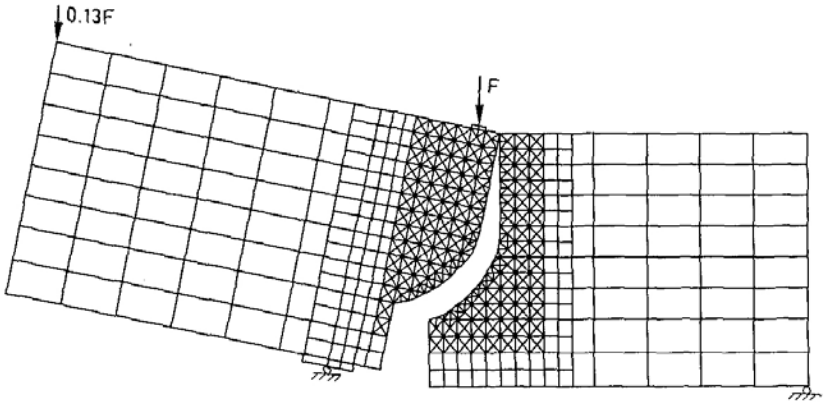

Figure 2.4 Simulation of crack propagation in a four-point shear test on a single-edge notched concrete beam, with predefined crack-path using discrete interfaces in Rots [320].

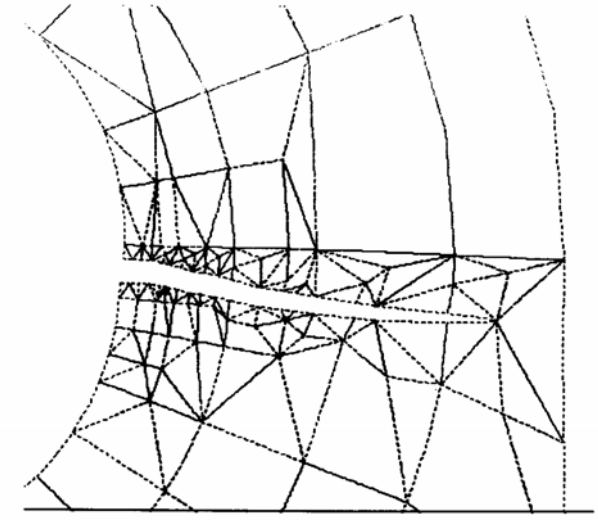

Figure 2.5 Remeshing in the simulation of a propagating crack within a lug in Saouma and Zatz [337].

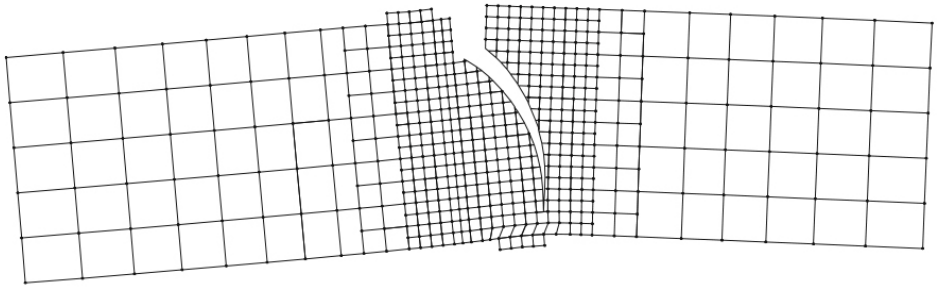

Figure 2.6 Simulation of crack propagation in a four-point shear test on a single-edge notched concrete beam with the Discrete Strong Discontinuity Approach by Dias-da-Costa et al. [105].

approach raised much interest in the years to come and different versions of elements with embedded strong discontinuities were developed (e.g. [10, 186, 189, 252, 256, 336, 354, 403]) (Fig. 2.3d). The recently proposed *Discrete Strong Discontinuity Approach* is based on the same concepts as E-FEM but, as implied by its name, represents the cracks as actual discontinuities by introducing global nodes in the elements crossed by the crack-path [105] (Fig. 2.6). Early reviews of the different variations of embedded strong discontinuity methods are given by Jirásek [176] and Oliver et al. [263].

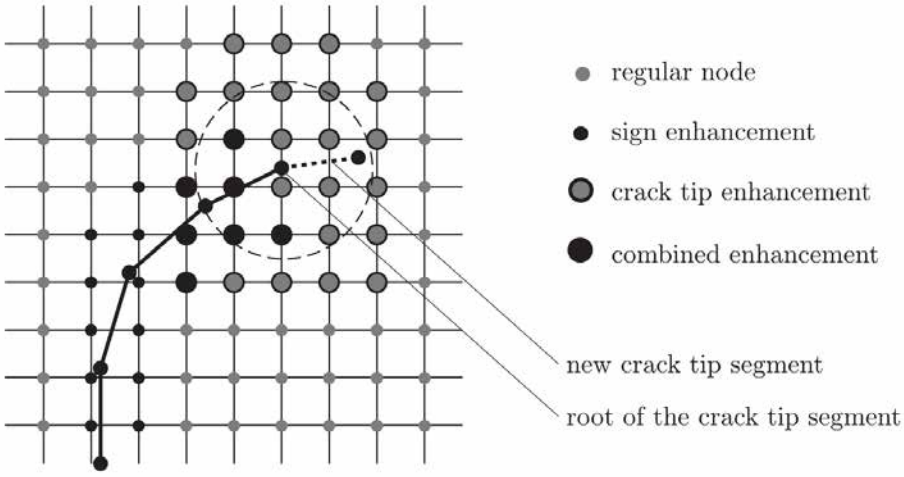

Figure 2.7 Nodal enrichment of elements crossed by a crack and surrounding the crack-tip in the eXtended Finite Element Method (X-FEM). (Image from Dumstorff and Meschke [113])

In the end of the 20th century, Belytschko et al. [30] and Möes et al. [235] proposed as an alternative to the existing approaches the *eXtended Finite Element Method (X-FEM)*. In X-FEM, the displacement discontinuities are captured through the kinematic enrichment of the nodes at elements crossed by a crack, based on the partition of unity concept [19,224] (Fig. 2.3c). Additional enrichments are applied to the nodes surrounding the crack-tip within a certain area (see Fig. 2.7), which are used for the computation of the near-tip stress intensity factors and thus the stress field. The method became very popular, since it avoids the use of remeshing algorithms, and saw many variations in the following years such as the *Hansbo method* [153] and the *Generalised Finite Element Method* [109, 366–368]. Reviews of the different versions of the X-FEM can be found in [1, 33, 136, 183, 369], while comparisons between the E-FEM and X-FEM can be found in [106, 177, 265].

A common characteristic for many of the aforementioned strong discontinuity approaches is the use of devices that define the crack propagation direction and ensure crack-path continuity, the so-called *tracking algorithms*. Through them, the potential location of the crack, and thus the elements or nodes that require the kinematic enrichment can be identified. It should be noted here that the use of tracking algorithm is, in principle, unnecessary in E-FEM [335, 336]. However, potential misalignment of the embedded discontinuities across neighbouring elements provokes spurious stress locking [176, 179, 195]. For this reason, tracking algorithms are commonly adopted by E-FEM approaches.

To overcome the necessity of crack-path continuity through tracking algorithms, Remmers et al. [312, 313] developed the *cohesive segments method*. Here, the crack is represented, as shown in Fig. 2.8, with a collection of overlapping cohesive segments that extend through three consecutive finite elements . Displacement discontinuities are captured exploiting the partition of unity method by nodal enrichment and their magnitude is governed by cohesive relationships. The *cracking node method* by Song and Belytschko [362]

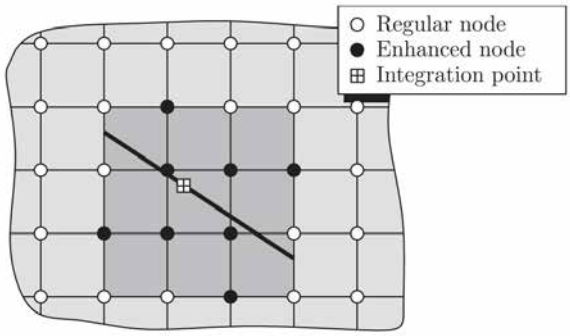

Figure 2.8 Representation of a crack increment in the cohesive segments method by Remmers et al. [312]. A crack is introduced at the integration point when the failure criterion is satisfied and extends through three elements. Nodes in black are enhanced according to the partition of unity method to represent the displacement jump (Image from Remmers et al. [313]).

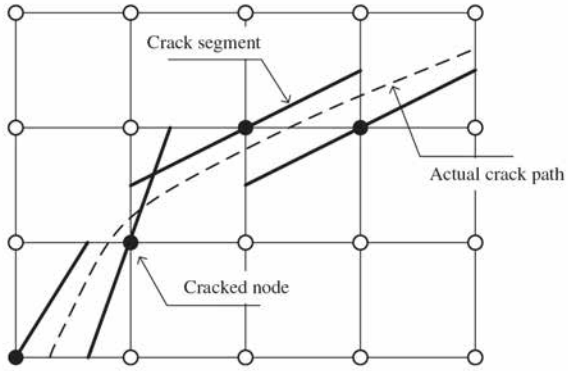

Figure 2.9 Representation of a crack in the cracking node method by Song and Belytschko [362]. Nodes in black are enhanced according to the partition of unity method to represent the displacement jump. The dashed line represents the crack-path approximation (Image from Song and Belytschko [362]).

is a similar approach in which cracks are forced to pass through nodes, instead of integration points as done in the cohesive segments method, and cross two elements (see Fig. 2.9).

During the last years, efforts to unify the design and structural analysis resulted in the development of the *isogeometric analysis*. Fracture propagation using isogeometric analysis is still at its infancy, with the first approaches exploring the potential of the method using the partition of unity concept for modelling the cracks using the discrete crack approach [144, 375].

The above enriching approaches, either at elemental or nodal level, aim to capture strong discontinuities upon crack initiation by improving the kinematics of the finite elements. In this sense, they can be interpreted as a way to limit the discretization error in the non-linear range. In addition to that, directional mesh-bias independency is improved in many of these approaches through the use of tracking algorithms, which define explicitly the location of a propagating crack within the structure.

2.3.4 Smeared crack approaches

The Smeared Crack Approach (SCA) is the numerical counterpart of continuum solid mechanics. Contrary to discrete crack approaches, the effect of a crack is represented as smeared over a part of the finite element mesh, where the stress is reducing for an increasing strain according to a defined constitutive law (see Fig. 2.3d). This smeared representation of the material degradation matches well the diffused damage in reinforced concrete structures, and unsurprisingly the first application dealt with simulation of crack-

ing in prestressed concrete vessels by Rashid [311].

In the years following Rashid's work, smeared crack approaches almost monopolized the simulation of cracking in quasi-brittle materials. The reason for this are two important practical advantages of the methodology compared to discrete crack approaches. Firstly, the fact that a crack is smeared within one or more elements poses no restriction on the orientation of the crack planes with respect to the element sides orientation. Secondly, the implementation at every conventional finite element code requires merely a subroutine with a constitutive model.

The popularity of the method dropped when it was realised that the dissipated energy was directly associated with the size of the used finite elements [198,240]. In the following years particular efforts were made to address the problem [304], leading to the crack-band width approach by Bažant and Oh [28]. According to this, the traction-displacement relationship of the cohesive-zone model is adjusted to a stress-strain relationship considering equivalence of the dissipated energy per unit area of a crack. The regularization of the stress-strain relationship is possible considering the band over which the crack is smeared, h in Figs. 2.1b, 2.1d. In *local* smeared crack approaches this band is associated to the width of a single finite element (Fig. 2.3e). Constitutive models based on the local SCA are today part of almost every commercial finite element code, and are still one of the most famous approaches used by practitioners for crack propagation analysis in large- and small-scale structures.

As soon as the problem of the mesh-size dependency was successfully overcome, the trust over local smeared discontinuities approaches was once more lessened due to the directional mesh-bias dependency. Considering the fact that well-aligned meshes, referring to meshes with the element sides aligned to the crack propagation, produced good results, the first remedy was once again remeshing algorithms [407, 408] (Fig. 2.3f).

On a different line, specific finite element formulations have been developed, within the context of local SCA, aiming to overcome the directional mesh-bias dependency through the limitation of the discretization error. To this aim, Ortiz et al. [275] and Belytschko et al. [32] proposed the enrichment of the strain field for the simulation of kinematic modes induced by a crack. This methodology was further elaborated by Simo et al. [352, 355] and resulted in the class of *Enhanced Assumed Strain (EAS)* finite elements (Fig. 2.3d). A more recent application of such an elemental enrichment in a smeared cracking context is the *mesh-corrected orthotropic damage model* [67, 68], being the weak counterpart of the previously presented E-FEM.

The beneficial use of the tracking algorithms in discrete crack approaches could not be unnoticed, and during the last decade tracking algorithms have been used as an auxiliary device aiming to improve the directional mesh-bias independency of local smeared crack approaches. This strategy was introduced in a smeared cracking context by Cervera and Chiumenti [69, 70] and their aim was to define the location of cracks and restrict their evolution within a single row of finite elements (Fig. 2.10). Different formulations of

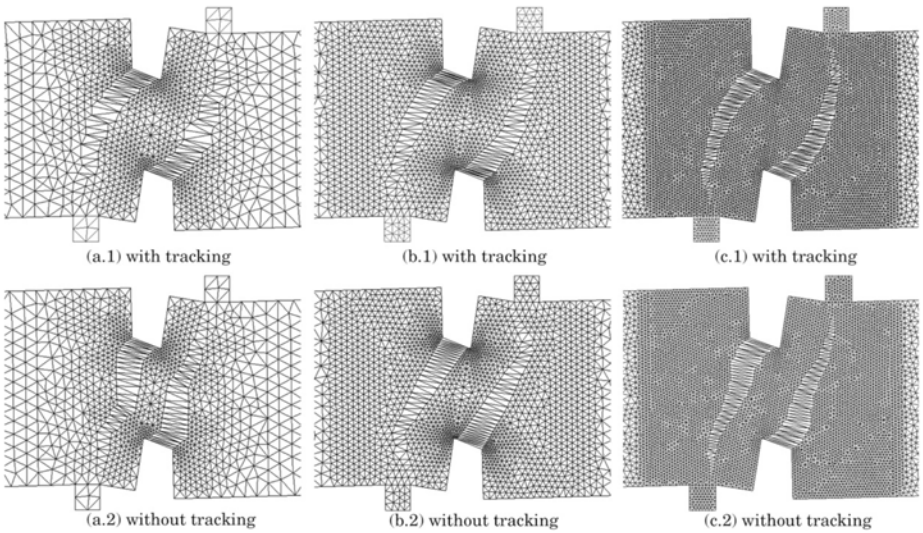

Figure 2.10 Crack propagation analysis of a double-edge notched concrete specimen under four-point bending using meshes with increasing refinement from left to right. Analysis with an isotropic local damage model and a tracking algorithm (top) and without a tracking algorithm (bottom). (Image from Cervera and Chiumenti [70]).

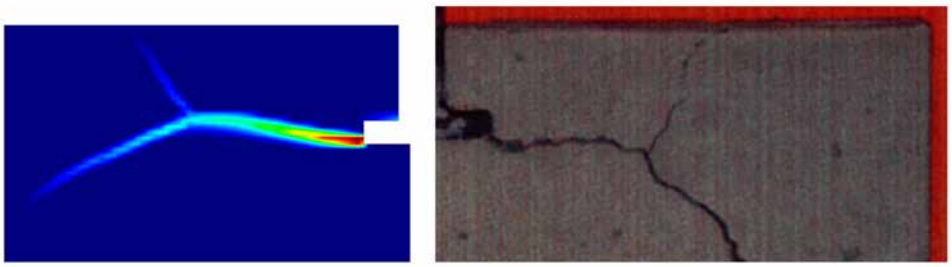

Figure 2.11 Comparison between numerically obtained crack pattern using a mixed strain/displacement formulation by Benedetti et al. [37] and the experimental result of a pull-out test on a concrete specimen. (Image from Benedetti et al. [37]).

tracking algorithms within smeared crack approaches have been presented in the last years by Cervera et al. [77], Slobbe et al. [360] and Burnett [56].

The *mixed methods*, introduced in the mid 1960s [133], offer another possibility for reducing the discretization error. The approach aims to consider apart from the nodal displacements additional variables as the primary unknowns of the boundary value problem under question. Despite their long use in computational fluid dynamics, due to their good performance in incompressible situations, mixed formulations were used only during the last decade of the 20th century in strain localization problems by Zienkiewicz et al. [408] and Pastor et al. [286, 287]. In the last years, several mixed methods have been developed and applied to strain localization problems, including mixed pressure-displacement [66,71,82,83,334], stress-displacement [73,74] and strain-displacement [35–37,72,73] finite elements (Fig. 2.11).

2.3.5 Regularized smeared crack approaches

In the 1990s, academic effort focused on the development of new formulations that aimed to recover the well-possessedness of the boundary value problem. The fruit of these efforts have been the so-called *regularised* smeared crack approaches, including *micropolar*, *non-local*, *gradient-enhanced* and *phase-field* models. In *micro-polar* or *Cosserat* models the underlying continuum description is enriched by adding rotational degrees-of-freedom to the conventional translational degrees-of-freedom [95, 363]. In *non-local* models the local stress does not depend on the local strain but on an averaged strain computed over a defined area [26, 27]. A similar approach is followed in *gradient-enhanced* models, in which non-locality is considered by introducing higher order deformation gradients in the constitutive relationship [97, 237, 381]. For a comparison between non-local and gradient-enhanced models see Peerlings et al. [290] and non-local models and X-FEM in Bobiński and Tejchman [47]. In the last years, Griffith's variational approach to fracture has been revived through the *phase-field* models [51,52,134,228] (Fig. 2.12) (for a review see Ambati et al. [7]). Despite their different origin, de Borst and Verhoosel [100] have presented recently the close mathematical relationship between gradient-enhanced and phase-field models. A common standpoint of the above models is the use of an internal length (different than the mesh size), which acts as a localization limiter, as well as the use of highly refined meshes within this length (see for instance [100,154]) to capture the material degradation [262]. Finally, strain-rate dependent *viscous-regularised* models [96, 241] have been considered as an alternative solution that recovers the well-posedness of the boundary value problem through the addition of viscous effects in the constitutive relationship.

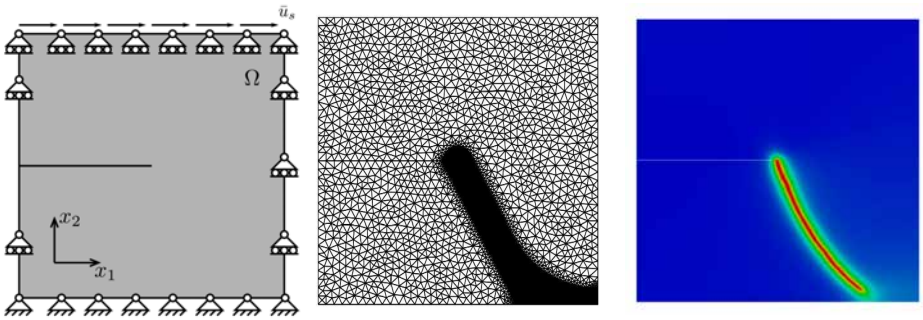

Figure 2.12 (a) Single edge notched pure shear test setup, (b) Used mesh, and (c) Phase-field simulation by de Borst and Verhoosel [100]. (Collection of images from de Borst and Verhoosel [100]).

2.3.6 Hybrid crack approaches

Apart from representing a crack exclusively with either a discrete or a smeared crack approach, there is the possibility also to combine them as shown in Fig. 2.13. In these hybrid strategies initial micro-cracking is simulated with the use of a smeared crack ap-

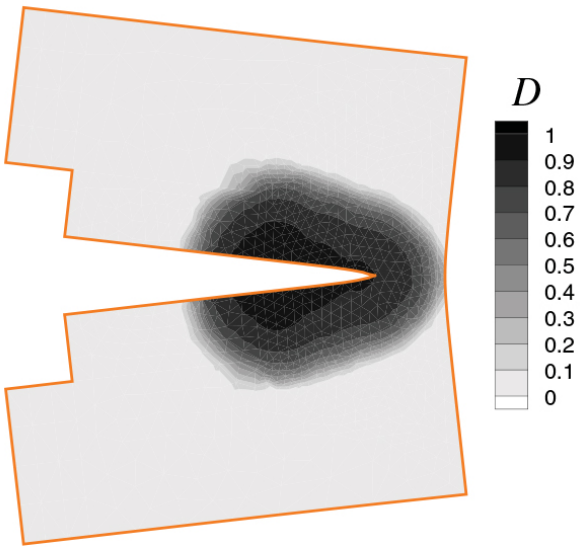

Figure 2.13 Representation of a crack in a wedge splitting test combing a non-local damage model with X-FEM by Comi et al. [91]. D represents the value of the non-local damage variable.

proach. Then, at a second stage, in which material degradation has increased to a defined level, the crack formation is simulated through the introduction of a strong discontinuity.

In the majority of these hybrid crack approaches, smeared cracking is simulated with a different kind of a regularised SCA model such as non-local [91, 179], viscous-regularised [392], or gradient-enhanced [356]. The use of a strong discontinuity at a later stage of damage evolution allows for the localized representation of cracking, which otherwise due to their non-local definition is smeared over a defined, and usually highly refined, region of the mesh (Fig. 2.13). An alternative approach to the use of regularised models for the smeared crack representation was adopted by Belytschko et al. [31], in which a transition between a local damage model and an X-FEM with cohesive enrichment is applied for the simulation of dynamic cracks. Aiming to a better estimation of the localization field prior to the introduction of a strong discontinuity Oliver et al. [259] and Lloberas-Valls et al. [197] have recently proposed the use of mixed strain-displacement and enhanced assumed strains formulations respectively.

2.4 Tracking algorithms

Tracking algorithms are an important part of many finite element approaches to cracking. Their role is to identify the crack propagation direction, and designate the consolidated and extended crack-path within the discretized domain during the numerical simulation. Then, according to the selected crack representation, a smeared or discrete crack approach is used at the elements within the crack-path to simulate the effect of the crack in the material, while the rest of the elements outside the crack are usually prevented from failure.

According to Cervera et al. [77] tracking algorithms benefit the numerical solution in three ways. First, they aid to the identification of the expected solution by minimizing the number of the potential ones. This is done through the use of a crack propagation

criterion which defines the crack direction. Secondly, they result in a more realistic crack representation, especially in the case of mixed-mode problems with curved cracks. Finally, they minimize or limit the energy dissipation outside of the crack band. The significance of the latter is particularly high since the stress-strain law in local smeared crack approaches, or traction-displacement law in discrete ones, is usually regularised considering that only one crack propagates within a single row of finite elements.

The definition of the crack-path becomes very important in discrete crack approaches for two more reasons. Firstly, it avoids numerical instability, since the kinematic enrichment is applied to only a narrow band within the mesh where the crack is expected to develop. Secondly, it guarantees the crack-path continuity, improving in this way the robustness of the method. As discussed, crack-path continuity of the introduced strong discontinuities in DCA is important to ensure compatibility between the deformation modes of adjacent elements, which if not guaranteed may result in spurious stress locking [127, 179, 333]. The above justify the long tradition of tracking algorithms in discrete crack approaches.

The successful applications of tracking algorithms in discrete crack approaches pointed on their potential benefits in a smeared cracking context, an approach which was introduced in [69, 70]. In SCA, tracking algorithms identify the elements crossed by the crack-path allowing them to damage according to the selected constitutive law, while prevents the ones outside it to fail.

The following of this section aims to outline some of the most used tracking algorithms in the available literature. First, a categorization of tracking algorithms is performed in terms of the information necessary for the definition and storage of the crack-path. According to this, four categories are defined and presented including: (i) local, (ii) global, (ii) partial domain tracking algorithms and (iv) tracking algorithms based on an underlying damage-related field. Following that, the crack propagation criteria, which can be used for most of the tracking algorithms independently of their category, are summarized.

2.4.1 Local algorithms

Local tracking algorithms identify the location of a crack within the mesh in an element by element manner. The crack propagation direction is computed locally, using information available at element-level or within a restricted area surrounding it. The new crack segment within an element can then be defined considering this direction and the locus of adjacent crack edges (if any) in neighbouring elements. The same strategy is followed for each crack that may exist in the analysed structure, starting from the first element of the crack (referred hereafter as *crack-root*) or the last element at the crack-front (referred as *crack-tip* in two-dimensions or *crack-face* in three-dimensions).

The above general procedure followed by a local tracking algorithm for constructing the crack-path is illustrated in Fig. 2.14. The necessary ingredients are the crack propagation

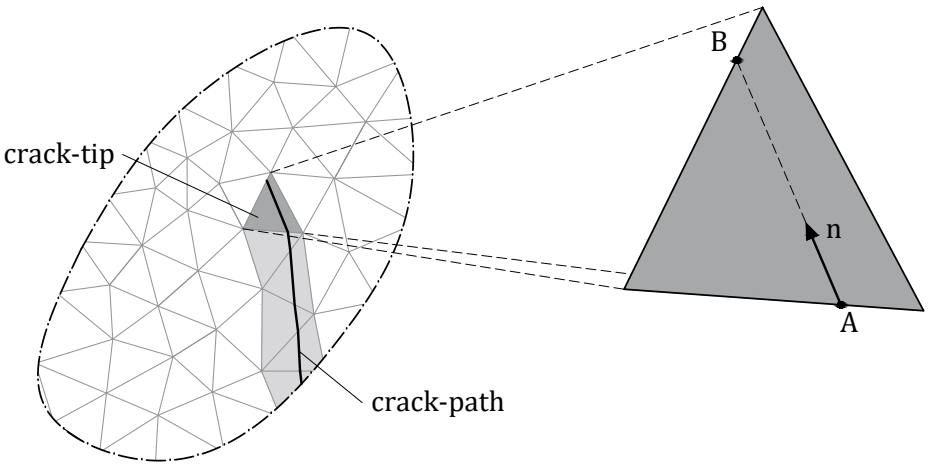

Figure 2.14 Crack propagation in a part of the mesh using local tracking algorithms.

direction **n** and the crack-entry coordinates. Starting from the crack-entry point (Point A in Fig. 2.14), the exit point of the crack at the crack-tip element is easily identified as the intersection between the extension of the vector **n** and one of the element's sides (Point B in Fig. 2.14). The shared side with one of the neighbouring elements and the intersection point define the next crack-tip element and the locus of its crack-entry point, respectively.

Owing to their quite simple and robust strategy, local tracking algorithms have been used in various discrete and smeared crack approaches. Their implementation is likewise straightforward, needing a strategy for the calculation of the crack propagation direction, as in all tracking algorithms, and a side-connectivity array indicating the elements sharing side with a given one. The latter can be easily constructed at the beginning of the analysis and stored for the rest of it (provided that no remeshing is used). The propagation direction, on the other hand, is continuously updated at the crack-tip element of each crack.

Despite the intrinsic simplicity of the above procedure, the literature riddles with diverse formulations of local tracking algorithms. The reason for this lies on their strong dependence on the finite element technology used. As it will be shown in the following, the crack propagation path within an element may vary depending to the interpolation strategy used, while the procedure followed for identifying the crack-exit/entry points depends on the shape of the used finite elements (triangles, quadrilaterals, tetrahedra, hexahedra etc.).

Local tracking algorithms were the first used for the simulation of propagating cracks in finite element applications. Their role was to define the direction and length of a new crack segment, which was then simulated, as we saw, through remeshing and nodal separation techniques [165, 166, 337] or later with the introduction of cohesive interface elements [167].

A common characteristic of local tracking algorithms is the construction of a piece-wise

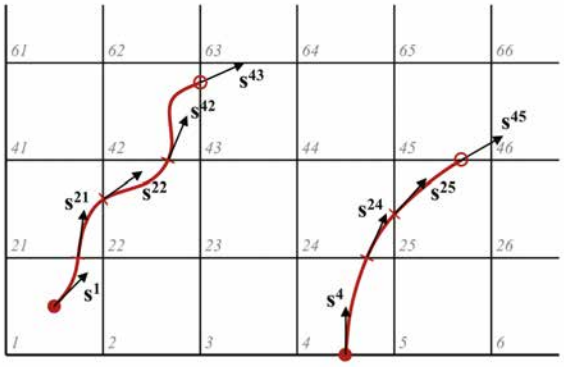

Figure 2.15 C^1 continuous crack-path proposed by Slobbe et al. [360]. S^i denotes the crack propagation direction entry from the preceding element i.

continuous crack-path (see Fig. 2.14). This intrinsic crack-path continuity of the method is a key feature for the limitation of stress locking in approaches with embedded strong discontinuities. In that sense, local tracking algorithms blend very well with E-FEM and numerous implementations exist in the literature [6, 105, 196, 215, 254, 257, 398]. The first applications of X-FEM employed, likewise, local tracking algorithms for recognizing the crack-path and enriching accordingly the nodes of the elements crossed by it [30, 235]. Note that in X-FEM a crack-edge (i.e. the last point of the crack-tip or surface of a crack front) can exist within the element, contrary to E-FEM in which lies always on the element side.

Complementary to their long tradition in discrete crack approaches, the use of local tracking algorithms in a smeared cracking context was proposed relatively recently by Cervera and co-workers [77, 84, 85, 292]. In those applications, material degradation was simulated in the elements within the crack-path through the use of local continuum damage mechanics models, while the rest maintained a linear elastic stress-strain behaviour. Pelá et al. [294, 296] extended this tracking algorithm for the simulation of cracking in orthotropic materials such masonry and wood.

In most local tracking algorithms, the crack propagation is updated at each new element and kept fixed during its propagation through it (or a part of it). This choice naturally gives a C^0 continuous crack-path constructed by linear piecewise segments. Slobbe et al. [359, 360] have recently proposed a local tracking algorithm in a SCA context, which can alternatively provide C^1 crack continuity among elements (see Fig. 2.15). This is achieved by constructing the crack propagation field within a crack-tip element considering the propagation directions at its integration points and the crack-entry direction from the previous element. The method needs the assignment of crack propagation directions at the corner nodes through a weighted linear least squares approximation using the known propagation directions at the crack-entry point and the integration points. Then the crack-path field can be constructed at any location within the element using its shape functions. The reconstruction of the crack-path at any moment during the analysis requires the storage of the propagation directions at the integration points as soon as an element is considered a consolidated part of the crack.

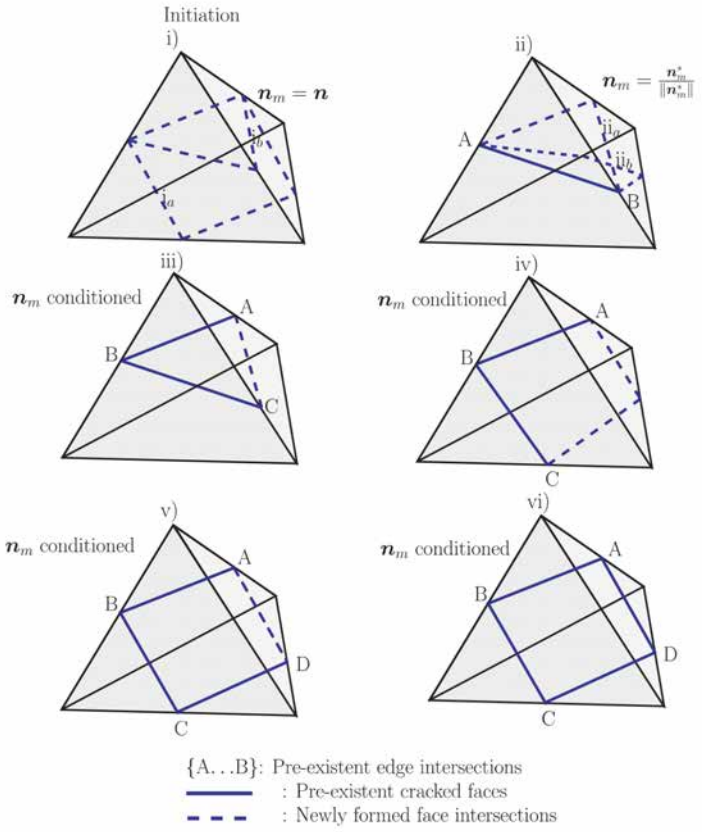

Figure 2.16 Local tracking algorithm for the definition of a new crack surface in Areias and Belytschko [9]. $\boldsymbol{n}_m$ denotes the defined crack propagation direction according to the propagation criterion and $\boldsymbol{n}_m$ the modified one computed respecting pre-existing crack faces in adjacent elements. (Image from Areias and Belytschko [9]).

Due to their simplicity and numerical efficiency, local tracking algorithms have been a preferable choice in three-dimensional (3D) problems. In the case of planar cracks their extension to 3D is straightforward (see [226]). Difficulties, however, may arise for representing the crack surface in non-planar cracks, where an adequate strategy needs to ensure crack-path continuity. To this aim, several approaches can be distinguished in the available literature. In Areias and Belytschko [9], the new crack surface in the crack-tip element is defined considering a modified crack propagation direction. This depends on the local crack direction defined at element level and the pre-existing crack faces (i.e. the intersecting facets of neighbouring cracks with the current element) in neighbouring elements (see Fig. 2.16). A drawback of this approach is that it may be impossible to construct a new crack plane in the case that the crack faces do not fall within the same plane on the crack-tip element [172]. Gasser and Holzapfel proposed two alternatives to overcome the above problem by relaxing the requirement of a crack-path continuity among the different crack faces. In their first proposal [142], a new crack surface can be uniquely defined by its normal vector and a single point located at the crack. The first is computed considering the underlying stress field, while the definition of the latter depends on the adjacent crack-edges. The authors, however, observed that in some cases

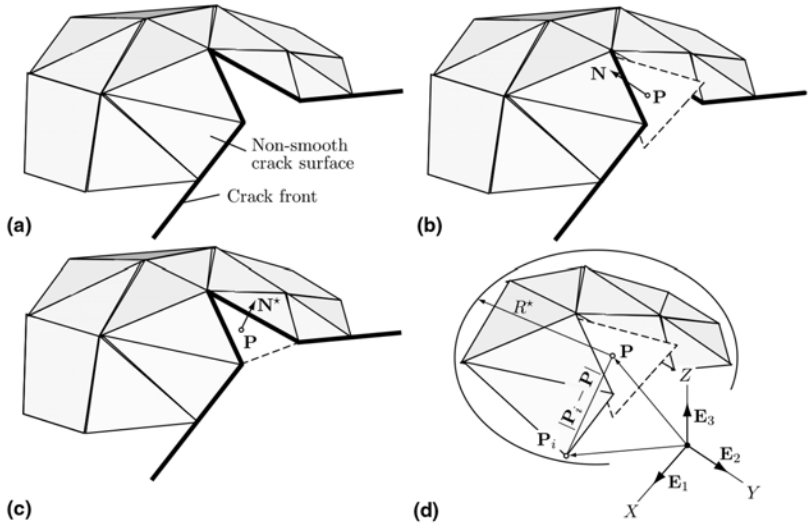

Figure 2.17 Local tracking algorithm for the definition of a new crack surface in Gasser and Holzapfel [9]. $\boldsymbol{N}$ denotes the defined crack propagation direction according to the propagation criterion, $\boldsymbol{N}^\star$ the modified one and $\boldsymbol{P}$ a point used for the definition of the new crack surface. (a) Existing non-smooth crack and crack surface, (b) prediction of the new crack surface using $\boldsymbol{N}$ and $\boldsymbol{P}$, (c) correction of the new crack surface using $\boldsymbol{N}^\star$ and $\boldsymbol{P}$, (d) patch of elements used for the definition of $\boldsymbol{N}^\star$. (Image from Gasser and Holzapfel [143]).

this approach may result in very irregular crack surfaces which may lead to (non-physical) crack bifurcations [143]. As a solution to this shortcoming, they proposed the addition of a corrector phase that follows the first prediction of the crack surface with the above procedure [143]. The corrector phase is responsible for adjusting the predicted crack plane to fit the neighbouring cracks surfaces such that patch-wise linear or quadratic crack representations are possible (see Fig. 2.17). This tracking algorithm is more robust compared to what Areias and Belytschko [9] proposed, but fails to give smooth crack-paths. Jäger et al. [172] present a comparison between the tracking algorithm proposed by Areias and Belytschko [9] and the one by Gasser and Holzapfel [143].

2.4.2 Global algorithms

Contrary to local methods, global tracking algorithms compute simultaneously all the potential crack-paths at each step of the analysis. This is achieved through the solution of a linear boundary value problem involving the whole analysed domain. The approach was proposed by Oliver and co-workers [260, 264] and since then has been applied in various contexts for the propagation of two-dimensional (2D) and three-dimensional (3D) cracks.

The basic idea of the global tracking algorithm is to construct a scalar function θ whose isolines represent the crack propagation directions within the analysed structure. The procedure is presented in the following keeping the notation used in [260] to facilitate the comparison with Fig. 2.18.

The scalar function θ, used for the definition of the potential crack-paths, is computed

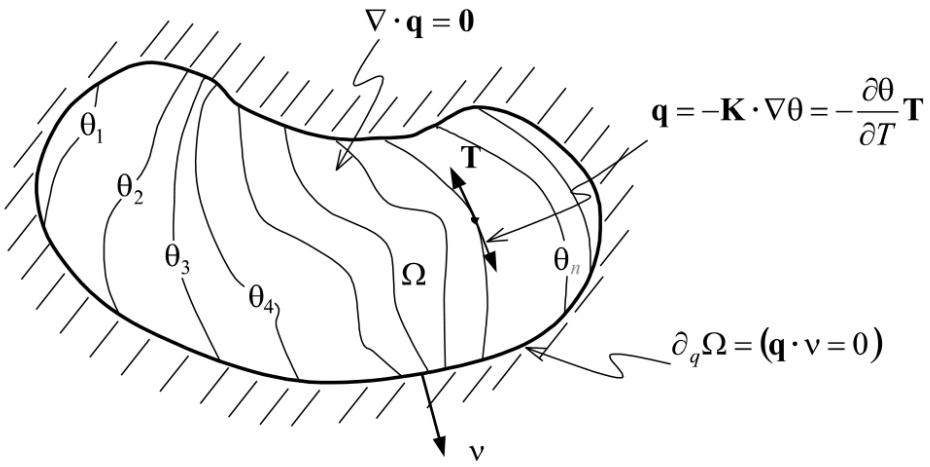

Figure 2.18 The heat conduction problem used for the computation of the thermal isolines representing potential crack-paths in the global tracking algorithm proposed by Oliver and Huespe [260] (Image from Oliver et al. [260]).

through the solution of an anisotropic heat-conduction-like boundary value problem which can be defined as*

$$\nabla \cdot \mathbf{q} = 0 \quad \text{in } \Omega \tag{2.1a}$$

$$\mathbf{q} = -\mathbf{K} \cdot \nabla\theta = -\mathbf{T}\frac{\partial\theta}{\partial \mathrm{T}} - \left[\mathbf{S}\frac{\partial\theta}{\partial \mathrm{S}}\right] \quad \text{in } \Omega \tag{2.1b}$$

$$\mathbf{q} \cdot \mathbf{v} = (\mathbf{v} \cdot \mathbf{T})\frac{\partial\theta}{\partial \mathrm{T}} - \left[(\mathbf{v} \cdot \mathbf{S})\frac{\partial\theta}{\partial \mathrm{S}}\right] \quad \text{on } \partial\Omega. \tag{2.1c}$$

In the above equations $\mathbf{q}$ is the heat flux, $\mathbf{v}$ is the outnormal to the boundary $\partial\Omega$, $\mathbf{S}$ and $\mathbf{T}$ are arbitrary unit vectors having the direction of the failure plane. $\mathbf{K}$ is an anisotropic conductivity-like tensor defined as

$$\mathbf{K} = \mathbf{T} \otimes \mathbf{T} + [\mathbf{S} \otimes \mathbf{S}] + \varepsilon\,\mathbf{I}. \tag{2.2}$$

where $\mathbf{I}$ represents the unit tensor and ε is a small perturbation parameter introduced to avoid the singularity of $\mathbf{K}$, the effect of which was studied in [29]. The parts within the brackets in the above equations are necessary for the use of the tracking algorithm in 3D problems and irrelevant for 2D ones.

Adopting a finite element discretization, the above boundary value problem is solved through a system of linear algebraic equations

$$[\mathbf{K}]\,\{\boldsymbol{\theta}\} = \{\mathbf{0}\} \tag{2.3}$$

*Equations (2.1a, (2.2) (2.3)) adopt the same notation introduced in Oliver et al. [260] for facilitating the interpretation of the different quantities in correspondence to Fig. 2.18. Therefore, for these equations, the global notation used throughout this thesis does not hold.

with [**K**] being the stiffness matrix of the heat conduction-like finite element problem and $\{\boldsymbol{\theta}\}$ the vector of temperature-like nodal unknowns [264]. The solution of the problem needs the definition of the **T** and **S** vectors. If a vector **N** represents the crack propagation direction, computed according to the selected propagation criterion, the **T** and **S** are selected as orthogonal to **N**. Finally, in order to provide a non-uniform field for θ, two arbitrary values for θ need to be prescribed at two nodes. Considering a different value for θ the location of these nodes becomes irrelevant.

As soon as the failure condition is reached at an element i its corresponding value $\theta_i = \theta_0$ is computed. The crack-path can then be identified by constructing the isoline corresponding to this value θ_i, starting from the centroid of the crack root element. Fracture is simulated by applying the chosen crack representation approach at the elements crossed by the θ_i isoline. In the original approach by Oliver et al. [260, 264] this was done by introducing strong discontinuities. Later, Huespe et al. [162, 163] followed the same approach for the simulation of ductile failure, whereas Dumstorff and Meschke [113] used the global algorithm in the context of X-FEM. On a different line, Cervera and Chiumenti [69,70] used the algorithm in a smeared cracking context, and cracks were simulated through the use of an isotropic continuum damage model in the elements crossed by the crack-path.

Recently, Riccardi et al. [315] have further elaborated the global tracking algorithm by proposing an alternative mathematical formulation for the construction of the θ scalar field. The motivation in their work is the eradication of the user-defined perturbation parameter used for the definition of **K** in Eq. (2.2). The first results of their approach have shown to increase the stability of the global tracking algorithm, albeit the precision seems to reduce for coarse meshes [315] compared to the original approach. In the same work, the authors propose the update of the crack-root at each numerical step and to construct the isoline of an existing crack considering the θ value of the crack-tip. This approach seems to alleviate problems associated with the loss of crack-path continuity.

Global tracking algorithms are in general more demanding from an algorithmic point of view [172] and more code invasive compared to local ones [77, 259]. This is because the tangent field to the crack $\boldsymbol{T}$ (and $\boldsymbol{S}$ in 3D) should be computed all over the domain, even at locations away from cracks and the global problem needs to be solved for each step. An additional limitation rises from their inability to handle merging, intersecting or branching cracks. On the contrary, one important advantage, evidenced from Eqs. (2.3) is the straightforward extension to 3D problems as shown in Chaves [78] and Jäger et al. [173]. In addition to that, there is no strong dependence on the finite element technology, as it is in local tracking algorithms.

2.4.3 Partial-domain algorithms

Partial-domain tracking algorithms are a compromise between local and global ones. In these approaches, the crack location is tracked through the solution of a boundary value problem at each numerical step within a sub-domain rather than in the whole structure.

The most famous partial-domain tracking algorithm is the level set method. Originally, it was proposed by Osher and Sethian [276] for the representation of the motion of interfaces as the zero of a function, called the level set function. Much later than this first application, Belytschko et al. [34] and Stolarska et al. [365] introduced the use of level set methods for the crack representation within the context of X-FEM.

A level set function is any continuous function dividing a domain into two parts and taking negative values in one, and positive in the other. The zero level set of this function defines the location of the interface of interest. Contrary to the original approach [276, 341], which focused on the motion of closed interfaces, cracks are open ones. Consequently, their representation necessitates one level set for representing the signed distance to the crack surface, and an additional one for each crack-tip representing the signed distance from it (see Fig. 2.19).

The necessary components for the tracking of cracks with the level set method are: (i) the level set functions for each crack, (ii) an update algorithm for these level set functions, (iii) the crack propagation direction, which normally is based on local criteria and the computation of the stress intensity factors and (iv) the crack propagation velocity or crack increment size which is used for the extension of the crack during one step and can be defined according to mechanical laws (e.g. [34, 90, 149]) or explicitly by the user (e.g. [364, 382]).

At the beginning of the numerical analysis, a crack is introduced and a function ψ is

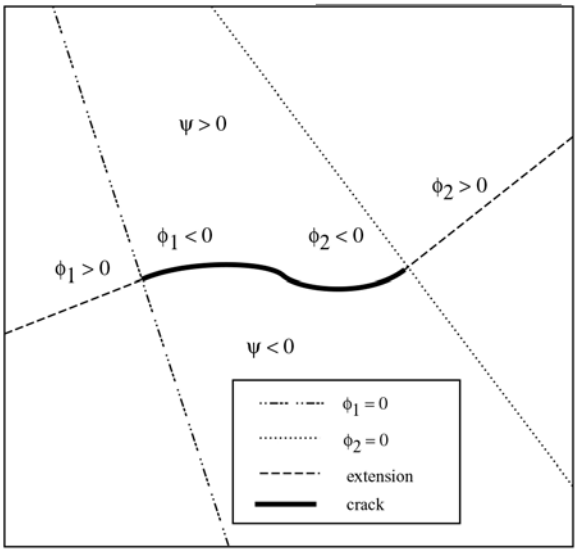

Figure 2.19 Level set functions for the representation of a crack in Stolarska et al. [365]. ψ is the signed distance function from the crack and $\varphi_{1,2}$ are the signed distances from the normal to each crack-tip.(Image from Stolarska et al. [365].

constructed using the signed distance function from the crack

$$\psi(\boldsymbol{x}, t=0) = \pm \min ||\boldsymbol{x} - \boldsymbol{x}_{\gamma_0}|| \tag{2.4}$$

while the additional functions for each crack-tip $\varphi_{1,2}$ are defined as

$$\varphi_i(\boldsymbol{x}, t=0) = (\boldsymbol{x} - \boldsymbol{x}_{\gamma_0}) \cdot \hat{\boldsymbol{t}}_i. \tag{2.5}$$

In the above equations, $\boldsymbol{x}$ represents the coordinates of a point within the structure, $\boldsymbol{x}_{\gamma_0}$ are the coordinates of a point belonging to the initially defined crack γ_0 and $\hat{\boldsymbol{t}}_i$ is a unit vector tangent to the crack at its tip i. The sign of the minimum distance in Eq. (2.4) depends on which side of the interface a point $\boldsymbol{x}$ is located. As can be seen in Fig. 2.19 with these definitions the crack loci can be defined as

$$\gamma_t = \{\boldsymbol{x} : \psi(\boldsymbol{x}, t) = 0 \cap \varphi(\boldsymbol{x}, t) \leq 0)\} \tag{2.6}$$

where

$$\varphi(\boldsymbol{x}, t) = \max_i(\varphi_i). \tag{2.7}$$

In the level set method, the crack is represented in an implicit way. The location of the crack is identified through interpolation of the level set values, which are stored at the nodes, using the same shape functions of the displacements. Hence, the crack representation depends on the interpolation strategy of the chosen finite elements. Aiming to reduce the high computational cost and storage requirements, a partial domain around the crack is usually considered for the computation, update and storage of the level sets at the nodes of elements within it [365].

Having defined the initial level set functions for each crack, its location and propagation is monitored with the update of its level sets during the numerical analysis. To this end, several proposals exist to update the level set functions, which can be defined through geometrical evolutions and non-differential equations [89, 111, 364, 365, 382], fast marching algorithms [343, 370], partial differential equations [149] or hybrid approaches based on both geometrical and differential equation approaches [90, 111]. Fries and Baydoun [135] proposed an alternative approach for the crack extension. In their work, cracks are represented by level set functions but the crack extension is made with the use of a local tracking procedure starting from the crack-tip. When the crack-extension is identified, then the level sets are updated to include the new crack-path. Similar approaches have been recently presented by Holl et al. [161] and Sadeghirad et al. [325].

The proper update of the level set functions is very important for the accuracy of the numerical solution in X-FEM. This is due to the variable roles that level sets have within X-FEM methods, the most important of which is the proper identification of the crack

propagation and, thus, the nodal enrichment of the elements that are crossed by the crack, as well as those surrounding the crack-tip. Additionally, level sets are important for the calculation of auxiliary variables, such as the near-tip displacement and stress field and the stress-intensity factors, which in turn define the propagation direction. Duflot [111] gives an excellent review of different level set update methods and their role within X-FEM. The generality of some of the update schemes as well of the definitions for the level set functions allows their almost straightforward extension to 3D problems (e.g. [49, 89, 236, 288]).

The level set methods have been used almost exclusively by X-FEM applications. This is due to the fact that the propagation depends heavily on the crack-tip stresses, which can be accurately computed with the use of the enrichment functions. Contrariwise, in E-FEM methods, the stresses can be far from accurate in the crack-tip because a crack propagates from one element to the other [403]. For this reason, level set methods cannot be applied in E-FEM without important elaboration at the crack-tip stress field [403], with recent developments in this direction presented in [152].

Another partial-domain tracking algorithm can be considered the one presented by Feist and Hofstetter [127, 128]. This approach is based on the global tracking algorithm presented in the previous Section 2.4.2, with the main difference that the scalar field θ is constructed only within a partial domain of the whole structure. This domain is occupied by elements already or potentially crossed by the crack. The approach is, similarly to the global tracking algorithm, easily extended to 3D cases [129], see also [11]. A comparison of the partial-domain and the global tracking algorithms is available in [127].

2.4.4 Algorithms based on an underlying damage-related field

In the last years a new class of tracking algorithms has emerged, in which the crack-path is identified considering an underlying scalar field representing material degradation in a smeared manner. These tracking algorithms are used in hybrid discontinuity approaches, presented in Section 2.3.6, and their aim is to monitor the evolution of the material degradation modelled with a smeared crack approach, and define the location where a strong discontinuity will be inserted to simulate the localized jump in the displacements. Apparently, the use of tracking algorithms within these approaches aims to enhance the localization process and the correct representation of the crack kinematics rather than the enhancement of the mesh-objectivity, which was merely the purpose of the algorithms presented in the previous sections. The latter is achieved, as discussed in Section 2.3.6, through the use of alternative smeared crack approaches such as regularised models, mixed formulations or finite elements with embedded weak discontinuities.

One of the first tracking algorithms in this category can be found in the work of Comi et al. [91], where a non-local damage model is used as the underlying field for the tracking of the crack. Here, the crack-path passes through the element that has the maximum damage within the crack-band. For curved cracks, where the crack direction is

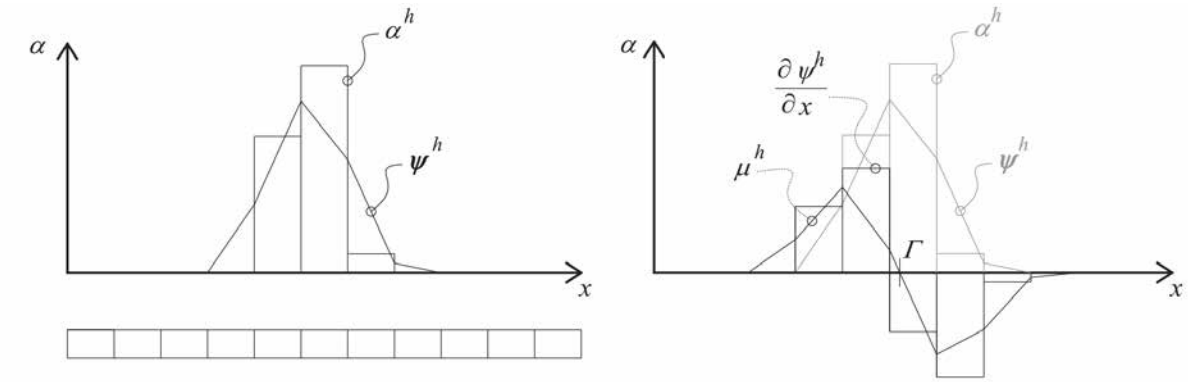

Figure 2.20 One dimensional illustration of the strain localization field α^h and its directional derivative ψ^h (left) and the crack-path-field Γ as the zero level of μ^h, which is the continuous approximation of ψ^h (right) (Image from Dias et al. [104]).

not trivial to define as in straight ones, the crack-path is recovered thought the best-fitting of the damage at Gauss points with a complete fourth-order polynomial. Then, the crack propagation direction for the next discontinuous element is considered as orthogonal to the direction of maximum curvature of the interpolating polynomial at the crack-tip.

The recently proposed *crack-path-field* tracking algorithm by Dias et al. [102, 103] and Oliver et al. [259] determines the position of a discrete crack considering a diffuse strain localization field α^h (see Fig. 2.20), which is obtained by non-linear local constitutive models equipped with strain softening. The crack-path-field is defined as the location where the selected scalar field α^h takes its maximum value. The procedure for defining the crack-path is composed by four steps including the computation of: (i) the smooth continuous approximation of variable α^h denoted as ψ^h, (ii) its directional derivative $\partial\psi^h/\partial x$, (iii) a smooth continuous approximation of this directional derivative μ^h and (iv) its zero level set Γ. The above fields are illustrated in Fig. 2.20 for an one-dimensional case. The crack-path-field algorithm is used in the last part of a kinematic enhancement series employed for the mesh-objective localization of fracture. The first kinematic enhancement is applied to elements in which material bifurcation is about to occur [197] or has already occurred [104, 259]. This enhancement intents to acquire a better approximation of field α^h in potential locations of strain localization. Then, at a defined a-priori stage of the localisation process, a strong discontinuity is inserted at the aforementioned elements that are already enhanced in a weak manner and are crossed by the zero level set of the crack-path-field Γ. The algorithm has been used in two-dimensional simulations of quasi-static [104, 255, 259] and dynamic crack propagation [197].

Feld-Payet et al. [130] recently proposed a similar tracking algorithm to the crack-path-field. The so-called *marching ridges* tracking algorithm is based on the identification of the crack-path as the zero level set of a scalar product involving the gradient of a regularised degradation-related field and an orthoradial vector $\underline{e}_\theta$ defined on a polar grid centred on the crack-tip or crack origin (see Fig. 2.21). The algorithm has been used for both 2D and 3D problems.

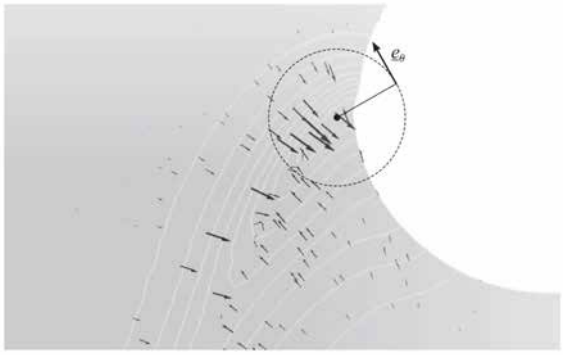

Figure 2.21 Damage gradient vectors and an orthoradial vector $\underline{e}_\theta$ at the crack-tip of a potential crack in the marching ridges algorithm of Feld-Payet et al. [130]. (Image from Feld-Payet et al. [130])

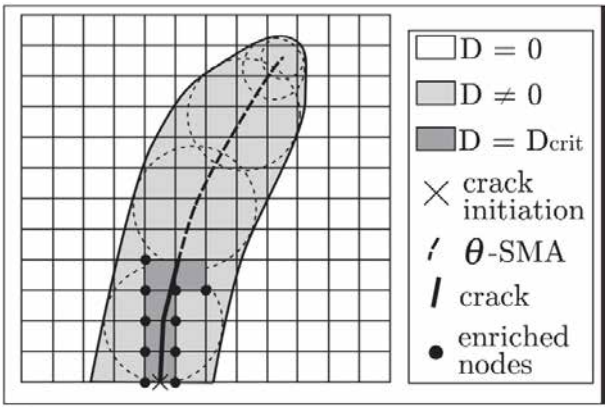

Figure 2.22 Geometrical tracking algorithm proposed in [374] for the calculation of the crack-path as the simplified medial axis (θ-SMA) of bi-tangent interior circles to a regularised damage field. (Image from Tamayo-Mas and Rodríquez-Ferran [374])

In the continuous-discontinuous approach of Tamayo-Mas and Rodríquez-Ferran [372, 373] the transition between regularised and discrete damage is through the use of a geometrical tracking algorithm. The crack-path is constructed as the simplified medial axis (denoted as θ-SMA in Fig. 2.22) of an area where regularised damage overpasses a defined damage threshold. The θ-SMA is the loci of centres of bi-tangent interior circles to the aforementioned damaged area (see Fig. 2.22). In 3D, a damaged volume is considered instead of an area and the crack is defined in a similar way by its medial surface. The algorithm has been used as a transition between a gradient-enhanced damage model and traction-free cracks in [373] or cohesive cracks in [374].

2.4.5 Crack propagation direction in tracking algorithms

The crack propagation criterion is a vital part of a tracking algorithm. This stems from the theory of Fracture Mechanics, empirical or physical considerations. In the following, a summary of the most used propagation criteria within tracking algorithms is endeavoured. Comparative studies between different propagation criteria used in tracking algorithms have been presented by Bouchard et al. [50], Dumstorff and Meschke [113] and Unger et al. [380].

Linear Elastic Fracture Mechanics criteria

Linear Elastic Fracture Mechanics (LEFM) have provided three criteria with significant use in tracking algorithms: (i) the maximum circumferential (or maximum

hoop/tangential) stress, (ii) the minimum strain energy density, and (iii) the maximum energy release.

The *maximum circumferential stress* criterion, proposed by Erdogan and Sih [119], states that a crack propagates from its tip at a polar angle θ_c in which the circumferential stress $\sigma_{\theta\theta}$ reaches its maximum. As the circumferential stress in the crack propagation direction is a principal stress, the angle θ_c can be determined analytically by setting the shear circumferential stress $\sigma_{r\theta}$ to zero

$$\sigma_{r\theta} = \frac{1}{2\,\pi\,r}\,\cos(\theta/2)\left(\frac{1}{2}\,K_I\,\sin\theta + \frac{1}{2}\,K_{II}(3\,\cos\theta - 1)\right) = 0 \tag{2.8}$$

where θ and r are the local polar co-ordinates at the crack-tip and K_I, K_{II} the stress intensity factors under mode I and mode II loading, respectively. The solution of the above equation gives

$$\theta_c = 2\,\arctan\left[\frac{1}{4}\left(K_I/K_{II} \pm \sqrt{K_I/K_{II}^2 + 8}\right)\right]. \tag{2.9}$$

Between the two possible directions given by Eq. (2.9), the one with the maximum $\sigma_{\theta\theta}$ is selected for the propagation. The extension of the maximum circumferential stress criterion to 3D has been presented by Shöllmann et al. [339].

Instead of considering stresses, the coeval *minimum strain energy density* criterion [346–348] looks at the strain energy density distribution around the crack-tip for the definition of the crack propagation direction. Here, crack propagation takes place when the strain-energy density factor S reaches a critical S_c (assumed to be a material property) at a neighbourhood of the crack-tip and in a direction determined by the stationary value of S

$$\left.\frac{\partial S}{\partial \theta}\right|_{\theta=\theta_c} = 0 \tag{2.10a}$$

$$\left.\frac{\partial^2 S}{\partial \theta^2}\right|_{\theta=\theta_c} \geq 0 \tag{2.10b}$$

The strain energy density is defined as [346]

$$S = \alpha_{11}\,K_I^2 + 2\,\alpha_{12}\,K_I\,K_{II} + \alpha_{22}\,K_{II}^2 + \alpha_{33}\,K_{III}^2 \tag{2.11}$$

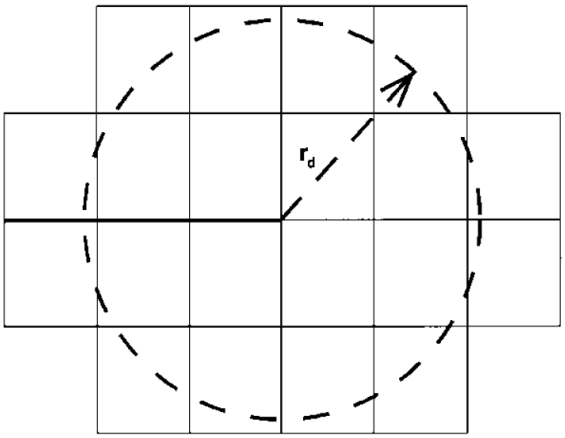

Figure 2.23 Selected elements surrounding the crack-tip for the calculation of the interaction integral in the computation of the crack propagation direction within X-FEM. (Image from Moës et al. [235]).

where

$$\alpha_{11} = \frac{1}{16\,G}\left[(\kappa - \cos\theta)(1+\cos\theta)\right] \tag{2.12a}$$

$$\alpha_{12} = \frac{1}{16\,G}\,\sin\theta\left[2\cos\theta - (\kappa - 1)\right] \tag{2.12b}$$

$$\alpha_{22} = \frac{1}{16\,G}\left[(\kappa+1)(1-\cos\theta) + (1+\cos\theta)(3\cos\theta - 1)\right] \tag{2.12c}$$

$$\alpha_{33} = \frac{1}{4\,G} \tag{2.12d}$$

with ν being the Poisson ratio and G the shear modulus. Finally, κ is defined as

$$\kappa = \begin{cases} 3 - 4\,\nu & \text{for plane strain} \\ (3-\nu)/(1+\nu) & \text{for plane stress.} \end{cases} \tag{2.13}$$

As can be seen from Eqs. (2.9) and (2.11), the use of the maximum stress and the minimum strain energy density criteria necessitates the computation of the stress intensity factors. In the first applications of these local propagation criteria [165,166,337], the stress intensity factors were computed with the use of special singularity finite elements around the crack-tip (e.g. [24, 57, 379]). A coeval alternative to these elements was the use of isoparametric quadratic elements with simple modifications on the position of the internal nodes [23, 155], such that the singular stress fields near a crack-tip could be reproduced [194]. Considering recent applications, the maximum circumferential stress criterion is very popular within the X-FEM. In this context, the stress intensity factors are calculated using domain forms of the interaction integrals over a selected area circumscribed by a radius r_d, which is normally defined as a factor of the finite element characteristic length, (see Fig. 2.23). Applications of the maximum circumferential stress criterion in the context of partition of unity methods can be found in [30, 89, 234, 235, 239, 386, 406].

The *maximum release energy* criterion stems from the original Griffith's energy release theory concept [150, 151] and was later reconsidered in [119, 247, 395]. Contrary to the above criteria, which depend on a local near-tip variable (i.e. the stress or strain energy

density), the maximum release energy criterion depends on a global energy state. In particular, a crack propagates from the crack-tip along a direction defined by the polar angle θ_c, which maximizes the global released energy of the structure G. This can be stated by the following conditions

$$\frac{\partial G}{\partial \theta}\Big|_{\theta=\theta_c} = 0 \tag{2.14a}$$

$$\frac{\partial^2 G}{\partial \theta^2}\Big|_{\theta=\theta_c} \leq 0. \tag{2.14b}$$

Propagation is initiated when the released energy G reaches a critical value G_c, which is a material constant.

Early applications of the maximum energy release criterion in the context of the finite element method can be found in [166, 400]. Much later, Meschke and Dumstorff [113, 227] used the maximum energy release criterion in the context of X-FEM. In their formulation, the crack propagation direction as well as its extension length are introduced as global unknowns to the problem, which is then solved enforcing a minimization of the total energy of the body. Similar criteria have been used afterwards by Unger et al. [380] and Zhang et al. [403]. In the latter approaches, an iterative procedure is used and the global energy of the structure is computed for different angles and crack extensions. The case minimizing the global energy is finally selected for the new increment. This iterative procedure increases importantly the computational cost of these methods [380].

In their first applications in the context of FEM the above LEFM criteria were commonly implemented in the same code and used for comparative studies using remeshing and nodal relaxation methods (see for instance [166, 167]). The same procedure was followed later by Bouchard et al. [50]. A common outcome of these studies was the similar performance of the maximum circumferential stress and the maximum release energy criteria, while the use of the minimum strain energy density was normally giving less accurate results regarding the expected crack propagation [50, 166].

Maximum Principal Stress criterion

When resisting forces are assumed to apply at the crack surfaces, either through a cohesive-traction separation law or from a stress-strain continuum model, the singularity at the crack-tip considered by linear elastic fracture mechanics is cancelled [406]. In such cases, the use of the presented propagation criteria of LEFM need some further modifications. One very common modification concerns the maximum circumferential stress criterion, which turns into the *maximum principal stress (MPS)* criterion.

The maximum principal stress criterion states that a crack will propagate at a direction orthogonal to the maximum principal stresses. Due to its straightforward implementation, as well as the good accuracy for straight and slightly curved cracks, this criterion has been one of the most used for crack propagation in both discrete [48, 65, 139, 225, 383, 391] and

smeared crack approaches [56, 77, 85, 294, 329, 360].

A common practice used for the improvement of the reliability of the stresses at the vicinity of the crack is to use an average stress tensor, which is computed using smoothing/averaging techniques around the crack-tip [105, 129, 313, 391] or non-local stress/strain tensors [179] (see Fig. 2.24).

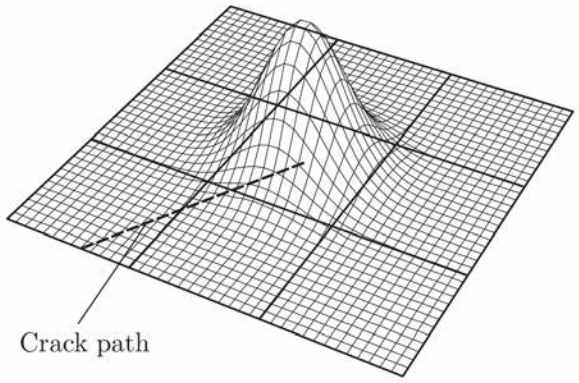

Figure 2.24 Computation of the crack propagation considering an averaged value of stresses of the crack-tip and neighbouring elements through Gaussian weight functions in Dumstorff and Meschke [113]

Discontinuous material bifurcation analysis

Discontinuous material bifurcation analysis is commonly used for the computation of the propagation direction. The method dates back to the work of Hill [158] who associated the strong ellipticity character of the acoustic (or localization) tensor $\boldsymbol{Q}$ to the existence of discontinuous acceleration waves. In subsequent works the loss of the ellipticity (or hyperbolicity) character of the governing equations was linked likewise to the strain localization in an elastoplastic [278, 316, 323] or a softening solid [253, 289, 354].

The criterion for loss of the material stability and therefore onset of strain localization can be defined as

$$\det \boldsymbol{Q}(\mathbf{n}) \leq 0 \tag{2.15}$$

where the acoustic/localization tensor $\boldsymbol{Q}$ is a function of the constitutive tangent matrix $\boldsymbol{C}$ and the normal vector to the material discontinuity $\mathbf{n}$

$$\boldsymbol{Q} = \mathbf{n} \cdot \boldsymbol{C} \cdot \mathbf{n}. \tag{2.16}$$

The above equations define that the material loses its stability (or, in other words, the material bifurcates) when the determinant of the acoustic tensors ceases to be positive in a direction defined by a vector $\mathbf{n}$. Inversely, the crack propagation direction can be computed by finding the normal vector $\mathbf{n}$ which gives the minimum determinant of $\boldsymbol{Q}$ and checking whether the inequality of Eq. (2.15) is satisfied.

For simple cases, analytical derivations are possible for the discontinuous material bifurcation analysis [158, 257, 260, 324], while more general cases necessitate the numerical

solution of the problem with proper algorithms [158, 261]. Recent contributions on analytical strain localization analyses have been presented for many associative plasticity and damage constitutive models by Wu and Cervera [396, 397].

Another limitation of the approach, is that the solution of the problem normally gives two possible directions that minimize the acoustic tensor [75, 261, 266, 306]. The selection of the propagation direction necessitates then the use of an additional criterion. Rabczuk and Belytschko used either the normal which is closer to the direction of the principal tensile stress [307] or later the direction corresponding to the maximum displacement gradient in the localization direction [308]. Similar criteria considering the gradient of the instantaneous (or the rate of the) displacement field have been considered by Oliver et al. [262] and Weed et al. [388].

Crack branching

Cracking branching refers to the splitting of a crack at its crack-tip in one or more parts (branches) during its propagation within a solid. The phenomenon is more likely to occur under dynamic loading, although crack branching has been observed also under quasi-static loading.

The simulation of crack branching with tracking algorithms is not a trivial task, as it necessitates two additional criteria that specify the moment of the crack-branching and the direction of the new branches. Today, a robust predictive theory that can give answers to the above conditions is missing. As a consequence, the criteria used in tracking algorithms for the definition of crack branching are heuristic or empirical based on experimental evidence.

Belytschko et al. [31] allow a crack to branch when the propagation directions ahead of the crack-tip, obtained with a discontinuous material bifurcation analysis, vary significantly from the previous crack direction. The same criterion was used by Song et al. [361], with the difference that in this case the crack propagation directions are computed with a maximum principal stress criterion. A similar criterion was used later by Song and Belytschko [362] in their cracking nodes method. They allowed new cracks to emerge from elements next to existing ones when the propagation directions at them diverge from the crack direction of the main crack with a higher angle compared to a defined threshold.

In Linder and Armero [196] (see also [12]) the crack branching is associated with the Rayleigh wave speed. In particular, a crack is allowed to branch as soon as the propagation velocity at the crack tip reaches a critical value, expressed as a fraction of the Rayleigh wave speed and is user-defined. The approach is implemented in quadrilateral elements and as soon as the branching criterion is satisfied the two elements that fall out of the crack propagation direction at the crack-tip are selected as the new crack-tips (see Fig. 2.25). From them, the crack propagates following the direction of the maximum principal stress.

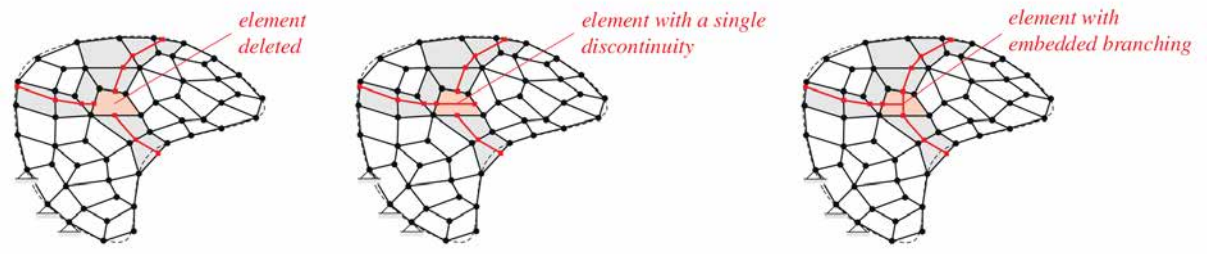

Figure 2.25 Branching of a crack in Linder and Armero [196] and different strategies for the branching element: element deletion (left), element with a single discontinuity (middle) and element with embedded branching (right). (Image from Linder and Armero [196]).

Fig. 2.25 demonstrates another implication that needs to be considered in the modelling of crack branching with strong discontinuity methods. This is the special construction of the branching elements, which is necessary to ensure compatibility between the kinematics of discontinuities in the neighbouring elements at the crack branches. Implementations of these elements in the context of partition of unity methods can be found in [93, 110], while for embedded strong discontinuities in [196, 197].

2.5 Finite element analysis of masonry structures

The inventory of numerical methods applied to the simulation of masonry structures has expanded significantly during the last decades. This is, first, due to the diversity of the composite materials known as masonry, in terms of components' typology and their geometrical arrangement, which has provoked the development of various approaches providing different levels of detail regarding the material modelling. Additionally, as presented in Section 2.3, there exist several possibilities for the numerical representation of cracking. Certainly, up to date, there is no panacea for the simulation of masonry and the analyst should weigh up carefully the choice among the available numerical tools considering the purpose of the structural analysis (e.g. capacity, ductility, crack distribution), the complexity and scale of the structure (e.g. single structural member or whole building) and the available resources (e.g. computational cost, knowledge of geometry and material properties).

The following of this chapter presents an overview of finite element methods employed in the analysis of masonry structures following a categorization according to the level of detail in the material representation into: (i) micro-mechanical, (ii) multi-scale, (iii) discontinuous, (iv) macro-element, and (v) macro-mechanical approaches. It is acknowledged that the finite element method is only a family of the computational methods used in the study of masonry structures, which includes limit analysis software [46, 145, 230, 273] or the lately increasing application of discrete element methods [193, 223, 282, 349]. For a review on these topics, as well as on analytical approaches dedicated to masonry structures we refer to the review papers of Lourenço [204], Roca et al. [317] and Theodossopoulos and

Sinha [378].

2.5.1 Micro-mechanical approach

Micro-mechanical approaches adopt a distinct modelling of the masonry components. This strategy allows to account for different mechanical properties and constitutive law for each component. Various micro-mechanical approaches have been proposed on the literature considering a different level of detail for the representation of the composite nature of masonry.

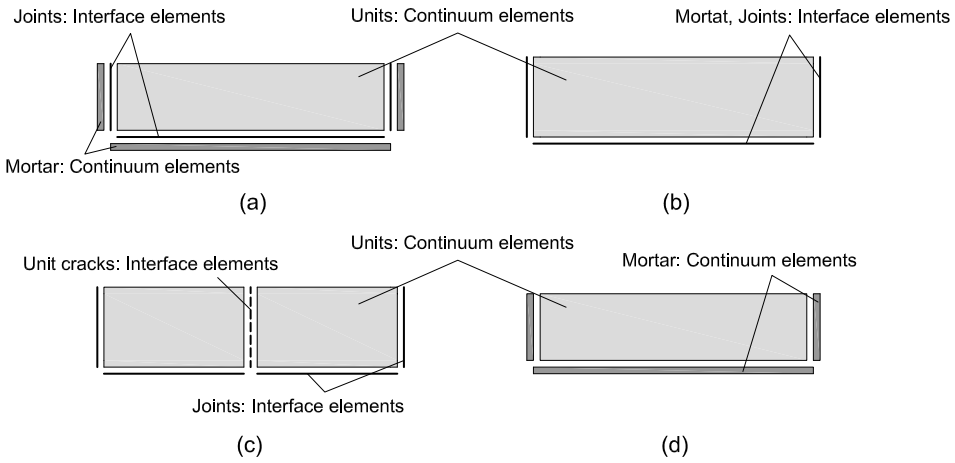

Figure 2.26 Different level of detail in micro-mechanical models: (a) Detailed micro-model, (b) Simplified micro-model with mortar and unit/mortar behaviour lumped in interface elements, (c) Simplified micro-model with additional interfaces for vertical cracking in bricks, (d) Continuous micro-model with modelling of units and mortar with continuum elements.

In a *detailed micro-model*, all the components are included in the numerical simulation, namely the units, mortar and the unit/mortar interface (Fig. 2.26a). Units and mortar are discretized with continuum elements, while unit/mortar interface through the use of discontinuous interface elements. The explicit modelling of all the components results naturally in a very accurate simulation of the local response of masonry. However, due to their high computational cost, their application has been strictly restrained to the analysis of masonry specimens (e.g. [108]) (see Fig. 2.27a).

Considering the fact that the weakest zone in masonry is commonly the mortar and the unit/mortar interface, a simplification of the detailed micro-model is possible, decreasing at the same time the computational burden. This is the purpose of the *simplified micro-models*, in which the non-linear behaviour of masonry is lumped into interface elements that are positioned between the units following the staggering pattern [80,81,279,280,322]. In this strategy the dimensions of units are expanded considering the mortar thickness and are modelled with linear elastic continuum elements (Fig. 2.26b). Alternatively, the non-linear behaviour of the units can be considered in the numerical analysis either by using a smeared cracking approach (e.g. [199, 302]) or discretely by introducing a

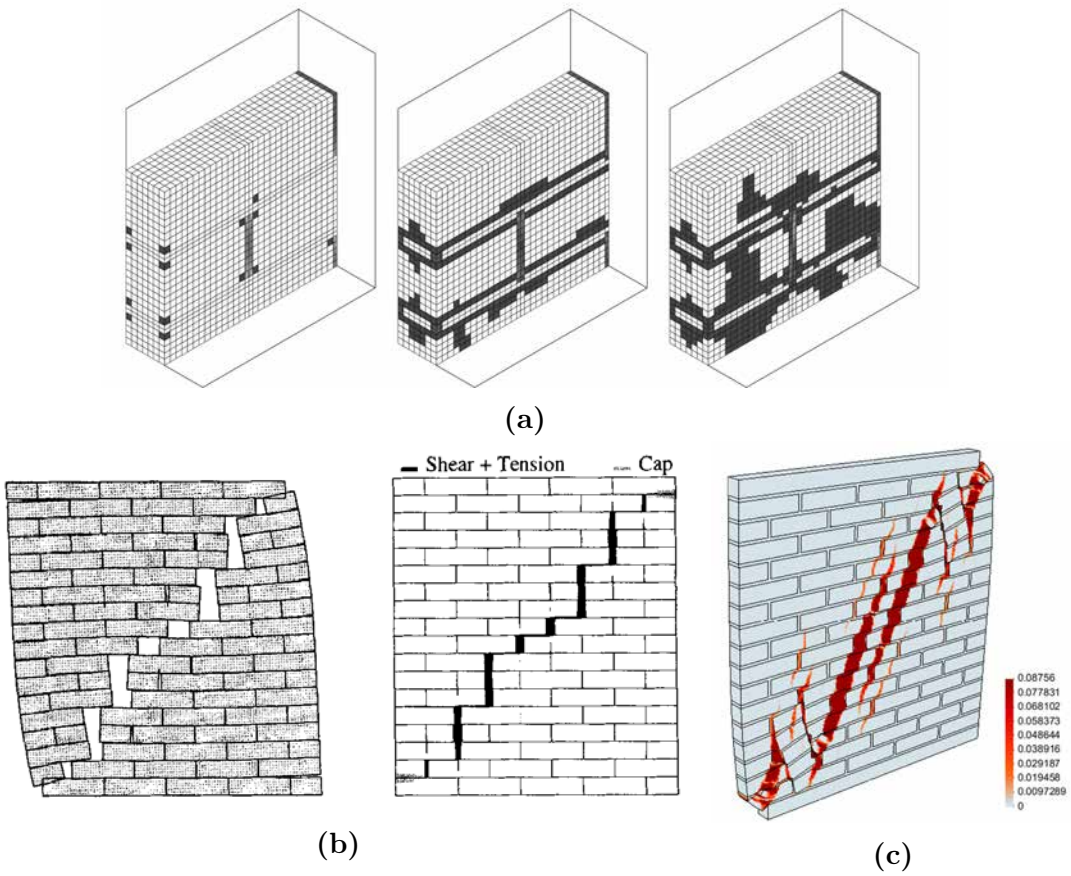

Figure 2.27 Applications of different levels of micro-modelling: (a) Evolution of damage for increasing levels of compression (from left to right) in a masonry prism with a detailed micro-model by Drougkas et al. [107], (b) Deformation (left) and damage (right) in the analysis of a shear wall with simplified micro-model by Lourenço et al. [206] and (c) Maximum principal strain in the analysis of the same shear wall with a 3D-Continuous micro-model by Petracca et al. [302].

discontinuous interface at the middle of the units for representing a vertical crack (Fig. 2.26c and Fig. 2.27b) (see [140, 202, 206, 210, 250, 340]). A final alternative considers the modelling of both units and mortar with continuum elements with a smeared crack representation of damage, disregarding the use of discontinuous interface elements (Figs. 2.26d, 2.27c) [21, 39, 285, 299, 302]. These models can be identified as *continuous micro-models*, due to the representation of masonry as a continuous material.

The above micro-mechanical models, with the unique exception of continuum micro-models, are based on the discrete interface approach for the representation of cracking. When cracking is simulated with continuum finite elements, local smeared, plasticity or damage models are usually used in a smeared cracking format, while a transient gradient enhanced non-local damage model has been recently presented in [175].

The explicit representation of masonry's components in terms of geometrical and mechanical properties can give very accurate results regarding the stress-state in the linear and non-linear range, as well as the damage pattern and collapse mechanism. On the other hand, a corollary of this detailed modelling is the increased effort for the model preparation, and the high cost in terms of computing time and memory resources. For

this reason, the application of micro-mechanical approaches is usually limited to small structural members or parts of a structure. Efforts towards the extension of their applicability into larger structures have been made during the last years through the use of partitioned modelling and parallel computing [211, 212].

2.5.2 Multi-scale approach

Multi-scale approaches refer to the analysis of a masonry structure through the solution of two Boundary Value Problems (BVP) in two different scales (Fig. 2.28). The approach takes advantage of the repetitive pattern of a Representative Volume Element (RVE), which can be identified in regular masonry typologies. At macro-scale level, the whole structure is considered and masonry is modelled as a homogeneous material. The problem is completely stated, apart from the knowledge of the constitutive law, which is obtained through the solution of the micro-scale BVP at each integration point. The micro-scale BVP is a micro-mechanical model of the selected RVE, considering the geometry and mechanical properties of the units, the mortar and, if desired, their interface. The solution of the micro-scale problem using the proper boundary conditions determines the micro-level stress field, which then is transformed to the macroscopic stress using proper bridging conditions between the two scales. Note that the selection of the boundary conditions for the RVE is not an easy task. Difficulties arise especially after cracking appears within the structure, when the simplifications regarding the periodicity of the boundary conditions of the cracked RVE do no hold. For a general review of multi-scale models for the analysis of composite materials see Otero et al. [277].

The micro-scale BVP is discretized using one of the presented alternatives of micro-mechanical models. Concerning the macro-scale BVP, different approaches have been

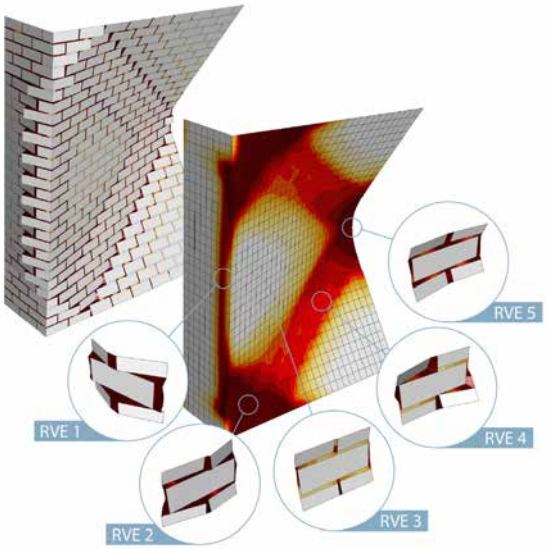

Figure 2.28 Front: Damage distribution at macro-scale and in selected RVEs in the multi-scale analysis of an out-of-plane loaded wall by Petracca et al. [301]. Back: Damage distribution in the continuum micro-model of the same wall. (Image from Petracca et al. [301]).

used in the literature, always in the context of smeared crack approaches. Higher-order or enriched Cosserat-based models have been used in [3–5, 20, 53, 94, 217], embedded discontinuities in [220], while other applications using standard local smeared cracking models can be found in [58, 299–301, 305, 344, 409].

Multi-scale models are more efficient compared to micro-mechanical models, especially in terms of model preparation. This is due to the fact that only the geometry of the RVE needs to follow the selected masonry's pattern and not of the whole structure as in the former. Nevertheless, their computational cost is still very high since the micro-scale problem needs to be solved at each step for each integration point. For this reason, their applicability in large-scale structures in engineering practice is, for the moment, limited.

2.5.3 Discontinuous approach

Instead of adopting a detailed description of the masonry's texture, as in micro-modelling and multi-scale approaches, several *discontinuity approaches* have been proposed that simulate strong discontinuities between the different blocks or parts of a structure by distributing selectively within the structure non-linear interfaces. This category of FE methods is based on the fact that structural collapse in masonry is characterized by the formation of global or local mechanisms, provoked by the separation of different parts of the structure due to crack propagation. Consequently, one of the most important ingredients for a realistic structural assessment of masonry structures is the identification and correct simulation of the emerging collapse mechanism.

Unlike micro-modelling approaches, there is no general methodology for the distribution of the discontinuities within the structure and various approaches have been reported over the years. For instance, Blasi and Sorare [45] simulated the cracking of the historical dome of Tempio di Romolo in Rome by introducing non-linear interface elements along

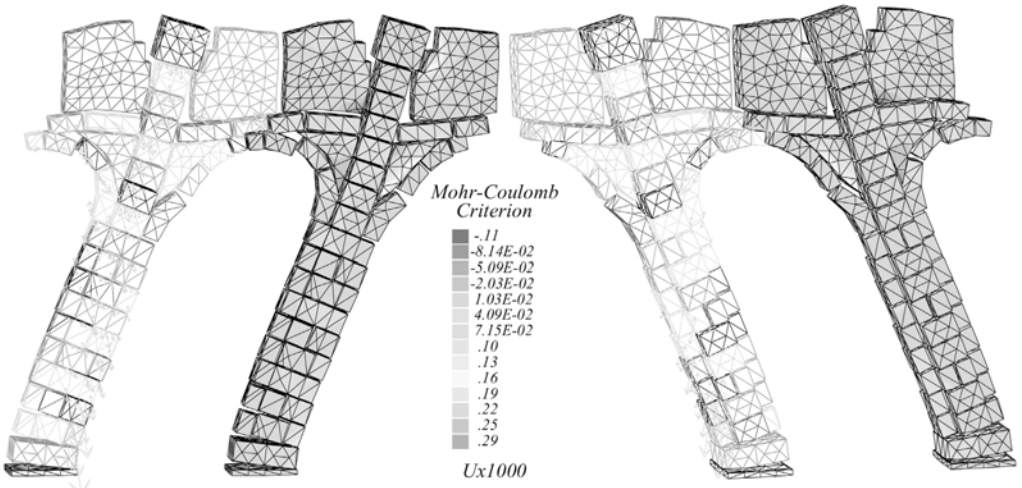

Figure 2.29 Simulation of the cloister of S. Vicente de Fora monastery in Portugal with the use of a discontinuous approach by Pegon et al. [291]

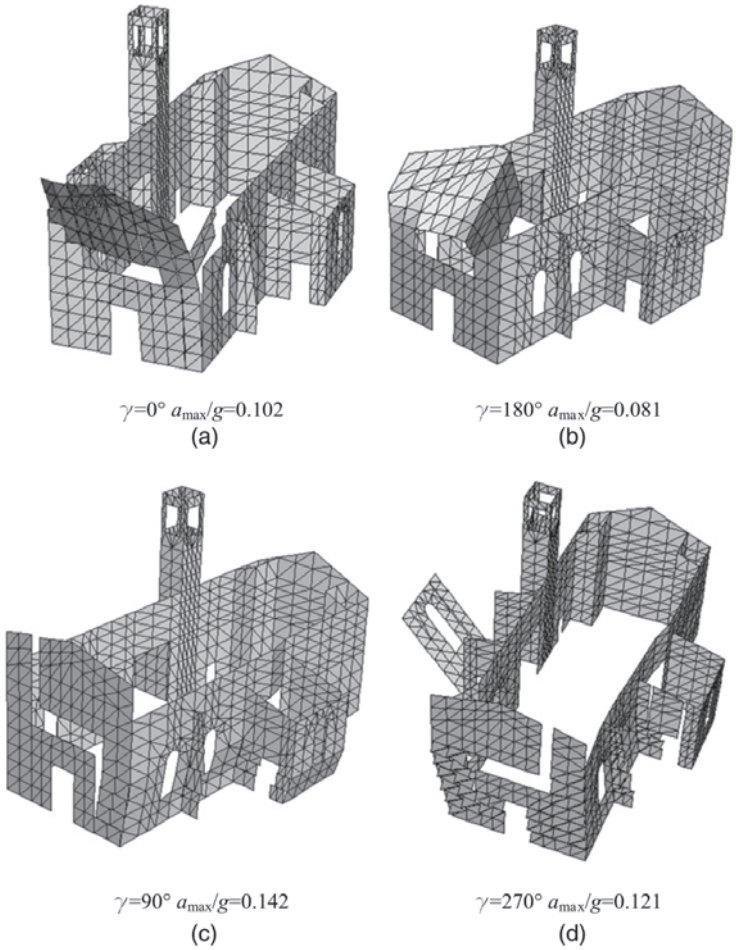

Figure 2.30 Discontinuous analysis of the church of St. Anna in Anitrella, in Italy by Milani and Venturini [233], using elastoplastic interfaces with softening at predefined locations obtained through preliminary limit analysis. Deformed shape at the end of the simulations for a loading direction towards the: (a) west $\gamma = 0^{\circ}$, (b) east $\gamma = 180^{\circ}$, (c) south $\gamma = 90^{\circ}$, (d) north $\gamma = 270^{\circ}$. (Image from Milani and Venturini [233]).

its meridians, allowing crack-opening by assuming zero tensile strength and modelling sliding with a Mohr-Coulomb friction law. Pegon et al. [291] employed a more dense network of non-linear interfaces enhanced with an elastic-plastic Coulomb friction law to simulate the block-to-block and block-to-masonry interaction in the seismic analysis of the cloisters of São Vicente de Fora Monastery in Lisbon (Fig. 2.29). More recently, Milani and Venturini [233] proposed a two step approach for the simulation of collapse in masonry churches. In the first step, a limit analysis is carried-out which helps to identify the emerging collapse mechanism. In the second step, elastic-plastic interfaces with material softening, considering the homogenized properties of masonry, are used in pre-defined locations such as the collapse mechanism can be reproduced during a pushover analysis (Fig. 2.30).

The above approaches, show the importance of the proper localization of damage for the realistic assessment of the structural capacity in masonry structures. However, the correct identification of the most vulnerable collapse mechanism is the sine qua non for

their successful application. In these cases, this could be guaranteed by the high expertise and deep insight of the involved analysts. Notwithstanding, their general application would need either the assessment of many different collapse mechanisms, or the use of robust preliminary analyses that could point on the emerging collapse mechanism. Both of the above cases increase the computational cost since more than one models need to be prepared and analysed for a single case study.

2.5.4 Macro-element approach

Macro-element approaches simplify the analysis of a masonry structure by discretizing it as an assembly of rigid and deformable macro-elements. During the last decades, the engineering community has shown permanent interest in the development of such simplified approaches aiming to reduce the high computational cost associated with the analysis of large-scale structures.

Along this line of research, Casolo and Peña [62] adopted a mechanistic rigid body spring model (RBSM), consisting of a collection of plane quadrilateral rigid elements connected to each other by two normal springs and one shear spring at each side. The developed macro-element aims to reproduce tensile, shear and compressive post-peak response accounting for hysteretic behaviour of a representative volume element of the analysed masonry. The proposed methodology has been used for the simulation of 2D regular [62] and irregular masonry structures [63] under both static and dynamic actions.

In regular masonry structures it is easy to recognize the contributing structural elements, which are the piers, walls, spandrels and lintels, as well as the interconnecting elements between them. This structural categorization has motivated the development of another macro-element approach, the *Equivalent Frame Method (EFM)*, in which the structure is idealized into a simplified frame system composed by vertical elements, which

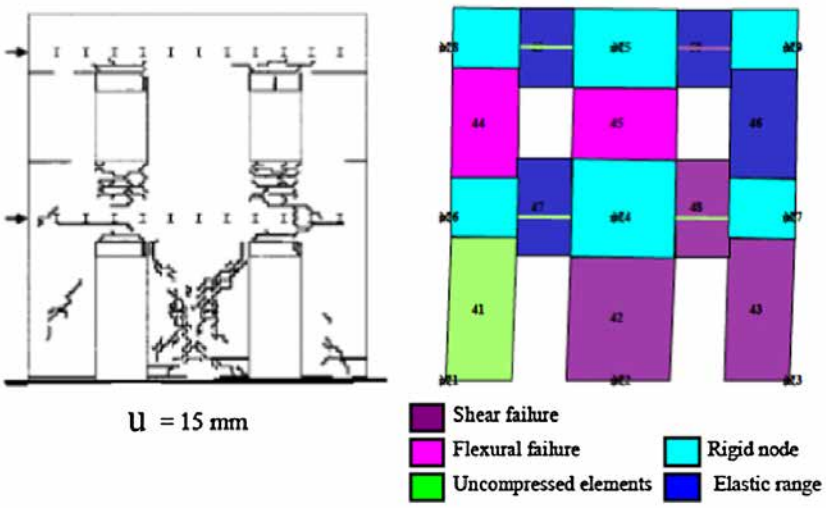

Figure 2.31 Analysis with an equivalent frame method of a façade wall tested by Calvi and Magenes [59] (left) using the equivalent frame method developed by Lagomarsino et al. [188] (right). (Picture adapted from Lagomarsino et al. [188]).

represent the piers or walls, and horizontal ones for modelling the spandrels or lintels above the openings. These vertical and horizontal elements are interconnected with the use of rigid nodes (Fig. 2.31). In most of EFM approaches, material non-linearity is lumped into the nodes at the ends or centre of the used macro-elements [2, 17, 188, 214, 283]. The material behaviour is simulated through proper constitutive laws that can account for the different failure mechanisms of each structural element. A more detailed representation of the damage across the macro-element is possible using a spread non-linear constitutive behaviour as proposed in the work of Raka et al. [310].

The idealization of a structure as an assembly of a limited number of macro-elements decreases dramatically the number of degrees of freedom of the numerical model. Corollary of this strategy is the extremely efficient simulation of whole masonry structures, which has established macro-element methods, and especially EFM models, as famous tools in engineering practice. Nevertheless, macro-element approaches present important limitations, as the predefinition of the damage zones along the edges or centre of the macro-elements and the necessity for generalized constitutive laws for describing the different collapse mechanism of each structural element. Additionally, EFM models are incapable of simulating irregular layouts [345] and simplify significantly the complex stress transfer between spandrels and piers by assuming a rigid connection among them.

2.5.5 Macro-mechanical approach

Macro-mechanical approaches or more commonly known as *macro-modelling* and *continuum finite element* approaches consider masonry as a homogeneous material with average properties, i.e. no distinction is made between masonry's components. These approaches are better suited to large and practice-oriented numerical simulations, where more importance is given to the global capacity of the structure and the local or global collapse mechanisms, rather than on the detailed representation of the heterogeneous local stress-state due to the composite nature of masonry.

The material behaviour in macro-mechanical approaches is represented using continuum finite elements with proper constitutive laws for the simulation of the linear and non-linear elastic behaviour. In a realistic macro-mechanical model the constitutive law should at least be able to represent the different behaviour of masonry under tensile and compressive loads, through the proper assignment of constitutive laws and failure surfaces. Although the vast majority of used material models do not account for different directional properties, sophisticated models considering the linear and non-linear anisotropy of masonry have also been proposed [38, 203, 207, 281, 292, 295, 296]. The limited use of the latter is attributed to the difficulties associated with the derivation of, mainly, the non-linear directional mechanical properties of masonry which are necessary for the definition of these models. Another alternative is the derivation of a macro-mechanical constitutive law accounting for the material anisotropy through homogenization techniques

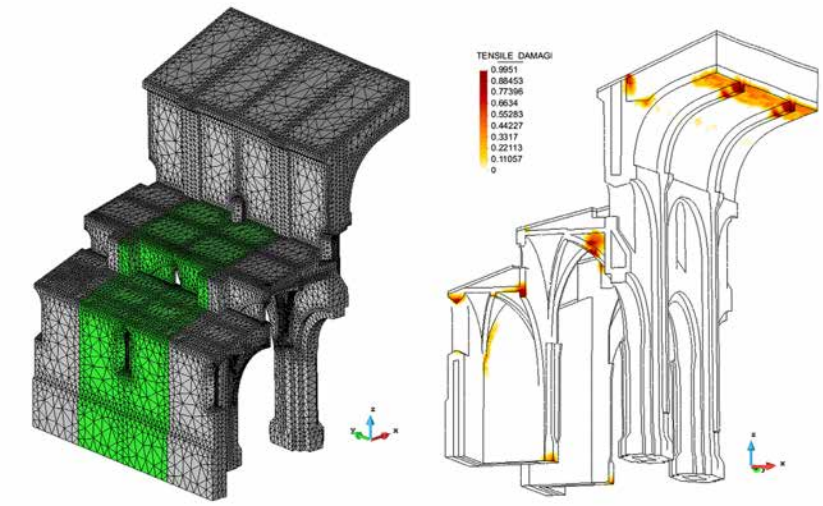

Figure 2.32 Macro-mechanical simulation of the demolition of a later nave in the church of the Poblet monastery by Saloustros et al. [332]. Left: Finite element discretization with the demolished bay in green. Right: Damage distribution at the end of the analysis.

(e.g. [200, 201, 410]).

Due to their intrinsic simplicity in model preparation and low computational cost, macro-modelling approaches are probably the most commonly used for the numerical simulation of large-scale masonry structures (e.g. [60, 61, 64, 117, 118, 208, 232, 318, 332]) (Figs. 2.32, 2.33), offering a good balance between efficiency and accuracy [205, 317]. Macro-mechanical approaches usually adopt a smeared representation of damage using standard irreducible finite element formulations and smeared crack approaches based on the crack-band approach. As discussed in Section 2.2, this strategy may result in serious directional mesh-bias dependency with immediate effects on the correct assessment of the structural capacity. Despite the extended application of macro-mechanical models, this mesh-dependency of the numerical solution is usually overlooked by the engineering community. Additionally, the damage usually appears as smeared over large areas within the structure, which does not represent the localized cracking exhibited by unreinforced masonry and hampers the interpretation of local, and global collapse mechanisms (see Figs. 2.32, 2.33, 2.34).

Alternative approaches that can alleviate the mesh-bias dependency, as the use of enhanced continua and regularised models, are difficult to apply at this scale, since these models necessitate highly refined meshes to capture properly the material degradation within the localization band. Additionally, it is not clear if the introduced internal length scale is a material property, which should be associated with the type of masonry used, or a numerical one. Regarding the use of discrete crack approaches in macro-mechanical models, some promising applications have been presented concerning the simulation of small-scale masonry beams with embedded cohesive crack models [314]. Nevertheless, discrete crack approaches are still hardly applicable to large-scale analyses, due to the intrinsic difficulties of the method in handling multiple cracks with crack intersection for

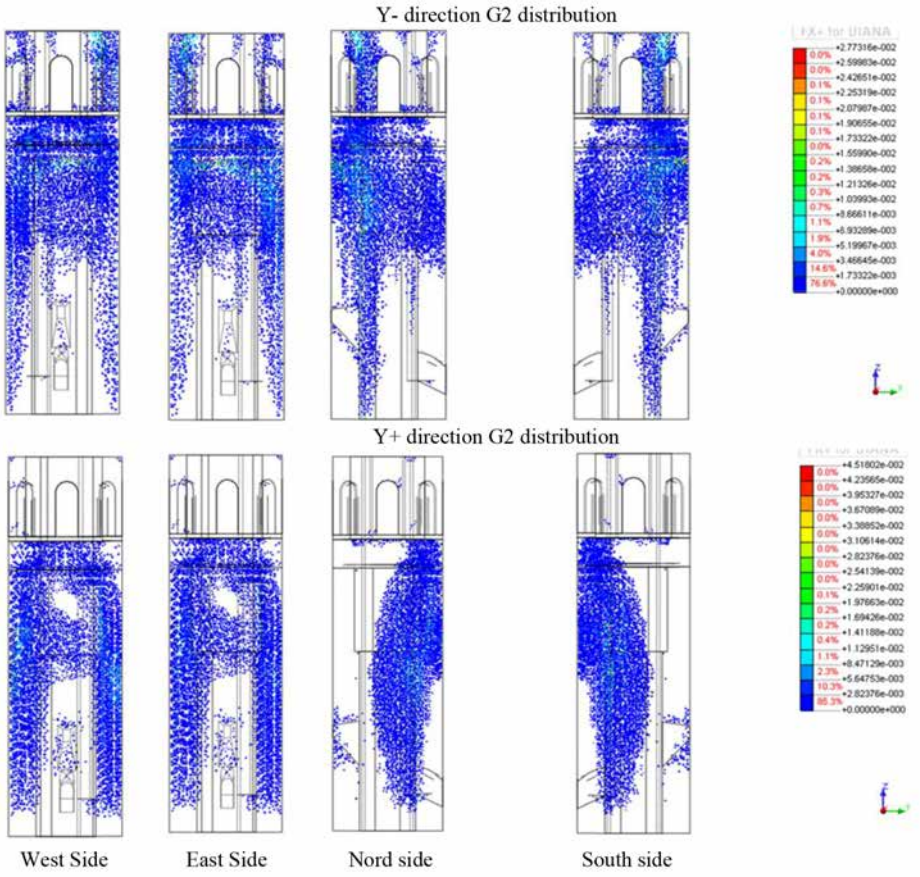

Figure 2.33 Cracking pattern obtained with a pushover analysis using a macro-mechanical approach and a local isotropic smeared cracking model by Milani et al. [229].

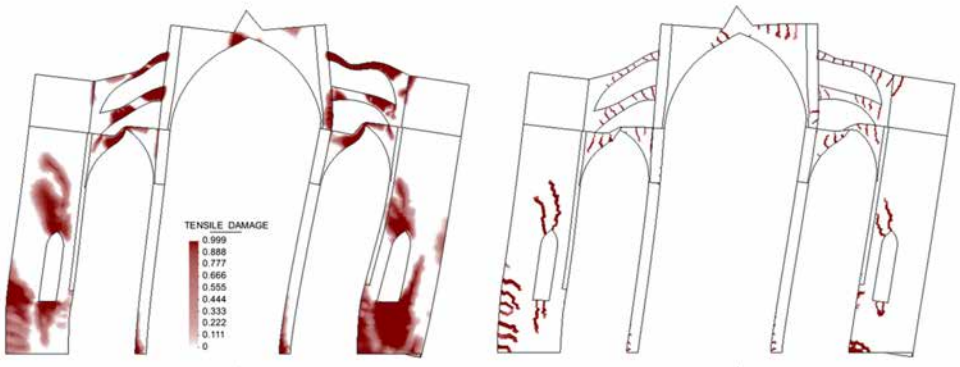

Figure 2.34 Analysis of a representative macro-element of Mallorca cathedral against horizontal loadings by Roca et al. [318]. Left: Classical smeared crack approach using a local continuum damage model. Right: enhancement using the use of a local tracking algorithm. (Image adapted from Roca et al. [318].)

a reasonable computational cost.

An interesting approach on this direction has been presented by researchers in the Technical University of Catalonia (BarcelonaTech-UPC) in Spain [77, 84, 85, 294]. They propose the use of a local tracking algorithm within the context of the smeared crack approach and local damage models. The method presents some important features for the realistic simulation of cracking in masonry structures. First, a more realistic crack representation is provided due to the localization of damage in single rows of finite elements.

This results in the better interpretation of the damage pattern and the emerging collapse mechanism, which is a key feature for the accurate diagnosis and design of strengthening or repairing interventions in damaged structures (see Fig. 2.34) [296, 303, 318]. Additionally, this localization technique allows a better control of the dissipated energy due to crack propagation compared to the classical SCA, which results in a smeared damage over large areas. In this way, mesh-size independency is also achieved. Another key characteristic is the improvement of the directional mesh-bias independency of classical irreducible finite element formulations, in a computationally efficient manner.

2.6 Summary

This chapter has presented the framework of this thesis in four thematic units. The first one has considered the early fracture research, which set the basis for many approaches in the field of computational failure mechanics. The second thematic unit has presented an overview of the different finite element approaches to cracking and the motivation behind their development. Tracking algorithms have been identified as an important tool for many of the presented FE methods applied to crack propagation analysis. The different proposed techniques for tracking the path of a crack have been the context of the third thematic unit. Finally, the last part of the chapter has focused on the finite element methods applied to the simulation of cracking in masonry structures.

As a driving force behind the development of a wide variety of strategies for crack simulation in solids has been recognized the directional mesh-bias dependency. The origin for it has been traditionally a matter of controversy and the prevailing interpretations have been presented. According to these arguments, finite element methods have been proposed altering the continuum formulation or the constitutive model, while other reducing the discretization error. The different approaches have been presented considering the adopted crack representation (i.e. discrete or smeared crack approach).

An important part of the chapter has focused on a review on tracking algorithms. These are auxiliary devices, defining the crack location within the mesh and ensuring its continuity in many finite element methods. The different methodologies used for tracking the consolidated part of a crack and predicting their propagation have been detailed. A unified approach for determining the crack propagation direction, at least for quasi-brittle materials, is still missing. For this reason, the different propagation criteria adopted in the literature have been presented.

The presentation of the finite element methods applied for the simulation of masonry structures has been performed on the basis of the detail in the material description. Highly detailed models, incorporating the different components of the material into the numerical model result in a very accurate analysis, but at high computational cost, and they are used mostly for academic purposes. On the other hand, the efficient cost of simplified approaches makes their use favourable in engineering practice. However, these approaches

adopt many simplifications in terms of material representation and cracking simulation.

The review of the above topics points out a contradiction in the application of finite element approaches to fracture. Most of the presented approaches are used and validated through the simulation of unreinforced concrete structures. Nevertheless, real-life concrete structures present some type of reinforcement, making cracking just a part of the material failure and in many cases not the determinant parameter. On the contrary, cracking in unreinforced masonry structures is decisive for the evolution of the collapse mechanism. Up to date, discontinuous interface elements consist the most common localization technique used in these types of structures, which are either positioned according to the material texture or to pre-defined locations to simulate the expected collapse mechanism. Apart from that, it seems that the obtained know-how of computational failure mechanics has not yet been transferred into the analysis of masonry structures. This thesis makes an endeavour towards this direction by proposing and applying a strain localization technique based on a tracking algorithm and a smeared crack approach for the realistic simulation of cracking in masonry structures.

This page is intentionally left blank.

3

Constitutive Model

This chapter presents the constitutive model used in this research for simulating the response of masonry under monotonic and cyclic loading conditions. This is a continuum damage model with two damage indices, which allow the distinct modelling of tensile and compressive damage and the consideration of unilateral effects under load reversal. The formulation of this model is presented in Section 3.2, after a short introduction (Section 3.1), while the damage criteria in Section 3.3. An existing model for the evolution of the irreversible strains is revisited, and its limitations and advantages are shown (Section 3.4.1). Considering this study, a novel formulation is proposed for the evolution of the irreversible strains (3.4.2). Section 3.5 presents the tensile and compressive evolution laws. These expressions are based on new definitions for the discrete softening parameters, aiming to the objective regularization of the dissipated energy with and without the consideration of irreversible strains. Aspects regarding the thermodynamic admissibility of the model (Section 3.6) and numerical implementation (Section 3.7) are also discussed. The chapter closes with the validation of the proposed model with experimental results on concrete and masonry available in the literature (Section 3.8).

3.1 Introduction

Since the first applications of numerical methods to the analysis of masonry structures [14, 25] a large variety of computational approaches have been developed and applied for the simulation of the linear and non-linear response of the composite material. Still, today, there is no general methodology applicable for the simulation of masonry. Among those existing in the literature, the proper choice is based mostly on two parameters: (i) the knowledge level of the (linear and non-linear) properties of masonry's components or of the composite itself and (ii) the bearable computational cost.

Masonry is an anisotropic material, with its properties defined by the relative position, dimensions and properties of the units and the mortar, which may or may not exist as in dry brick/stone masonry. As discussed in Section 2.5, there are different ways to consider these characteristics. In micro-mechanical models, the components of masonry are physically defined in a simplified or detailed way (see [187, 202, 210, 279, 302, 322]) and different properties are assigned to each of them. In computational homogenization techniques and multi-scale methods, the geometry of the components and their properties are considered only for the analysis of a representative volume element of the analysed masonry, from which the average stresses and strains are computed and can be used in a homogenized continuum finite element model [4, 141, 200, 220, 230, 300, 301, 305, 409]. Finally, another possibility for modelling the anisotropic behaviour of masonry without a geometrical distinction of the constituents in the structural model or in a representative volume element, is through the use of anisotropic continuum material models. Such models have been developed within the framework of plasticity [203, 207] and continuum damage mechanics [38, 281, 295].

An important issue regarding these approaches is the large number of material properties that are necessary for the definition of the numerical model. The micro-parameters of the components or the anisotropic properties of the composite need specialized test procedures which are usually difficult to apply in-situ. Additionally, more than one masonry typologies may coexist in large historical structures corresponding to the construction of the different structural elements (e.g. vaults, columns, buttresses). The acquisition of the micro-properties of each one of these requires extensive experimental campaigns which are usually inapplicable in engineering practice due to the involved cost and restrictions raised by the cultural value of the structure.

Alternatively, a common practice is the simulation of masonry as a homogeneous material with average properties (e.g [42, 60, 64, 118, 208, 232, 298, 317, 318, 332]). In the linear range, the material is assumed as isotropic without an explicit association of the stiffness to the directionality of the staggering. In the non-linear range, the cracking and crushing of the material are modelled using constitutive models based on smeared crack approach [98,320], theory of plasticity [54,293], continuum damage mechanics [76,122,123] or a combination of the latter two [190, 209]. These models usually consider different properties under tensile and compressive loading, such as strength, dissipated energy and hardening/softening response, in order to simulate correctly the different fracture processes under cracking and crushing. The material properties that are necessary in these models are easily assessed with in-situ tests [44] or laboratory experiments from samples obtained from the structure [216, 297].

This thesis considers the use of a continuum damage model with damage induced orthotropic behaviour for modelling the constitutive behaviour of masonry. Due to their solid theoretical basis on the thermodynamics of irreversible processes, damage mechanics have been a powerful framework for the development of a wide variety of constitutive

models for different materials in the last decades (e.g. [76, 92, 122, 182, 191, 209, 221, 222, 353, 384, 399]). Damage models are appealing for large-scale computations, because they do not require the costly return-mapping algorithms of plasticity models. Additionally, the use of complex failure surfaces or the combination of more than one is relatively straightforward and does not affect the computational robustness.

The constitutive model used in this thesis is based on the work of Faria et al. [122, 123] and Cervera et al. [66, 76]. It is a continuum damage model with two scalar damage variables for distinguishing between tensile and compressive damage and thus cracking and crushing of the material. The decomposition of the effective stress tensor into positive and negative parts, as well as the use of the two damage variables, allows to consider the unilateral effect under tension-compression cyclic loading. Comparing to the aforementioned models, this work introduces two different damage surfaces in tension and compression, and proposes a novel formulation for the definition of the irreversible strains. Another contribution concerns the definition of the discrete softening parameters for the objective regularization of the dissipated energy according to the crack-band theory. The above properties, as well as the limited number of involved material parameters and the simple explicit formulation, make it a suitable model for the seismic analysis of large concrete and masonry structures.

In the following sections, the main components of the constitutive model are outlined using compact notation. Lowercase bold letters in italics stand for second order tensors (e.g. $\boldsymbol{\sigma}$), uppercase bold letters in italics for fourth order tensors (e.g. $\boldsymbol{C_0}$) and lowercase bold letters for vectors (e.g. $\mathbf{n_i}$).

3.2 Constitutive law

Adopting the hypothesis of strain equivalence [181, 192], the effective stress tensor $\bar{\boldsymbol{\sigma}}$ is defined in this thesis as in [121–123]

$$\bar{\boldsymbol{\sigma}} = \boldsymbol{C_0} : \boldsymbol{\varepsilon}^e. \tag{3.1}$$

In the above equation, $\boldsymbol{C_0}$ is the isotropic linear-elastic constitutive tensor, (:) denotes the double contraction and $\boldsymbol{\varepsilon}^e$ the elastic strain tensor which has the following form

$$\boldsymbol{\varepsilon}^e = \boldsymbol{\varepsilon} - \boldsymbol{\varepsilon}^i. \tag{3.2}$$

Equation (3.2) reveals a split of the total strains into an elastic $\boldsymbol{\varepsilon}^e$ and an inelastic part $\boldsymbol{\varepsilon}^i$, which is a common standpoint of the current damage mechanics model and those based on a plasticity framework. The association of the effective stresses with the elastic strain tensor instead of the total strain tensor, shown in Eq. (3.1), is the extension of the classical concept of the effective stress tensor [191] proposed by Faria and Oliver [122]

that allows the convenient consideration of irreversible deformations, when cyclic loading is of interest, without changing the nature of the original orthotropic continuum damage model.

The effective stress tensor is decomposed into a tensile $\bar{\boldsymbol{\sigma}}^+$ and a compressive part $\bar{\boldsymbol{\sigma}}^-$. Such tensors are respectively defined in a similar way to Faria et al. [124] and Pelà [292] as

$$\bar{\boldsymbol{\sigma}}^+ = \boldsymbol{P}^+ : \bar{\boldsymbol{\sigma}} \tag{3.3a}$$

$$\bar{\boldsymbol{\sigma}}^- = \bar{\boldsymbol{\sigma}} - \bar{\boldsymbol{\sigma}}^+ = \boldsymbol{P}^- : \bar{\boldsymbol{\sigma}} \tag{3.3b}$$

where $\boldsymbol{P}^+$ and $\boldsymbol{P}^-$ are projection tensors with the following form

$$\boldsymbol{P}^+ = \sum_{i=1} H[\bar{\sigma}_i]\, \boldsymbol{p_{ii}} \otimes \boldsymbol{p_{ii}} \tag{3.4a}$$

$$\boldsymbol{P}^- = \boldsymbol{I} - \boldsymbol{P}^+. \tag{3.4b}$$

and the symmetric tensor $\boldsymbol{p_{ij}}$ is defined as

$$\boldsymbol{p_{ij}} = \boldsymbol{p_{ji}} = \frac{1}{2}\left(\mathbf{n_i} \otimes \mathbf{n_j} + \mathbf{n_j} \otimes \mathbf{n_i}\right). \tag{3.5}$$

In the above, $H[\bar{\sigma}_i]$ denotes the Heaviside step function ($H[x] = 1$ for $x \geq 0$ or $H[x] = 0$ for $x < 0$) computed for the ith eigenvalue of the elastic stress tensor σ_i and $\mathbf{n_i}$ is the corresponding normalized eigenvector. Finally, $\otimes$ corresponds to the tensor product.

Two internal damage indices are introduced denoting the tensile d^+ and the compressive d^- damage. Their values vary between 0 and 1, referring to an undamaged and a fully damaged state, respectively. The constitutive relation can now be defined as

$$\boldsymbol{\sigma} = (1 - d^+)\, \bar{\boldsymbol{\sigma}}^+ + (1 - d^-)\, \bar{\boldsymbol{\sigma}}^-. \tag{3.6}$$

The split of the effective stress tensor into a tensile and a compressive part, as well as the use of the two distinct damage indices $d^{\pm}$ aim to the application of different damage criteria under tensile and compressive stress states. This strategy permits the simulation of materials with different behaviour under tensile and compressive loading conditions, such as concrete, stone or masonry. Additionally, this choice allows to account for stiffness recovery upon load reversal in tension-compression loading cycles. This phenomenon, known as *unilateral effect*, is crucial for seismic analysis [76, 125], which is one of the objectives of this thesis.

The constitutive law can be expressed as a function of the secant matrix by substituting the tensile and compressive effective stress tensors of Eq. (3.3) into Eq. (3.6) as presented

in [295]

$$\boldsymbol{\sigma} = (\boldsymbol{I} - \boldsymbol{D}) : \boldsymbol{C_0} : \boldsymbol{\varepsilon}^e \tag{3.7}$$

where $\boldsymbol{I}$ is the identity tensor and $\boldsymbol{D}$ a function of the projection tensors $\boldsymbol{P}^+$ and $\boldsymbol{P}^-$ as well as the damage indices d^+ and d^-

$$\boldsymbol{D} = d^+ \boldsymbol{P}^+ + d^- \boldsymbol{P}^- \tag{3.8}$$

The elastic secant stiffness matrix, which will be used in this thesis within a secant scheme for the solution of the non-linear algebraic equations, can then be written as

$$\boldsymbol{C}_s = (\boldsymbol{I} - \boldsymbol{D}) : \boldsymbol{C_0}. \tag{3.9}$$

The selection of the secant matrix aims to enhance the stability of the numerical solution. The loss of the convergence rate, stemming from this choice instead of the use of a tangent stiffness matrix, will be partially overcome using a line search procedure during the numerical iterations.

3.3 Damage criteria

Loading, unloading and reloading conditions are distinguished with the use of two scalar positive quantities, one for tension τ^+ and a second for compression τ^-, termed as equivalent stresses. Their values are defined according to the functions proposed by Petracca et al. [299, 300]

$$\tau^+ = H_0 \left[\bar{\sigma}_{max}\right] \left[\frac{1}{1-a}\left(a\,\bar{I}_1 + \sqrt{3\,\bar{J}_2} + b\,\langle\bar{\sigma}_{max}\rangle\right)\frac{f^+}{f^-}\right] \tag{3.10}$$

$$\tau^- = H_0 \left[-\bar{\sigma}_{min}\right] \left[\frac{1}{1-a}\left(a\,\bar{I}_1 + \sqrt{3\,\bar{J}_2} + \kappa_1\,b\,\langle\bar{\sigma}_{max}\rangle\right)\right] \tag{3.11}$$

$$a = \frac{\left(f_b^-/f^-\right) - 1}{2\left(f_b^-/f^-\right) - 1} \tag{3.12}$$

$$b = (1-a)\,\frac{f^-}{f^+} - (1+a)\,. \tag{3.13}$$

In the above, f^+ and f^- stand for the tensile and compressive uniaxial strengths respectively and f_b^- for the biaxial compressive strength. $\bar{I}_1$ is the first invariant of the

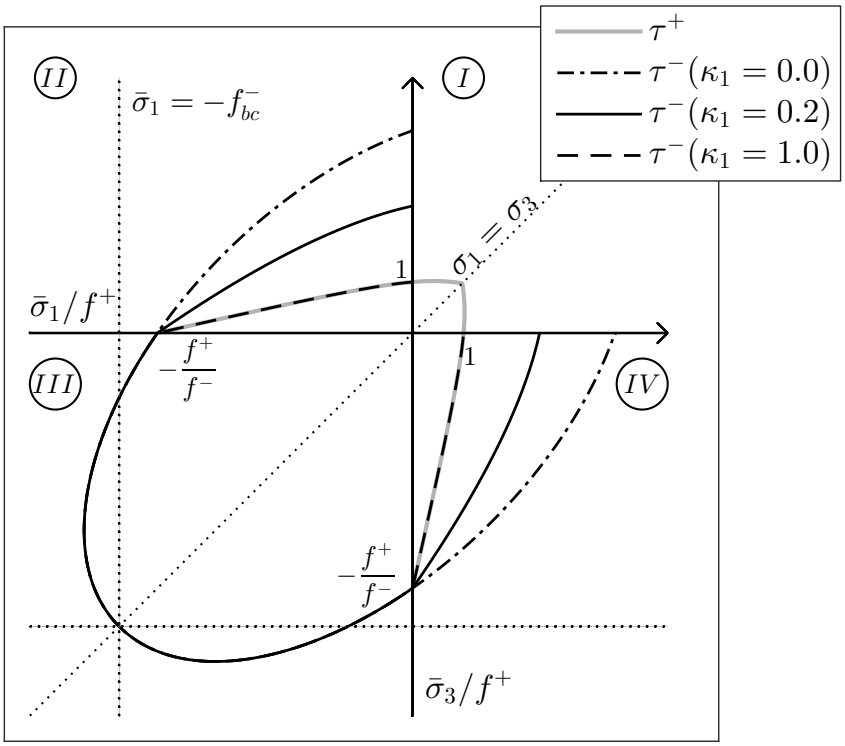

Figure 3.1 Effect of the τ^- function to the shape of the d^- failure surface in the shear quadrants for the plane stress case.

effective stress tensor and $\bar{J}_2$ the second invariant of the deviatoric effective stress tensor. Finally, $\bar{\sigma}_{max}$ and $\bar{\sigma}_{min}$ designate the maximum and minimum principal effective stresses respectively. The specific Heaviside function H_0 is defined as

$$H_0[x] = \begin{cases} 1 & if \;\; x > 0 \\ 0 & if \;\; x \leq 0. \end{cases} \tag{3.14}$$

Function H_0 is used in Eqs. (3.10, 3.11) to activate the τ^+ for tensile and shear stress states (I, II and IV quadrants in Fig. 3.1), and the τ^- for compressive and shear stress states (II, III and IV quadrants in Fig. 3.1).

The κ_1 variable in Eq. (3.11) was introduced by Petracca et al. [299,300] to control the shape of the compressive damage surface in the shear quadrants (II and IV in Fig. 3.1), and through this the dilatant behaviour of the material under shear stress states. Its value varies between 0 (i.e. the Drucker-Prager criterion) and 1 (i.e. the criterion proposed by Lubliner et al. [209]), with lower values resulting in higher dilatancy (see [302]).

Fig. 3.1 presents the shape of the damage surfaces, for the plane stress case, obtained through the definitions of Eqs. (3.10, 3.11) for different values of κ_1. Note that κ_1 affects the shape of the compressive damage surface only at the shear quadrants, while $\tau^{\pm}$ surfaces at the tensile and compressive quadrants remain unaltered.

Two additional internal variables r^+ and r^- are introduced representing the stress thresholds and thus the damage history under tension and compression, respectively.

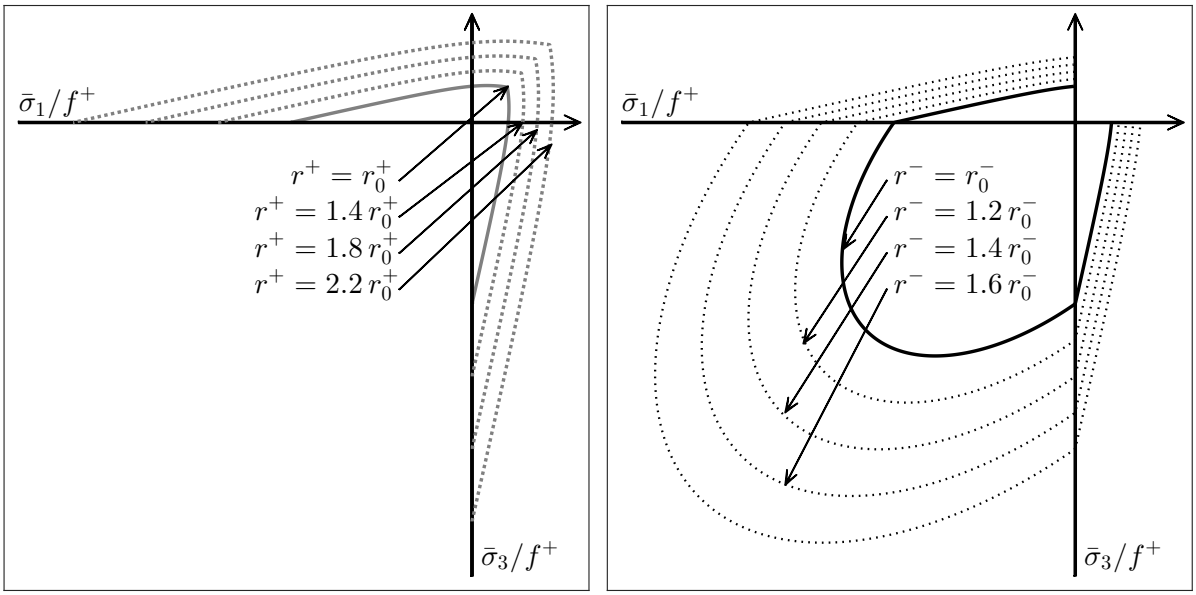

(a) **(b)**

Figure 3.2 Evolution of the stress threshold and the respective damage surfaces for increasing damage and $\kappa_1 = 1.0$: (a) r^+ and (b) r^-.

Their initial values are equal to the uniaxial tensile and compressive strength at the moment of damage initiation. For compression, if hardening occurs before the peak strength, then $r_0^- = f_0^-$, with f_0^- denoting the strength at the onset of hardening (see Section 3.5). If no hardening is considered then $r_0^- = f^-$, and f^- is the uniaxial compressive strength. The tensile threshold is equal to the uniaxial tensile strength $r_0^+ = f^+$, since no hardening is considered under tensile loading (see Section 3.5). After damage is triggered, both thresholds become equal to the maximum attained values by the equivalent stresses $\tau^\pm$ and can be explicitly computed for a generic time instant t as

$$r_t^\pm = \max\left[r_0^\pm, \max_{i\,\in\,(0,t)}\left(\tau_i^\pm\right)\right]. \tag{3.15}$$

Fig. 3.2 illustrates the evolution of the tensile r^+ and compressive r^- stress thresholds for different times instances with increasing damage. The area bounded by $r^\pm$ is the area of admissible effective stresses not inducing damage evolution. If the effective stresses, during the new time/load increment do not fall within this area, there will be an increase of the r^+ and/or r^- (depending on the effective stress state) and a respective damage evolution with an expansion of the damage surfaces in the effective stress space shown by the dotted lines in Fig. 3.2.

Following the above, the damage criteria for tension Φ^+ and compression Φ^- are introduced as

$$\Phi^\pm(r^\pm, \tau^\pm) = \tau^\pm - r^\pm \leq 0. \tag{3.16}$$

3.4 A continuum damage model with irreversible strains

The chosen definitions of the effective stresses in Eq. (3.1) and the split of the total strains in Eq. (3.2) allow to conveniently consider the effect of irreversible strains by treating them as an internal variable. This approach was introduced by Faria and Oliver [122] for the efficient simulation of irreversible deformations occurring in large concrete structures under cyclic loading [121–123, 125]. This work follows the same approach with the irreversible strains considered as an internal variable computed through a novel evolution law compared to the one used in the aforementioned works. The new formulation aims to overcome the difficulty in the calibration of the user-defined parameter presented in the model of Faria et al. [122, 123].

The section is composed by two parts. In the first one the formulation of Faria et al. [122,123] is revisited. Basing on its advantages and aiming to overcome its limitations, the second part of this section presents the novel formulation for the evolution of the irreversible strains.

Note that in the following the irreversible strains are designated as $\boldsymbol{\varepsilon}^i$ instead of $\boldsymbol{\varepsilon}^p$. This choice aims to make a distinction of the current model, which is based exclusively on the theory of continuum damage mechanics, with relative formulations combining both damage and plasticity theories as in [190, 209, 399] among others.

3.4.1 Irreversible strain evolution law by Faria & Oliver 1993

The evolution law for the irreversible strains is defined by Faria et al. [122, 123] as

$$\dot{\boldsymbol{\varepsilon}}^i = \beta\, E\, H[\dot{d}^-]\, \frac{\langle \bar{\boldsymbol{\sigma}} : \dot{\boldsymbol{\varepsilon}} \rangle}{\bar{\boldsymbol{\sigma}} : \bar{\boldsymbol{\sigma}}}\, \boldsymbol{C_0}^{-1} : \bar{\boldsymbol{\sigma}} \tag{3.17}$$

where E denotes the Young's modulus and $\beta \geq 0$ is a material parameter that defines the magnitude of the rate of the irreversible strains. The Heaviside step function couples the evolution of the irreversible strains with that of the compressive damage. In this way, there is no evolution of $\boldsymbol{\varepsilon}^i$ during unloading and reloading or before reaching the initial compressive threshold, i.e. for cases when $\Phi^- < 0$. The use of the Macaulay brackets ensures a non-negative dissipation, posing, however, a restriction on the evolution of the irreversible strains in cases where the product of the effective stresses and the increment of the total strains might be negative.

As noted by Faria et al. [123] the above definition aims to account for the irreversible strains in a computationally efficient way that fits in the purpose of large time consuming seismic analysis. Contrary to plasticity or plastic-damage models, the definition of a flow rule is absent, and the physical direction of the irreversible deformations coincides with that of the elastic strain tensor $\boldsymbol{\varepsilon}^e = \boldsymbol{C_0}^{-1} : \bar{\boldsymbol{\sigma}}$.

Another difference with classical plasticity concerns the unloading modulus. In this model, unloading occurs according to a damaged modulus, which is an improvement compared to plasticity models, where the elastic modulus is used during the unloading.

The scalar parameter $\beta \geq 0$ controls the rate of the irreversible deformation. For $\beta = 0$ an elastic-damage material is recovered, and the effect of the irreversible deformations is disregarded. The definition of Eq. (3.17) makes, however, laborious the evaluation of the upper bound of β, which actually depends on the Poisson's ratio and the loading scenario, as demonstrated in the following.

An insight of the range of variation of β is possible by considering some basic loading scenarios at material level. Let us consider first a uniaxial compressive loading case with the following strain state ($\varepsilon_{xx} = 0$, $\varepsilon_{yy} < 0$, $\gamma_{xy} = 0$) in plane stress conditions. For Poisson's ratio equal to zero ($\nu = 0$), the stress and strain state can be represented using Voigt's notation as $\boldsymbol{\varepsilon} = [0 \ \varepsilon_{yy} \ 0]$, $\bar{\boldsymbol{\sigma}} = [0 \ \bar{\sigma}_{yy} \ 0]$ and $\Delta\boldsymbol{\varepsilon} = [0 \ \Delta\varepsilon_{yy} \ 0]$. Under these conditions, and considering increasing damage (i.e. $H[\dot{d}^-] = 1$), the only non-zero incremental component of the irreversible strains tensor is, according to Eq. (3.17),

$$\Delta\varepsilon^i_{yy} = \beta\, E\, H[\dot{d}^-]\, \frac{\langle \bar{\sigma}_{yy}\, \Delta\varepsilon_{yy} \rangle}{\bar{\sigma}_{yy}\, \bar{\sigma}_{yy}}\, \varepsilon_{yy} \tag{3.18a}$$

$$= \beta\, \Delta\varepsilon_{yy} \tag{3.18b}$$

For this particular case, β determines the irreversible fraction of the total strain increment and its range of values lies between 0 and 1. For $\beta = 1$ the total strain increment will be irreversible, i.e. $\Delta\boldsymbol{\varepsilon}^e = 0$, while for $\beta = 0$ the total strain increment will be considered as elastic $\Delta\boldsymbol{\varepsilon}^e = \Delta\boldsymbol{\varepsilon}$.

Let us consider now the same uniaxial compressive test but with Poisson's ratio $\nu \neq 0$. The stress and strain states now are $\boldsymbol{\varepsilon} = [0 \ \ \varepsilon_{yy} \ \ 0]$, $\bar{\boldsymbol{\sigma}} = [\nu\, \bar{\sigma}_{yy} \ \ \bar{\sigma}_{yy} \ \ 0]$ and the incremental strains are $\Delta\boldsymbol{\varepsilon} = [0 \ \ \Delta\varepsilon_{yy} \ \ 0]$. The only non-zero component of the irreversible strains is now

$$\Delta\varepsilon^i_{yy} = \beta\, \frac{1 - \nu^2}{1 + \nu^2}\, \Delta\boldsymbol{\varepsilon}_{yy}. \tag{3.19}$$

The use of a non-zero value for the Poisson's ratio changes the possible ranges of values for β. In this case, a value of $\beta \geq 1$ is necessary to get $\Delta\varepsilon^i_{yy} = \Delta\boldsymbol{\varepsilon}_{yy}$.

A third case is investigated, with a pure shear distortion strain state ($\varepsilon_{xx} = 0$, $\varepsilon_{yy} = 0$, $\gamma_{xy} \neq 0$). For $\nu = 0$, the stress and strain states will be $\boldsymbol{\varepsilon} = [0 \ \ 0 \ \ \gamma_{xy}]$, $\bar{\boldsymbol{\sigma}} = [0 \ \ 0 \ \ \bar{\sigma}_{xy}]$ and

Table 3.1 Range of β for different loading scenarios and Poisson's ratio according to the model for inelastic strains proposed by Faria & Oliver [122].

Cases	Uniaxial Compression $\nu = 0$	Uniaxial Compression $\nu \neq 0$	Simple shear $\nu = 0$
$\Delta\boldsymbol{\varepsilon}$	$[0 \;\; \Delta\boldsymbol{\varepsilon}_{yy} \;\; 0]$	$[0 \;\; \Delta \;\; \boldsymbol{\varepsilon}_{yy} 0]$	$[0 \;\; 0 \;\; \Delta\gamma_{xy}]$
$\Delta\boldsymbol{\varepsilon}^i$	$[0 \;\; \beta\Delta\boldsymbol{\varepsilon}_{yy} \;\; 0]$	$[0 \;\; \beta \frac{1-\nu^2}{1+\nu^2} \Delta\boldsymbol{\varepsilon}_{yy} \;\; 0]$	$[0 \;\; 2\,\beta\,\Delta\gamma_{xy} \;\; 0]$
Range of β	$0 \leq \beta \leq 1$	$0 \leq \beta \leq \frac{1+\nu^2}{1-\nu^2}$	$0 \leq \beta \leq 2$

$\Delta\boldsymbol{\varepsilon} = [0 \;\; 0 \;\; \Delta\gamma_{xy}]$, resulting in the following increment of the irreversible strains

$$\Delta\gamma^i_{xy} = \beta\, E\, H(\dot{d}^-)\, \frac{\langle \bar{\sigma}_{xy}\, \Delta\gamma_{xy} \rangle}{\bar{\sigma}_{xy}\, \bar{\sigma}_{xy}} \gamma_{xy} \tag{3.20a}$$

$$= \beta\, \frac{E\gamma_{xy}}{\bar{\sigma}_{xy}}\, \Delta\gamma_{xy} \tag{3.20b}$$

$$= 2\,\beta\,\Delta\gamma_{xy} \tag{3.20c}$$

which implies that β in this case can vary between 0 and 0.5, with the first case giving zero irreversible strains and the latter zero elastic strains.

The above examples, summarized in Table (3.1), demonstrate that the range of variation of β depends on the loading state, as well as on the Poisson's ratio. The former implies that β varies according to the expected stress state driving the damage and the simulated material. The above characteristic of Eq. (3.17) hampers its use in the simulation of seismic loading of masonry structures, which can result in damage due to both shear and compression stress states.

3.4.2 A novel evolution law for irreversible strains*

Despite the attractive simplicity of the evolution law presented in Eq. (3.17), it has been shown in Section 3.4.1 that there is a difficulty in the control of the magnitude of the irreversible strains through the use of β parameter. Here, we propose a novel formulation for the evolution of the irreversible strains, in which there is an explicit control of the increment of the irreversible strains through a single scalar parameter, for which the notation β is maintained. The underlying idea is that of expressing the increment of inelastic deformation as a function of β and two scalar internal variables instead of the stress and strain tensors as performed in [122, 123]. These internal variables are the stress threshold, for which a new function is proposed, and a new internal variable representing the stress threshold in the new time/load increment at the absence of irreversible strains.

*This section is based on a section of Reference [326]

In the following, the procedure for deriving such formulation is presented in an incremental way. The symbol "Δ" denotes the increment of a specific quantity from time step n to n+1. For the sake of simplicity, the indices $(\pm)$ are dropped as the approach can be equally applied for the tension or compression variables.

Let us assume that the new time step $n+1$ in an incremental numerical analysis is characterized by an increment on the total strains $\Delta\boldsymbol{\varepsilon}_{n+1}$. We define $\tilde{\bar{\boldsymbol{\sigma}}}$ as the effective stresses in the absence of increment of irreversible strains at time step $n+1$ as

$$\tilde{\bar{\boldsymbol{\sigma}}}_{n+1} = (\bar{\boldsymbol{\sigma}}|_{\Delta\boldsymbol{\varepsilon}^i=0})_{n+1} = \bar{\boldsymbol{\sigma}}_n + \boldsymbol{C_0} : \Delta\boldsymbol{\varepsilon}_{n+1}. \tag{3.21}$$

The corresponding equivalent stresses $\tau(\tilde{\bar{\boldsymbol{\sigma}}})$ can be computed as a function of the effective stresses using Eqs. (3.10, 3.11) and the corresponding threshold $r(\tilde{\bar{\boldsymbol{\sigma}}})$ in a manner analogous to Eq. (3.15) as

$$r(\tilde{\bar{\boldsymbol{\sigma}}}_{n+1}) = \max\left[r_n, \tau(\tilde{\bar{\boldsymbol{\sigma}}}_{n+1})\right]. \tag{3.22}$$

The increment of the stress threshold in the absence of an increment in the irreversible strains is

$$\Delta r^{max}_{n+1} = r(\tilde{\bar{\boldsymbol{\sigma}}}_{n+1}) - r_n \geq 0 \tag{3.23}$$

where the superscript max has been used to denote that Δr^{max}_{n+1} represents the maximum value that the actual stress threshold increment Δr_{n+1} can take for the case with $\Delta\boldsymbol{\varepsilon}^i = 0$. Note that Δr^{max}_{n+1} is always non-negative due to the definition of $r(\tilde{\bar{\boldsymbol{\sigma}}}_{n+1})$ in Eq. (3.22) as a monotonic function with lower bound the r_n.

Let us assume now that a part of the total strains is irreversible. Considering the definitions for effective stresses (in Eq. (3.1)) and the elastic strains (in Eq. (3.2)), the increment of the effective stresses will be smaller than that of $\tilde{\bar{\boldsymbol{\sigma}}}_{n+1}$. In the same manner, the increment of the stress threshold at the generic step ($\Delta r_{n+1} = r_{n+1} - r_n$) will be also smaller than Δr^{max}_{n+1}. Therefore, this increment can be expressed as

$$\Delta r_{n+1} = (1-\beta)\,\Delta r^{max}_{n+1} \tag{3.24}$$

with $\beta = [0, 1]$. Parameter β determines explicitly the magnitude of the stress threshold increment, and consequently, as will be shown later, the incremental elastic and irreversible strains for the current step of the analysis. The actual stress threshold at $n+1$

can be computed considering that $\Delta r_{n+1} = r_{n+1} - r_n$ along with Eq. (3.24)

$$
\begin{aligned}
r_{n+1} &= r_n + \Delta r_{n+1} && \text{(3.25a)}\\
&= r_n + (1-\beta)\,\Delta r_{n+1}^{max} && \text{(3.25b)}\\
&= r_n + (1-\beta)\,(r(\tilde{\tilde{\boldsymbol{\sigma}}}_{n+1}) - r_n) && \text{(3.25c)}\\
&= (1-\beta)\,r(\tilde{\tilde{\boldsymbol{\sigma}}}_{n+1}) + \beta\, r_n && \text{(3.25d)}\\
&= \left[1 - \beta\left(1 - \frac{r_n}{r(\tilde{\tilde{\boldsymbol{\sigma}}}_{n+1})}\right)\right] r(\tilde{\tilde{\boldsymbol{\sigma}}}_{n+1}) && \text{(3.25e)}\\
&= \lambda\, r(\tilde{\tilde{\boldsymbol{\sigma}}}_{n+1}) && \text{(3.25f)}
\end{aligned}
$$

with the scalar λ being a scaling factor equal to

$$
\lambda = 1 - \beta\left(1 - \frac{r_n}{r(\tilde{\tilde{\boldsymbol{\sigma}}}_{n+1})}\right). \tag{3.26}
$$

Owing to the chosen definitions of Eqs. (3.10, 3.11), the equivalent stresses are linearly dependent on the effective stresses, so that

$$
\mu\,\tau(\bar{\boldsymbol{\sigma}}) = \tau(\mu\,\bar{\boldsymbol{\sigma}}) \tag{3.27}
$$

for any scalar μ. The same holds for the stress thresholds (see Eq. (3.15)) yielding

$$
r(\tau(\mu\,\bar{\boldsymbol{\sigma}})) = r(\mu\,\tau(\bar{\boldsymbol{\sigma}})) = \mu\, r(\tau(\bar{\boldsymbol{\sigma}})) \tag{3.28}
$$

The above property allows to perform the desired scaling of the threshold increment, shown in Eq. (3.25f), through the scaling of the effective stresses as

$$
\bar{\boldsymbol{\sigma}}_{n+1} = \lambda\,\tilde{\tilde{\boldsymbol{\sigma}}}_{n+1} \tag{3.29}
$$

A further elaboration of expression (3.29) is possible using expressions in Eqs. (3.2,3.21)

$$
\begin{aligned}
\bar{\boldsymbol{\sigma}}_{n+1} &= \lambda\,(\bar{\boldsymbol{\sigma}}_n + \boldsymbol{C_0} : \Delta\boldsymbol{\varepsilon}_{n+1}) \Rightarrow && \text{(3.30a)}\\
\boldsymbol{C_0} : \boldsymbol{\varepsilon}^e_{n+1} &= \lambda\,(\boldsymbol{C_0} : \boldsymbol{\varepsilon}^e_n + \boldsymbol{C_0} : \Delta\boldsymbol{\varepsilon}_{n+1}) \Rightarrow && \text{(3.30b)}\\
\boldsymbol{\varepsilon}^e_{n+1} &= \lambda\,\boldsymbol{\varepsilon}^e_n + \lambda\,(\Delta\boldsymbol{\varepsilon}^e_{n+1} + \Delta\boldsymbol{\varepsilon}^i_{n+1}) \Rightarrow && \text{(3.30c)}\\
\boldsymbol{\varepsilon}^e_{n+1} &= \lambda\,\boldsymbol{\varepsilon}^e_n + \lambda\,\boldsymbol{\varepsilon}^e_{n+1} - \lambda\,\boldsymbol{\varepsilon}^e_n + \lambda\,\Delta\boldsymbol{\varepsilon}^i_{n+1} \Rightarrow && \text{(3.30d)}\\
\Delta\boldsymbol{\varepsilon}^i_{n+1} &= \frac{1-\lambda}{\lambda}\,\boldsymbol{\varepsilon}^e_{n+1} && \text{(3.30e)}
\end{aligned}
$$

The increment of the irreversible strains can now be obtained substituting Eq. (3.26) into Eq. (3.30e) and making use of Eqs. (3.23, 3.24)

$$
\Delta\boldsymbol{\varepsilon}^i_{n+1} = \beta\,\frac{r(\tilde{\tilde{\boldsymbol{\sigma}}}_{n+1}) - r_n}{r_{n+1}}\,\boldsymbol{\varepsilon}^e_{n+1} \tag{3.31}
$$

Table 3.2 Ranges of β for different loading scenarios and Poisson's ratio according to the proposed model for inelastic strains.

Cases	Uniaxial Compression $\nu = 0$	Uniaxial Compression $\nu \neq 0$	Simple shear $\nu = 0$
$\Delta\boldsymbol{\varepsilon}$	$[0 \;\; \Delta\boldsymbol{\varepsilon}_{yy} \;\; 0]$	$[0 \;\; \Delta \;\; \boldsymbol{\varepsilon}_{yy} 0]$	$[0 \;\; 0 \;\; \Delta\gamma_{xy}]$
$\Delta\boldsymbol{\varepsilon}^i$	$[0 \;\; \beta\Delta\boldsymbol{\varepsilon}_{yy} \;\; 0]$	$[0 \;\; \beta\,\Delta\boldsymbol{\varepsilon}_{yy} \;\; 0]$	$[0 \;\; \beta\,\Delta\gamma_{xy} \;\; 0]$
Range of β	$0 \leq \beta \leq 1$	$0 \leq \beta \leq 1$	$0 \leq \beta \leq 1$

The above definition implies that the direction of the incremental irreversible strains coincides with that of the elastic strains in an analogous manner to the original approach of Faria et al. [122, 123].

An important property of the proposed methodology is its explicit calculation for each new time step. This is due to the definitions chosen for $\tilde{\bar{\boldsymbol{\sigma}}}$ (Eq. 3.21), the effective stresses $\bar{\boldsymbol{\sigma}}$ (3.29) and the stress threshold r (Eq. (3.25f)), which involve parameters that can be calculated from the values of total strains only (see also Section 3.7). The postulation of Eq. (3.24) sets the margins of β strictly between 0 and 1, with the consequent control of the evolution of the irreversible strains. This is illustrated in Table (3.2), presenting the range of variation of β for the three different basic stress states studied before, but using now expression (3.31) and the irreversible strains driven by the compressive entities (i.e. compressive stress thresholds and equivalent stresses have been used in Eqs. (3.22-3.31)) and the parameter $\kappa_1 = 1.0$ in Eq. (3.11). For all the cases, the scaling of the incremental irreversible strains can be properly defined through β, with $\beta = 0$ resulting to zero increment of the irreversible strains, and $\beta = 1$ to zero increment of the stress threshold and thus null incremental elastic strains. Figure (3.3) illustrates the effect of β for the third loading case with simple shear distortion, in which it is possible to visualize the role of $\tilde{\bar{\boldsymbol{\sigma}}}$ and the scaling of the effective stresses through Eq. (3.29).

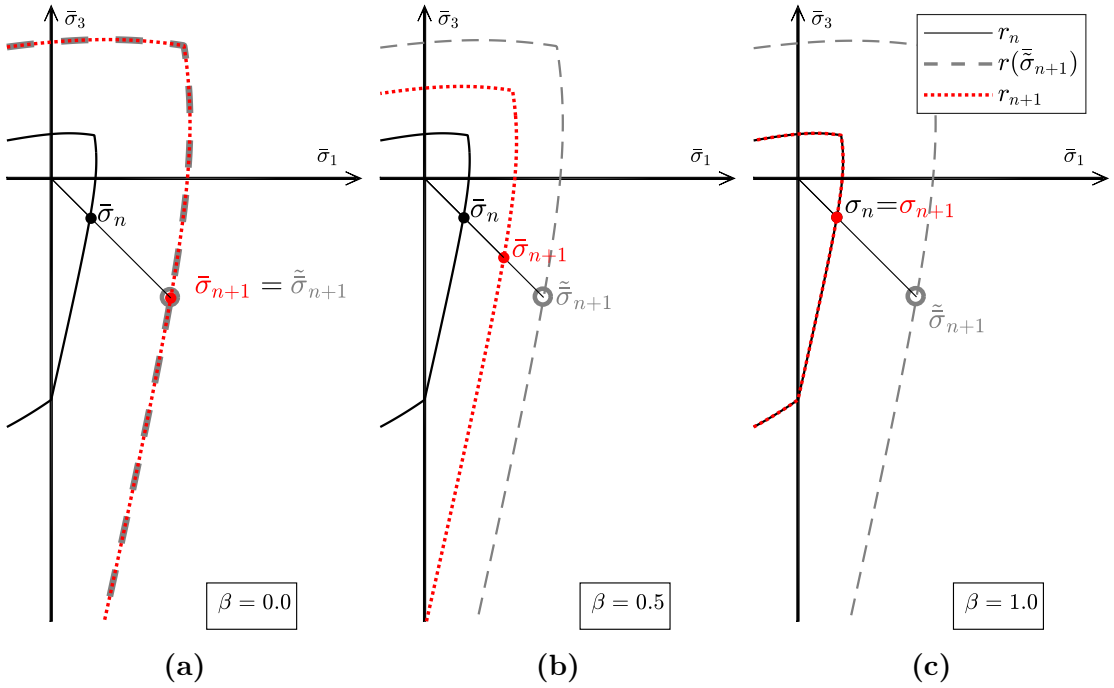

Figure 3.3 Effect of the β parameter to the evolution of the effective stresses and damage surfaces according to the proposed model for inelastic strains: (a) $\beta = 0.0$, (b) $\beta = 0.5$, (c) $\beta = 1.0$.

3.5 Damage variables

The damage indices in the constitutive equation (3.6) are explicitly defined as functions of the stress thresholds, i.e. $d^{\pm} = d^{\pm}(r^{\pm})$. Both are monotonically increasing functions varying from 0 for intact material to 1 for a completely damaged material. Tensile damage is characterized by an exponential softening function according to Oliver et al. [258], triggered after reaching the uniaxial tensile strength $r_0^+ = f^+$ and varying thereafter according to

$$d^+ = 1 - \frac{r_0^+}{r^+} \exp\left\{ 2H_d^+ \left(\frac{r_0^+ - r^+}{r_0^+} \right) \right\} \qquad r^+ \geq r_0^+ . \tag{3.32}$$

Fig. 3.4 illustrates the stress-strain relationship using the proposed constitutive model and the above expression for d^+ for an uniaxial tensile test.

Compressive damage is defined according to the expressions proposed by Cervera in [66] and is composed by two parts. The first part occurs for stress thresholds from r_0^- to r_p and is defined through the parabolic hardening law

$$d^- = A_d \frac{r_e}{r^-} \left(\frac{r^- - r_0^-}{r_p - r_0^-} \right)^2 \qquad r_0^- \leq r^- \leq r_p \tag{3.33}$$

where,

$$A_d = \frac{r_p - r_e}{r_e} \tag{3.34}$$

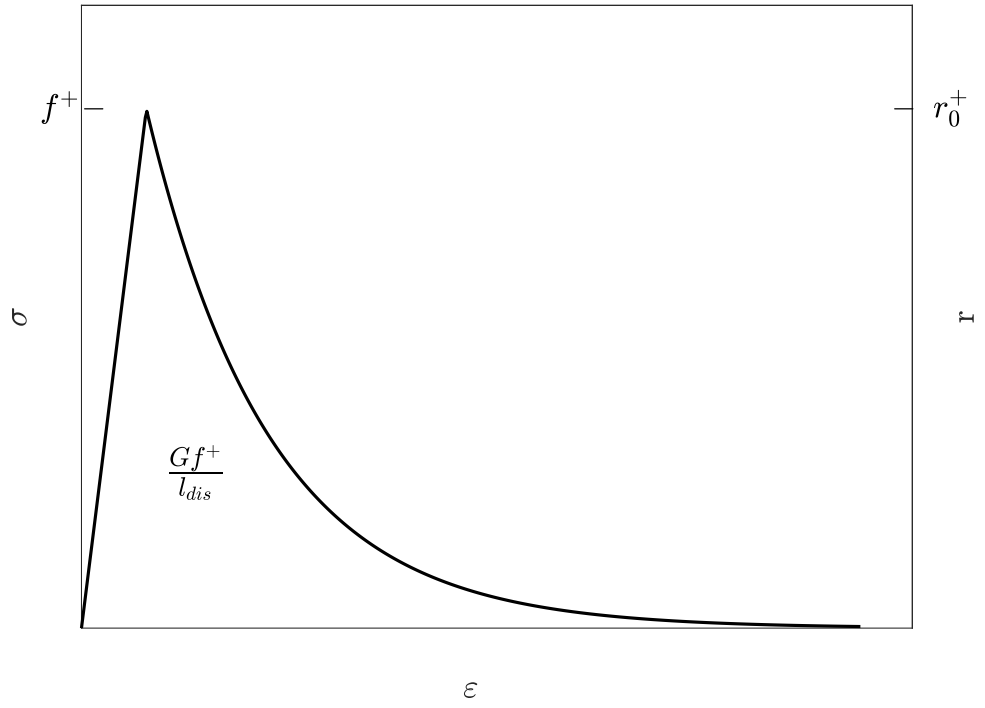

Figure 3.4 Exponential softening law for tensile damage.

The stress threshold $r_0^- = f_0^-$ corresponds to the bounding damage surface for the onset of damage and the $r_p = f_p$ to the bounding damage surface at peak compressive strength, while $r_e = f^-$. Such surfaces are represented in Fig. 3.5.

The second part occurs for stress thresholds greater than r_p, for which an exponential softening law is considered

$$d^- = 1 - \frac{r_e}{r^-} \exp\left\{2H_d^- \left(\frac{r_p^- - r^-}{r_e^-}\right)\right\} \qquad r^- \geq r_p. \tag{3.35}$$

Fig. 3.6 presents an example of the compressive uniaxial law described by Eqs. (3.33) to (3.35).

Tension and compression evolution laws consider respectively the positive G_f^+ and negative G_f^- fracture energies, as well as the characteristic finite element width l_{dis}, through the corresponding discrete softening parameter $H_d^\pm$ ensuring mesh-size independent energy dissipation according to the crack-band theory [28, 251]. As will be shown in Section 3.6, energy is dissipated due to the evolution of both damage and irreversible strains. These two contributions to the dissipated energy are considered in this thesis through the proposal of two novel expressions for the discrete softening parameters. For the case of tensile damage this is (see Appendix A)

$$\frac{1}{H_d^+} = (1-\beta)\,\frac{l_{mat}^+ - l_{dis}}{l_{dis}}. \tag{3.36}$$

For the case of compressive damage, the discrete softening parameter H_d^- is defined

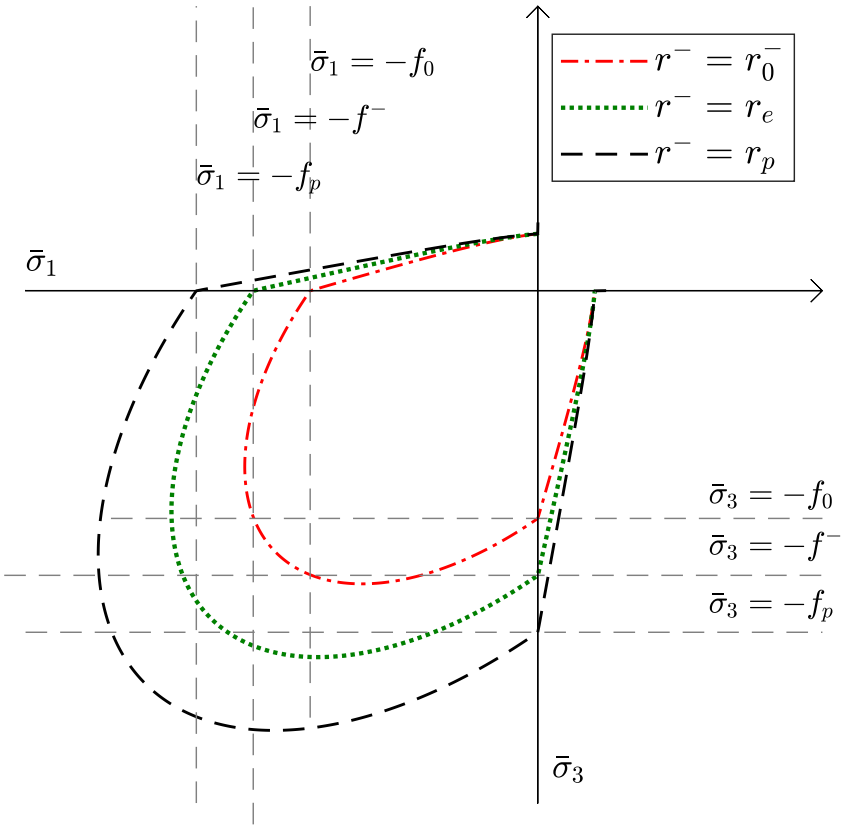

Figure 3.5 Bounding damage surfaces r_0 and r_p for damage under compression.

as (see Appendix A)

$$\frac{1}{H_d^-} = (1-\beta)\left(\frac{l_{mat}^-}{l_{dis}} - \tilde{A}_d - \frac{r_p}{r_e} - \frac{\beta}{1-\beta} B_d\right) \tag{3.37}$$

where

$$\tilde{A}_d = \frac{A_d\,(r_p^3 - 3\,r_p\,r_0^2 + 2\,r_0^3)}{3\,r_e(r_p - r_0^-)^2} \tag{3.38}$$

$$B_d = \frac{(r_p - r_0^-)(3\,r_p - 2\,A_d\,r_e + 3\,r_0^-)}{3\,r_e^2}. \tag{3.39}$$

Note that for $r_0^- = r_e = r_p$ exponential softening starts immediately after reaching the peak compressive strength and the discrete softening modulus is equivalent to the tensile one

$$\frac{1}{H_d^-} = (1-\beta)\,\frac{l_{mat}^- - l_{dis}}{l_{dis}}. \tag{3.40}$$

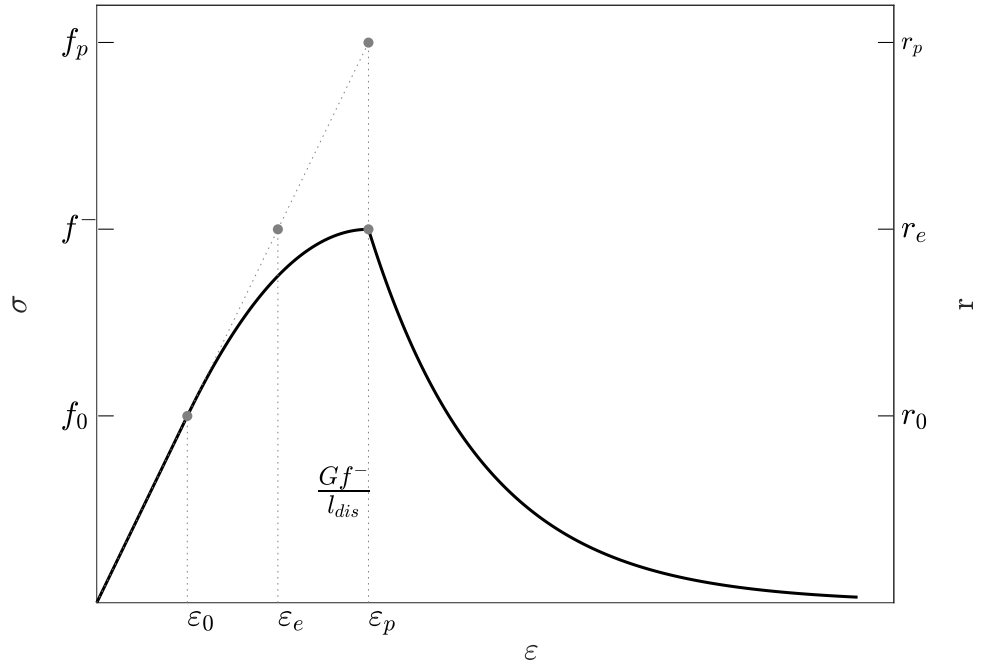

Figure 3.6 Uniaxial law for compressive damage d^-

In the above, the material characteristic length for tension and compression is defined

$$l_{mat}^{\pm} = \frac{2EG_f^{\pm}}{(f^{\pm})^2}. \tag{3.41}$$

It is noted that the above expressions of the discrete softening parameters vary from the original ones presented in [66] due to the presence of the β parameter used for the definition of the irreversible deformations in Eq. (3.31). In this way, the softening response is regularised according to the selected value of β by considering the contributions to the dissipated energy of both the evolution of the irreversible strains and the compressive damage (see Appendix A).

The effect of the new proposed functions is illustrated in Fig. 3.7 presenting a cyclic uniaxial tensile test (Figs. 3.7a & c) and a cyclic uniaxial compressive test (Figs. 3.7b & d) using the proposed discrete softening parameters of Eqs. (3.36) and (3.37) and those presented in [66] which correspond to $\beta = 0$. Figs. 3.7a and 3.7b demonstrate that the use of the new softening modulus results in a consistent energy dissipation according to the input value of Gf^- independently of the choice of β.

Note that all the parameters included in the presented constitutive model can be defined through uniaxial tensile and compressive tests. The first is sufficient to define the tensile strength of the material f^+ and the tensile fracture energy G_f^+ necessary for the definition of the tensile softening law of Eq. (3.32). The stress-strain relationship of the uniaxial compressive test will define f_0^- as the stress at the initiation of the hardening during the ascending loading path, f^- as the maximum compressive strength, whereas $f_p = E\,\boldsymbol{\varepsilon}_p$ where E is the elastic modulus and $\boldsymbol{\varepsilon}_p$ the strain at the beginning of the softening

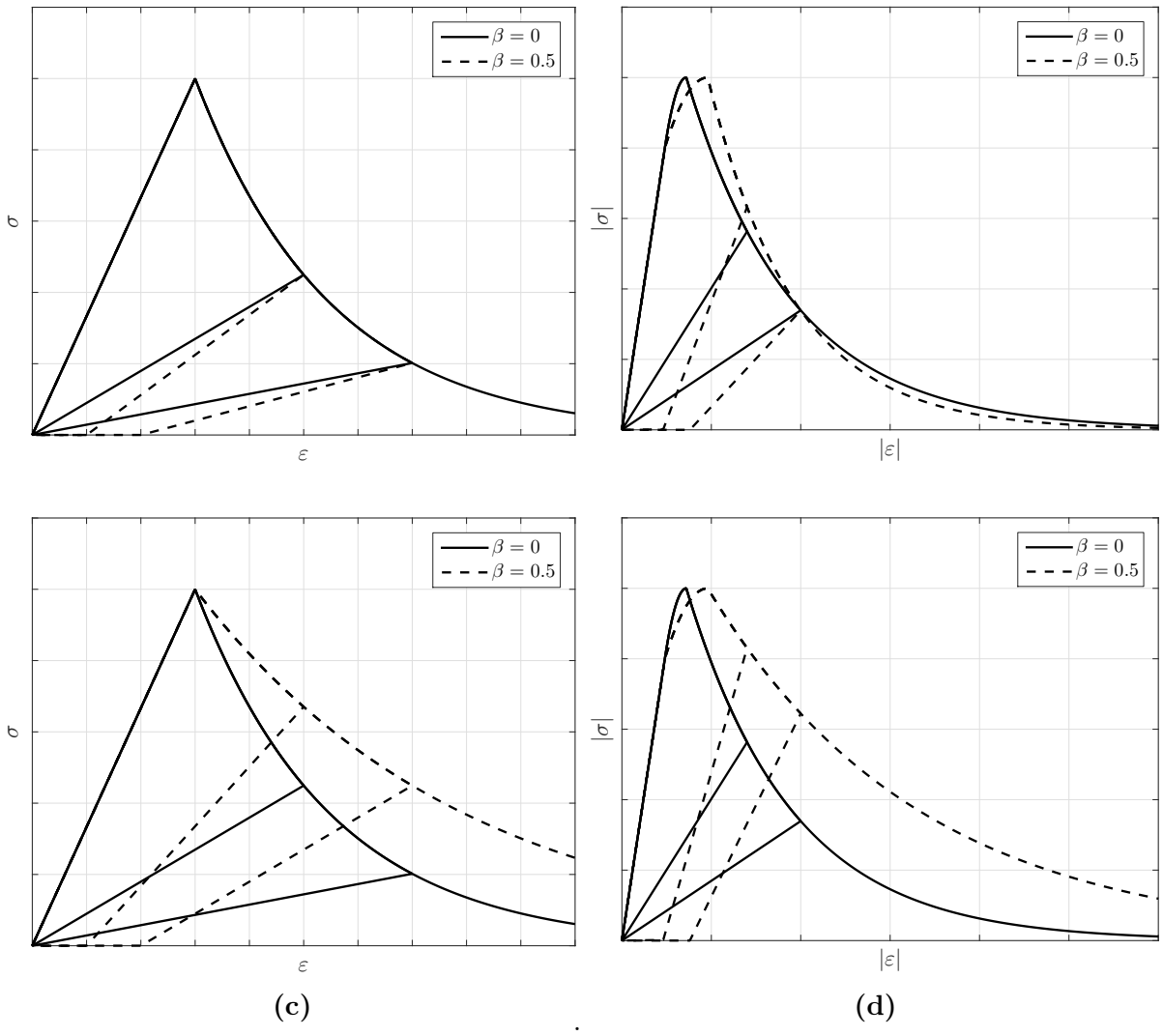

Figure 3.7 Effect of the discrete softening modulus in the dissipated energy. Case with the proper regularization of the softening modulus presented in Eqs. (3.36), (3.37): (a) uniaxial cyclic tensile test, (b) uniaxial cyclic compressive test. Case without the proper regularization of the softening modulus: (c) uniaxial cyclic tensile test, (d) uniaxial cyclic compressive test

(see Fig. 3.6). Similarly to the tensile test, the area under the stress displacement curve can be associated with the compressive fracture energy G_f^-. If irreversible strains are considered, then these tests need to be cyclic, in order to capture the level of irreversible strains during the unloading cycles.

Finally, the characteristic length is calculated according to the finite elements size in order to ensure size independent energy dissipation. In this work, constant strain triangular elements will be used with $l_{dis} = \sqrt{A_{fe}}$ and A_{fe} representing the area of the finite element. This is a standard procedure which can be refined to consider the crack direction and the finite element size according to [67, 258, 358].

3.6 Thermodynamic admissibility

The rate of the mechanical dissipation γ of the current model is [122]

$$\dot{\gamma} = -\frac{\partial \psi}{\partial d^+}\dot{d}^+ - \frac{\partial \psi}{\partial d^-}\dot{d}^- - \frac{\partial \psi}{\partial \boldsymbol{\varepsilon}^i} : \dot{\boldsymbol{\varepsilon}}^i \geq 0 \tag{3.42}$$

where ψ is the Helmholtz free energy and $\psi_0^{\pm}$ elastic free energies having the following form [122]

$$\psi = (1 - d^+)\,\psi_0^+ + (1 - d^-)\,\psi_0^- \tag{3.43}$$

$$\psi_0^+ = \frac{1}{2}\,\bar{\boldsymbol{\sigma}}^+ : \boldsymbol{C}_{\mathbf{0}}^{-1} : \bar{\boldsymbol{\sigma}} \tag{3.44}$$

$$\psi_0^- = \frac{1}{2}\,\bar{\boldsymbol{\sigma}}^- : \boldsymbol{C}_{\mathbf{0}}^{-1} : \bar{\boldsymbol{\sigma}}. \tag{3.45}$$

It is possible to distinguish two parts that contribute to the total dissipation in Eq. (3.42). The first concerns the dissipation due to the damage evolution, with a rate defined as $\dot{\gamma}^d$ and the second due to the evolution of the irreversible strains, which is similarly defined as $\dot{\gamma}^i$. These contributions can be presented as

$$\dot{\gamma}^d = -\frac{\partial \psi}{\partial d^+}\,\dot{d}^+ - \frac{\partial \psi}{\partial d^-}\,\dot{d}^- \tag{3.46a}$$

$$\dot{\gamma}^i = -\frac{\partial \psi}{\partial \boldsymbol{\varepsilon}^i} : \dot{\boldsymbol{\varepsilon}}^i. \tag{3.46b}$$

According to the second law of thermodynamics, the rate of the energy dissipation $\dot{\gamma}$ must be non-negative to ensure the irreversibility of the damage process. As the presented model can simply vary through the definition of one scalar from an elastic-damage model to an elastic-damage model with irreversible deformations, the above condition must hold for both cases. This means that both $\dot{\gamma}^d$ and $\dot{\gamma}^i$ should be always non-negative.

Let us begin with the dissipation rate due to the damage evolution $\dot{\gamma}^d$, for which the following procedure has been presented in [123] and is repeated here for the sake of completeness.

The partial derivative of the Helmholtz free energy with respect to the damage indices are

$$\frac{\partial \psi}{\partial d^+} = -\psi_0^+ \tag{3.47a}$$

$$\frac{\partial \psi}{\partial d^-} = -\psi_0^- \tag{3.47b}$$

By virtue of the above, $\dot{\gamma}^d$ turns to be

$$\dot{\gamma}^d = \psi_0^+\,\dot{d}^+ + \psi_0^-\,\dot{d}^-. \tag{3.48}$$

A little manipulation of the elastic free energies $\psi_0^{\pm}$, considering the stress split presented in Eqs. (3.3a) and (3.3b) is necessary to show that they always have non-negative values, i.e. $\psi_0^{\pm} \geq 0$ (see [123]). The same holds for the damage indices, which are monotonically increasing functions due their definitions in Eqs. (3.32), (3.33) and (3.35), meaning in fact that damage is irrecoverable $\dot{d}^{\pm} \geq 0$. Following these observations it can be concluded that the rate of the energy dissipation due to the damage evolution is always non-negative

$$\dot{\gamma}^d \geq 0. \tag{3.49}$$

The above result ensures the non-negative dissipation for the considered elastic-damage model. The only task remaining to ensure non-negative dissipation for the generalized case with irreversible deformations is to show that $\dot{\gamma}^i \geq 0$.

Considering the strain split presented in Eq. (3.2), the partial derivative of the Helmholtz free energy with respect to the irreversible strains is

$$\frac{\partial \psi}{\partial \boldsymbol{\varepsilon}^i} = \frac{\partial \psi}{\partial \boldsymbol{\varepsilon}^e} \frac{\partial \boldsymbol{\varepsilon}^e}{\partial \boldsymbol{\varepsilon}^i} = -\frac{\partial \psi}{\partial \boldsymbol{\varepsilon}^e} \tag{3.50}$$

and considering the definition of ψ in Eq. (3.43) we have

$$\frac{\partial \psi}{\partial \boldsymbol{\varepsilon}^e} = (1 - d^+) \frac{\partial \psi_0^+}{\partial \boldsymbol{\varepsilon}^e} + (1 - d^-) \frac{\partial \psi_0^-}{\partial \boldsymbol{\varepsilon}^e} \tag{3.51}$$

Some observations are necessary at this point. The first one concerns the linear dependency between the effective stress tensors and the elastic strains (see Eq. (3.1)), which considering also the stress split of Eqs. (3.3a) and (3.3b) gives

$$\bar{\boldsymbol{\sigma}}^{\pm}(\mu \boldsymbol{\varepsilon}^e) = \mu \, \bar{\boldsymbol{\sigma}}^{\pm}(\boldsymbol{\varepsilon}^e) \tag{3.52}$$

for any arbitrary scalar μ. The above result proves that the tensile and compressive effective stress tensors are first degree homogeneous functions of $\boldsymbol{\varepsilon}^e$ and thus Euler's theorem holds for both of them yielding

$$\bar{\boldsymbol{\sigma}}^{\pm}(\boldsymbol{\varepsilon}^e) = \frac{\partial \bar{\boldsymbol{\sigma}}^{\pm}}{\boldsymbol{\varepsilon}^e} : \boldsymbol{\varepsilon}^e. \tag{3.53}$$

Due to the above properties, the partial derivative of the elastic free energies with respect to the elastic strains are

$$\frac{\partial \psi_0^{\pm}}{\partial \boldsymbol{\varepsilon}^e} = \frac{1}{2} \frac{\partial \bar{\boldsymbol{\sigma}}^{\pm}}{\boldsymbol{\varepsilon}^e} : \boldsymbol{\varepsilon}^e + \frac{1}{2} \bar{\boldsymbol{\sigma}}^{\pm} \overset{(3.53)}{=} \bar{\boldsymbol{\sigma}}^{\pm} \tag{3.54}$$

and consequently Eq. (3.51) can be now expressed as

$$\frac{\partial \psi}{\partial \boldsymbol{\varepsilon}^e} = (1-d^+)\,\bar{\boldsymbol{\sigma}}^+ + (1-d^-)\,\bar{\boldsymbol{\sigma}}^- \tag{3.55}$$

Considering now the definition of the irreversible strains presented in Section 3.4, the equivalent rate form of Eq. (3.31) can be expressed as

$$\dot{\boldsymbol{\varepsilon}}^i = \beta \lim_{\Delta t \to \infty} \left(\frac{r(\tilde{\bar{\boldsymbol{\sigma}}}) - r_t}{\Delta t} \right) \frac{1}{r_{t+\Delta t}}\, \boldsymbol{\varepsilon}^e = m\, \boldsymbol{\varepsilon}^e \tag{3.56}$$

where $m \geq 0$ is a non-negative scalar due to the definitions of $r(\tilde{\bar{\boldsymbol{\sigma}}})$, β and r in Section (3.4). Considering Eqs. (3.50), (3.55) and 3.56 the rate of the energy dissipation due to the evolution of irreversible strains is

$$\dot{\gamma}^i = -\frac{\partial \psi}{\partial \boldsymbol{\varepsilon}^i} : \dot{\boldsymbol{\varepsilon}}^i \tag{3.57a}$$

$$= \left[(1-d^+)\,\bar{\boldsymbol{\sigma}}^+ + (1-d^-)\,\bar{\boldsymbol{\sigma}}^-\right] : m\,\boldsymbol{\varepsilon}^e \tag{3.57b}$$

$$= m\,\left[(1-d^+)\,\bar{\boldsymbol{\sigma}}^+ : \boldsymbol{\varepsilon}^e + (1-d^-)\,\bar{\boldsymbol{\sigma}}^- : \boldsymbol{\varepsilon}^e\right] \tag{3.57c}$$

$$= 2\,m\,\psi \geq 0 \tag{3.57d}$$

which is also always non-negative. Owing to the results of Eqs. (3.49) and (3.57d) it is proved that the presented formulation satisfies the basic thermodynamic requirements ensuring the irreversibility of damage and irreversible deformations

$$\dot{\gamma} = \dot{\gamma}^d + \dot{\gamma}^i \geq 0. \tag{3.58}$$

3.7 Numerical implementation

Table 3.3 presents the steps involved in the numerical implementation of the proposed constitutive model. It adopts a strain driven format, which makes its implementation straightforward into standard displacement-based or mixed strain and displacement based finite element codes (e.g. [74]). Moreover, the explicit closed-form format of all the internal variables enhances the computational efficiency, which is of primary importance when analyses of large-scale structures are carried out. These steps can be illustrated with the help of Figs. 3.8a-b for the cases with and without irreversible deformations respectively.

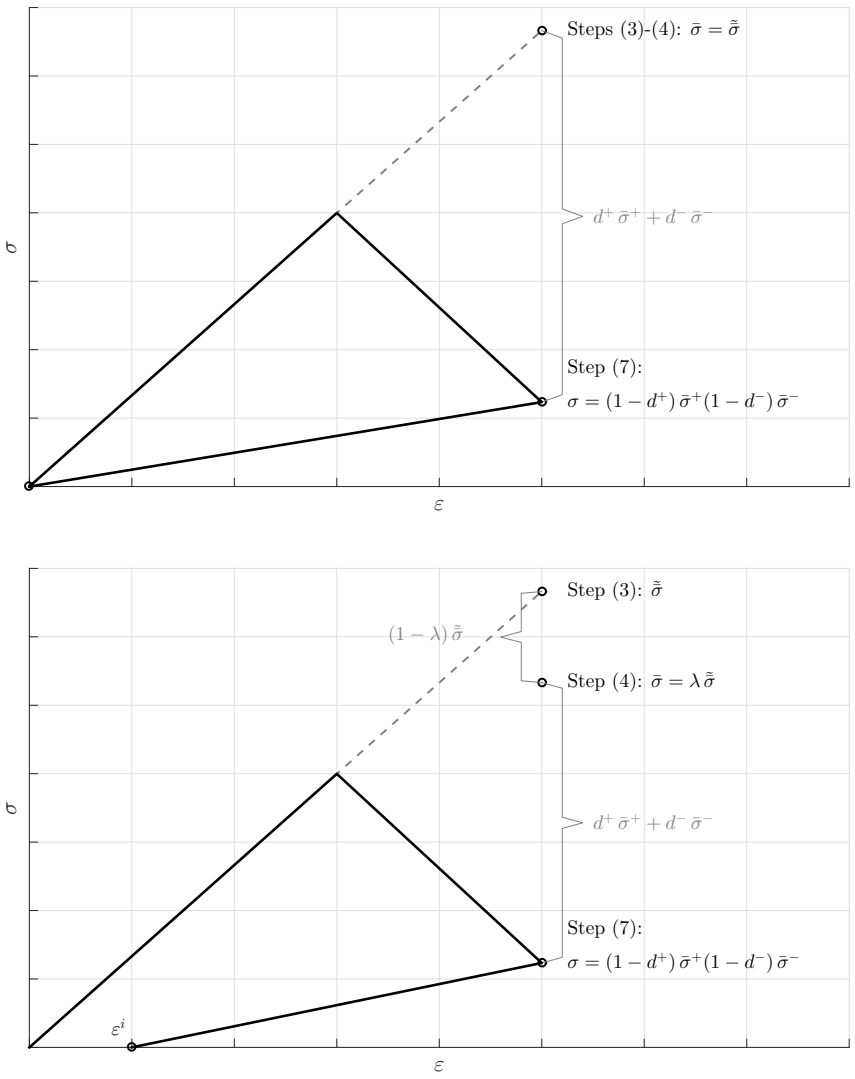

(b)

Figure 3.8 Illustration of the different steps of the numerical computation for a uniaxial case (a) without and (b) with irreversible strains.

Table 3.3 Algorithm used for the constitutive model with irreversible strains associated to the compressive stress thresholds and equivalent stresses.

START

Step $n = 0$

(1) Initialize the stress thresholds and the damage indices:
$r^+_{n+1} = r^+_0$, $r^-_{n+1} = r^-_0$, $d^+_{n+1} = 0$, $d^-_{n+1} = 0$

Step $n + 1$

(2) Compute $\boldsymbol{\varepsilon}_{n+1}$.

(3) Calculate $\tilde{\bar{\boldsymbol{\sigma}}}_{n+1}$ using Eq. (3.21).

(4) Is $\beta > 0$?

YES:

(i) Calculate $\tau(\tilde{\bar{\boldsymbol{\sigma}}}_{n+1})$ using Eq. (3.10) or Eq. (3.11) and $r(\tilde{\bar{\boldsymbol{\sigma}}}_{n+1})$ using Eq. (3.22).

(ii) Compute λ using Eq. (3.26). Set $\bar{\boldsymbol{\sigma}}_{n+1} = \lambda\, \tilde{\bar{\boldsymbol{\sigma}}}_{n+1}$ and continue to step (5).

NO: No evolution of irreversible strains is considered. Set $\bar{\boldsymbol{\sigma}}_{n+1} = \tilde{\bar{\boldsymbol{\sigma}}}_{n+1}$ and continue to step (5).

(5) Compute τ^+_{n+1} and τ^-_{n+1} according to Eqs. (3.10) and (3.11), respectively.

(6) If $\tau^+_{n+1} > r^+_n$ or $\tau^-_{n+1} > r^-_n$ update damage thresholds $r^\pm_{n+1}$ according to Eq. (3.15). Update damage indices d^+_{n+1} and d^-_{n+1} according to (3.32), (3.33) and (3.35)

(7) Compute the Cauchy stress tensor $\boldsymbol{\sigma}_{n+1}$ according to Eq. (3.6).

EXIT

3.8 Applications under uniaxial cyclic loading

The presented constitutive model is applied in this section to the simulation of uniaxial cyclic tensile and compressive experimental tests available in the literature. Four case studies are considered with the first three referring to uniaxial tests on concrete specimens (one tensile and two compressive) and the final one referring to a uniaxial compressive test on brick masonry. Contrary to concrete, cyclic tests on masonry specimens are scarce in the literature and according to the author's knowledge there is no reported tensile cyclic test. The simulations are performed at material level with a characteristic length of $l_{dis} = 55\,mm$.

3.8.1 Uniaxial tensile cyclic loading

The first case study concerns the uniaxial tensile cyclic test reported by Gopalaratnam and Shah [147]. The adopted material parameters are $E = 3.1 \times 10^4\ MPa$, $f^+ = 3.48\ MPa$ and $G_f^+ = 40\,J/m^2$ and are extracted from Lee & Fenves [190]. The evolution of the irreversible strains is associated with the evolution of the tensile damage, thus the tensile stress threshold r^+ and the tensile equivalent stress τ^+ are used in Eqs. (3.22) to (3.31). A value of $\beta = 0.975$ has been used to define the incremental magnitude of the irreversib

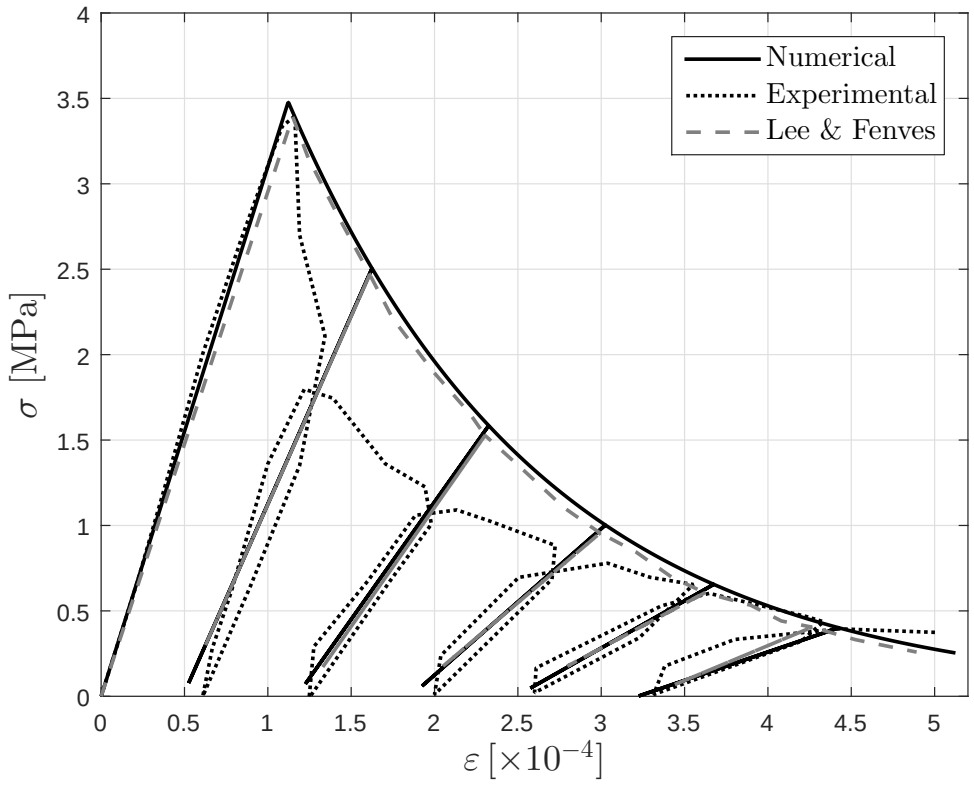

Figure 3.9 Numerical solution of an uniaxial tensile cyclic loading test compared with the experimental result by Gopalaratnam and Shah [147].

The experimental stress-strain curve, as reported by Gopalaratnam and Shah [147], is presented with the dotted line in Fig. 3.9. It has been constructed by dividing the applied displacement by the length of the strain gauge, which was 82.6 mm. The same figure shows with a solid line the numerical results obtained with the proposed formulation, and with a dashed line those reported by Lee & Fenves [190] using a plastic-damage model.

The obtained results show that the constitutive model can simulate the stiffness degradation, as well as the magnitude of the irreversible strains at the end of each cycle. More important differences can be observed immediately after the peak strength, where there exists a sudden drop of the capacity in the experimentally obtained curve. The same difference between numerical and experimental results has been reported using diverse models available in the literature (see for instance [157, 243, 272, 399]), and can be also observed in the numerical results of Lee & Fenves shown in Fig. 3.9. A possible explanation was given by Lee & Fenves [190] and concerns the length of the strain gauge used in the experiment which should have been limited to a smaller zone where the localization occurred. In general, the numerical model can capture in a satisfying way the experimentally obtained stress-strain relationship, and shows a very good agreement with the widely used plastic-damage model of Lee & Fenves [190].

3.8.2 Uniaxial compressive cyclic loading

The two case studies on cyclic compressive loading consider the tests reported by Karson and Jisra [184] and Sinha et al. [357]. The adopted material parameters are $E = 3.17 \times 10^4$ MPa, $f^- = 27.6$ MPa, $Gf^- = 9500\, J/m^2$, $f_0^- = 0.70 f^-$ and $\beta = 0.55$ for the simulation of the test by Karson and Jisra [184] and $E = 1.9 \times 10^4$ MPa, $f^- = 27.0$ MPa, $Gf^- = 10000\, J/m^2$, $f_0^- = 0.82\, f^-$ and $\beta = 0.75$ for the test of Sinha et al. [357]. The results of these two simulations are reported in Fig. 3.10 and Fig. 3.11 respectively.

The test on the brick masonry was carried-out by Naraine and Sinha [238]. The dimensions of the test specimens were $700 \times 700 \times 230\, mm^3$ constructed with frogged clay bricks of size $230 \times 110 \times 70\, mm^3$ and bed joint mortar with a thickness of $10\, mm$. The following properties have been used for its simulation $E = 3.0 \times 10^3$ MPa, $f^- = 5.3$ MPa, $Gf^- = 20000\, J/m^2$, $f_0^- = 0.35 f^-$ and $\beta = 0.56$. The results of this simulation are reported in Fig. 3.12. For all the cases with compressive loading the evolution of the irreversible strains is associated with the evolution of the compressive damage, and consequently the compressive stress threshold r^- and the compressive equivalent stress τ^- are used in Eqs. (3.22) to (3.31).

The numerical results of all the analysed cases demonstrate that the proposed model can capture correctly the experimental stress-strain envelope (Figs. 3.10, 3.11 and 3.12). Contrary to the tensile case, and considering the concrete specimens, the unloading paths are concave while the reloading ones present a more or less linear pattern which starts to become non-linear also during the last cycles. In the presented model unloading and

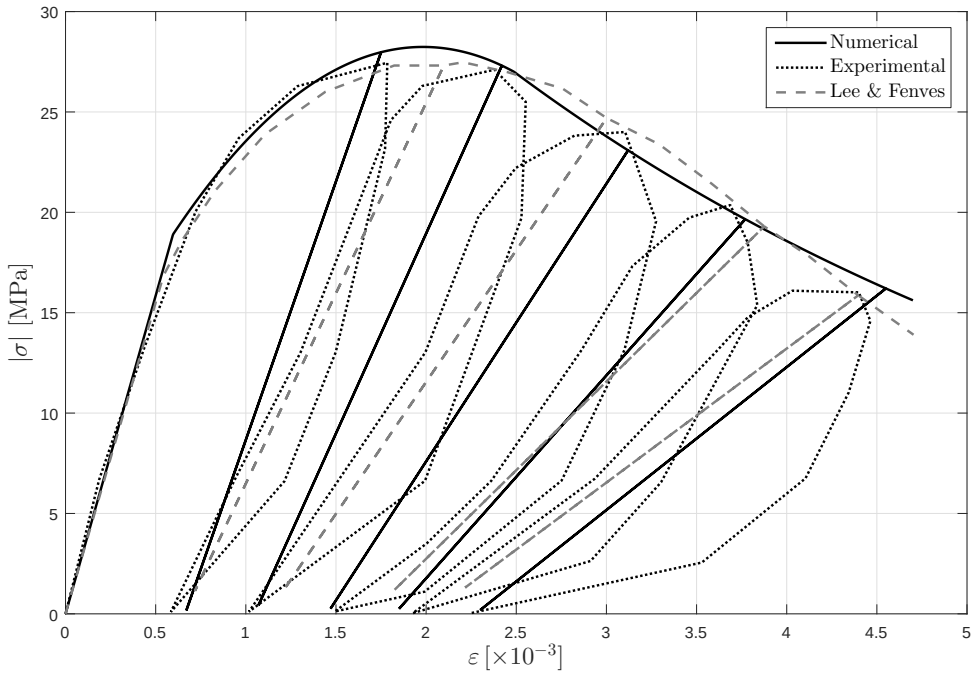

Figure 3.10 Numerical solution of an uniaxial compressive cyclic test compared with the experimental result by Karsan and Jirsa [184].

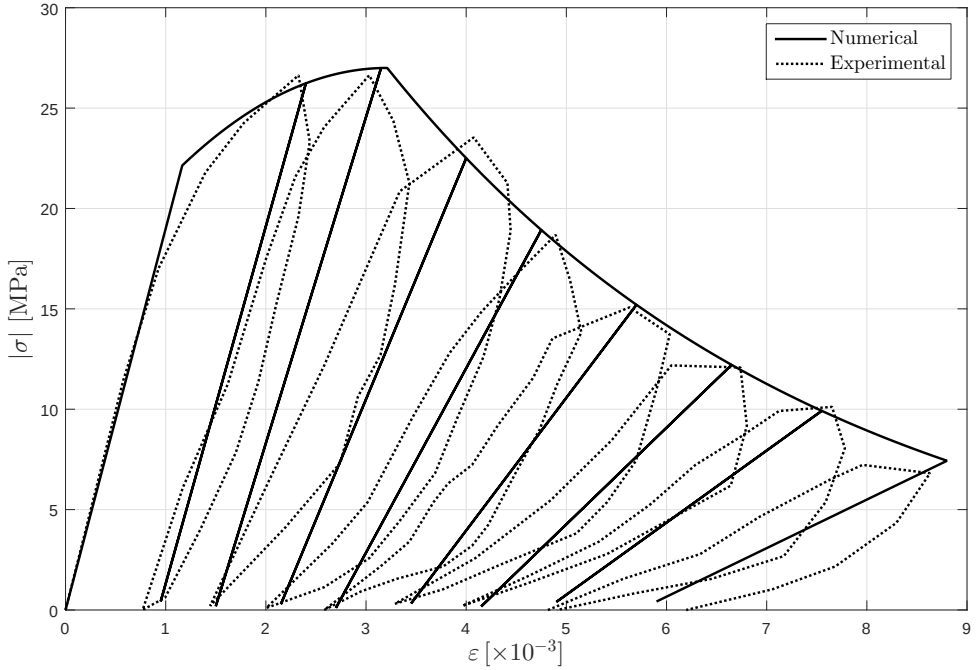

Figure 3.11 Numerical solution of an uniaxial compressive cyclic test compared with the experimental result by Sinha et al. [357].

reloading occurs following straight paths and no further degradation is considered similar to other damage and plastic-damage models [123, 148, 174, 190, 272, 385, 399, 405], as well as the plastic-damage model of Lee & Fenves shown with the dashed line in Fig. 3.10. Despite this approximation of the unloading-reloading paths, the explicit strain-driven proposed model can represent closely the irreversible deformation at the end of each cycle for both cases of the tests on concrete specimens (Figs. 3.10, 3.11).

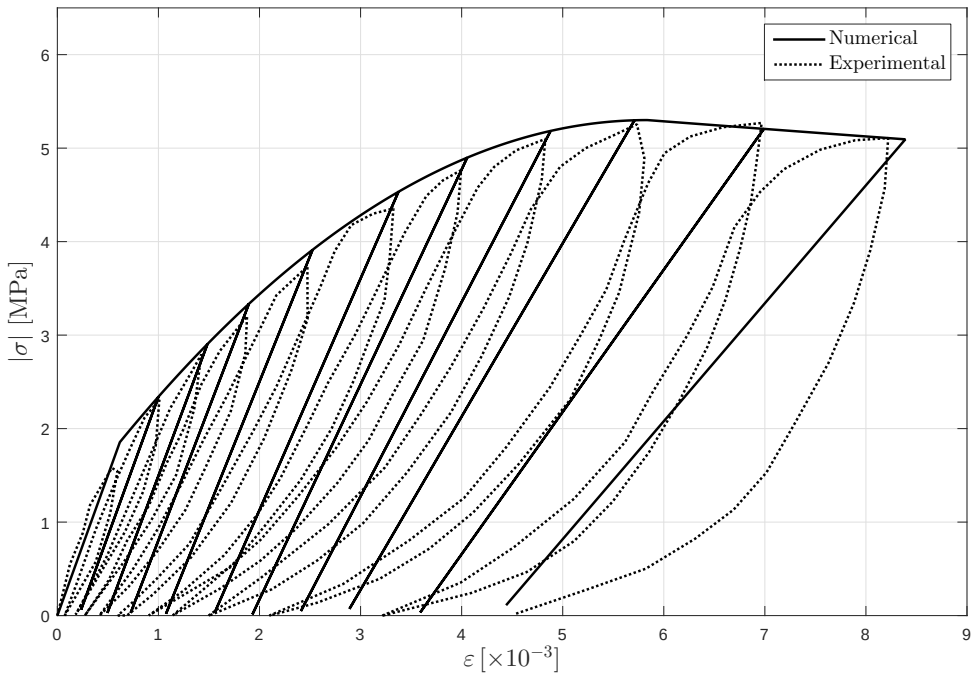

Figure 3.12 Numerical solution of an uniaxial compressive cyclic test compared with the experimental result by Naraine and Sinha. [238].

Considering the compressive test on the brick masonry in Fig. 3.12, it can be observed a high non-linear behaviour during unloading and reloading paths. For this case, the adopted strategy seems to overestimate the irreversible strains during the first steps of the hardening, but giving better estimations for the last cycles, when softening has started. The early stop of the experiment does not allow to draw further conclusions concerning the performance of the model during the post-peak region.

3.8.3 Remarks

The obtained results using the proposed formulation applied to tensile and compressive cyclic tests on concrete and masonry specimens have showed some important features. Firstly, the numerical predicted capacity curves resemble very closely the experimental results. This is an important characteristic of the presented constitutive model which makes it suitable for capacity-oriented structural analysis. Secondly, a good agreement has been found regarding the level of irreversible deformation on the concrete specimens at the end of each cycle when compared to the experimental results. This feature becomes very important for the proper modelling of crack opening-closing and stiffness recovery (i.e. the unilateral effect) phenomena in seismic analysis.

Differences, however, have been found considering the un-loading and reloading paths, which are more evident in the case of the masonry specimen. Such phenomena can be considered with a more elaborated definition of the damage evolution laws during the unloading paths and reloading paths. Up to date, very few models for concrete and masonry have been proposed in the literature that can capture this effect (e.g. [249, 350]),

but at the cost of an important number of parameters involved in the model definition. The simplification adopted in this work regarding the linear modelling of unloading and re-loading paths, aims to consider irreversible strains as an overall effect in the structural response ensuring high algorithmic efficiency and limited required number of numerical and material parameters.

3.9 Summary

This chapter presents the constitutive model used in this thesis for simulating the response of masonry under monotonic and cyclic loading. Masonry is approximated as a homogeneous material with average material properties. The presented continuum damage mechanics model results in damage-induced orthotropic behaviour in the non-linear range. This is achieved through a split of the effective stress tensor into a tensile and a compressive part, for which different damage surfaces and damage evolution laws are adopted. This strategy allows to consider the distinct behaviour of masonry under tensile and compressive loading and to simulate stiffness recovery under tensile-compressive loading cycles.

A novel formulation is proposed for the evolution of the irreversible strains within the framework of continuum damage mechanics. This formulation is compared to the one proposed by Faria et al. [122, 123] for simple analytical tests, showing that it allows a better control of the level of irreversible strains through the use of a single scalar variable. The performance of the model is also investigated through the simulation of experimental results on concrete specimens under tensile and compressive cyclic loading and on a masonry specimen under compressive cyclic loading. The results show that the model can provide a good estimation of the capacity curve and the level of irreversible deformation during the loading history. The proposed model will be further validated in the future as more experimental tests under tensile and compressive cyclic loading will be available.

Concerning the evolution of the damage indices, two formulations for the discrete softening parameters under tension and compression have been proposed. These ensure the proper regularization of the softening regions considering both the contribution of dissipated energy due to the evolution of damage and irreversible strains resulting to objective results in line with crack-band approach.

An essential feature of the model is its algorithmic efficiency owed to the explicit computation of all the internal variables. For this reason, and due to its strain-driven format, its implementation into standard displacement based or mixed strain-displacement based finite element codes is straightforward.

4

Fixed and multi-directional local tracking algorithm*

Crack localization and mesh-objectivity of the classical smeared crack approach are enhanced in this thesis through the use of a local tracking algorithm. This approach aims to identify and designate crack paths within the structure so that damage localizes only at the elements crossed by them. This chapter presents novel local tracking algorithms for the simulation of arbitrary, multiple and intersecting cracks. Two alternative procedures are proposed for crack-nucleation, referred hereafter as "fixed" and "multi-directional". The "fixed tracking algorithm" aims to the simulation of cases under monotonic loading, whereas cyclic loading is treated with the "multi-directional tracking algorithm". The different procedures followed for crack nucleation are presented in Section 4.2.1 and Section 4.2.8 for the fixed and multi-directional tracing algorithm, respectively. Common procedures used in both algorithms, such as crack propagation, completion and intersection are detailed in Sections 4.2.2-4.2.7. The chapter closes with Section 4.2.9 discussing implementation aspects.

4.1 Introduction

Tracking algorithms have a long tradition in computational modelling of fracture. Their development has been closely linked with that of the discrete crack approach (DCA) and indeed they consist an indivisible part for many algorithms introducing strong discontinuities in the classical finite element method. Their use in DCA is important for mainly two reasons. First, they define the strain localization zones, and thus the respective locations for the nodal or elemental enhancement. This explicit definition of the localization zone limits the computational overhead associated with the enhancement of the original finite

*This chapter presents a summary of the gradually developed algorithm in References [326, 328–330]

element solution and increases solubility of the non-linear problem. Secondly, tracking algorithms are used to ensure the compatibility between the newly deformation modes of the enhanced finite elements/nodes. In this way, severe stress locking is alleviated [403].

On the other hand, tracking algorithms within the smeared crack approach (SCA) are relatively new in the field of computational failure mechanics. Their first application was presented by Cervera & Chiumenti [69,70] who used a global tracking algorithm proposed earlier by Oliver et al. [264] in a DCA context. In the smeared crack approach, the aim of tracking algorithms is to define the path where cracks are assumed to propagate (referred hereafter as *crack-paths*) and allow only the elements crossed by them to experience damage. This approach has shown to enhance the mesh objectivity of the classical smeared crack approach in the same way that it does for the discrete crack one, and has motivated the development of new local tracking algorithms combined with the SCA during the last decade [56,77,85,360].

Notwithstanding the aforementioned advantages, tracking algorithms are commonly designed with important assumptions regarding the initiation, propagation and completion of the simulated cracks. These assumptions are usually associated with the difficulties in modelling complex crack patterns, such as crack-opening and closing as well as crack intersection phenomena, within the context of the discrete crack approach, where tracking algorithms have a long tradition. It is mainly due to this reason that tracking algorithms have been mostly used for the simulation of structural problems with small number of cracks emerging under monotonic loading.

This thesis aims to extend the use of tracking algorithms to a broader field of structural problems involving multiple cracks under monotonic and cyclic loadings. One of the most important challenges towards this objective, along with the ones mentioned above, is the numerical efficiency of the methodology in terms of computing time and memory resources such that the cost becomes affordable by practitioners in the engineering field. For this purpose, the local tracking algorithm developed by researchers in the Technical University of Catalonia [77,84,85,292] is an adequate basis for the development of such a numerical tool. The particular approach is formulated within the smeared crack concept and succeeds in efficiently representing localized cracking in large-scale structures [294, 303,318], improving the mesh-objectivity of the numerical solution. However, the available format of the aforementioned tracking algorithm restricts the nucleation of cracks only from the boundary of the finite element mesh and precludes the intersection of propagating cracks.

This chapter presents two novel tracking algorithms, defined as *fixed* and *multi-directional*, that have been developed in the course of this thesis for the simulation of cracking in masonry structures. The difference of the two algorithms lies on the criteria used for the crack initiation. The fixed tracking algorithm aims to simulate cracking under monotonic loading and addresses issues such as arbitrary crack nucleation, propagation and intersection. The multi-directional tracking algorithm keeps these characteristics but

introduces criteria for crack opening and closing, allowing the nucleation of new cracks close to existing ones due to important changes in the structure's stress state under cyclic loading.

4.2 Proposed tracking algorithms

The purpose of the tracking algorithm is to limit the damage localization to crack-paths composed of a series of consecutive finite elements. This is performed through the execution of a sequence of tasks at each solution step, load or time increment, including the identification of new cracks and monitoring of their propagation, in addition to existing ones that have consolidated in previous steps.

As soon as the crack paths are defined, a labelling system is used to categorize the elements falling within or outside of them. The elements within a crack respond according to the constitutive law presented in Chapter 3. The rest of the elements maintain a linear elastic stress-strain relationship.

The presented tracking algorithm is devised for triangular constant strain finite elements. Despite their known limitations, these elements ensure a straightforward implementation in any finite element code and allow for the easier meshing of irregular geometries, which are a common characteristic of many historical masonry structures. The extension of this approach to other element typologies could be performed in a similar way to [56, 360].

4.2.1 Crack nucleation - Fixed-directional tracking

Crack-roots

The first task of the tracking algorithm is to identify the nucleation of new cracks. A new crack can start at an undamaged element satisfying the tensile damage criterion defined in Section 3.3, which is repeated here for a load/time increment $n+1$

$$\Phi^{+}_{n+1} = \tau^{+}_{n+1} - r^{+}_{n+1} = 0 \qquad \text{and} \qquad \tau^{+}_{n+1} > r^{+}_{n} \tag{4.1}$$

The algorithm checks this condition for all the existing undamaged elements of the mesh, and the ones fulfilling it are temporarily labelled as *potential crack-root* elements. Note that contrary to most existing tracking algorithms, the above procedure is indiscriminately applied to all the elements of the mesh. This strategy aims to account for two issues. The first one is to allow cracks to initiate at locations where the defined damaged criterion is satisfied depending on the simulated structural problem, without their a-priori definition by the analyst. The second one is to model cracks initiating both from the boundary and the interior of the structure. As presented in Chapter 2, internal cracking has not been

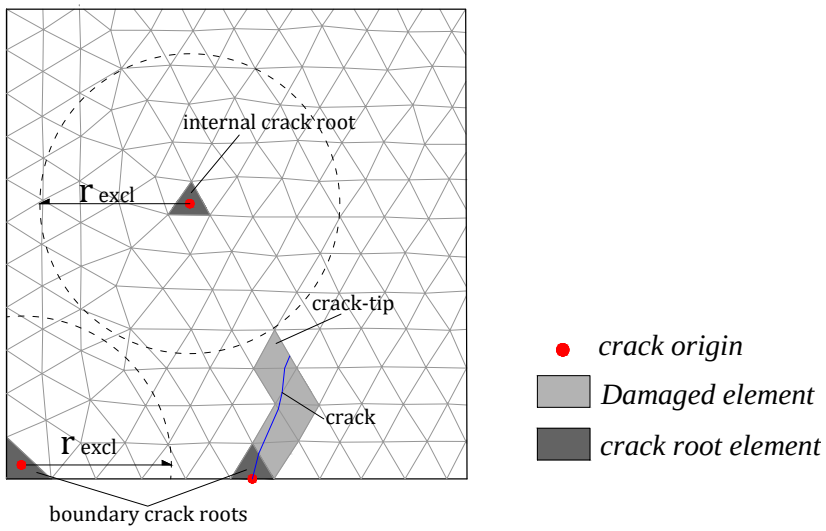

Figure 4.1 Illustration of some basic elements of the proposed tracking algorithm. Crack-roots are the origin elements of the cracks, crack-tips are the last elements at the propagating front and crack-origins refer to the locus within an element where a crack begins.

object of study for tracking algorithms, since most of the applications have considered case studies with cracks starting from the boundaries of the simulated structures.

The control of the damage dispersion over a small part of the discretized domain, and thus the simulation of separate and individual cracks, is possible with the use of an *exclusion radius criterion*. This criterion, introduced in [84, 85], states that a new crack can originate at an element which is located in an area without any other existing crack. This area is circumscribed by the *exclusion radius* r_{excl}, which is defined by the user (see Fig. 4.1). The definition of an exclusion radius averts the initiation of secondary spurious cracking surrounding existing cracks, a pathology that may spoil the correct damage localization in later steps of the simulation [264, 362]. Similar criteria have been also used by Oliver et al. [264] and Song and Belytschko [362], where the equivalent exclusion area (named as shielding zone in [264]) is defined as a multiple of the finite element size. Note that the exclusion radius controls only the nucleation of new cracks at a certain distance to existing ones and does not preclude the propagation of cracks close to others as in [264]. A similar use the exclusion radius to the one presented here can be considered in the tracking algorithm presented by Slobbe et al. [360], whereas in Alfaiate et al. [6] the exclusion radius prevents the initiation of new cracks only around the crack-tip. A similar approach has been recently used by Wu et al. [398].

Apart from its aforementioned numerical purpose, the exclusion radius has a second functionality when a composite material, such as masonry, is simulated. More specifically, r_{excl} can be defined according to the average distance between the weak zones of the composite and heterogeneous material. For many masonry typologies, the weak zones are the interfaces between the mortar and the units due to the contact of two different materials, or the mortar joints themselves, and consequently the distance between cracks can be defined by the size of the brick or stone units [132, 202]. In such cases, the staggering

of the masonry can be considered using an exclusion radius equivalent to the unit's size.

With the above definitions, a potential crack-root element without any existing crack within the area circumscribed by the exclusion radius is defined as a *crack-root element*. Crack-root elements with one or more sides on the boundary of the mesh are referred to as *boundary crack-root* elements, while those with no sides on the boundary of the mesh are *internal crack-root* elements. If more than one finite elements are defined as potential crack-roots at the same increment, and the distance between them is less than the exclusion radius, the one with the highest value of the tensile equivalent stress τ^+ (see Eq. (3.10)) is selected as a crack-root. Figure 4.1 presents an example of boundary and internal crack-roots.

4.2.2 Crack-origin coordinates

Following the identification of the new crack-roots, the coordinates of the *crack-origin* points are defined and stored. These depend on the location of the crack-root element within the discretized domain. For cracks initiating at corners or at internal elements, the centroid of the triangular element is selected as the crack-origin. For the case of a crack starting at an element with one side on the boundary, the crack-origin is located at the midpoint of the boundary side. Figure 4.1 presents examples for crack-origins at corner, boundary and internal elements.

4.2.3 Crack propagation

The propagation of new and existing cracks at each step of the numerical analysis starts from the *crack-root* and *crack-tip* elements respectively. A crack-tip is a damaged element lying on the propagating front of a crack that has already formed in a previous step of the analysis (see Fig. 4.1). The tracking algorithm is capable of simulating crack propagation in one or two directions depending on the position of the crack-root element. Cracks originating from elements at the boundary (i.e. boundary crack-roots) can propagate towards one direction, while those originating from an internal element (i.e. internal crack-roots) can propagate in two opposite directions. The procedure for each case is presented in the following.

Propagation towards one direction

The crack propagation from boundary crack-root and crack-tip elements is performed in the way presented in [77,84,85,292] and is illustrated in Fig. 4.2. For each boundary crack-root element, a vector is drawn, starting from the crack-origin location, with a direction orthogonal to the one defined by the maximum principal effective stress. This direction is calculated using a stress tensor constructed from the average values of the effective stresses at the nodes of each element. The use of smoothed values of stresses is a common practice

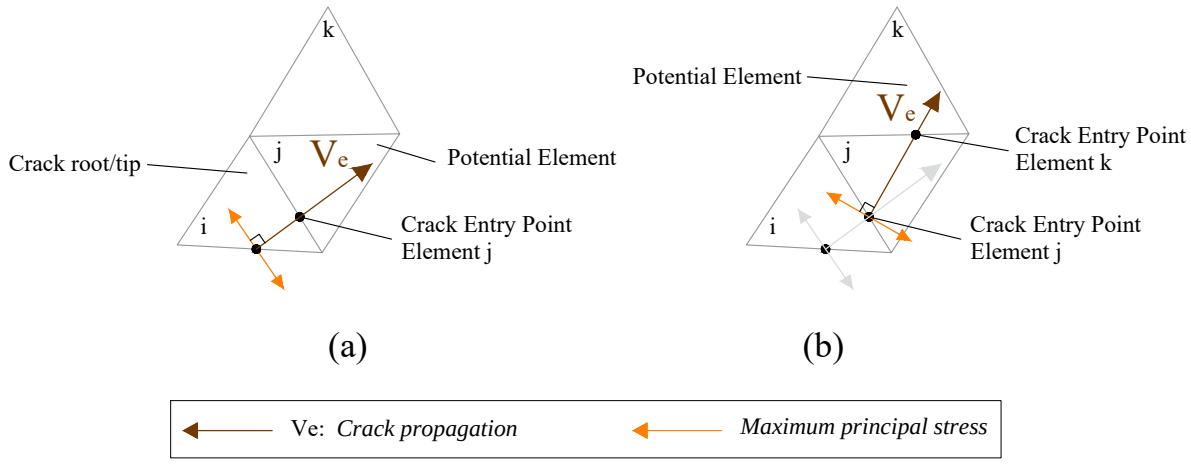

Figure 4.2 Procedure for crack propagation (picture adapted from [292]).

in local tracking algorithms aiming to increase the reliability of the stress directions at the crack-tip (see for instance [143, 218, 225, 308, 391]). The intersection of this vector with the neighbouring element defines the exit point and the next *potential element* of the crack (Fig. 4.2a). Similarly, starting from this point the following potential elements of the crack are recognised (Fig. 4.2b). The same procedure is followed for identifying the propagation path of consolidated cracks from the crack-tip elements. In this case the crack-origin point is the exit point of the crack at the previous cracked element.

Propagation towards two opposite directions

Contrary to cracking starting from the boundary, other cracks, such as shear ones, initiate from the interior and propagate along two opposite directions in this thesis. The tracking algorithm is enhanced with a new procedure that allows to identify internal crack-root elements and monitor the crack propagation from it in two opposite directions. The procedure is presented in Fig. 4.3 and is detailed in the following.

Starting from the crack-origin point of the internal crack-root element, two vectors ($V_{e,1}$) and ($V_{e,2}$) are defined, having a direction orthogonal to that of the maximum principal effective stress but opposing orientations (Fig. 4.3a). Following this, the crack path is recognized in two steps. First, the elements pertaining to the path defined by the orientation of vector ($V_{e,1}$) are identified starting from the crack-origin point and following the same process as described above for the boundary crack-root and crack-tip elements (Fig. 4.3b). Upon concluding the labelling towards that side of the crack, the elements lying at the opposite face can be recognised starting again from the crack-origin point of the internal crack-root, but using the orientation of vector ($V_{e,2}$) (Fig. 4.3c).

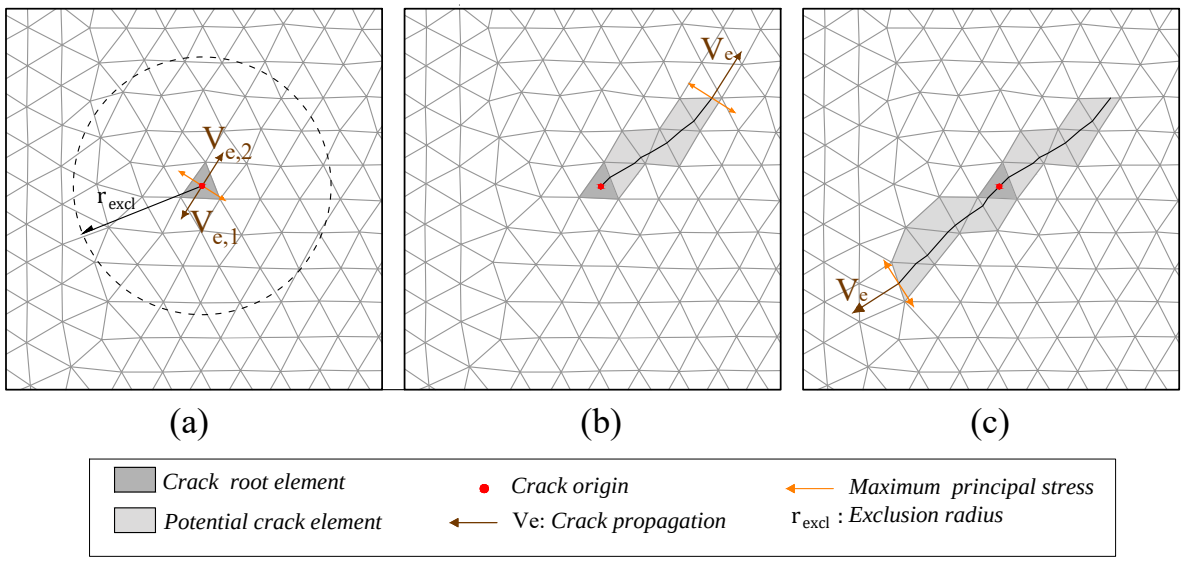

Figure 4.3 Simulation of internal cracking with the tracking technique: (a) *internal crack-root* element with the two opposite vectors of the crack propagation, (b) labelling of the *potential crack* elements towards the first side of the crack, (c) labelling of the *potential crack* elements towards the second side of the crack.

4.2.4 End of the labelling procedure

The described procedure for the definition of crack propagation stops when one at least of the following criteria are satisfied:

(i) *Boundary criterion*: a crack reaches the mesh boundary, and at least one of the elements in the wake of the crack with a distance from the crack-tip lower than the exclusion radius does not have sides or nodes on the boundary of the mesh.

(ii) *Stress threshold criterion*: the stress-state of a potential element is lower than a pre-defined threshold. This threshold can be conveniently defined in terms of the tensile equivalent stress and previous works [77,84,292,296] have demonstrated that labelling can be completed when the inequality $\tau^+ < 0.75 f^+$ holds. The aim of this condition is to limit the computational cost, as the crack path is not sought through the entire domain until the crack meets the boundary. This is a common strategy in tracking algorithms, for instance, Stolarska et al. [365] define a certain number of elements in which the level set function is updated and thus the crack can propagate during a numerical step in their X-FEM formulation.

Once the stress threshold or the boundary criterion is satisfied, the crack is assumed as complete for the current step and the algorithm continues with the propagation of the next crack. The same procedure is followed until the propagation of all the new and existing cracks has been identified.

A common local mechanism of masonry structures is the rocking of piers due to the formation of flexural cracks along the two boundaries. A similar case is illustrated in Fig.

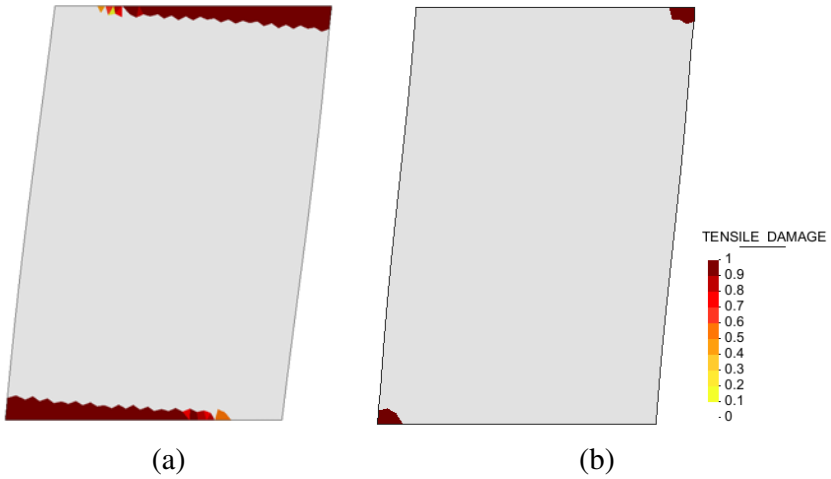

Figure 4.4 Flexural crack propagation on top and bottom of a shear wall for a top displacement of $\delta = 2\,mm$: (a) with and (b) without proper definition of the boundary criterion.

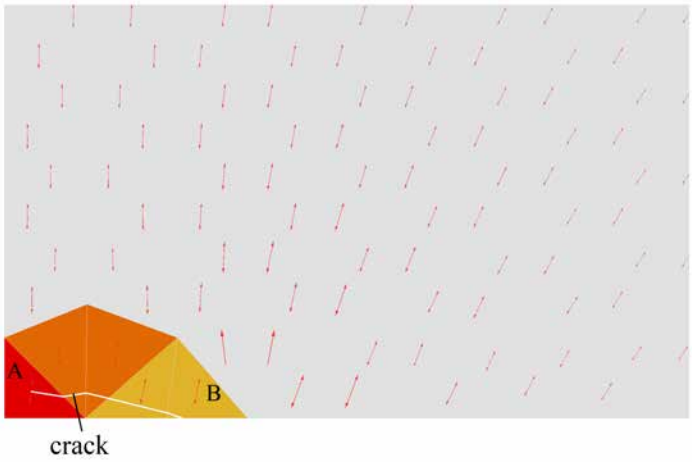

Figure 4.5 Flexural crack at the bottom of a shear wall exiting the mesh.

4.4a, where cracks originate from the corner of the wall and propagate towards the interior. A zoom in at the region of the crack-tip during the loading, shown in Fig. 4.5, reveals that the directions of the principal stresses may not be parallel to the boundary, due to the effect of the self-weight and also the constraints at the top and bottom of the wall that restrain the vertical displacement. Under these conditions, it is possible that the crack originating from the corner of the wall (element A in Fig. 4.5) exits the mesh at its lower boundary (element B in Fig. 4.5). The new definition of the aforementioned *boundary criterion*, aims to overcome this issue. In this way, if a crack reaches the boundary but condition (i) is not fulfilled, the crack direction is corrected and defined as parallel to the boundary of the mesh where the crack exits. The labelling process in this case will end if this crack reaches again another boundary of the mesh, as for instance the vertical end of the wall for the case of Fig. 4.4. As will be shown through the various analyses carried out in Chapter 5, the above definition succeeds in identifying correctly complete or incomplete cracks that should propagate across the boundary. Instead, the improper definition of the *boundary criterion* leads to the result of Fig. 4.4b, where the two cracks

stop as soon as the crack fronts reach the boundary of the mesh, which leads to improper identification of the collapse mechanism and load capacity.

4.2.5 Crack intersection

In previous works the criteria for ending the crack propagation were complemented with an additional one, the *crack meeting criterion* [77,84,85,292]. The latter condition was based on the hypothesis that, if a crack met another one during its propagation, it should be assumed as complete, and the two cracks were considered as a single one. This assumption has shown to be valid in case studies with monotonically increasing loads [77, 85, 292, 303, 318]. Similar strategies are common to tracking algorithms as in [6, 56, 264, 309, 360], among others.

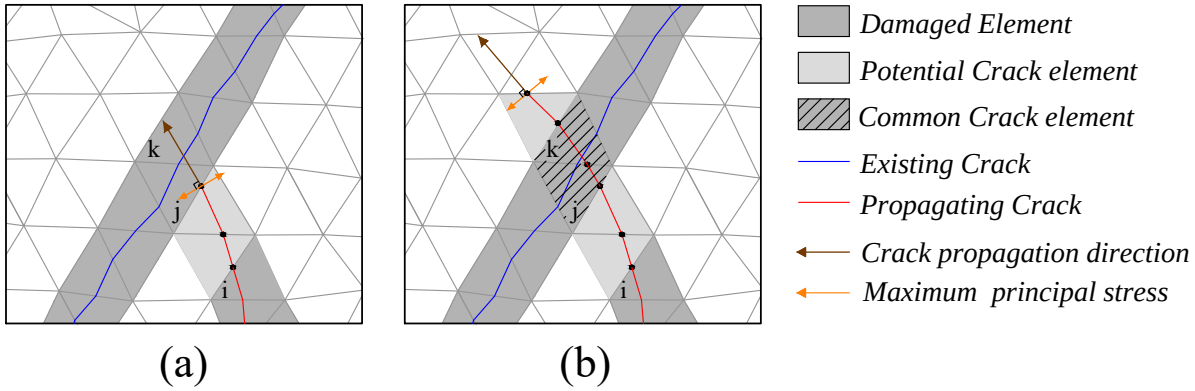

Figure 4.6 Case with the intersection of two cracks.

Contrary to monotonic loads, cyclic ones (e.g. due to earthquakes) may cause complex cracking in unreinforced masonry structures, and cases including crack opening and closing as well as crack intersection should be anticipated. Evidently, the above assumption of the crack meeting criterion becomes insufficient for the simulation of cyclic loads. To overcome this, the current algorithm is designed to account for intersection of propagating cracks with existing ones that fall within their trajectory. The propagation procedure when a crack meets another remains the same as if the crack-tip was not a part of an existing crack. The crack direction is identified as orthogonal to the direction of the maximum principal effective stresses of the, now common, element and the next elements of the crack are sought. An example of crack intersection is presented in Fig. 4.6, where the propagating crack (in red) starting from the crack-tip element "i" meets an existing crack (in blue) towards its propagation. As shown in Fig. 4.6a, the crack-direction at the current crack-tip element "j", which is a part of the existing crack, is defined as in the same way as for intact elements. Note that the crack propagation direction is computed considering the values of the effective stresses and, in this way, even if the common element is completely damaged, the direction of the crack propagation direction can be still computed. In the same manner, the crack continues its propagation through the existing crack as shown in

Fig. 4.6b, with the elements "j" and "k" being common crack elements now.

As it can be seen from the above procedure, the modelling of crack intersection can be easily pursued within the context of the proposed tracking algorithm. Contrary to X-FEM and E-FEM methods, no change is necessary at nodal or elemental level (see [93, 196]) or any refinement in order to separate crack-tips for the proper calculation of the stress intensity factors and consequently the computation of the propagation direction [369]. The correct crack propagation, of course, relies on the correct strain localization, which depends on the kinematics of the chosen finite elements. In any case, the correction of the crack propagation with the maximum curvature criterion presented later can account for local errors in the crack propagation direction.

As soon as cracks are allowed to intersect, an element may belong to more than one crack, implying that it will have as many crack-entry points as the number of the cracks crossing it. It is recalled that the storage of the crack-entry point is necessary for two functions. The first one is when the element is the crack-tip of a crack and thus the crack-entry coordinates are necessary to identify the starting point for the crack propagation. The second one concerns the use of the maximum curvature criterion which is presented later in Section 4.2.7. In the maximum curvature criterion, the crack-entry points at elements on the wake of the crack-tip are recovered in order to opportunely correct the propagation of the crack. To this aim, a matrix is introduced that saves the potential crack-entry coordinates for each side of the element. In the case that more than one crack enter from the same side, two options are possible: (i) to add elements in the matrix corresponding to each new crack-entry coordinates, (ii) to use an average crack-entry point for that side. The first choice favours accuracy, but increases the numerical cost since there is the need for dynamically allocating memory, as well as the use of additional arrays to associate the crack-entry point with the number of each crack. Due to the above, the second choice has been selected in this work in favour of computer memory usage and robustness, which are necessary for the analysis of structures with a large number of cracks.

4.2.6 Element labelling and crack-path continuity

Element labelling

As soon as the procedure for the crack propagation of all the cracks has been completed, each element of the mesh is labelled with a flag representing its crack state for the current step. This can be one of the following three:

- *Intact element, unable to damage*: element outside of a crack-path. Its stress-strain relationship will remain linear elastic for the current step.
- *Potential crack element*: undamaged element falling within a crack-path at the current step. If it satisfies the damage criterion, its stress-strain relationship will be

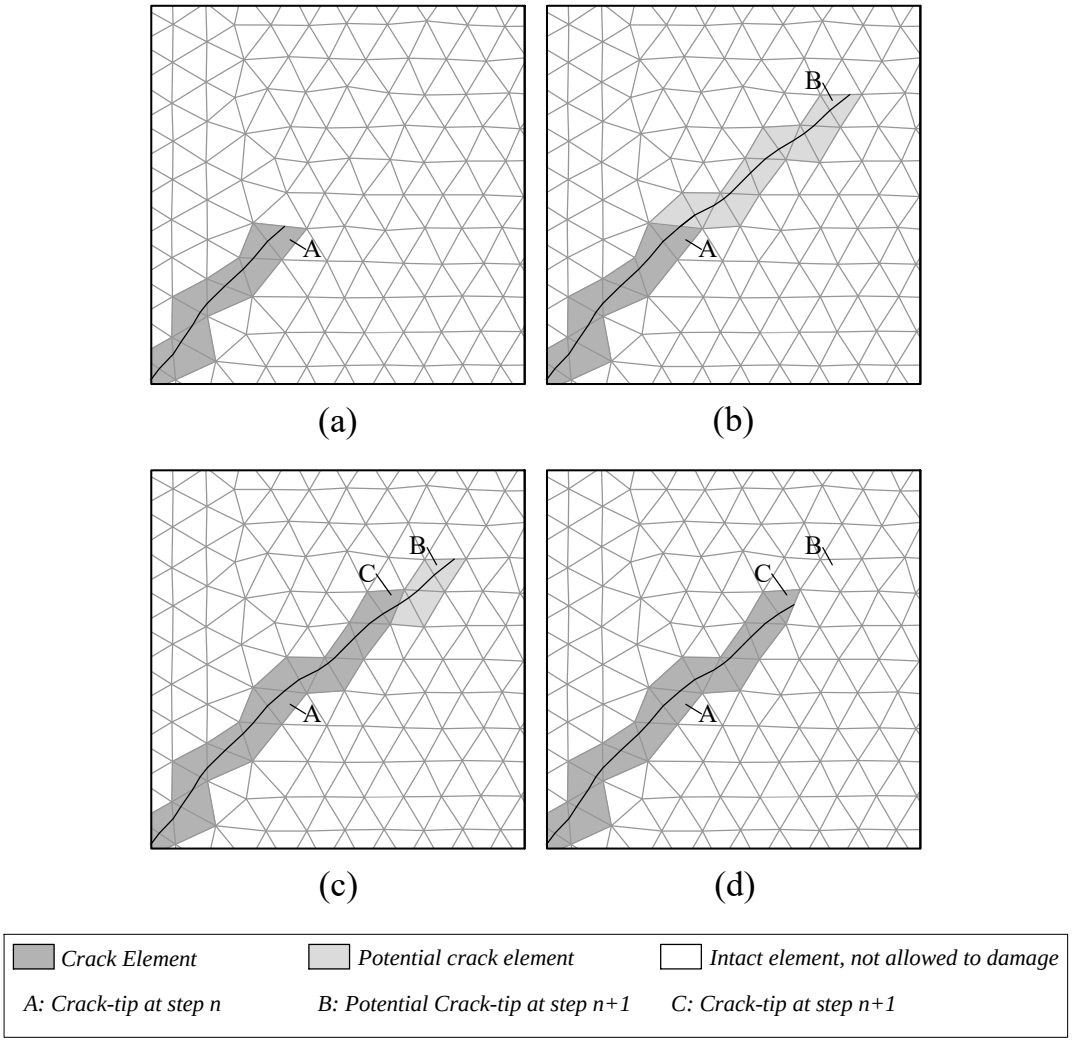

Figure 4.7 Assigned flags at the elements of the mesh for a propagating crack: (a) consolidated crack prior to crack propagation, (b) potential crack path at step $n+1$, (c) consolidated crack after convergence of the current step $n+1$, (d) labelling status at the end of the current step $n+1$.

defined according to the continuum damage model presented in Chapter 3.

- *Crack element*: belonging to a consolidated crack at a previous step that has already experienced damage. Its stress-strain relationship is characterized by the continuum damage model presented in Chapter 3.

The above categorization of elements is illustrated in Fig. 4.7 showing the propagation of a crack and the labelling procedure during a step of the numerical analysis. Figure 4.7a presents the consolidated part of the crack, which has propagated up to element A in the previous step n. In the new step $n+1$, the tracking algorithm identifies that the crack can potentially propagate up to element B (see Fig. 4.7b), which is the last one satisfying the *stress threshold criterion* presented in Section 4.2.4. A flag is assigned to all the elements between A and B categorizing them as *potential crack elements*. This flag activates the constitutive law presented in Chapter 3 for these elements, while the rest will remain linear elastic. At the end of the iterations of step $n+1$, the updated

flag system of the elements in the crack is illustrated in Fig. 4.7c. All the elements up to element C have damaged, while the rest potential elements did not satisfy the damage criterion and therefore remained linear elastic. Before proceeding to the new load/time increment, the tracking algorithm is called to update the crack status for a last time. The status of all potential elements that remained intact is initialized to *Intact element, unable to damage* as shown in Fig. 4.7d. This ensures that during the new step, $n+2$, the crack will propagate from element C, with a crack propagation direction according to the new converged stress state.

Crack path continuity

Let us consider now the same case of the single propagating crack, but assuming that two elements D and E, prior to element C have not damaged at the end of the step $n+1$ even if they have been identified as *potential crack elements*, as shown in Fig. 4.8. If no further consideration is made, the status of elements D and E is initialized to *Intact element, unable to damage* at the end of the step, and the crack loses its continuity breaking in more than one parts (see Fig. 4.8c). This is avoided by the current algorithm through the implementation of a crack path continuity procedure. According to this, the damage state of all the elements of the crack is inspected after convergence starting from the potential crack-tip elements and going backwards towards the crack-tip at the beginning of the step. For the current example, this means starting from element B and going backwards up to element A. As soon as, a damaged element is found, in this case element C, the rest of the status of all the preceding elements is changed to *Damaged*. The procedure stops as soon as the crack-tip element at the beginning of the current step is met, (element A in Fig. 4.8).

The above procedure implies that the algorithm stores for each crack the crack-tip of the consolidated crack (e.g. element A in Fig. 4.8) and the potential crack-tip at the end of the labelling procedure (e.g. element B in Fig. 4.8). Additionally, each element is associated with the crack(s) it belongs to. In this way, the crack-path of each crack can be recovered at any moment, starting from the (potential) crack-tip and going backwards considering elements belonging to the same crack.

4.2.7 Maximum curvature criterion

The selection of the elements of a crack depending on the local values of the stresses justifies the "local" nature of the presented tracking algorithm. This choice is very convenient for handling cases with multiple cracks and in terms of computational efficiency compared to global tracking algorithms [77]. Nevertheless, local tracking algorithms can encounter some difficulties under bending stress states, when the local calculation of the principal stress directions may be relatively poor due to the high stress-gradients, resulting in spurious changes in the crack direction.

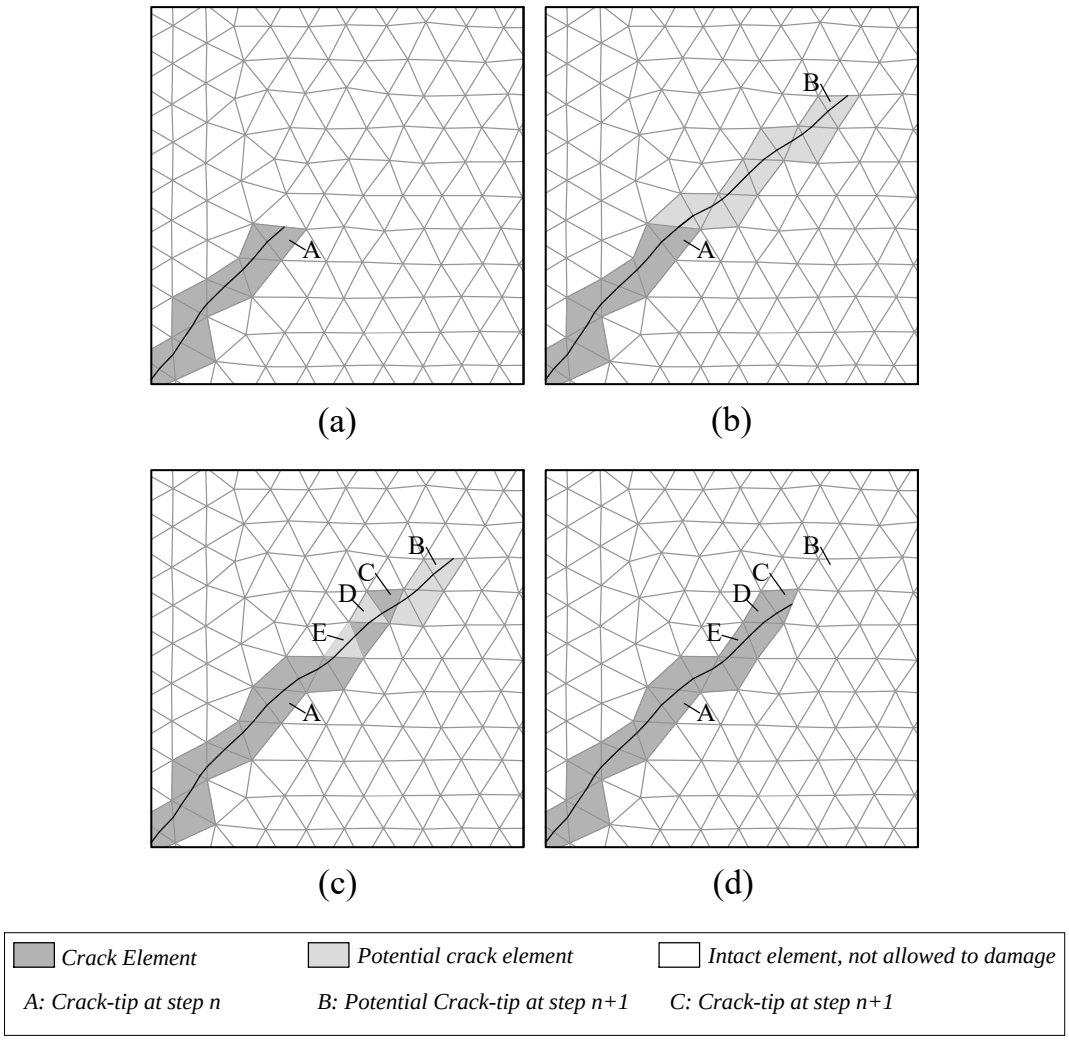

Figure 4.8 Assigned flags at the elements of the mesh for a propagating crack: (a) consolidated crack prior to crack propagation, (b) potential crack path at step $n+1$, (c) consolidated crack after convergence of the current step $n+1$, (d) labelling status at the end of the current step $n+1$ after the crack path continuity procedure.

To avoid such non-realistic result, Clemente et al. [77,85] proposed the enhancement of the algorithm with a procedure for the apropos correction of the crack propagation. This procedure, termed as *maximum curvature criterion*, is activated at each element lying at the propagating front of the crack (i.e. the crack-tip elements) before the selection of the next potential element. The idea is to compare the crack propagation direction defined at the crack-tip element (V_e) according to the principal stresses, with the vector sum of the crack directions (V_c) of both the potential and the damaged elements within a neighbourhood of radius r_{neigh} (see Fig. 4.9). If the relative angle among them is larger than a maximum angle a_{max}, the vector V_c is used for the definition of the crack direction.

The parameters involved in the use of the maximum curvature criterion are the r_{neigh} radius and the a_{max} angle. As presented in [77,292], the proper selection of the number of elements considered for the crack correction through the radius of r_{neigh} is important in cases with curved cracks. Contrariwise, the effect of r_{neigh} is limited for cracks which are

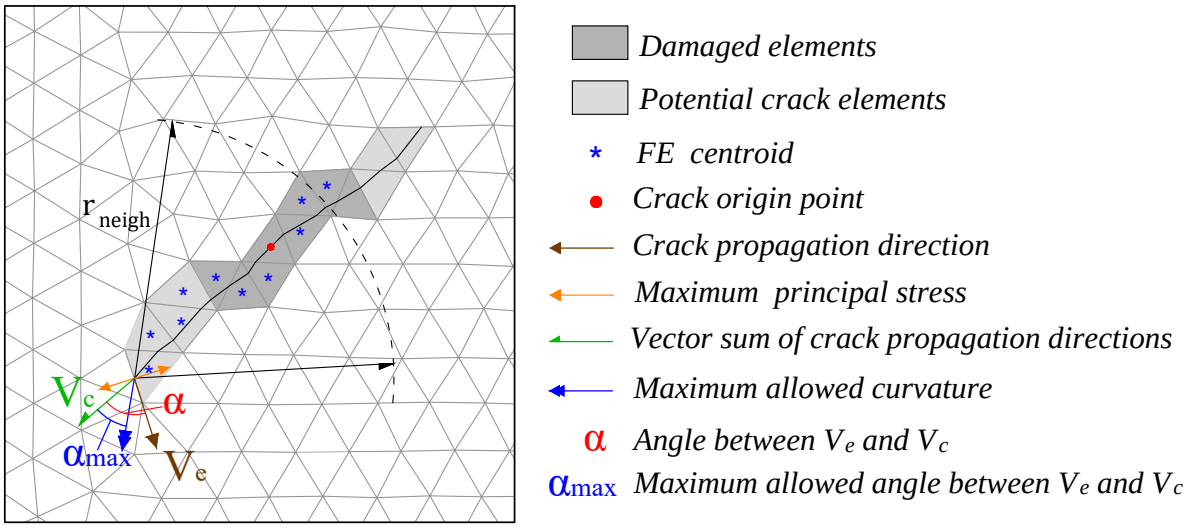

Figure 4.9 The maximum curvature criterion applied during the propagation of an internal crack.

straight or exhibit small curvature. A general conclusion of the obtained experience using the maximum curvature criterion shows that curved cracks necessitate values of r_{neigh} involving a small number of elements, and values of a_{max} sufficiently large such that the curvature of the crack is not restrained, but spurious U-turns are excluded. The effect of these parameters will be further investigated in this thesis for the cases of shear and flexural cracks.

The use of similar criteria aiming to prevent sudden turns in propagating cracks are common in tracking algorithms. For instance, Jäger et al. [172] use the same criterion in their 3D local tracking algorithm and a value between $\pi/6$ and $\pi/4$ is proposed for the equivalent maximum curvature angle. In the tracking algorithm of Zhang et al. [403] the new crack direction in the crack-tip is defined using the consolidated crack direction at the previous element and the mean value of the crack directions of the next two new crack elements, obtained through a global energy-based tracking method. This smoothing strategy aims to alleviate sudden turning of the crack (see [402,403]). An alternative to the explicit control of the crack diverging angle has been presented by Slobbe et al. [359, 360] also in the context of local tracking algorithms. The main concept is to postpone the crack path fixation up to the moment that a certain level of damage is reached at an element crossed by a potential crack (named as damage path). The idea resembles closely the strategy used by Jirásek and Zimmerman [179] and Sancho et al. [335, 336] for the adaptation of embedded strong discontinuities until a certain crack width is reached, which can be defined according to the material parameters. Similar assumptions are common also in continuous-discontinuous models, in which a strong discontinuity is inserted during a later stage of damage localization to represent the displacement discontinuity of the crack (e.g. [130,373]). Despite the potentiality of this method demonstrated in the context of an embedded crack model [139,314,335,336], Slobbe et al. [359,360] show that delayed crack path fixation may provide ambiguous results concerning the appearance of spurious crack

tortuosity, while the criteria for the proper definition of the parameter controlling the moment of crack path fixation (damage/crack-width limit) are still under research. In the same work, the preclusion of the crack overturning is also enhanced by considering a C^1 continuous crack using the crack-entry direction for the definition of the new propagation direction within a new element of the crack [360].

4.2.8 Crack nucleation - Multi-directional tracking

The criteria for crack initiation, presented in Section 4.2.1, define that new cracks can start at a certain distance from existing ones, which is determined by the exclusion radius r_{excl}. As will be shown in Chapter 5, this procedure is robust for structural cases with monotonic loading, where the crack directions do not show sudden changes during the loading history (see also previous works [77, 296, 318]). However, cyclic loading (e.g. due to earthquakes) may induce *multi-directional cracking* with cracks initiating in the same region of existing cracks but with a different direction. To illustrate this, consider the simplified case of a shear wall, shown in Fig. 4.10, subjected to cyclic shear loading at its top (restraining the rotation). The top displacement towards the left produces a diagonal shear crack, starting from the middle of the wall and propagating towards its two opposite corners (Fig. 4.10a). The reversal of the loading cycle finds the wall at its initial configuration with the crack closed (Fig. 4.10b). The loading in the opposite direction results in the opening of a new crack that propagates diagonally towards the other two corners (Fig. 4.10c). If the first crack is completely closed, the structural condition before the opening of the two cracks will very be similar resulting to the possible origin of the second crack very close to the origin of the first one.

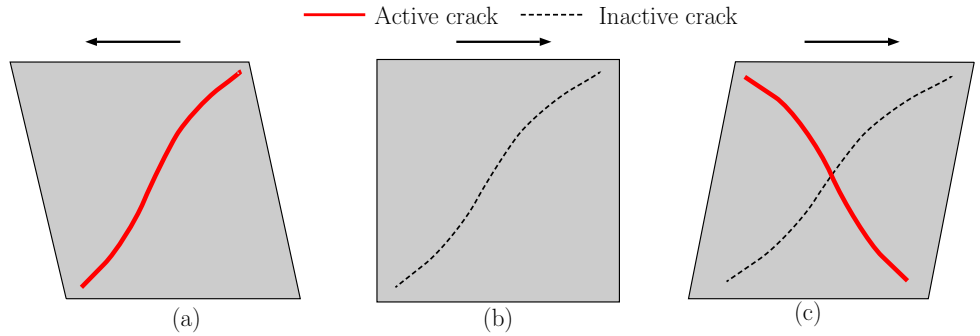

Figure 4.10 Example of cracking under the shear loading of a wall: (a) Opening of one crack during the loading towards the left, (b) closing of the crack when returning to the initial configuration and (c) opening of a second crack, diagonal to the first during the reverse loading.

The simulation of such cases needs a different approach regarding crack initiation from the one presented in Section 4.2.1. For instance, in the specific case of the shear wall in Fig. 4.10, this approach should allow the initiation of the second crack at the finite element that satisfies the failure criterion after the reversal of the loading cycle, independently of its distance to the closed crack.

The modelling of cases involving the nucleation of cracks due to different stress-states at a region of existing cracks is possible through the categorization of cracks into "*active*" and "*inactive*". Prior to the definition of these two categories, two new versors are introduced:

- *Crack direction* ($\hat{v}_{cr}$)*:* a versor denoting the average direction of a consolidated crack. The crack direction of a crack is calculated using the coordinates of the two ends of a crack. These are the coordinates of the crack origin and the crack-tip for single-direction propagating cracks (with a boundary crack-root), and the coordinates of the two crack-tips for double-direction propagating cracks (with an internal crack-root).

- *Crack closure direction* ($\hat{v}_{cl}$): a versor denoting the average direction orthogonal to the maximum principal effective stress of all the elements within the crack. This versor shows the average crack propagation direction of all the elements within a crack at each time/load increment of the analysis.

The crack direction and crack closure direction versors are updated at the end of each step for each of the consolidated cracks. A crack i is defined as "*active*" if the angle between its crack direction versor $\hat{v}^i_{cr}$ and its crack closure direction versor $\hat{v}^i_{cl}$ is lower than a predefined limit angle a_{lim}. The crack status can be formally expressed through the use of the following function

$$H^i[|\hat{v}^i_{cr} \cdot \hat{v}^i_{cl}| - cos(a_{lim})] = \begin{cases} 0 & \text{Inactive crack} \\ 1 & \text{Active crack} \end{cases} \qquad i = 1, N_{cr} \tag{4.2}$$

where $(\cdot)$ is the dot product, the subscript $i = 1, N_{cr}$ is used to denote the versor values for each crack of the total existing cracks N_{cr} and $H[\bullet]$ is the Heaviside step function

$$H[x] = \begin{cases} 0 & \text{for} \quad x < 0 \\ 1 & \text{for} \quad x \geq 0 \end{cases} \tag{4.3}$$

Following the above, an element is a crack-root when all of the following criteria are satisfied:

(i) The failure condition, as defined by the constitutive model (Eq. 4.1), is reached.

(ii) There is no "*active*" crack within a distance defined by the exclusion radius r_{excl}.

(iii) There is no crack within a distance defined by the exclusion radius r_{excl} with a crack direction making an angle with the crack propagation direction of the crack-root lower than the limit angle α_{lim}.

The first two conditions imply that new cracks can initiate at locations where the current stress-state has resulted in the closing of the pre-existing cracks. The third one prevents the presence of spurious cracking with similar direction to nearby cracks. To illustrate this, Fig. 4.11 illustrates how the algorithm models the two shear cracks at the middle of the wall for the example of Fig. 4.10. Fig. 4.11a shows the stress-state within the crack at the moment of the opening of the crack during the movement towards the left. The two versors of the crack ($\hat{v}_{cr}$ and $\hat{v}_{cl}$, shown in one of the two crack-tips of the crack) coincide, as the crack direction has been defined according to the crack-propagation direction of each element within it. The crack is active and can continue its propagation. Figure 4.11b presents the stress state for a step during the reversal of the cycle. The wall is now deforming towards the right and the existing crack is closed. This can be seen by the direction of the principal stresses which have rotated compared to when the crack was open. The crack closure ($\hat{v}_{cr}$) and crack direction versors ($\hat{v}_{cl}$) form an angle which is greater than the limit angle α_{lim}. The existing crack is therefore identified as inactive, and new cracks are allowed to open. This happens at a later instance, shown in Fig. 4.11c, when a crack initiates very close to the existing crack and propagates thereafter.

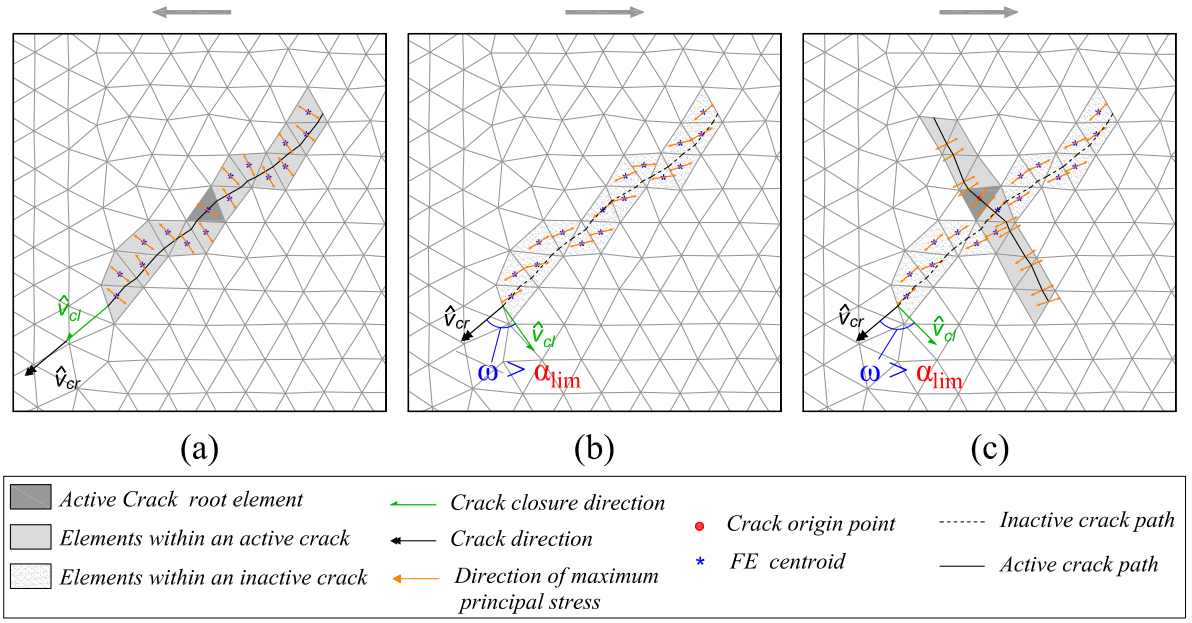

Figure 4.11 Crack propagation in the middle of a shear wall: (a) propagation of a shear crack for the loading towards the left, (b) deactivation of the crack due to the change in the stress state, (c) initiation and propagation of a second crack next to the inactive one.

The use of a limit angle, as a way to identify the closure of existing cracks and the possibility of new ones to open, resembles the concept used to model multiple cracks at constitutive level in the smeared crack models by de Borst and Nauta [98]. A similar concept was used also by Song & Belytschko aiming to model crack branching for propagating cracks [362] under dynamic fracture. Likewise, the limit angle introduced in this work (α_{lim}) is a numerical parameter aiming to deactivate the use of the exclusion radius

when the strain state of the crack has exceeded the margins set by Eq. (4.2) and thus to allow new cracks to emerge close to existing ones.

4.2.9 Implementation

The local nature of the proposed tracking algorithm allows its straightforward implementation to any standard finite element code. The algorithm can be defined as two subroutines, which are called at different instances of each numerical step. The first subroutine is responsible for the propagation of new and existing cracks and is called at the beginning of each step before the calculation of the stress state of each element. The second subroutine is called upon convergence of the numerical solution and is responsible for the crack-path continuity of each crack and the update of the flag system of each element according to its damaged status. Table 4.1 presents the structure of the two above parts of the tracking algorithm.

Table 4.1 The two subroutines used for the implementation of the fixed and multi-directional tracking algorithms.

Start - Part I

(i) Recovery of the crack-tip elements and their crack-entry coordinates.

(ii) Propagation of existing cracks.

(iii) Search for *potential crack-roots* for elements satisfying Eq. (4.1).

(iv) Multi-directional tracking considered?

YES : Find the *crack-roots* according to procedure presented in Section 4.2.8

NO : Find the *crack-roots* according to procedure presented in Section 4.2.1

(v) Propagation of new cracks

End - Part I

Start - Part II

(i) Check for crack path continuity

(ii) Update crack status of finite elements

End - Part II

The above structure of the proposed algorithm allows for further modifications concerning the use of the tracking algorithm during each numerical step. For instance, in this work the first part of the algorithm is called only once at the beginning of each step, and the propagation of new and existing paths is based on on the converged stress state of the previous step. The aim of this choice is twofold. Firstly, an increased resolution of the step size is normally necessary for the accurate simulation of highly non-linear problems, which

is the case of this thesis, and therefore no important errors are anticipated in the crack paths from the selected strategy. Secondly, it is an efficient choice in terms of computing time, suited for the analysis of structural cases with a large number of cracks, as complex masonry structures. This strategy is common in tracking algorithms (e.g. [259, 373]).

Nevertheless, an increase of this first order accuracy (the error is proportional to the size of the time step) it is possible by including the tracking algorithm during the prediction-correction process, calling it at the beginning of each equilibrium iteration. In this way, the predicted strain (and thus effective stress) state can be considered for the crack propagations at the cost of an increasing computational time. This choice, however, entails the danger of serious convergence problems. On a different line, a second (or higher) order prediction of the stresses at the current steps can be done considering the stresses at the two (or more) previous time steps [77]. This strategy will reduce the dependence of the crack paths on the size of the time step by increasing the memory requirements according to the stored number of the previous steps.

Other implementation issues of the proposed tracking algorithm concern some topological information and the storage requirements. Regarding the first, the connectivity between all the elements, as well as their relative position within the mesh is recognized and stored at the beginning of the analysis. The rest of the information that needs to be saved and retrieved during the analysis is: (i) the crack-origin and crack-tip(s) of each crack, (ii) the crack-origin and crack-entry coordinates of each element, (iii) the identity number of the crack(s) each damaged element belongs to and (iv) the flag status of each element.

4.3 Summary

This chapter presents novel local tracking algorithms for the simulation of localized cracks in a smeared cracking context. The purpose of the algorithms is to identify at each load/time increment of the numerical analysis the nucleation of new cracks and designate their propagation, along with that of existing cracks, within the mesh. A crack is simulated as a continuous row of finite elements, which experience damage at their Gauss points according to the presented continuum damage mechanics model in Chapter 3. The rest of the finite elements outside of a crack maintain a linear elastic stress-strain relationship. The user has the possibility to determine the distance between new and existing cracks. In case of masonry, this distance can be defined making reference to the unit's size or the bond pattern.

This thesis proposes several developments in the context of tracking algorithms that make possible the analysis of large structures experiencing multiple and arbitrary cracking against monotonic and cyclic loading. The first contribution of this thesis concerns the simulation of new cracks under monotonic loading, which is possible with the use of the *fixed tracking algorithm*. Contrary to most existing tracking algorithms, cracks are allowed

to nucleate from any location of the discretized domain, at elements satisfying the failure criterion of the selected continuum damage model. Then, their propagation depends on the location of the crack-origin element. For internal crack-origins, a new methodology is proposed allowing cracks to propagate in two opposite directions. For elements starting from the boundary, the original approach presented in [77, 84, 85, 292] is maintained and cracks can propagate towards a single direction. At this point, a novel enhancement is presented that allows the modelling of cracks running parallel to the mesh boundary, such as cracks at the end of walls or piers.

Two more novel procedures are proposed for the simulation of cracking under cyclic loading. The first one is a methodology that allows the intersection of cracks during their propagation. This is another improvement compared to existing tracking algorithms, which is possible due to the local nature and the smeared cracking basis of the proposed approach. The second novelty refers to the definition of active and inactive cracks. For active cracks, the exclusion radius criterion is considered, and new cracks are allowed to open only at the specified distance from existing ones. Contrariwise, inactive cracks do not restrict the opening of new ones next to them. This procedure for the crack nucleation is referred as *multi-directional tracking algorithm* and it is used for the simulation of cases with in-plane cyclic loads. Additionally, this chapter presents a procedure ensuring crack-path continuity in both fixed and multi-directional tracking algorithms.

The local nature of the tracking algorithms is characterized by a straightforward implementation to any standard finite element code. For this purpose, implementation details are presented in the last section of this chapter. The tracking algorithms are defined as two subroutines called at the beginning and at the end of each load/time increment of the numerical analysis. Finally, the algorithms can be combined easily with other material models as shown in [294, 327]. This allows their future use with more sophisticated material models considering the linear and non-linear anisotropy of masonry.

5

Structural Applications*

This chapter presents structural applications of the proposed tracking algorithm and constitutive model. The first case study considers the simulation of a standardized experiment resulting in a single internal crack, i.e. the Brazilian splitting test (Section 5.2). The next case study considers a real-scale masonry frame tested in laboratory against in-plane monotonic loading (Section 5.3). Section 5.4 deals with the simulation of a shear masonry wall tested against cyclic in-plane loading. The last case study (Section 5.5) presents the seismic analysis of a real-scale 5-storey masonry structural wall through an equivalent non-linear static analysis. The proposed approach is validated through comparison of the obtained numerical results with analytical and experimental data, as well as with the results from other numerical approaches available in the literature. Issues such as mesh-objectivity, influence of the numerical parameters, in addition to computational cost are also examined.

5.1 Introduction

A common practice used for the validation of localization techniques in numerical analysis is the comparison with experimental benchmark tests including a limited number of cracks in concrete specimens (e.g. [69,100,227,265,356,404]). Concrete, however, is scarcely used in engineering practice without some type of reinforcement. The common use of steel rebars provides damage patterns characterised commonly by distributed cracking, whose formation and propagation is usually simulated by classical smeared crack approaches. In these cases, cracking of the concrete is only one of the damage pathologies leading to collapse, while other issues, as the failure of the reinforcement, become equally important.

*This chapter presents a summary of the numerical results presented in References [326, 328–330]

Masonry structures, on the other hand, are commonly constructed without any reinforcement and exhibit localized cracks that determine the collapse mechanism and the structural capacity. The use of localization techniques seems to suit very well the purpose of the realistic structural analysis of masonry buildings. For this reason, the proposed localized damage model, based on the combination of the continuum damage model and the tracking algorithm presented in Chapters 3 and 4 respectively, is used in the following for the analysis of small and large-scale masonry structures. The choice of the case studies are made considering the availability of experimental data, as well as simulations with alternative numerical methods in the literature.

The simulated case studies adopt a macro-mechanical and continuum modelling of masonry material. It is noted that the deduction of the homogenized masonry properties from experimental in-situ and laboratory tests is a very difficult task. This is due to the lack of experimental methods for the assessment of the critical tensile and shear properties of the composite, but also due to the wide scattering of data in the cases that those exist. For this reason, the main task of this work is to assess the capacity of the proposed methodology to capture the emerging collapse mechanisms rather than a close quantitative reproduction of the experimental results.

5.2 Brazilian splitting test[†]

The first numerical application considers the simulation of the Brazilian splitting laboratory test. This benchmark example has three objectives. Firstly, to validate the capacity of the proposed algorithm to simulate cracking that initiates from the interior of the discretized domain and propagates along two opposite orientations. Secondly, to investigate the dependency of the tracking algorithm on the mesh discretization, both in terms of direction and size of the finite elements. Finally, to provide information regarding the computational cost induced by the use of the tracking algorithm.

5.2.1 Experimental set-up and failure pattern

In the Brazilian splitting test, the tested specimen has a circular cross-section of diameter D and a depth l (Fig. 5.1). The test consists in applying a compressive force along the diameter of the tested cylinder until failure occurs. The failure pattern is characterized by a crack, starting from the interior of the tested specimen and propagating towards the boundaries following the direction of the applied compressive forces, i.e. along the diameter of the tested specimen. The obtained value of the maximum load is used to define the splitting tensile strength of the tested material. The Brazilian splitting test is a standard method for the estimation of the splitting tensile strength of geomaterials such as concrete [15] and rocks [16].

[†]This section is based on Reference [329]

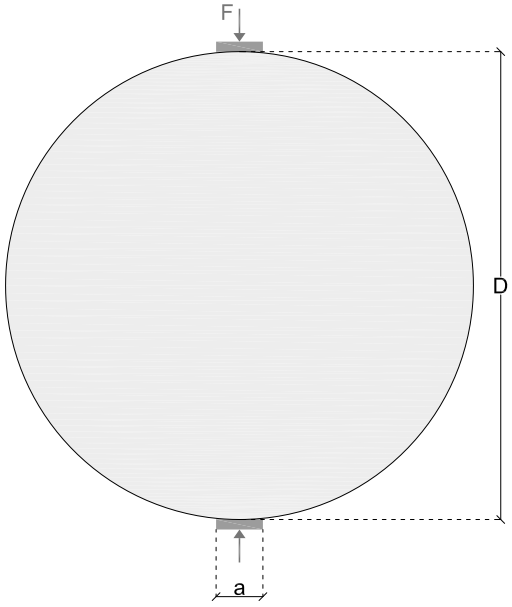

Figure 5.1 Geometry and testing scheme of the Brazilian splitting test.

5.2.2 Numerical simulation

The dimensions considered in the numerical simulation, with respect to Fig. 5.1, are $D = 15\ cm$, $a = D/10 = 1.5\ cm$. The cylinder is analysed under plane strain conditions. Typical material properties for concrete have been adopted: $E = 30.1\ GPa$, $f^+ = 2.2\ MPa$, $v = 0.25$, $f^- = 20\ MPa$, $= 2400\ kg/m^3$, $G_f^+ = 50\ J/m^2$, $G_f^- = 15000\ J/m^2$. The fixed-tracking algorithm has been used with the following parameters r_{excl}= 0.5 cm, $a_{max} = 45°$ and $r_{neigh} = 0.5\ cm$. The experiment is simulated by imposing a vertical displacement at the top of the upper bearing plate, and restraining the vertical displacement at the bottom. At each step of the analysis, the corresponding non-linear equations are solved with the use of a secant (Picard's) method along with a line-search procedure. Convergence of an increment is attained when the ratio between the iterative residual forces and the norm of the total external forces is lower than 10^{-3} (0.1%).

5.2.3 Mesh-dependency

This section focuses on the sensitivity of the numerical solution to the typology of the used discretization, both in terms of orientation and size of the finite elements. Figure 5.2 presents the four meshes used for studying the dependence of the numerical solution on the directionality of the finite elements sides within the mesh. The first two are discretized in an unstructured manner with average element sizes, at the region where damage is expected, $h_e = 50\,mm$ (984 nodes, Fig. 5.2a) and $h_e = 25\,mm$ (1711 nodes, Fig. 5.2b), respectively. The same region is discretized in a structured manner in the last two meshes, with average element sizes $h_e = 50\,mm$. It is noted that these meshes have been designed avoiding the alignment of the predominant directions of the triangular

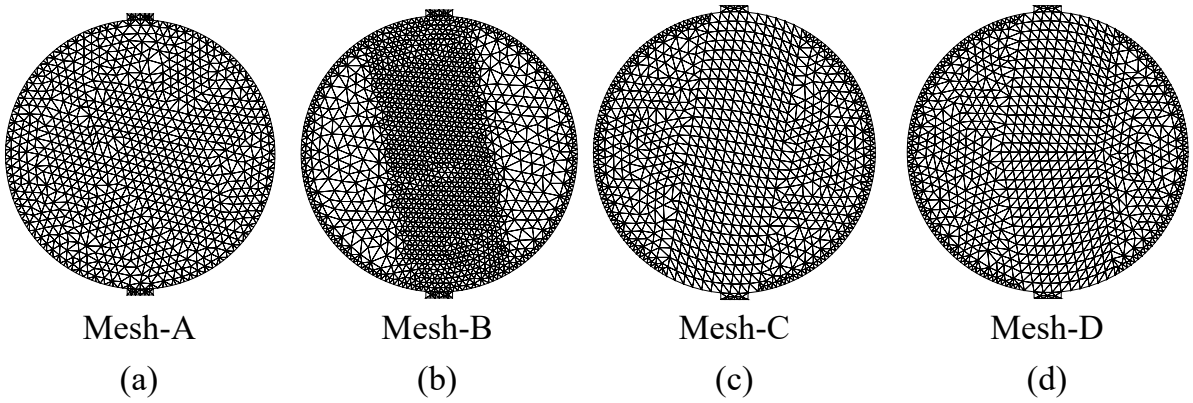

Figure 5.2 The four meshes used for the directional mesh-bias sensitivity study.

elements with the vertical axis, where the cracking is expected to occur. This has been done to investigate the capability of the proposed localized damage model to provide results that are independent on the orientation of the used mesh. In particular, for the structured mesh Mesh-C (994 nodes, Fig. 5.2c) the sides of the rectangular triangles create angles of around -10°, 80°, 125° with the horizontal axis. In the structured mesh Mesh-D (1016 nodes, Fig. 5.2d) the structured region has been split into two, with the triangles in the lower part being a mirror of the ones in the upper part.

Figure 5.3 presents the contour of the d^+ tensile damage index for both the analyses with and without the use of the proposed tracking algorithm. The results using the classical smeared crack approach present a large spreading of damage within the discretized domain. Additionally, the localization of damage depends spuriously on the mesh. This can be better visualised in the plot of the maximum principal strains, in Fig. 5.4. The use of the tracking algorithm successfully addresses the aforementioned flaws of the classical smeared crack approach, resulting in a vertical crack starting from the interior of the mesh and propagating along the loading direction for all the used meshes.

Apart from the sensitivity of the numerical solution on the directionality of the mesh, the effect of the finite element size is also investigated. To this aim, simulations have been performed with two additional meshes keeping the mesh-orientation of Mesh-C, but changing the sizes of the finite elements. Mesh-C' has mean element sizes $h_e = 75\,mm$ (384 nodes, Fig. 5.5a), while in Mesh-C" $h_e = 25\,mm$ (1983 nodes, Fig. 5.5c).

The refinement of the mesh has no positive effect on the simulation of the expected crack direction using the classical smeared crack-approach (Figs. 5.6a and 5.7a). A vertical crack could not be simulated, even in the finer mesh, and the spurious spreading of damage around the localized band does not reduce on mesh refinement (Fig. 5.6a). On the other hand, the use of the tracking algorithm predicts the expected vertical crack pattern independently of the discretization size (Fig. 5.6b and Fig. 5.7b).

Table 5.1 presents a comparison between the peak load obtained for each of the performed analysis and the analytical solution. The latter is calculated through the formula

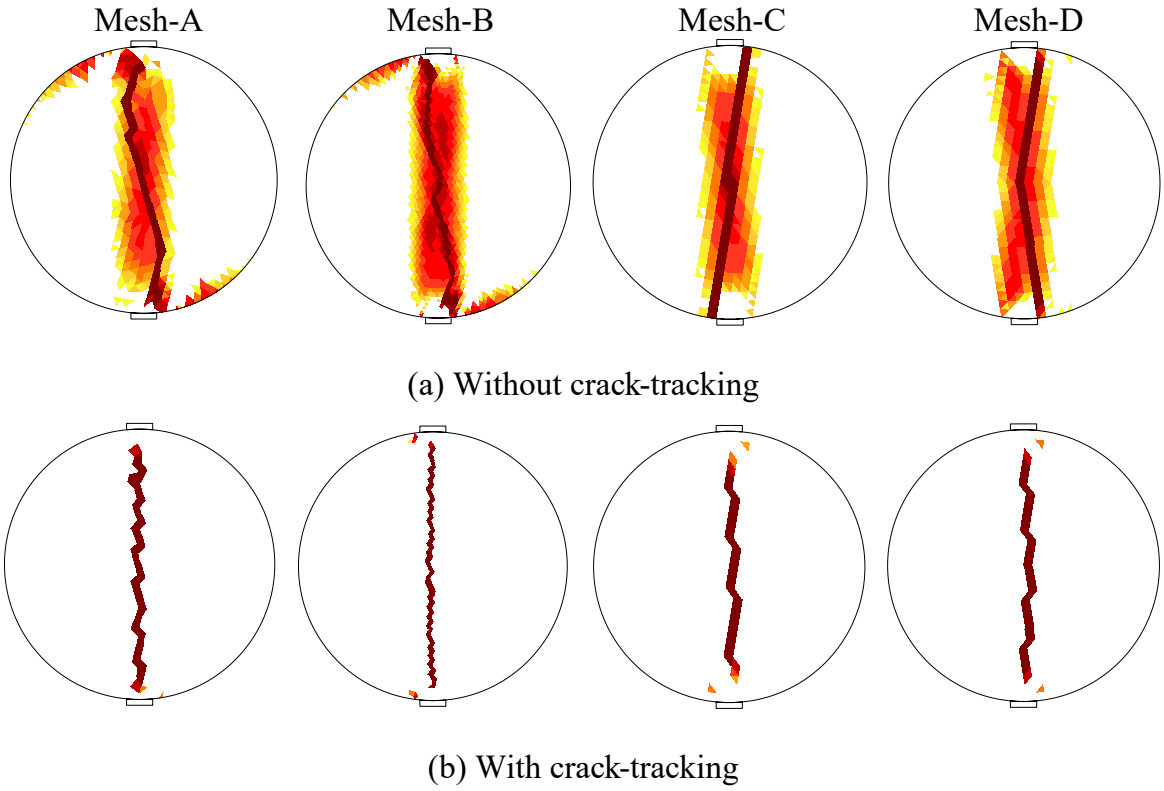

Figure 5.3 Directional mesh-bias sensitivity. Contour of the tensile damage index (d^+) after the peak load for four different meshes: (a) without the tracking algorithm, (b): with the tracking algorithm.

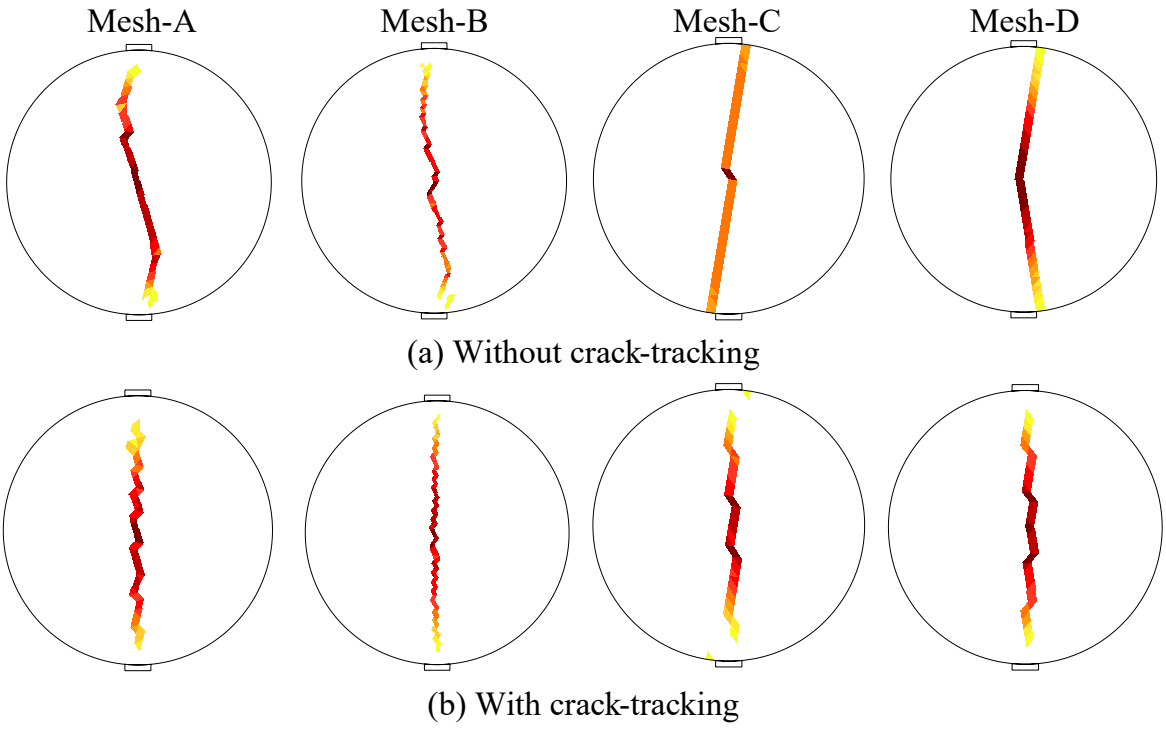

Figure 5.4 Directional mesh-bias sensitivity. Contour of the maximum principal strains after the peak load for the four different meshes: (a) without the tracking algorithm, (b): with the tracking algorithm.

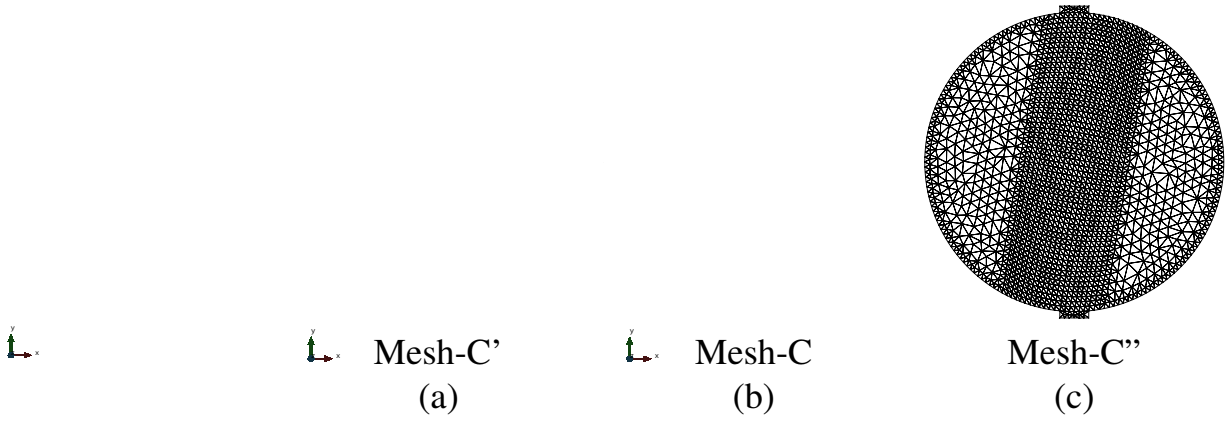

Figure 5.5 The three meshes used for the mesh-size sensitivity study.

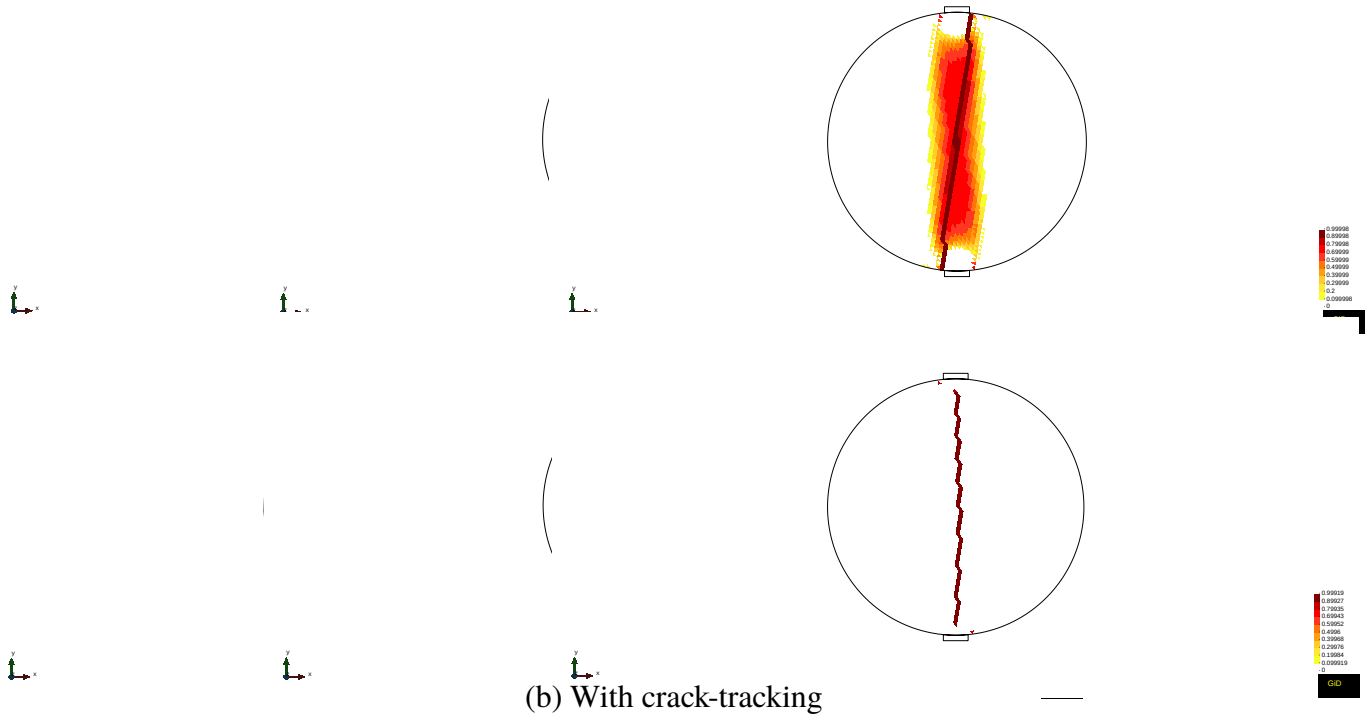

Figure 5.6 Mesh-size sensitivity. Contour of the tensile damage index (d^+) after the peak load for four different meshes: (a) without the tracking algorithm, (b): with the tracking algorithm.

proposed by [15, 16] that is

$$P/l = \frac{\pi D f_{sp}}{2} \tag{5.1}$$

where P/l is the capacity per unit length and f_{sp} is the splitting tensile strength. Its value is considered equal to $f_{sp} = f^+/0.9$ according to Eurocode 2 [115]. The results of both approaches are close to the analytical predicted value. The use of the tracking algorithm gives results which are closer to the analytical ones for all the studied meshes. Contrariwise, the large spreading of damage in the numerical solution without the tracking

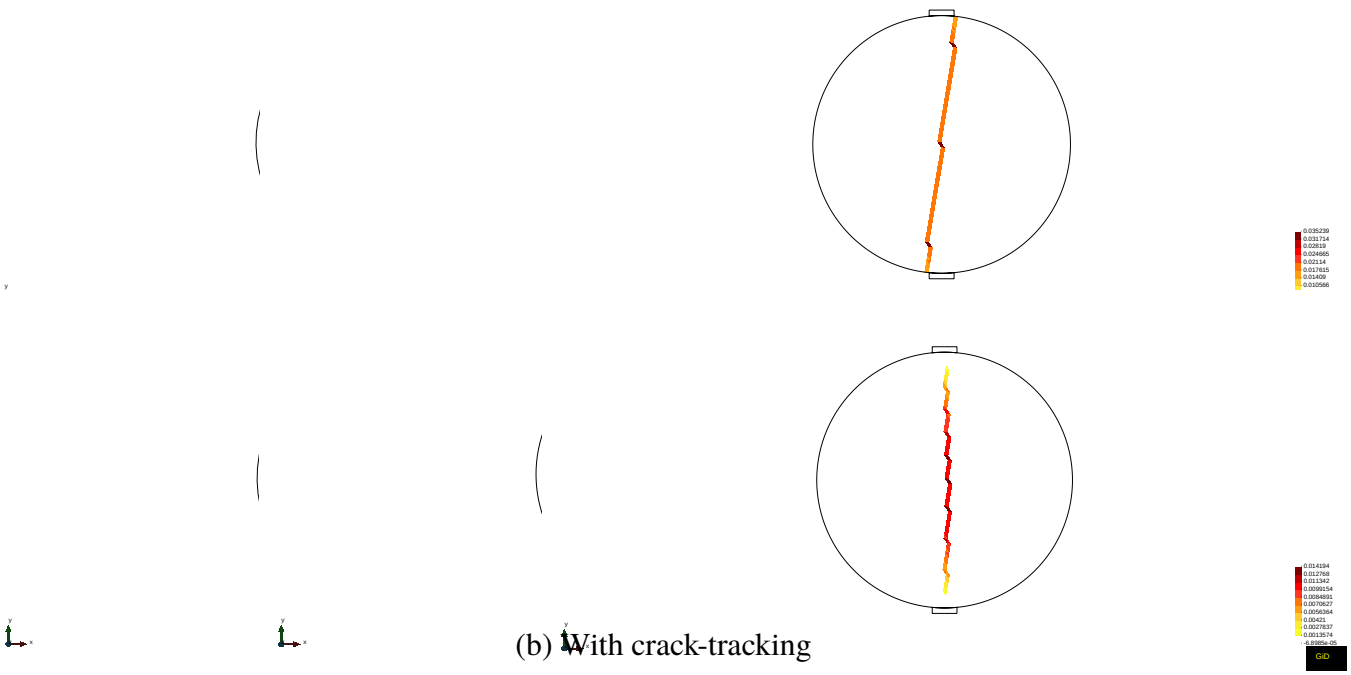

(b) With crack-tracking

Figure 5.7 Mesh-size sensitivity. Contour of the maximum principal strains after the peak load for the four different meshes: (a) without the tracking algorithm, (b): with the tracking algorithm.

algorithm seems to result in an underestimation of the specimen's capacity. The minor variations of the load-capacity, despite that a straight crack path has been obtained using the tracking algorithm for all the meshes, are attributed to the selected definition of the characteristic length as a function of the finite element's area (see Section 3.5). A more precise definition, concerning the crack geometry as the ones presented in [56, 251, 358], is expected to reduce the observed differences.

Table 5.1 Comparison between numerical and analytical results with and without the tracking algorithm for the Brazilian splitting test.

		No-Tracking		Tracking	
Mesh	Analytical capacity $[kN/m]$	Capacity $[kN/m]$	Difference from analytical [%]	Capacity $[kN/m]$	Difference from analytical [%]
Mesh-A	575.96	537.56	-6.67	579.39	0.60
Mesh-B	—"—	538.22	-6.55	585.29	1.62
Mesh-C'	—"—	514.98	-10.06	539.65	-6.30
Mesh-C	—"—	529.66	-8.04	544.44	-5.47
Mesh-C"	—"—	532.35	-7.57	549.10	-4.66
Mesh-D	—"—	529.14	-8.13	554.09	-3.80

5.2.4 Computational cost

Table 5.2 presents the computational cost, in terms of time and memory resources, needed for the performed analyses with and without the tracking algorithm. All the numerical analyses in this thesis have been performed in a single machine equipped with an Intel Core i7-4790-3.60GHz CPU and 16.0 GB RAM.

As can be seen, the tracking algorithm is very efficient both in terms of memory requirements and computational time. The necessary arrays, presented in Chapter 4, result in additional memory requirements of around 17 % using the tracking algorithm. The performed analyses show that the computational time overhead using tracking increases, as expected, with the increase of the number of degrees of freedom, with a maximum overhead of around 31% for the case of the refined Mesh-C". Note that in some cases (Mesh-A and Mesh-B) the computational cost using the tracking algorithm is lower than a calculation done without using it. This is a result that has been seen in many of the forthcoming analysis of this thesis and is attributed to the improvement of the non-linear iterations convergence rate due to the correct damage localization when using the tracking algorithm.

Table 5.2 Computational cost with and without the use of the tracking algorithm for the Brazilian splitting test.

		No-Tracking		Tracking		Overhead using tracking	
Mesh	Number of nodes	Memory [Mb]	CPU-time [s]	Memory [Mb]	CPU-time [s]	Memory [%]	CPU-time [%]
Mesh-A	984	1.33	14.52	1.56	13.06	17.29	-10.06
Mesh-B	1711	2.37	28.66	2.78	24.96	17.30	-12.91
Mesh-C'	384	0.52	4.38	0.61	5.07	17.31	15.75
Mesh-C	994	1.35	10.47	1.58	13.15	17.04	25.60
Mesh-C"	1983	2.76	24.98	3.24	32.74	17.39	31.06
Mesh-D	1016	1.38	10.61	1.62	13.48	17.39	27.05

5.3 Masonry frame[‡]

This section investigates the capacity of the proposed algorithm to simulate the response of a large-scale structural problem exhibiting multiple cracking. The simulated experiment consists of a real-scale unreinforced masonry frame with an opening tested under in-plane lateral loading by Augenti et al. [18]. This structural example has been selected due

[‡]This section is based on References [328, 329]

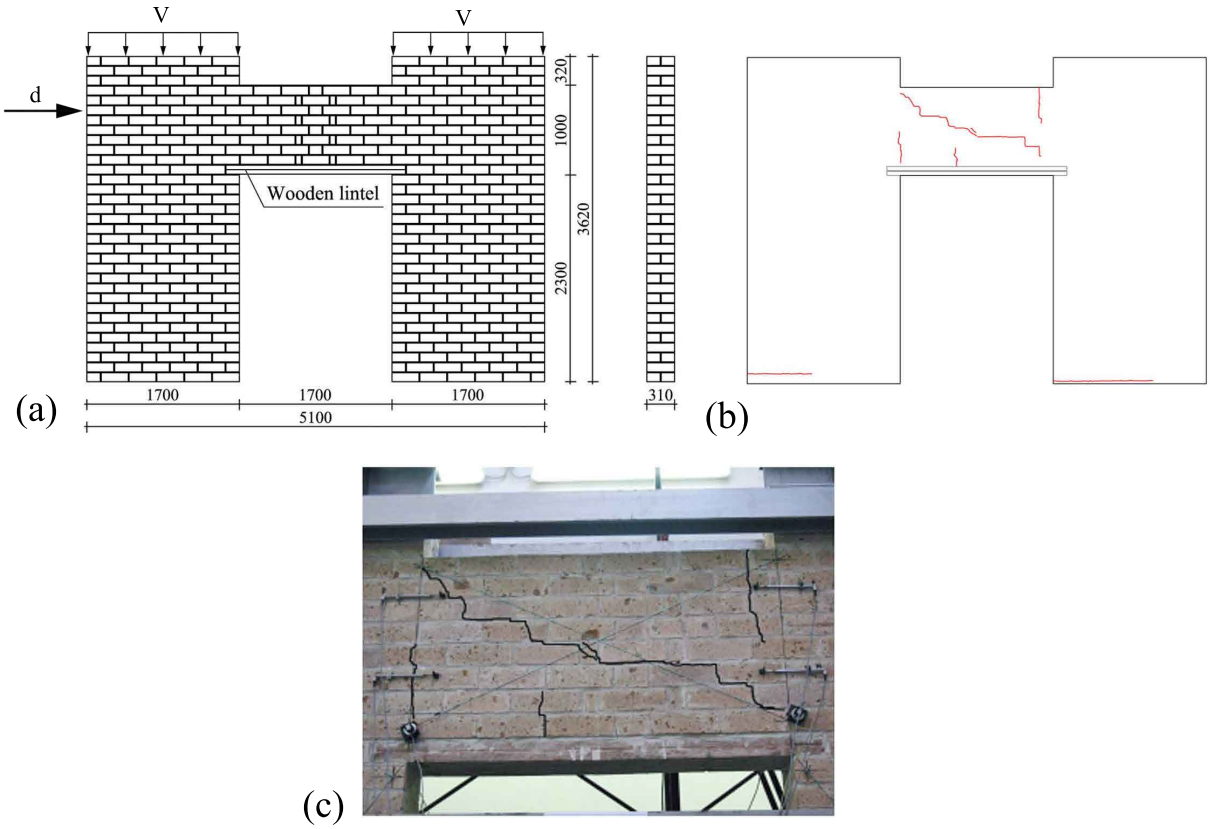

Figure 5.8 (a) Geometry and load configuration of the experiment. Cracking at the end of the experiment of (b) the whole frame and (c) the spandrel. (Picture adapted from [18]).

to the complexity given by the structural interaction among the piers and the spandrel, representing a meaningful case with different types of cracks due to traction, shear and flexure. In fact, this test can show the capacity of the used approach to represent both the experimental cracking pattern and the redistribution of actions among structural members as soon as the different cracks appear.

5.3.1 Experimental setting and results

The masonry is built of yellow tuff bricks with dimensions 150 $\times$ 300 $\times$ 100 mm^3 and hydraulic mortar of 10 mm thickness. The wall has overall dimensions of 5100 mm length, 3620 mm height and 310 mm thickness. The spandrel above the opening lies over a timber lintel with bond length of 150 mm at both sides.

The experimental test was performed in two steps. Initially, a distributed load was applied at the top of each pier with a resultant $V = 200\ kN$. This was followed by the application of a horizontal displacement d at the left of the wall keeping the vertical load constant. Figure 5.8a illustrates the geometry and the load configuration of the experiment. Figures 5.8b and 5.8c show the resulted cracking in the whole structure and the spandrel, respectively. The in-plane loading activated different failure phenomena in masonry resulting in a complex cracking of the structure. In particular, two horizontal cracks formed at the base of the piers due to the debonding between the units and the

Table 5.3 Material parameters for the masonry frame wall.

f^+ $[MPa]$	f^- $[MPa]$	G_f^+ $[J/m^2]$	G_f^- $[J/m^2]$	E $[GPa]$	ρ $[kg/m^3]$	v $[-]$
0.13	3.9	5	35000	1.54	1200	0.2

mortar. Flexural cracking, crossing both the units and mortar-units interface, appeared in three locations at the lower and the upper part of the spandrel. Finally, the last reported damage was a diagonal shear crack starting from the middle of the spandrel and extending diagonally towards its opposite corners. For a detailed description of the experimental setup, the loading procedure and the damage pattern the reader is referred to the original work of Augenti et al. [18].

5.3.2 Numerical simulation

The experimental test is simulated using the fixed tracking algorithm presented in Chapter 4. The material of the wall is idealized as homogeneous with its properties derived from the available experimental data [18], while appropriate values from the literature are chosen for the non-available material parameters, see Table 5.3. It is noted that the selected value for the Young's modulus is lower than the experimentally obtained value for the composite material (i.e. around $2.2\,GPa$). The adopted value coincides with the experimentally measured Young's modulus of the bricks and the mortar (i.e. $1.54\ GPa$ and $1.52\ GPa$ respectively) [18], which is a value that represents closely the linear stiffness of the tested frame. The influence of the above material parameters on the structural response has been presented in [328]. The ratio between uniaxial and biaxial compressive strength is considered as $f_b^-/f^- = 1.15$. Linear elastic behaviour is assumed for the timber lintel with Young's modulus $E = 15\ GPa$. The connection between the masonry and the timber lintel is modelled with care in order to provide a realistic representation of the actual interaction between the two neighbouring materials. This interconnection is modelled through a soft layer with thickness of $10\ mm$ and limited strength and stiffness aiming to account for some relative rotation of the lintel with respect to the masonry ($E = 0.02\ GPa$, $f^+ = 0.01\ MPa$, $v = 0.2$, $f^- = 3.9\ MPa$, $G_f^+ = 5\ J/m^2$, $G_f^- = 35000\ J/m^2$). This zone can be seen as the continuous counterpart of a discontinuous interface with almost zero tensile strength.

Similar to the experiment, the numerical simulation consists of two stages. At the first one, the dead load is applied along with a vertical force equal to $200\ kN$ at the top of each pier. During the second stage, a horizontal displacement at the left part of the structure is applied in an incremental fashion, keeping the load of the first step constant. Similar to the Brazilian test, a secant (Picard's) method has been used for solving the non-linear equilibrium equations at each numerical step of the analysis along with a line

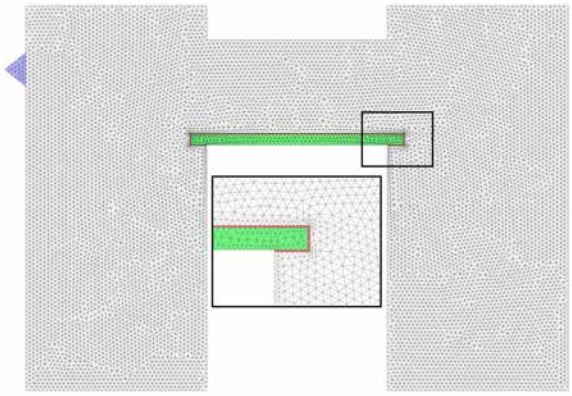

Figure 5.9 Finite element mesh used in the numerical simulation.

search procedure. Convergence of a numerical step is attained when the ratio between the iterative residual forces and the norm of the total external forces is lower than 10^{-2} (1%).

The masonry frame is discretized in an unstructured mesh of 2D plane-stress three-noded triangles with average mesh size of $h_e = 4\,mm$ (10678 nodes) (Fig. 5.9). In the reference case studied in this section, the input parameters for the tracking algorithm are $r_{excl} = 300\ mm$ (equal to the length of the bricks), $a_{max} = 45°$ and $r_{neigh} = 200\ mm$. The influence of these values is investigated in Section 5.3.5.

5.3.3 Results and discussion

Figure 5.10 illustrates the sequence of the tensile cracks obtained from the numerical analysis. In the first part of the numerical simulation, which includes the application of the dead load as well as the load of 200 kN at the top of the piers, no damage occurs. Two vertical cracks at the corners of the spandrel are the first damage affecting the structure during the second stage of the analysis (Fig. 5.10a). An increase of the horizontal displacement results in the formation of two horizontal cracks at the base of the piers (Fig. 5.10b) and their subsequent rocking. Following this, internal cracking starts to form within the spandrel (Fig. 5.10c-d). Finally, at a horizontal displacement of 21 mm, a diagonal shear crack has totally formed and secondary flexural cracks are observed at the top and bottom of the spandrel (Fig. 5.10e).

It can be appreciated in Fig. 5.10f that the obtained damage is in good agreement with the resulted cracking pattern of the experiment (cf. Figs. 5.8b-c). The open localized cracks at the end of the analysis, displayed by the contour of the maximum principal strains in Fig. 5.10f, are located at the both ends of the spandrel, at its middle and at the bottom of the piers as in the experiment.

It is noted that the numerical simulation of this particular example would be impossible using a tracking algorithm without the enhancement for internal cracking presented in Chapter 4. Apart from the internal shear cracking affecting the middle of the spandrel, the flexural cracks at its left bottom do not start from the boundary of the numerical

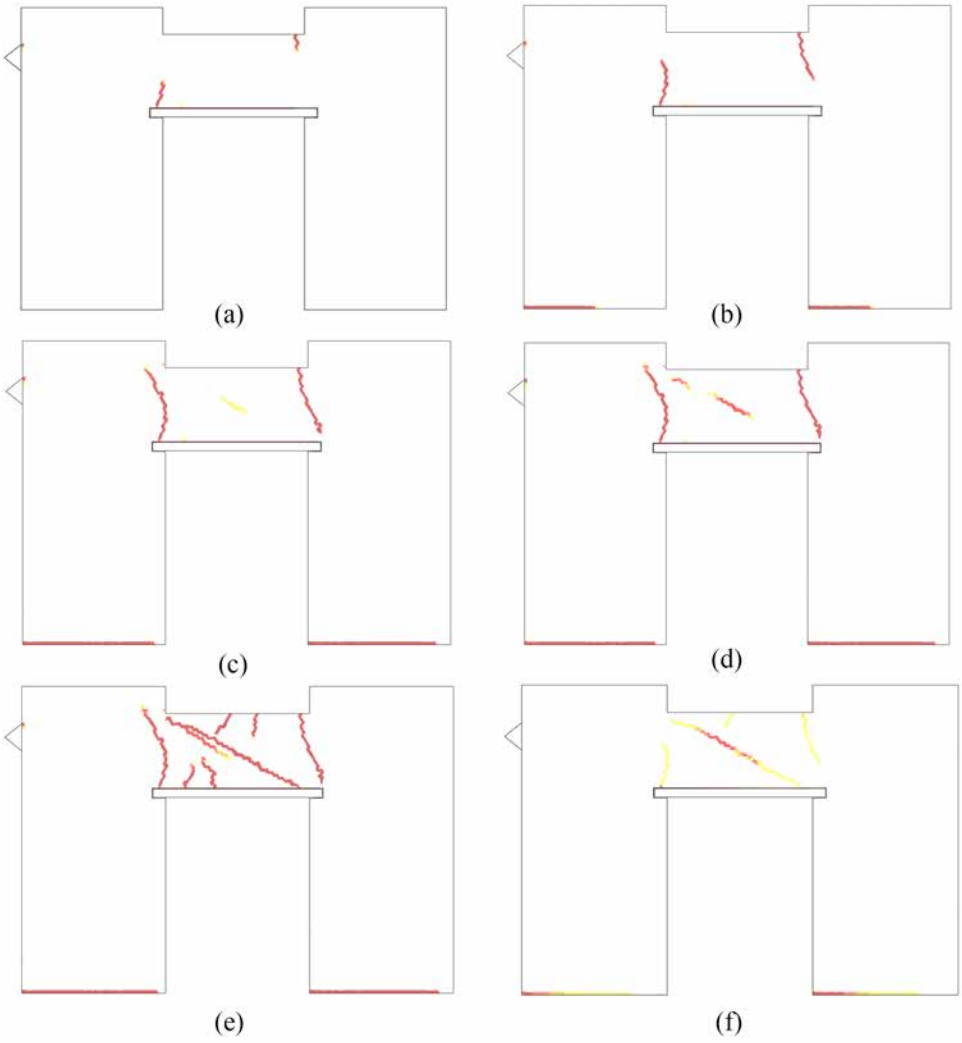

Figure 5.10 Tensile damage contour for: (a) $d = 1.5\ mm$, (b) $d = 3.3\ mm$, (c) $d = 12.3\ mm$, (d) $d = 17.3\ mm$, (e) $d = 20.7\ mm$. (f) Maximum principal strains contour for $d = 20.7\ mm$.

domain.

The numerical result using the classical smeared crack approach, without the enhancement given by a tracking algorithm, is illustrated in Fig. 5.11. Cracking at the base of the piers is almost localized within a single row of elements, facilitated by the alignment of the mesh with the expected crack direction. Contrarily, a dispersion of the damage can be observed at the region of the flexural cracks at the spandrel, where the solution is biased by the mesh topology. This spurious spreading of the damage results in the unrealistic reduction of the structural stiffness due to the spurious spreading of damage. As a consequence, the capacity of the structure reduces before reaching the necessary force for the opening of the internal shear crack that was observed experimentally. This limitation of the classical smeared crack approach prevents to capture correctly the experimental obtained damage.

The tested masonry frame has been analysed by Parisi et al. [285] with the use of the continuous micro-model presented in Fig. 5.12a. Note that no discontinuous interfaces were used for simulating the joints' behaviour, and that the timber frame was not included

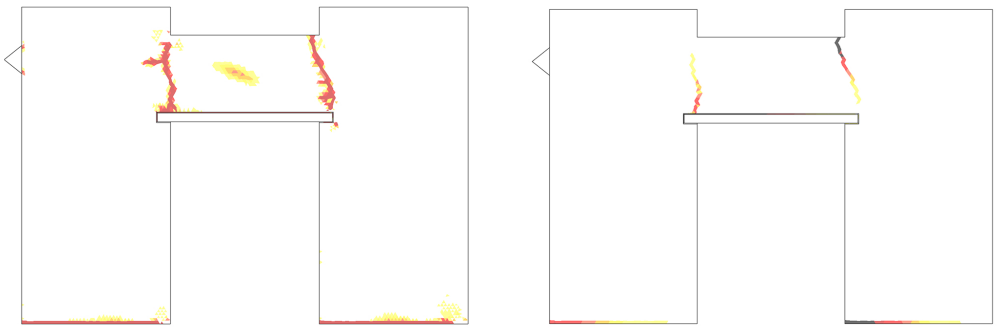

Figure 5.11 Tensile damage contour (left) and maximum principal strains (right) for the analysis with the smeared crack approach without a tracking algorithm (horizontal displacement $d = 25\ mm$).

in the numerical simulation. Figure 5.12b presents the smeared cracking strain field resulted from the analysis with the micro-model. Overall, the damage pattern obtained with the tracking algorithm (see Fig. 5.10e & Fig. 5.10f) agrees with that simulated by the micro-model, with however a more clear representation of the obtained cracks using the proposed approach. This result, in addition to the realistic representation of the cracking pattern, makes the proposed approach an efficient alternative for the analysis of similar structural cases.

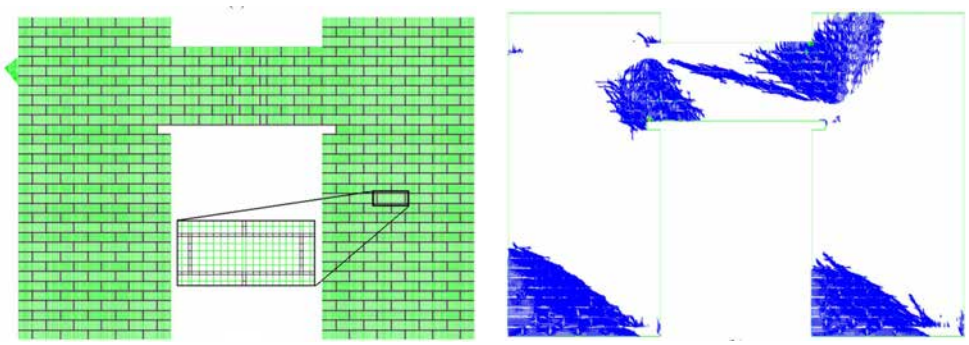

(a) **(b)**

Figure 5.12 Micro-model used in [285] for the simulation of the in-plane loaded masonry frame: (a) mesh, (b) smeared cracking strain field. (Pictures adapted from [285]).

Figure 5.13 presents the comparison between the numerical and experimental load-displacement diagrams. The use of the tracking algorithm allows to capture correctly the experimentally obtained failure curve, both in terms of maximum strength and ductility of the structure. The first significant loss of stiffness is related to the rocking of the piers and the relative cracking at their base, which results in the increasing opening of the flexural cracks at the two opposite ends of the spandrel (see Figure 5.10b). The latter damage is the dominating cause for the loss of stiffness of the structure until the shear crack forms in the spandrel, which results in the sudden drop of the applied force for a displacement of about 20 mm.

An important aspect of the numerical result is its capacity to reproduce satisfactorily the loss of structural stiffness occurring due to all the different fracture phenomena

throughout the loading history. This is essential for the evaluation of the seismic capacity of an existing structure, or the design of a new one, since common procedures (e.g. [116,120]) rely on the realistic estimation of the initial stiffness, the ductility and the strength reduction. When the tracking algorithm is not used, the load versus displacement graph fails to represent the correct sequence of fracture in the non-linear range, as the brittle shear cracking in the spandrel.

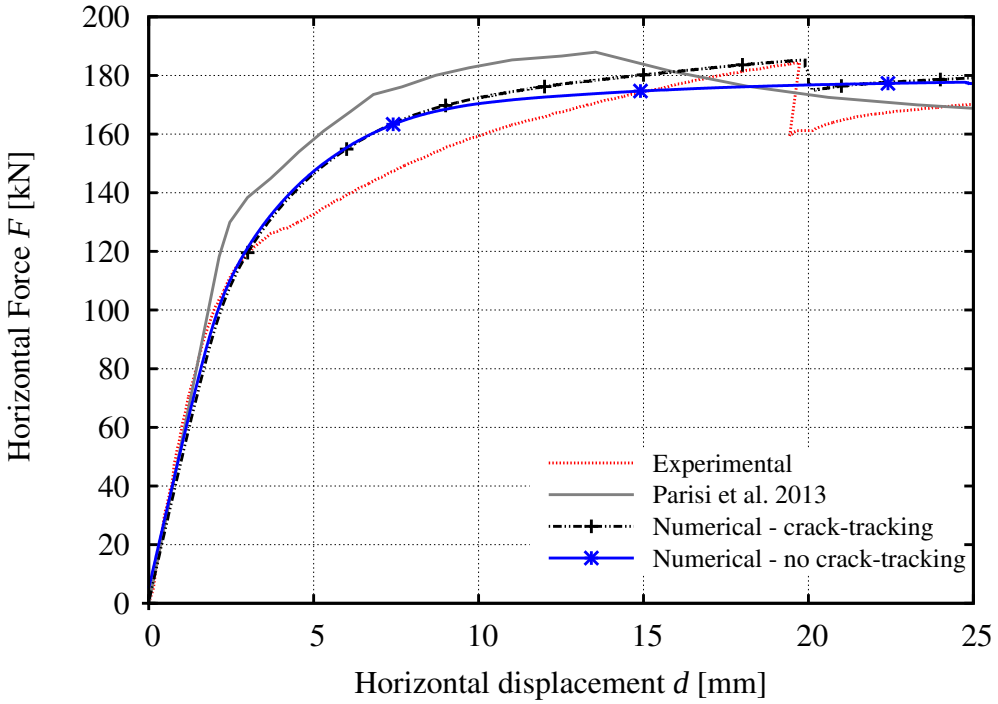

Figure 5.13 Load-displacement graph of the experimental test and the numerical analyses.

5.3.4 Computational cost

As in the example of the Brazilian splitting test, Table 5.4 presents information regarding the computational cost with and without the use of the tracking algorithm for the particular example. The additional requirements in memory lie within the same range of values as in the Brazilian splitting test, i.e around 16% higher using the tracking algorithm. The processing time with the proposed technique is around 11% higher than that of the classical smeared crack approach.

5.3.5 Influence of tracking parameters

This section presents a sensitivity analysis on the tracking parameters aiming to assess their influence on the numerical results. Figure 5.14 presents the obtained damage pattern with four different values of the exclusion radius r_{excl}= [0.1; 0.2; 0.3; 0.5 m]. As expected, the exclusion radius r_{excl} has significant effect in the numerical simulation, affecting the distribution of cracking within the analysed structure. Values lower than the unit size

result in a denser cracking within the spandrel, changing the response of the structure and the damage pattern. In particular, for $r_{excl} = 0.1\ m$ various cracks appear at the both ends of the spandrel, facilitating the rocking mode of the whole structure, while the shear crack at the middle of the spandrel cannot be reproduced. This change in the structural response can be appreciated in the load vs displacement graphs of Fig. 5.15, where for $r_{excl} = 0.1\ m$ the typical graph for a rocking failure mode is obtained, without however, the sudden drop attributed to the shear cracking of the spandrel. On the contrary, when values higher of 0.2 m are chosen, the numerical model reproduces the experimental obtained structural response (Fig. 5.14b-d and Fig. 5.15). Actually, a value of the exclusion radius lower than 0.2 m does not take into account the internal microstructure of masonry defined by the size of the brick.

The above results demonstrate the utility of the exclusion radius. The failure mechanism of masonry structures is determined by the relative position of the cracks and consequently the division of the whole structure into macroblocks. The relative geometry and strength of the components play a decisive role in the type of cracking of masonry structures. This can be appreciated in the experimental test under investigation, in which cracking occurred mainly at the joints between bricks and mortar. A continuum finite element model ignores the internal geometry of the composite and therefore fails to capture failure mechanisms determined by it. This drawback can be partially overcome with the use of the exclusion radius, which can be perceived as an implicit way to take into account the size effect of the units within a continuum finite element model. On the contrary, a micro-model could simulate this cracking phenomenon in a more direct way due to the explicit detailed geometrical definition of the problem, at the cost of a computation time largely higher than that of the proposed approach. This disadvantage of micro-models renders them hardly applicable to the analysis of large and complex structures. Instead, the used methodology shows to be a good compromise between accuracy and computational cost.

Figures 5.16 and 5.17 present the cracking affecting the spandrel and the relative load against displacement curves respectively for nine different combinations of a_{max} and r_{neigh} for $r_{excl} = 0.3\ m$. Once the exclusion radius is well defined, a_{max} and r_{neigh} have a marginal influence to the global response of the structure. The shear cracking at the middle of the spandrel is identical for all combinations of the above correction parameters. This is

Table 5.4 Computational cost with and without the use of the tracking algorithm for the masonry frame wall.

No-Tracking		Tracking		Overhead using tracking	
Memory [Mb]	CPU-time [s]	Memory [Mb]	CPU-time [s]	Memory [%]	CPU-time [%]
16.97	238.06	19.62	264.03	15.61	10.90

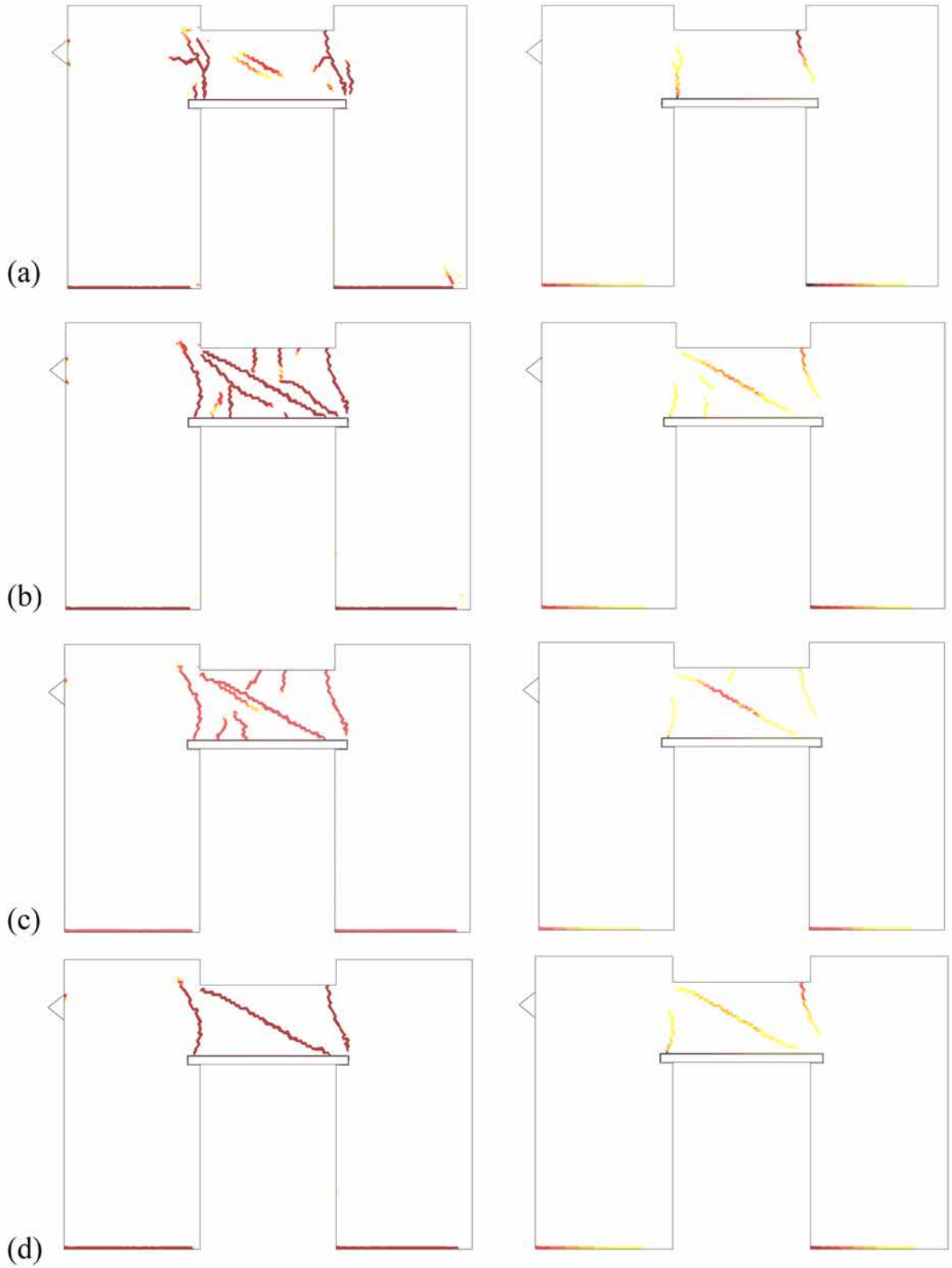

Figure 5.14 Contour of tensile damage (left) and maximum principal strain (right): (a) $r_{excl} = 0.1\ m$, (b) $r_{excl} = 0.2\ m$, (c) $r_{excl} = 0.3\ m$, (d) $r_{excl} = 0.5\ m$ (horizontal displacement $d = 0.21\ m$).

to be anticipated, since shear cracking, dominant in this case, is not affected by these parameters, in contrast to cracking under bending stress states (see [77]). Restricting the change in the crack curvature with low values of a_{max} has a small effect on the secondary

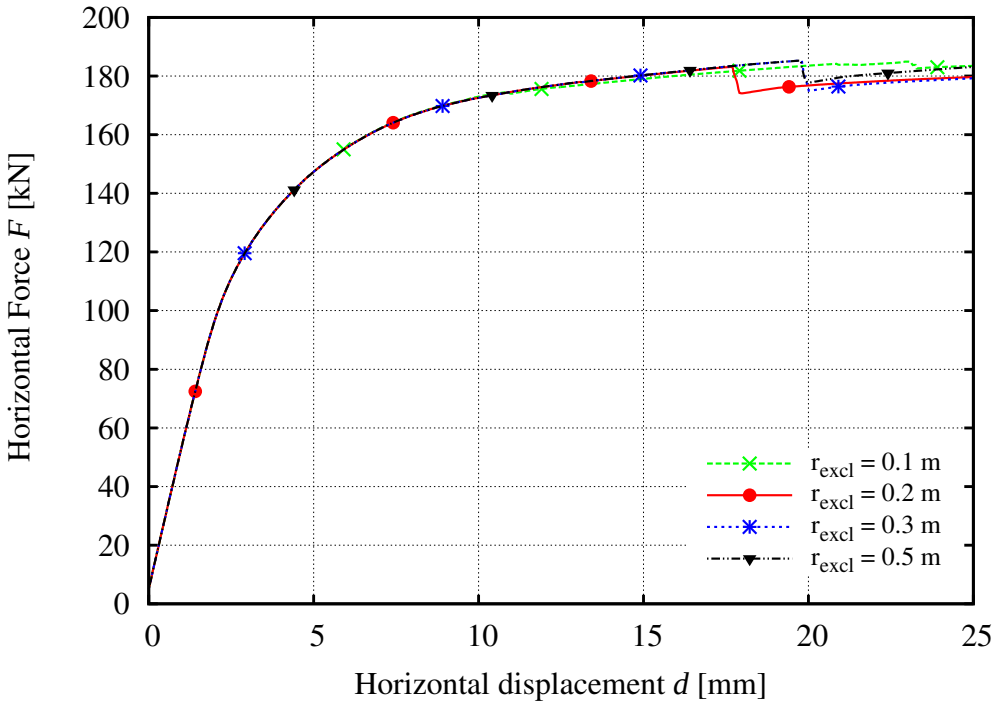

Figure 5.15 Sensitivity of the structural capacity of the masonry frame to r_{excl}.

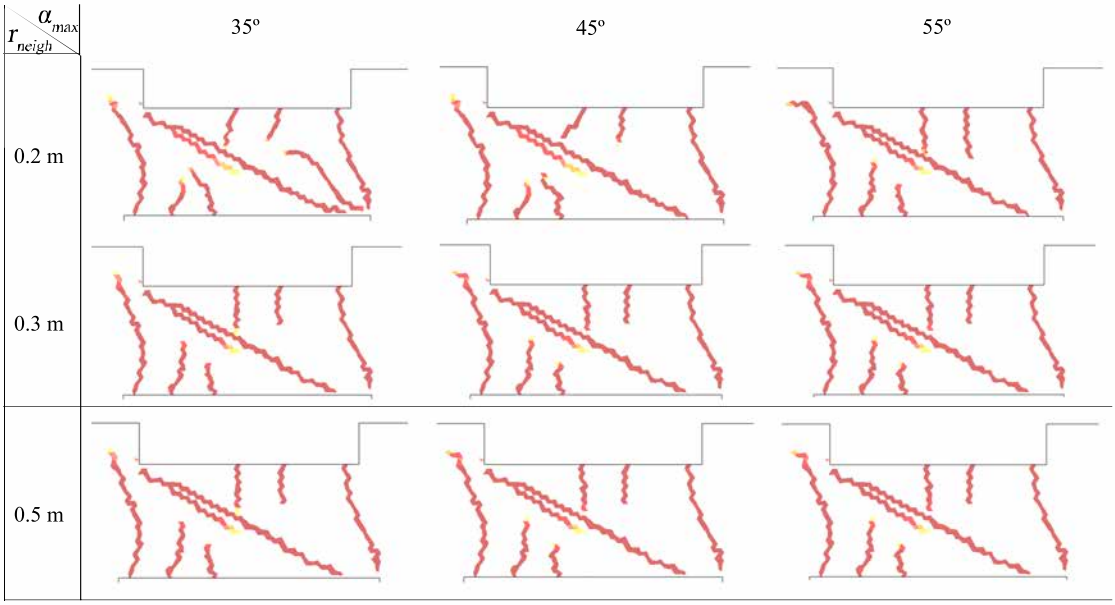

Figure 5.16 Sensitivity of damage distribution at the spandrel to a_{max} and r_{neigh}.

flexural cracking affecting the lower and upper boundaries of the spandrel. In any case, the collapse mechanism and the capacity of the structure is identical for all the investigated valu es of a_{max} and r_{neigh}.

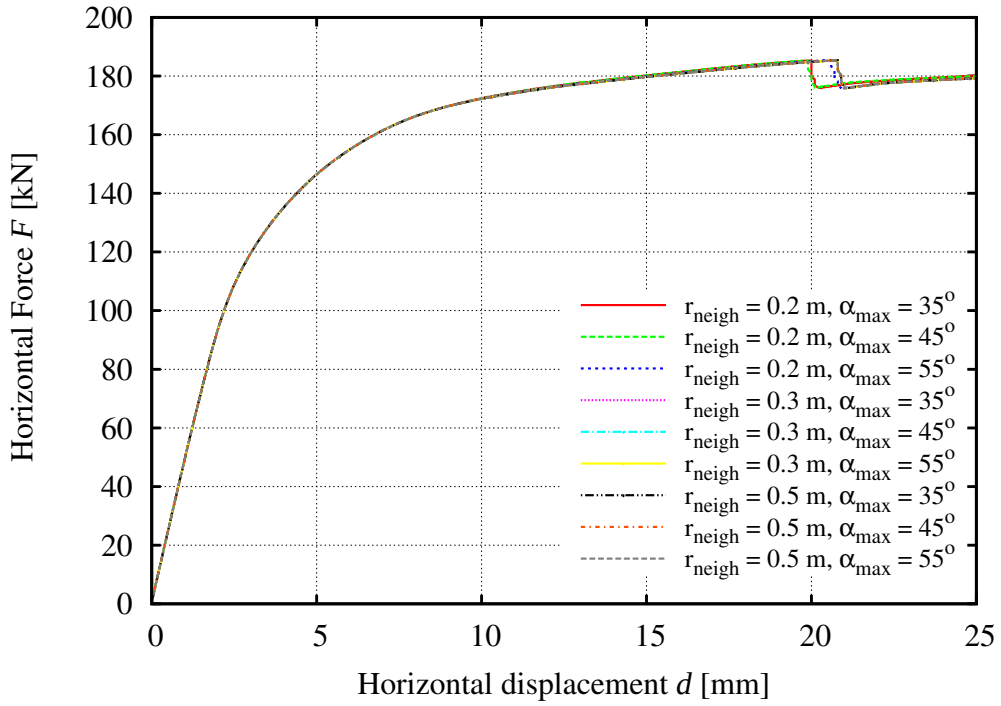

Figure 5.17 Sensitivity of structural capacity of the masonry frame to a_{max} and r_{neigh}

5.4 Shear wall under cyclic loading[§]

5.4.1 Experimental and numerical set-up

This section presents an application of the proposed multi-directional tracking algorithm and the constitutive law with the consideration of irreversible deformations on an experimental case study. The test was performed by Antoine et al. [8] and considers the in-plane response of a masonry wall under quasi-static shear loading. The tested specimen has a width of 1.00 m and a height of 1.35 m, while its thickness is 0.25 m. The masonry is constructed using an English bond pattern with unit dimensions of $55 \times 120 \times 250$ mm^3 and 10 mm mortar joint thickness. A vertical load of 150 kN was distributed at the top part of the wall and was maintained constant during the whole experiment, aiming to represent gravitational loading acting on the top of the masonry wall during a seismic event. The seismic action was reproduced by applying a horizontal displacement at the top of the wall. Proper boundary conditions were used to avoid its top and bottom rotation. Figure 5.18a shows a sketch of the adopted experimental set-up for the execution of the cyclical shear tests.

The experimentally obtained shear load against displacement graph is illustrated in Fig. 5.18b. The wall presents the typical behaviour for shear dominating failure. This is characterised by an overall drop in the capacity for increasing load cycles and appreciable energy dissipation throughout the whole loading history, as represented by the area of the

[§]This section is based on Reference [326]

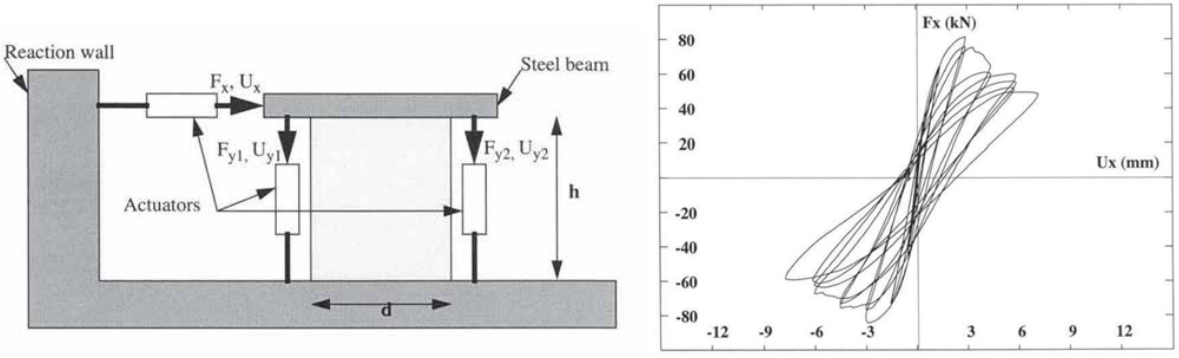

(a) (b)

Figure 5.18 (a) Experimental set-up and (b) experimentally obtained force against displacement graph of the tested masonry wall. (Pictures adapted from [8]).

Table 5.5 Material parameters for the masonry shear wall.

f^+ $[MPa]$	f^- $[MPa]$	G_f^+ $[J/m^2]$	G_f^- $[J/m^2]$	E $[MPa]$	ρ $[kg/m^3]$	v $[-]$
0.15	6.2	80.0	14000	1490	1750	0.2

hysteretic cycles of the load-displacement curve. The quasi-brittle character of the shear failure is due to the decrease of strength produced by the formation of two systems of crossing diagonal cracks in the wall [8, 213].

The wall has been discretized for the purposes of the numerical analysis using 3-noded constant-strain triangles (2836 nodes). The material parameters are presented in Table 5.5. The compressive strength, the density and the Young's modulus are equal to the values obtained through experimental tests on stack bond prisms reported in [44, 213]. The rest of the mechanical properties of the materials, and the parameters of the constitutive model have been chosen in order to calibrate correctly the shear response of the material, on the basis on the discussion presented in [326]. To this aim, a value of $\kappa_1 = 0.15$ has been chosen which is similar to the value used in other available studies on masonry shear walls [300–302]. Due to the lack of experimental results on cyclic tensile tests on masonry, discussed in Chapter 3, the evolution of the irreversible strains has been associated with the compressive damage. This means that r^- and τ^- have been used instead of r and τ respectively in Eqs. (3.22) to (3.31) in Chapter 3 and a value of $\beta = 0.95$ has been selected for the definition of the irreversible strains magnitude. Regarding the tracking parameters, the exclusion radius has been set equal to $r_{excl} = 0.20\ m$, which is a value between the length and the width of the masonry units, while the parameters for the maximum curvature criterion are $\alpha_{max} = 25°$, $r_{neigh} = 0.60\ m$. The limit angle used for the activation-deactivation of the cracks under the cyclic loading is $\alpha_{lim} = 40°$. This value means that three additional cracks with an orientation varying by 40° can initiate next to an existing crack. To visualize this, and considering that the exclusion radius has been defined equivalent to the units size, the above value implies that a total of four

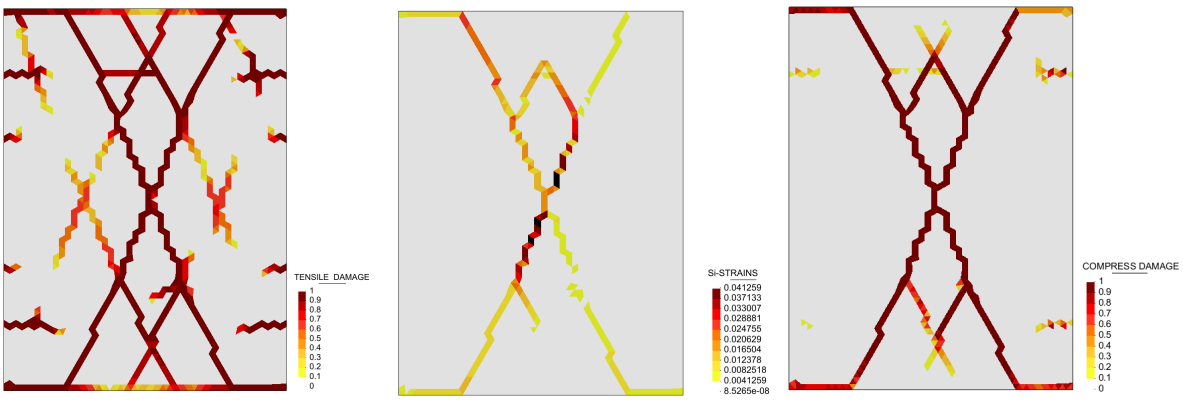

(a) (b) (c)

Figure 5.19 Contours of: (a) the d^+ damage index, (b) the maximum principal strains at the end of the analysis, (c) the d^- damage index at the end of the cyclic analysis of the shear masonry wall.

cracks with different orientations can initiate from the same unit. The influence of this parameter is investigated in Section 5.4.4.

The wall has been analysed under plane stress conditions and the simulation has been performed in two stages. The first one includes the application of the self-weight and the vertical compressive load at the top of the wall. In the second stage, a cyclic horizontal displacement is applied at the top of the wall with increasing magnitude, as in the experiment. Vertical displacement at the top is restrained, precluding the rotation of the wall. The numerical solution is performed in an incremental manner. At each time/load increment, the non-linear equations are solved with the use of a secant (Picard's) method. Convergence is achieved when the ratio between the norm of the iterative residual forces and the norm of the total external forces is lower than 10^{-2} (1%).

5.4.2 Numerical simulation

Figure 5.19 presents the contours of the tensile d^+ and compressive d^- damage indices, as well as that of the maximum principal strains at the end of the analysis. The wall is dominated by diagonal shear cracking, which is in agreement with the reported experimental damage pattern [8, 213]. There is evidence of flexural cracking at the lower and bottom parts of the wall, as well as at the two sides. Despite the opened cracks during the loading history, the main degradation of the wall is concentrated at the two diagonal cracks that have opened in the middle of the wall, as shown by the contour of the maximum principal strains. The use of the tracking algorithm results in a very clear representation of the localized cracks, aiding the identification of the occurring collapse mechanism at the wall.

Figure 5.20a presents the damage evolution and Figure 5.20b the state of the cracks for the opposite top displacements of the first cycle. For demonstration purposes, the contour value 1 (red) in Fig. 5.20b is used for the active cracks and -1 (white) for the inactive ones, while the elements outside of the crack maintain value equal to 0 (orange). It is visible that all cracks are active for the maximum displacement of the first cycle with

a loading direction towards the right. Two flexural cracks at the two corners of the wall consist the first occurring damage. After those, a shear crack initiated at the middle of the wall (left column of Fig. 5.20). The results with the same top displacement but opposite direction are presented in the right column of Fig. 5.20. All the previously opened cracks have now closed and are correctly identified as inactive. New horizontal cracks appear at the two opposite corners, as well as a diagonal shear crack at the middle of the wall, intersecting the existing crack. The proposed multi-directional tracking algorithm is capable of simulating both the correct initiation of new cracks close to the existing ones, as well as their intersection.

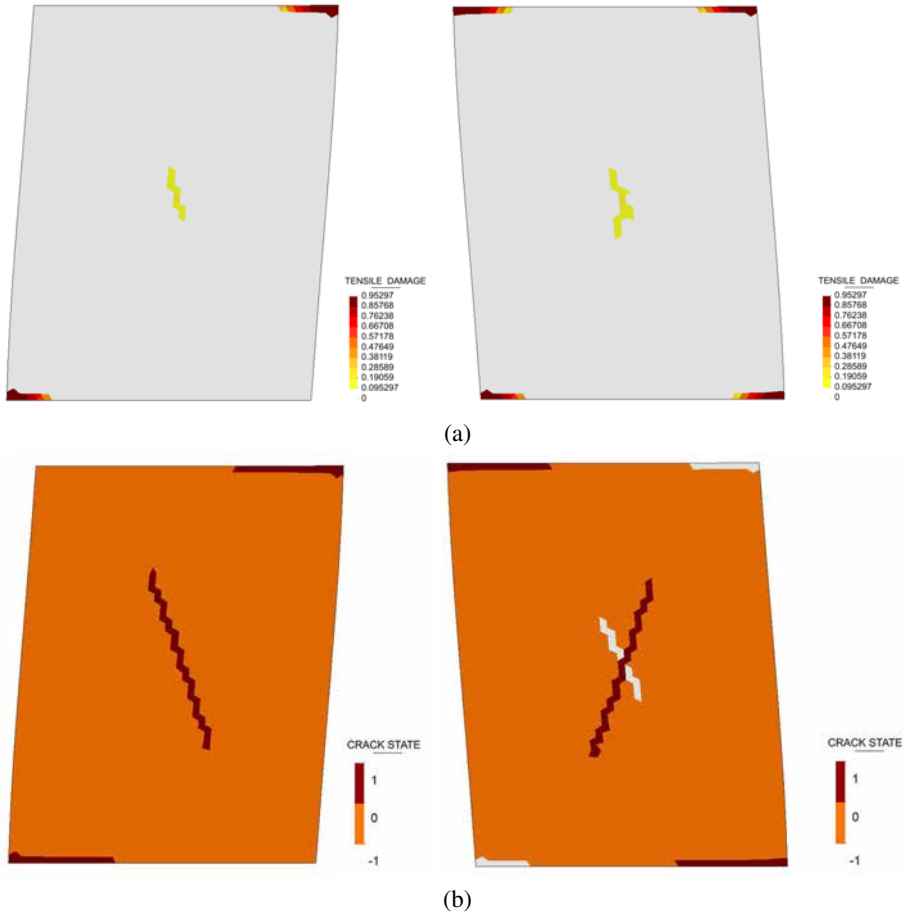

Figure 5.20 (a) Tensile damage contour d^+ and (b) crack state during the first loading cycle for the maximum displacement towards the right (left column) and the maximum displacement towards the left (right column) (deformed mesh $\times 100$).

Figure 5.21 presents the damage pattern during the loading cycle with a maximum displacement at the top equal to $d = \pm 3.0\,mm$. After the initial damage shown in Fig. 5.20, additional shear cracks have opened, with the deformation, however, localizing at the initial diagonal crack at the middle of the wall (see center column of Fig. 5.21). Some flexural cracks initiate at the two lateral sides of the wall and propagate horizontally towards the interior. Note that the cracks opened during an opposite loading direction have been correctly identified as closed (right column in Fig. 5.21).

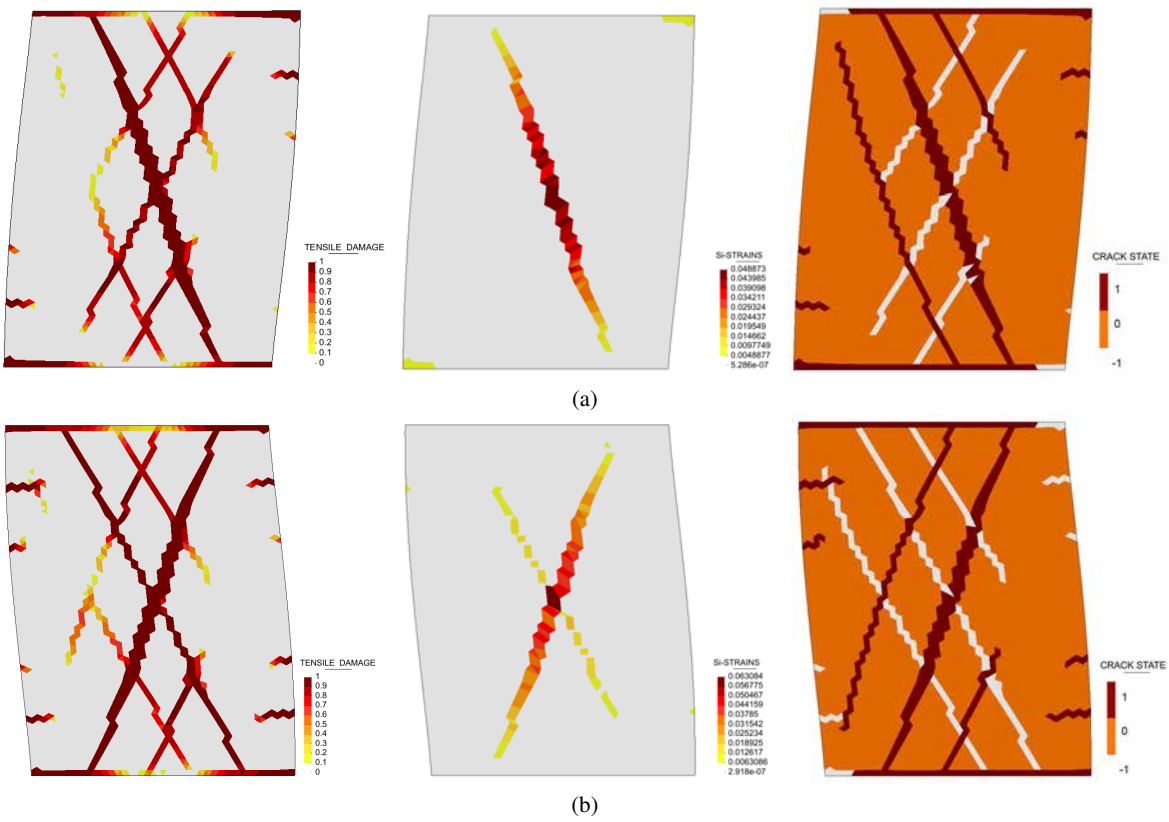

Figure 5.21 Contours of tensile d^+ damage (left), maximum principal strains (center) and crack state (right) for a top displacement of 3.0 mm towards the right (a) and left (b), (deformed mesh $\times 50$).

The response of the wall in terms of horizontal load against horizontal displacement is presented in Fig. 5.22. The numerical simulation captures the shear failure of the wall, which is characterized by an overall softening branch and stiffness degradation after exceeding the maximum capacity. The first cycles of the loading are characterized by an almost linear behaviour, due to the small amount of damage, as shown in Fig. 5.20. A significant drop in the capacity occurs after the complete degradation of the diagonal cracks at the middle of the wall, which occurs during the loading cycles with the maximum displacement of 3.0 mm, as in the experiment. After that, the increase of the displacement results in the drop of the stiffness due to the degradation of the additional shear cracks, yielding the final damage pattern and strain state of Fig. 5.19.

The used constitutive model is able to represent satisfactorily the cyclic damaging behaviour of the wall. There is a slight underestimation of the magnitude of the hysteretic loops shown in the last cycles of the experiment which is connected to the choice for the association of the evolution of the irreversible strains to only that of the compressive damage variable d^-. In fact, as can be seen in Fig. 5.19c, compressive damage d^- appears only at the two diagonal cracks at the middle of the wall, making them the only source of the irreversible deformations. As discussed, the coupling of the irreversible strains with the evolution of the tensile damage is straightforward with the proposed formulation presented in Eq. (3.31) of Section 3.4.2. However, as discussed in Chapter 3, this possibility has not been followed in this thesis due to the lack of experimental evidence for irreversible

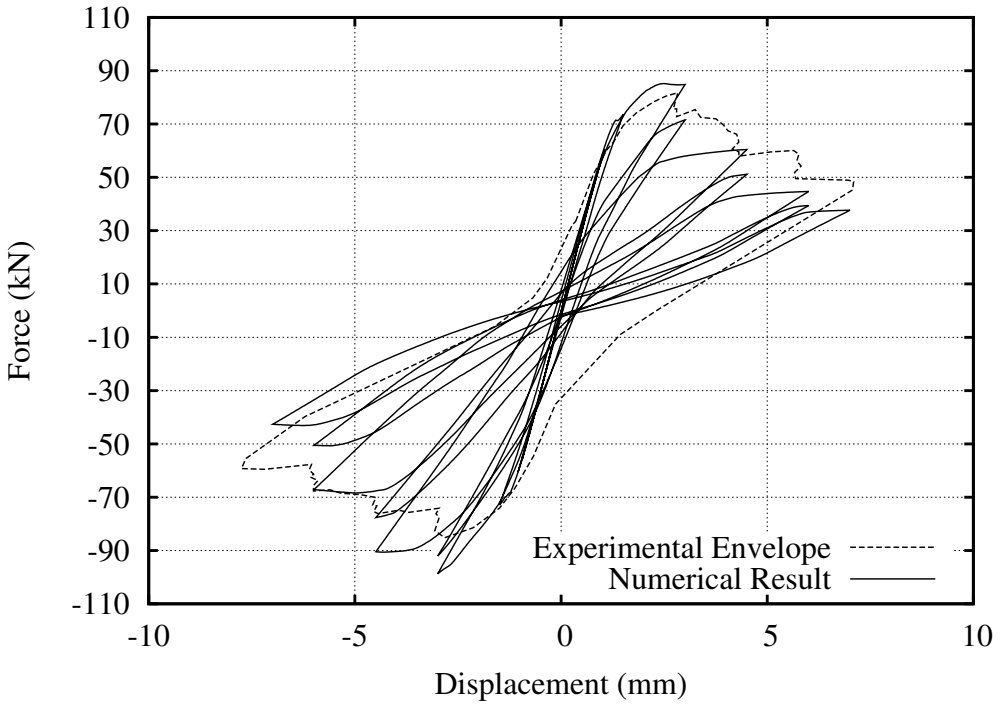

Figure 5.22 Force against horizontal displacement graphs for the masonry shear wall obtained through the numerical analysis.

deformations under tensile loading which would allow the validation of such a choice.

5.4.3 Mesh-dependency

As shown in the previous sections, the tracking algorithm has shown to improve the mesh objectivity in structural analyses with monotonically propagating cracks. In this section, the shear wall is analysed with an additional mesh aiming to study the mesh dependency of the presented approach for the more demanding case of cyclic loading. The first column of Fig. 5.23 shows the different discretization used in the mesh dependency analyses. The first mesh, denoted hereafter as Mesh-A, is mesh used for the aforementioned results with 5470 elements. The second mesh, Mesh-B, presents a constant structured pattern in the greatest part of the wall with equilateral triangles making angles of 30°, 90° and 150° with the horizontal axis and has a lower number of elements (3704) compared to Mesh-A.

The different columns of Fig. 5.23 present the damage pattern at the end of the different cycles during the loading history. Diagonal shear cracking dominates the main part of the wall in both cases, while flexural cracks appear at the boundaries. The damage pattern is very similar for the greatest loading history of the wall, with some differences occurring in the last cycles, during which the coarser mesh (Mesh-B) presents some additional shear cracking.

Figure 5.24 illustrates the force against the applied displacement graphs overlapped for the two meshes. The two analyses bare important similarities illustrating the mesh-objective behaviour of the proposed approach. The predicted capacity of the wall shows

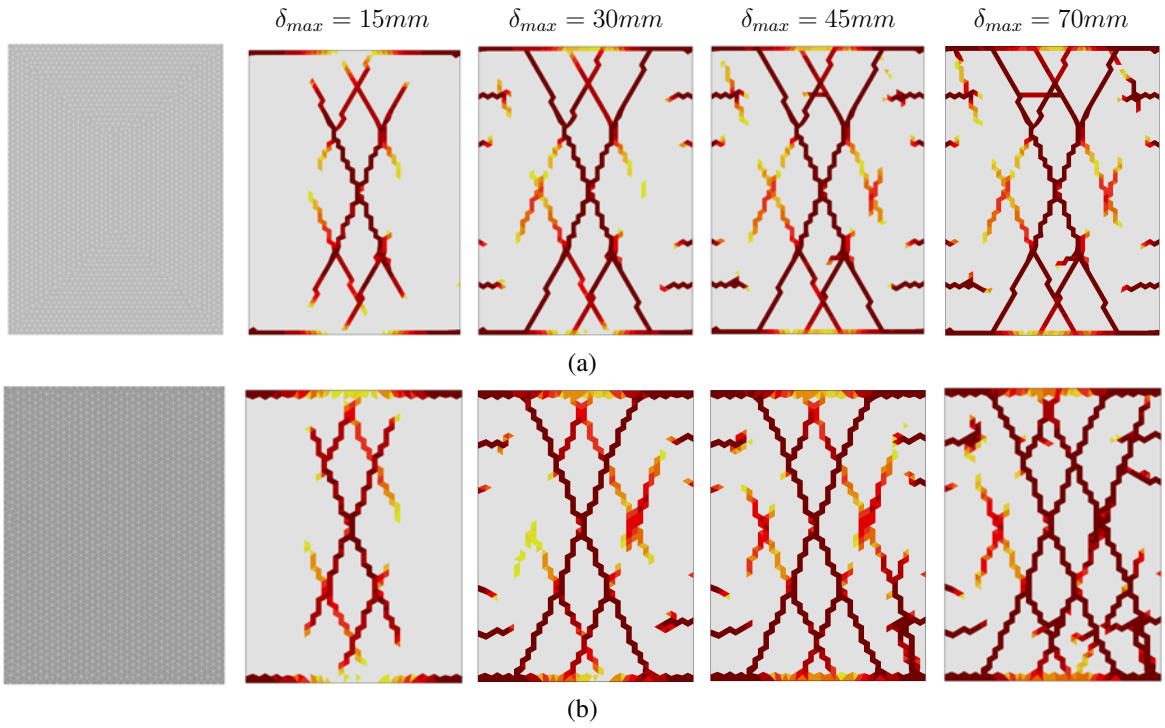

Figure 5.23 The used discretization (first column) and the contours of the tensile damage at the end of the various cycles with increasing maximum displacement δ_{max}: (a) Mesh-A, (b) Mesh-B

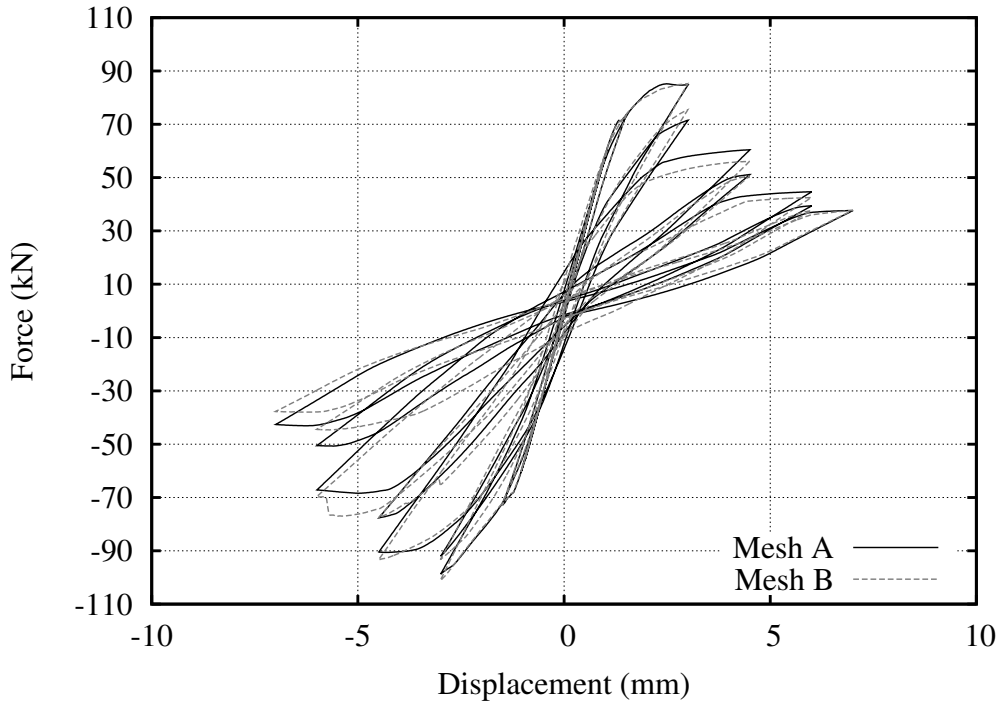

Figure 5.24 Horizontal force against displacement at the top of the wall for Mesh-A and Mesh-B

a variation of less than 3% and is attained at the second loading cycle for a displacement of 3.0 mm. Following that, the structure presents a softening response with dropping capacity and energy dissipation due to the further opening of the cracks. As presented in Fig. 5.23, after the first two loading cycles most of the cracks have already formed, and

the diagonal cracks at the middle of the wall as well as the boundary cracks at the top and bottom ends of the wall have completely opened. Upon this point, the numerical responses reflect the small differences regarding the positions of the cracks and the appearance of more cracks at the coarser mesh (Mesh-B), slightly alternating the residual response of the wall.

5.4.4 Influence of the limit angle α_{lim}

The use of the limit angle α_{lim} controls the activation and deactivation of the existing cracks, and thus the possibility for new ones to nucleate. To estimate its influence in the analysis, eight additional analyses of the shear walls have been performed. In these, the value of α_{lim} ranges from 15° to 55° with an increment of 5°. It is recalled that the reference value used in the presented analysis is 40°.

In the considered structural case the maximum limit angle depends on the pre-compression level. If there was no pre-compression or self-weight acting on the wall, the principal stresses would swap between ±45° for the opposite top displacements. In that case, a limit angle slightly smaller than 90° would be sufficient for the correct estimation of the cracks' state. Instead, when there is an initial stress state due to the vertical forces, the principal stress directions swing continuously during the interchange of the loading directions making angles between their maximum limits smaller than ±90°. Evidently, the maximum limit angle will decrease for increasing vertical loads.

Figure 5.25 shows the force against displacement graphs for the different values of α_{lim}. Each of them is compared with the reference case of Fig. 5.22. It can be seen, that for $25° \leq \alpha_{lim} \leq 45°$ there is no observable change in the structural response of the wall, whereas there exist some small differences for $\alpha_{lim} \leq 20°$. More important variations are identified for $\alpha_{lim} \geq 50°$, where there is a lower residual capacity after the first cycles of the analysis.

The above observations stand also for the obtained damage patterns, shown in Fig. 5.26. The cases with $25° \leq \alpha_{lim} \leq 45°$ demonstrate an almost identical crack pattern, with some very small differences of some additional cracks the appearance of which does not reflect on the capacity and the structural response of the wall, as shown in Fig. 5.25. The selection of $\alpha_{lim} \geq 50°$ seems inappropriate for estimating the correct closure of the diagonal crack in the middle of the wall. This is shown in Fig. 5.27, where the crack state is plotted at the end of the cycle with a maximum displacement 3.0 mm towards the left. The crack in the middle is erroneously identified as "active" and therefore, a new crack cannot nucleate at its neighbourhood defined by the exclusion radius. This happens at a later stage, when the increased lateral displacement results in the sufficient rotation of the principal stress axes to allow for the deactivation of the crack.

From these results, it may seem tempting to use very low values of the limit angle. However, this may lead to the early consideration of a crack as "inactive" due to the

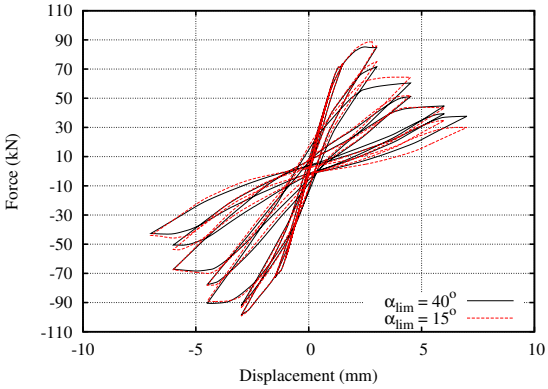

$\alpha_{lim} = 15°$

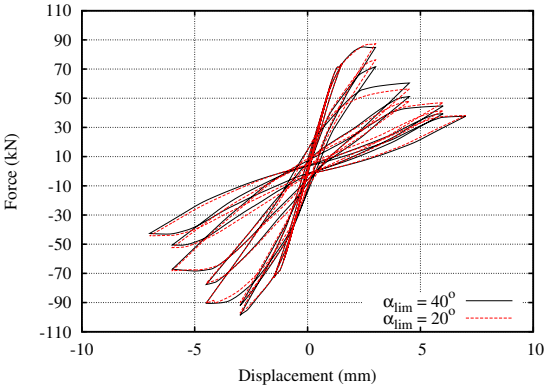

$\alpha_{lim} = 20°$

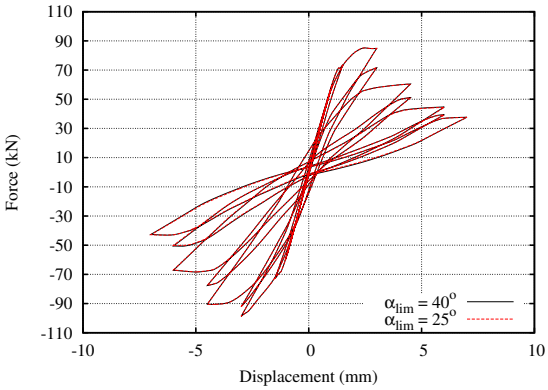

$\alpha_{lim} = 25°$

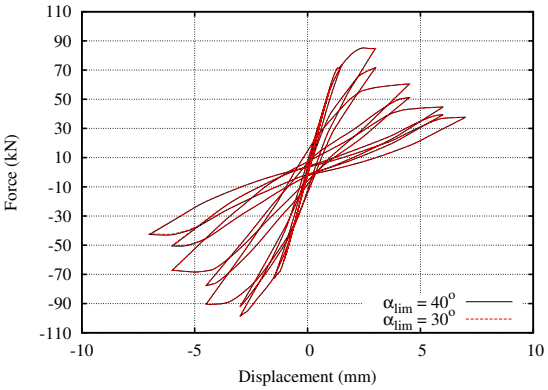

$\alpha_{lim} = 30°$

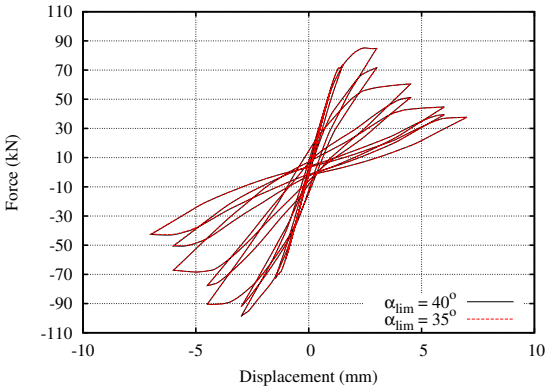

$\alpha_{lim} = 35°$

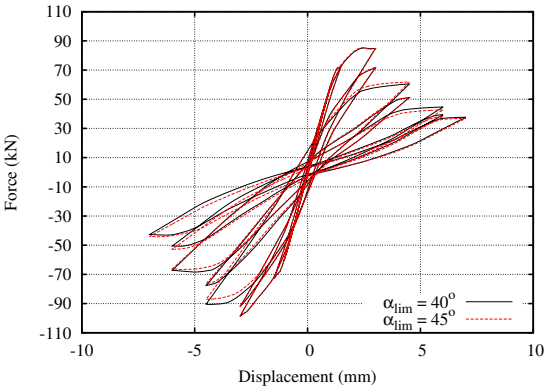

$\alpha_{lim} = 45°$

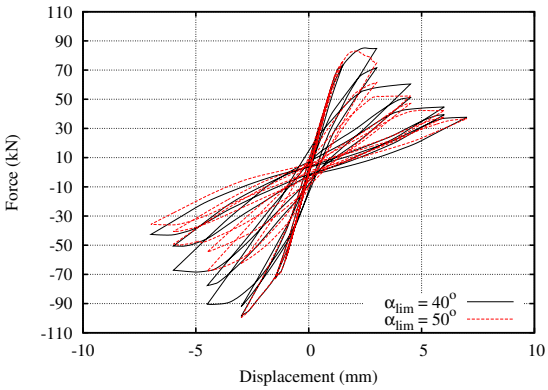

$\alpha_{lim} = 50°$

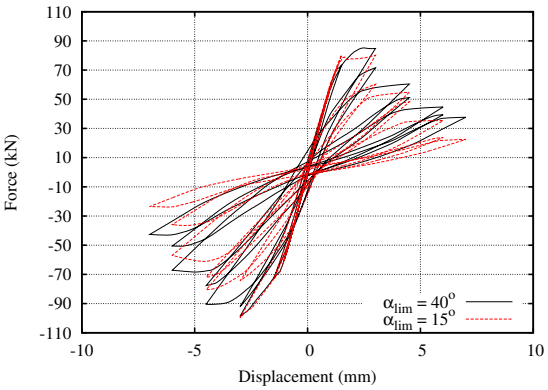

$\alpha_{lim} = 55°$

Figure 5.25 Influence of α_{lim} in the structural response of the shear wall

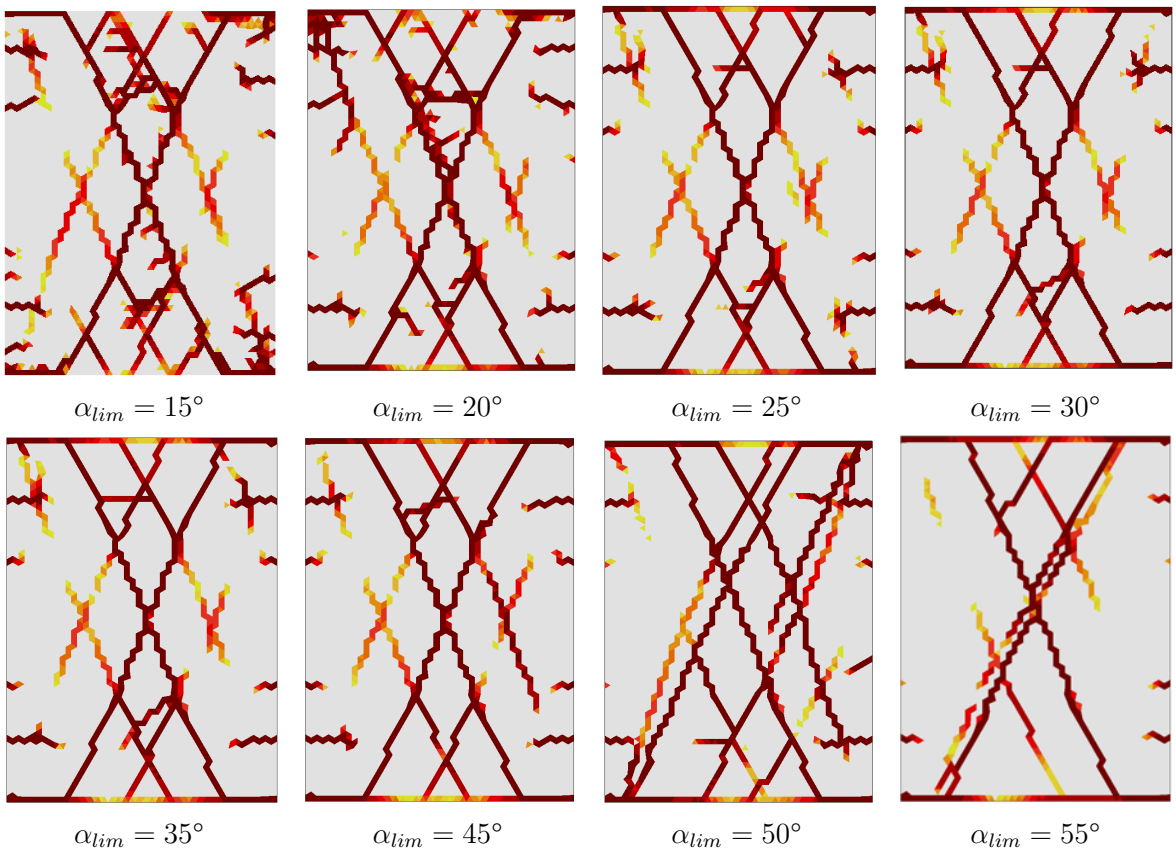

Figure 5.26 Influence of α_{lim} in the damage pattern of the shear wall

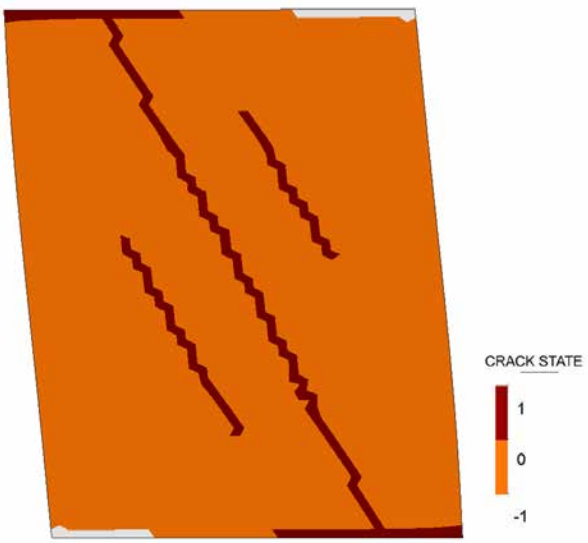

Figure 5.27 Crack state at the end of a cycle with a maximum displacement 3.0 mm towards the left for $\alpha_{lim} = 50°$.

rotation of the principal directions of the cracked element during its propagation by more than α_{lim}. In this example, this happens for the cases with $\alpha_{lim} \leq 20^{\circ}$ for the boundary cracks at the top of the wall and the diagonal crack at the middle of it, resulting to spurious crack initiation around them. Nevertheless, it is noted that these secondary cracks do not propagate significantly and the damage pattern remains the same as for the rest of the cases with $\alpha_{lim} \leq 45^{\circ}$. This is attributed to the correct damage localization at the main diagonal and horizontal cracks that leads to the unloading of the elements surrounding them.

5.5 Large-scale wall[¶]

The proposed tracking algorithm is now applied to the in-plane analysis of a large-scale masonry structure. The case study concerns a five floor interior structural wall of the masonry building situated in Via Martoglio, Catania Italy [55]. This is a well-known case study in the literature, analysed with diverse numerical tools as will be presented in Section 5.5.4. Its selection aims to validate the proposed tracking algorithm with a real-scale structure experiencing extensive cracking and to compare with other approaches used in the literature.

Figure 5.28a presents the geometry and dimensions of the analysed structure. The wall has regular openings symmetrically distributed along its central axis. The symmetry of the structure is interrupted by an opening at the right corner of the top floor, whereas there exists also a large door opening at the middle of the base floor. Clay brick vaults supported on concrete girders comprise the floor structural system, while the roof is a timber structure. The masonry is of regular units with dimensions $250 \times 120 \times 55\, mm^3$ (brick UNI5628/65). All the lintels are made of masonry but that of the central door at the base, which is made of reinforced concrete.

The numerical simulation aims to investigate the structural response of the wall against seismic actions by means of a non-linear equivalent static analysis. Two stages of loading are considered. The first one corresponds to the application of the self-weight of the walls and floors and the live load as defined in [55]. In the second stage, the seismic actions are simulated as horizontal forces applied at the level of each floor. The loading pattern is proportional to the height and the vertical loading of each floor as suggested by the Italian Code [171].

As no information is available regarding the rigidity of the floors, two models have been considered. In the first one (denoted hereafter as Model A), the same material parameters are used for both the masonry walls and floors assuming the existence of a flexible diaphragm (Material A in Table 5.6). In the second model (denoted hereafter as Model B), the floors are simulated as linear elastic with the double stiffness of the

[¶]This section is based on Reference [330]

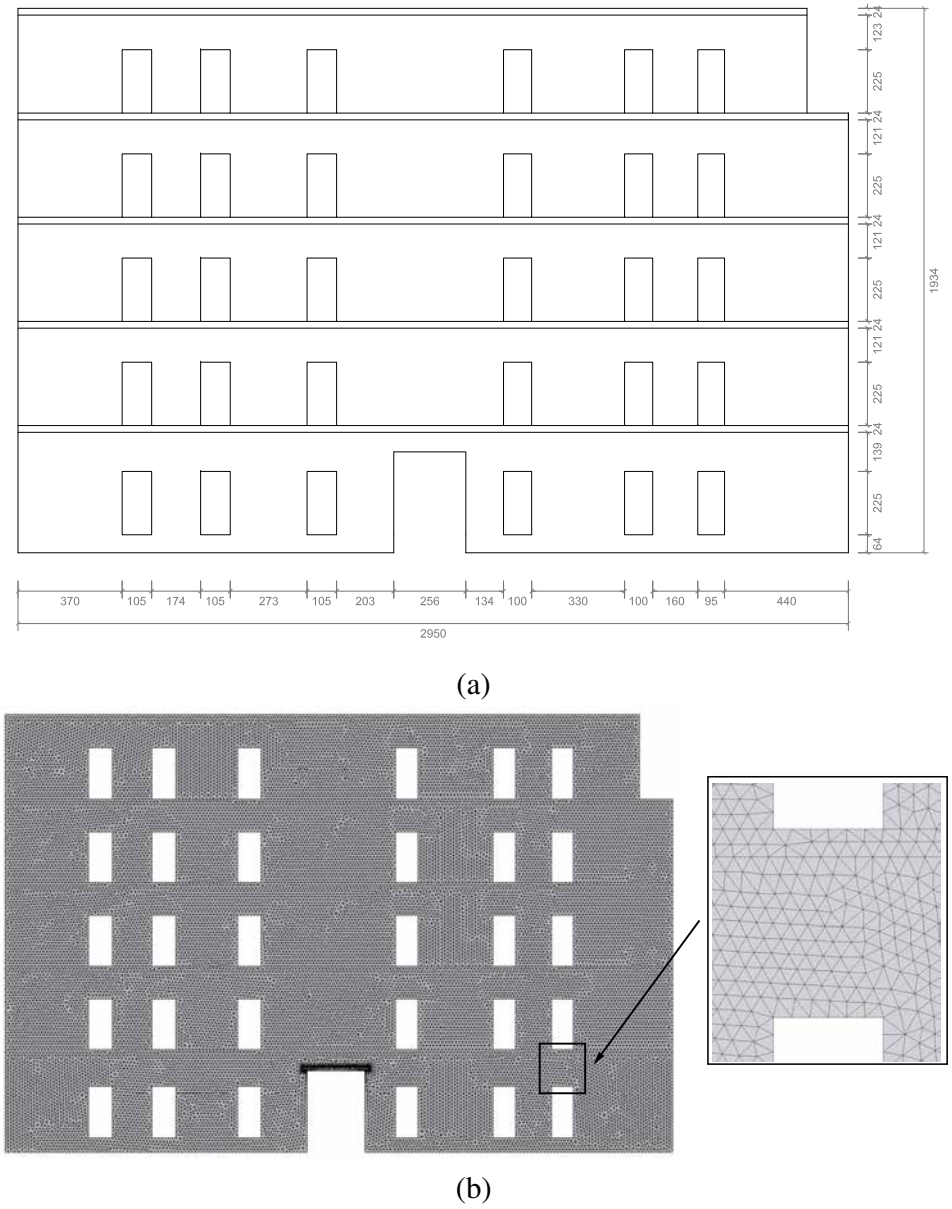

Figure 5.28 (a) Geometry of the analysed wall (in cm) and (b) the used unstructured mesh.

masonry aiming to consider the effect of a stiff diaphragm (Material B in Table 5.6). The latter material has been used in both models for modelling the concrete lintel above the central opening at the ground floor. The material properties have been extracted from previous analyses on the same building [55, 231]. κ_1 parameter is considered equal to 0.45 resulting to a shear strength of 0.15 MPa, which is the value used in the previous reference studies [55, 231]. The ratio between biaxial and uniaxial compression is equal to 1.15. Due to the monotonic nature of the loading, the fixed tracking algorithm is used also in this case. Following the obtained experience of the previous case study (Section 5.3) an exclusion radius $r_{excl} = 250\,mm$ is used, which is equal to the bricks length, while the rest of the tracking parameters are $a_{max} = 45°$ and $r_{neigh} = 50\,mm$. The last two are minimum values that prevent the overturning of cracks.

Table 5.6 Material parameters adopted in the numerical simulations of Via Martoglio structural wall.

Material	f^+ $[MPa]$	f^- $[MPa]$	G_f^+ $[J/m^2]$	G_f^- $[J/m^2]$	E $[MPa]$	ρ $[kg/m^3]$	v $[-]$
A	0.10	3.0	100	50000	2.5	1700	0.2
B	[-]	[-]	[-]	[-]	5.0	1700	0.2

Table 5.7 Materials assigned to the different structural elements of Model-A and Model-B.

Material	Model A	Model B
A	Walls & Floors	Walls
B	Lintel	Floors & Lintel

The structure is discretized using an unstructured mesh with two-dimensional constant strain triangles under plane stress conditions. The average size of the finite elements is $150\,mm$ resulting in a total number of 51052 elements (Fig. 5.28b). The analysis is performed using an arc-length method along with a line-search procedure.

5.5.1 Model A - Flexible diaphragm

The structural response of the Model A with flexible floors is presented in terms of base shear against top horizontal displacement in Fig. 5.29. The structure has a maximum capacity of 635 kN. The post-peak response is characterized by a softening part leading to a residual strength of around 530 kN.

The first drop in the stiffness occurs for a base shear of around 350 kN (Point A in Fig. 5.29). This coincides with the occurrence of shear and flexural cracking at the spandrels of the second and third floor as shown in Fig. 5.30a. The increase of the horizontal load results in the extension of damage to the great majority of the spandrels, see Fig. 5.30b. Flexural cracks initiate from the corner of the openings and propagate vertically within the spandrels. On the contrary, shear cracks emerge from the interior of the spandrels, at their middle height, and continue their propagation diagonally in two directions. Figure 5.31 presents the evolution of this damage pattern for the spandrel at the 4th floor and second column of openings (counting from the right side). Cracking due to bending initiates at the two ends of the spandrel and propagates towards the interior (Fig. 5.31a). At a later stage, shear cracks emerge at the interior (Fig. 5.31b) of the spandrel and evolve diagonally towards the two ends of the spandrel (Fig. 5.31c). This cracking is characteristic of a strong-pier weak spandrel configuration [43, 284, 331] and resembles very closely the failure pattern of the masonry frame presented in Section 5.3.

Figure 5.30c shows the tensile damage distribution just after the maximum capacity of the structure. The vertical piers of the right side start to behave as cantilevers owing

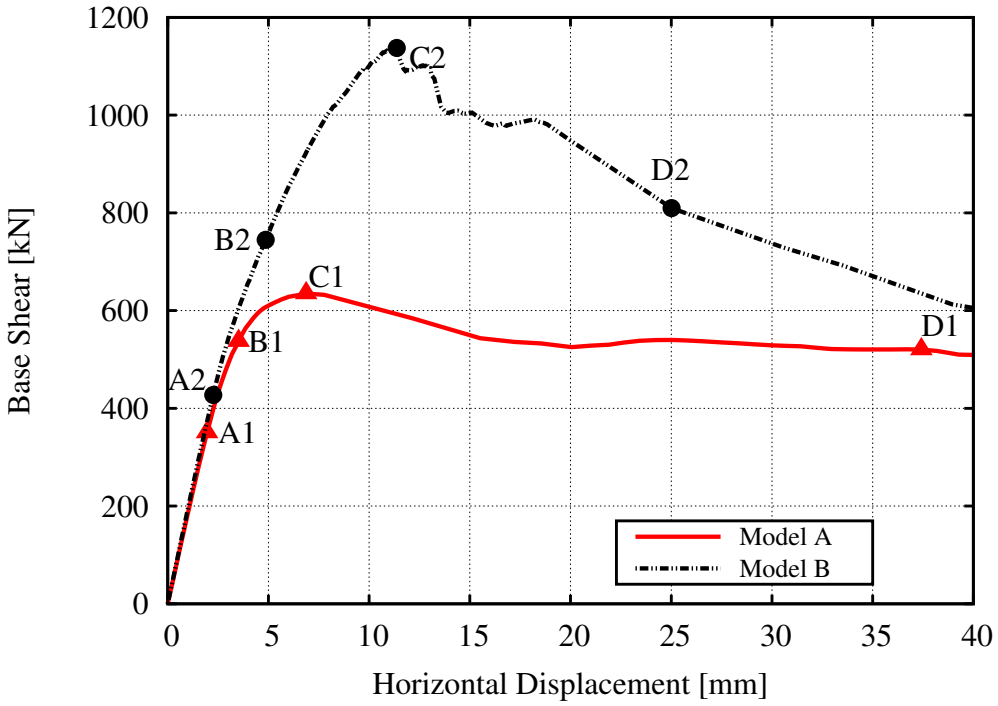

Figure 5.29 Base shear versus horizontal displacement at the top right corner of the structure for the flexible diaphragm case (Model A) and for the stiff diaphragm case (Model B).

to the extensive damage of the weak spandrels. The collapse mechanism is determined by the rotation of the right corner after the progression of damage at the spandrels of all floors of the extreme right side at levels sufficient to allow its detachment from the rest of the structure. The rest of the analysis finds the right corner rotating around its base, resulting to important shear cracking at the base wall (Fig. 5.30d). The analysis stops when the flexural cracks at the spandrels are entirely opened, resulting to their complete partition from their adjacent piers.

5.5.2 Model B - Stiff diaphragm

The assumption of a stiff and elastic diaphragm has an important effect in the response of the structure. The capacity increases around 80%, reaching a horizontal load of 1139 kN (Fig. 5.29). The displacement of the structure for the capacity load increases in the same order, being of 11 mm instead of 6.6 mm for Model A.

The initiation of damage is similar to that of Model A, affecting the spandrels of the second and third floor at the fourth column of openings (counting from the left side) for a base shear of around 425 kN, see Fig. 5.32a. Contrary to Model A, the increase of the horizontal force results in a more uniform distribution of damage at the spandrels. This can be observed in Fig. 5.32b, showing the tensile damage contour for a base shear of around 750 kN. After the spreading of damage at the spandrels, shear cracks start affecting the piers of the base floor. Important cracking seems to affect the pier next to the base door, which is probably due to a hammering effect of the rigid lintel above it.

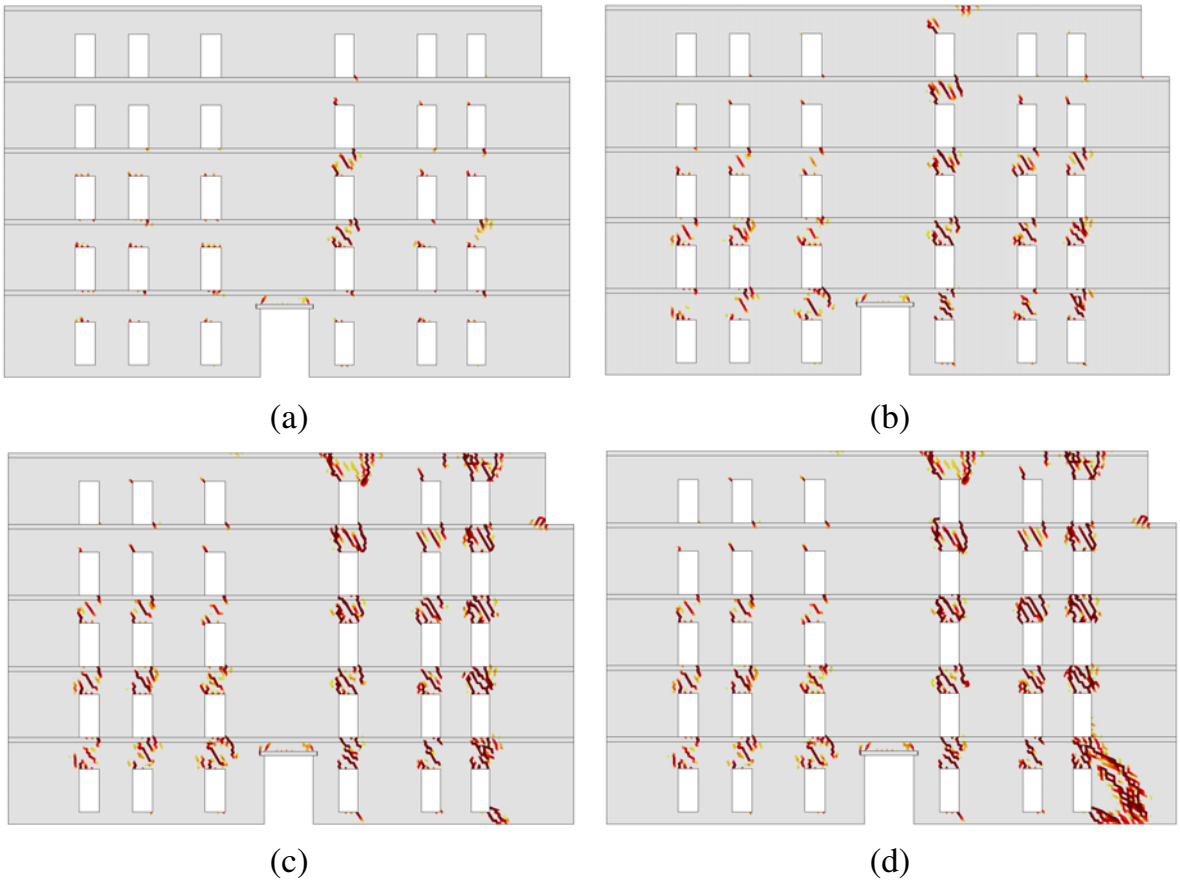

Figure 5.30 Tensile damage contour of Model A for a horizontal displacement at the right top of: (a) 2 *mm* (point A1 in Fig. 5.29), (b) 3.5 *mm* (point B1 in Fig. 5.29), (c) 6.9 *mm* (point C1 in Fig. 5.29) and (d) 37 *mm* (point D1 in Fig. 5.29).

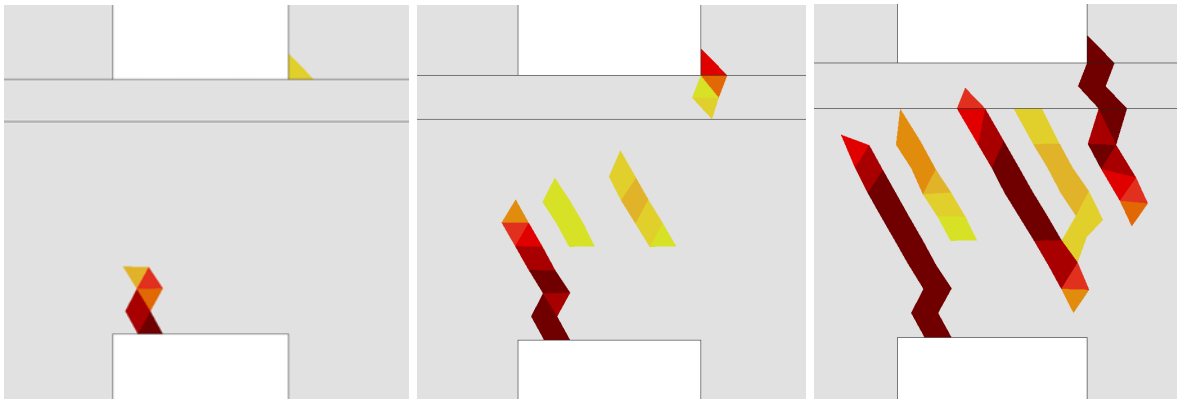

Figure 5.31 Flexural and shear cracking evolution at the spandrel of the 4th floor, second column of openings (counting from the right side) for a displacement at the top of: (a) $d = 2.9\,mm$ (b) $d = 4.0\,mm$ (c) $d = 11.9\,mm$.

The tensile damage distribution after reaching the maximum capacity is shown in Fig. 5.32c. The stiffer floors have restrained the rotation of the vertical piers despite the severe damage at the spandrels and mobilized the shear response of the piers. Flexural cracks start appearing at the lower left corner, while shear cracks are now evident in many piers

of the structure mostly at the right side and the base. The shear failure of these piers determines the capacity of the structure, which can be seen as the drop of the base shear after the peak in the graph of Fig. 5.29. The shear capacity of the rest piers results in a residual strength of the structure as shown by the horizontal plateau in the post-peak response. This is followed by another sudden drop in the residual strength of the structure due to the shear failure of the rest of the piers at the left part of the structure as shown in Fig. 5.32d. The analysis stops when the shear capacity of all the base piers is exhausted.

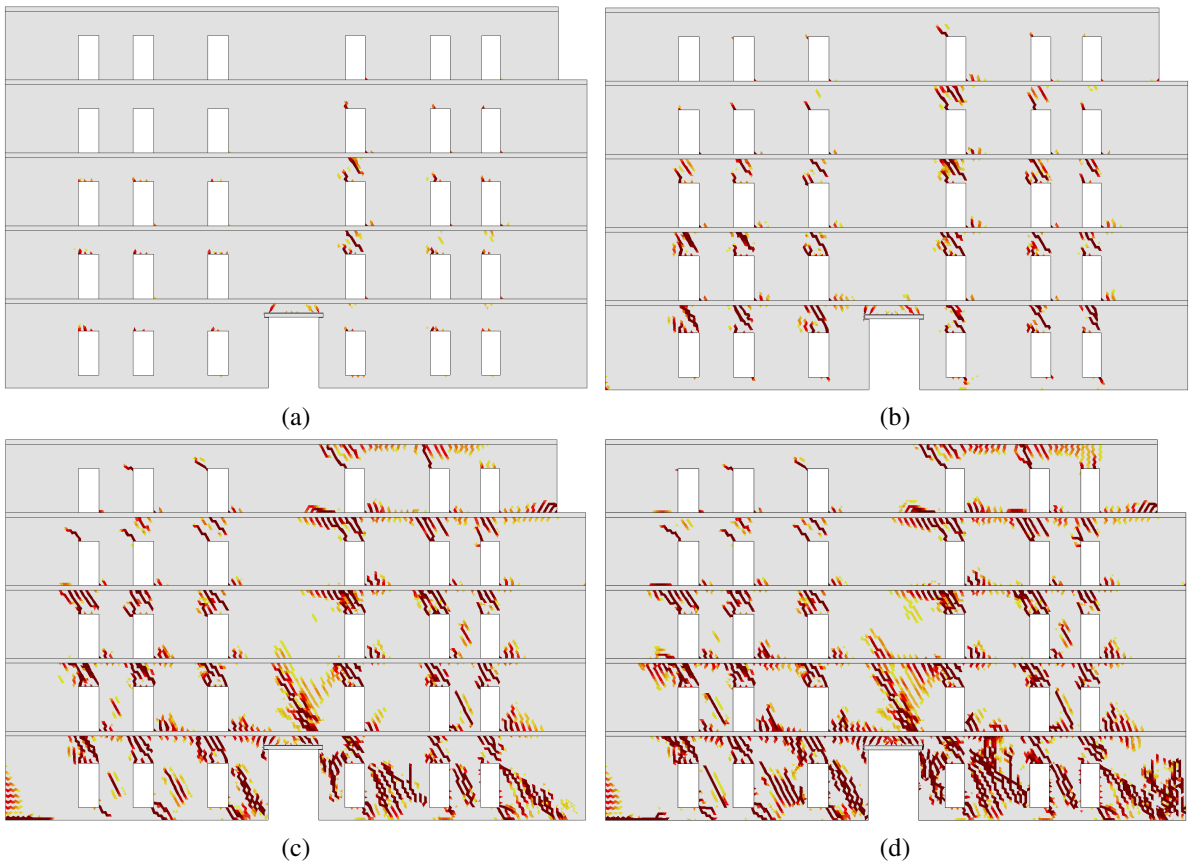

Figure 5.32 Tensile damage contour of Model B for a horizontal displacement at the right top of: (a) 2.2 *mm* (point A2 in Fig. 5.29), (b) 4.8 *mm* (point B2 in Fig. 5.29), (c) 11.4 *mm* (point C2 in Fig. 5.29) and (d) 25.1 *mm* (point D2 in Fig. 5.29).

5.5.3 Discussion of the diaphragm effect on the structural response

The different assumptions regarding the rigidity and strength of the floors lead to substantial changes of the structural response. Stiff floors increase the integrity of the structure and the collaboration among the vertical piers even after the damage at the spandrels.

The collapse mechanism in Model A is triggered by the flexural cracking at the spandrels. This induces the cantilever behaviour of the last three vertical piers of the right side, which rotate around their base with almost no interaction among them. Failure of the structure is eventually determined by the collapse of the right side, as shown in

Fig. 5.33a. On the contrary, the stiff floor in Model B results in the mobilisation of the shear response of the piers, the strength of which determines the global capacity of the structure. Collapse in this case is due to the shear failure of the piers at the base of the structure, as shown in Fig 5.33b. The capacity of the tracking algorithm to model internal cracks with two orientations, i.e. shear cracks, is crucial for the realistic simulation of the current case study.

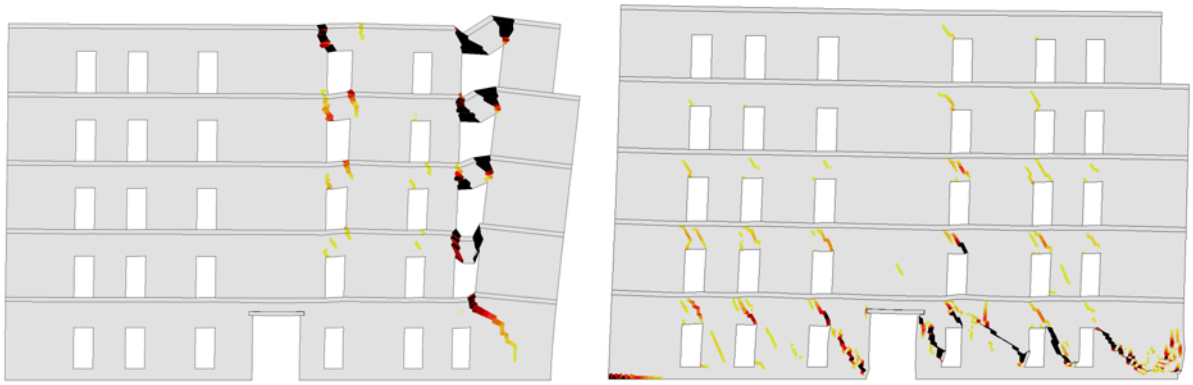

(a) (b)

Figure 5.33 Contour of the maximum principal strains on a deformed (×30) mesh for (a) Model A and (b) Model B.

The different non-linear response between the shear failure and the flexural one can be appreciated through a comparison of the base shear versus displacement graphs in Fig. 5.29. Flexural failure in Model A and rocking of the vertical piers is characterized by a smooth post-peak response. Differently, in Model B the shear failure of the piers at the base results in sudden drops of the load-caring capacity of the structure after the peak-strength.

A common characteristic of both models is the weakness of the spandrels. The most prone to failure are those with massive piers at their both sides. This is the case of the spandrels at the fourth column (counting from the left side), which are the first to experience damage during the loading history (see Figs 5.30a and 5.32a) for both models. Nevertheless, the damage pattern at the spandrels seems to change from mainly vertical flexural cracks to diagonal shear cracking when the floor has an increased stiffness compared to that of the masonry walls.

5.5.4 Comparison with other approaches

Figure 5.34 presents a comparison between the results obtained with the macro-model proposed in this work and three alternatives from the literature: a finite element model with inserted discontinuities [55], a limit analysis software [231] and an equivalent frame approach [2].

The capacity obtained using Model A (635 kN) is very similar to the one calculated using the lower bound approach (691 kN) in Milani et al. [231] considering the case

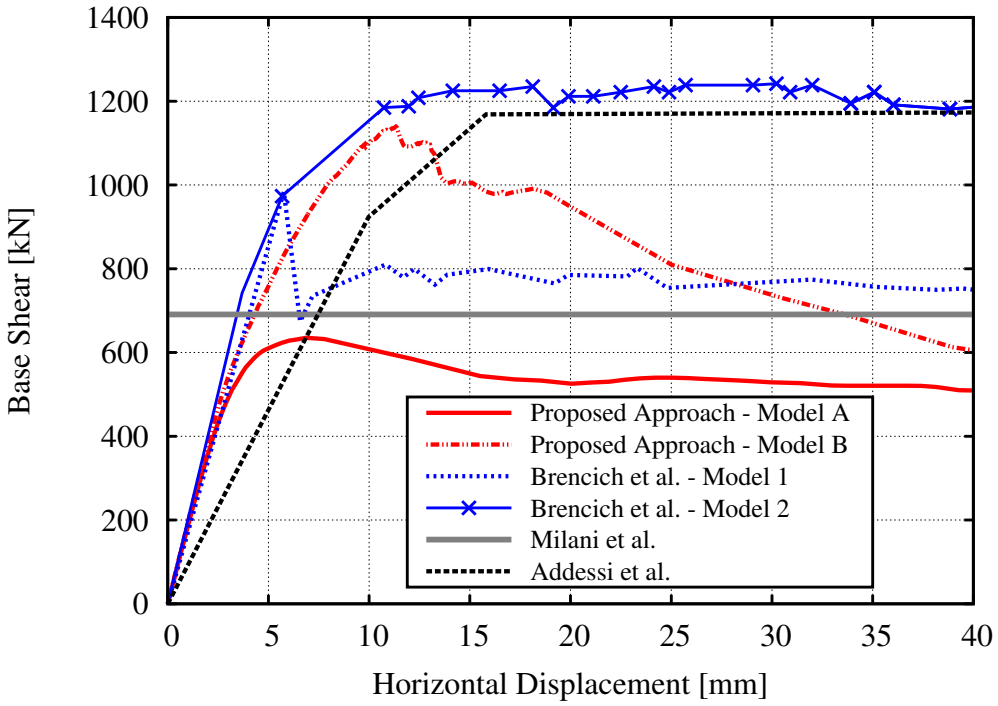

Figure 5.34 Comparison of the global response of the Via Martoglio masonry wall as obtained by different numerical approaches.

with flexible diaphragms. Note that in [231] the self-weight of masonry was applied as a concentrated load at the floor levels, compared to its application at the masonry surfaces in this work. This difference could explain the lower capacity of the present model since more load is actually located at higher levels of the structure.

Two models are reported from the work of Brencich et al. [55]. In Model 1 the concrete floors were assumed to have the same properties as the masonry (as in Model A here), while in Model 2 they were modelled as elastic with an elastic modulus of 5.0 GPa (as in Model B here). In these models, damage could localize only along discontinuities distributed within the structure at horizontal layers and separated by quadrilateral finite elements. Vertical interfaces were positioned only at the location of the masonry lintels at each floor and for a single element height. The different treatment of damage and the above restrains in the propagation of vertical cracks resulted in an increased capacity compared to the one estimated here for both models. This difference is more important for the case of Model 1 and Model A, where the analyses show that failure is characterized by vertical cracking due to bending at the spandrels. Nevertheless, the damage distribution within the structure is equivalent in both approaches and for both models. In Models 1 and A, damage is mainly localized at the spandrels, while in Models 2 and B significant damage affects the piers of the structure, and especially those of the lower floor.

Finally, the maximum capacity obtained using Model B is very close to the one predicted by Addessi et al. [2] for a model with the assumption of elastic diaphragms and using an equivalent frame approach with force-based beam finite elements. The differences

existing in the linear response are due to the use of a different value of elastic modulus for the walls of the structure.

The obtained results using the proposed approach are in overall agreement with those existing in the literature. The enhanced capacity of the tracking algorithm to simulate the propagation of damage within the structure results in a more detailed representation of the post-peak response, as shown especially for the case of Model B. The presented approach models appropriately the structural response of large structures, providing valuable information regarding the behaviour of the different structural members and the local collapse mechanisms occurring within the structure.

5.5.5 Mesh-dependency

This section investigates the dependency of the proposed approach to the discretization size and structure of the mesh. The performed analyses consider the properties of Model A using two additional meshes, and the obtained results are compared with the reference mesh of Fig. 5.28b.

Mesh-size dependency

The mesh-size dependency is investigated using a refined unstructured mesh with average element size equal to 75 mm. This increased refinement results in a total number of 204729 elements, i.e. 4 times more than in the reference model. The difference of the refinement level is illustrated in Fig. 5.35.

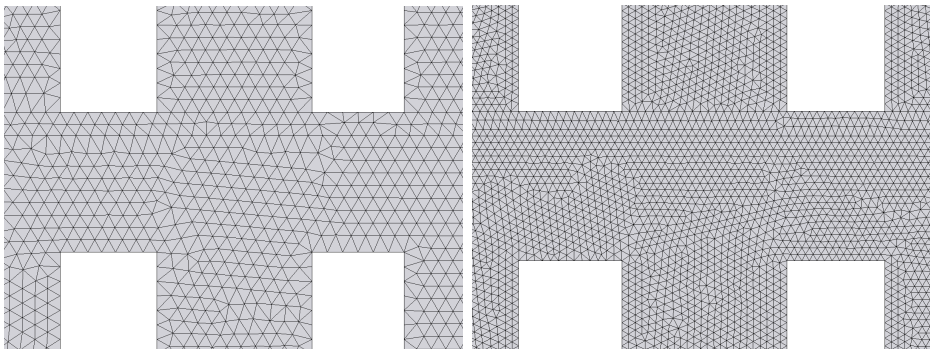

Figure 5.35 Detail of the meshes used for the mesh-size dependency analyses with average element size of (a) $h_e = 150\,mm$, (b) $h_e = 75\,mm$.

Figure 5.36 shows the global response of the structure for the two unstructured meshes with the different element sizes. The two graphs almost coincide providing identical capacity for both cases and a very similar post-peak response. As illustrated in Fig. 5.37a, the damage pattern is comparable for both cases. The same occurs for the obtained collapse mechanism, shown with the contour of the maximum principal strains in Fig. 5.37b. The proposed enhanced macro-model gives results that are mesh-size independent.

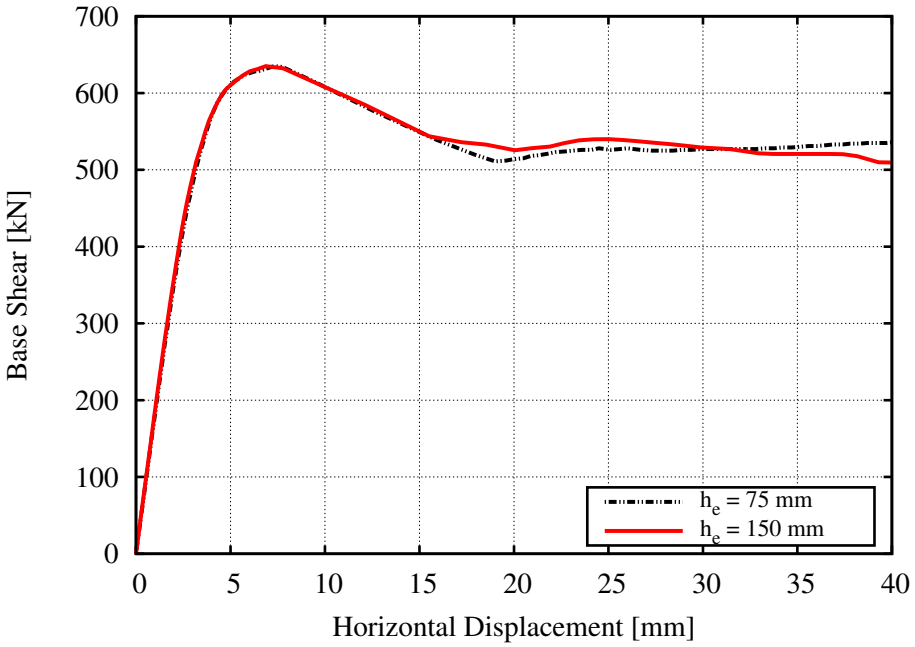

Figure 5.36 Base shear versus horizontal displacement at the top right corner of the structure using a mesh with different element size.

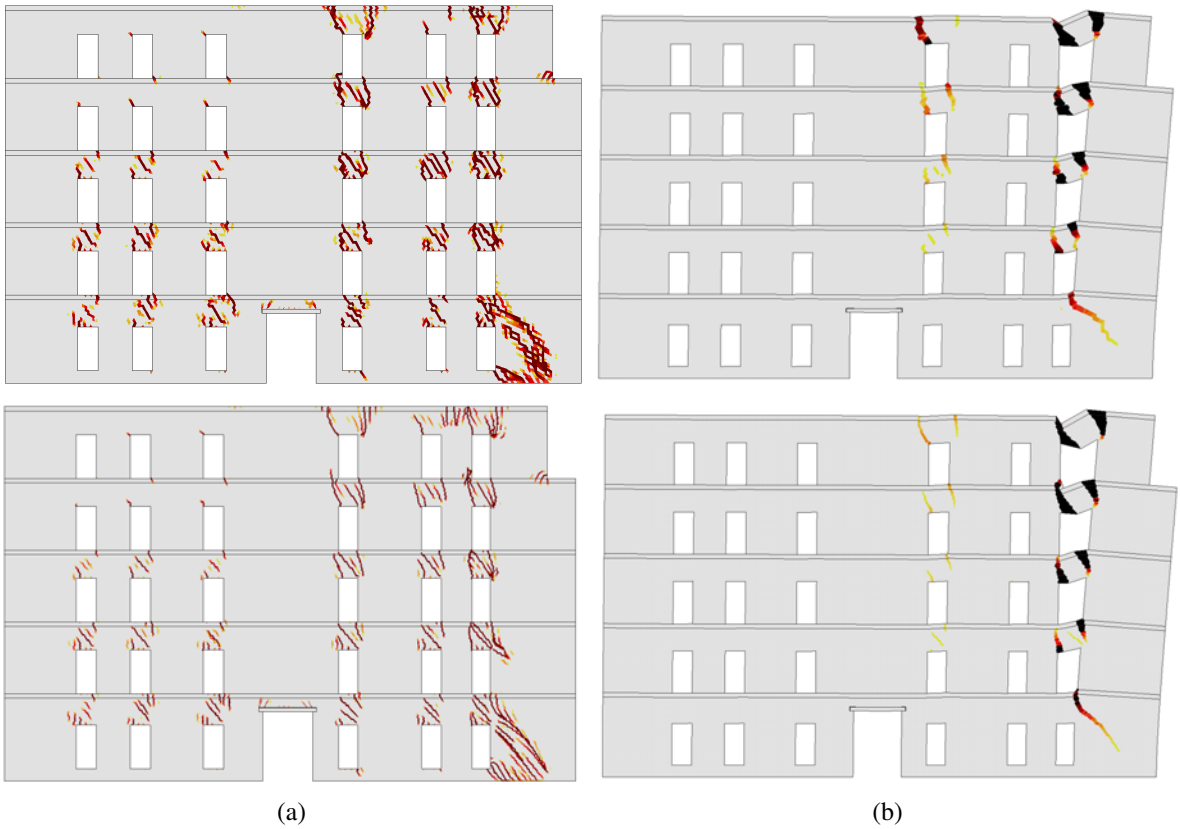

Figure 5.37 Contours of (a) tensile damage, (b) maximum principal strains on a deformed ($\times 40$) mesh for a displacement at the top right corner of 37 mm. Top row: unstructured mesh with average element size of 150 mm, Bottom row: unstructured mesh with average element size of 75 mm.

This is due to both the correct localization of the damage and the regularization of the constitutive law according to the finite element's characteristic length as presented in

Chapter 3.

Directional mesh-bias dependency

The directional mesh-bias dependency is investigated by comparing the results obtained with the mesh of Fig. 5.28b, with a structured mesh presented in Fig. 5.38. The sides of the orthogonal triangles make angles of 0°, 45°, 90°and 135°with the horizontal direction and have a mean length of 150 mm (44852 elements). Analyses with this mesh are carried-out with both the classical smeared crack approach and the tracking algorithm.

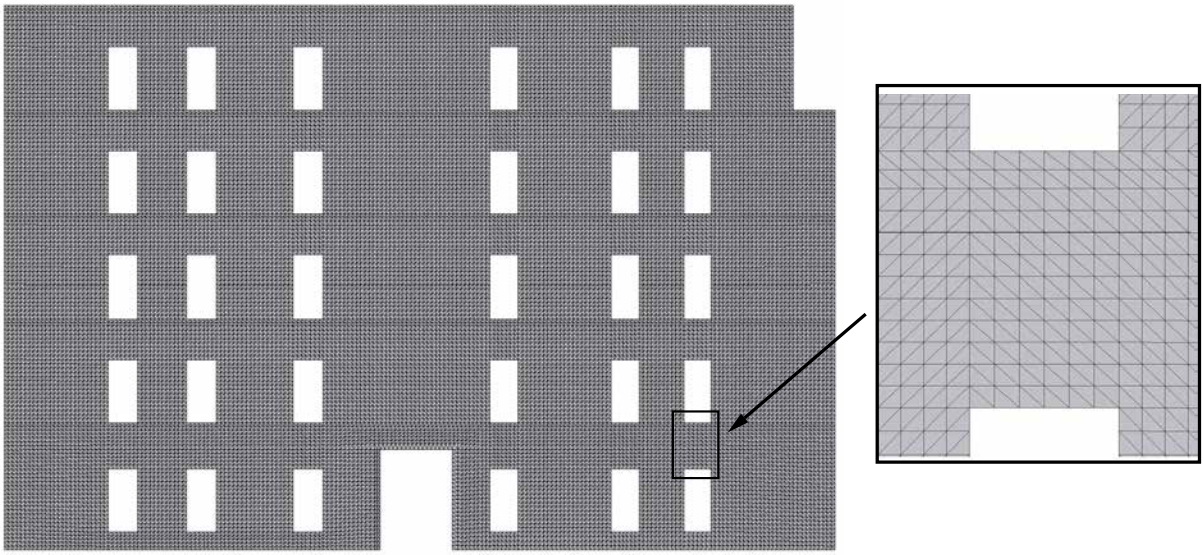

Figure 5.38 Structured mesh used in the mesh-bias sensitivity analysis.

The damage distribution as well as the localized strains for a horizontal displacement of approximately 21 mm using the two different meshes and the enhanced macro-model are presented in Fig. 5.39. The obtained results are in good agreement. The damage typology at the spandrels is similar in both cases, with flexural cracks being present at the two corners of the openings and shear cracks at the middle of the spandrels. Good agreement is found also for the localized cracks and the occurring collapse mechanism, determined by the overturning of the right corner as shown in Fig. 5.39b and Fig. 5.39d.

The effectiveness of the tracking algorithm to address the directional mesh-bias dependency is better demonstrated when compared with the numerical simulations carried-out without it. To this aim, both meshes of Fig. 5.28b and Fig. 5.38 are analysed using the classical smeared crack approach. Figure 5.40a presents the contours of tensile damage using the unstructured mesh of Fig. 5.28b, for a horizontal displacement at the top of the structure equal to 15.4 mm. Severe damage affects the spandrel walls resulting to their separation from the adjacent piers and the rotation of the vertical walls at the right side of the structure. Note the direction of the cracks that have opened during the loading history, but also the open cracks after reaching the capacity of the structure (Fig. 5.40b); they are mostly diagonal, referring to a prevailing shear failure at the spandrels. Consider

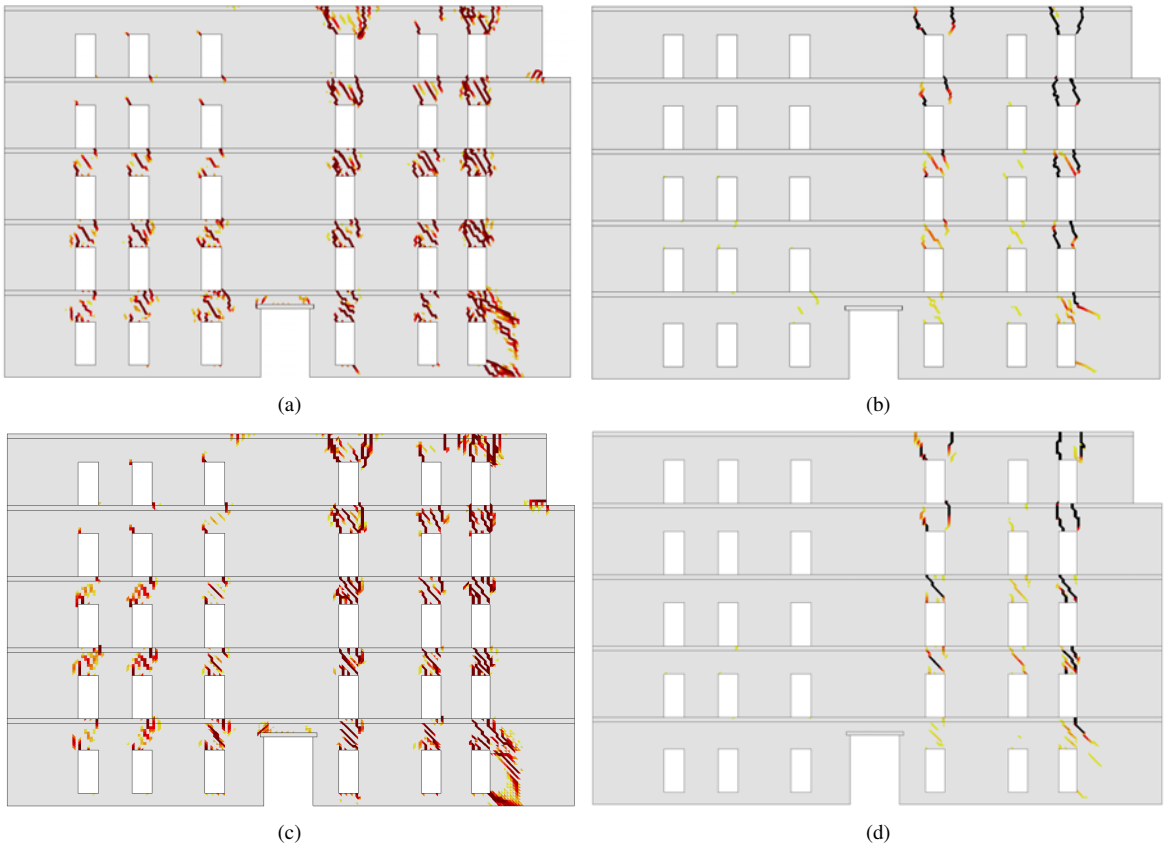

Figure 5.39 Simulation of Model A using the proposed tracking algorithm. (a) Tensile damage and (b) maximum principal strains using the unstructured mesh for a horizontal displacement of 20.9 *mm* (Point 1 in Fig. 5.41). (c) Tensile damage and (d) maximum principal strains using the structured mesh for a horizontal displacement of 21.2 *mm* (Point 2 in Fig. 5.41).

now the results of the numerical analysis using the structured mesh of Fig. 5.38. Figure 5.40c presents the contour of the tensile damage for a displacement of 15.5 *mm* at the top of the structure. Cracking once again prevails at the spandrels, but this time the crack orientation is vertical in the great majority of the existing cracks. This is better observed with the contour of the maximum principal strains showing the localized cracks in Fig. 5.40d.

It is obvious that when the tracking algorithm is not used, the numerical solution depends on the directionality of the mesh for both of the used discretizations. This numerical pathology inhibits the assessment of the actual local collapse mechanisms. On the contrary, the tracking algorithm shows to be robust, even for the structured mesh with orientations that facilitate the opening of vertical cracks, as the case of the classical smeared crack approach has demonstrated.

The different response of the structure for the two meshes is clear in the base shear against horizontal displacement graphs of Fig. 5.41. The capacity of the structure without the use of the tracking algorithm is lower by around 14% when the structured mesh is used, compared to the result with the structured one. This is due to the mesh-biased cracking at the spandrels, being vertical at the case of the structured mesh and diagonal

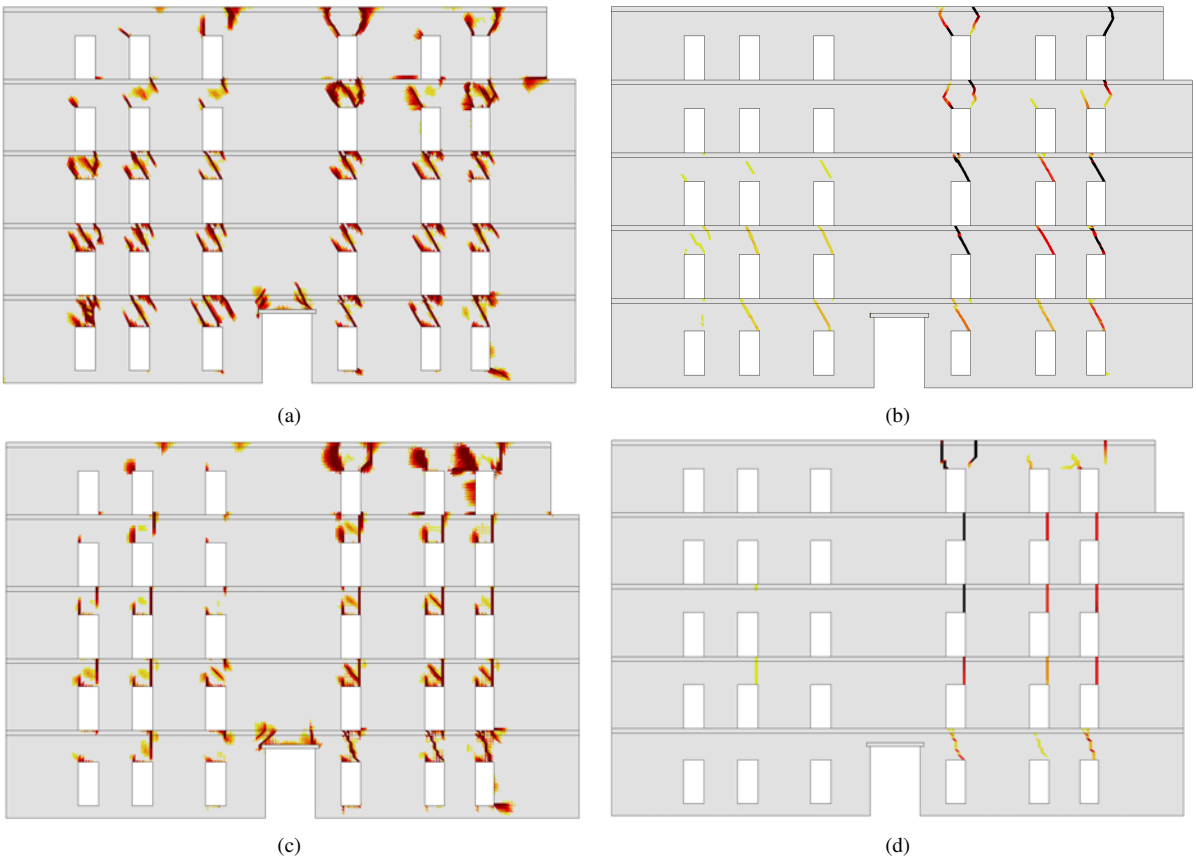

Figure 5.40 Simulation of Model A using the classical smeared crack approach. (a) Tensile damage and (b) maximum principal strains using the unstructured mesh for a horizontal dis-placement of 15.4 *mm* (Point 3 in Fig. 5.41). (c) Tensile damage and (d) maximum prin-cipal strains using the structured mesh for a horizontal displacement of 15.5 *mm* (Point 4 in Fig. 5.41).

for the unstructured one. Quite different response is also observed in the post-peak range with a sharper decrease of the residual capacity. On the contrary, the results using the tracking algorithm are in good agreement among them for both used meshes (Fig. 5.41). The capacity is lower by around 2% for the case with the structured mesh. Despite this, the structural response is clearly similar for both cases, even in the post-peak response. A comparison between the graphs obtained with and without the tracking algorithm reveals the impact of the erroneous localization of damage with the smeared crack approach.

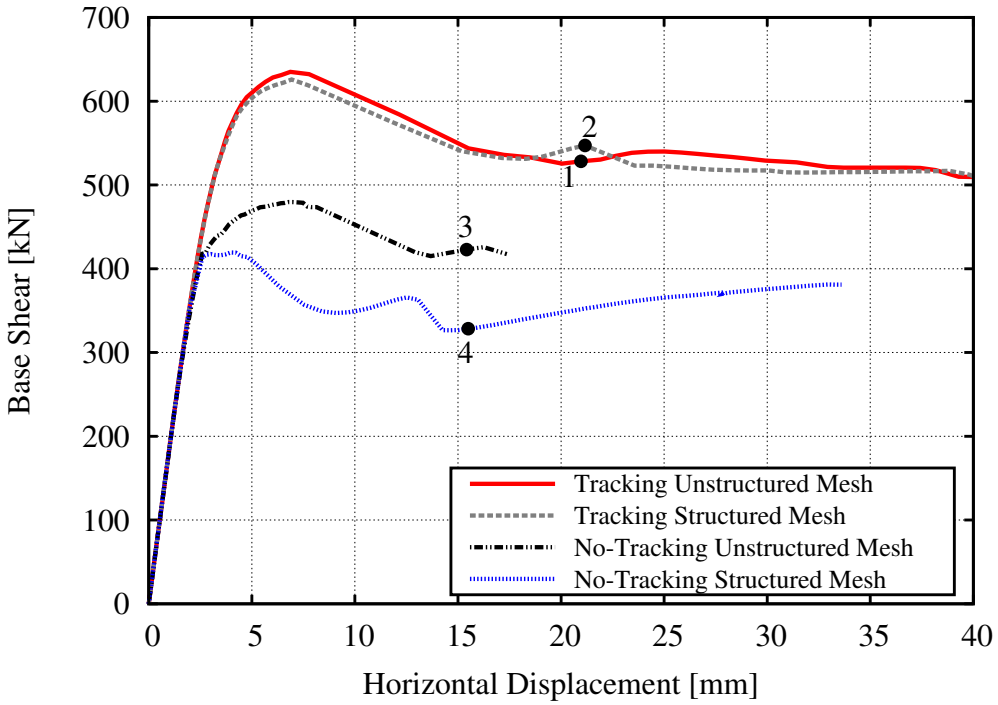

Figure 5.41 Base shear versus horizontal displacement at the top right corner of the structure using two different meshes (structured and unstructured), with and without the proposed tracking algorithm.

5.6 Summary

This chapter evaluates the application of the local tracking algorithm and the continuum damage model to four case studies differing in scale, total number of cracks and collapse mechanisms. The proposed methodology is validated through its comparison with analytical and experimental results, as well as different numerical approaches available in the literature. The following aspects are investigated regarding the tracking algorithm and the constitutive model: (i) their capacity to simulate the collapse mechanism and strength characteristics of masonry structures, (ii) the mesh-objectivity of the results, (iii) the computational cost, (iv) their performance compared to existing numerical approaches, and (v) the influence of the numerical parameters used in the tracking algorithm on the simulation.

The analysis of the Brazilian test, presented in Section 5.2, is a benchmark for the correct simulation of internal cracking. The proposed approach succeeds in capturing correctly the vertical crack at the middle of the specimen. The results using the tracking algorithm are compared with those using the classical smeared crack approach without the enhancement of the tracking algorithm. This comparison shows that the presented localization technique improves the mesh-size and directional mesh-bias objectivity of the numerical simulations. The results are also compared to analytical formulas from structural codes, showing a good agreement between numerical and analytical results.

The next case study is an experimental campaign on a masonry frame with a door

opening performed by Augenti et al. [18]. The numerical model simulates correctly the collapse mechanism, characterized by a combination of flexural cracks at the piers and the spandrels and a shear crack at the middle of the spandrel. The obtained results are further compared with those of a micro-model available in the literature, showing that the proposed methodology can be an efficient alternative for simulating this common collapse mechanism of masonry frame elements. This case study is utilized to demonstrate the influence of the tracking parameters due to the appearance of both shear and flexural cracks. The results of the sensitivity analysis suggest that in masonry structures with localized cracking affecting mainly the masonry joints, an exclusion radius equivalent to the unit's size can be used to capture correctly the collapse mechanism. Regarding the parameters used for the crack propagation correction, the observations of previous works [77, 84, 85, 293, 294] are confirmed, showing that the effect of these parameters is more significant for flexural cracks. For the particular case study, the variation of these two parameters shows a minor influence in the structural response.

The experimentally tested masonry wall against in-plane shear loading by Anthoine et al. [8] is a challenging case study since it necessitates the proper simulation of crack opening and closing effects by both the tracking algorithm and the constitutive model. The novel multi-directional tracking algorithm has captured correctly the crack opening and closing making possible the simulation of the diagonal crossing cracks which characterized the failure of the wall. The constitutive model plays an important role on this, since the information provided to the tracking algorithm for the characterization of the crack status depends on the correct estimation of the damage state at element level. The irreversible deformations under shear are considered due to the proper definition of the compressive damage surface and the novel proposed evolution law for the irreversible strains. Nevertheless, the results suggest that the evolution of the irreversible strains only under compressive damage may underestimate the hysteretic response of the structure.

The final validation case considers the analysis of the structural wall situated in Via Martoglio, Catania, Italy, which represents a large-scale application of the proposed approach. The results demonstrate that the tracking algorithm can simulate structural cases with extensive cracking and aid in the identification of the varying failure pattern according to the structural assumptions, as the floor's rigidity in the particular example. The mesh-sensitivity analysis confirms that the proposed methodology improves the mesh-objectivity of the numerical solution. A comparison with the classical smeared crack approach illustrates the importance of the correct crack localization, both in terms of predicting the capacity of the structure and the local and global failure mechanisms. The comparison of the results with other established numerical techniques shows the utility of the proposed approach when detailed information on the occurring (local and global) collapse mechanisms is necessary.

6

Crack Propagation in Cohesive-Frictional Materials*

This chapter presents an investigation of the implications given by alternative failure criteria in the simulation of cracking in cohesive-frictional materials. A novel tracking algorithm is presented with varying crack propagation criteria under tensile and shear failure. The mechanical behaviour is described with an isotropic damage model adopting a Mohr-Coulomb failure surface (Section 6.2). A new procedure is proposed for the selection of the crack propagation among the two alternative fracture planes proposed by the Mohr-Coulomb theory, based on the maximization of the energy release (Section 6.3). The theoretical and numerical implications emerged by the categorization of the failure modes and the existence of more than one potential fracture plane are presented and discussed through the simulation of the Nooru-Mohamed mixed-mode tests in concrete specimens (Section 6.4).

6.1 Introduction

As discussed in Chapter 2, most of the existing tracking algorithms are based on the assumption that a crack propagates having a direction orthogonal to the maximum principal stress/strain direction (see Section 2.4.5). In continuum solid mechanics, this hypothesis is consistent with the Rankine maximum tensile stress failure criterion, in which cracking occurs when the maximum stress reaches the tensile strength of the material on a plane orthogonal to the first stress eigenvector (see Fig. 6.1). However, for different failure criteria, as for instance Tresca or Mohr-Coulomb as shown in Fig. 6.1, the failure condition is satisfied in two potential planes diverging from the plane on which the maximum

*This chapter is based on Reference [327]

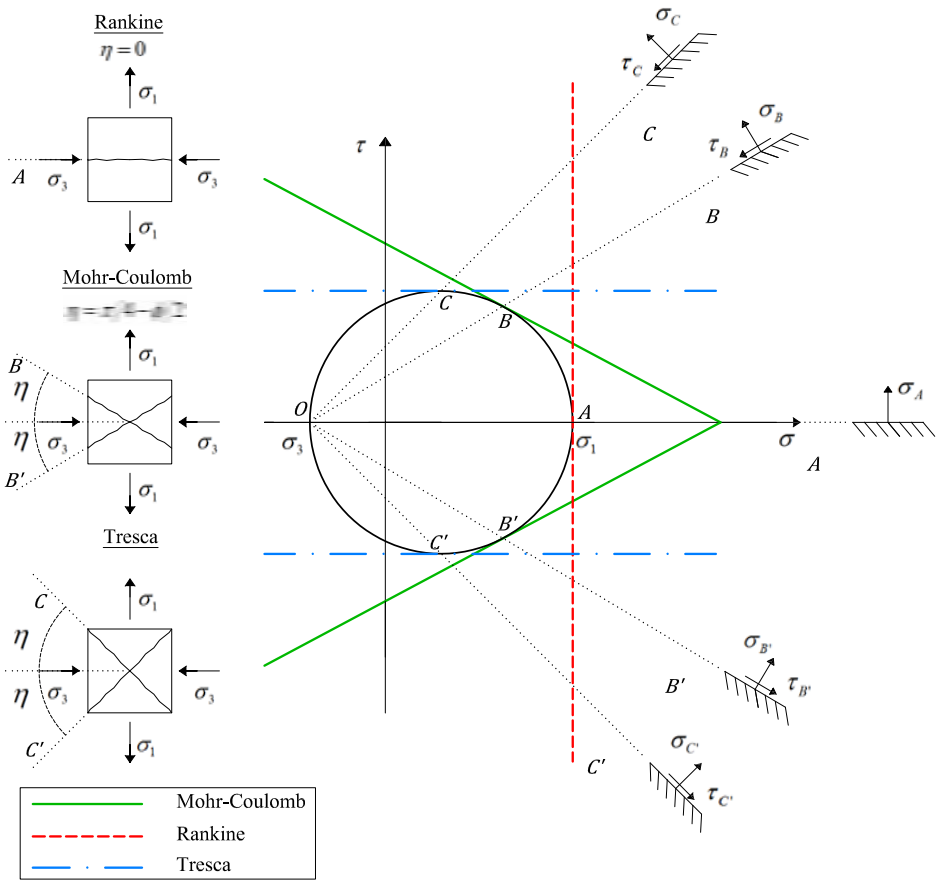

Figure 6.1 Failure planes of Mohr-Coulomb, Rankine and Tresca failure criteria in the σ, τ plane.

principal stress acts by an angle η (see for instance [75, 397]). Similarly, as presented in Section 2.4.5, the problem of more than one potential failure surfaces is present when the crack propagation is sought through a discontinuous material bifurcation analysis.

The existence of more than one potential fracture planes is a challenge for tracking algorithms, since by design they monitor the crack propagation along a single direction. The possibility of tracking a crack along all the potential fracture planes, allowing for crack-branching, is tempting but involves important algorithmic complications. One of this is the large number of branches that could be produced from a single crack, since new crack branches could emerge from each crack-front at each step of the analysis. A way to avoid this excessive and unrealistic branching would be to apply a branching criterion at the crack-front to define the moment of branching. However, as discussed in Section 2.4.5, such reliable criteria are still missing.

This chapter investigates the implications in the design of a tracking algorithm equipped with a crack propagation criterion that results in more than one potential fracture plane. As a first step towards this direction, this thesis considers the Mohr-Coulomb theory of rupture, which is commonly used for the simulation of shear failure in geomaterials. The designed algorithm makes a distinction between two failure modes, each of them having a different crack propagation. Under pure tension, a crack is defined to propagate along a direction orthogonal to the direction of the maximum principal stress, which is a

well-established assumption for the considered family of materials. Under shear, the crack propagation direction is defined according to the Mohr-Coulomb planes of fracture. To this end, the answer to the dilemma on the correct selection among the two alternative potential fracture planes defined by the Mohr-Coulomb theory is sought with the use of an energy criterion based on the maximization of the released energy.

After this introduction, the rest of the chapter is organized as follows. Section 6.2 briefly presents the Mohr-Coulomb theory of rupture. The novel parts of the tracking algorithm are presented in Section 6.3. The application of the new algorithm to the analysis of Nooru-Mohamed mixed mode tests on concrete is assessed in Section 6.4. Finally, Section 6.5 closes the chapter presenting some summarizing comments.

6.2 The Mohr-Coulomb theory of rupture

Otto Mohr's criterion, dating from 1900, states that failure occurs on a plane where the normal (σ) and the shear (τ) stresses reach a critical combination. For isotropic materials, in which the strength properties are the same when the shear stress is reversed, this critical combination can be expressed as

$$f = \tau \mp g(\sigma) = 0. \tag{6.1}$$

The above expression states that the limiting shear stress τ depends on the normal stress σ acting on the same plane at a point of the continuum. Mohr did not favour any particular shape for the failure envelopes $g(\sigma)$. A special case is when these are straight lines in the form of Coulomb's equation

$$g(\sigma) = c - \sigma \tan\varphi \tag{6.2}$$

where c is the cohesion and φ the internal friction angle of the material. The use of Coulomb's model of friction Eq. (6.2) in Eq. (6.1) results in the Mohr-Coulomb failure criterion

$$|\tau| = c - \sigma \tan\varphi. \tag{6.3}$$

In the σ-τ plane, shown in Fig. 6.2, Eq. (6.3) represents two straight lines symmetrical to the σ-axis. A Mohr's circle representing a critical stress state becomes tangent to these lines at two locations represented by the points B and B' in Fig. 6.2, symmetrical with respect to the σ-axis. Lines OB and OB' connecting the pole O with the points B and B' respectively represent the orientation of the failure surfaces. These form an angle with respect to the plane on which the maximum principal stress acts, which is equal to $\eta = \pm(\pi/4 - \varphi/2)$.

An alternative way for presenting Mohr-Coulomb's failure criterion is in terms of the

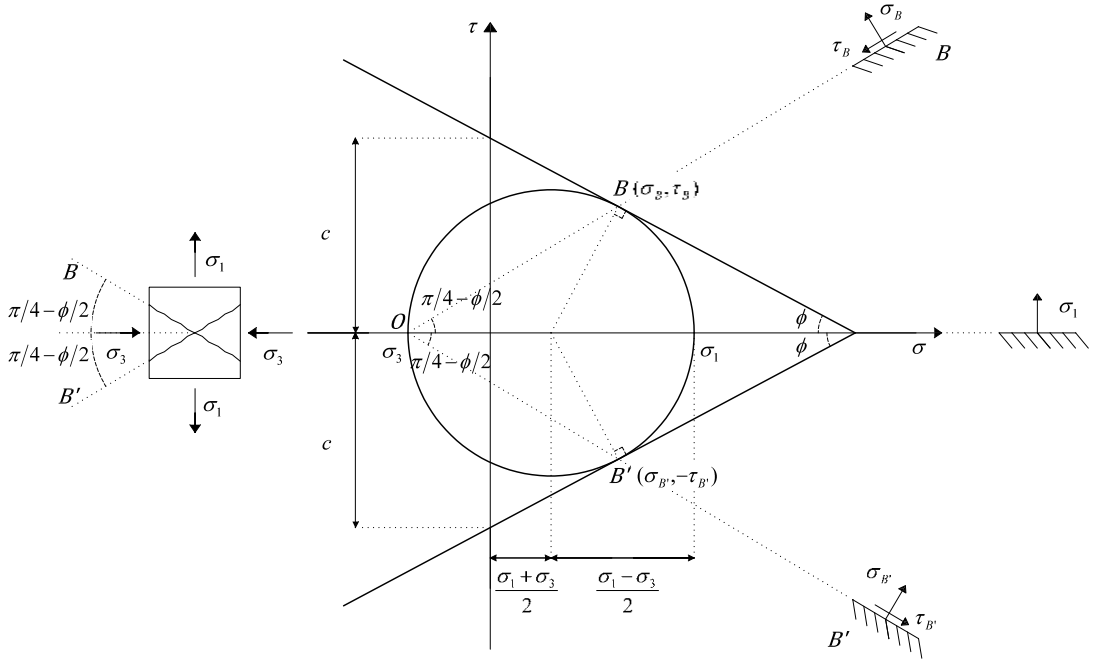

Figure 6.2 Mohr-Coulomb failure criterion in the σ, τ plane.

principal stresses [79, 389]

$$f(\sigma_1, \sigma_3) = \frac{\sigma_1}{f^+} - \frac{\sigma_3}{f^-} - 1 = 0, \qquad \sigma_1 \geq \sigma_2 \geq \sigma_3 \tag{6.4}$$

where the tensile f^+ and compressive f^- strengths of the material can be expressed as a function of the frictional-cohesive characteristics of the material [79]

$$f^+ = \frac{2\,c\,\cos\varphi}{1+\sin\varphi} \tag{6.5a}$$

$$f^- = \frac{2\,c\,\cos\varphi}{1-\sin\varphi}. \tag{6.5b}$$

Alternatively, a little manipulation of Eqs. (6.5) results in expressions for the friction angle and the cohesion in terms of the tensile and the compressive strength

$$\varphi = \sin^{-1}\left(\frac{f^-/f^+ - 1}{f^-/f^+ + 1}\right), \qquad 0 \leq \varphi < \pi/2 \tag{6.6a}$$

$$c = \frac{1}{2}\sqrt{f^-\,f^+}. \tag{6.6b}$$

Fig. 6.3 illustrates the dependence of the failure surface on the compressive to tensile strength ratio (or the friction angle and cohesion) under plane stress conditions. Two limit cases can be distinguished for varying values of f^-/f^+. For equal compressive and tensile strengths ($f^-/f^+ = 1$) the friction angle is zero ($\varphi = 0$) and the Mohr-Coulomb failure criterion coincides with Tresca's hexagon. In this case, the two symmetrical fracture planes make an angle of $\eta = \pm\pi/4$ with the plane of the maximum principal stress,

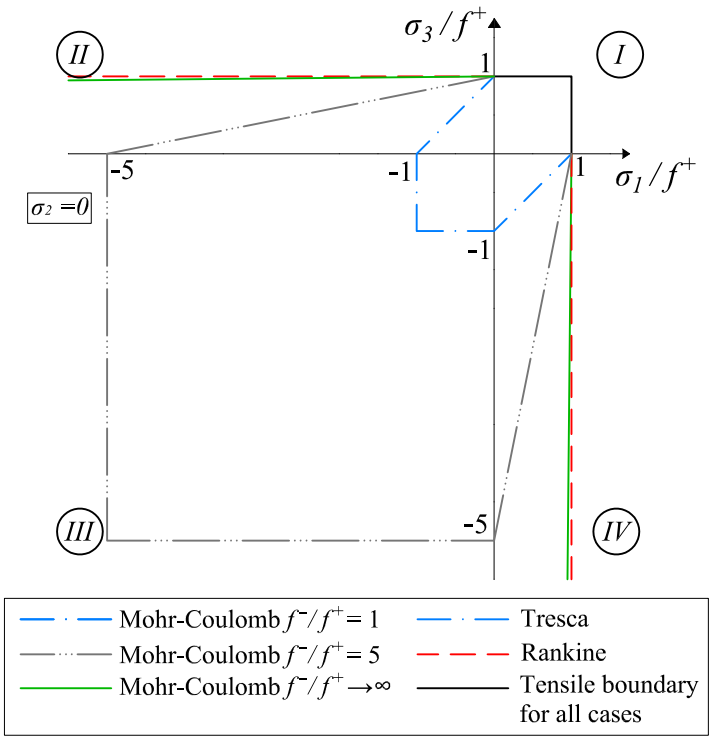

Figure 6.3 Comparison of Mohr-Coulomb failure criterion with Tresca and Rankine for the plane stress case.

corresponding to the plane of maximum shear stress (see Fig. 6.1). On the other end, a large compressive to tensile strengths ratio ($f^-/f^+ \to \infty$ or $\varphi \to \pi/2$) results in the coincidence of the Mohr-Coulomb failure surface with Rankine's one (Fig. 6.3). This assumption leads to the collapse of the two fracture planes into a single one, which as shown in Fig. 6.1 is the one of the maximum principal stress.

6.3 Tracking algorithm

6.3.1 Failure modes and propagation directions

The tracking algorithm used in this chapter is based on on the *fixed* one presented in Chapter 4. The main difference concerns the selection of the crack propagation direction, which here is associated with the stress state at the moment of failure. According to the latter, two types of failure modes are distinguished: a) tensile failure and b) shear failure. These are defined as follows:

(a) *Tensile failure.* An element fails in tension when all its principal stresses are non-negative, i.e. $\sigma_1 \geq \sigma_2 \geq \sigma_3 \geq 0$ and the failure criterion is violated in the first quadrant of the principal stress space shown in Fig. 6.3. In this case, the crack is defined to propagate with a direction orthogonal to the maximum principal stress. This crack propagation angle is represented with respect to the horizontal axis of a Cartesian xy-coordinate system with ω.

(b) *Shear failure.* An element fails in shear when it has one tensile and one compressive principal stresses, i.e. $\sigma_1\sigma_3 < 0$. This corresponds to a stress-state within the second or fourth quadrant of the principal stress space as presented in Fig. 6.3. Under such conditions, the normal and shear stresses reach a critical combination on two planes. These planes, with a direction defined by lines OB and OB' in Fig. 6.2, are symmetrical with respect to the plane on which the maximum principal stress acts and diverge from it with an angle $\eta = \pm(\pi/4 - \varphi/2)$. With reference to the horizontal axis of a Cartesian xy-coordinate system, these two angles are defined as $\theta_{1,2}$

$$\theta_1 = \omega + \left(\frac{\pi}{4} - \frac{\varphi}{2}\right) \tag{6.7a}$$

$$\theta_2 = \omega - \left(\frac{\pi}{4} - \frac{\varphi}{2}\right). \tag{6.7b}$$

Due to the above, an additional procedure needs to be pursued in order to identify the failure mode, and in case of shear failure to choose among the two potential fracture planes proposed by the Mohr-Coulomb theory of rupture. The selection among these two fracture planes is decided in this work with the use of an energy-based criterion that will be presented in Section 6.3.3.

It is acknowledged that the selected crack propagation direction under the tensile failure mode corresponds to the Rankine failure criterion. This is usually represented using a maximum-tensile-strength cut-off in combination with the Mohr-Coulomb failure surfaces. Since the aim of the current contribution is to investigate the implications of selecting the proper crack propagation direction with a tracking algorithm under shear failure, the incorporation of a maximum-tensile-strength cut-off has been disregarded. Nevertheless, it is noted that in the presented applications shear failure is dominant, and therefore the difference expected in terms of capacity between the chosen model and one with a tensile cut-off criterion is expected to be negligible. However, it is acknowledged that the combination of these two criteria should be considered for the estimation of structural capacity under a combination of mode I and mixed mode fracture.

6.3.2 Selection of the crack propagation direction

Figure 6.4 presents a flowchart of the tracking algorithm. The new part, considering the selection of the crack propagation direction, comes into play after the crack-root and crack-tip elements have been identified. At this point, a loop starts over all the crack-roots of new cracks and crack-tips of consolidated cracks. At each loop, the crack propagation direction of the crack and in particular the crack propagation angle at the crack-root/tip (denoted hereafter as ψ^0) is identified through the following procedure:

(A) The values of the principal stresses and the eigenvectors of the crack-root/tip are

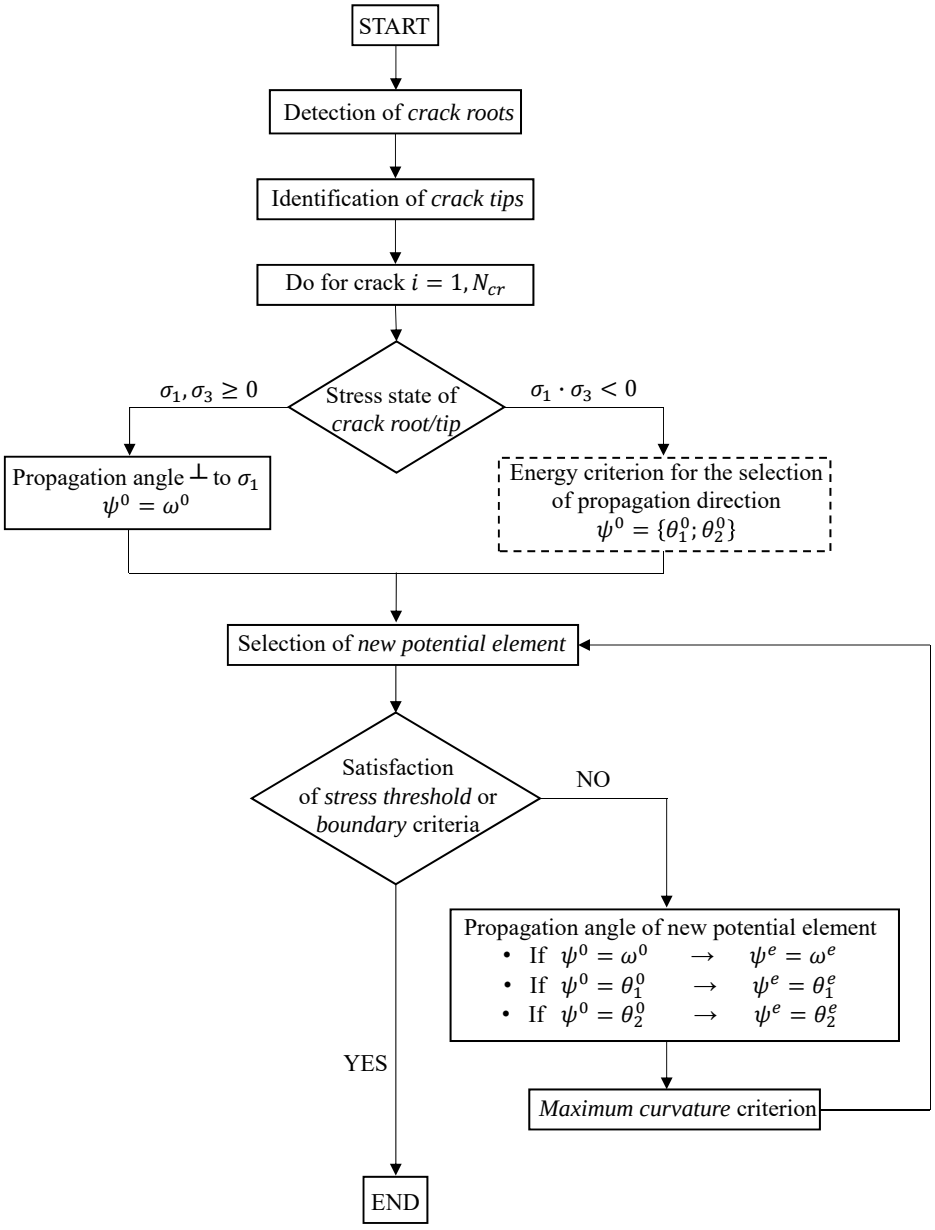

Figure 6.4 Flowchart of the modified fixed tracking algorithm with crack-propagation selected according to the stress-state at the crack-root/tip element.

computed considering a stress-tensor obtained as the average of the smoothed stress field at the nodes of the element. Note that in the following, the principal stresses are ordered such as the relationship $\sigma_1 \geq \sigma_2 \geq \sigma_3 \geq 0$ holds. According to those, the following two cases leading to cracking are recognised:

(A_I) All the principal stresses are non-negative, i.e. $\sigma_3 \geq 0$: the crack propagation direction is orthogonal to the direction of the maximum principal stresses and is defined by the angle $\psi^0 = \omega^0$.

(A_{II}) The maximum and minimum principal stresses have different signs, i.e. $\sigma_1 \, \sigma_3 < 0$: the crack propagation direction follows one of the two possible fracture planes defined by the Mohr-Coulomb theory of rupture. One of the two possible

propagation directions is selected, i.e. $\psi^0 = \theta_1$ or $\psi^0 = \theta_2$, according to the procedure presented in Section 6.3.3.

(B) Once the propagation direction and ψ^0 for the crack has been chosen, the new crack-path can be identified. Starting from the crack-root/tip element, the adjacent element crossed by the defined crack propagation direction is labelled as the new potential element. To this end, two actions are carried-out:

(B_I) Control of the satisfaction of the two crack ending criteria (i.e. stress-threshold and boundary criteria) are satisfied. If so, the crack propagation has ended, and the procedure is repeated from step (A) for the next crack. If not, the algorithm continues to step (B_{II}).

(B_{II}) Determination of the crack angle of the new potential element. During an increment each crack will propagate in the direction determined from the crack-root/tip element, i.e. either orthogonal to the direction of the maximum principal stress or along one the Mohr-Coulomb fracture planes according to Eq. (6.7). Note that the value of the cracking angle of the new potential element (denoted as ψ^e) is calculated according to its own stress-state, i.e.

$$\begin{aligned} &\text{if} \quad \psi^0 = \omega^0 \quad \text{then} \quad \psi^e = \omega^e \\ &\text{if} \quad \psi^0 = \theta_1^0 \quad \text{then} \quad \psi^e = \theta_1^e \\ &\text{if} \quad \psi^0 = \theta_2^0 \quad \text{then} \quad \psi^e = \theta_2^e. \end{aligned}$$

(B_{III}) Control and correction of the propagation angle. Contrary to pure bending states, the mixed mode failure investigated in this chapter is not characterised by high stress gradients at the crack-tip that may affect significantly the stress directions. For this reason, the application of the maximum curvature criterion has shown to be unnecessary in the analyses performed here. Nevertheless, the opportune correction of the crack propagation angle using the maximum curvature criterion is possible with a small variation compared to the procedure presented in Chapter 4. Here, only elements belonging to the same fracture plane are considered for the computation of the crack vector V_c representing the average crack direction at the wake of the crack-tip.

6.3.3 Energy-based criterion for the selection of the crack propagation direction

It has been shown in the preceding sections that Mohr-Coulomb theory of rupture predicts two equally possible fracture planes. Following thermodynamic principles, the selected potential crack direction should maximize the released energy. In this work, this is done by evaluating the total elastic strain energy fields of the two possible crack paths prior to

their opening. The selected path is the one with the larger stored total elastic strain energy density. This choice is based on the premise that upon fracture the material neighbouring to the fracture zone will unload elastically. In this way, if the crack crosses a region with higher elastic strain energy, the amount of energy release is maximized, minimizing the total strain energy of the body. This procedure, minimizes the energy dissipated during the development of the fracture.

This is not the first time that a strain energy based criterion is used for the estimation of the crack propagation angle. In particular, similar criteria have proved to be successful in geotechnical engineering simulations for determining the propagation of fracture in faults (see [248, 271]). In fracture mechanics, a similar condition is implied by the T-Criterion [376, 377]. According to this, a crack propagates towards the direction of the maximum dilatational strain energy density.

The procedure used for the selection of the crack propagation direction starts after the crack-tip and crack-root elements are defined (see Fig. 6.4). Then for each crack-root/tip element the following steps are considered, which are illustrated in Fig. 6.5:

1. The two possible crack-propagation angles at the crack-root/tip element are defined.
2. For each of these two angles, the two possible crack paths are determined and the composing potential elements on each of them are recognized (Fig. 6.6). This occurs in the following order:
   i. The crack propagation direction of the crack-root/tip element is set equal to θ_1.
   ii. For this crack propagation direction, the next element of the crack is identified.
   iii. The distance δ_κ between the centroid of the new element and the centroid of the crack-root/tip is computed.
   iv. If the new potential element lies within the limit of the radius r_{crack} (defined in the following step (vii)) the total elastic strain energy W^e of the element is computed

$$W^e = \int_{V_e} \frac{1}{2}\, \boldsymbol{\sigma} : \boldsymbol{\varepsilon}\, dV \tag{6.9}$$

   where $\boldsymbol{\sigma}$ and $\boldsymbol{\varepsilon}$ are the stress and strain tensors of the new element and V^e its volume.
   v. The propagation angle of the new element is calculated as $\psi^e = \theta_1^e$ and (if chosen) the maximum curvature criterion is applied.
   vi. The new element is named as current crack-tip and the steps (ii)-(vi) are repeated.

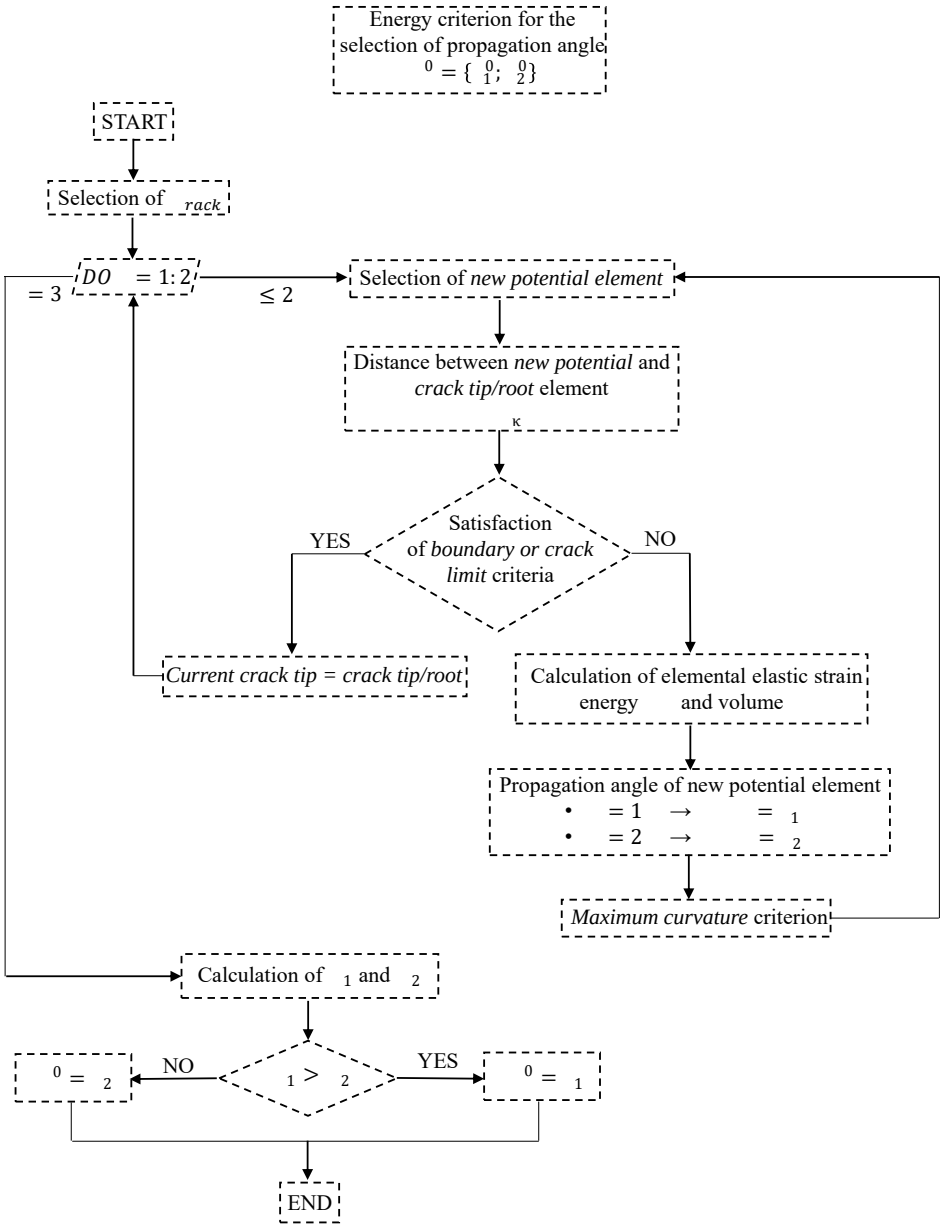

Figure 6.5 Flowchart with the procedure for the selection of the frictional crack propagation direction θ_1 or θ_2.

vii. The procedure stops when the *boundary criterion* or the *crack limit criterion* is satisfied. The first is the same criterion as described in Chapter 4. The crack limit criterion is satisfied when the distance between the crack-root/tip and the new element of the crack δ_κ overpasses a radius r_{crack} (see Fig. 6.6). This radius is calculated for each crack at each load increment. It is the minimum between a radius defined by the user r_{crit} and the distance between the crack-root/tip and the last potential element before the crack meets a mesh boundary *or another crack*.

viii. When one of the above criteria is satisfied, the steps from (ii) to (vii) are repeated, considering this time the crack propagation direction of the crack-

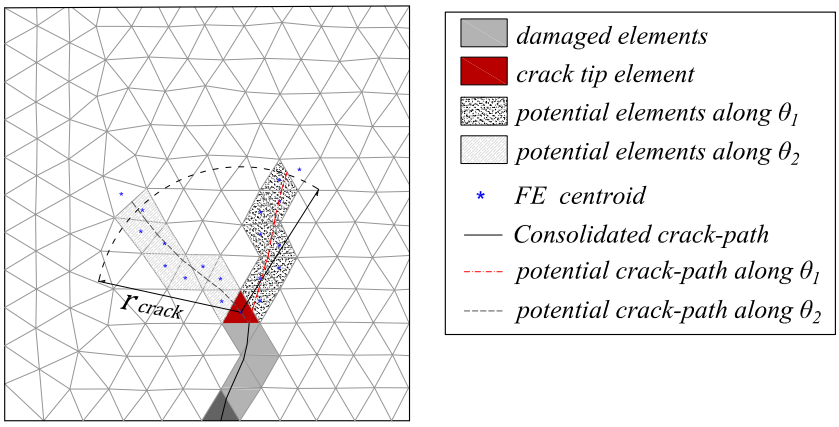

Figure 6.6 Illustration of the procedure used for the selection of the crack propagation direction between θ_1 and θ_2.

root/tip element as $\psi^0 = \theta_2$ (in step (ii)) and that of the following elements as $\psi^e = \theta_2^e$ (in step (v)).

3. To this end, the composing elements of the two potential crack propagations from the crack-tip and the strain energy and volume of each are computed. The total strain energy per crack volume for each of the two potential crack propagations is defined as

$$w_1 = \frac{1}{V_1} \sum_{i}^{n} W_i^e \tag{6.10a}$$

$$w_2 = \frac{1}{V_2} \sum_{j}^{m} W_j^e. \tag{6.10b}$$

The crack volume at each direction (V_1, V_2) is the sum of the volume of the elements (V^e) pertaining to the crack path

$$V_1 = \sum_{i}^{n} V_i^e \tag{6.11a}$$

$$V_2 = \sum_{j}^{m} V_j^e \tag{6.11b}$$

where $i = 1, n$ are the elements on the direction of the crack determined with θ_1 and $j = 1, m$ are the elements on the direction of the crack determined with θ_2.

4. The selected crack direction for the particular increment is the direction with the greatest strain energy per crack volume.

As presented in the Chapter 2, there exist in the literature different methods for choosing the crack propagation direction among more than one equally probable. For instance, in Unger et al. [380] and Zhang et al. [403] an iterative procedure is followed

in which the stored elastic strain energy is calculated for different crack directions. This approach could be also considered here for the two potential fracture planes. However, this choice implies a much higher computational cost since the non-linear system of equations needs to be solved for both potential crack planes at each step. Additionally, in cases of multiple cracking, various combinations of potential crack propagations of the different cracks should be checked for identifying the one minimizing the total elastic energy of the body. Another possibility is to compare the two possible directions with the gradient of the instantaneous displacement field close to the crack-tip/origin as in references [262, 308, 388].

6.4 Simulation of mixed-mode tests on concrete

6.4.1 Experimental and numerical set-up

The proposed formulation has been applied to the analysis of three benchmark problems for mixed mode fracture in concrete. They correspond to a series of experiments on double edge notched (DEN) specimens under non-proportional loading, performed by Nooru-Mohamed [246]. The tested concrete specimen is square shaped with dimensions $200 \times 200 \times 50\ mm^3$ and two notches with a depth of 25 mm and height of 5 mm at each lateral side. The DEN specimen was glued to four platens in the configuration of Fig. 6.7a. The numerical simulations correspond to the load-path 4 of the experimental campaign, which was performed in two steps. In the first one, a compressive load was applied to the lateral platens in displacement control up to a value P_s. Subsequently, a traction load P was applied over the top platen in displacement control keeping the lateral force P_s constant under load control. Figure 6.7b illustrates the cracking patterns observed at the DEN specimens after the experiments for the load paths 4a (specimen 48-03), 4b (specimen 46-05) and 4c (specimen 47-06) corresponding to lateral force $P_s = 5$ kN, 10 kN and 27.5 kN, respectively. Two concrete specimens were tested for load-path 4b, whereas only one specimen was tested for load-paths 4a and 4c.

Although the experiment itself, as well as the experimental apparatus were sophisticatedly designed, Nooru-Mohamed mentions that undesirable eccentricities could be provoked by the skew-symmetric bonding of the specimen to the steel platens, the possible relative rotations between the two used coupled frames and the non-symmetric behaviour of the springs (in the longitudinal direction) that were used to avoid the in-plane rotation of the DEN specimen. For a comprehensive discussion on the experimental procedure, apparatus and problems the reader is referred to the original work [245, 246].

The non-linear behaviour of the concrete is simulated using an isotropic continuum damage model. The constitutive model is easily obtained from the orthotropic damage model presented in Chapter 3 by using a single equivalent stress and damage index instead of two different for tensile and compressive damage. The choice of a single damage index

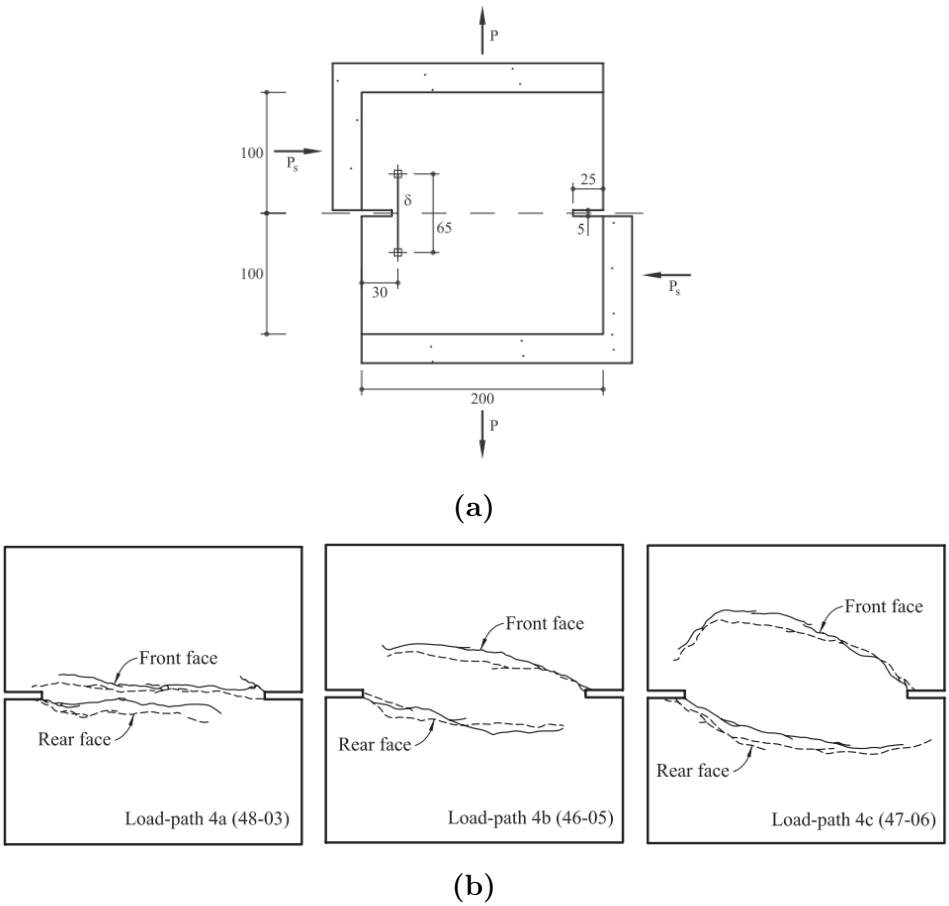

Figure 6.7 (a) Geometry and load configuration for the Double Edge Notched (DEN) specimen, (b) Experimentally obtained crack patterns in the front (solid lines) and rear (dashed lines) faces of the tested DEN specimens by Nooru-Mohamed [246].

emerges from the fact that only damage due to cracking affects the analysed specimens. The Mohr-Coulomb failure criterion (Eq. 6.3) is used for defining the damage surface while the exponential softening law presented in Chapter 3, Eq. (3.32), is used for the evolution of the damage index. For further details on this isotropic damage model see Saloustros et al. [327]. The material parameters are defined according to the data provided by Nooru-Mohamed [246]: tensile strength $f^+ = 3.0\ MPa$, Young Modulus $E = 30\ MPa$, Poisson's ratio $= 0.2$, and fracture energy $G_f^+ = 110\ J/m^2$.

The three experiments are discretized in an unstructured mesh with average mesh size of $h_e = 2.5$ mm (8394 nodes). The discretization consists of 2D plane stress 3-noded linear triangular elements. The computational boundary conditions are exactly skew-symmetric, with the central node of the mesh being fixed in the horizontal and vertical degrees of freedom. Regarding the input parameters for the local tracking algorithm, $r_{excl} = 0.12\,m$ and $r_{crit} = 0.03\,m$. As discussed previously, the definition of α_{max} and r_{neigh} has been unnecessary.

The discrete weak form of the problem is solved incrementally in a step-by-step manner. At each load increment, the corresponding non-linear equations are solved with the use of a secant scheme (Picard's method) along with a line search procedure. Convergence

of an increment is attained when the ratio of the norm of the iterative residual forces and the norm of the total external forces is lower than 10^{-2} (1%).

The outline of the simulated experiment is as follows. Firstly, the two possible solutions indicated by the Mohr-Coulomb theory of rupture are presented. It is noted that for these analyses the procedure for the angle selection has been turned-off and the angle of the fracture is selected explicitly to be equal to θ_1 or θ_2 according to the studied case. Following this, the capacity of the presented tracking algorithm and the energy-based criterion to model the frictional characteristics of quasi-brittle materials is demonstrated by presenting the numerical solutions for three different compressive to tensile strength ratios $f^-/f^+ = [5; 20; \infty]$. For comparison purposes, each example is simulated also with the use of the fixed tracking algorithm in which the propagation direction and failure criterion are based on the maximum-tensile-stress criterion of Rankine [77].

The numerical simulation of the three experiments has given similar results in terms of: (i) the capacity of the energy-based criterion to select the direction that maximizes the released energy, (ii) the effect of the friction angle, (iii) the mesh-size and directional mesh-bias sensitivity of the numerical result and (iv) the representation of the collapse mechanism. For this reason, the following section presents in detail only the results concerning load-case 4b. For more information about the results derived from load-cases 4a and 4c, the interested reader is referred to Saloustros et al. [327].

6.4.2 Results and discussion

For load-path 4b the lateral compressive force applied at the first stage of the analysis is P_s=10 kN. At the second stage, a vertical traction is imposed by increasing gradually the vertical displacement (denoted in the graphs of Figs. 6.8, 6.9 as "δ") maintaining constant the lateral load P_s.

As commented, the numerical analysis of the specimen starts by presenting the two possible solutions according to the Mohr-Coulomb criterion, for $f^-/f^+ = 20$. Hence, the results presented in Fig. 6.8 have been produced by turning off the procedure described in Section 6.3.3 for the selection of the crack propagation direction. In these analyses, the fracture under shear propagates at a constant angle θ_1 (Fig. 6.8a) or θ_2 (Fig. 6.8b). Note that when damage occurs under pure tension the fracture propagates with a direction orthogonal to the maximum principal stresses (i.e. ω). The results show that the two cracks initiate under a pure tensile state of stress, but soon after, they evolve under a shear stress state. As a consequence, the crack propagation direction plays an important role to both the curvature of the crack and the dissipated energy, which can be appreciated in Fig. 6.8a & b and Fig. 6.8c, respectively. In this case it is evident that a crack propagating at a direction θ_1 leads to a shorter crack with less curvature and to less dissipated energy.

The following numerical simulations are carried-out using the energy-criterion presented in Section 6.3.3 for selecting between the two possible crack propagation directions.

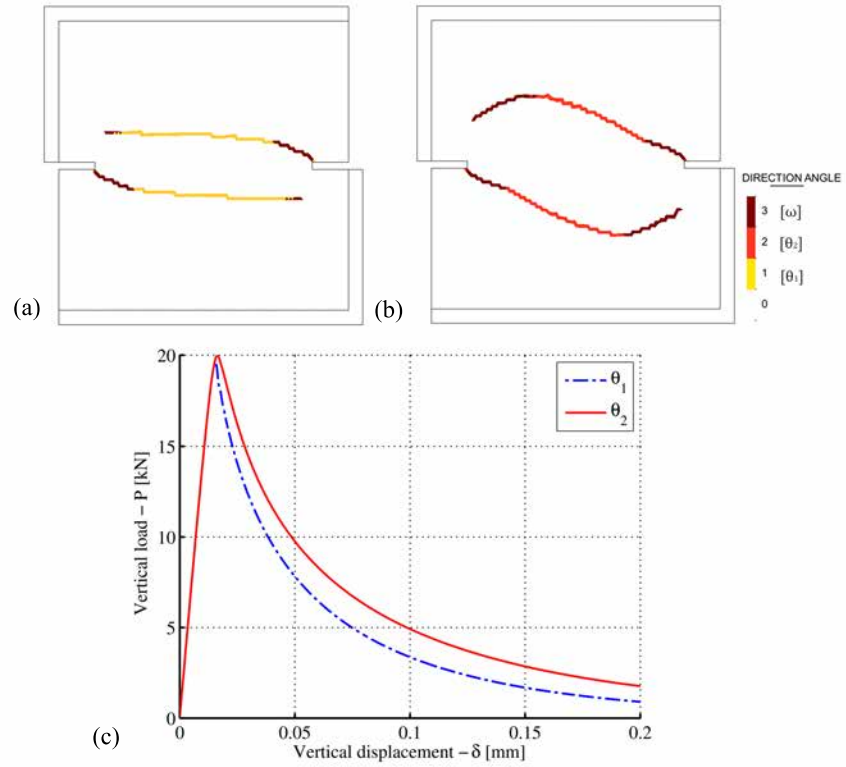

Figure 6.8 Load-path 4b for $f^-/f^+ = 20$: contour of the selected crack propagation direction in the damaged elements (a) case θ_1 , (b) case θ_2, and (c) load vs displacement (P-δ) for the two possible fracture planes.

Three different compressive to tensile strength ratios $f^-/f^+ = [5; 20; \infty]$ are considered referring to different cohesive-frictional characteristics. Figure 6.9 presents the results of these analysis in terms of obtained crack pattern and load against vertical displacement curves. The contour shown in Figs. 6.9a-d represents the choice of the propagation angle, with θ_1 represented with yellow, θ_2 with orange and ω with red. The results show that for all three ratios of f^-/f^+, the energy-based criterion has chosen correctly θ_1 as a propagation angle, which as seen before (Fig. 6.8) is the one minimizing the total stored elastic strain energy of the specimen. The same result has been observed for the other load cases 4a and 4c not presented here (see [327]). These results point-out that the proposed approach based on a total elastic strain energy criterion can be useful for the selection between more than one potential propagation directions in mixed mode problems. Concerning the failure pattern, cracking is induced due to shear at its greater extend. Pure tensile stresses are driving the first part of the crack for all the different f^-/f^+ studied cases. Among the studied cases, those with more curved crack patterns present also tensile failure towards the end of the analysis, when the central part of the crack specimen undergoes important rotation due to the opening of the existing cracks. A comparison with the other two experiments performed under a different lateral force P_s, shown in Fig. 6.10, demonstrates the effect of the lateral compressive force to the crack curvature and failure pattern. The low lateral force in load path 4a leads practically to a mode I failure

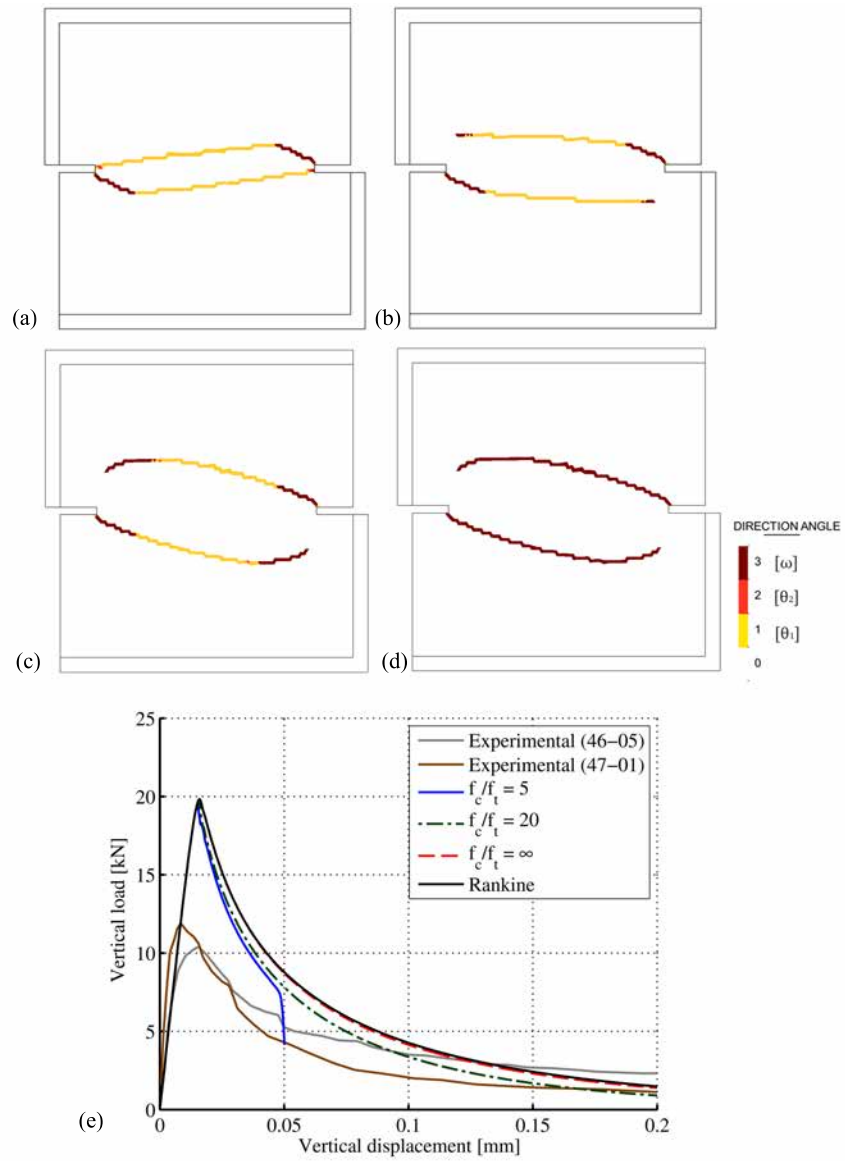

Figure 6.9 Load-path 4b: contour of the selected crack propagation direction in the damaged elements for Mohr-Coulomb's criterion and (a) $f^-/f^+ = 5$, (b) $f^-/f^+ = 20$, (c) $f^-/f^+ = \infty$; (d) for Rankine's criterion and $f^-/f^+ = 20$, and (e) load vs displacement (P-δ) for different compressive to tensile strength ratios.

(Fig. 6.10a). On the other end, load path 4c fails exclusively under shear (Fig. 6.10c) and the presented here load path 4b consists an intermediate case (Fig. 6.10b).

Apart from the efficiency of the energy-based criterion, the algorithm captures the varying response for the varying f^-/f^+ values. Lower compressive to tensile strength ratios result in a smaller curvature of the crack trajectory and in less dissipated energy (see Fig. 6.9e). For the ratio $f^-/f^+ = 5$ the two cracks reach the opposite notch and the specimen starts rotating around the developed compressive strut, resulting in the sudden drop of load, as can be appreciated in Fig. 6.9e. On the other end, we can see that the curvature of the crack using the Mohr-Coulomb failure criterion with $f^-/f^+ \approx \infty$ (Fig. 6.9c) is identical to that obtained by using Rankine (Fig. 6.9d). This outcome illustrates that the (unrealistic) use of a friction angle of almost $\pi/2$ results in the coincidence of

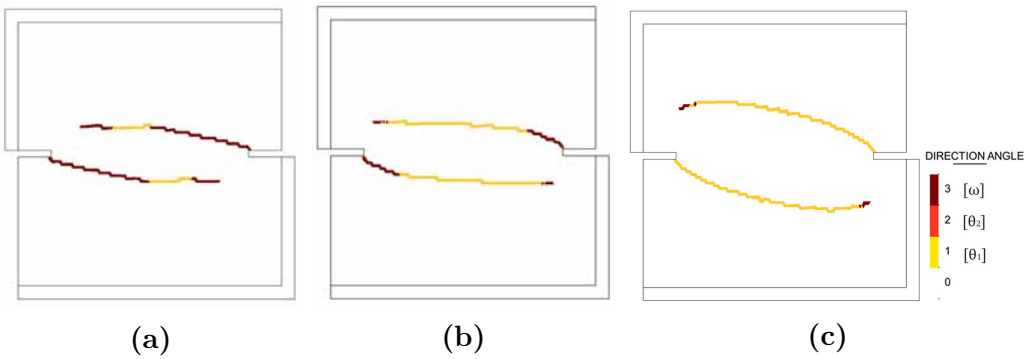

Figure 6.10 Effect of the lateral force P_s on the crack propagation and failure pattern for $f^-/f^+ = 20$. (a) Load-path 4a with $P_s = 5\,kN$, (b) Load-path 4b with $P_s = 10\,kN$, (c) Load-path 4c with $P_s = 27.5\,kN$.

the Mohr-Coulomb failure criterion with that of the Rankine for tensile and shear stress states ($\psi \approx \pi/2 \Rightarrow \left(\frac{\pi}{4} - \frac{\varphi}{2}\right) \approx 0$) as presented previously in Section 6.2 and Fig. 6.3.

With regards to the prediction of the cracking pattern, a better agreement between the numerical and experimental results is obtained for $f^-/f^+ \geq 20$ and thus high friction angles $\varphi \geq 64°$. Considering Eq. (6.7), such high values of φ result in very small deviations of the failure planes predicted by the MC theory compared with the Rankine failure plane. The same conclusion has been drawn for the other two load paths 4a and 4c (see [327] and Fig. 6.10). These results show that for the current mixed mode tests, cracking is driven by the maximum principal stress, i.e. a local Mode I crack-growth can be used to simulate the crack propagation within the analysed concrete specimens. Gálvez et al. [137, 138] made a similar observation in the simulation of a series of mixed mode tests on concrete. In those tests, the crack paths could be predicted accurately using a finite element method with a crack propagation defined by the maximum tangential stress criterion of linear elastic fracture mechanics. The above justify the popularity of using a maximum principal stress criterion for the definition of the crack propagation angle for mode I and mixed mode cracking problems in concrete.

Regarding the obtained load vs. displacement graphs (Fig. 6.9e), these show an overestimation of the predicted peak load compared to the experimentally obtained one. The same discrepancies have been observed by other authors (see for instance references [101, 106, 113, 160, 319, 360]) and it is probably the reason that several authors have used lower values for the tensile strength and fracture energy (e.g. [69, 157]). As commented before, the reason for this divergence may be due to the possible experimental eccentricities, which do not exist in the numerical simulation.

Finally, it should be noted that the correlation between the friction angle in geomaterials given by Eq. (6.6a) and the ratio of the compressive and tensile strengths drops for increasing f^-/f^+. For instance, the compressive strength of the concrete specimens used in the particular example are around 46 MPa, resulting in $f^-/f^+ \approx 15$ and $\varphi \approx 61°$, which is a high value for concrete. This limitation makes the application of the classical Mohr-Coulomb theory unsuitable for the simulation of materials with very distinct com-

pressive to tensile strength (e.g concrete, masonry) and has motivated the proposal of a modified Mohr-Coulomb criterion by Oller [267].

6.4.3 Mesh-dependency

A second mesh with average element size of $h_e = 5\,mm$ (2162 nodes) has been used to investigate the mesh-dependency of the proposed numerical method. Figure 6.11 presents the results obtained with the two different meshes for load path 4b with $f^-/f^+ = 20$ and using the procedure for selecting the crack propagation direction of Section 6.3.3. In the same figure, the difference of the discretization level between the two meshes can be appreciated. The analyses show that the crack propagation direction θ_1, which maximizes the released energy, has been correctly selected independently of the degree of refinement of the mesh. In both cases two skew-symmetric cracks start from the two notches and propagate towards the interior of the specimen. The crack curvature is very similar for the two meshes and no spurious mesh-bias is observed. Figure 6.3.3c depicts the load versus displacement curves for these two simulations. The two graphs present the same trend, with the dissipated energy being almost identical upon mesh-refinement.

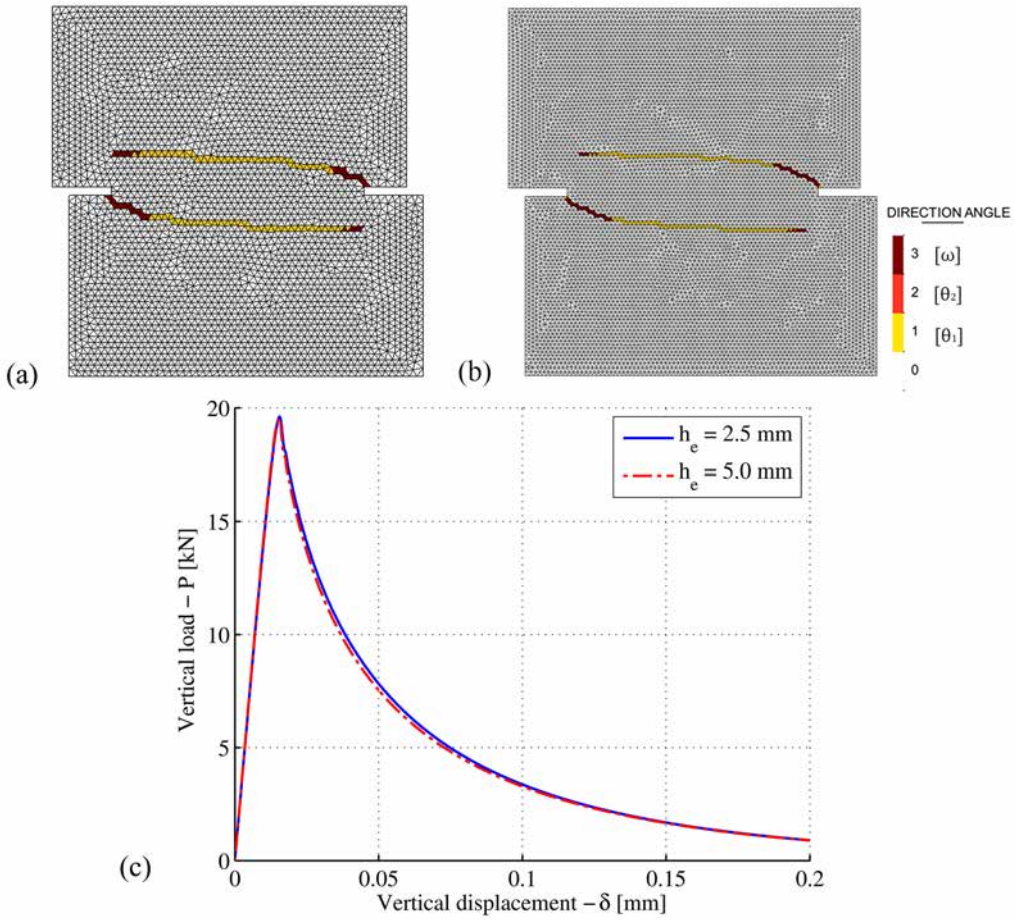

Figure 6.11 Load-path 4b: contour of the selected crack propagation direction in the damaged elements for mesh with element size (a) $h_e = 5\,mm$ and (b) $h_e = 2.5\,mm$. (c) Load vs. displacement (P_δ) for the two different meshes, $f^-/f^+ = 20$.

6.5 Summary

This chapter presents a tracking algorithm for crack propagation depending on the frictional characteristics of the simulated material. The algorithm distinguishes between tensile and shear failure and defines accordingly the crack propagation direction. Under pure tension, the crack propagates with a direction orthogonal to the direction of the maximum principal stress. Under shear failure, the crack propagation criterion is consistent with the Mohr-Coulomb theory of rupture, which gives two mutually possible fracture planes. The selection among the two of them is made through the use of a novel procedure based on a criterion for the maximization of the released energy, which is applied at the propagating front of each crack prior to each opening. According to this, the two potential crack propagation paths are identified from the crack-tip and the total elastic strain energy per crack volume for each of them is computed. The crack is then defined to propagate towards the direction with the maximum stored total elastic strain energy per crack volume.

The proposed algorithm is applied to the analysis of a non-proportional mixed mode test carried-out on double notched concrete specimens. The results show that the algorithm successfully presents the expected sensitivity to the changes of the material frictional characteristics, resulting in varying crack curvatures for different frictional angles. Moreover, the used energy criterion is capable of selecting the fracture plane that minimizes the dissipated energy and maximizes the released energy among the two fracture planes predicted by the Mohr-Coulomb theory of rupture. The separation of the failure types into tensile and shear by the algorithm, is proved to be an effective tool for understanding fracture phenomena under mixed mode loading tests.

This page is intentionally left blank.

7

Conclusions

7.1 Summary

Advanced computational methods are important tools for the analysis and conservation of existing masonry structures and the design of new ones. Their effectiveness in achieving the aforementioned goals depends on their capacity to address a number of contradicting parameters, namely accuracy in material and damage representation, versatility of the loading hypothesis, and efficiency regarding the pre/post-processing and computational cost.

The high capacity of most masonry typologies under compressive loads, compared to their low tensile strength, renders cracking critical for the security of masonry structures. The first part of Chapter 2 of this thesis, covers a review of the numerical methods developed for the simulation of cracking in quasi-brittle materials, such as masonry and concrete. Focus is placed on approaches developed within the Finite Element Method (FEM), due to their versatility and broad use in academia and industry. The immense interest of the engineering community to understand and describe cracking phenomena, in addition to the unexpected numerical obstacles encountered during this endeavour, has resulted in the development of a wide diversity of finite element (FE) methods for the analysis of structural problems involving cracks.

The second part of Chapter 2 focuses on the application of these approaches to the analysis of masonry structures. From this review, it becomes evident that a limited number of tools for accurate crack representation have been applied to the analysis of masonry structures. Notably, when this happens it concerns only small-scale masonry structural elements. This practice is commonly imposed by the high computational cost of accurate strain localization techniques, which prohibits their application to large-scale problems. Other reasons are associated with the inapplicability of many advanced approaches for cracking to versatile loading and boundary conditions or multiple-crack problems. On the other hand, the simulation of large-scale problems has not been equally benefited from the

acquired knowledge in the field of computational failure mechanics. At this geometrical scale, high computational efficiency is usually preferred to accuracy, and consequently sophisticated models are not applied due to their excessive computational cost. Therefore, the analysis of a large structure usually resorts to simplified methods, such macro-element approaches, by adopting important assumptions concerning the geometrical and material representation. Another famous choice are macro-mechanical FE models using classical smeared crack approaches. Even though these models can account for a detailed modelling of the structural geometry, they often result in a mesh-dependent numerical solution and a non-realistic crack representation.

By virtue of the above, the aim of this thesis is to propose a computational tool that allows the realistic crack representation in the non-linear analysis of masonry structures. Computational efficiency has been set as a key feature, such that the analysis of large-scale masonry structures can be feasible for both research and engineering practice purposes. Following the state-of-the-art presented in Chapter 2, the enhancement of the classical smeared crack approach with a tracking algorithm has been recognized as an appropriate methodology for the accomplishment of the above aim.

The constitutive model used for the representation of masonry is presented in Chapter 3. It is a Continuum Damage Mechanics (CDM) model with two damage indices for the distinct representation of compressive and tensile damage, i.e. crushing and cracking respectively. Particular focus is given to the simulation of the effect of irreversible strains, which are important for the modelling of cyclic actions. For this reason, an existing CDM formulation is revisited. Considering its advantages, and aiming to overcome its limitations, a new formulation is proposed. Additionally, novel expressions are developed for the discrete softening parameters, which are responsible for the regularization of the softening response according to the fracture energy, following the principles of the crack-band approach. In this way, mesh-size objectivity is ensured at constitutive level. In the same chapter, the model is applied to the simulation of cyclic tests on concrete and masonry specimens. This application shows that the presented model can capture with sufficient accuracy the stress-strain response and the level of irreversible strains at the end of each load cycle under softening. The strain-driven format and the explicit computation of all the internal variables of the model ensure high algorithmic efficiency, which is one of the desirable features in large-scale computations.

Chapter 4 describes two novel tracking algorithms for the simulation of localized cracking under monotonic and cyclic loading, referred as *fixed* and *multi-directional* tracking algorithm, respectively. These algorithms aim to enhance the directional mesh-bias independency of the numerical solution and to allow the realistic representation of cracking. This work proposes several developments aiming to model complex cracking phenomena that may occur under versatile loading conditions in masonry structures. First, a new approach is developed that makes possible the simulation of both boundary and internal cracking, propagating towards one or two directions respectively. This approach allows

the simulation of arbitrary cracking, starting from any location of the structure. Following that, it is shown that the smeared crack basis of the algorithm is a key feature towards the simulation of crack intersection without the use of any special finite element, as in X-FEM or E-FEM. Finally, the challenges in modelling of cyclic loads with a tracking algorithm are discussed and a novel approach is proposed to define the crack initiation. According to this, a categorization of cracks in active and inactive is devised as a method to allow crack initiation close to existing ones.

The proposed macro-mechanical approach, developed in Chapters 3 and 4, is applied to the simulation of several structural problems in Chapter 5. The selected case studies cover different structural scales, number of cracks and loading conditions. The first case study concerns an experiment on small-scale specimens, and in particular the Brazilian splitting test. Following that, two experimental cases from the literature on masonry structural elements are analysed. The first refers to a masonry frame with one door opening, tested under in-plane monotonic loading. The second is a shear wall, which was tested under cyclic in-plane horizontal loading. Finally, the analysis of a real-scale masonry façade from an existing building is considered under monotonic in-plane horizontal loading. This latter case study has been extensively analysed in the literature with various simplified and advanced numerical approaches. In all the examples, the algorithm can reproduce accurately and efficiently the collapse mechanism, either experimentally obtained or analytically predicted. The proposed numerical method shows robustness and the post-peak behaviour can be followed up to the end of the analysis without serious numerical problems. The use of different meshes in size and orientation demonstrates that the proposed approach improves significantly the mesh-objectivity of the classical smeared crack approach. An important characteristic is the effectiveness in representing the collapse mechanisms, despite being a macro-mechanical approach. Indeed, the definition of the minimum distance between new and existing cracks according to the unit size seems to help in capturing the collapse mechanism and aids the correct interpretation of local collapse mechanisms within the structure. The effect of the numerical parameters used in the definition of the numerical model is also assessed.

Simulation of crack propagation in cohesive-frictional materials, its implications and proposed measures are described in Chapter 6. A new crack propagation criterion is presented, which identifies and distinguishes crack propagation under tension and shear stress-states. For tensile failure the maximum principal stress (MPS) criterion is adopted, whereas for shear failure the crack propagation direction is defined according to the Mohr-Coulomb (MC) theory of rupture. Adopting this assumption, the material's friction angle can have an influence in the crack propagation under shear failure. The prediction of two potential failure planes by the MC theory of rupture points to a particular challenge for tracking algorithms. This is the necessity for selecting the propagation direction among more than one possible failure planes. As discussed in Chapter 2, the possibility of more than one failure planes is common when a propagation criterion different from the MPS

is chosen. To address this issue, a novel procedure is proposed based on the maximization of the released energy. According to this, the energy density of both potential crack planes is computed, and the one with the maximum is chosen for the definition of the crack propagation. The tracking algorithm with the above propagation criterion is applied to the simulation of the Nooru-Mohamed mixed-mode tests on concrete specimens. For comparison purposes, analyses are also carried-out with the previously presented tracking algorithms, which are based exclusively on the MPS criterion. The obtained results indicate that the proposed procedure for the crack propagation can correctly select the direction that maximizes the energy release. The separation between tensile and shear failure aids the evaluation of the stress-state driving cracking under the imposed mixed-mode loading. Additionally, the algorithm shows the required sensitivity to changes in the material frictional characteristics. Nevertheless, the numerical results imply that, under the studied loading conditions, cracking is driven by the maximum principal stress, as the MC theory has given less curved cracking patterns than the experimental ones. Finally, the model has demonstrated a mesh-size objectivity even for curved crack patterns.

7.2 Conclusions

The conclusions of this work can be summarized in the following:

Constitutive Model

- The use of a continuum damage model with two damage indices captures the distinct characteristics of masonry under tensile and compressive loading and simulates crack-opening/closing phenomena with stiffness recovery. The differentiation between tensile and compressive damage enhances the interpretation of the accumulated cracking and crushing of the material during the loading history.

- The developed formulation of the irreversible strains in a continuum damage mechanics (CDM) format allows its straightforward implementation in existing CDM models. The proposed closed-form expression for the computation of the irreversible strains blends well with the explicit format of the constitutive model. Its application to various case studies on concrete and masonry specimens, in addition to a masonry shear wall, has given promising results that can be further exploited in the future.

- The regularization of the dissipated energy at element level through the proper definition of two novel discrete softening parameters guarantees the mesh-size objectivity of the proposed numerical method.

- The constitutive model shows robustness for all the analysed case studies without producing significant convergence problems.

- The strain-driven format of the model leads to a simple and explicit formulation with high algorithmic efficiency, tailored to the analysis of non-linear large-scale problems.

Tracking Algorithm

- The enhancement of the classical smeared crack approach with a tracking algorithm results in the realistic and accurate representation of cracking in quasi-brittle materials and especially in masonry structures. The simulation of localized damage enhances the interpretation of the obtained local and global collapse mechanism compared to existing numerical approaches at macro-mechanical level.

- The original developments proposed in the context of the fixed tracking algorithm make possible the simulation of multiple tensile, flexural and shear cracking under monotonic loading. This capacity has been exhibited through the simulation of novel and real-life case studies that have not been possible to simulate up to date by numerical approaches based on tracking algorithms.

- Two novel developments presented within the context of the multi-directional tracking algorithm allow the simulation of quasi-static cyclic loading. The first concerns the modelling of crack intersection, and the second the proposal of a criterion for identifying opened and closed cracks during the analysis. The latter permits new cracks to initiate without any restriction next to closed ones.

- The computational overhead of the tracking algorithm is relatively small for practical applications. The additional memory requirements compared to the classical SCA lie between 15% and 20%. The estimation of the time cost is more difficult owning to the fact that the solutions obtained with and without the tracking algorithm are different. As an average, the tracking algorithm leads to a time overhead of around 15%. Nevertheless, in many cases, and particularly when multiple cracking is involved, the time-gain due to the improvement of the convergence rate using the tracking algorithm balances the time consumed by the tracking subroutines within the FE formulation. As a result, there have been cases in which the analysis time with the tracking algorithm has been lower than without it.

- The tracking algorithm greatly enhances the directional mesh-bias objectivity of the numerical results. This has been corroborated using meshes of different typologies (structured-unstructured) and sizes in the various analysed loading scenarios. Additionally, the localization of damage into a singe row of finite elements blends well with the crack-band approach, adopted by local smeared crack approaches.

- The proposed tracking algorithm can be easily extended to account for different crack propagation criteria or combinations of them. The use of a crack propagation

criterion different from the MPS implies the potential of more than one crack directions. The proposed crack-path selection procedure based on the energy density fields ahead of the crack is successful in selecting the crack-path that maximizes the released energy, minimizing the internal strain energy of the structure.

- The use of a MPS crack propagation criterion results in a better representation of the experimental cracking on mixed-mode tests on concrete compared to the MC-based one. This has been further confirmed by the rest of the examples, where a good agreement with the experimental cracking pattern has been obtained with a MPS-based propagation. Nevertheless, the majority of the analysed cases have been under relatively low compressive loading compared to their compressive capacity. Therefore, more analyses should be carried-out before drawing conclusions regarding the applicability of the MPS criterion under mixed-mode loading cases.

- The proposed tracking algorithms show remarkable robustness. Post-peak behaviour has been captured in all the analyses.

Structural Applications

- The proposed numerical model can predict correctly the sequence of the formation and propagation of tensile, flexural and shear cracks within the structure. This feature is manifested in the simulation of the masonry frame tested by Augenti et al. [18], where the sequence of crack initiation and propagation are predicted in a remarkable agreement with the experimental result. The realistic modelling of the cracking sequence is a valuable tool for identifying the correct collapse mechanism and the structural ductility.

- The numerical results on the analysed masonry structures demonstrate the capability of the proposed model to reproduce the loss of structural stiffness due to the occurring fracture phenomena throughout the loading history. This feature is essential for the evaluation of the seismic capacity of an existing structure, or the design of a new one, with non-linear procedures considered in modern Codes.

- The analysis of the shear wall tested by Anthoine [8] under cyclic loading shows that the methodology proposed for the separation of cracks into open and closed (or active and inactive respectively) aids the interpretation of the sequence of the damage phenomena and the evaluation of the energy dissipation throughout the loading cycles.

- The developed numerical model can simulate structural effects, such as the diaphragm rigidity in the analysis of the "Via-Martoglio" façade. The different assumptions regarding the stiffness of the floors have led to a realistic variation of the collapse mechanism and, consequently, of the load and displacement capacities.

- The simulation of damage as localized cracks in the proposed model is a powerful tool for the correct identification of local and global damage mechanisms. In particular, pier rocking, as well as flexural and shear failure of the spandrel, are correctly reproduced in the analysis of the masonry frame tested by Augenti et al. [18]. Diagonal shear failure is properly predicted in the shear wall tested by Anthoine [8]. All the above local mechanisms are also detected in the complex real case study of the "Via Martoglio" façade [55] leading to the evolution of the overturning of one of its corners or the shear collapse of the ground floor, considering flexible or stiff diaphragms respectively.

- The developed numerical model can accurately simulate the post-peak non-linear response of a structure, giving important information regarding its stability. This is demonstrated in the analysis of the "Via Martoglio" façade with the assumption of rigid diaphragms, where the successive failure of the shear walls at the base can be traced after the structure has overpassed its maximum load capacity.

7.3 Main contributions

This research provides the following original contributions:

- The development of local tracking algorithms oriented to the simulation of complex crack patterns. These include the modelling of:

  (i) Arbitrary cracking without a-priori definition of the crack locations;
  (ii) Boundary and internal crack with uni-directional and bi-directional crack propagation, respectively;
  (iii) Crack intersection;
  (iv) Crack-opening/closing and multi-directional cracking under cyclic loading.

  The above developments address several challenges involved in the crack simulation by tracking algorithms and amplify their application to the simulation of multiple crack problems with tensile, shear and flexural cracks under monotonic and cyclic loading.

- The development of a tracking algorithm that is capable of utilising different propagation criteria or a combination of them. The numerical and practical possibilities and implications of this choice have been demonstrated and evaluated. In this context, a novel procedure has been proposed for the selection among more than one potential failure planes based on the maximization of the released energy.

- The proposal and implementation of a novel formulation for the simulation of the irreversible strains within the context of a two-parameters continuum damage model.

The methodology is characterized by a strain-driven formulation, and the irreversible strains are implemented as an internal variable allowing their explicit computation. Comparison with experimental results on concrete and masonry under tensile and compressive loading illustrates that, despite its simplicity, the model can represent experimentally obtained stress-strain curves and irreversible strain levels in the post-peak response.

- The definition of two novel expressions for the discrete softening parameters in the constitutive model. The new expressions ensure the mesh-size objectivity of the constitutive model under monotonic and cyclic load cases.

- The investigation of the failure pattern of three common mixed mode tests on concrete. The comparison of the crack propagation criteria has shown that for the particular experiments, the crack propagation is driven by the maximum principal stress.

- The development of a novel numerical tool that allows the realistic simulation of cracking in masonry structures and the assessment of local and global collapse mechanisms and post-peak behaviour in an efficient way.

- The application of the developed tool to real-scale case studies for the assessment of their structural behaviour. In this context, the proposed methodology has been validated and compared to available experimental results and well-established numerical tools oriented to the analysis of masonry structures.

7.4 Suggestions for future work

Finally, this thesis closes with the following suggestions for future work:

- The further improvement of the mesh-size objectivity. As demonstrated throughout the thesis, the proposed methodology improves significantly the mesh-size independency of the numerical solution. Nevertheless, some minor variations of the load-capacity in the case of the Brazilian splitting test have been observed, despite the fact that in all the cases a straight crack path has been obtained using the tracking algorithm. As discussed in Section 5.2.3, a more accurate result would be possible using an adaptive characteristic length, considering the number of elements orthogonal to the crack direction. Such approaches already exist in the literature (e.g. [56,251,358]) and their application to this algorithm would further enhance its mesh-size objectivity.

- The investigation on the possibilities for simulating crack branching. The problem of crack-branching is not addressed in the present work. The reason for this is

the lack of reliable criteria for predicting the moment that a crack should branch. Notwithstanding, the procedure developed for defining the crack initiation in the multi-directional tracking algorithm (Section 4.2.8) can be used in a similar way to Song and Belytschko [362] for allowing new crack branches from existing cracks. According to this, new cracks can initiate next to existing ones when their propagation direction differs more than a predefined angle from the direction of existing cracks in a defined neighbourhood.

- Extension of the model to dynamic cases. It is certainly of interest to investigate whether the multi-directional tracking algorithm can simulate properly the crack-opening/closing effects considering the inertial effects of a dynamic analysis.

- The increase in the level of detail in the material representation (I). The formulation of the tracking algorithm allows its combination with different constitutive models. One possibility is to extend the presented model using the *mapped stress tensor* concept, introduced by Betten [40, 41] and refined by Oller [268–270], in a similar way that was applied by Pelà et al. [292, 294–296], so that the elastic and inelastic directional properties of masonry are considered in the analysis. Another possibility is to substitute the constitutive model with one from the available literature accounting for the anisotropic behaviour of masonry (e.g. [207]). It is noted, however, that anisotropic models need expensive experimental tests on masonry assemblages in order to obtain the orthotropic linear and non-linear material parameters.

- The increase in the level of detail in the material representation (II). Another interesting approach for a more detailed material representation, would be the combination of the tracking algorithm with homogenization procedures (e.g. [200, 300, 409]). This methodology would permit to account the elastic and inelastic behaviour of a wide variety of masonry typologies, without the requirement of detailed experimental tests, which are necessary for the definition of anisotropic material models.

- The extension of the developed numerical strategy to 3D problems. As presented in Section 2.4.1, there have been reported in the literature several successful implementations of local tracking algorithms in 3D. Nevertheless, it is acknowledged that the implementation procedure is not easy and the modelling of non-planar cracks can be cumbersome. On the contrary, the tensorial formulation of the constitutive model renders it readily applicable to 3D structural problems.

- The implementation of the tracking algorithm into thick shell elements. Analysis of 3D masonry walls accounting for the proper modelling of the transverse shear has given accurate results for some masonry typologies (e.g. [203, 301]). The implementation of the proposed algorithm into shell elements is considered as a more straightforward choice compared to 3D solid elements, since the tracking of the

crack-path could be done in two-dimensions instead of three. Of course, this happens under the assumption that cracks remain planar through the thickness of a masonry wall.

- The further validation of the crack-propagation direction for different masonry typologies and consideration of different crack-propagation criteria. For many masonry typologies with low strength mortar (e.g. hydraulic mortar in historical structures) the crack-direction is physically biased by the staggering pattern. In these cases, the association of the crack propagation direction with the staggering can have a positive influence in the more accurate representation of damage pattern and collapse mechanisms.

- The application of the crack-propagation selection criterion developed in Chapter 6 to multiple-crack problems. In this thesis, the studied examples are characterized by two dominating cracks. Further investigation should be pursued regarding its applicability to multiple-crack cases with crack interaction.

- The further validation of the proposed formulation for the simulation of irreversible strains. A necessary step towards this direction is the comparison with experimental results on masonry under tensile, shear and compressive cyclic loading. Up to date, this has been hampered by the limited well-documented cyclic experiments available in the literature and the common high dispersion that masonry experiments present.

- The application of the developed numerical method to the simulation of other types of cracking materials. For instance, structures made of adobe or timber commonly present collapse mechanisms characterized by localized cracks, making the present methodology as a possible tool for their structural assessment.

Appendices

Appendix A

Discrete softening parameter

In this Appendix the procedure for the derivation of the expressions for the discrete softening parameters is presented.

As presented in Section 3.6 the rate of the mechanical dissipation γ of the continuum damage model presented is

$$\dot{\gamma} = -\frac{\partial \psi}{\partial \boldsymbol{\varepsilon}^i} : \dot{\boldsymbol{\varepsilon}}^i - \frac{\partial \psi}{\partial d^+}\dot{d}^+ - \frac{\partial \psi}{\partial d^-}\dot{d}^- = \dot{\gamma}^i + \dot{\gamma}^d \geq 0 \tag{A.1}$$

where ψ is the Helmholtz free energy and $\psi_0^{\pm}$ elastic free energies presented in Eqs. (3.43), (3.44), (3.45) and repeated here for convenience

$$\psi = (1 - d^+)\,\psi_0^+ + (1 - d^-)\,\psi_0^- \tag{A.2}$$

$$\psi_0^+ = \frac{1}{2}\,\bar{\boldsymbol{\sigma}}^+ : \boldsymbol{C}_{\mathbf{0}}^{-1} : \bar{\boldsymbol{\sigma}} \tag{A.3}$$

$$\psi_0^- = \frac{1}{2}\,\bar{\boldsymbol{\sigma}}^- : \boldsymbol{C}_{\mathbf{0}}^{-1} : \bar{\boldsymbol{\sigma}} \tag{A.4}$$

From Eq. (A.1), the evolutions of both damage $\dot{\gamma}^d$ and irreversible strains $\dot{\gamma}^i$ dissipated energies contribute to the total dissipated energy of the solid, with each part being

$$\dot{\gamma}^i = -\frac{\partial \psi}{\partial \boldsymbol{\varepsilon}^i} : \dot{\boldsymbol{\varepsilon}}^i \geq 0 \tag{A.5}$$

$$\dot{\gamma}^d = \psi_0^+\,\dot{d}^+ + \psi_0^-\,\dot{d}^- \geq 0 \tag{A.6}$$

Having defined the above, the total dissipated energy per unit volume g_f is obtained as the sum of the dissipated energy due to evolution of the damage and the irreversible strains

$$g_f = \int_0^t \dot{\gamma}^i\,dt + \int_0^t \dot{\gamma}^d\,dt \tag{A.7}$$

The discrete softening parameter can be defined similarly to [69] considering an ideal uniaxial compressive test, with a monotonic increment of the compressive strain (denoted hereafter as ε^e) from an initial unstressed state to full degradation. The stress-strain curve is obtained considering the generalised case with parabolic hardening for $r_0 \leq r \leq r_p$ and exponential softening for $r > r_p$. In the following, we drop the superindex $(-)$ for simplicity. During the loading, and considering Eqs. (3.11) and (3.15) the stress threshold will be

$$r = E\,\varepsilon^e \tag{A.8}$$

The dissipation due to damage evolution is computed considering Eqs. (A.6) and (A.8) and $\dot{d} = d'\,\dot{r}$ as

$$\gamma^d = \int_0^\infty \dot{\gamma}^d\,dt \tag{A.9a}$$

$$= \int_0^t \psi_0\,\dot{d}\,dt \tag{A.9b}$$

$$= \int_0^t \frac{1}{2}\,\sigma\,\varepsilon\,\dot{d}\,dt \tag{A.9c}$$

$$= \frac{1}{2E}\int_{r_0}^\infty r^2\,d'\,dr \tag{A.9d}$$

$$= \frac{1}{2E}\left[\int_{r0}^{r_p} r^2\,d'\,dr + \int_{r_p}^\infty r^2\,d'\,dr\right] \tag{A.9e}$$

$$= \frac{1}{2E}\left[\frac{A_d\,r_e\,(r_p^3 - 3\,r_p\,r_0^2 + 2\,r_0^3)}{3\,(r_p - r_0)^2} + \frac{r_e^2}{H_d} + r_p\,r_e\right] \tag{A.9f}$$

The contribution of the irreversible strains to the total dissipated energy can be computed considering

$$\dot{\varepsilon}^i = \beta\,\frac{E\dot{\varepsilon}}{E\,\varepsilon^e}\varepsilon^e \tag{A.10a}$$

$$= \beta\,\dot{\varepsilon} \tag{A.10b}$$

$$= \frac{\beta}{1-\beta}\dot{\varepsilon}^e \tag{A.10c}$$

and

$$-\frac{\partial\psi}{\partial\varepsilon^i} = (1-d)\,r \tag{A.11}$$

where Eqs. (3.56), (A.2), (A.4) and (A.8) have been used.

Substituting Eqs. (A.10c) and (A.11) into (A.5) and considering the evolution laws of

the damage index presented in Eqs. (3.33) and (3.33) gives

$$\gamma^i = \int_0^\infty -\frac{\partial \psi}{\partial \boldsymbol{\varepsilon}^i} : \dot{\boldsymbol{\varepsilon}}^i \tag{A.12a}$$

$$= \int_0^t (1-d)\, r\, \frac{\beta}{(1-\beta)}\, \dot{\varepsilon}^e dt \tag{A.12b}$$

$$= \frac{\beta}{E\,(1-\beta)} \int_{r0}^{r} (1-d)\, r\, dr \tag{A.12c}$$

$$= \frac{\beta}{E\,(1-\beta)} \left[\int_{r_0}^{r_p} (1-d)\, r\, dr + \int_{r_p}^{r} (1-d)\, r\, dr \right] \tag{A.12d}$$

$$= \frac{\beta}{2\,E\,(1-\beta)} \left[\frac{(r_p - r_0)(3\,r_p - 2\,A_d\,r_e + 3\,r_0)}{3} + \frac{r_e^2}{H_d} \right] \tag{A.12e}$$

According to the crack-band theory [28, 251], the specific dissipation energy γ should be scaled according to the characteristic length of each finite element l_dis such as that

$$\gamma = \frac{G_f}{l_{dis}} \tag{A.13}$$

where G_f is the measured fracture energy. Substituting Eqs. (A.9f) and (A.12e) into Eq. (A.13) we can derive the discrete softening modulus as

$$\frac{1}{H_d} = (1-\beta) \left(\frac{l_{mat}}{l_{dis}} - \tilde{A}_d - \frac{r_p}{r_e} - \frac{\beta}{1-\beta}\, B_d \right) \tag{A.14a}$$

where

$$\tilde{A}_d = \frac{A_d\,(r_p^3 - 3\,r_p\,r_0^2 + 2\,r_0^3)}{3\,r_e (r_p - r_0)^2} \tag{A.15}$$

$$B_d = \frac{(r_p - r_0)(3\,r_p - 2\,A_d\,r_e + 3\,r_0)}{3\,r_e^2} \tag{A.16}$$

Note that for $r_0 = r_e = r_p$, exponential softening starts immediately after reaching the peak strength and the discrete softening modulus becomes

$$\frac{1}{H_d} = (1-\beta)\, \frac{l_{mat} - l_{dis}}{l_{dis}}. \tag{A.17}$$

If the effect of the irreversible deformations is neglected (i.e. $\beta = 0$), the discrete softening modulus for parabolic hardening and exponential softening is

$$\frac{1}{H_d} = \left(\frac{l_{mat}}{l_{dis}} - \tilde{A}_d - \frac{r_p}{r_e} - \frac{\beta}{1-\beta}\, B_d \right) \tag{A.18}$$

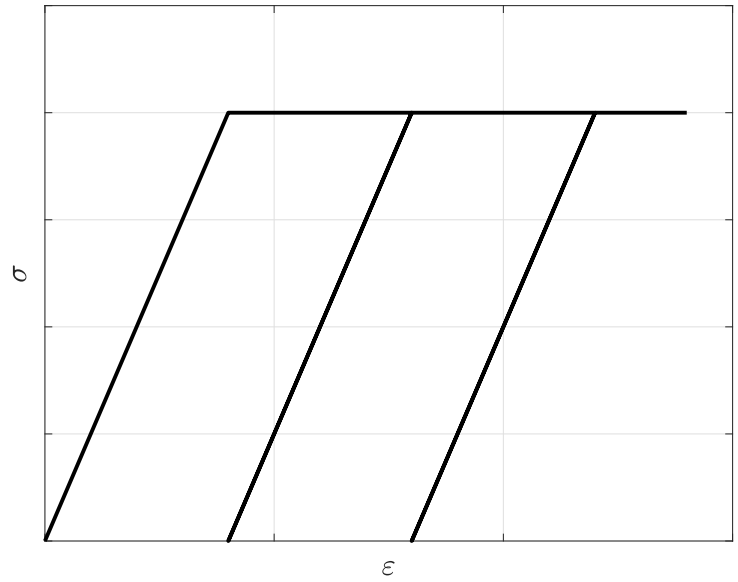

Figure A.1 Example of a perfectly plastic behaviour recovered for $\beta = 1.0$.

and for exponential softening

$$\frac{1}{H_d} = \frac{l_{mat} - l_{dis}}{l_{dis}} \tag{A.19}$$

which are known results for an elastic-damage model [66].

Note that for the limit case of $\beta = 1$, Eq. (A.10b) limits to $\dot{\varepsilon}^i = \dot{\varepsilon}$ and consequently $\dot{\varepsilon}^e = 0$. This results in $\Delta r = 0$, which means that there is no damage evolution and hence no softening. In that case, energy is dissipated only due to the evolution of the irreversible strains, which using Eqs. (A.5), (A.8), (A.11) will be

$$\gamma^i = E\,\varepsilon_0^e \int_0^t \dot{\varepsilon}\,dt \tag{A.20a}$$

$$= E\,\varepsilon_0^e \int_{\varepsilon_0}^e d\varepsilon \tag{A.20b}$$

$$= E\,\varepsilon_0^e\,[\varepsilon - \varepsilon_0^e] \tag{A.20c}$$

with ε_0^e being the elastic strain at the peak strength. According to the above, the dissipation will keep increasing linearly with the increase of the strains, resembling the behaviour of a perfectly plastic material as shown in Fig. A.1.

Bibliography

[1] Abdelaziz, Y., and Hamouine, A. A survey of the extended finite element. *Computers and Structures 86*, 11-12 (2008), 1141–1151.

[2] Addessi, D., Liberatore, D., and Masiani, R. Force-Based Beam Finite Element (FE) for the Pushover Analysis of Masonry Buildings. *International Journal of Architectural Heritage 9*, 3 (2015), 231–243.

[3] Addessi, D., Marfia, S., Sacco, E., and Toti, J. Modeling Approaches for Masonry Structures. *The Open Civil Engineering Journal*, 2 (2014), 288–300.

[4] Addessi, D., and Sacco, E. A multi-scale enriched model for the analysis of masonry panels. *International Journal of Solids and Structures 49*, 6 (2012), 865–880.

[5] Addessi, D., Sacco, E., and Paolone, A. Cosserat model for periodic masonry deduced by nonlinear homogenization. *European Journal of Mechanics, A/Solids 29*, 4 (2010), 724–737.

[6] Alfaiate, J., Wells, G. N., and Sluys, L. J. On the use of embedded discontinuity elements with crack path continuity for mode-I and mixed-mode fracture. *Engineering Fracture Mechanics 69*, 6 (2002), 661–686.

[7] Ambati, M., Gerasimov, T., and De Lorenzis, L. A review on phase-field models of brittle fracture and a new fast hybrid formulation. *Computational Mechanics 55*, 2 (2014), 383–405.

[8] Anthoine, A., Magenes, G., and Magonette, G. Shear compression tensting and analysis of brick masonry walls. In *10th European Conference on Earthquake Engineering* (Vienna, 1994), pp. 1657–1662.

[9] Areias, P. M. A., and Belytschko, T. Analysis of three-dimensional crack initiation and propagation using the extended finite element method. *International Journal for Numerical Methods in Engineering 63*, 5 (2005), 760–788.

[10] Armero, F., and Garikipati, K. An analysis of strong discontinuities in multiplicative finite strain plasticity and their relation with the numerical simulation of strain localization in solids. *International Journal of Solids and Structures 33*, 20-22 (1996), 2863–2885.

[11] Armero, F., and Kim, J. Three-dimensional finite elements with embedded strong discontinuities to model material failure in the infinitesimal range. *International Journal for Numerical Methods in Engineering 91*, 12 (2012), 1291–1330.

[12] Armero, F., and Linder, C. Numerical simulation of dynamic fracture using finite elements with embedded discontinuities. *International Journal of Fracture 160*, 2 (2009), 119–141.

[13] Armero, F., and Oller, S. A general framework for continuum damage models. I. Infinitesimal plastic damage models in stress space. *International Journal of Solids and Structures 37* (2000), 7409–7436.

[14] Arrigoni, R., Nascè, V., Pistone, G., and Strona, P. Numerical Models for the Original Structure of the "Mole Antonelliana". In *1st International Conference on Structural Repairs and Maintanance of Historical Buildings* (Florence, Italy, 1989), C. Brebbia, Ed., Computational Mechanics Publications, UK, pp. 245–254.

[15] ASTM:C496/C496M. Standard Test Method for Splitting Tensile Strength of Cylindrical Concrete Specimens. *ASTM International*, 336 (2011), 1–5.

[16] ASTM:D3967-08. Standard Test Method for Splitting Tensile Strength of Intact Rock Core Specimens. *ASTM International* (2008).

[17] Augenti, N. *Il calcolo sismico degli edifici in muratura*. UTET Libreria, Turin.

[18] Augenti, N., Parisi, F., Prota, A., and Manfredi, G. In-Plane Lateral Response of a Full-Scale Masonry Subassemblage with and without an Inorganic Matrix-Grid Strengthening System. *Journal of Composites for Construction 15*, 4 (2011), 578–590.

[19] Babuška, I., and Melenk, J. M. The partition of unity method. *International Journal for Numerical Methods in Engineering 40*, 4 (1997), 727–758.

[20] Bacigalupo, A., and Gambarotta, L. Computational two-scale homogenization of periodic masonry: Characteristic lengths and dispersive waves. *Computer Methods in Applied Mechanics and Engineering 213-216* (2012), 16–28.

[21] Barbosa, C. S., Lourenço, P. B., and Hanai, J. B. On the compressive strength prediction for concrete masonry prisms. *Materials and Structures 43*, 3 (2009), 331–344.

[22] Barenblatt, G. I. The Mathematical Theory of Equilibrium of Crack in Brittle Fracture. *Adv. Appl. Mech. 7* (1962), 55–129.

[23] Barsoum, R. S. On the use of isoparametric finite elements in linear fracture mechanics. *International Journal for Numerical Methods in Engineering 10*, 1 (jan 1976), 25–37.

[24] Barsoum, R. S. Triangular quarter-point elements as elastic and perfectly-plastic crack tip elements. *International Journal for Numerical Methods in Engineering 11*, 1 (1977), 85–98.

[25] Barthel, R. Analysis and Structural Behaviour of Masonry Cross Vaults. In *1st International Conference on Structural Repairs and Maintanance of Historical Buildings* (Florence, Italy, 1989), C. Brebbia, Ed., Computational Mechanics Publications, UK, pp. 119–128.

[26] Bažant, Z. P., and Jirásek, M. Nonlocal Integral Formulations of Plasticity and Damage: Survey of Progress. *Journal of Engineering Mechanics 128*, 11 (2002), 1119–1149.

[27] Bažant, Z. P., and Lin, F. B. Nonlocal Smeared Cracking Model for Concrete Fracture. *Journal of Structural Engineering 114*, 11 (1988), 2493–2510.

[28] Bažant, Z. P., and Oh, B. Crack band theory for fracture of concrete. *Materials and Structures 16* (1983), 155–177.

[29] Beese, S., Loehnert, S., and Wriggers, P. Modeling of Fracture in Polycrystalline Materials. In *Advances in Discretization Methods*. Springer, Cham, 2016, pp. 79–102.

[30] Belytschko, T., and Black, T. Elastic crack growth in finite elements with minimal remeshing. *International Journal for Numerical Methods in Engineering 45*, 5 (1999), 601–620.

[31] Belytschko, T., Chen, H., Xu, J., and Zi, G. Dynamic crack propagation based on loss of hyperbolicity and a new discontinuous enrichment. *International Journal for Numerical Methods in Engineering 58*, 12 (2003), 1873–1905.

[32] Belytschko, T., Fish, J., and Engelmann, B. E. A finite element with embedded localization zones. *Computer Methods in Applied Mechanics and Engineering 70*, 1 (1988), 59–89.

[33] Belytschko, T., Gracie, R., and Ventura, G. A review of extended/generalized finite element methods for material modeling. *Modelling and Simulation in Materials Science and Engineering 17* (2009), 043001.

[34] Belytschko, T., Moës, N., Usui, S., and Parimi, C. Arbitrary discontinuities in finite elements. *International Journal for Numerical Methods in Engineering 50*, 4 (2001), 993–1013.

[35] Benedetti, L. *Mixed finite element formulations for strain localization and failure in plasticity.* PhD thesis, Universitat Politècnica de Catalunya (BarcelonaTech-UPC), 2017.

[36] Benedetti, L., Cervera, M., and Chiumenti, M. Stress-accurate Mixed FEM for soil failure under shallow foundations involving strain localization in plasticity. *Computers and Geotechnics 64* (mar 2015), 32–47.

[37] Benedetti, L., Cervera, M., and Chiumenti, M. High-fidelity prediction of crack formation in 2D and 3D pullout tests. *Computers & Structures 172* (2016), 93–109.

[38] Berto, L., Saetta, A., Scotta, R., and Vitaliani, R. An orthotropic damage model for masonry structures. *International Journal for Numerical Methods in Engineering 55*, 2 (2002), 127–157.

[39] Berto, L., Saetta, A., Scotta, R., Vitaliani, R. Failure mechanism of masonry prism loaded in axial compression: computational aspects. *Materials and Structures 38*, 276 (2005), 249–256.

[40] Betten, J. Creep Theory of Anisotropic Solids. *Journal of Rheology 25*, 6 (1981), 565.

[41] Betten, J. Applications of tensor functions to the formulation of yield criteria for anisotropic materials. *International Journal of Plasticity 4*, 1 (1988), 29–46.

[42] Betti, M., and Vignoli, A. Numerical assessment of the static and seismic behaviour of the basilica of Santa Maria all'Impruneta (Italy). *Construction and Building Materials 25*, 12 (2011), 4308–4324.

[43] Beyer, K., and Dazio, A. Quasi-Static Cyclic Tests on Masonry Spandrels. *Earthquake Spectra 28*, 3 (aug 2012), 907–929.

[44] Binda, L., Mirabella Roberti, G., Tiraboschi, C., and Abbaneo, S. Measuring Masonry Material Properties. *U.S.-Italy Workshop on Guidelines for Seismic Evaluation and Rehabilitation of Unreinforced Masonry Buildings* (1994), 326–347.

[45] Blasi, C., and Sorace, S. Special Finite Element Approaches to the Study of Masonry Domes. Comparative Numerical Analyses and Experimental Researches. In *1st International Conference on Structural Repairs and Maintanance of Historical Buildings* (Florence, Italy, 1989), C. Brebbia, Ed., Computational Mechanics Publications, UK, pp. 603–611.

[46] Block, P., Ciblac, T., and Ochsendorf, J. Real-time limit analysis of vaulted masonry buildings. *Computers & Structures 84*, 29-30 (2006), 1841–1852.

[47] Bobiński, J., and Tejchman, J. Comparison of continuous and discontinuous constitutive models to simulate concrete behaviour under mixed-mode failure conditions. *International Journal for Numerical and Analytical Methods in Geomechanics 40*, 3 (2016), 406–435.

[48] Bocca, P., Carpinteri, A., and Valente, S. Mixed mode fracture of concrete. *International Journal of solids and structures 27*, 9 (1991), 1139–1153.

[49] Bordas, S., and Moran, B. Enriched finite elements and level sets for damage tolerance assessment of complex structures. *Engineering Fracture Mechanics 73*, 9 (2006), 1176–1201.

[50] Bouchard, P., Bay, F., and Chastel, Y. Numerical modelling of crack propagation: automatic remeshing and comparison of different criteria. *Computer Methods in Applied Mechanics and Engineering 192*, 35-36 (2003), 3887–3908.

[51] Bourdin, B., Francfort, G. A., and Marigo, J. J. Numerical experiments in revisited brittle fracture. *Journal of the Mechanics and Physics of Solids 48*, 4 (2000), 797–826.

[52] Bourdin, B., Francfort, G. A., and Marigo, J. J. *The variational approach to fracture*. No. April. Springer, 2008.

[53] Brasile, S., Casciaro, R., and Formica, G. Multilevel approach for brick masonry walls - Part II: On the use of equivalent continua. *Computer Methods in Applied Mechanics and Engineering 196*, 49-52 (2007), 4801–4810.

[54] Brasile, S., Casciaro, R., and Formica, G. Finite Element formulation for nonlinear analysis of masonry walls. *Computers and Structures 88*, 3-4 (2010), 135–143.

[55] Brencich, A., Gambarotta, L., and Lagomarsino, S. Catania Project: Research on the seismic response of two masonry buildings. Chapter 6: Analysis of a masonry building in Via Martoglio. *CNR Gruppo Nazionale per la Difesa dei Terremoti* (2000), 107–143.

[56] Burnett, D. J. *A Mesh Objective Algorithm for Modeling Mode-I Cracks Using a Standard Finite Element Formulation*. Phd thesis, University of New Mexico, 2015.

[57] Byskov, E. The calculation of stress intensity factors using the finite element method with cracked elements. *International Journal of Fracture Mechanics 6*, 2 (1970), 159–167.

[58] Calderini, C., and Lagomarsino, S. A micromechanical inelastic model for historical masonry. *Journal of Earthquake Engineering 10*, 4 (2006), 453–479.

[59] Calvi, G., and Magenes, G. Experimental research on Response of URM Building systems. In *US-Italian Workshop on Guidelines for Seismic Evaluation and Rehabilitation of Unreinforced Masonry Buildings* (NCEER-SUNY Buffalo, 1994), Technical Report NCEER-94-0021.

[60] Carvalho, J., Ortega, J., Lourenço, P. B., Ramos, L. F., and Roman, H. Safety analysis of modern heritage masonry buildings: Box-buildings in Recife, Brazil. *Engineering Structures 80* (2014), 222–240.

[61] Casati Calzada, M. J., and Gálvez Ruiz, J. C. The influence of the masonry mechanical properties in the structural behaviour of the Leon's cathedral. *Materiales de Construcción 59*, 294 (2009), 75–96.

[62] Casolo, S., and Peña, F. Rigid element model for in-plane dynamics of masonry walls considering hysteretic behaviour and damage. *Earthquake Engineering and Structural Dynamics 36*, 8 (2007), 1029–1048.

[63] Casolo, S., and Sanjust, C. A. Seismic analysis and strengthening design of a masonry monument by a rigid body spring model: The Maniace Castle of Syracuse. *Engineering Structures 31*, 7 (2009), 1447–1459.

[64] Castellazzi, G., D'Altri, A. M., de Miranda, S., and Ubertini, F. An innovative numerical modeling strategy for the structural analysis of historical monumental buildings. *Engineering Structures 132* (2017), 229–248.

[65] Cendón, D. A., Gálvez, J. C., Elices, M., and Planas, J. Modelling the fracture of concrete under mixed loading. *International journal of fracture 103*, 3 (2000), 293–310.

[66] Cervera, M. *Viscoelasticity and Rate-dependent Continuum Damage Models, Monography N-79.* CIMNE, Barcelona, 2003.

[67] Cervera, M. A smeared-embedded mesh-corrected damage model for tensile cracking. *International Journal for Numerical Methods in Engineering 76*, July (2008), 1930–1954.

[68] Cervera, M. An orthotropic mesh corrected crack model. *Computer Methods in Applied Mechanics and Engineering 197*, 17-18 (2008), 1603–1619.

[69] Cervera, M., and Chiumenti, M. Mesh objective tensile cracking via a local continuum damage model and a crack tracking technique. *Computer Methods in Applied Mechanics and Engineering 196*, 1-3 (2006), 304–320.

[70] Cervera, M., and Chiumenti, M. Smeared crack approach: back to the original track. *International Journal for Numerical and Analytical Methods in Geomechanics 30*, 12 (2006), 1173–1199.

[71] Cervera, M., Chiumenti, M., and Agelet de Saracibar, C. Shear band localization via local J2 continuum damage mechanics. *Computer Methods in Applied Mechanics and Engineering 193*, 9-11 (2004), 849–880.

[72] Cervera, M., Chiumenti, M., Benedetti, L., and Codina, R. Mixed stabilized finite element methods in nonlinear solid mechanics. Part III: Compressible and incompressible plasticity. *Computer Methods in Applied Mechanics and Engineering 285* (2015), 752–775.

[73] Cervera, M., Chiumenti, M., and Codina, R. Mixed stabilized finite element methods in nonlinear solid mechanics. Part I: Formulation. *Computer Methods in Applied Mechanics and Engineering 199*, 37-40 (2010), 2559–2570.

[74] Cervera, M., Chiumenti, M., and Codina, R. Mixed stabilized finite element methods in nonlinear solid mechanics. Part II: Strain localization. *Computer Methods in Applied Mechanics and Engineering 199*, 37-40 (2010), 2571–2589.

[75] Cervera, M., Chiumenti, M., and Di Capua, D. Benchmarking on bifurcation and localization in J2 plasticity for plane stress and plane strain conditions. *Computer Methods in Applied Mechanics and Engineering 241-244* (2012), 206–224.

[76] Cervera, M., Oliver, J., and Faria, R. Seismic evaluation of concrete dams via continuum damage models. *Earthquake Engineering & Structural Dynamics 24*, 9 (1995), 1225–1245.

[77] Cervera, M., Pelà, L., Clemente, R., and Roca, P. A crack-tracking technique for localized damage in quasi-brittle materials. *Engineering Fracture Mechanics 77*, 13 (2010), 2431–2450.

[78] Chaves, E. W. V. Tracking 3D Crack Path. In *International Conference on Mathematical and Statistical Modeling in Honor of Enrique Castillo.* (Ciudad Real, Spain, 2006).

[79] Chen, W.-F. *Plasticity in reinforced concrete.* McGraw-Hill, 1982.

[80] Chiostrini, S., Foraboschi, P., and Sorace, S. Problems Connected with the Arrangement of a Non-linear Finite Element Method to the Analysis of Masonry Structures. In *1st International Conference on Structural Repairs and Maintanance of Historical Buildings* (1989), C. Brebbia, Ed., Computational Mechanics Publications, UK, pp. 525–534.

[81] Chiostrini, S., and Vignoli, A. Application of a Numerical Method to the study of Masonry Panels with Various Geometry under Seismic Loads. In *1st International Conference on Structural Repairs and Maintanance of Historical Buildings* (1989), pp. 309–317.

[82] Chiumenti, M., Valverde, Q., Agelet de Saracibar, C., and Cervera, M. A stabilized formulation for incompressible elasticity using linear displacement and pressure interpolations. *Computer Methods in Applied Mechanics and Engineering 191*, 46 (nov 2002), 5253–5264.

[83] Chiumenti, M., Valverde, Q., Agelet de Saracibar, C., and Cervera, M. A stabilized formulation for incompressible plasticity using linear triangles and tetrahedra. *International Journal of Plasticity 20*, 8-9 (aug 2004), 1487–1504.

[84] Clemente, R. *Análysis estructural de edificios históricos mediante modelos localizados de fisuración*. PhD thesis, Universitat Politècnica de Catalunya (BarcelonaTech-UPC), 2006.

[85] Clemente, R., Cervera, M., and Roca, P. Localized damage model applied to the analysis of masonry structures. *Revista Internacional de Métodos Numéricos para Cálculo y Diseño en Ingeniería 24*, 1 (2008), 67–91.

[86] Clough, R. The stress distribution of Norfork Dam. *Structures and Materials Research 100*, 19 (1962), 1–108.

[87] Coker, E. The application of optical methods to technical problems of stress distribution. *Nature 90*, 2249 (1912), 383–386.

[88] Coker, E. G. The effects of holes and semicircular notches on the distribution of stress in tension members. In *Proc. Phys. Soc. Lond.* (1912), vol. 25, pp. 95–105.

[89] Colombo, D. An implicit geometrical approach to level sets update for 3D non planar X-FEM crack propagation. *Computer Methods in Applied Mechanics and Engineering 237-240* (2012), 39–50.

[90] Colombo, D., and Massin, P. Fast and robust level set update for 3D non-planar X-FEM crack propagation modelling. *Computer Methods in Applied Mechanics and Engineering 200*, 25-28 (2011), 2160–2180.

[91] Comi, C., Mariani, S., and Perego, U. An extended FE strategy for transition from continuum damage to mode I cohesive crack propagation. *International Journal for Numerical and Analytical Methods in Geomechanics 31*, 2 (2007), 213–238.

[92] Comi, C., and Perego, U. Fracture energy based bi-dissipative damage model for concrete. *International Journal Of Solids And Structures 38*, 36-37 (2001), 6427–6454.

[93] Daux, C., Moes, N., and Dolbow, J. Arbitrary branched and intersecting cracks with the extended finite element method. *International Journal for Numerical Methods in Engineering 48*, September 1999 (2000), 1741–1760.

[94] De Bellis, M. L., and Addessi, D. A Cosserat Based Multi-Scale Model for Masonry Structures. *International Journal for Multiscale Computational Engineering 9*, 5 (2011), 543–563.

[95] de Borst, R. Simulation of Strain Localization: a Reappraisal of the Cosserat Continuum. *Engineering Computations 8*, 4 (1991), 317–332.

[96] de Borst, R. Fracture in quasi-brittle materials: A review of continuum damage-based approaches. *Engineering Fracture Mechanics 69* (2001), 95–112.

[97] de Borst, R., and Mühlhaus, H.-B. Gradient-dependent plasticity: Formulation and algorithmic aspects. *International Journal for Numerical Methods in Engineering 35*, 3 (1992), 521–539.

[98] de Borst, R., and Nauta, P. Non-orthogonal cracks in a smeared finite element model. *Engineering Computations 2*, 1 (1985), 35–46.

[99] de Borst, R., Sluys, L., Mühlhaus, H.-B., and Pamin, J. Fundamental issues in Finite Element Analyses of localization of deformation. *Engineering Computations 10*, 2 (1993), 99–121.

[100] de Borst, R., and Verhoosel, C. V. Gradient damage vs phase-field approaches for fracture: Similarities and differences. *Computer Methods in Applied Mechanics and Engineering 312* (2016), 78–94.

[101] DeJong, M. J., a.N. Hendriks, M., and Rots, J. G. Sequentially linear analysis of fracture under non-proportional loading. *Engineering Fracture Mechanics 75*, 18 (2008), 5042–5056.

[102] Dias, I. F. *Crack path field and strain injection techniques in numerical modeling of propagating material failure*. PhD thesis, Universitat Politècnica de Catalunya (BarcelonaTech-UPC), 2012.

[103] Dias, I. F., Oliver, J., and Huespe, A. Strain injection techniques in numerical modeling of propagating material failure. *Monography CIMNE 134* (2012).

[104] Dias, I. F., Oliver, J., Lemos, J. V., and Lloberas-Valls, O. Modeling tensile crack propagation in concrete gravity dams via crack-path-field and strain injection techniques. *Engineering Fracture Mechanics 154* (2016), 288–310.

[105] Dias-da Costa, D., Alfaiate, J., Sluys, L. J., and Júlio, E. Towards a generalization of a discrete strong discontinuity approach. *Computer Methods in Applied Mechanics and Engineering 198*, 47-48 (2009), 3670–3681.

[106] Dias-Da-Costa, D., Alfaiate, J., Sluys, L. J., and Júlio, E. A comparative study on the modelling of discontinuous fracture by means of enriched nodal and element techniques and interface elements. *International Journal of Fracture 161*, 1 (2010), 97–119.

[107] Drougkas, A., Roca, P., and Molins, C. Numerical prediction of the behavior, strength and elasticity of masonry in compression. *Engineering Structures 90* (2014), 15–28.

[108] Drougkas, A., Roca, P., and Molins, C. Strength and elasticity of pure lime mortar masonry. *Materials and Structures* (2014).

[109] Duarte, C., Babuška, I., and Oden, J. Generalized finite element methods for three-dimensional structural mechanics problems. *Computers & Structures 77*, 2 (2000), 215–232.

[110] Duarte, C. A., Reno, L. G., Simone, A., and Van Der Giessen, E. Hp generalized finite elements for three-dimensional branched cracks and polycrystals. *AIP Conference Proceedings 973*, February (2008), 39–44.

[111] Duflot, M. A study of the representation of cracks with level sets. *International Journal for Numerical Methods in Engineering 70*, 11 (2007), 1261–1302.

[112] Dugdale, D. Yielding of steel sheets containing slits. *Journal of the Mechanics and Physics of Solids 8*, 2 (1960), 100–104.

[113] Dumstorff, P., and Meschke, G. Crack propagation criteria in the framework of X-FEM-based structural analyses. *International Journal for Numerical and Analytical Methods in Geomechanics 31*, 2 (2007), 239–259.

[114] Dvorkin, E. N., Cuitiño, A. M., and Gioia, G. Finite elements with displacement interpolated embedded localization lines insensitive to mesh size and distortions. *International Journal for Numerical Methods in Engineering 30*, 3 (1990), 541–564.

[115] EN 1992 (Eurocode 2). Design of concrete structures. Tech. rep., London, 1992.

[116] EN 1998-1 (Eurocode 8). Design of structures for earthquake resistance, Part 1 General rules seismic actions and rules for buildings, 2003.

[117] Endo, Y. *Modelling and Structural Analysis of historical masonry systems including vaulted structure.* PhD thesis, Universitat Politècnica de Catalunya (BarcelonaTech-UPC), 2015.

[118] Endo, Y., Pelà, L., Roca, P., da Porto, F., and Modena, C. Comparison of seismic analysis methods applied to a historical church struck by 2009 L'Aquila earthquake. *Bulletin of Earthquake Engineering 13*, 12 (2015), 3749–3778.

[119] Erdogan, F., and Sih, G. On the Crack Extension in Plates under Loading and Transverse Shear. *Journal of Fluids Engineering 85*, 4 (1963), 519–527.

[120] Fajfar, P. Capacity spectrum method based on inelastic demand spectra. *Earthquake Engineering & Structural Dynamics 28*, 9 (sep 1999), 979–993.

[121] Faria, R. *Seismic behaviour of concrete dams evaluated via a continuum damage model.* PhD thesis, Porto University, Portugal, 1994.

[122] Faria, R., and Oliver, J. *A Rate Dependent Plastic-Damage Constitutive Model for Large Scale Computations in Concrete Structures, Monography N-17.* CIMNE, 1993.

[123] Faria, R., Oliver, J., and Cervera, M. A strain-based plastic viscous-damage model for massive concrete structures. *International Journal of Solids and Structures 35*, 14 (1998), 1533–1558.

[124] Faria, R., Oliver, J., and Cervera, M. On Isotropic Scalar Damage Models for the Numerical Analysis of Concrete Structures, Monography N-198. 1–38.

[125] Faria, R., Oliver, J., and Cervera, M. Modeling material failure in concrete structures under cyclic actions. *Journal of Structural Engineering*, December (2004), 1997–2005.

[126] Feenstra, P. H., and de Borst, R. A composite plasticity model for concrete. *International Journal of Solids and Structures 33*, 5 (1996), 707–730.

[127] Feist, C. *A numerical model for cracking of plain concrete based on the strong discontinuity approach.* PhD thesis, Universität Innsbruck, 2004.

[128] Feist, C., and Hofstetter, G. An embedded strong discontinuity model for cracking of plain concrete. *Computer Methods in Applied Mechanics and Engineering 195*, 52 (2006), 7115–7138.

[129] Feist, C., and Hofstetter, G. Three-dimensional fracture simulations based on the SDA. *International Journal for Numerical and Analytical Methods in Geomechanics 31*, 2 (2007), 189–212.

[130] Feld-Payet, S., Chiaruttini, V., Besson, J., and Feyel, F. A new marching ridges algorithm for crack path tracking in regularized media. *International Journal of Solids and Structures 71* (2015), 57–69.

[131] Felippa, C. A. A historical outline of matrix structural analysis: A play in three acts. *Computers and Structures 79*, 14 (2001), 1313–1324.

[132] Fouchal, F., Lebon, F., and Titeux, I. Contribution to the modelling of interfaces in masonry construction. *Construction and Building Materials 23*, 6 (2009), 2428–2441.

[133] Fraeijs de Veubeke, B. M. Displacement and equilibrium models. In *Stress Analysis*, O. C. Zienkiewicz and H. G., Eds. Wiley, London, 1965, pp. 145–197.

[134] Francfort, G., and Marigo, J.-J. Revisiting brittle fracture as an energy minimization problem. *Journal of the Mechanics and Physics of Solids 46*, 8 (1998), 1319–1342.

[135] Fries, T.-P., and Baydoun, M. Crack propagation with the extended finite element method and a hybrid explicit-implicit crack description. *International Journal for Numerical Methods in Engineering 89*, 12 (2012), 1527–1558.

[136] Fries, T.-P., and Belytschko, T. The extended/generalized finite element method: An overview of the method and its applications. *International Journal for Numerical Methods in Engineering 84*, 3 (2010), 253–304.

[137] Gálvez, J. C., Červenka, J., Cendón, D. A., and Saouma, V. A discrete crack approach to normal/shear cracking of concrete. *Cement and Concrete Research 32*, 10 (2002), 1567–1585.

[138] Gálvez, J. C., Elices, M., and Planas, J. Mixed mode fracture of concrete under proportional and nonproportional loading. *International Journal of Fracture 94* (1999), 267–284.

[139] Gálvez, J. C., Planas, J., Sancho, J. M., Reyes, E., Cendón, D. a., and Casati, M. J. An embedded cohesive crack model for finite element analysis of quasi-brittle materials. *Engineering Fracture Mechanics 109* (2013), 369–386.

[140] Gambarotta, L., and Lagomarsino, S. Damage models for the seismic response of brick masonry shear walls. Part I: The mortar joint model and its applications. *Earthquake Engineering & Structural Dynamics 26*, 4 (apr 1997), 423–439.

[141] Gambarotta, L., and Lagomarsino, S. Damage Models for the Seismic Response of Brick Masonry Shear Walls. Part II: the Continuum Model and Its Applications. *Earthquake Engng. Struct. Dyn. 26*, March 1996 (1997), 441–462.

[142] Gasser, T. C., and Holzapfel, G. A. Modeling 3D crack propagation in unreinforced concrete using PUFEM. *Computer Methods in Applied Mechanics and Engineering 194*, 25-26 (2005), 2859–2896.

[143] Gasser, T. C., and Holzapfel, G. A. 3D Crack propagation in unreinforced concrete. A two-step algorithm for tracking 3D crack paths. *Computer Methods in Applied Mechanics and Engineering 195*, 37-40 (2006), 5198–5219.

[144] Ghorashi, S. S., Valizadeh, N., and Mohammadi, S. Extended isogeometric analysis for simulation of stationary and propagating cracks. *International Journal for Numerical Methods in Engineering 89*, 9 (2012), 1069–1101.

[145] Gilbert, M., Casapulla, C., and Ahmed, H. Limit analysis of masonry block structures with non-associative frictional joints using linear programming. *Computers & Structures 84*, 13-14 (may 2006), 873–887.

[146] Goodman, R., Taylor, R., and Brekke, T. A model for the mechanics of jointed rock. *Journal of Soil Mechanics & Foundations Div 94*, 3 (1968), 637–659,.

[147] Gopalaratnam, V. S., and Shah, S. P. Softening Response of Plain Concrete in Direct Tension. *ACI Journal 82*, 3 (1985), 310–323.

[148] Grassl, P., and Jirásek, M. Damage-plastic model for concrete failure. *International Journal of Solids and Structures 43*, 22-23 (2006), 7166–7196.

[149] Gravouil, A., Moës, N., and Belytschko, T. Non-planar 3D crack growth by the extended finite element and level sets-Part II: Level set update. *International Journal for Numerical Methods in Engineering 53*, 11 (2002), 2569–2586.

[150] Griffith, A. The theory of rupture. In *First International Congress of Applied Mechanic* (Delft, 1924), C. Biereno and J. Burgers, Eds., pp. 54–63.

[151] Griffith, A. A. The Phenomena of Rupture and Flow in Solids. *Philosophical Transactions of the Royal Society A: Mathematical, Physical and Engineering Sciences 221* (1921), 163–198.

[152] Haghighat, E., and Pietruszczak, S. On modeling of discrete propagation of localized damage in cohesive-frictional materials. *International Journal for Numerical and Analytical Methods in Geomechanics 39*, 16 (2015), 1774–1790.

[153] Hansbo, A., and Hansbo, P. A finite element method for the simulation of strong and weak discontinuities in solid mechanics. *Computer Methods in Applied Mechanics and Engineering 193*, 33-35 (2004), 3523–3540.

[154] He, W., Wu, Y. F., Xu, Y., and Fu, T. T. A thermodynamically consistent nonlocal damage model for concrete materials with unilateral effects. *Computer Methods in Applied Mechanics and Engineering 297* (2015), 371–391.

[155] Henshell, R. D., and Shaw, K. G. Crack tip finite elements are unnecessary. *International Journal for Numerical Methods in Engineering 9*, 3 (1975), 495–507.

[156] Heyman, J. The stone skeleton. *International Journal of Solids and Structures 2*, 2 (1966), 249–279.

[157] Hien Poh, L., and Swaddiwudhipong, S. Over-nonlocal gradient enhanced plastic-damage model for concrete. *International Journal of Solids and Structures 46*, 25-26 (2009), 4369–4378.

[158] Hill, R. Acceleration waves in solids. *Journal of the Mechanics and Physics of Solids 10*, 1 (1962), 1–16.

[159] Hillerborg, A., Modéer, M., and Petersson, P.-E. Analysis of crack formation and crack growth in concrete by means of fracture mechanics and finite elements. *Cement and Concrete Research 6*, 6 (1976), 773–781.

[160] Hofstetter, G., Feist, C., Lehar, H., Theiner, Y., Valentini, B., and Winkler, B. Plasticity based crack models and applications. Springer, Vienna, 2011, pp. 161–219.

[161] Holl, M., Rogge, T., Loehnert, S., Wriggers, P., and Rolfes, R. 3D multiscale crack propagation using the XFEM applied to a gas turbine blade. *Computational Mechanics 53*, 1 (2014), 173–188.

[162] Huespe, A. E., Needleman, A., Oliver, J., and Sánchez, P. J. A finite thickness band method for ductile fracture analysis. *International Journal of Plasticity 25*, 12 (2009), 2349–2365.

[163] Huespe, A. E., Needleman, A., Oliver, J., and Sánchez, P. J. A finite strain, finite band method for modeling ductile fracture. *International Journal of Plasticity 28*, 1 (2012), 53–69.

[164] Inglis, C. E. Stresses in a plate due to the presnce of cracks and sharp corners. *Trans. Inst. Naval Arch. 55* (1913), 219–239.

[165] Ingraffea, A. R., Gerstle, W., Gergely, P., and Saoume, V. Fracture mechanics of bond in reinforced concrete. *Journal of Structural Engineering 110*, 4 (1984), 871–890.

[166] Ingraffea, A. R., and Heuze, F. Finite element models for rock fracture mechanics. *International Journal for Numerical and Analytical Methods in Geomechanics 4*, 1 (1980), 25–43.

[167] Ingraffea, A. R., and Saouma, V. Numerical modeling of discrete crack propagation in reinforced and plain concrete. In *Fracture mechanics of concrete: Structural application and numerical calculation*. Springer Netherlands, Dordrecht, 1985, pp. 171–225.

[168] Irwin, G. Fracture Dynamics. In *Fracturing of Metals*. American Society for Metals, Cleveland, 1948.

[169] Irwin, G. Analysis of Stresses and Strains Near the End of a Crack Traversing a Plate. *Journal of Applied Mechanics 24*, September (1957), 361–364.

[170] Irwin, G. Fracture. *Handbook der Physik 6* (1958), 551–590.

[171] Italian Ministry of Infrastructure and Transport. *Circolare 2 febbraio 2009, n. 617, Istruzioni per l'applicazione delle "Nuove norme tecniche per le costruzion" di cui al decreto ministeriale 14 gennaio 2008.* Rome, Italy, 2009.

[172] Jäger, P., Steinmann, P., and Kuhl, E. On local tracking algorithms for the simulation of three-dimensional discontinuities. *Computational Mechanics 42*, 3 (2008), 395–406.

[173] Jäger, P., Steinmann, P., and Kuhl, E. Towards the treatment of boundary conditions for global crack path tracking in three-dimensional brittle fracture. *Computational Mechanics 45*, 1 (2009), 91–107.

[174] Jason, L., Huerta, A., Pijaudier-Cabot, G., and Ghavamian, S. An elastic plastic damage formulation for concrete: Application to elementary tests and comparison with an isotropic damage model. *Computer Methods in Applied Mechanics and Engineering 195*, 52 (2006), 7077–7092.

[175] Jelvehpour, A. *Development of a transient gradient enhanced non local continuum damage mechanics model for masonry.* PhD thesis, Queensland University Technology, 2016.

[176] Jirásek, M. Comparative study on finite elements with embedded discontinuities. *Computer Methods in Applied Mechanics and Engineering 188*, 1-3 (2000), 307–330.

[177] Jirásek, M., and Belytschko, T. B. Computational resolution of strong discontinuities. In *Fifth world congress on computational mechanics* (Vienna, 2002), pp. 7–12.

[178] Jirásek, M., and Grassl, P. Evaluation of directional mesh bias in concrete fracture simulations using continuum damage models. *Engineering Fracture Mechanics 75*, 8 (2008), 1921–1943.

[179] Jirásek, M., and Zimmermann, T. Embedded crack model. Part II. Combination with smeared cracks. *International Journal for Numerical Methods in Engineering 50*, 6 (2001), 1291–1305.

[180] Johnson, C., and Scott, R. A Finite Element Method for Problems in Perfect Plasticity Using Discontinuous Trial Functions. In *Nonlinear Finite Element Analysis in Structural Mechanics.* Springer Berlin Heidelberg, Berlin, Heidelberg, 1981, pp. 307–324.

[181] Ju, J. W. On energy-based coupled elastoplastic damage theories: Constitutive modeling and computational aspects. *International Journal of Solids and Structures 25*, 7 (1989), 803–833.

[182] Kachanov, L. M. Time of the rupture process under creep conditions. *Izvestiya Akademii Nauk SSSR Otdelenie Tekniches 8* (1958), 26–31.

[183] Karihaloo, B. L., and Xiao, Q. Z. Modelling of stationary and growing cracks in FE framework without remeshing: A state-of-the-art review. *Computers and Structures 81* (2003), 119–129.

[184] Karsan, I., and Jirsa, J. Behavior of concrete under compressive loadings. *Journal of Structural Engineering (ASCE) 95*, 12 (1969), 310–323.

[185] Kirsch, E. Die Theorie der Elastizität und die Bedürfnisse der Festigkeitslehre. *Zeitschrift des Vereines deutscher Ingenieure 42* (1898), 797–807.

[186] Klisinski, M., Runesson, K., Sture, S., and Others. Finite element with inner softening band. *Journal of engineering mechanics 117*, 3 (1991), 575.

[187] Kumar, N., Amirtham, R., and Pandey, M. Plasticity based approach for failure modelling of unreinforced masonry. *Engineering Structures 80* (2014), 40–52.

[188] Lagomarsino, S., Penna, A., Galasco, A., and Cattari, S. TREMURI program: An equivalent frame model for the nonlinear seismic analysis of masonry buildings. *Engineering Structures 56* (2013), 1787–1799.

[189] Larsson, R., Runesson, K., and Ottosen, N. S. Discontinuous displacement approximation for capturing plastic localization. *International Journal for Numerical Methods in Engineering 36*, 12 (1993), 2087–2105.

[190] Lee, J., and Fenves, G. L. Plastic-Damage Model for Cyclic Loading of Concrete Structures. *Journal of Engineering Mechanics 124*, 8 (1998), 892–900.

[191] Lemaitre, J. How to use damage mechanics. *Nuclear Engineering and Design 80*, 2 (1984), 233–245.

[192] Lemaitre, J., and Chaboche, J. L. Aspect Phenomenologique de la Rupture par Endommagement. *Journal de Mécanique Appliquée 2*, 3 (1978).

[193] Lemos, J. V. Discrete Element Modeling of Masonry Structures. *International Journal of Architectural Heritage 1*, 2 (may 2007), 190–213.

[194] Lim, I. L., Johnston, I. W., and Choi, S. K. A finite element code for fracture propagation analysis within elasto-plastic continuum. *Engineering fracture mechanics 53*, 2 (1996), 193–211.

[195] Linder, C., and Armero, F. Finite elements with embedded strong discontinuities for the modeling of failure in solids. *International Journal for Numerical Methods in Engineering 72*, 12 (2007), 1391–1433.

[196] Linder, C., and Armero, F. Finite elements with embedded branching. *Finite Elements in Analysis and Design 45*, 4 (2009), 280–293.

[197] Lloberas-Valls, O., Huespe, A. E., Oliver, J., and Dias, I. F. Strain injection techniques in dynamic fracture modeling. *Computer Methods in Applied Mechanics and Engineering 308* (2016), 499–534.

[198] Lo, K. Y., and Lee, C. F. Stress analysis and slope stability in strain-softening materials. *Geotechnique 23*, 1 (1973), 1–11.

[199] Lofti, H. R., and Shing B.P. Interface model applied to fracture of masonry structures. *Journal of Structural Engineering 120*, 1 (1994), 63–80.

[200] Lopez, J., Oller, S., Oñate, E., and Lubliner, J. A homogeneous constitutive model for masonry. *International Journal for Numerical Methods in Engineering 46*, 10 (1999), 1651–1671.

[201] Lourenço, P., Krakowiak, K., Fernandes, F., and Ramos, L. Failure analysis of Monastery of Jerónimos, Lisbon: How to learn from sophisticated numerical models. *Engineering Failure Analysis 14*, 2 (2007), 280–300.

[202] Lourenço, P. B. *Computational strategies for masonry structures.* PhD thesis, Delft University of Technology, 1996.

[203] Lourenço, P. B. Anisotropic Softening Model for Masonry Plates and Shells. *Journal of Structural Engineering 126*, 9 (2000), 1008–1016.

[204] Lourenço, P. B. Computations on historic masonry structures. *Progress in Structural Engineering and Materials 4*, July (2002), 301–319.

[205] Lourenço, P. B., and Pina-Henriques, J. Validation of analytical and continuum numerical methods for estimating the compressive strength of masonry. *Computers & Structures 84*, 29-30 (nov 2006), 1977–1989.

[206] Lourenço, P. B., and Rots, J. G. Multisurface Interface Model for Analysis of Masonry Structures. *Journal of Engineering Mechanics 123*, 7 (1997), 660–668.

[207] Lourenço, P. B., Rots, J. G., and Blaauwendraad, J. Continuum Model for Masonry: Parameter Estimation and Validation. *Journal of Structural Engineering 124*, 6 (1998), 642–652.

[208] Lourenço, P. B., Trujillo, A., Mendes, N., and Ramos, L. F. Seismic performance of the St. George of the Latins church: Lessons learned from studying masonry ruins. *Engineering Structures 40* (2012), 501–518.

[209] Lubliner, J., Oliver, J., Oller, S., and Oñate, E. A plastic-damage model for concrete. *International Journal of Solids and Structures 25*, 3 (1989), 299–326.

[210] Macorini, L., and Izzuddin, B. A. A non-linear interface element for 3D mesoscale analysis of brick-masonry structures. *International Journal for Numerical Methods in Engineering 85*, 12 (2011), 1584–1608.

[211] Macorini, L., and Izzuddin, B. A. Nonlinear analysis of masonry structures using mesoscale partitioned modelling. *Advances in Engineering Software 60-61* (2013), 58–69.

[212] Macorini, L., Izzuddin, B. a., and Asce, M. Nonlinear Analysis of Unreinforced Masonry Walls under Blast Loading Using Mesoscale Partitioned Modeling. *Journal of Structural Engineering 140* (2011), 1–10.

[213] Magenes, G., and Calvi, G. M. In-plane seismic response of brick masonry walls, 1997.

[214] Magenes, G., and Della Fontana, A. Simplified Non-linear Seismic Analysis of Masonry Buildings. *Proceedings of the British Masonry Society*, December (1998), 8;190–195.

[215] Manzoli, O. L. Predição de propagação de fissuras através de modelos constitutivos locais e técnica de construção progressiva da trajetória de descontinuidade. *Revista Internacional de Metodos Numericos para Calculo y Diseno en Ingenieria 27*, 3 (2011), 180–188.

[216] Marastoni, D. *Advanced Minor Destructive Testing for the Assessment of Existing Masonry*. PhD thesis, University of Bologna, 2016.

[217] Marfia, S., and Sacco, E. Multiscale damage contact-friction model for periodic masonry walls. *Computer Methods in Applied Mechanics and Engineering 205-208*, 1 (2012), 189–203.

[218] Mariani, S., and Perego, U. Extended finite element method for quasi-brittle fracture. *International Journal for Numerical Methods in Engineering 58*, 1 (2003), 103–126.

[219] Martha, L., Wawrzynek, P., and Ingraffea, A. Arbitrary crack representation using solid modeling. *Engineering with Computers* (1993), 63–82.

[220] Massart, T. J., Peerlings, R. H. J., and Geers, M. G. D. An enhanced multi-scale approach for masonry wall computations with localization of damage. *International Journal for Numerical Methods in Engineering 69*, 5 (2007), 1022–1059.

[221] Mazars, J., Hamon, F., and Grange, S. A new 3D damage model for concrete under monotonic, cyclic and dynamic loadings. *Materials and Structures* (2014), 3779–3793.

[222] Mazars, J., and Pijaudier-Cabot, G. Continuum damage theory - application to concrete. *Journal of Engineering Mechanics 115*, 2 (1989), 345–365.

[223] McInerney, J., and DeJong, M. Discrete Element Modeling of Groin Vault Displacement Capacity. *International Journal of Architectural Heritage 9*, 8 (2015), 1037–1049.

[224] Melenk, J., and Babuška, I. The partition of unity finite element method: Basic theory and applications. *Computer Methods in Applied Mechanics and Engineering 139*, 1-4 (1996), 289–314.

[225] Mergheim, J., Kuhl, E., and Steinmann, P. A finite element method for the computational modelling of cohesive cracks. *International Journal for Numerical Methods in Engineering 63*, 2 (2005), 276–289.

[226] Mergheim, J., Kuhl, E., and Steinmann, P. Towards the algorithmic treatment of 3D strong discontinuities. *Communications in Numerical Methods in Engineering 23*, 2 (2006), 97–108.

[227] Meschke, G., and Dumstorff, P. Energy-based modeling of cohesive and cohesionless cracks via X-FEM. *Computer Methods in Applied Mechanics and Engineering 196*, 21-24 (2007), 2338–2357.

[228] Miehe, C., Hofacker, M., and Welschinger, F. A phase field model for rate-independent crack propagation: Robust algorithmic implementation based on operator splits. *Computer Methods in Applied Mechanics and Engineering 199*, 45-48 (2010), 2765–2778.

[229] Milani, G., Casolo, S., Naliato, A., and Tralli, A. Seismic Assessment of a Medieval Masonry Tower in Northern Italy by Limit, Nonlinear Static, and Full Dynamic Analyses. *International Journal of Architectural Heritage 6*, 5 (sep 2012), 489–524.

[230] Milani, G., Lourenço, P., and Tralli, A. Homogenised limit analysis of masonry walls, Part I: Failure surfaces. *Computers & Structures 84*, 3-4 (2006), 166–180.

[231] Milani, G., Lourenço, P., and Tralli, A. Homogenised limit analysis of masonry walls, Part II: Structural examples. *Computers & Structures 84*, 3-4 (2006), 181–195.

[232] Milani, G., Valente, M., and Alessandri, C. The narthex of the Church of the Nativity in Bethlehem: A non-linear finite element approach to predict the structural damage. *Computers and Structures* (2017).

[233] Milani, G., and Venturini, G. Safety Assessment of Four Masonry Churches by a Plate and Shell FE Non-linear Approach. *Journal of Performance of Constructed Facilities*, February (2011), 230.

[234] Moës, N., and Belytschko, T. Extended finite element method for cohesive crack growth. *Engineering Fracture Mechanics 69*, 7 (2002), 813–833.

[235] Moës, N., Dolbow, J., and Belytschko, T. A finite element method for crack growth without remeshing. *International Journal for Numerical Methods in Engineering 46*, 1 (1999), 131–150.

[236] Moës, N., Gravouil, A., and Belytschko, T. Non-planar 3D crack growth by the extended finite element and level sets-Part I: Mechanical model. *International Journal for Numerical Methods in Engineering 53*, 11 (2002), 2549–2568.

[237] Muhlhaus, H. B., and Aifantis, E. C. The influence of microstructure-induced gradients on the localization of deformation in viscoplastic materials. *Acta Mechanica 89*, 1-4 (1991), 217–231.

[238] Naraine, K., and Sinha, S. Behaviour of Brick Masonry under Cyclic Compressive Loading. *Journal of Structural Engineering 115*, 2 (1989), 1432–1445.

[239] Natarajan, S., Mahapatra, R., and Bordas, S. Integrating strong and weak discontinuities without integration subcells and example applications in an XFEM/GFEM framework. *International journal for numerical methods in engineering 83* (2010), 269–294.

[240] Nayak, G. C., and Zienkiewicz, O. C. Elasto-Plastic Stress Analysis. a Generalization for Various Constitutive Relations Including Strain Softening. *International Journal for Numerical Methods in Engineering 5* (1972), 113–135.

[241] Needleman, A. Material rate dependence and mesh sensitivity in localization problems. *Computer Methods in Applied Mechanics and Engineering 67*, 1 (1988), 69–85.

[242] Ngo, D., and Scordelis, C. Finite Element Analysis of Reinforced Concrete Beams. *ACI Journal 64*, 3 (1967), 152–163.

[243] Nguyen, G. D., and Houlsby, G. T. A coupled damage-plasticity model for concrete based on thermodynamic principles: Part I: Model formulation and parameter identification. *International Journal for Numerical and Analytical Methods in Geomechanics 32*, 4 (2008), 353–389.

[244] Nilson, A. H. Nonlinear Analysis of Reinforced Concrete by the Finite Element Method. *ACI Journal 65*, 9 (1968), 757–766.

[245] Nooru-Mohamed, M., Schlangen, E., and van Mier, J. G. Experimental and numerical study on the behavior of concrete subjected to biaxial tension and shear. *Advanced Cement Based Materials 1*, 1 (1993), 22–37.

[246] Nooru-Mohamed, M. B. M. *Mixed-mode fracture of concrete: an experimental approach*. PhD thesis, Delft University of Technology, 1992.

[247] Nuismer, R. J. An energy release rate criterion for mixed mode fracture. *International Journal of Fracture 11*, 2 (1975), 245–250.

[248] Okubo, C., and Schultz, R. Evolution of damage zone geometry and intensity in porous sandstone: insight gained from strain energy density. *Journal of the Geological Society 162*, Engelder 1974 (2005), 939–949.

[249] Oliveira, D. V., and Lourenço, P. B. Implementation and validation of a constitutive model for the cyclic behaviour of interface elements. *Computers and Structures 82*, 17-19 (2004), 1451–1461.

[250] Oliveira, D. V., Lourenço, P. B., and Roca, P. Cyclic behaviour of stone and brick masonry under uniaxial compressive loading. *Materials and Structures 39*, 2 (2007), 247–257.

[251] Oliver, J. A consistent characteristic length for smeared cracking models. *International Journal for Numerical Methods in Engineering 28*, 2 (1989), 461–474.

[252] Oliver, J. Continuum modelling of strong discontinuities in solid mechanics using damage models. *Computational Mechanics 17*, 1-2 (1995), 49–61.

[253] Oliver, J. Modelling strong discontinuities in solid mechanics via strain softening constitutive equations. Part 1: fundamentals. *International Journal for Numerical Methods in Engineering 39*, 21 (1996), 3575–3600.

[254] Oliver, J. Modelling strong discontinuities in solid mechanics via strain softening constitutive equations. Part 2: Numerical simulation. *International Journal for Numerical Methods in Engineering 39*, 21 (1996), 3601–3623.

[255] Oliver, J., Caicedo, M., Roubin, E., Huespe, A., and Hernández, J. Continuum approach to computational multiscale modeling of propagating fracture. *Computer Methods in Applied Mechanics and Engineering 294* (2015), 384–427.

[256] Oliver, J., Cervera, M., and Manzoli, O. On the Use of Strain-Softening models for the Simulation of Strong Discontinuities in Solids. In *Material Instabilities in Solids*, R. de Borst and E. V. D. Giessen, Eds. John Wiley & Sons, Ltd, 1998, pp. 104–123.

[257] Oliver, J., Cervera, M., and Manzoli, O. Strong discontinuities and continuum plasticity models: the strong discontinuity approach. *International Journal of Plasticity 15*, 3 (1999), 319–351.

[258] Oliver, J., Cervera, M., Oller Martinez, S. H., and Lubliner, J. Isotropic damage models and smeared crack analysis of concrete. *Proc. SCI-C Computer Aided Analysis and Design of Concrete Structures*, February (1990), 945–957.

[259] Oliver, J., Dias, I. F., and Huespe, A. E. Crack-path field and strain-injection techniques in computational modeling of propagating material failure. *Computer Methods in Applied Mechanics and Engineering 274* (2014), 289–348.

[260] Oliver, J., and Huespe, A. E. Continuum approach to material failure in strong discontinuity settings. *Computer Methods in Applied Mechanics and Engineering 193*, 30-32 (2004), 3195–3220.

[261] Oliver, J., Huespe, A. E., Cante, J. C., and Díaz, G. On the numerical resolution of the discontinuous material bifurcation problem. *International Journal for Numerical Methods in Engineering 83*, 6 (2010), 786–804.

[262] Oliver, J., Huespe, a. E., and Dias, I. F. Strain localization, strong discontinuities and material fracture: Matches and mismatches. *Computer Methods in Applied Mechanics and Engineering 241-244* (2012), 323–336.

[263] Oliver, J., Huespe, A. E., and Samaniego, E. A study on finite elements for capturing strong discontinuities. *International Journal for Numerical Methods in Engineering 56*, 14 (2003), 2135–2161.

[264] Oliver, J., Huespe, a. E., Samaniego, E., and Chaves, E. W. V. Continuum approach to the numerical simulation of material failure in concrete. *International Journal for Numerical and Analytical Methods in Geomechanics 28*, 78 (2004), 609–632.

[265] Oliver, J., Huespe, A. E., and Sánchez, P. J. A comparative study on finite elements for capturing strong discontinuities: E-FEM vs X-FEM. *Computer Methods in Applied Mechanics and Engineering 195*, 37-40 (2006), 4732–4752.

[266] Oliver, J., Linero, D. L., Huespe, A. E., and Manzoli, O. L. Two-dimensional modeling of material failure in reinforced concrete by means of a continuum strong discontinuity approach. *Computer Methods in Applied Mechanics and Engineering 197*, 5 (2008), 332–348.

[267] Oller, S. Numerical Modelling of Frictional Materials - Monography N-3. *CIMNE* (1991), (in spanish).

[268] Oller, S., Botello, S., Miquel, J., and Oñate, E. An anisotropic elastoplastic model based on an isotropic formulation. *Engineering Computations 12* (1995), 245–262.

[269] Oller, S., Car, E., and Lubliner, J. Definition of a general implicit orthotropic yield criterion. *Computer Methods in Applied Mechanics and Engineering 192*, 7-8 (2003), 895–912.

[270] Oller, S., Oñate, E., and Miquel, J. Mixing anisotropic formulation for analysis of composites. *Communications in numerical methods in engineering 12*, 8 (1996), 471–482.

[271] Olson, E. L., and Cooke, M. L. Application of three fault growth criteria to the Puente Hills thrust system, Los Angeles, California, USA. *Journal of Structural Geology 27*, 10 (2005), 1765–1777.

[272] Omidi, O., and Lotfi, V. Continuum large cracking in a rate-dependent plastic-damage model for cyclic-loaded concrete structures. *International Journal for Numerical and Analytical Methods in Geomechanics 37*, 10 (2013), 1363–1390.

[273] Orduña, A. n., and Lourenço, P. B. Cap Model for Limit Analysis and Strengthening of Masonry Structures. *Journal of Structural Engineering 129*, 10 (2003), 1367–1375.

[274] Orowan, E. Fracture and strength of solids. *Reports on Progress in Physics 12*, 1 (1949), 185.

[275] Ortiz, M., Leroy, Y., and Needleman, A. A finite element method for localized failure analysis. *Computer Methods in Applied Mechanics and Engineering 61*, 2 (1987), 189–214.

[276] Osher, S., and Sethian, J. A. Fronts propagating with curvature-dependent speed: Algorithms based on Hamilton-Jacobi formulations. *Journal of Computational Physics 79*, 1 (1988), 12–49.

[277] Otero, F., Oller, S., and Martinez, X. Multiscale Computational Homogenization : Review and Proposal of a New Enhanced-First-Order Method. *Archives of Computational Methods in Engineering* (2016).

[278] Ottosen, N. S., and Runesson, K. Discontinuous bifurcations in a nonassociated Mohr material. *Mechanics of Materials 12*, 3-4 (1991), 255–265.

[279] Page, A. W. Finite element model for masonry. *Journal of the Structural Division 104*, 8 (1978), 1267–1285.

[280] Page, A. W. A Model for the In-Plane Behaviour of Masonry and a Sensitivity Analysis of its CriticaI Parameters. In *5th International Brick Masonry Conference* (1979), pp. 262–267.

[281] Papa, E. A unilateral damage model for masonry based on a homogenisation procedure. *Mechanics of Cohesive-Frictional Materias 1*, February (1996), 349–366.

[282] Papastamatiou, D., and Psycharis, I. N. Seismic response of classical monuments-a numerical perspective developed at the Temple of Apollo in Bassae, Greece. *Terra Nova 5*, 6 (1993), 591–601.

[283] Parisi, F. *Non-Linear Seismic Analysis of Masonry Buildings*. PhD thesis, University of Naples Federico II, 2010.

[284] Parisi, F., Augenti, N., and Prota, A. Implications of the spandrel type on the lateral behavior of unreinforced masonry walls. *Earthquake Engineering & Structural Dynamics 43*, 12 (2014), 1867–1887.

[285] Parisi, F., Lignola, G. P., Augenti, N., Prota, a., and Manfredi, G. Nonlinear Behavior of a Masonry Subassemblage Before and After Strengthening with Inorganic Matrix-Grid Composites. *Journal of Composites for Construction 15*, 5 (2011), 821–832.

[286] Pastor, M., Li, T., Liu, X., and Zienkiewicz, O. C. Stabilized low-order finite elements for failure and localization problems in undrained soils and foundations. *Computer Methods in Applied Mechanics and Engineering 174*, 1-2 (1999), 219–234.

[287] Pastor, M., Quecedo, M., and Zienkiewicz, O. C. A mixed displacement-pressure formulation for numerical analysis of plastic failure. *Computers & Structures 62*, 1 (1997), 13–23.

[288] Paul, B., Ndeffo, M., Massin, P., and Moës, N. An integration technique for 3D curved cracks and branched discontinuities within the extended Finite Element Method. *Finite Elements in Analysis and Design 123*, May 2016 (2017), 19–50.

[289] Peerlings, R. H. J., de Borst, R., Brekelmans, W. A. M., and Geers, M. G. D. Localisation issues in local and nonlocal continuum approaches to fracture. *European Journal of Mechanics, A/Solids 21*, 2 (2002), 175–189.

[290] Peerlings, R. H. J., Geers, M. G. D., de Borst, R., and Brekelmans, W. A. M. A critical comparison of nonlocal and gradient-enhanced softening continua. *International Journal of Solids and Structures 38*, 44-45 (2001), 7723–7746.

[291] Pegon, P., Pinto, A. V., and Géradin, M. Numerical modelling of stone-block monumental structures. *Computers & Structures 79*, 22-25 (2001), 2165–2181.

[292] Pelà, L. *Continuum Damage Model for Nonlinear Analysis of Masonry Structures*. PhD thesis, Universitat Politècnica de Catalunya (BarcelonaTech-UPC), 2009.

[293] Pelà, L., Aprile, A., and Benedetti, A. Seismic assessment of masonry arch bridges. *Engineering Structures 31*, 8 (2009), 1777–1788.

[294] Pelà, L., Cervera, M., Oller, S., and Chiumenti, M. A localized mapped damage model for orthotropic materials. *Engineering Fracture Mechanics 124-125* (2014), 196–216.

[295] Pelà, L., Cervera, M., and Roca, P. Continuum damage model for orthotropic materials: Application to masonry. *Computer Methods in Applied Mechanics and Engineering 200*, 9-12 (2011), 917–930.

[296] Pelà, L., Cervera, M., and Roca, P. An orthotropic damage model for the analysis of masonry structures. *Construction and Building Materials 41* (2013), 957–967.

[297] Pelà, L., Roca, P., and Benedetti, A. Mechanical Characterization of Historical Masonry by Core Drilling and Testing of Cylindrical Samples. *International Journal of Architectural Heritage 10*, 2-3 (2016), 360–374.

[298] Penna, A. Seismic assessment of existing and strengthened stone-masonry buildings: critical issues and possible strategies. *Bulletin of Earthquake Engineering 13*, 4 (2014), 1051–1071.

[299] Petracca, M. *Computational Multiscale Analysis of Masonry Structures*. PhD thesis, University G. d'Annunzio of Chieti- Pescara (UNICH) - Universitat Politècnica de Catalunya (BarcelonaTech-UPC), 2016.

[300] Petracca, M., Pelà, L., Rossi, R., Oller, S., Camata, G., and Spacone, E. Regularization of first order computational homogenization for multiscale analysis of masonry structures. *Computational Mechanics 57*, 2 (2016), 257–276.

[301] Petracca, M., Pelà, L., Rossi, R., Oller, S., Camata, G., and Spacone, E. Multiscale computational first order homogenization of thick shells for the analysis of out-of-plane loaded masonry walls. *Computer Methods in Applied Mechanics and Engineering 315* (2017), 273–301.

[302] Petracca, M., Pelà, L., Rossi, R., Zaghi, S., Camata, G., and Spacone, E. Micro-scale continuous and discrete numerical models for nonlinear analysis of masonry shear walls. *Construction and Building Materials 149* (2017), 296–314.

[303] Petromichelakis, Y., Saloustros, S., and Pelà, L. Seismic assessment of historical masonry construction including uncertainty. In *9th International Conference on Structural Dynamics, EURODYN 2014* (2014), Á. Cunha, E. Caetano, P. Ribeiro, C. Papadimitriou, C. Moutinho, and F. Magalhães, Eds., pp. 297–304.

[304] Pietruszczak, S., and óz, Z. Finite element analysis of deformation of strainâĂŘsoftening materials. *International Journal for Numerical Methods in Engineering 17*, 3 (1981), 327–334.

[305] Quinteros, R. D., Oller, S., and Nallim, L. G. Nonlinear homogenization techniques to solve masonry structures problems. *Composite Structures 94*, 2 (2012), 724–730.

[306] Rabczuk, T. Computational Methods for Fracture in Brittle and Quasi-Brittle Solids : State-of-the-art Review and Future Perspectives. *ISRN Applied Mathematics 2013* (2012), 1–61.

[307] Rabczuk, T., and Belytschko, T. Cracking particles: A simplified meshfree method for arbitrary evolving cracks. *International Journal for Numerical Methods in Engineering 61*, 13 (2004), 2316–2343.

[308] Rabczuk, T., and Belytschko, T. A three-dimensional large deformation meshfree method for arbitrary evolving cracks. *Computer Methods in Applied Mechanics and Engineering 196*, 29-30 (2007), 2777–2799.

[309] Rabczuk, T., Bordas, S., and Zi, G. A three-dimensional meshfree method for continuous multiple-crack initiation, propagation and junction in statics and dynamics. *Computational Mechanics 40*, 3 (2007), 473–495.

[310] Raka, E., Spacone, E., Sepe, V., and Camata, G. Advanced frame element for seismic analysis of masonry structures: model formulation and validation. *Earthquake Engineering & Structural Dynamics 44*, 14 (nov 2015), 2489–2506.

[311] Rashid, Y. Ultimate strength analysis of prestressed concrete pressure vessels. *Nuclear Engineering and Design 7*, 4 (1968), 334–344.

[312] Remmers, J. J. C., de Borst, R., and Needleman, A. A cohesive segments method for the simulation of crack growth. *Computational Mechanics 31*, 1-2 SPEC. (2003), 69–77.

[313] Remmers, J. J. C., de Borst, R., and Needleman, A. The simulation of dynamic crack propagation using the cohesive segments method. *Journal of the Mechanics and Physics of Solids 56*, 1 (2008), 70–92.

[314] Reyes, E., Gálvez, J. C., Casati, M. J., Cendón, D. A., Sancho, J. M., and Planas, J. An embedded cohesive crack model for finite element analysis of brickwork masonry fracture. *Engineering Fracture Mechanics 76*, 12 (2009), 1930–1944.

[315] Riccardi, F., Kishta, E., and Richard, B. A step-by-step global crack-tracking approach in E-FEM simulations of quasi-brittle materials. *Engineering Fracture Mechanics 170* (2017), 44–58.

[316] Rice, J. R., and Rudnicki, J. W. A note on some features of the theory of localization of deformation. *International Journal of Solids and Structures 16*, 7 (1980), 597–605.

[317] Roca, P., Cervera, M., Gariup, G., and Pelà, L. Structural Analysis of Masonry Historical Constructions. Classical and Advanced Approaches. *Archives of Computational Methods in Engineering 17*, 3 (2010), 299–325.

[318] Roca, P., Cervera, M., Pelà, L., Clemente, R., and Chiumenti, M. Continuum FE models for the analysis of Mallorca Cathedral. *Engineering Structures 46* (2013), 653–670.

[319] Roth, S.-N., Léger, P., and Soulaïmani, A. A combined XFEM-damage mechanics approach for concrete crack propagation. *Computer Methods in Applied Mechanics and Engineering 283* (2015), 923–955.

[320] Rots, J. *Computational modeling of concrete fracture*. PhD thesis, Delft University of Technology, 1988.

[321] Rots, J. G., Nauta, P., Kusters, G. M. a., and Blaauwendraad, J. Smeared Crack Approach and Fracture Localization in Concrete. *Heron 30*, 1 (1985).

[322] Rots. J.G., Berkers, W., and van den Heuvel, H. Towards fracture mechanics based design rules for movement-joint spacing. In *10th International Brick and Block Masonry Conference* (Calgary, Canada, 1994), N. Shrive and A. Huizer, Eds., pp. 707–718.

[323] Rudnicki, J. W., and Rice, J. R. Conditions for the localization of deformation in pressure-sensitive dilatant materials. *Journal of the Mechanics and Physics of Solids 23*, 6 (1975), 371–394.

[324] Runesson, K., Saabye Ottosen, N., and Dunja, P. Discontinuous bifurcations of elastic-plastic solutions at plane stress and plane strain. *International Journal of Plasticity 7*, 1-2 (1991), 99–121.

[325] Sadeghirad, A., Chopp, D. L., Ren, X., Fang, E., and Lua, J. A novel hybrid approach for level set characterization and tracking of non-planar 3D cracks in the extended finite element method. *Engineering Fracture Mechanics 160* (2016), 1–14.

[326] Saloustros, S., Cervera, M., and Pelà, L. Tracking multi-directional intersecting cracks in numerical modelling of masonry shear walls under cyclic loading. *Meccanica* (2017), (in press).

[327] Saloustros, S., Pelà, L., and Cervera, M. A crack-tracking technique for localized cohesive-frictional damage. *Engineering Fracture Mechanics 150* (2015), 96–114.

[328] Saloustros, S., Pelà, L., Cervera, M., and Roca, P. A macro-modelling finite element technique for the realistic simulation of cracking in masonry structures. *Structural Analysis of Historical Constructions - Anamnesis, diagnosis, therapy, controls*, 2010 (2016), 284–290.

[329] Saloustros, S., Pelà, L., Cervera, M., and Roca, P. Finite element modelling of internal and multiple localized cracks. *Computational Mechanics 59*, 2 (2016), 299–316.

[330] Saloustros, S., Pelà, L., Cervera, M., and Roca, P. An Enhanced Finite Element Macro-Model for the Realistic Simulation of Localized Cracks in Masonry Structures: A Large-Scale Application. *International Journal of Architectural Heritage* (2017), (in press).

[331] Saloustros, S., Pelà, L., Cervera, M., Roca, P., and D'Ayala, D. F. Effect of pier-spandrel geometry on the in-plane response of masonry structures. In *16th International Brick and Block Masonry Conference* (Padova, Italy, 2016), C. Modena, F. da Porto, and M. Valluzzi, Eds., CRC Press 2016, pp. 339–346.

[332] Saloustros, S., Pelà, L., Roca, P., and Portal, J. Numerical analysis of structural damage in the church of the Poblet monastery. *Engineering Failure Analysis 48* (2014), 41–61.

[333] Samaniego, E. *Contributions to the continuum modelling of strong discontinuities in two-dimensional solids*. PhD thesis, Universitat Politècnica de Catalunya (UPC-BarcelonaTech), 2003.

[334] Sánchez, P. J., Sonzogni, V. E., and Huespe, A. E. Study of a stabilized mixed finite element with emphasis on its numerical performance for strain localization problems. *Communications in Numerical Methods in Engineering 24*, 4 (2007), 297–320.

[335] Sancho, J. M., Planas, J., Cendón, D. A., Reyes, E., and Gálvez, J. C. An embedded crack model for finite element analysis of concrete fracture. *Engineering Fracture Mechanics 74*, 1-2 (2007), 75–86.

[336] Sancho, J. M., Planas, J., Gálvez, J. C., Reyes, E., and Cendón, D. A. An embedded cohesive crack model for finite element analysis of mixed mode fracture of concrete. *Fatigue & Fracture of Engineering Materials & Structures 29*, 12 (dec 2006), 1056–1065.

[337] Saouma, V. E., and Zatz, I. J. An automated finite element procedure for fatigue crack propagation analyses. *Engineering Fracture Mechanics 20*, 2 (1984), 321–333.

[338] Schäfer, H. A contribution to the solution of contact problems with the aid of bond elements. *Computer Methods in Applied Mechanics and Engineering 6*, 3 (1975), 335–353.

[339] Schöllmann, M., Richard, H. A., Kullmer, G., and Fulland, M. A new criterion for the prediction of crack development in multiaxially loaded structures. *International Journal of Fracture 117*, 2 (2002), 129–141.

[340] Serpieri, R., Albarella, M., and Sacco, E. A 3D microstructured cohesive-frictional interface model and its rational calibration for the analysis of masonry panels. *International Journal of Solids and Structures 123* (2017), 110–127.

[341] Sethian, J. A., and Sethian, J. A. *Level set methods and fast marching methods : evolving interfaces in computational geometry, fluid mechanics, computer vision, and materials science*. Cambridge University Press, 1999.

[342] Shephard, M. S., Yehia, N. A. B., Burd, G. S., and Weidner, T. J. Automatic crack propagation tracking. *Computers and Structures 20*, 1-3 (1985), 211–223.

[343] Shi, J., Chopp, D., Lua, J., Sukumar, N., and Belytschko, T. Abaqus implementation of extended finite element method using a level set representation for three-dimensional fatigue crack growth and life predictions. *Engineering Fracture Mechanics 77*, 14 (2010), 2840–2863.

[344] Shieh-Beygi, B., and Pietruszczak, S. Numerical analysis of structural masonry: mesoscale approach. *Computers and Structures 86*, 21-22 (2008), 1958–1973.

[345] Siano, R., Sepe, V., Camata, G., Spacone, E., Roca, P., and Pelà, L. Analysis of the performance in the linear field of Equivalent-Frame Models for regular and irregular masonry walls. *Engineering Structures 145* (2017), 190–210.

[346] Sih, G. Some basic problems in fracture mechanics and new concepts. *Engineering Fracture Mechanics 5*, 2 (1973), 365–377.

[347] Sih, G. C., and Macdonald, B. Fracture mechanics applied to engineering problems-strain energy density fracture criterion. *Engineering Fracture Mechanics 6*, 2 (1974), 361–386.

[348] Sih, G. C. G. Strain-energy-density factor applied to mixed mode crack problems. *International Journal of fracture 10*, 3 (1974), 305–321.

[349] Silva, L. C., Lourenço, P. B., and Milani, G. Nonlinear discrete homogenized model for masonry walls out-of-plane loaded. *ASCE Journal of Structural Engineering 143*, 9 (2017).

[350] Sima, J. F., Roca, P., and Molins, C. Cyclic constitutive model for concrete. *Engineering Structures 30*, 3 (2008), 695–706.

[351] Simo, J., and Hughes, T. *Computational Inelasticity*, vol. 7. Springer, 1998.

[352] Simo, J. C., and Armero, F. Geometrically non-linear enhanced strain mixed methods and the method of incompatible modes. *International Journal for Numerical Methods in Engineering 33*, 7 (1992), 1413–1449.

[353] Simo, J. C., and Ju, J. W. Strain- and stress-based continuum damage models-I. Formulation. *International Journal of Solids and Structures 23*, 7 (1987), 821–840.

[354] Simo, J. C., Oliver, J., and Armero, F. An analysis of strong discontinuities induced by strain-softening in rate-independent inelastic solids. *Computational Mechanics 12*, 5 (1993), 277–296.

[355] Simo, J. C., and Rifai, M. S. A class of mixed assumed strain methods and the method of incompatible modes. *International Journal for Numerical Methods in Engineering 29*, 8 (1990), 1595–1638.

[356] Simone, A., Wells, G. N., and Sluys, L. J. From continuous to discontinuous failure in a gradient-enhanced continuum damage model. *Computer Methods in Applied Mechanics and Engineering 192*, 41-42 (2003), 4581–4607.

[357] Sinha, B. P., Gerstle, K. H., and Tulin, L. G. Stress-Strain Relations for Concrete Under Cyclic Loading. *ACI Journal Proceedings 61*, 2 (1964), 195–211.

[358] Slobbe, A., Hendriks, M., and Rots, J. Systematic assessment of directional mesh bias with periodic boundary conditions: Applied to the crack band model. *Engineering Fracture Mechanics 109* (2013), 186–208.

[359] Slobbe, A. T. *Propagation and band width of smeared cracks.* PhD thesis, Delft University of Technology, 2015.

[360] Slobbe, A. T., Hendriks, M. A. N., and Rots, J. G. Smoothing the propagation of smeared cracks. *Engineering Fracture Mechanics 132* (2014), 147–168.

[361] Song, J. H., Areias, P. M. A., and Belytschko, T. A method for dynamic crack and shear band propagation with phantom nodes. *International Journal for Numerical Methods in Engineering 67*, 6 (2006), 868–893.

[362] Song, J. H., and Belytschko, T. Cracking node method for dynamic fracture with finite elements. *International Journal for Numerical Methods in Engineering 77*, 3 (2009), 360–385.

[363] Steinmann, P., and William, K. Localization within the framework of micropolar elastoplasticity. In *Advances in Continuum Mechanics VI*. Springer, 1991, pp. 293–313.

[364] Stolarska, M., and Chopp, D. L. Modeling thermal fatigue cracking in integrated circuits by level sets and the extended finite element method. *International Journal of Engineering Science 41*, 20 (2003), 2381–2410.

[365] Stolarska, M., Chopp, D. L., Moës, N., and Belytschko, T. Modelling crack growth by level sets in the extended finite element method. *International Journal for Numerical Methods in Engineering 51*, 8 (2001), 943–960.

[366] Strouboulis, T., Babuška, I., and Copps, K. The design and analysis of the Generalized Finite Element Method. *Computer Methods in Applied Mechanics and Engineering 181*, 1 (2000), 43–69.

[367] Strouboulis, T., Copps, K., and Babuska, I. The generalized finite element method: an example of its implementation and illustration of its performance. *International Journal for Numerical Methods in Engineering*, May 1999 (2000), 1–16.

[368] Strouboulis, T., Copps, K., and Babuška, I. The generalized finite element method. *Computer Methods in Applied Mechanics and Engineering 190*, 32 (2001), 4081–4193.

[369] Sukumar, N., Dolbow, J. E., and Moës, N. Extended finite element method in computational fracture mechanics: a retrospective examination. *International Journal of Fracture 196*, 1-2 (2015), 189–206.

[370] Sukumar, N., and Prévost, J. H. Modeling quasi-static crack growth with the extended finite element method Part I: Computer implementation. *International Journal of Solids and Structures 40*, 26 (2003), 7513–7537.

[371] Swenson, D. V., and Ingraffea, A. Modeling mixed-mode dynamic crack propagation using finite elements: Theory and applications. *Computational Mechanics 3* (1988), 381–397.

[372] Tamayo-Mas, E. *Continuous-discontinuous modelling for quasi-brittle failure : propagating cracks in a regularised bulk.* PhD thesis, Universitat Politècnica de Catalunya (BarcelonaTech-UPC), 2013.

[373] Tamayo-Mas, E., and Rodríguez-Ferran, A. A new continuous-discontinuous damage model: Cohesive cracks via an accurate energy-transfer process. *Theoretical and Applied Fracture Mechanics 69* (2014), 90–101.

[374] Tamayo-Mas, E., and Rodríguez-Ferran, A. A medial-axis-based model for propagating cracks in a regularised bulk. *International Journal for Numerical Methods in Engineering 101*, 7 (2015), 489–520.

[375] Tambat, A., and Subbarayan, G. Isogeometric enriched field approximations. *Computer Methods in Applied Mechanics and Engineering 245-246* (2012), 1–21.

[376] Theocaris, P. S., and Andrianopoulos, N. P. The mises elastic-plastic boundary as the core region in fracture criteria. *Engineering Fracture Mechanics 16*, 3 (1982), 425–432.

[377] Theocaris, P. S., and Andrianopoulos, N. P. The T-criterion applied to ductile fracture. *International Journal of Fracture 50* (1982), 125–130.

[378] Theodossopoulos, D., and Sinha, B. A review of analytical methods in the current design processes and assessment of performance of masonry structures. *Construction and Building Materials 41* (2013), 990–1001.

[379] Tracey, D. Finite elements for determination of crack tip elastic stress intensity factors. *Engineering Fracture Mechanics 3*, 3 (1971), 255–265.

[380] Unger, J. F., Eckardt, S., and Könke, C. Modelling of cohesive crack growth in concrete structures with the extended finite element method. *Computer Methods in Applied Mechanics and Engineering 196* (2007), 4087–4100.

[381] Vardoulakis, I. A gradient flow theory of plasticity for granular materials. *Acta Mechanica 87* (1991), 197–217.

[382] Ventura, G., Budyn, E., and Belytschko, T. Vector level sets for description of propagating cracks in finite elements. *International Journal for Numerical Methods in Engineering 58*, 10 (2003), 1571–1592.

[383] Verhoosel, C. V., Remmers, J. J. C., and Gutiérrez, M. A. A partition of unityâĂŘbased multiscale approach for modelling fracture in piezoelectric ceramics. *International Journal for Numerical Methods in Engineering 82*, 8 (2010), 966–994.

[384] Voyiadjis, G. Z., Taqieddin, Z. N., and Kattan, P. I. Anisotropic damage-plasticity model for concrete. *International Journal of Plasticity 24*, 10 (2008), 1946–1965.

[385] Vu, V. D., Mir, A., Nguyen, G. D., and Sheikh, A. H. A thermodynamics-based formulation for constitutive modelling using damage mechanics and plasticity theory. *Engineering Structures 143* (2017), 22–39.

[386] Vu-Bac, N., Nguyen-Xuan, H., Chen, L., Lee, C. K., Zi, G., Zhuang, X., Liu, G. R., and Rabczuk, T. A phantom-node method with edge-based strain smoothing for linear elastic fracture mechanics. *Journal of Applied Mathematics 2013*, 1 (2013).

[387] Wawrzynek, P. A., and Ingraffea, A. R. Interactive finite element analysis of fracture processes: An integrated approach. *Theoretical and Applied Fracture Mechanics 8*, 2 (1987), 137–150.

[388] Weed, D. A., Foster, C. D., and Motamedi, M. H. A robust numerical framework for simulating localized failure and fracture propagation in frictional materials. *Acta Geotechnica 12*, 2 (2017), 253–275.

[389] Weihe, S., Ohmenhäuser, F., and Kröplin, B. A phenomenological approach to decompose geometrical and constitutive aspects of failure induced anisotropy. *Computational Materials Sceince 13* (1998), 177–194.

[390] Wells, A. The Condition of Fast Fracture in Aluminimum Alloys with Particular Reference to Comet Failures. Tech. rep., British Welding Research Association Report, 1955.

[391] Wells, G. N., and Sluys, L. J. A new method for modelling cohesive cracks using finite elements. *International Journal for Numerical Methods in Engineering 50*, 12 (2001), 2667–2682.

[392] Wells, G. N., Sluys, L. J., and de Borst, R. Simulating the propagation of displacement discontinuities in a regularized strain-softening medium. *International Journal for Numerical Methods in Engineering 53*, 5 (2002), 1235–1256.

[393] Westergaard, H. M. Bearing pressures and cracks. *Journal of Applied Mechanics 61* (1939), A49–A53.

[394] Williams, M. L. Investigation of structural failures of welded ships. *Welding Journal 32* (1953), 498–528.

[395] Wu, C.-H. Fracture Under Combined Loads by Maximum-Energy-Release-Rate Criterion. *Journal of Applied Mechanics, Transactions ASME 45*, 3 (1978), 553–558.

[396] Wu, J. Y., and Cervera, M. A thermodynamically consistent plastic-damage framework for localized failure in quasi-brittle solids: Material model and strain localization analysis. *International Journal of Solids and Structures 88-89* (2015), 227–247.

[397] Wu, J.-Y., and Cervera, M. On the equivalence between traction- and stress-based approaches for the modeling of localized failure in solids. *Journal of the Mechanics and Physics of Solids 82* (2015), 137–163.

[398] Wu, J. Y., Li, F. B., and Xu, S. L. Extended embedded finite elements with continuous displacement jumps for the modeling of localized failure in solids. *Computer Methods in Applied Mechanics and Engineering 285* (2015), 346–378.

[399] Wu, J. Y., Li, J., and Faria, R. An energy release rate-based plastic-damage model for concrete. *International Journal of Solids and Structures 43*, 3-4 (2006), 583–612.

[400] Xie, M., Gerstle, W. H., and Rahulkumar, P. Energy-Based Automatic Mixed-Mode Crack-Propagation Modeling. *Journal of Engineering Mechanics 121*, 8 (1995), 914–923.

[401] Yarema, S. Y. On the contribution of G. R. Irwin to fracture mechanics. *Materials Science 31*, 5 (1996), 617–623.

[402] Zhang, Y. *Simulation methods for durability assessment of concrete structures: multifield framework and strong discontinuity embedded approach.* PhD thesis, Vienna University of Technology, 2013.

[403] Zhang, Y., Lackner, R., Zeiml, M., and Mang, H. a. Strong discontinuity embedded approach with standard SOS formulation: Element formulation, energy-based crack-tracking strategy, and validations. *Computer Methods in Applied Mechanics and Engineering 287* (2015), 335–366.

[404] Zhang, Y., Macorini, M., and Izzudin, B. A. Mesoscale Partitioned Analysis of Brick-Masonry Arches. *Engineering Structures to appear* (2016), 142–166.

[405] Zhou, F., and Cheng, G. A coupled plastic damage model for concrete considering the effect of damage on plastic flow. *Mathematical Problems in Engineering 2015* (2015).

[406] Zi, G., and Belytschko, T. New crack-tip elements for XFEM and applications to cohesive cracks. *International Journal for Numerical Methods in Engineering 57*, 15 (2003), 2221–2240.

[407] Zienkiewicz, O. C., and Huang, G. C. A note on localization phenomena and adaptive finite-element analysis in forming processes. *Communications in Applied Numerical Methods 6*, 2 (1990), 71–76.

[408] Zienkiewicz, O. C., Huang, M., and Pastor, M. Localization problems in plasticity using finite elements with adaptive remeshing. *International Journal for Numerical and Analytical Methods in Geomechanics 19*, 2 (1995), 127–148.

[409] Zucchini, A., and Lourenço, P. A micro-mechanical homogenisation model for masonry: Application to shear walls. *International Journal of Solids and Structures 46*, 3-4 (2009), 871–886.

[410] Zucchini, A., and Lourenço, P. B. A micro-mechanical model for the homogenisation of masonry. *International Journal of Solids and Structures 39*, 12 (2002), 3233–3255.

This page is intentionally left blank.

Part II - Publications

This page is intentionally left blank.

A crack-tracking technique for localized cohesive-frictional damage

Savvas Saloustros · Luca Pelà · Miguel Cervera

Engineering Fracture Mechanics, 2015, Vol. 150, p. 96-114
doi: 10.1016/j.engfracmech.2015.10.039

Accepted Manuscript in *Engineering Fracture Mechanics*
DOI: 10.1016/j.engfracmech.2015.10.039

A crack-tracking technique for localized cohesive-frictional damage

Savvas Saloustros · Luca Pelà · Miguel Cervera

Submitted: 15 May 2015
Revised: 14 September 2015
Accepted 26 October 2015

Abstract This paper extends the use of crack-tracking techniques within the smeared crack approach for the numerical simulation of cohesive-frictional damage on quasi-brittle materials. The mechanical behaviour is described by an isotropic damage model with a Mohr-Coulomb failure surface. The correct crack propagation among the two alternative fracture planes proposed by the Mohr-Coulomb theory is selected with the use of an energy criterion based on the total elastic strain energy. The simulation of three benchmark problems of mixed-mode fracture in concrete demonstrates that the proposed methodology can reproduce the material's frictional characteristics, showing robustness, as well as mesh-size and mesh-bias independence.

Keywords Continuum Damage Model · Crack-Propagation · Cracking · Strain Localization · Mohr-Coulomb

Savvas Saloustros · Luca Pelà · Miguel Cervera

Department of Civil and Environmental Engineering
Universitat Politècnica de Catalunya (UPC-BarcelonaTech)
Jordi Girona 1-3, 08034 Barcelona, Spain.

International Center for Numerical Methods in Engineering (CIMNE)
Gran Capità, S/N, 08034 Barcelona, Spain.

E-mail: savvas.saloustros@upc.edu
E-mail: luca.pela@upc.edu
E-mail: miguel.cervera@upc.edu

Highlights

- A new crack propagation criterion consistent with the Mohr-Coulomb theory.
- A local crack-tracking technique accounting for material's frictional behaviour.
- Crack propagation direction evaluated by an energy criterion.
- Numerical simulation of mixed mode tests on concrete specimens.

1 Introduction

The accurate structural assessment of existing structures and the efficient design of new ones necessitate, apart from the comprehensive knowledge of the construction materials' characteristics, the realistic simulation of fracture phenomena, potentially leading to structural failure. Geomaterials, such as concrete, mortar and bricks, are typically found in the existing buildings. Owing to their high competence under compressive loading, the critical state in such materials is usually determined by their shear or tensile capacity. Under these two stress states, fracture initiates upon reaching the material's ultimate capacity and propagates exhibiting a drop in the stress (i.e. stress softening) for increasing strain. It is for this reason that these materials are termed as *quasi-brittle materials*.

Simulation of fracture in quasi-brittle materials within the computational failure mechanics is possible by means of two alternative ways: the discrete and the smeared crack approaches. In the discrete crack approach, cracking is modelled as an actual discontinuity within the discretized finite element domain. In

most of the numerical strategies of the discrete crack approach the onset and the propagation of the modelled crack bases on energy criteria. On the contrary, in the smeared crack approach the fracture is initiated by a stress/strain criterion and is modelled as smeared within the area of a finite element by modifying its mechanical properties (stiffness and strength). For a comprehensive review of discrete and smeared crack approaches the reader is referred to [13, 18, 20, 6, 5, 35].

Independently of the approach chosen to simulate fracture, it was soon realised that the numerical solution was strongly dependent on the discretization characteristics of the analysed domain, i.e. there was a strong mesh-bias dependence. To overcome this drawback, the aforementioned numerical strategies are usually enhanced by means of an integrated crack-tracking procedure. The use of crack-tracking techniques permits to identify the path for the crack propagation and allow in this way the application of the selected numerical strategy on a restricted part of the mesh. This necessity for the prediction of the crack propagation has triggered the research on the methodology to identify the correct crack path. Within the discrete crack method, a variety of procedures have been proposed. These include on one hand the use of local criteria, where the crack propagates towards the direction of the maximum circumferential stress at the vicinity of the crack tip [2, 40, 23, 44] or perpendicular to the direction of the maximum principal stress of an averaged stress/strain tensor at the vicinity of the advancing crack [42, 19]. On the other hand, global criteria have been proposed by Oliver and co-workers [27, 28] and Meschke & Dumstorff [22]. In the first methodology the crack-direction is determined by iso-lines running perpendicular to the maximum principal stresses, while in the latter both the crack orientation and extension are included as additional unknowns in the variational formulation. A comparison of the above methodologies is available in [16]. The inventory of crack propagation criteria within the smeared crack approach is still narrow. In the first application of crack-tracking techniques within the smeared approach Cervera & Chiumenti [5, 6] determined the crack direction using the aforementioned global criterion of Oliver and co-workers [28, 27]. Later, the concept of tracking of the crack path was applied at a local level [11] with the crack orientation determined to be perpendicular to the direction of the maximum principal stresses at the crack tip. Within this local criterion, spurious changes of propagation direction can be avoided by the opportune correction of the crack orientation based on potentially and consolidated damaged elements [11] or by means of delayed crack path fixation [39]. Another competent way for modelling strain localization within the smeared crack approach is the use of mixed stress/displacement or strain/displacement formulations [8, 9, 1, 7]. An important feature of these mixed formulations is their general applicability to two and three-dimensional problems without the necessity of an auxiliary crack-tracking technique.

A common ground of the majority of the presented crack propagation criteria is the explicit or implicit assumption that the crack propagates in a direction perpendicular to the maximum principal stress direction. This hypothesis is consistent with the Rankine failure criterion, in which cracking occurs when the maximum stress reaches the tensile strength of the material on a plane orthogonal to the first stress eigenvector (see Figure 1). However, for a failure criterion different from Rankine's (e.g. Tresca or Mohr-Coulomb, see Figure 1), the failure condition is satisfied in two potential planes diverging from the direction of the minimum principal stresses by an angle β [10, 43]. Inevitably, these cases require a crack propagation criterion that a) is consistent with the used failure criterion and b) is capable to select the correct propagation direction between the two potential ones.

The aim of this work is to propose a crack-propagation criterion that is consistently connected to the assumed failure criterion. The study focuses on the simulation of fracture in geomaterials, which present cohesive-frictional characteristics under shear failure. Therefore, cracks due to shear or tension are considered separately, with different propagation criteria for

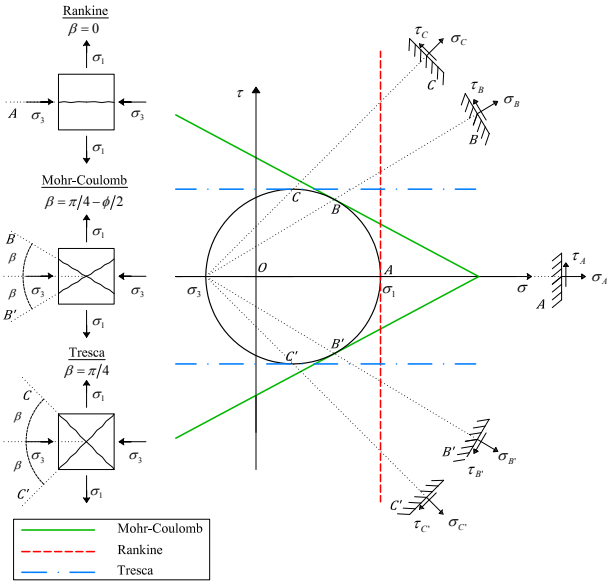

Fig. 1: Failure planes of Mohr-Coulomb, Rankine and Tresca failure criteria in the σ, τ plane.

each case. Crack propagation in the direction perpendicular to the maximum principal stresses is attained only for the case of pure tension. Under shear, the crack propagation direction is defined according to the Mohr-Coulomb planes of failure. To this end, the answer to the dilemma on the correct selection among the two alternative potential fracture planes defined by the Mohr-Coulomb theory is sought with the use of an energy criterion based on the total elastic strain energy.

The paper is organized in the following way. Section 2 includes a brief review of the Mohr-Coulomb theory, as well as the description of the tensile and shear failures considered in this work. Section 3 presents an overview of the used continuum damage model. Then, the proposed local crack-tracking algorithm is described in detail in Section 4. Section 5 presents numerical examples for the validation of the algorithm's capacity to simulate the frictional characteristics in quasi-brittle materials. The paper ends with some concluding remarks in Section 6.

2 Criterion for crack initiation and propagation

2.1 The Mohr-Coulomb theory of rupture

Geomaterials such as rocks, concrete and mortar, exhibit quite different strength in tension and compression. As a consequence, the simulation of fracture in these materials requires a pressure dependent criterion. Such criterion occurs in the Mohr-Coulomb theory of failure. Mohr's postulate, dating from 1900, states that failure occurs on a plane where the normal (σ) and the shear (τ) stresses reach a critical combination. For isotropic materials, in which the strength properties are the same when the shear stress is reversed, this critical combination can be expressed as

$$f = \tau \mp g(\sigma) = 0 \tag{1}$$

A special case of Mohr's postulate is when the bounding curves g(σ) are straight lines in the form of Coulomb's equation, dating from 1773

$$g(\sigma) = c - \sigma \tan\phi \tag{2}$$

where c is the cohesion and ϕ the internal friction angle of the material. The use of Coulomb's model of friction in Equation (1) results in the Mohr-Coulomb failure criterion

$$|\tau| = c - \sigma \tan\phi \tag{3}$$

In the σ, τ plane, Equation (3) represents two straight lines symmetrical to the σ-axis (see Figure 2). An alternative way for presenting Mohr-Coulomb's failure criterion is in terms of the principal stresses

$$f(\sigma_1, \sigma_3) = \frac{\sigma_1}{f_t} - \frac{\sigma_3}{f_c} - 1 = 0, \qquad \sigma_1 \geq \sigma_2 \geq \sigma_3 \tag{4}$$

where f_t and f_c are the tensile and compressive strength of the material equal to

$$f_t = \frac{2\,c\,\cos\phi}{1+\sin\phi} \tag{5a}$$

$$f_c = \frac{2\,c\,\cos\phi}{1-\sin\phi} \tag{5b}$$

From Equations (5) the friction angle and cohesion can be expressed in terms of the tensile and the compressive strength

$$\phi = \sin^{-1}\left(\frac{f_c/f_t - 1}{f_c/f_t + 1}\right) \qquad 0 \leq \phi < \pi/2 \tag{6a}$$

$$c = \frac{1}{2}\sqrt{f_c\, f_t} \tag{6b}$$

Figure 3 illustrates the dependence of the failure surface on the compressive to tensile strength ratio (or the friction angle and cohesion). As expected, for $f_c/f_t = 1$ ($\phi = 0$) the Mohr-Coulomb failure criterion coincides with Tresca's hexagon. On the other end, a large compressive to tensile strengths ratio ($f_c/f_t \to \infty$ or $\phi = \pi/2$) results in the coincidence of the Mohr-Coulomb failure surface with Rankine's one (Figure 3).

2.2 Failure types

In the present work, under plane stress conditions, two types of failure are considered depending on the stress-state at the location of the crack origin: a) tensile failure and b) shear failure. Tensile failure occurs under a stress state of pure tension, i.e. the criterion is violated in the first quadrant in Figure 3, and is characterized by a crack forming in a direction perpendicular to the maximum principal stress/strain. Shear failure occurs when $\sigma_1\sigma_3 < 0$, viz. the criterion in Figure 3 is violated either in the second or fourth quadrant. Under such conditions, the normal and shear stresses reach a critical combination on two planes. These planes, noted by the points B and B' in Figure 2, are symmetrical with respect to the direction of the minimum principal stress diverging from it by an angle $\beta = \pm(\pi/4 - \phi/2)$, depending on the frictional characteristics of the material.

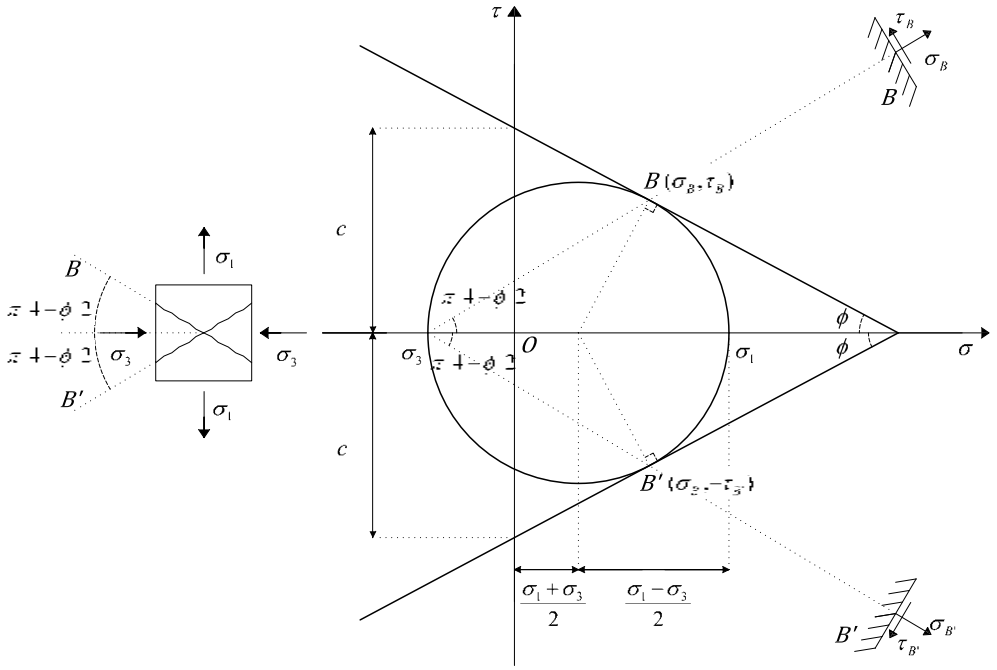

Fig. 2: Mohr-Coulomb failure criterion in the σ, τ plane.

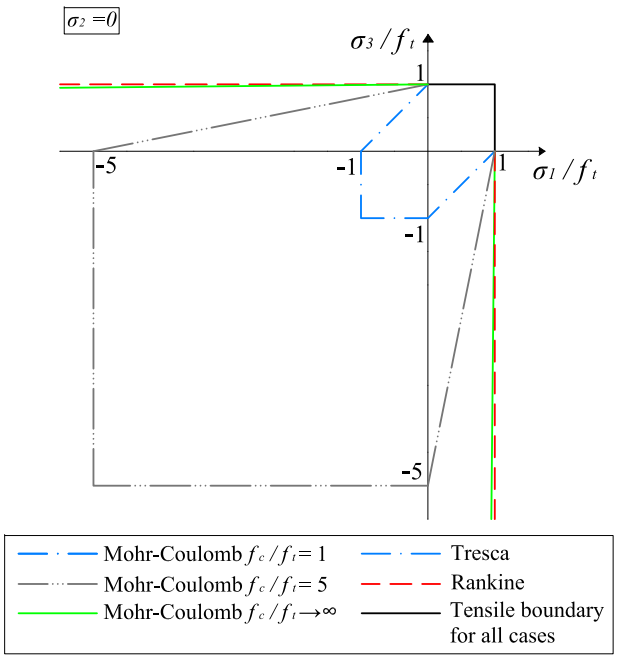

Fig. 3: Comparison of Mohr-Coulomb failure criterion with Tresca and Rankine in the biaxial stress plane.

3 Continuum damage model

In this work, fracture of material is simulated by the use of a constitutive model based on continuum damage mechanics [3]. This model has proven to be adequate for the analysis of structures made of quasi-brittle materials such as concrete (e.g. [5, 6]) and masonry (e.g. [32, 33, 31]).

The constitutive equation for the damage model is defined as

$$\boldsymbol{\sigma} = (1 - d)\,\bar{\boldsymbol{\sigma}} = (1 - d)\,\boldsymbol{C} : \boldsymbol{\varepsilon} \tag{7}$$

where $\bar{\boldsymbol{\sigma}}$ denotes the effective stress tensor [21] computed in terms of the total strain tensor $\boldsymbol{\varepsilon}$ and $\boldsymbol{C}$ is the usual fourth order isotropic linear-elastic constitutive tensor. The damage index d represents the damage state of the material, varying from zero when the material is undamaged to one when the material is completely damaged. In this work, the use of a single damage variable is justified by our aim to investigate fracture due to only tensile and shear stress states. In the general case, where damage due to compression may be critical, an equivalent damage model with two separate damage variables for compressive and tensile damage can be used (see [36, 34, 38, 30]).

The equivalent stress is a positive scalar depending on the effective stress tensor and the failure criterion assumed. In the current work, according to the Mohr-Coulomb theory, it assumes the following form

$$\Sigma = \bar{\sigma}_1 - \frac{f_t}{f_c}\,\bar{\sigma}_3 \tag{8}$$

where $\bar{\sigma}_1$ and $\bar{\sigma}_3$ are the maximum and minimum effective principal stresses, respectively.

The damage criterion can be expressed as

$$\Phi(\Sigma, r) = \Sigma - r \leq 0. \tag{9}$$

The internal stress-like variable r represents the current damage threshold. Its value is determined as the maximum between $r_0 = f_t$ and the greatest value ever attained by the equivalent stress Σ during the loading history [3]

$$r = \max[r_0, max(\Sigma)]. \tag{10}$$

Following the above, the internal damage variable d can be defined in terms of the corresponding current value of the threshold $d = d(r)$, so that it is a monotonically increasing function such that $0 \leq d \leq 1$. In particular, the following exponential function is considered

$$d(r) = 1 - \frac{r_0}{r}\exp\left\{-2\,H_d\frac{r - r_0}{r_0}\right\} \quad r_0 \leq r \tag{11}$$

where $H_d \geq 0$ is the discrete softening parameter. For ensuring mesh-size independence the specific dissipated energy D is adjusted for each damaged finite element so that the equation

$$D = \left(1 + \frac{1}{H_d}\right)\frac{(f_t)^2}{2\,E}. \tag{12}$$

Using Equations (11) and (12) the discrete softening parameter is defined as

$$H_d = \frac{l_{dis}}{l_{mat} - l_{dis}} \tag{13}$$

where the material characteristic length $l_{mat} = 1/H_{mat}$, with $H_{mat} = (f_t)^2/(2\,E\,G_f)$, depends only on the material properties. Finally, the discrete crack characteristic width can be taken as the representative size of the element $l_{dis} = l_e = \sqrt{2\,A_e}$, being A_e the surface of the triangular element.

4 The local crack-tracking algorithm

The proposed crack-tracking technique is based on the algorithm developed by Cervera and co-workers [11]. This section includes an overview of the algorithm, focusing on the added features for the simulation of cohesive-frictional damage.

The methodology bases on a labelling system and is applied at the beginning of each load increment. According to the stress field of the previous converged load increment, the algorithm identifies new cracks within the discretized domain. Following this, the propagation of the old and the new cracks is defined according to the stress state of the crack tip or the crack origin elements, respectively. Then, the elements lying on the crack path are recognized and labelled as able to damage. This labelling system remains un-changed during the equilibrium equations of the current load increment, when the stress field is evaluated activating the constitutive law presented in Section 2 only for the labelled as able to damage elements. Figure 4 illustrates the main steps of the proposed algorithm that are detailed in the following sections.

4.1 New crack detection

The crack-tracking algorithm starts with the detection of new cracks. For the purposes of this work, new cracks originate at the boundaries of the domain, at elements satisfying Mohr-Coulomb's failure criterion, as defined in Equation (8). In the case of several elements reaching failure at the same increment, an *exclusion radius* criterion is applied [11]. Under this criterion, the element with the highest value of $f(\sigma_1, \sigma_3)$ within a defined by the user radius r_{excl} is labelled as a *crack root* element.

4.2 Crack propagation

The next step of the algorithm consists in determining the crack propagation direction for new and old cracks. This procedure takes place either at the *crack root* elements for new cracks or at the *crack tip* elements for consolidated cracks. A *crack tip* element is an element located at the propagating front of an old crack.

Depending on the stress-state of the *crack tip/root* element, two types of failure may occur and, consequently, two alternative values of the propagation angle ψ^0 can be defined for the crack tip element:

(a) *Tensile failure.* An element fails in tension when its principal stresses are greater or equal to zero. In this case, the crack propagates towards a direction

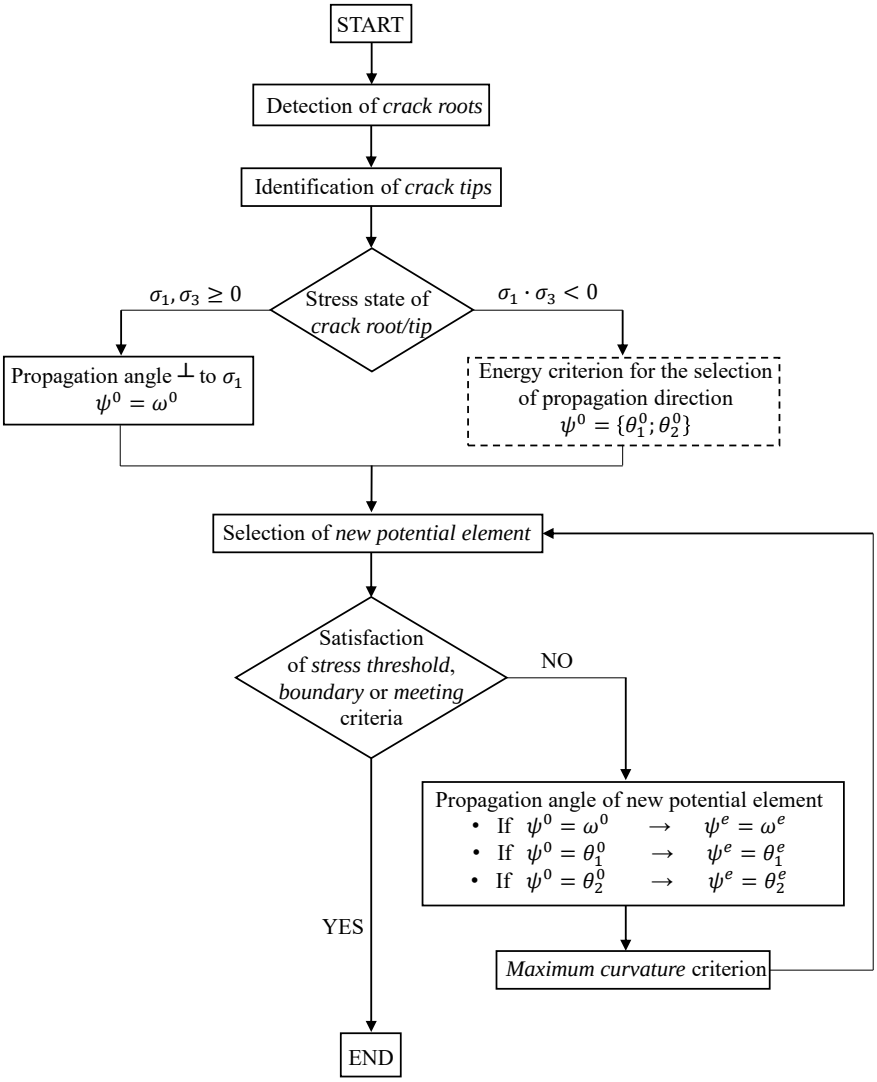

Fig. 4: Flowchart with the basic steps of the proposed local crack-tracking algorithm.

ω, perpendicular to the direction of the maximum principal stress.

(b) *Shear failure*. An element fails in shear when it has at least one tensile and one compressive principal stresses. As described in Section 2.2, in this case failure can occur in two possible planes according to the Mohr-Coulomb theory of fracture, see Figure 2. The two possible crack-propagation directions $\theta_{1,2}$ are

$$\theta_1 = \omega + \left(\frac{\pi}{4} - \frac{\phi}{2}\right) \tag{14a}$$

$$\theta_2 = \omega - \left(\frac{\pi}{4} - \frac{\phi}{2}\right) \tag{14b}$$

The selection among these two fracture planes is decided in this work with the use of an energy-based criterion that will be presented in Section 4.3.

Once the propagation direction for each crack is decided, then the path of each crack is evaluated and the elements pertaining to it are labelled as *potential elements* to damage in the current load increment. Figure 5b illustrates this procedure. Starting from the *crack tip/root* element, the neighbour element lying on the defined crack propagation direction is labelled as the *new potential element*. To this end two actions are carried-out:

1. Determination of the crack angle of the new potential element. During an increment each crack will propagate in the direction determined from the

crack tip/root element, i.e. either perpendicular to the direction of the maximum principal stress or according to Equations (14). However, the value of the cracking angle of the *new potential element* (ψ^e) is calculated according to its own stress state and therefore is denoted by ω, θ_1^e, or θ_2^e.

2. Control and correction of the propagation angle. The *maximum curvature criterion* ensures that no spurious change occurs in the crack direction [11]. To achieve this purpose, the angle a between the vector $\overrightarrow{V}_e$ and the vector $\overrightarrow{V}_c$ is calculated. The vector $\overrightarrow{V}_e$ denotes the crack direction for the new potential element. The vector $\overrightarrow{V}_c$ represents the vector sum of the crack directions of both the potential elements and the consolidated damaged elements within a neighbourhood of radius r_{neigh} (see Figure 5b). The radius r_{neigh} is a length defined by the user and it is measured from the centroid of the current tip potential element. In case of $\alpha \leq \alpha_{max}$, the vector $\overrightarrow{V}_e$ is used for the crack propagation direction of the new potential element. In case of $\alpha > \alpha_{max}$, the vector $\overrightarrow{V}_c$ is used for the definition of the crack propagation direction

Following these two actions, the *next potential element* lying on the crack path can be recognised. The above procedure continues until two cracks coalesce (crack meeting criterion), a crack reaches the mesh boundary (boundary criterion) or the value $f(\sigma_1, \sigma_3)$ (see Equation (4)) of the new potential element is lower than a threshold defined by the user (stress threshold criterion). In this work the threshold used is $f(\sigma_1, \sigma_3) = -0.25$ [11].

After performing the above procedure for all the new and old cracks of the analysed domain, each element is clarified into two categories. The first one declares the cracking state of the element:

- *Intact & unable to damage element:* element that does not belong to any crack and will remain linear elastic.
- *Intact & able to damage element:* element that belongs to a crack path and it is allowed to damage during the current load increment.
- *Damaged element:* element belonging to a consolidated crack and has entered the non-linear regimen.

The second category denotes the selected crack propagation direction of each damaged element.

- ω: damaged element with crack propagation direction perpendicular to the direction of the maximum principal stress.
- θ_1: damaged element with crack propagation direction equal to $\theta_1 = \omega + (\pi/4 - \phi/2)$.
- θ_2: damaged element with crack propagation direction equal to $\theta_2 = \omega - (\pi/4 - \phi/2)$.

4.3 Mohr-Coulomb failure plane selection

The selection between the two possible failure planes proposed by the Mohr-Coulomb theory is of great importance within the proposed algorithm, since it determines the out-come of the crack propagation. In this work, a solution to this dilemma is given by evaluating the elastic strain energy fields of the two possible crack paths prior to their opening. The selected path is the one with the highest stored elastic strain energy. This choice is based on the premise that upon fracture the material neighbouring to the fracture zone will unload elastically. In this way the strain energy release is maximized, minimizing the total strain energy of the body. This procedure also minimizes the energy dissipated during the development of the fracture. Similar criteria have proved to be successful in geotechnical engineering simulations for determining the propagation of fracture in faults (see [29, 26]).

The process for the selection of the crack propagation direction starts after the crack tip and crack root elements are defined (see Figure 4). Then for each crack tip/root element the procedure, illustrated in Figure 6, for determining the crack propagation direction is as follows:

1. The two possible angles for the crack propagation of the *crack tip/root* element are defined.
2. For each of these two angles, the two possible crack paths are determined and the composing potential elements on each of them are defined (Figure 5a). This occurs in the following order:
   i. The crack propagation direction of the crack tip element is defined at the direction of θ_1.
   ii. For this crack propagation direction, the *new potential element* is identified.
   iii. The distance δ_κ between the centroid of the *new potential element* and the centroid of the *crack tip/root element* is computed.
   iv. If the new potential element lies within the limit of the radius r_{crack} (defined in the step (vii) of this section) the total strain energy W^e on the volume V^e are computed

$$W^e = \int_{V_e} \frac{1}{2} \boldsymbol{\sigma} : \boldsymbol{\varepsilon} \, dV \tag{15}$$

where $\boldsymbol{\sigma}$ and $\boldsymbol{\varepsilon}$ are the stress and strain tensors of the *new potential element* and V^e is the volume of the element.

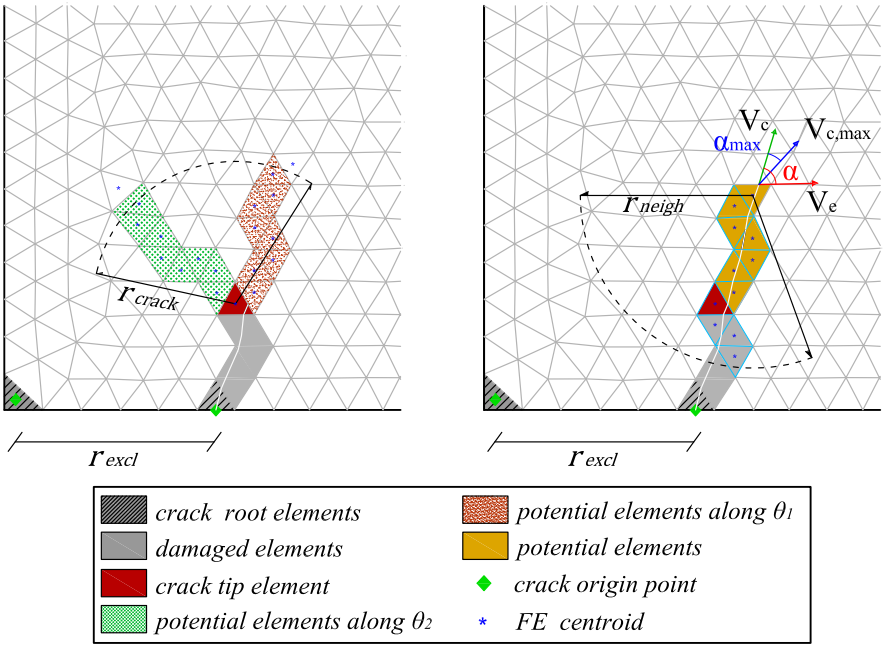

Fig. 5: Basic steps of the proposed local crack-tracking algorithm: selection between the two possible crack propagation directions for frictional failure (a) and labelling of potential elements with angle correction (b).

v. The propagation angle of the *new potential element* is calculated and the maximum curvature criterion is applied.
vi. The *new potential element* is named as *current crack tip* and the above steps are repeated.
vii. The procedure stops when the *crack meeting criterion*, *the boundary criterion* or the *crack limit criterion* is satisfied. The first two are the same criteria as described in Section 4.2. The crack limit criterion is satisfied when the distance between the crack tip/root and the new potential element δ_κ overpasses a radius r_{crack} (see Figure 5a). This radius is calculated for each crack at each load increment. It is the minimum between a radius defined by the user r_{crit} and the distance between the crack tip/root and the last potential element before the crack meets a mesh boundary or another crack.
viii. When one of the above criteria is met, the steps from (ii) to (vii) are repeated with the crack propagation direction of the crack tip/root element set as θ_2.

3. To this end, with the composing elements of the two possible cracks and their strain energy and volume defined, the total strain energy per crack volume for each of the two cracks can be defined as

$$w_1 = \frac{1}{V_1}\sum_{i}^{n} W_i^e \tag{16a}$$

$$w_2 = \frac{1}{V_2}\sum_{j}^{n} W_j^e \tag{16b}$$

The crack volume at each direction (V_1, V_2) is defined as the sum of the volume of the elements (V^e) pertaining to the crack path,

$$V_1 = \sum_{i}^{n} V_i^e \tag{17a}$$

$$V_2 = \sum_{j}^{n} V_j^e \tag{17b}$$

where $i = 1, n$ are the elements on the direction of the crack determined with θ_1 and $j = 1, m$ are the elements on the direction of the crack determined with θ_2.
Finally, the selected crack direction for the particular increment is the direction with the greatest strain energy per crack volume.

5 Numerical Examples

In this section, the proposed formulation is applied to the analysis of three benchmark problems for mixed

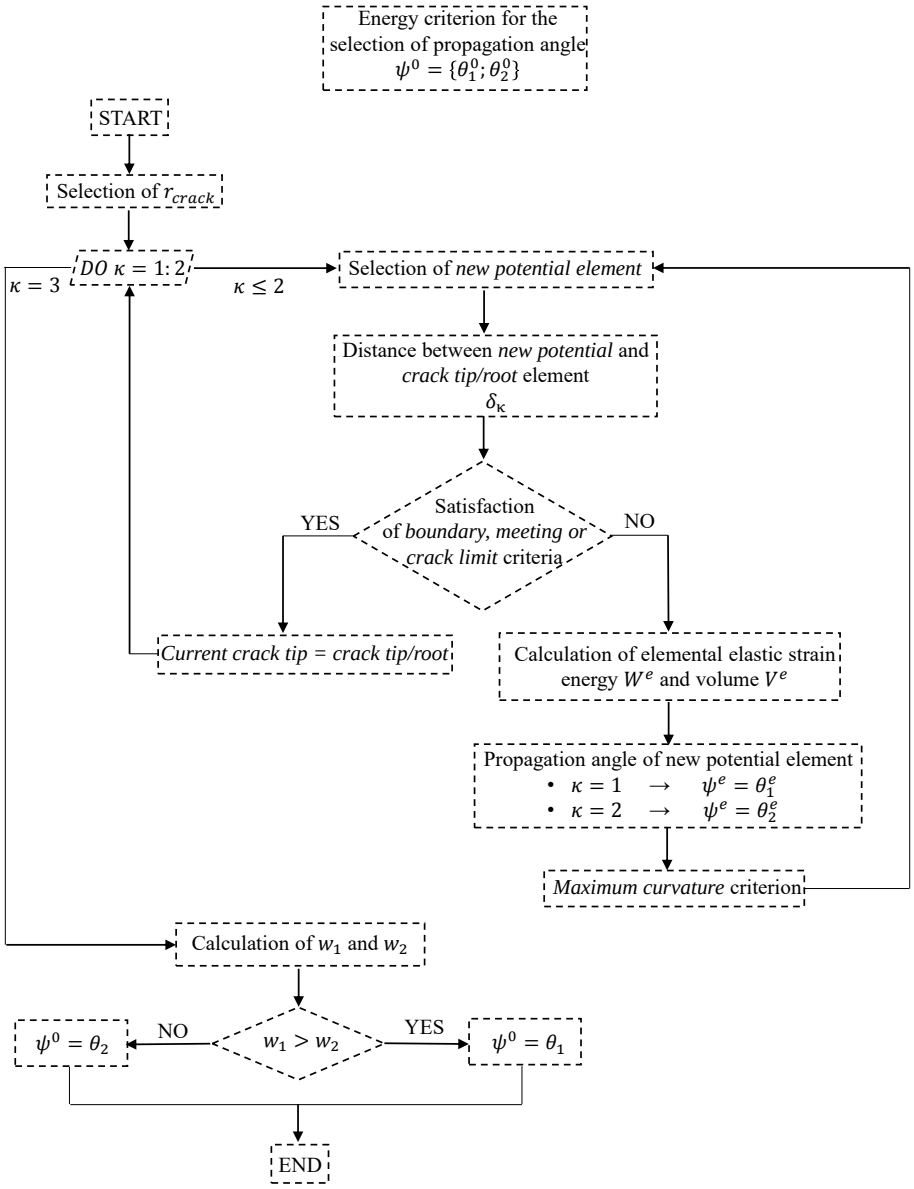

Fig. 6: Flowchart with the procedure for the selection of the frictional crack propagation direction θ_1 or θ_2.

mode fracture in concrete. They correspond to a series of experiments on a double edge notched (DEN) specimen under non-proportional loading, performed by Nooru-Mohamed [25]. The tested concrete specimen is square shaped with dimensions $200 \times 200 \times 50\ mm^3$ and two notches with a depth of 25 mm and height of 5 mm at each lateral side. The DEN specimen was glued to four platens in the configuration of Figure 7. The numerical simulations correspond to the load-path 4 of the experimental campaign, which was performed in two steps. In the first one, a compressive load was applied to the lateral platens in displacement control up to a value P_s. Subsequently, a traction load P was applied over the top platen in displacement control keeping the lateral force Ps constant under load control. Figure 8 illustrates the cracking patterns observed at the DEN specimens after the experiments for the load paths 4a (specimen 48-03), 4b (specimen 46-05) and 4c (specimen 47-06) corresponding to lateral force $P_s = 5\ kN$, $10\ kN$ and $27.5\ kN$ respectively. Two concrete specimens were tested for load-path 4b, whereas only one specimen was tested for load-paths 4a and 4c. Nooru-Mohamed mentions that although the experiment itself as well as the experimental apparatus were sophisticatedly designed, undesirable eccentricities in the experiment can be provoked by the skew-symmetric bonding

of the specimen to the steel platens, the possible relative rotations between the two used coupled frames and the non-symmetric behaviour of the springs (in the longitudinal direction) that were used to avoid the in-plane rotation of the DEN specimen. For a comprehensive discussion on the experimental procedure, apparatus and problems the reader is referred to the original work [25, 24].

The material parameters used for the numerical simulation are based on the data provided by Nooru-Mohamed [Nooru-Mohamed 1992] and are the same for the three different load paths: tensile strength $f_t = 3.0$ MPa, Young Modulus $E = 30$ MPa, Poisson's ratio $= 0.2$, and mode I fracture energy $G_f = 110$ J/m^2.

The three experiments are discretized in an unstructured mesh with average mesh size of $h_e = 2.5$ mm (8394 nodes). For load path 4c a second mesh is used, with average mesh size of $h_e = 5$ mm (2162 nodes), aiming to investigate the mesh-size and mesh-bias dependency of the algorithm. The discretization consists of 2D plane-stress 3-noded linear triangular elements. The computational boundary conditions are exactly skew-symmetrical, with the central node of the mesh being fixed in the horizontal and vertical degrees of freedom. Regarding the input parameters for the local crack-tracking algorithm, r_{excl}=0.12 m and r_{crit}=0.03 m for all the presented examples. The definition of α_{max} and r_{neigh} has been unnecessary since no important bending occurs.

Calculations are performed with an enhanced version of the finite element program COMET [4, 12], while pre and post-processing with GiD [17]. Both software have been developed at the International Center for Numerical Methods in Engineering (CIMNE), in Barcelona. The discrete weak form of the problem is solved incrementally in a step-by-step manner. At each load increment, the corresponding nonlinear equations are solved with the use of a modified Newton-Raphson method (using the secant stiffness matrix) along with a line search procedure. Convergence of an increment is attained when the ratio between the iterative residual forces and the norm of the total residual forces is lower than 0.01 (1%).

The outline of each simulated experiment is as follows. Firstly, the two possible solutions indicated by the Mohr-Coulomb fracture criterion are presented. It is noted that for these analyses the procedure for the angle selection has been turned-off and the angle of the fracture is selected explicitly to be equal to θ_1 or θ_2 according to the studied case. Following this, the capacity of the local crack-tracking algorithm, proposed in Section 4, to model the frictional characteristics of quasi-brittle materials is demonstrated by presenting

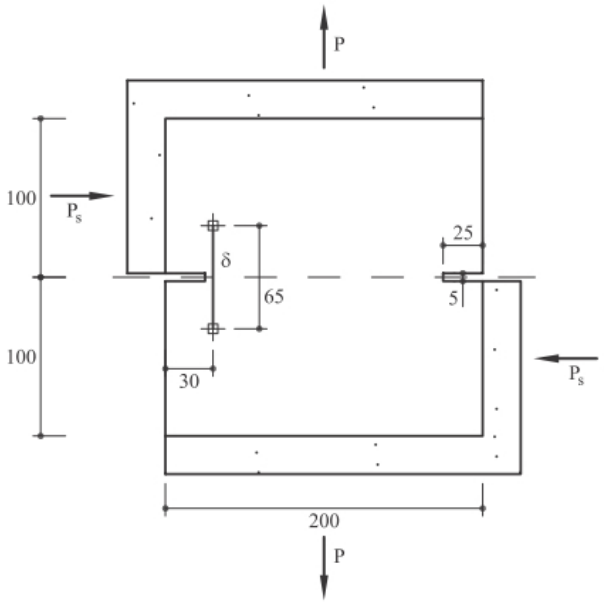

Fig. 7: Geometry and load for double edge notched specimen [25]

the numerical solutions for three different compressive to tensile strength ratios $f_c/f_t = 5$; 20, ∞. For comparison purposes, each example is simulated also with the use of the previous version of the local crack-tracking algorithm based in the Rankine failure criterion [11].

5.1 Load-path 4a

For load-path 4a the lateral compressive load applied during the first stage of the experiment is Ps $= 5$ kN. At the second stage, the vertical displacement δ is gradually increased keeping the lateral load P_s constant.

As commented, the numerical analysis of the specimen starts by presenting the two possible solutions according to the Mohr-Coulomb postulate, for $f_c/f_t = 20$. Hence, the results presented in Figure 9 have been produced by turning off the procedure described in Section 4.3 for the selection of the crack propagation direction. In these analyses, the fracture under shear propagates at a constant angle θ_1 (Figure 9a) or θ_2 (Figure 9b) depending on the case. Note that when damage occurs under pure tension the fracture propagates at a direction perpendicular to the maximum principal stresses (i.e. ω). It can be seen in Figures 9a and 9b that, for this load-path, the cracking of the specimen is mostly defined by tensile failure. It is only a small part at the middle of the crack that fails under shear and where the direction of the crack is different in the two analysed cases. As a result, the dissipated energy is very similar

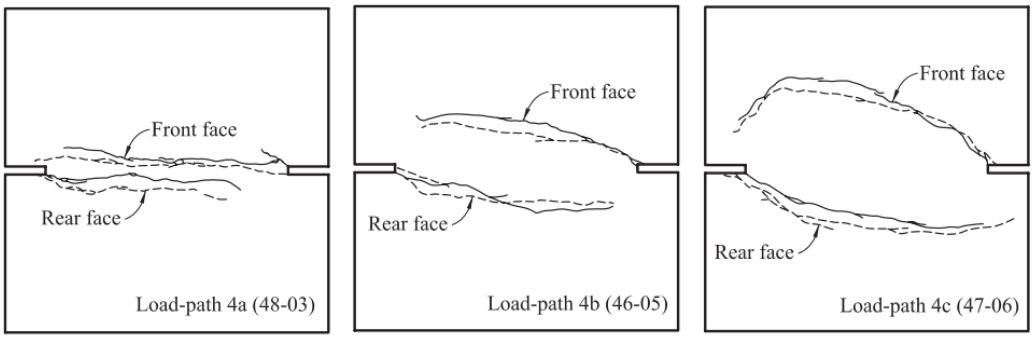

Fig. 8: Experimentally obtained crack patterns in the front (solid lines) and rear (dashed lines) faces for double edge notched specimens [25].

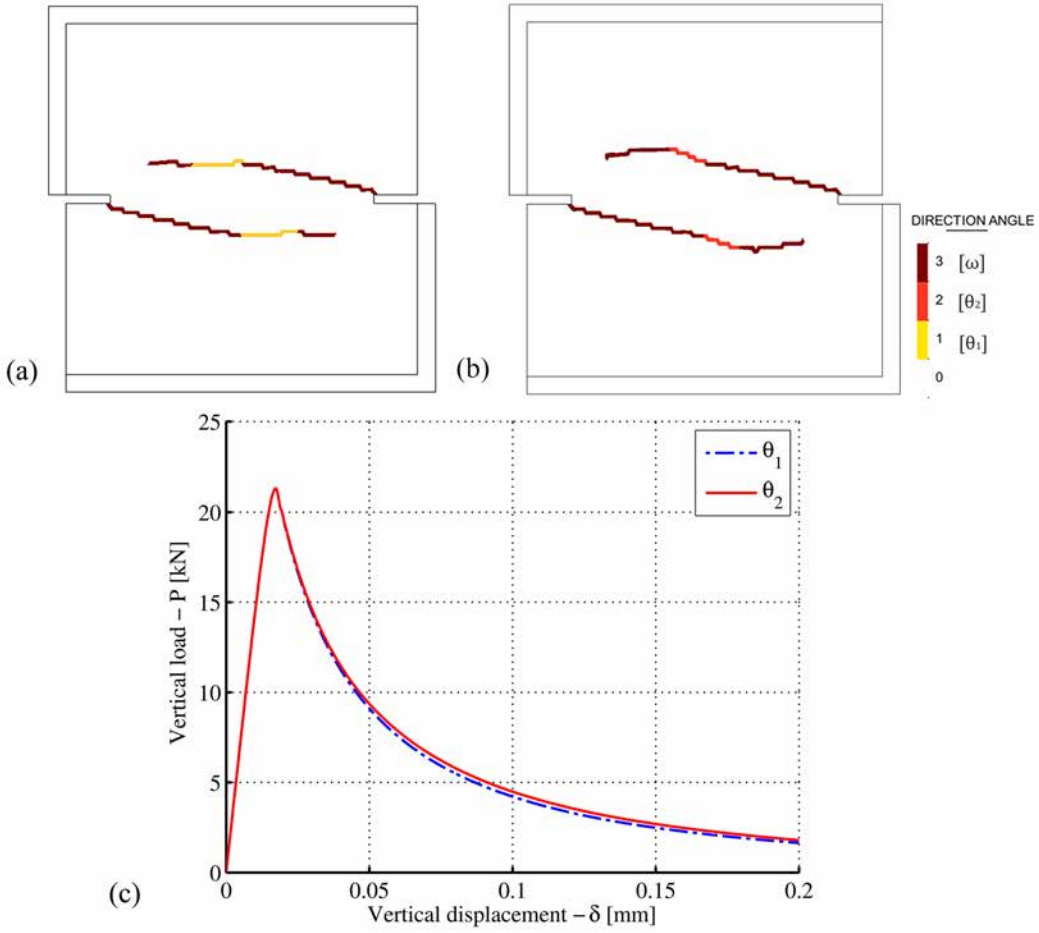

Fig. 9: Load-path 4a for $f_c/f_t = 20$: contour of the selected crack propagation direction in the damaged elements case θ_1 (a), case θ_2 (b) and load vs displacement (P-δ) for the two possible fracture planes (c).

for both cases. Nevertheless, the less curved crack for a propagation direction θ_1 results in the slightly lower dissipated energy, see Figure 9c.

The capacity of the local crack-tracking algorithm to capture the effect of the material's frictional properties is demonstrated by considering three different compressive to tensile strength ratios: $f_c/f_t = 5; 20; \infty$. As shown in Figure 10, the effect of the frictional angle is evident in the crack propagation direction of the part of the crack failing under shear. In the same figure,

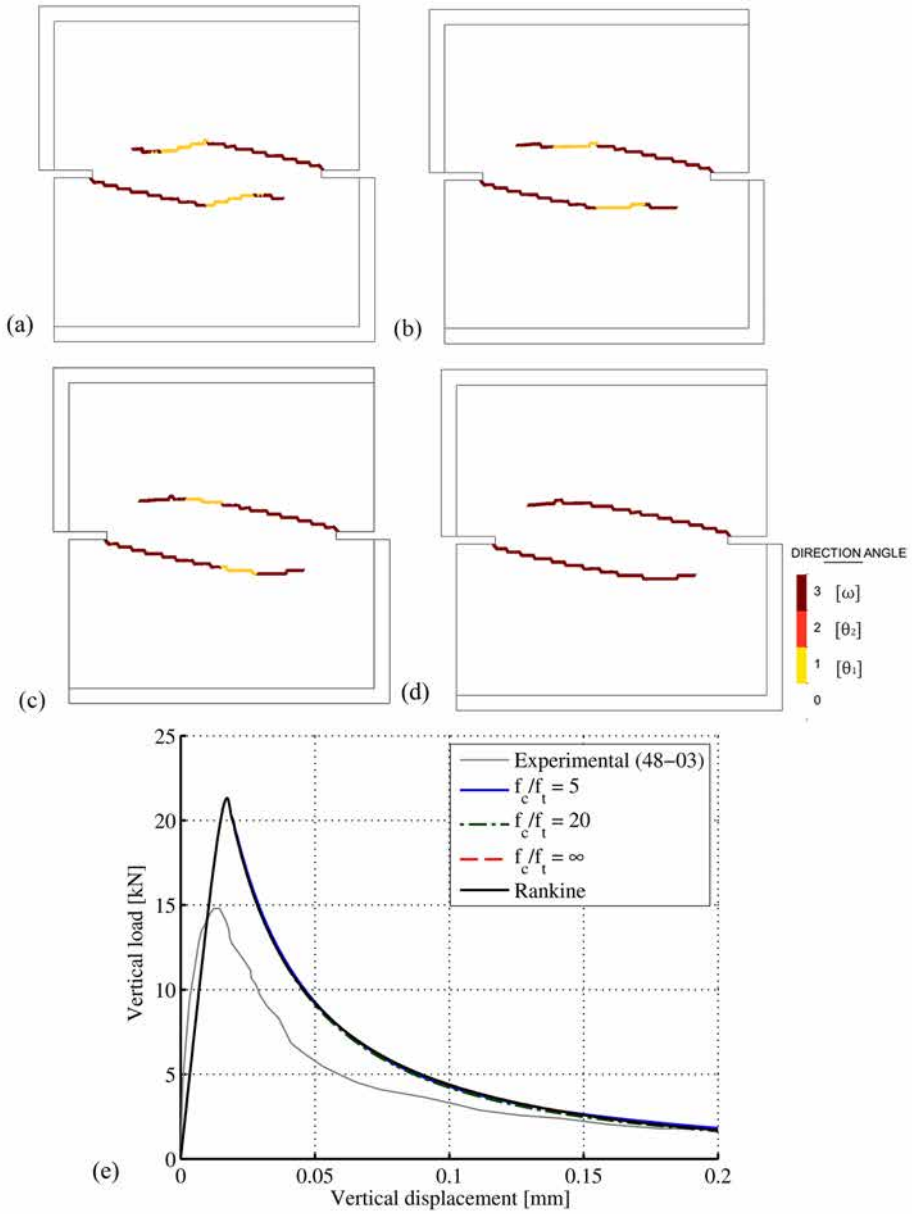

Fig. 10: Load-path 4a: contour of the selected crack propagation direction in the damaged elements for Mohr-Coulomb's criterion and $f_c/f_t = 5$ (a), $f_c/f_t = 20$ (b), $f_c/f_t \approx \infty$ (c); for Rankine's criterion and $f_c/f_t = 20$ (d) and load vs displacement (P-δ) for different compressive to tensile strength ratios (e).

we can see that the curvature of the crack using the Mohr-Coulomb failure criterion with $f_c/f_t \approx \infty$ (Figure 10c) is identical to that obtained by using Rankine (Figure 10d). This outcome illustrates that the (unrealistic) use of a friction angle of almost $\pi/2$ results in the coincidence of the Mohr-Coulomb failure criterion with that of the Rankine for tensile and shear stress states ($\psi \approx \pi/2 \Rightarrow \left(\frac{\pi}{4} - \frac{\phi}{2}\right) \approx 0$) as presented previously in section 2.1, Figure 3.

The small part of the crack failing under shear leads to the insignificant differences in the dissipated energy for the specific load path for the different values of f_c/f_t, as illustrated in the graph of Figure 10e. In overall, the obtained load vs. displacement curves follow the same pattern as the experimental one presenting a slowly curving part when the cracks propagate and finally entering into a softening branch upon the cracks have sufficient length to develop the failure mechanism. However, differences exist in terms of peak load and dissipated energy. This divergence has been observed

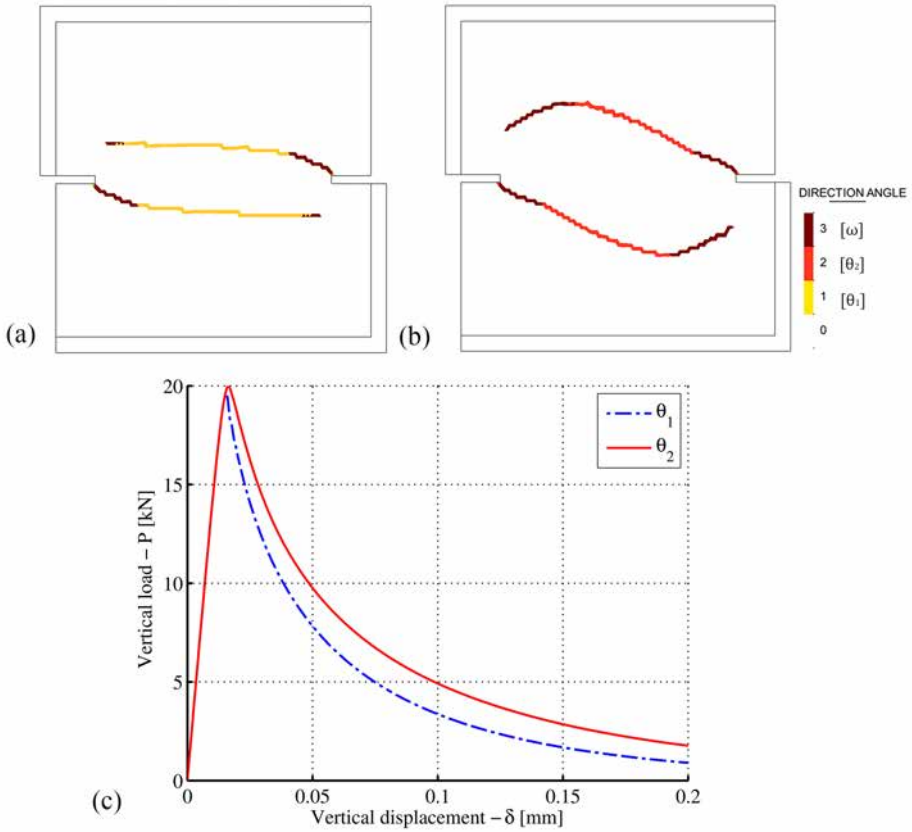

Fig. 11: Load-path 4b for $f_c/f_t = 20$: contour of the selected crack propagation direction in the damaged elements case θ_1 (a), case θ_2 (b) and load vs displacement (P-δ) for the two possible fracture planes (c).

by several authors (e.g., [15, 41, 14, 37]) simulating the same test and can be possibly attributed to the experimental problems previously described.

5.2 Load-path 4b

In this load-path the lateral compressive force applied in the first step is P_s=10 kN. Then, a vertical traction is imposed by increasing gradually the vertical displacement δ under the constant effect of P_s.

As for load-path 4a, first the procedure for the angle selection is turned-off and the two possible solutions according to the Mohr-Coulomb postulate, i.e. θ_1 or θ_2 for failure under shear are presented for $f_c/f_t = 20$. As shown in Figure 11, the two cracks initiate under tension, but soon after, they evolve under a shear stress state. As a consequence, the crack propagation direction plays an important role to both the curvature of the crack and the dissipated energy, which can be appreciated in Figures 11 a & b and Figure 11c, respectively. In this case it is evident that a crack propagating at a direction θ_1 leads to a shorter crack with less curvature and to less dissipated energy.

The effect of the material frictional characteristics is evident in Figure 12, which presents the obtained crack trajectories for $f_c/f_t = 5; 20; \infty$. As it is shown, the proposed formulation succeeds both in capturing the frictional properties of the material and in selecting the θ_1 crack propagation direction in all the cases. Smaller compressive to tensile strengths ratios result in a smaller curvature of the crack trajectory and in less dissipated energy (see Figure 12e). For the ratio $f_c/f_t = 5$ the two cracks reach the opposite notch and the specimen starts rotating around the developed compressive strut, resulting in the sudden drop of load, as can be appreciated in Figure 12e. Once again, when a high compressive to tensile strength ratio is selected, the solution approaches the Rankine's one (see Figure 12c & d). Note that when f_c/f_t tends to infinity the two potential crack propagation directions are almost equal (i.e. $\theta_1 \approx \theta_2$) in Mohr-Coulomb's criterion, resulting in an identical possible crack path in most cases.

Comparing to the experimental results, the obtained load vs. displacement graphs (Figure 12e) show an

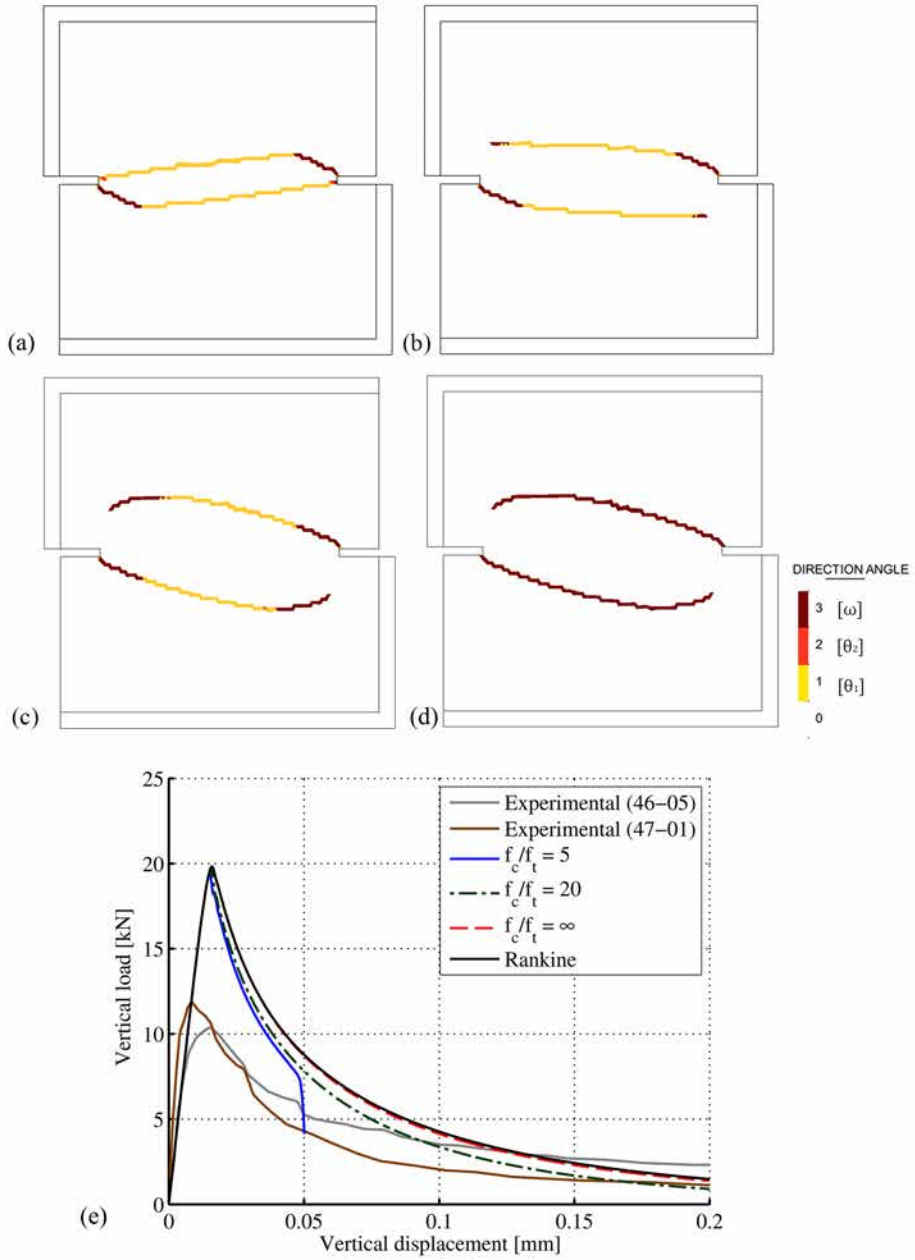

Fig. 12: Load-path 4b: contour of the selected crack propagation direction in the damaged elements for Mohr-Coulomb's criterion and $f_c/f_t = 5$ (a), $f_c/f_t = 20$ (b), $f_c/f_t \approx \infty$ (c); for Rankine's criterion and $f_c/f_t = 20$ (d) and load vs displacement (P-δ) for different compressive to tensile strength ratios (e).

overestimation of the predicted peak load. The same discrepancies have been observed in references (e.g. [16, 14, 39, 37]). As commented before, the reason for this divergence may be due to the possible experimental eccentricities.

5.3 Load-path 4c

For load-path 4c the lateral load applied in the first stage P_s is equal to 27.5 kN. During the second stage of the simulation the axial vertical displacement δ is increased under the constant effect of the lateral load P_s.

Figures 13a-b present the two possible crack paths, for $f_c/f_t = 20$, according to the Mohr-Coulomb pos-

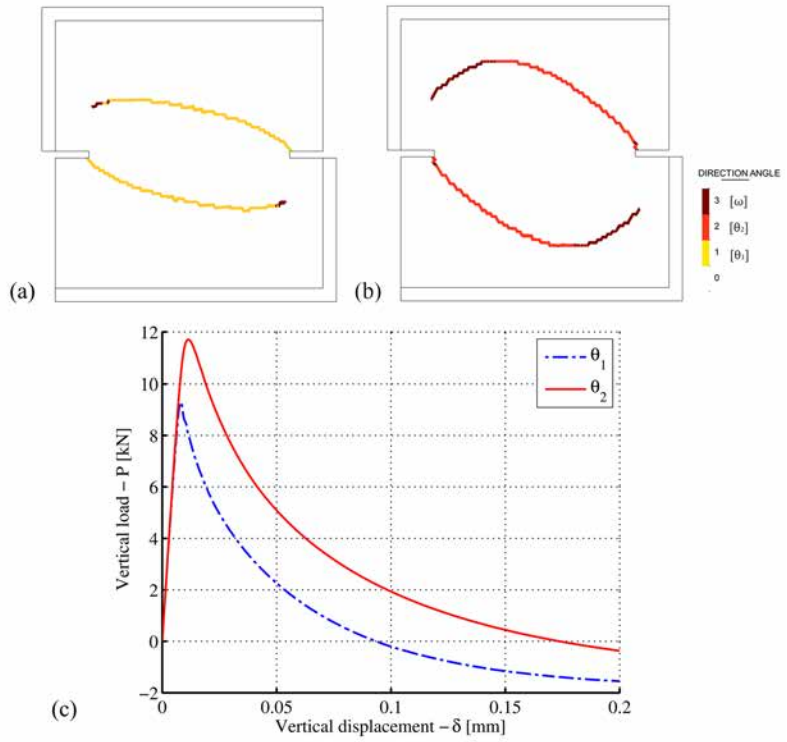

Fig. 13: Load-path 4c for $f_c/f_t = 20$: contour of the selected crack propagation direction in the damaged elements case θ_1 (a), case θ_2 (b) and load vs displacement (P-δ) for the two possible fracture planes (c).

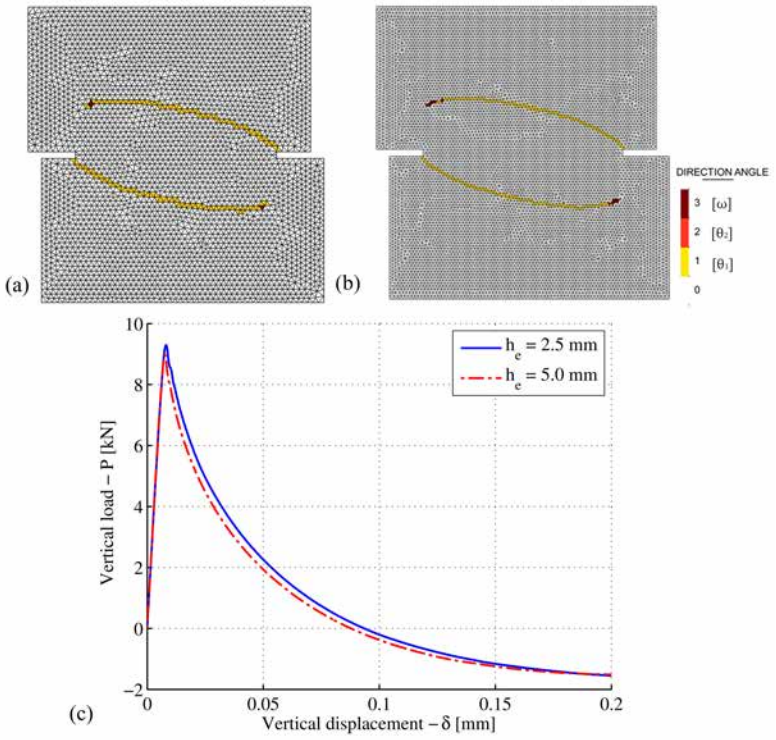

Fig. 14: . Load-path 4c: contour of the selected crack propagation direction in the damaged elements for mesh with element size $h_e = 5.0mm$ (a) and $h_e = 2.5mm$ (b) and load vs. displacement (P-δ) for two different meshes (c).

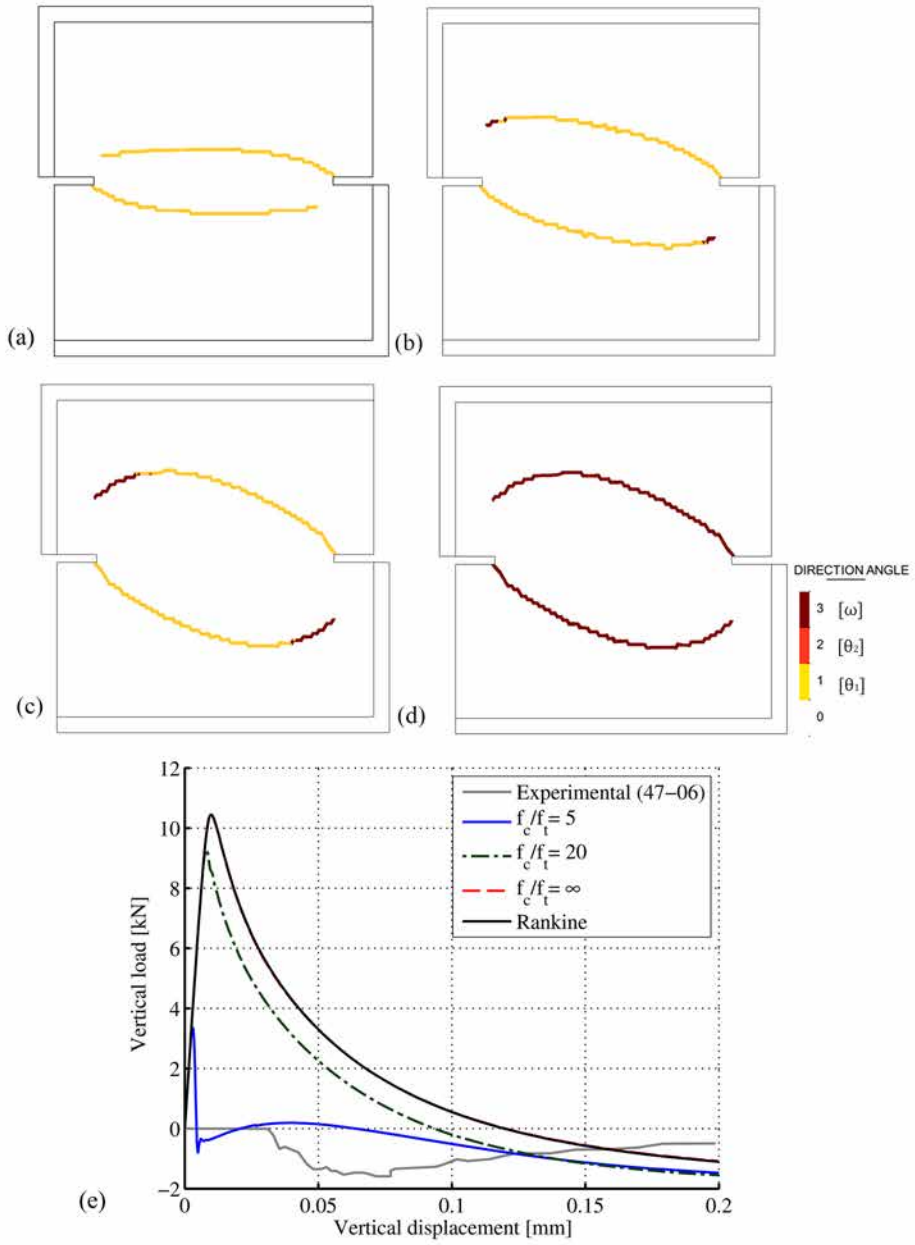

Fig. 15: Load-path 4c: contour of the selected crack propagation direction in the damaged elements for Mohr-Coulomb's criterion and $f_c/f_t = 5$ (a), $f_c/f_t = 20$ (b), $f_c/f_t \approx \infty$ (c); for Rankine's criterion and $f_c/f_t = 20$ (d) and load vs displacement (P-δ) for different compressive to tensile strength ratios (e).

tulate. Contrarily to the previous two load-paths, and due to the high value of the lateral load P_s, the two cracks start and progress in this case mostly due to shear. Failure under pure tension is visible only at the end of the cracks and when the collapse mechanism is completely developed. As a consequence, the difference between the crack trajectories is important for the two possible crack propagation directions θ_1 and θ_2. This importance of the selected crack path is also reflected in the difference of the dissipated energy visible in the load vs. displacement curves of Figure 13c.

Figure 14 presents the solutions using the proposed algorithm with two different meshes, including the procedure for selecting among the two possible crack propagation directions of Section 4.3. As shown, the crack propagation direction θ_1, which requires less dissipated energy to form, has been correctly selected independently of the degree of refinement of the mesh. The

difference in the level of discretization can be appreciated in Figure 14a and Figure 14b. In both cases two skew-symmetric cracks start from the two notches and propagate towards the interior of the specimen. The crack curvature is very similar for the two meshes and no spurious mesh bias is observed. Figure 14c shows the load versus displacement curves for these two simulations. The two graphs present the same trend, with the dissipated energy being almost identical upon mesh-refinement.

Figure 15 shows the effect of f_c/f_t for for load-path 4c in the obtained crack trajectories. Due to the shear failure that occurs along the greatest length of the crack, the effect of the f_c/f_t is clearly observed also in the load vs. displacement curves, presented in Figure 15e. As for load-path 4b, for a ratio $f_c/f_t = 5$ the two cracks form for very small values of vertical load, resulting in the sudden drop of the load and the rotation of the upper and lower parts of the specimen afterwards. Once again, the coincidence between the Mohr-Coulomb criterion with $f_c/f_t \approx \infty$ and the Rankine solution is evident both in terms of the crack-trajectory (Figure 15c & d) as well as of the dissipated energy (Figure 15e). Note that the proposed algorithm succeeds in selecting the crack propagation direction that minimizes the dissipated energy for all the studied ratios of f_c/f_t.

In general, the load displacement graphs attain the same shape as in the previous cases. However, the applied load needs to become compressive to keep stable the propagation of the crack. In the experimental results, a vertical compressive load needs to be applied from the beginning of the second stage of the experiment. This is related to the opening of the bottom crack during the application of the lateral force P_s at the first stage of the experiment, as reported by the authors of the experiments [25]. The fact that the rear side of the same crack opened later comparing to the front side reveals the out-of-plane bending effects experienced by the specimen, which may have affected the experiment and have led to the observed differences between numerical and experimental outcomes (e.g. [16, 37]). As a result of the earlier cracking at the left notch, the experimental obtained crack trajectory of the lower and upper crack is different. Contrarily, in the numerical solution the two cracks show an almost perfect skew-symmetry.

6 Conclusions

This paper has presented a crack-tracking algorithm oriented to the study of fracture in quasi-brittle materials with cohesive-frictional behaviour. To this aim, a new crack-propagation criterion is proposed that is consistent with the failure types suggested by the Mohr-Coulomb theory failure criterion under shear failure. This methodology extends the applicability of crack-tracking algorithms combined with the smeared crack approach to the simulation of mixed mode loading conditions in a larger family of construction materials.

The proposed crack-tracking algorithm categorizes cracking into shear and tensile. Under pure tension, cracking propagates towards a direction perpendicular to the direction of the maximum principal stress, whereas under shear cracking occurs at a failure plane proposed by the Mohr-Coulomb theory. As shown from the simulated experiments, this separation of the crack regimens is a valuable tool for understanding fracture phenomena in mixed mode problems. Another special feature of the presented algorithm is the ability to select among the two mutually possible fracture planes proposed by the Mohr-Coulomb failure criterion. To achieve this, an energy based criterion is applied at the propagating front of each crack prior to the crack opening. This procedure has proved capable to identify the crack path that maximizes the released strain energy and minimizes the dissipated energy in cracking of concrete under non-proportional loading.

The presented crack-tracking algorithm results in mesh-bias independency of the numerical solution, while the use of the local continuum damage model ensures mesh-size independency. These features allow for the realistic, in qualitative and quantitative terms, numerical simulation of cracking phenomena in geomaterials within the framework of the smeared crack approach. Additionally, the proposed algorithm offers a numerical solution with reasonable computational cost, since the overhead of using the crack-tracking technique is relatively small. This makes the study of structures with multiple cracks feasible. The proposed algorithm can be easily combined with different constitutive models or with discrete approaches such as the X-FEM and E-FEM.

7 Acknowledgements

This research has received the financial support from the MINECO (Ministerio de Economia y Competitividad of the Spanish Government) and the ERDF (European Regional Development Fund) through the MICROPAR project (Identification of mechanical and strength parameters of structural masonry by experimental methods and numerical micro-modelling, ref num. BIA2012-32234) and from the Excellence Programme for Knowledge Generation by MINECO,

through the EACY project (Enhanced accuracy computational and experimental framework for strain localization and failure mechanisms, ref. MAT2013-48624-C2-1-P).

References

1. Benedetti, L., Cervera, M., and Chiumenti, M. Stress-accurate Mixed FEM for soil failure under shallow foundations involving strain localization in plasticity. *Computers and Geotechnics 64* (mar 2015), 32–47.
2. Cendón, D. A., Gálvez, J. C., Elices, M., and Planas, J. Modelling the fracture of concrete under mixed loading. *International Journal of Fracture 103*, 3 (2000), 293–310.
3. Cervera, M. Viscoelasticity and Rate-dependent Continuum Damage Models, Monography N-79. Tech. rep., CIMNE, Barcelona, 2003.
4. Cervera, M., Agelet de Saracibar, C., and Chiumenti, M. COMET - data input manual version 5.0. Technical report IT-308. Tech. rep., CIMNE UPC, Barcelona, 2002.
5. Cervera, M., and Chiumenti, M. Mesh objective tensile cracking via a local continuum damage model and a crack tracking technique. *Computer Methods in Applied Mechanics and Engineering 196*, 1-3 (2006), 304–320.
6. Cervera, M., and Chiumenti, M. Smeared crack approach: back to the original track. *International Journal for Numerical and Analytical Methods in Geomechanics 30*, 12 (2006), 1173–1199.
7. Cervera, M., Chiumenti, M., Benedetti, L., and Codina, R. Mixed stabilized finite element methods in nonlinear solid mechanics. Part III: Compressible and incompressible plasticity. *Computer Methods in Applied Mechanics and Engineering 285* (2015), 752–775.
8. Cervera, M., Chiumenti, M., and Codina, R. Mixed stabilized finite element methods in nonlinear solid mechanics. Part I: Formulation. *Computer Methods in Applied Mechanics and Engineering 199*, 37-40 (2010), 2559–2570.
9. Cervera, M., Chiumenti, M., and Codina, R. Mixed stabilized finite element methods in nonlinear solid mechanics. Part II: Strain localization. *Computer Methods in Applied Mechanics and Engineering 199*, 37-40 (2010), 2571–2589.
10. Cervera, M., Chiumenti, M., and Di Capua, D. Benchmarking on bifurcation and localization in J2 plasticity for plane stress and plane strain conditions. *Computer Methods in Applied Mechanics and Engineering 241-244* (2012), 206–224.
11. Cervera, M., Pelà, L., Clemente, R., and Roca, P. A crack-tracking technique for localized damage in quasi-brittle materials. *Engineering Fracture Mechanics 77*, 13 (2010), 2431–2450.
12. COMET. Coupled Mechanical and Thermal analysis, http://www.cimne.com/comet/, 2016.
13. de Borst, R. Fracture in quasi-brittle materials: A review of continuum damage-based approaches. *Engineering Fracture Mechanics 69* (2001), 95–112.
14. DeJong, M. J., a.N. Hendriks, M., and Rots, J. G. Sequentially linear analysis of fracture under nonproportional loading. *Engineering Fracture Mechanics 75*, 18 (dec 2008), 5042–5056.
15. Di Prisco, M., Ferrara, L., Meftah, F., Pamin, J., de Borst, R., Mazars, J., and Reynouard, J. M. Mixed mode fracture in plain and reinforced concrete: Some results on benchmark tests. *International Journal of Fracture 103*, 1991 (2000), 127–148.
16. Dumstorff, P., and Meschke, G. Crack propagation criteria in the framework of X-FEM-based structural analyses. *International Journal for Numerical and Analytical Methods in Geomechanics 31*, 2 (2007), 239–259.
17. GiD. The personal pre and post-processor, http://www.gidhome.com/, 2014.
18. Jirásek, M., and Belytschko, T. Computational resolution of strong discontinuities. *Fifth world congress on computational mechanics* (2002), 7–12.
19. Jirásek, M., and Zimmermann, T. Embedded crack model. Part II. Combination with smeared cracks. *International Journal for Numerical Methods in Engineering 50*, 6 (2001), 1291–1305.
20. Karihaloo, B. L., and Xiao, Q. Z. Modelling of stationary and growing cracks in FE framework without remeshing: A state-of-the-art review. *Computers and Structures 81* (2003), 119–129.
21. Lemaitre, J., and Chaboche, J. L. Aspect Phenomenologique de la Rupture par Endommagement. *Journal de Mécanique Appliquée 2*, 3 (1978).
22. Meschke, G., and Dumstorff, P. Energy-based modeling of cohesive and cohesionless cracks via X-FEM. *Computer Methods in Applied Mechanics and Engineering 196*, 21-24 (2007), 2338–2357.
23. Moës, N., and Belytschko, T. Extended finite element method for cohesive crack growth. *Engineering Fracture Mechanics 69*, 7 (2002), 813–833.
24. Nooru-Mohamed, M., Schlangen, E., and van Mier, J. G. Experimental and numerical study on the behavior of concrete subjected to biaxial tension and shear. *Advanced Cement Based Materials 1*, 1 (oct 1993), 22–37.
25. Nooru-Mohamed, M. B. M. *Mixed-mode fracture of concrete: an experimental approach.* PhD thesis, Delft University of Technology, 1992.
26. Okubo, C., and Schultz, R. Evolution of damage zone geometry and intensity in porous sandstone: insight gained from strain energy density. *Journal of the Geological Society 162*, Engelder 1974 (2005), 939–949.
27. Oliver, J., and Huespe, A. Theoretical and computational issues in modelling material failure in strong discontinuity scenarios. *Computer Methods in Applied Mechanics and Engineering 193*, 27-29 (2004), 2987–3014.
28. Oliver, J., Huespe, a. E., Samaniego, E., and Chaves, E. W. V. Continuum approach to the numerical simulation of material failure in concrete. *International Journal for Numerical and Analytical Methods in Geomechanics 28*, 78 (2004), 609–632.
29. Olson, E. L., and Cooke, M. L. Application of three fault growth criteria to the Puente Hills thrust system, Los Angeles, California, USA. *Journal of Structural Geology 27*, 10 (oct 2005), 1765–1777.
30. Pelà, L., Bourgeois, J., Roca, P., Cervera, M., and Chiumenti, M. Analysis of the Effect of Provisional Ties on the Construction and Current Deformation of Mallorca Cathedral. *International Journal of Architectural Heritage 10*, 4 (2016), 418–437.
31. Pelà, L., Cervera, M., Oller, S., and Chiumenti, M. A localized mapped damage model for orthotropic materials. *Engineering Fracture Mechanics 124-125*, July (2014), 196–216.

32. Pelà, L., Cervera, M., and Roca, P. Continuum damage model for orthotropic materials: Application to masonry. *Computer Methods in Applied Mechanics and Engineering 200*, 9-12 (2011), 917–930.
33. Pelà, L., Cervera, M., and Roca, P. An orthotropic damage model for the analysis of masonry structures. *Construction and Building Materials 41* (2013), 957–967.
34. Petromichelakis, Y., Saloustros, S., and Pelà, L. Seismic assessment of historical masonry construction including uncertainty. In *9th International Conference on Structural Dynamics, EURODYN 2014* (2014), Á. Cunha, E. Caetano, P. Ribeiro, C. Papadimitriou, C. Moutinho, and F. Magalhães, Eds., pp. 297–304.
35. Rabczuk, T. Computational Methods for Fracture in Brittle and Quasi-Brittle Solids : State-of-the-art Review and Future Perspectives. *ISRN Applied Mathematics 2013* (2012), 1–61.
36. Roca, P., Cervera, M., Pelà, L., Clemente, R., and Chiumenti, M. Continuum FE models for the analysis of Mallorca Cathedral. *Engineering Structures 46* (2013), 653–670.
37. Roth, S.-N., Léger, P., and Soulaïmani, A. A combined XFEM-damage mechanics approach for concrete crack propagation. *Computer Methods in Applied Mechanics and Engineering 283* (jan 2015), 923–955.
38. Saloustros, S., Pelà, L., Roca, P., and Portal, J. Numerical analysis of structural damage in the church of the Poblet monastery. *Engineering Failure Analysis 48* (2014), 41–61.
39. Slobbe, A. T., Hendriks, M. A. N., and Rots, J. G. Smoothing the propagation of smeared cracks. *Engineering Fracture Mechanics 132* (2014), 147–168.
40. Stolarska, M., Chopp, D. L., Moës, N., and Belytschko, T. Modelling crack growth by level sets in the extended finite element method. *International Journal for Numerical Methods in Engineering 51*, 8 (2001), 943–960.
41. Unger, J. F., Eckardt, S., and Könke, C. Modelling of cohesive crack growth in concrete structures with the extended finite element method. *Computer Methods in Applied Mechanics and Engineering 196* (2007), 4087–4100.
42. Wells, G. N., and Sluys, L. J. A new method for modelling cohesive cracks using finite elements. *International Journal for Numerical Methods in Engineering 50*, 12 (2001), 2667–2682.
43. Wu, J.-Y., and Cervera, M. On the equivalence between traction- and stress-based approaches for the modeling of localized failure in solids. *Journal of the Mechanics and Physics of Solids 82* (2015), 137–163.
44. Zi, G., and Belytschko, T. New crack-tip elements for XFEM and applications to cohesive cracks. *International Journal for Numerical Methods in Engineering 57*, 15 (2003), 2221–2240.

Finite element modelling of internal and multiple localized cracks

Savvas Saloustros · Luca Pelà · Miguel Cervera · Pere Roca

Computational Mechanics, 2016, Vol. 59, p. 299-316
doi:10.1007/s00466-016-1351-6

Accepted Manuscript in *Computational Mechanics*
DOI: 10.1007/s00466-016-1351-6

Finite Element Modelling of Internal and Multiple Localized Cracks

Savvas Saloustros · Luca Pelà · Miguel Cervera · Pere Roca

Received: 14 June 2016
Accepted: 21 October 2016

Abstract Tracking algorithms constitute an efficient numerical technique for modelling fracture in quasi-brittle materials. They succeed in representing localized cracks in the numerical model without mesh-induced directional bias. Currently available tracking algorithms have an important limitation: cracking originates either from the boundary of the discretized domain or from predefined "crack-root" elements and then propagates along one orientation. This paper aims to circumvent this drawback by proposing a novel tracking algorithm that can simulate cracking starting at any point of the mesh and propagating along one or two orientations. This enhancement allows the simulation of structural case-studies experiencing multiple cracking. The proposed approach is validated through the simulation of a benchmark example and an experimentally tested structural frame under in-plane loading. Mesh-bias independency of the numerical solution, computational cost and predicted collapse mechanisms with and without the tracking algorithm are discussed.

Savvas Saloustros · Luca Pelà · Miguel Cervera · Pere Roca

Department of Civil and Environmental Engineering
Technical University of Catalonia, UPC-BarcelonaTech
Jordi Girona 1-3, 08034 Barcelona, Spain.

International Center for Numerical Methods in Engineering (CIMNE)
Gran Capità, S/N, 08034 Barcelona, Spain.

E-mail: savvas.saloustros@upc.edu
E-mail: luca.pela@upc.edu
E-mail: miguel.cervera@upc.edu
E-mail: pere.roca.fabregat@upc.edu

Keywords Continuum Damage Mechanics · Crack-Tracking · Damage Localization · Quasi-brittle materials · Shear/Flexural/Tensile Cracks

1 Introduction

Almost half a century after the pioneering works of Ngo & Scordelis [1] and Rashid [2], the numerical simulation of cracking in quasi-brittle materials is still a challenging task. Although a wide range of novel formulations has been proposed in the field of computational failure mechanics, up to date there is no such thing as a panacea for the realistic and efficient numerical analysis of failure in quasi-brittle materials. As a fact, the analyst has to consider at least three aspects before choosing the adequate numerical tool: the realistic numerical modelling of cracking, the accurate simulation of the material behaviour and the bearable computational cost.

Realistic modelling of cracking implies that the location and direction of cracks are not spuriously affected by the used mesh topology. This situation is commonly referred as *mesh-induced directional bias*. The dependency of the numerical simulation to the used mesh is a common limitation of both smeared and discrete crack approaches [3]. This defect has triggered the research, first, on the possible limitations in the numerical discrete problem and, second, on the adequate remedies to overcome them. The proposed solutions depend on the perception of the origin of the numerical problem. Some approaches intervene in the mathematical formulation of the continuum problem, such as gradient-enhanced [4, 5], non-local [6, 7] or micropolar [8, 9] models. Other formulations aim to overcome the error produced by the

spatial discretization of the continuum domain, such as mixed formulations [10], crack-tracking techniques with [11, 12, 13, 14] or without [15, 16, 17] enrichment of the used finite elements or nodes. Finally, another approach reported in the literature bases on the modification of the material model [18]. For a review on the issue the interested reader is referred to [19, 20].

Of equal importance to the numerically objective modelling of cracking, is the accurate simulation of the material behaviour. The description of the mechanical behaviour in quasi-brittle materials necessitates a proper failure criterion and a constitutive law with softening behaviour controlled by the fracture energy. To account for this behaviour various models have been applied for the simulation of quasi-brittle materials based on plasticity [21, 22, 23], continuum damage models [24, 25] or a combination of both [26, 27, 28]. The previous isotropic formulations have been complemented by anisotropic models [29, 30, 31]. In the last years, an increasing effort has been made to develop numerical methods that consider the interaction of components in composite materials (e.g. concrete, masonry). Such methodologies can be based on computational homogenization [32, 33, 34, 35, 36, 37, 38], or on micro-modelling techniques, also known as direct numerical simulations, including all the information about the material's micro-structure [39, 40].

The micro- and multi-scale modelling approaches, even though very sophisticated and characterized by a remarkable level of accuracy, are still hardly applicable to the study of large-scale structural problems experiencing multiple cracking. This is due to the significant computational cost required by these models. As a consequence, the Continuum Finite Element Modelling (also known as macro-modelling) based on the classical smeared crack-approach is still on the foreground of applications in large-scale concrete [41] and masonry structures [42, 43, 44].

The aim of this work is to apply the know-how of objective mesh-localization approaches to the analysis of structures made of quasi-brittle materials that experience multiple cracking. The adopted numerical technique is the classical smeared crack approach enhanced with a local crack-tracking algorithm [16]. This choice is justified by the following reasoning. Firstly, tracking algorithms provide numerical solutions that are free of mesh-induced directional bias [45, 16, 17, 46, 47, 48]. Secondly, the particular tracking algorithm can be effectively combined with constitutive models suitable for quasi-brittle materials, like anisotropic [31, 49] or isotropic ones [26]. Additionally, an important feature of the algorithm is the possibility to define a minimum distance between the discrete cracks. These exclusion zones surrounding a crack render it possible to consider indirectly the size of the material's mesoscale (e.g. masonry units), when the composite is simplified as a homogenized continuum in the numerical simulation. Finally, the overhead in the computational cost is limited, allowing the efficient simulation of multiple cracking problems in large-scale structures.

Up to date approaches using tracking algorithms have focused mostly on cracks nucleating from the boundary of the domain or from pre-existent flaws and propagating in a single orientation (see for instance [46, 47, 50, 51, 52, 53]). This confines the application of tracking algorithms to a very narrow family of structural problems, in which the origin of cracks is either known prior to the analysis, or it is imposed by including material or geometrical perturbations within the analysed numerical domain. Additionally, structural problems with cracking starting from an arbitrary point within the analysed domain and propagating in two opposite orientations have not been addressed.

The main novelty of the present work resides in the enhancement of a crack-tracking algorithm with a technique that allows the initiation and propagation of cracks at any element of the discretized domain. In particular, the proposed methodology extends the use of local crack-tracking algorithms to the simulation of cracking starting from the interior of the discretized domain and propagating along two opposite orientations. This novel contribution to the original methodology [16] makes possible the efficient simulation of localized cracks under shear, flexure and traction, without any *a priori* definition of their location by the analyst. Another original aspect of the proposed method is the identification of the potential crack path prior to the occurrence of the damage, differently from the approach recently proposed in [54].

The paper is structured in the following way. Section 2 presents the underlying continuum damage model. Section 3 outlines the methodology for the simulation of formation and propagation of internal cracking with the use of a crack-tracking algorithm. The proposed numerical strategy is validated with the simulation of a single-crack problem with internal fracture (Brazilian splitting test) and then with the analysis of a complex multi-crack problem (frame wall with one-door opening tested against horizontal loading), see Section 4. Finally, conclusions are summarized in Section 5.

2 Continuum Damage model

In this work, a constitutive model based on the continuum damage mechanics presented in [25] is used for the simulation of fracture. The model benefits from the

use of two separate damage scalar indexes to distinguish between tensile and compressive damage. This is an important characteristic for the simulation of degradation in materials such as concrete and masonry which have quite different capacity under tension and compression. Other local models based on the same concept have been proposed by Lee & Fenves [27], Comi & Perego [55], Wu et al. [28], Pelà et al. [56], Voyiadjis et al. [57], Mazars et al. [58]. He et al. [59] and Pereira et al. [60] have recently proposed nonlocal counterparts of some of the these models.

The constitutive model establishes on the concept of the effective stress tensor $\bar{\boldsymbol{\sigma}}$, which basing on the strain equivalence principle [61] is related to the strain tensor $\boldsymbol{\epsilon}$ according to the following equation

$$\bar{\boldsymbol{\sigma}} = \boldsymbol{C} : \boldsymbol{\epsilon} \tag{1}$$

where $\boldsymbol{C}$ stands for the isotropic linear-elastic co tutive tensor and (:) the tensor product contracte two indices. Aiming to model a different response u tension and compression, the effective stress is split a tensile $\bar{\boldsymbol{\sigma}}^+$ and a compressive part $\bar{\boldsymbol{\sigma}}^-$. Such ten are respectively defined as

$$\bar{\boldsymbol{\sigma}}^+ = \sum_{j=1}^{3} \langle \bar{\sigma}_j \rangle \, \boldsymbol{p_j} \otimes \boldsymbol{p_j}$$

$$\bar{\boldsymbol{\sigma}}^- = \bar{\boldsymbol{\sigma}} - \bar{\boldsymbol{\sigma}}^+$$

where $\bar{\sigma}_j$ stands for the *j-th* principal stress value f tensor $\bar{\boldsymbol{\sigma}}$ and $\boldsymbol{p_j}$ is the unit vector of the respective p cipal direction j. The symbol $\langle \bullet \rangle$ denotes the Maca brackets ($\langle x \rangle = x$, if $x \geq 0$,$\langle x \rangle = 0$, if $x < 0$).

Following that, two internal damage variables are introduced d^+ and d^-, with the first denoting the tensile damage and the second the compressive one. The constitutive relation can be expressed then as

$$\boldsymbol{\sigma} = (1 - d^+)\bar{\boldsymbol{\sigma}}^+ + (1 - d^-)\bar{\boldsymbol{\sigma}}^- \tag{4}$$

Loading, unloading and reloading conditions are distinguished with the use of two scalar positive quantities, one for tension τ^+ and a second for compression τ^-, termed as the equivalent stresses. Their values depend on the stress tensor and the assumed failure criteria. In this work, the failure criterion presented in [26] is used so that the values of the equivalent stresses for tension and compression are

$$\tau^+ = H\left[\bar{\sigma}_{max}\right] \frac{1}{1-\alpha} \left[\sqrt{3\bar{J}_2} + \alpha \bar{I}_1 + \beta \langle \bar{\sigma}_{max} \rangle \right] \frac{f^+}{f^-} \tag{5}$$

$$\tau^- = H\left[-\bar{\sigma}_{min}\right] \frac{1}{1-\alpha} \left[\sqrt{3\bar{J}_2{}^-} + \alpha \bar{I}_1{}^- + \beta \langle \bar{\sigma}_{max} \rangle \right] \tag{6}$$

$$\alpha = \frac{\left(f_b^- / f^-\right) - 1}{2\left(f_b^- / f^-\right) - 1} \tag{7}$$

$$\beta = (1-\alpha)\frac{f^-}{f^+} - (1+\alpha) \tag{8}$$

In the above equations f_b^- and f^- are the biaxial and uniaxial compressive strengths respectively, $\bar{I}_1$ denotes the first invariant of the effective stress tensor, $\bar{J}_2$ the second invariant of the effective deviatoric stress tensor, while $\bar{\sigma}_{max}$ and $\bar{\sigma}_{min}$ stand for the maximum and minimum principal stress respectively. The failure surface for the case of the plane stress is shown in Figure 1. $H\left[\bullet\right]$ denotes the Heaviside step function. Tensile damage is activated for stress states within the first, second and fourth quadrants of the principal stress space, see Figure 1, while compressive damage for stress states only within the third quadrant.

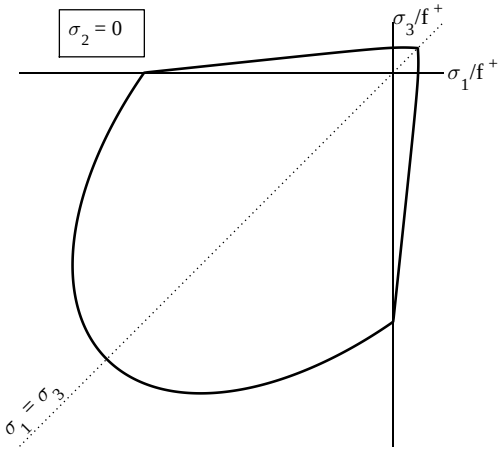

Fig. 1: Adopted damage surface under plane-stress conditions [26].

The damage criteria are defined then as [62]

$$\Phi^{\pm}\left(r^{\pm}, \tau^{\pm}\right) = \tau^{\pm} - r^{\pm} \leq 0 \tag{9}$$

where $r^{\pm}$ are internal stress-like variables that represent the current damage thresholds and the respective expansion of the damage surface. As a consequence, their initial values are equal to the uniaxial stress under tension $r_0^+ = f^+$ and compression $r_0^- = f^-$ and thereafter vary according to

$$r^{\pm} = max\left[r_0^{\pm}, \max_{i \in (0,n)} \left(\tau_i^{\pm}\right) \right] \tag{10}$$

The evolution of the internal damage variables $d^{\pm}$ is defined as [63]

$$d^{\pm} = 1 - \frac{r_0^{\pm}}{r^{\pm}} \exp\left\{ 2H_d^{\pm} \left(\frac{r_0^{\pm} - r^{\pm}}{r_0^{\pm}} \right) \right\} \tag{11}$$

In the above Equation (11), $H_d^{\pm} \geq 0$ stands for the discrete softening parameter, included to ensure mesh-size objective results considering the compressive and tensile fracture energy of the material $G_f^{\pm}$ and the characteristic finite element length. In particular, the specific dissipated energy (i.e. dissipated energy per unit of volume) in tension or compression $D^{\pm}$ is regularized considering the characteristic crack width l_{dis} related to the area (for two-dimensional elements) or volume (for three-dimensional elements) of each finite element in the crack band according to the equation [64]

$$D^{\pm} l_{dis} = G_f^{\pm} \tag{12}$$

The specific dissipated energy for a damage model with exponential softening is [65]

$$D^{\pm} = \left(1 + \frac{1}{H_d^{\pm}}\right) \frac{\left(f^{\pm}\right)^2}{2E} \tag{13}$$

From Equations (12) and (13) the previously introduced softening parameter is defined as

$$H_d^{\pm} = \frac{l_{dis}}{l_{mat} - l_{dis}} \tag{14}$$

For the current work, two-dimensional linear triangular elements are used with $l_{dis} = \sqrt{2A}$, where A denotes the area of each element. This selection can be refined according to the work of Oliver [66]. The material characteristic length l_{mat} and the discrete softening parameter H_{mat} depend only on the material properties according to [16, 65]

$$l_{mat} = \frac{1}{H_{mat}} = \frac{2EG_f^{\pm}}{\left(f^{\pm}\right)^2} \tag{15}$$

It is noted that regularized stress versus strain models, as the present one, can be shown to be equivalent to traction versus displacement jumps models such those used in fracture mechanics [67], X-FEM and E-FEM formulations [68].

3 Modelling of cracking with a local tracking technique

As discussed in the Introduction, most of the currently available crack-tracking algorithms focus on the simulation of cracks starting from the boundary of the discretized domain and propagating towards a single orientation. This drawback limits the application of such algorithms, which cannot be used for the analysis of structures experiencing internal cracking such as shear cracks. To overcome this limitation, in this work the local-crack tracking algorithm presented by Cervera et al. [16] is adequately enhanced for the simulation of cracking initiating from internal elements of the mesh and propagating along two opposite orientations. This section presents the main features of the algorithm focusing on its novel contributions. The method is here applied to constant strain three node elements but it can be extended to other types of two-dimensional finite elements (see [17]).

The local crack-tracking algorithm constitutes an enhancement of the classical smeared crack approach. The algorithm is called at the beginning of each load increment of the numerical analysis prior to the evaluation of the stresses. Its purpose is to identify and "label" the elements pertaining to a crack path for the current increment. For these elements, the evaluation of the stresses is computed according to the nonlinear constitutive law defined in Section 2. Contrariwise, the elements falling out of the crack path will keep their linear elastic stress-strain relation.

The first procedure carried-out by the crack-tracking algorithm is the identification of new cracks. A new crack starts at an element according to the tensile damage criterion defined by Equations (5) and (9). The above check is performed throughout the whole discretized domain and not only at the elements lying over the boundary as in existing crack-tracking algorithms. This is necessary to identify and allow the initiation of internal cracking. The elements satisfying the failure criterion of Equation (9) ($\Phi^+ = 0$) are defined as *crack root* elements.

The control of the damage dispersion over a small part of the discretized domain, and thus the simulation of separate and individual cracks, is possible with the use of an *exclusion radius* criterion. This criterion, introduced in [16], defines as a crack root element the one with the highest value of the tensile equivalent stress τ^+ within a radius r_{excl} (see Figure 2a). The value of r_{excl} is defined *a priori*, and may be according to the mesoscale geometry of the heterogeneous material.

Following the above procedure, the coordinates of the *crack origin* are defined and stored. These depend on the location of the crack root element within the discretized domain. For the family of internal crack root elements, the crack origin is defined as the centroid of the triangular element, i.e. the intersecting point of the medians (Figure 2a). The same holds for corner elements, whereas for the remaining boundary elements the midpoint of the side lying on the mesh boundary is selected.

The second part of the algorithm, after the definition of the crack root and crack tip elements, is the identification of the following elements pertaining to the crack path. The procedure is different for the two crack root elements, i.e. boundary and internal ones. For each

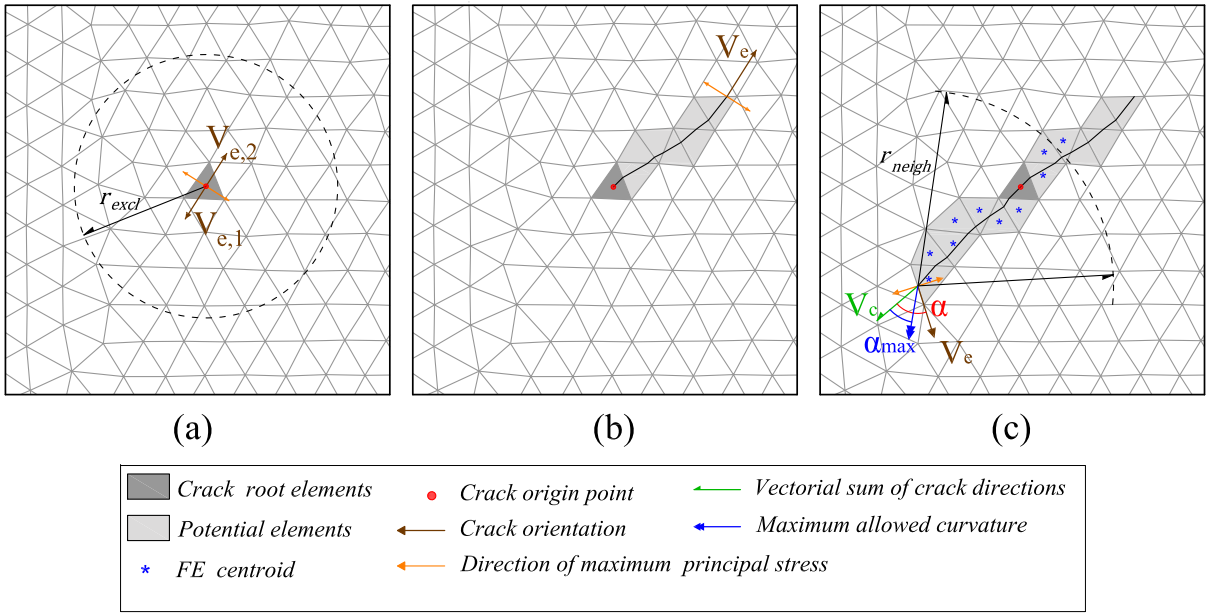

Fig. 2: Simulation of internal cracking with the crack-tracking technique: (a) *internal crack root* element with the two opposite vectors of the crack propagation, (b) labelling of the next potential elements towards the first side of the crack, (c) labelling of the next *potential* elements towards the second side of the crack and use of the *maximum curvature criterion*.

boundary crack root element, a vector is drawn, starting from the crack origin location, with a direction perpendicular to the one defined by the maximum principal stress. The intersection of this vector with the neighbouring element defines the exit point and the *next potential element* of the crack. Similarly, starting from this point the following next potential elements of the crack are recognised. The same procedure is followed for identifying the propagation path of consolidated cracks from the crack tip elements. In this case the crack origin point is the exit point of the crack at the previous cracked element.

Contrarily to cracking starting from the boundary, other cracks, such as shear ones, initiate from the interior and propagate along two opposite orientations. To account for this damage typology, the algorithm is enhanced with a different procedure. Starting from the crack origin point of the *internal crack root* element, two vectors $(\overrightarrow{V}_{e,1})$ and $(\overrightarrow{V}_{e,2})$ are defined, having a direction perpendicular to that of the maximum principal stress but opposite orientations (Figure 2a). Following this, the identification of the potential cracking elements within the current increment takes part in two steps. First, the elements pertaining to the path defined by the orientation of vector $(\overrightarrow{V}_{e,1})$ are identified starting from the crack origin point and following the same process as described above for the boundary crack root elements (Figure 2b). Upon concluding the labelling towards that side of the crack, the elements lying at the opposite face can be recognised starting again from the crack origin point of the internal crack root, but using the orientation of vector $(\overrightarrow{V}_{e,2})$ (Figure 2c). Figure 3 presents the main steps of the labelling in case of internal cracks.

The described procedure for the definition of crack propagation stops on three alternative conditions: (i) when the next potential element belongs to a different crack, i.e. when the crack joins another one (*meeting* criterion in Figure 3); (ii) when a crack reaches the mesh boundary (*boundary* criterion in Figure 3); (iii) when the stress-state of a potential element is lower than a pre-defined threshold (*stress threshold* criterion in Figure 3). This threshold can be conveniently defined in terms of the failure criterion and experience has demonstrated that labelling can be completed when the inequality $\frac{\tau^+}{f^+} < 0.75$ holds [16].

The selection of the elements of a crack depending on the local values of the stresses justifies the "local" nature of the presented crack-tracking algorithm. Even if this choice is very convenient in terms of computational efficiency and for cases of multiple cracks comparing to the global crack-tracking algorithms [16], it can meet some difficulties under bending stress states, when the local calculation of the principal stress di-

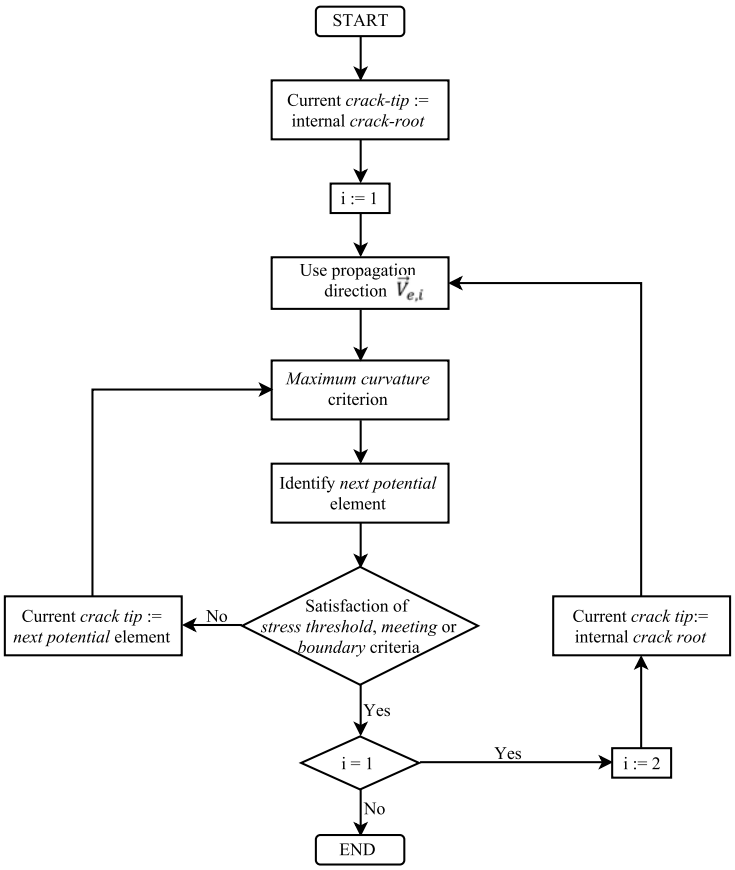

Fig. 3: Flowchart including the main steps of the crack-tracking algorithm for the identification of crack paths starting from the interior of the discretized domain.

rections may be relatively poor due to the high stress-gradients, resulting in spurious changes in the crack direction. To avoid such non-realistic result, the algorithm is enhanced with a procedure for the *apropos* correction of the crack propagation. This procedure, termed as *maximum curvature* criterion, is activated at each element lying at the propagating front of the crack before the selection of the next potential element. The idea is to compare the crack direction defined at the crack-tip element ($\overrightarrow{V_e}$), according to the principal stresses, to the direction of the vectorial sum of the crack directions ($\overrightarrow{V_c}$) of both the potential and the damaged elements within a neighbourhood of radius r_{neigh} (see Figure 2c). If the relative angle among them is larger than a maximum angle a_{max}, the vector $\overrightarrow{V_c}$ is used for the definition of the crack direction. The values of r_{neigh} and a_{max} are explicitly pre-defined.

Upon concluding the above procedure for all crack root and crack tip elements, the crack-tracking algorithm ends. The elements labelled as potential, as well as the already damaged ones, will be allowed to damage according to the constitutive model described in Section 2. For the rest, the stress-strain relationship will remain linear elastic for the current load increment.

The flexible design format of the presented algorithm can allow its possible enhancement to account for diverse problems. A branching criterion at the crack-root/tip elements would allow the simulation of crack-branching problems. However, the development of reliable criteria is necessary for a successful combination with tracking algorithms [20]. Another important extension, currently under development by the authors, concerns the modelling of intersecting cracks. This improvement can allow the simulation of problems including load-reversal (e.g. seismic actions).

4 Numerical examples

This section presents two examples to demonstrate the capacity of the proposed crack-tracking algorithm to simulate internal and multiple localized fracture in quasi-brittle materials. The first one is the Brazilian splitting

test, being a case of internal cracking propagating towards the two ends of the tested specimen. The second one is a frame wall with a door opening, tested against in-plane loading. Both examples demonstrate the capacity of the proposed technique to simulate boundary, internal and multiple localized cracks.

4.1 Benchmark for mesh objectivity: Brazilian splitting test

The first numerical application considers the simulation of the Brazilian splitting test. This example has three objectives. Firstly, to validate the capacity of the proposed algorithm to simulate cracking that initiates from the interior of the discretized domain and propagates along two opposite orientations. Secondly, to investigate the dependency of the used approach on the mesh discretization, both in terms of direction and size of the finite elements. Finally, to provide information regarding the computational cost induced by the use of the tracking algorithm.

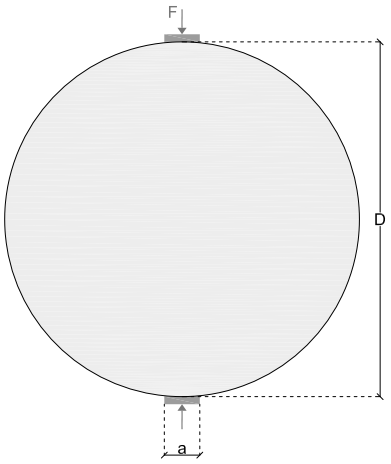

Fig. 4: Geometry and testing scheme of the Brazilian splitting test.

4.1.1 Experimental set-up and failure pattern

In the Brazilian splitting test, the tested specimen has a circular cross-section of diameter D and a depth l (Figure 4). The test consists in applying a compressive force along the diameter of the tested cylinder until failure occurs. The failure pattern is characterized by a tensile crack, starting from the interior of the tested specimen and propagating towards the boundaries following the direction of the applied compressive forces, i.e. along the diameter of the tested specimen. The obtained value of the maximum load is used to define the splitting tensile strength of the tested material. The Brazilian splitting test is a standard method for the estimation of the splitting tensile strength of geomaterials such as concrete [69] and rocks [70].

4.1.2 Numerical simulation

The dimensions considered in the numerical simulation, with respect to Figure 4, are $D = 15\ cm$, $a = D/10 = 1.5\ cm$. The cylinder is analysed under plane strain conditions. Typical material properties for concrete have been adopted: $E = 30.1\ GPa$, $f^+ = 2.2\ MPa$, $v = 0.25$, $f^- = 20\ MPa$, $\rho = 2400\ kg/m^3$, $G^+ = 50\ J/m^2$, $G^- = 15000\ J/m^2$. The tracking parameters are r_{excl}= 0.5 cm, $a_{max} = 45°$ and r_{neigh} = 0.5 cm.

The experiment is simulated by imposing a vertical displacement at the top of the upper bearing plate. The numerical solution of the discrete problem is performed in a step-by-step manner. At each step, the corresponding nonlinear equations are solved with the use of a full Newton-Raphson method along with a line-search procedure. Convergence of an increment is attained when the ratio between the iterative residual forces and the norm of the total external forces is lower than 10^{-3} (0.1%).

The numerical calculations are performed with an enhanced version of the finite element programme COMET [71], while pre- and post-processing with GiD [72]. Both software have been developed at the International Center for Numerical Methods in Engineering (CIMNE), in Barcelona.

4.1.3 Mesh-induced bias

This section focuses on the sensitivity of the numerical solution to the typology of the used discretization, both in terms of orientation and size of the finite elements.

Figure 5 presents the four meshes used for studying the dependency of the numerical solution on the direction of the mesh. The first two are discretized in an unstructured manner with average element sizes, at the region where damage is expected, h_e=0.5 cm (984 nodes, Figure 5a) and h_e=0.25 cm (1711 nodes, Figure 5b), respectively. The same region is discretized in a structured manner in the last two meshes, with average element sizes h_e=0.5 cm. It is noted these meshes have been designed avoiding the alignment of the predominant directions of the triangular elements with the vertical axis, where the cracking is expected to occur. This has been done to show the capability of the numerical

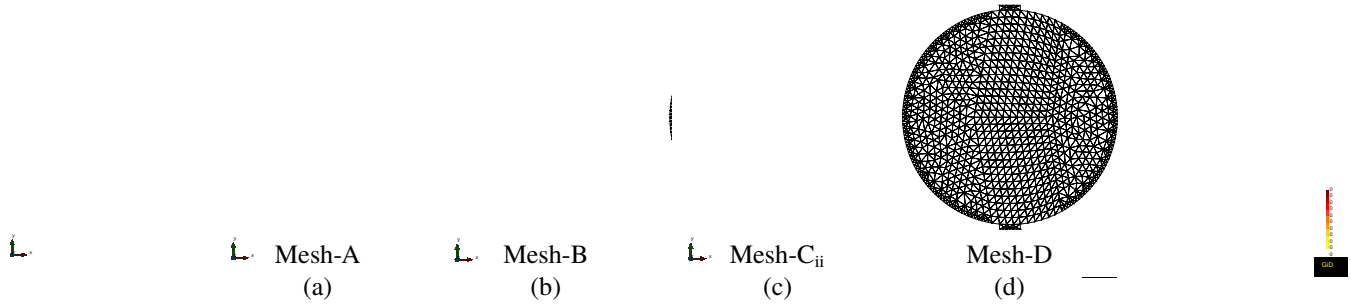

Fig. 5: The four meshes used for the mesh-induced directional bias study.

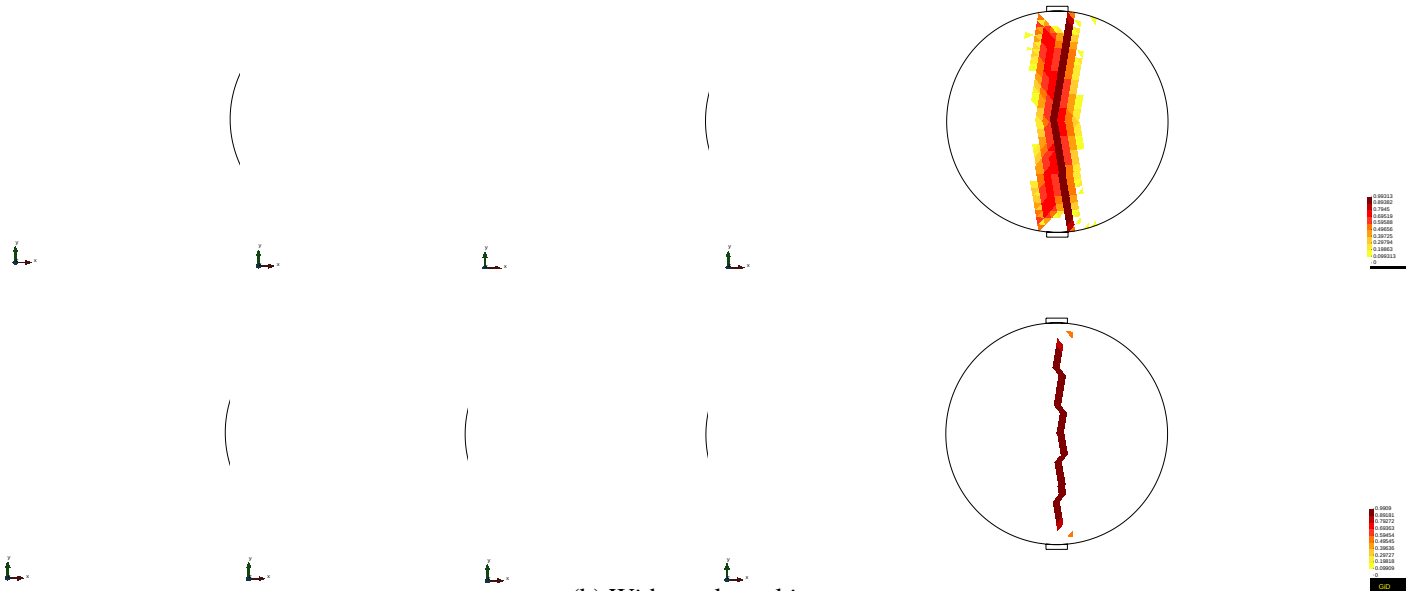

Fig. 6: Mesh-induced directional bias sensitivity. Contour of the tensile damage index (d^+) after the peak load for four different meshes: (a) without the crack-tracking algorithm, (b): with the crack-tracking algorithm.

technique to provide mesh-bias independent results. In particular, for the structured mesh Mesh-C (994 nodes, Figure 5c) the sides of the rectangular triangles create angles of around -10°, 80°, 125° with the horizontal axis. In the structured mesh Mesh-D (1016 nodes, Figure 5d) the structured region has been split into two, with the triangles in the lower part being a mirror of the ones in the upper part.

Figure 6 presents the contour of the d^+ tensile damage index for both the analyses with and without the use of the proposed tracking algorithm. The results using the classical smeared crack approach present a large spreading of damage within the discretized domain. In addition, the localization of damage depends spuriously on the mesh. This can be better visualised in the plot of the maximum principal strains, in Figure 7. The use of the tracking algorithm successfully addresses the aforementioned flaws of the classical smeared crack approach, resulting in a vertical crack emanating from the interior of the mesh and propagating along the loading direction for all the used meshes.

Apart from the sensitivity of the numerical solution on the directionality of the mesh, the effect of the finite element size is also investigated. To this aim, simulations have been performed with two additional meshes keeping the mesh-orientation of Mesh-C, but changing the sizes of the finite elements. Mesh-C' has mean element sizes h_e=0.075 m (384 nodes, Figure 8a), while in Mesh-C" h_e=0.025 m (1983 nodes, Figure 8c).

The refinement of the mesh has no positive effect on the simulation of the expected crack direction using the classical smeared crack-approach (Figures 9a and 10a).

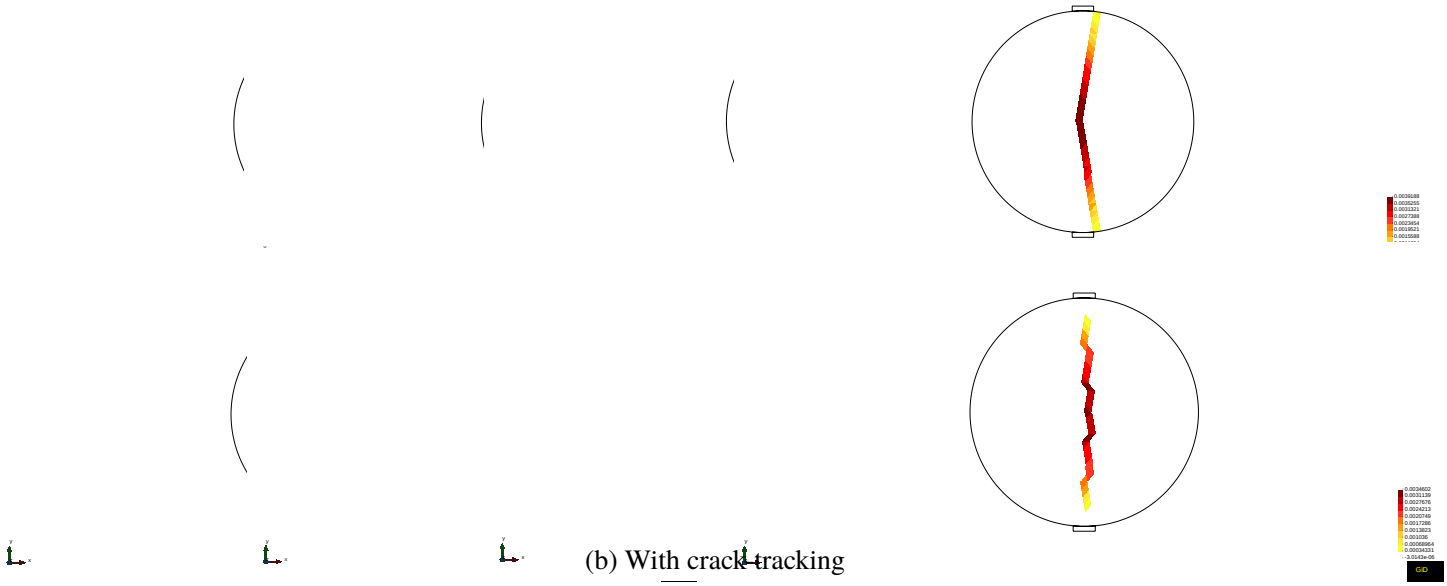

Fig. 7: Mesh-induced directional bias sensitivity. Contour of the maximum principal strains (ϵ_{max}) after the peak load for the four different meshes: (a) without the crack-tracking algorithm, (b): with the crack-tracking algorithm.

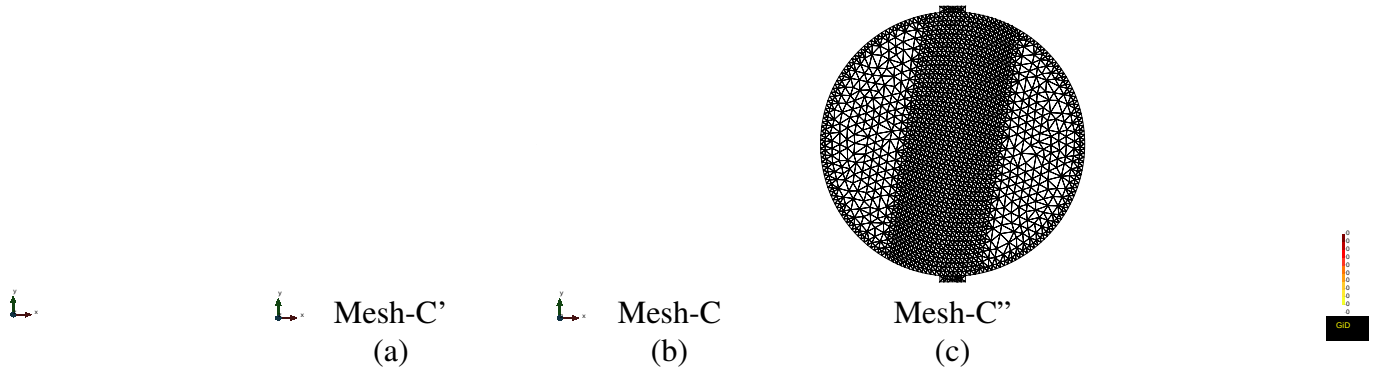

Fig. 8: The three meshes used for the mesh-size sensitivity study.

A vertical crack could not be simulated, even in the finer mesh, and the spurious spreading of damage around the localized band does not reduce on mesh refinement (Figure 9a). On the other hand, the use of the tracking algorithm predicts the expected vertical crack pattern independently of the discretization size (Figure 9b and Figure 10b.

Table 1 presents a comparison among the peak load obtained for each of the performed analysis and the analytical solution. The latter is calculated through the formula proposed by [69, 70] that is

$$P/l = \frac{\pi D f_{sp}}{2} \tag{16}$$

where P/l is the capacity per unit length and f_{sp} is the splitting tensile strength. Its value is considered equal to $f_{sp} = f^{+}/0.9$ according to Eurocode 2 [73]. Good agreement with the analytical result is achieved when the tracking algorithm is used. Contrariwise, the large spreading of damage in the numerical solution without the tracking algorithm lowers unrealistically the capacity of the specimen.

4.1.4 Computational cost

Table 2 presents the computational cost, in terms of time and memory resources, needed for the performed analyses with and without the tracking-algorithm. All the numerical analyses have been performed in a single machine equipped with an Intel Core i7-4790-3.60GHz CPU and 16.0 GB RAM.

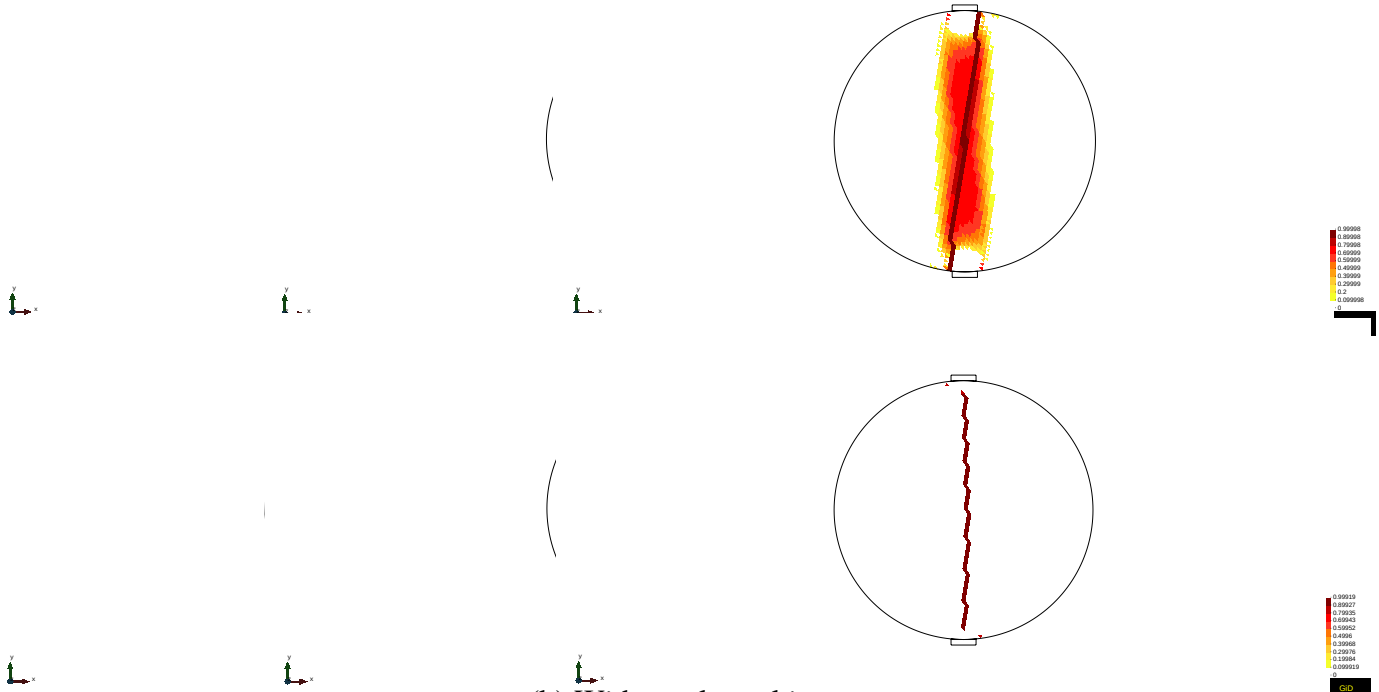

(b) With crack-tracking

Fig. 9: Mesh-size sensitivity. Contour of the tensile damage index (d^+) after the peak load for four different meshes: (a) without the crack-tracking algorithm, (b): with the crack-tracking algorithm.

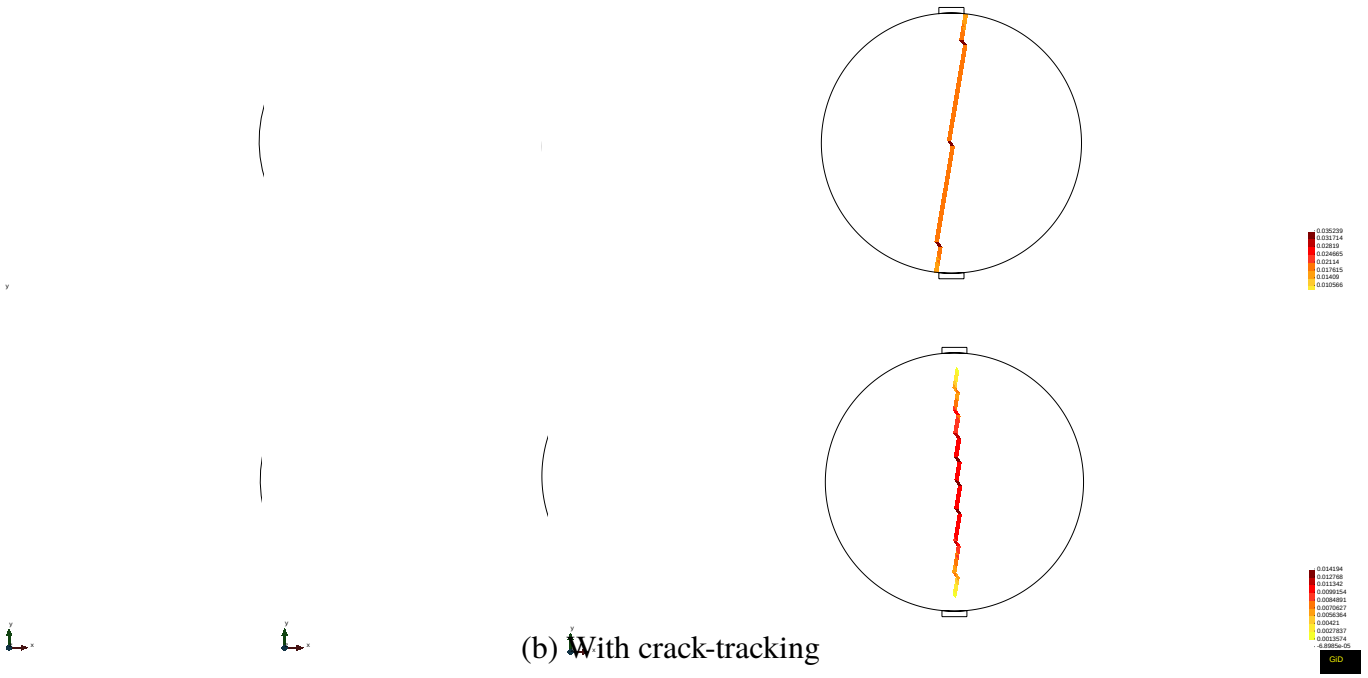

(b) With crack-tracking

Fig. 10: Mesh-size sensitivity. Contour of the maximum principal strains (ϵ_{max}) after the peak load for the four different meshes: (a) without the crack-tracking algorithm, (b): with the crack-tracking algorithm.

		No-Tracking		Tracking	
Mesh	Analytical capacity $[kN/m]$	Capacity $[kN/m]$	Difference from analytical [%]	Capacity $[kN/m]$	Difference from analytical [%]
Mesh-A	575.96	537.56	-6.67	579.39	0.60
Mesh-B	—"—	538.22	-6.55	585.29	1.62
Mesh-C'	—"—	514.98	-10.06	539.65	-6.30
Mesh-C	—"—	529.66	-8.04	544.44	-5.47
Mesh-C"	—"—	532.35	-7.57	549.10	-4.66
Mesh-D	—"—	529.14	-8.13	554.09	-3.80

Table 1: Comparison between numerical and analytical results with and without the proposed tracking algorithm for the Brazilian splitting test.

		No-Tracking		Tracking		Overhead using tracking	
Mesh	Number of nodes	Memory [Mb]	CPU-time [s]	Memory [Mb]	CPU-time [s]	Memory [%]	CPU-time [%]
Mesh-A	984	1.33	14.52	1.56	13.06	17.29	-10.06
Mesh-B	1711	2.37	28.66	2.78	24.96	17.30	-12.91
Mesh-C'	384	0.52	4.38	0.61	5.07	17.31	15.75
Mesh-C	994	1.35	10.47	1.58	13.15	17.04	25.60
Mesh-C"	1983	2.76	24.98	3.24	32.74	17.39	31.06
Mesh-D	1016	1.38	10.61	1.62	13.48	17.39	27.05

Table 2: Computational cost with and without the use of the tracking algorithm for the Brazilian splitting test.

As can be seen, the tracking algorithm is very efficient both in terms of memory requirements and computational time. The arrays necessary for the labelling system of the elements result to additional memory requirements of around 17 % using the tracking algorithm. The performed analyses show that the computational time overhead using tracking increases, as expected, with the increase of the number of degrees of freedom, with a maximum overhead of around 31% for the case of the refined Mesh-C". Note that in some cases (Mesh-A and Mesh-B) the computational cost using the tracking algorithm is lower than a calculation done without using it. This is because of the improvement of the non-linear iterations convergence rate due to the correct damage localization when using the tracking algorithm.

4.2 Structural Application: Frame wall with one door opening

In this section, we investigate the capacity of the proposed algorithm to simulate the response of a large-scale structural problem exhibiting multiple cracking. The simulated experiment consists in the in-plane lateral loading of a full-scale unreinforced masonry frame with an opening [74]. This structural example has been selected due to the complexity given by the structural interaction among the piers and the spandrel, representing a meaningful case with different types of cracks due to traction, shear and flexure. In fact, this test can show the capacity of the used approach to represent both the experimental cracking pattern and the redistribution of actions among structural members as soon as the different cracks appear.

4.2.1 Experimental setting and results

The masonry is built of yellow tuff bricks with dimensions 150 × 300 × 100 mm^3 and hydraulic mortar of 10 mm thickness. The wall has overall dimensions of 5100 mm length, 3620 mm height and 310 mm thickness. The spandrel above the opening lies over a timber lintel with bond length of 150 mm at both sides.

The experimental test was performed in two steps. Initially, a distributed load was applied at the top of each pier with a resultant $V = 200\ kN$. This was followed by the application of a horizontal displacement d at the left of the wall keeping the vertical load constant. Figure 11a illustrates the geometry and the load configuration of the experiment. Figure 11b and Figure 11c show the resulted cracking in the whole structure and the spandrel respectively. The in-plane loading activated different failure phenomena in masonry resulting in a complex cracking of the structure. In particular, two horizontal cracks formed at the base of the piers due to the debonding between the units and the mortar. Flexural cracking, crossing both the units and

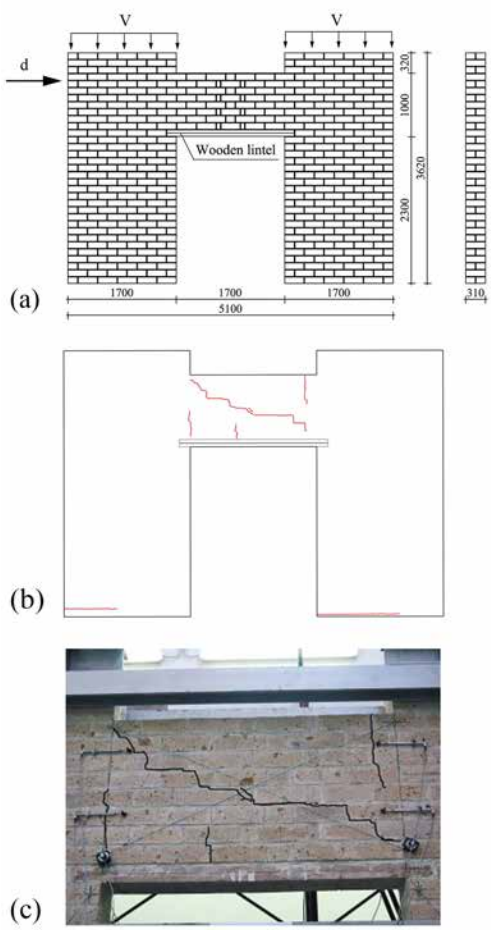

Fig. 11: (a) Geometry and load configuration of the experiment. Cracking after the end of the experiment of (b) the whole frame and (c) the spandrel (pictures adapted from [74]).

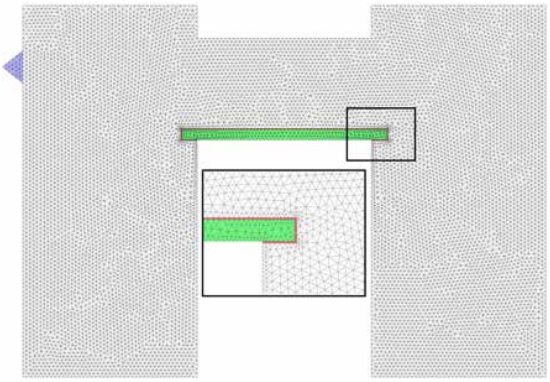

Fig. 12: Discretized domain used for the numerical simulation.

mortar-units interface, appeared in three locations at the lower and the upper part of the spandrel. Finally, the last reported damage was a diagonal shear crack starting from the middle of the spandrel and extending diagonally towards its opposite corners. For a detailed description of the experimental setup, the loading procedure and the damage pattern the reader is referred to the original work [74].

4.2.2 Numerical simulation

The experimental test is simulated using the numerical algorithm presented in Section 3. The material of the wall is idealized as homogeneous with its properties derived from the available experimental data [74], while appropriate values from the literature are chosen for the non-available material parameters. The constitutive model of Section 2 is used as an approximation of the masonry behaviour. In this work, focus is given on the capacity of the algorithm to simulate the different typologies of the localized cracking observed in the particular example.

For masonry, the selected material properties are $E = 1.54\ GPa$, $f^+ = 0.13\ MPa$, $v = 0.2$, $f^- = 3.9\ MPa$, $\rho = 1200\ kg/m^3$, $G^+ = 15\ J/m^2$, $G^- = 35000\ J/m^2$, while the ratio between uniaxial and biaxial compressive strength is considered as $f_b^-/f^- = 1.15$. Linear elastic behaviour is assumed for the timber lintel with Young's modulus $E = 15\ GPa$. The connection between the masonry and the timber lintel is modelled with care in order to provide a realistic representation of the actual interaction between the two neighbouring materials. This interconnection is modelled through a soft layer with thickness of 10 mm and limited strength and stiffness ($E = 0.02\ GPa$, $f^+ = 0.01\ MPa$, $v = 0.2$, $f^- = 3.9\ MPa$, $G^+ = 5\ J/m^2$, $G^- = 35000\ J/m^2$). This zone can be seen as the continuous counterpart of a no-tension discontinuous interface.

Following the experiment, the numerical simulation consists of two steps: first, the application of the dead load along with a vertical force equal to 200 kN at the top of each pier, and second, the incremental application of a horizontal displacement at the left part of the structure, keeping the load of the first step constant.

The masonry frame is discretized in an unstructured mesh of 2D plane-stress three-noded triangles with average mesh size of $h_e = 4\ cm$ (10678 nodes) (Figure 12). In the reference case the input parameters for the local crack-tracking algorithm are r_{excl}= 300 mm (equal to the length of the bricks), $a_{max} = 45°$ and r_{neigh} = 200 mm. The influence of these values is investigated in Section 4.2.5.

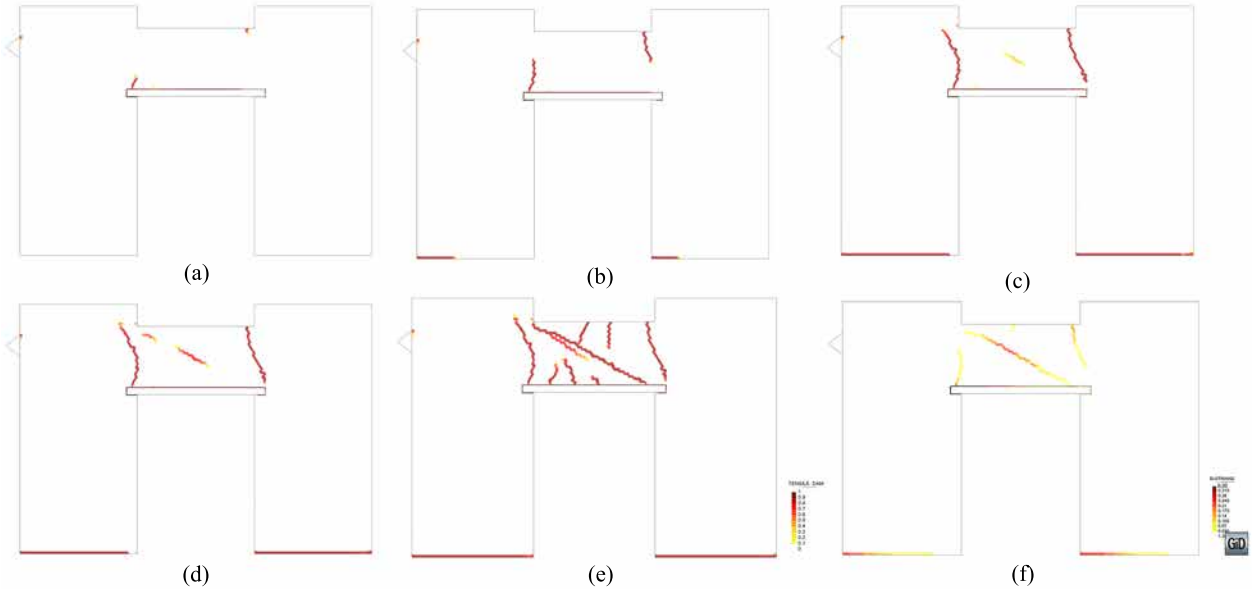

Fig. 13: Tensile damage contour for: (a) $d = 1.5\ mm$, (b) $d = 3.3\ mm$, (c) $d = 12.3\ mm$, (d) $d = 17.3\ mm$, (e) $d = 20.7\ mm$. (f) Maximum principal strains contour for $d = 20.7\ mm$.

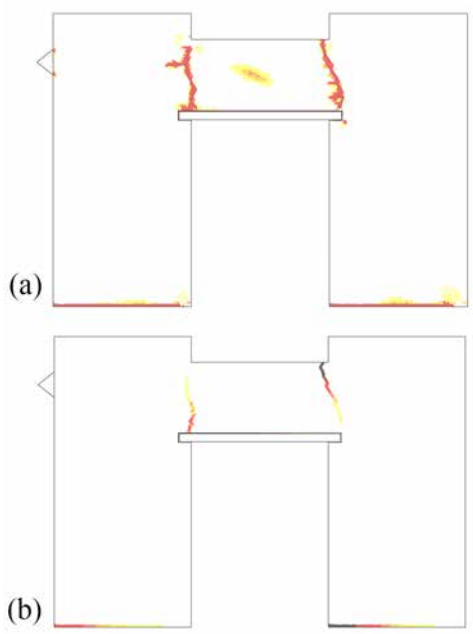

Fig. 14: Tensile damage contour (a) and maximum principal strains (b) for the analysis with the smeared crack approach without a crack-tracking technique (horizontal displacement $d = 25\ mm$)

4.2.3 Results and discussion

Figure 13 illustrates the sequence of the tensile cracks obtained from the numerical analysis. In the first part of the numerical simulation, which includes the application of the dead load as well as the load of 200 kN at the top of the piers, no damage occurs. Two vertical cracks at the corners of the spandrel are the first damage occurring in the structure during the second stage of the analysis (Figure 13a). An increase of the horizontal displacement results in the formation of two horizontal cracks at the base of the piers (Figure 13b) and their subsequent rocking. Following this, internal cracking starts to form within the spandrel (Figure 13c-d). Finally, at a horizontal displacement of 21 mm, a diagonal shear crack has totally formed and secondary flexure cracks are observed at the top and bottom of the spandrel (Figure 13e).

It can be appreciated in Figure 13f that the obtained damage is in good agreement with the resulted cracking pattern of the experiment (Figures 11b-c). The open localized cracks at the end of the analysis, displayed by the contour of the tensile principal strains in Figure 13f, are located at the both ends of the spandrel, at its middle and at the bottom of the piers as in the experiment.

Finally, it is noted that the numerical simulation of this particular example would be impossible using a crack-tracking technique without the enhancement for internal cracking. Apart from the internal shear cracking affecting the middle of the spandrel, the flexural cracks at its left bottom do not start from the boundary of the numerical domain.

The numerical result using the classical smeared crack approach, without the enhancement given by a crack-tracking technique, is illustrated in Figure 14.

Cracking at the base of the piers is almost localized within a single row of elements, facilitated by the alignment of the mesh with the expected crack direction. Contrarily, a dispersion of the damage can be observed at the region of the flexural cracks at the spandrel, where the solution is biased by the mesh topology. This spurious spreading of the damage results in the unrealistic release of elastic energy due to the elastic unloading of the elements surrounding the damaged ones. As a consequence, the capacity of the structure reduces before reaching the necessary force for the opening of the internal shear crack that was observed experimentally. This limitation of the classical smeared crack approach prevents to capture correctly the experimental obtained damage.

Figure 15 presents the smeared cracking strain field resulting from a numerical analysis of the same experiment performed with a micro-model approach by Parisi et al. [75]. The results obtained with the tracking algorithm (see Figure 13e & Figure 13f) agree with the damage pattern simulated by the micro-model.

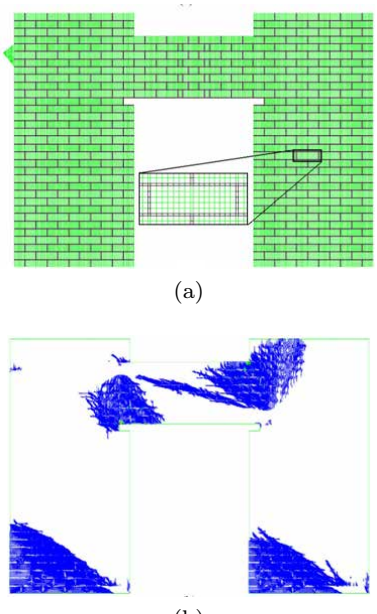

(a)

(b)

Fig. 15: Micro-model used in [75] for the simulation of the in-plane loaded masonry frame: (a) mesh, (b) smeared cracking strain field (pictures adapted from [75]).

Figure 16 presents the comparison between the numerical and experimental load-displacement diagrams. The use of the crack-tracking algorithm allows to capture correctly the experimentally obtained failure curve, both in terms of maximum strength and ductility of the

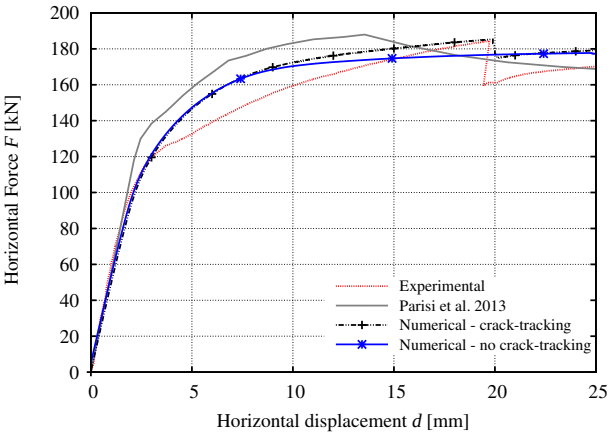

Fig. 16: Load-displacement graph of the experimental test and the numerical analyses.

structure. The first significant loss of stiffness is related to the rocking of the piers and the relative cracking at their base, which results in the increasing opening of the flexural cracks at the two opposite ends of the spandrel (see Figure 13b). The latter damage is the dominating cause for the loss of stiffness of the structure until the shear crack forms in the spandrel, which results in the sudden drop of the applied force for a displacement of about 20 mm.

An important aspect of the numerical result is its capacity to reproduce satisfactorily the loss of structural stiffness occurring due to all the different fracture phenomena throughout the loading history. This is essential for the evaluation of the seismic capacity of an existing structure, or the design of a new one, since common procedures (e.g. [76, 77]) rely on the realistic estimation of the initial stiffness, the ductility and the strength reduction. When the crack-tracking technique is not used, the load versus displacement graph fails to represent the correct sequence of fracture in the nonlinear range, as the brittle shear cracking in the spandrel.

4.2.4 Computational cost

As in the example of the Brazilian splitting test, Table 3 presents information regarding the computational cost with and without the use of the tracking algorithm for the particular example. The additional requirements in memory lie within the same range of values as in the Brazilian splitting test, i.e around 16% higher using the tracking algorithm. The processing time with the proposed technique is around 11% higher than that of the classical smeared crack approach.

No-Tracking		Tracking		Overhead using tracking	
Memory [Mb]	CPU-time [s]	Memory [Mb]	CPU-time [s]	Memory [%]	CPU-time [%]
16.97	238.06	19.62	264.03	15.61	10.90

Table 3: Computational cost with and without the use of the tracking algorithm for the frame wall with a door opening example.

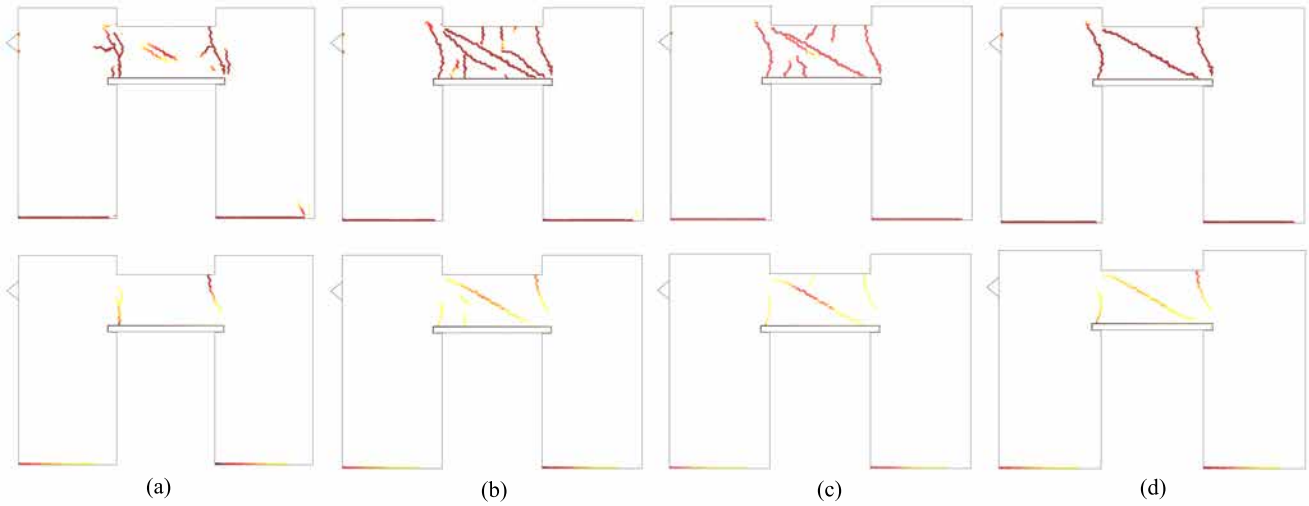

Fig. 17: Contour of tensile damage (top) and maximum principal strains (bottom): (a) $r_{excl} = 0.1\ m$, (b) $r_{excl} = 0.2\ m$, (c) $r_{excl} = 0.3\ m$, (d) $r_{excl} = 0.5\ m$ (horizontal displacement $d = 0.21\ m$).

4.2.5 Effect of tracking parameters

This section presents a sensitivity analysis on the crack-tracking parameters to assess their influence on the numerical results. Figure 17 presents the obtained damage pattern with four different values of the exclusion radius r_{excl}= [0.1; 0.2; 0.3; 0.5 m]. As expected, the exclusion radius r_{excl} has significant effect in the numerical simulation, affecting the distribution of cracking within the analysed structure. Values lower than the unit size result in a denser cracking within the spandrel, changing the response of the structure and the damage pattern. In particular, for $r_{excl} = 0.1\ m$ various cracks appear at the both ends of the spandrel, facilitating the rocking mode of the whole structure, while the shear crack at the middle of the spandrel cannot be reproduced. This change in the structural response can be appreciated in the load vs displacement graphs of Figure 18, where for $r_{excl} = 0.1\ m$ the typical graph for a rocking failure mode is obtained, without however, the sudden drop attributed to the shear cracking of the spandrel. On the contrary, when values higher of 0.2 m are chosen, the numerical model reproduces the experimental obtained structural response (Figure 17b-d and Figure 18). Actually, a value of the exclusion radius lower than 0.2 m does not take into account the internal microstructure of masonry defined by the size of the brick.

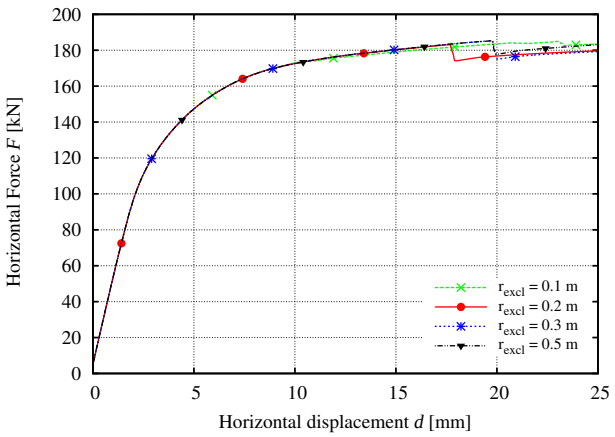

Fig. 18: Sensitivity of structural capacity to r_{excl}.

The above results demonstrate the utility of the exclusion radius. The failure mechanism of masonry structures is determined by the relative position of the cracks and consequently the division of the whole structure into macroblocks. The relative geometry and strength of the components play a decisive role in the type of cracking of masonry structures. This can be appreciated

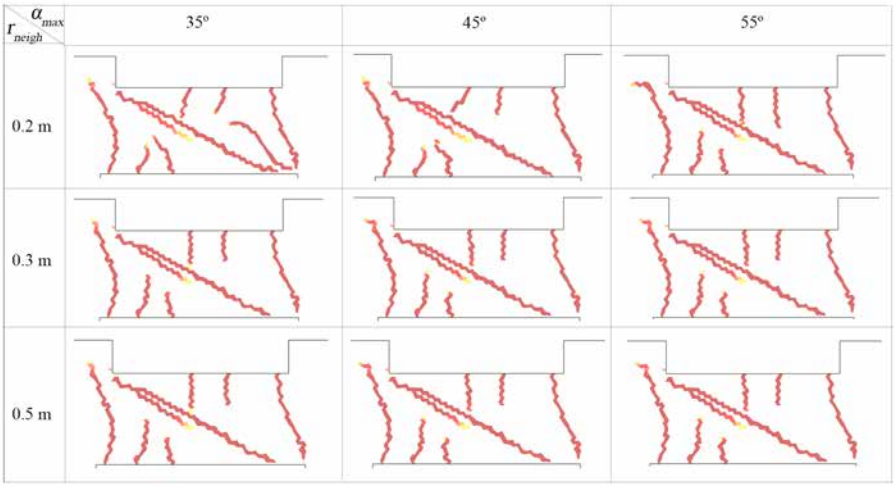

Fig. 19: Sensitivity of damage distribution at the spandrel to a_{max} and r_{neigh}.

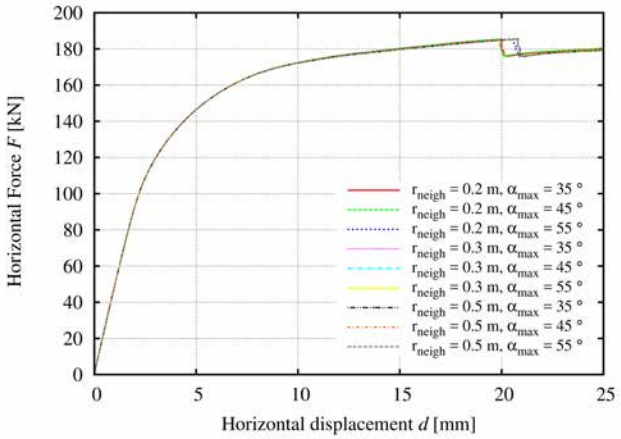

Fig. 20: Sensitivity of structural capacity to a_{max} and r_{neigh}

in the experimental test under investigation, in which cracking occurred mainly at the joints between bricks and mortar. A continuum finite element model ignores the internal geometry of the composite and therefore fails to capture failure mechanisms determined by it. This drawback can be partially overcome with the use of the exclusion radius, which can be perceived as a way to take into account the size effect of the units within a continuum finite element model. On the contrary, a micro-model could simulate this cracking phenomenon in a more direct way due to the *a priori* detailed geometrical definition of the problem, at the cost of a computation time largely higher than that of the proposed model. This disadvantage of micro-models renders them hardly applicable to the analysis of large and complex structures. The proposed model based on a crack-tracking method shows to be a good compromise between accuracy and computational cost.

Figures 19 and 20 present the cracking affecting the spandrel and the relative load against displacement curves respectively for nine different combinations of a_{max} and r_{neigh} for $r_{excl} = 0.3\ m$. Once the exclusion radius is well defined, the effect of a_{max} and r_{neigh} is minor to the global response of the structure. The shear cracking at the middle of the spandrel is identical for all combinations of the above correction parameters. This is to be anticipated, since shear cracking, dominant in this case, is not affected by these parameters, on contrary with cracking under bending stress states (see [16]). Restricting the change in the crack curvature with low values of a_{max} has a small effect on the secondary flexural cracking affecting the lower and upper boundaries of the spandrel. In any case, the collapse mechanism is identical for all the investigated values of a_{max} and r_{neigh}.

5 Conclusions

The structural behaviour of constructions made of quasi-brittle materials, such as concrete or masonry, is determined by the formation of discrete cracks that define the collapse mechanism. Continuum finite element approaches based on the classical smeared crack approach simulate poorly this complex response since (a) they may represent damage spread in an unrealistic way and (b) the numerical solution is determined by the mesh-induced directional bias.

To circumvent the above drawbacks, this article proposes the use of a crack-tracking technique for the realistic simulation of cracking in structures made of quasi-

brittle materials. A novel algorithm is presented for the simulation of cracking starting at any location within the discretized domain making possible the simulation of both boundary and internal cracking. This contribution, along with the capacity of the approach to allow the nucleation of new cracks without the *a priori* definition by the user, extends the application field of tracking algorithms to the structural assessment of new or existing structures.

Two numerical examples are used to validate the proposed algorithm: a Brazilian splitting test and the in-plane loading of a frame wall with a door opening. The numerical simulations prove the capability of the model to represent correctly the formation and propagation of tensile, flexural and shear cracks within the discretized domain. The accurate representation by the model of the cracking phenomena produces a realistic simulation of the experimental failure mechanisms and the correct estimation of the nonlinear response of the structure. The model yields a damage pattern more realistic than the well-known smeared crack approach.

The limited computational cost of the proposed approach and its accuracy render it a reliable tool for the analysis of complex structural problems experiencing multiple cracking. The tracking technique proposed for the modelling of internal cracking has shown to be robust and it can be used in conjunction with other finite element formulations and material models.

Acknowledgements This research has received the financial support from the MINECO (Ministerio de Economia y Competitividad of the Spanish Government) and the ERDF (European Regional Development Fund) through the the MULTIMAS project (Multiscale techniques for the experimental and numerical analysis of the reliability of masonry structures, ref. num. BIA2015-63882-P) and the EACY project (Enhanced accuracy computational and experimental framework for strain localization and failure mechanisms, ref. MAT 2013-48624-C2-1-P).

The authors gratefully acknowledge Dr. Fulvio Parisi for providing information regarding the experimental data.

References

1. D. Ngo and C. Scordelis, "Finite Element Analysis of Reinforced Concrete Beams," *ACI Journal*, vol. 64, no. 3, pp. 152–163, 1967.
2. Y. Rashid, "Ultimate strength analysis of prestressed concrete pressure vessels," *Nuclear Engineering and Design*, vol. 7, pp. 334–344, apr 1968.
3. J. Mosler and G. Meschke, "Embedded crack vs. smeared crack models: a comparison of elementwise discontinuous crack path approaches with emphasis on mesh bias," *Computer Methods in Applied Mechanics and Engineering*, vol. 193, no. 30-32, pp. 3351–3375, 2004.
4. R. H. J. Peerlings, R. De Borst, W. A. M. Brekelmans, and J. H. P. De Vree, "Gradient enhanced damage for quasi-brittle materials," *International Journal for Numerical Methods in Engineering*, vol. 39, no. 19, pp. 3391–3403, 1996.
5. A. Simone, G. N. Wells, and L. J. Sluys, "From continuous to discontinuous failure in a gradient-enhanced continuum damage model," *Computer Methods in Applied Mechanics and Engineering*, vol. 192, pp. 4581–4607, oct 2003.
6. Z. P. Bažant and F. B. Lin, "Nonlocal Smeared Cracking Model for Concrete Fracture," *Journal of Structural Engineering*, vol. 114, pp. 2493–2510, nov 1988.
7. J. de Vree, W. Brekelmans, and M. van Gils, "Comparison of nonlocal approaches in continuum damage mechanics," *Computers & Structures*, vol. 55, pp. 581–588, may 1995.
8. R. De Borst, "Simulation of strain localization: a reppraisal of the cosserat continuum," *Engineering Computations*, vol. 8, pp. 317–332, apr 1991.
9. R. De Borst, L. Sluys, H.-B. Mühlhaus, and J. Pamin, "Fundamental issues in Finite Element Analyses of localization of deformation," *Engineering Computations*, vol. 10, no. 2, pp. 99–121, 1993.
10. L. Benedetti, M. Cervera, and M. Chiumenti, "Stress-accurate Mixed FEM for soil failure under shallow foundations involving strain localization in plasticity," *Computers and Geotechnics*, vol. 64, pp. 32–47, mar 2015.
11. M. Jirásek and T. Zimmermann, "Embedded crack model. Part II. Combination with smeared cracks," *International Journal for Numerical Methods in Engineering*, vol. 50, no. 6, pp. 1291–1305, 2001.
12. G. N. Wells and L. J. Sluys, "A new method for modelling cohesive cracks using finite elements," *International Journal for Numerical Methods in Engineering*, vol. 50, no. 12, pp. 2667–2682, 2001.
13. N. Moës and T. Belytschko, "Extended finite element method for cohesive crack growth," *Engineering Fracture Mechanics*, vol. 69, pp. 813–833, may 2002.
14. P. Dumstorff and G. Meschke, "Crack propagation criteria in the framework of X-FEM-based structural analyses," *International Journal for Numerical and Analytical Methods in Geomechanics*, vol. 31, pp. 239–259, feb 2007.
15. M. Cervera and M. Chiumenti, "Mesh objective tensile cracking via a local continuum damage model and a crack tracking technique," *Computer Methods in Applied Mechanics and Engineering*,

vol. 196, no. 1-3, pp. 304–320, 2006.
16. M. Cervera, L. Pelà, R. Clemente, and P. Roca, "A crack-tracking technique for localized damage in quasi-brittle materials," *Engineering Fracture Mechanics*, vol. 77, no. 13, pp. 2431–2450, 2010.
17. A. Slobbe, M. Hendriks, and J. Rots, "Smoothing the propagation of smeared cracks," *Engineering Fracture Mechanics*, vol. 132, pp. 147–168, dec 2014.
18. M. Jirásek and P. Grassl, "Evaluation of directional mesh bias in concrete fracture simulations using continuum damage models," *Engineering Fracture Mechanics*, vol. 75, no. 8, pp. 1921–1943, 2008.
19. R. De Borst, "Fracture in quasi-brittle materials: A review of continuum damage-based approaches," *Engineering Fracture Mechanics*, vol. 69, pp. 95–112, 2001.
20. T. Rabczuk, "Computational Methods for Fracture in Brittle and Quasi-Brittle Solids : State-of-the-art Review and Future Perspectives," *ISRN Applied Mathematics*, vol. 2013, pp. 1–61, 2012.
21. W.-F. Chen, *Plasticity in reinforced concrete*. McGraw-Hill, 1982.
22. W.-F. Chen, *Constitutive Equations for Engineering Materials, Vol. 2 plasticity and modelling*. Elsevier, 1994.
23. P. H. Feenstra and R. De Borst, "A composite plasticity model for concrete," *International Journal of Solids and Structures*, vol. 33, pp. 707–730, feb 1996.
24. J. Mazars and G. Pijaudier-Cabot, "Continuum damage theory - application to concrete," *Journal of Engineering Mechanics*, vol. 115, no. 2, pp. 345–365, 1989.
25. M. Cervera, J. Oliver, and R. Faria, "Seismic evaluation of concrete dams via continuum damage models," *Earthquake Engineering & Structural Dynamics*, vol. 24, no. 9, pp. 1225–1245, 1995.
26. J. Lubliner, J. Oliver, S. Oller, and E. Oñate, "A plastic-damage model for concrete," *International Journal of Solids and Structures*, vol. 25, no. 3, pp. 299–326, 1989.
27. G. Lee and G. L. Fenves, "Plastic-Damage Model for Cyclic Loading of Concrete Structures," *Journal of Engineering Mechanics*, vol. 124, no. 8, pp. 892–900, 1998.
28. J. Y. Wu, J. Li, and R. Faria, "An energy release rate-based plastic-damage model for concrete," *International Journal of Solids and Structures*, vol. 43, no. 3-4, pp. 583–612, 2006.
29. E. Papa, "A unilateral damage model for masonry based on a homogenisation procedure," *Mechanics of Cohesive-Frictional Materias*, vol. 1, no. February, pp. 349–366, 1996.
30. P. B. Lourenço, "Anisotropic Softening Model for Masonry Plates and Shells," *Journal of Structural Engineering*, vol. 126, no. 9, pp. 1008–1016, 2000.
31. L. Pelà, M. Cervera, and P. Roca, "An orthotropic damage model for the analysis of masonry structures," *Construction and Building Materials*, vol. 41, pp. 957–967, 2013.
32. J. Lopez, S. Oller, E. Oñate, and J. Lubliner, "A homogeneous constitutive model for masonry," *International Journal for Numerical Methods in Engineering*, vol. 46, no. 10, pp. 1651–1671, 1999.
33. V. Kouznetsova, M. G. D. Geers, and W. A. M. Brekelmans, "Multi-scale constitutive modelling of heterogeneous materials with a gradient-enhanced computational homogenization scheme," *International Journal for Numerical Methods in Engineering*, vol. 54, pp. 1235–1260, jul 2002.
34. A. Zucchini and P. B. Lourenço, "A micro-mechanical model for the homogenisation of masonry," *International Journal of Solids and Structures*, vol. 39, pp. 3233–3255, jun 2002.
35. P. B. Lourenço, G. Milani, A. Tralli, and A. Zucchini, "Analysis of masonry structures: review of and recent trends in homogenization techniques.," *Canadian Journal of Civil Engineering*, vol. 34, no. 11, pp. 1443–1457, 2007.
36. C. Calderini and S. Lagomarsino, "Continuum Model for In-Plane Anisotropic Inelastic Behavior of Masonry," *Journal of Structural Engineering*, vol. 134, no. 2, pp. 209–220, 2008.
37. J. Oliver, M. Caicedo, E. Roubin, A. Huespe, and J. Hernández, "Continuum approach to computational multiscale modeling of propagating fracture," *Computer Methods in Applied Mechanics and Engineering*, vol. 294, pp. 384–427, 2015.
38. M. Petracca, L. Pelà, R. Rossi, S. Oller, G. Camata, and E. Spacone, "Regularization of first order computational homogenization for multiscale analysis of masonry structures," *Computational Mechanics*, dec 2015.
39. P. B. Lourenço and J. G. Rots, "Multisurface Interface Model for Analysis of Masonry Structures," *Journal of Engineering Mechanics*, vol. 123, no. 7, pp. 660–668, 1997.
40. L. Macorini and B. A. Izzuddin, "A non-linear interface element for 3D mesoscale analysis of brick-masonry structures," *International Journal for Numerical Methods in Engineering*, vol. 85, pp. 1584–1608, mar 2011.
41. S. Oliveira and R. Faria, "Numerical simulation of collapse scenarios in reduced scale tests of arch dams," *Engineering Structures*, vol. 28, no. 10,

pp. 1430–1439, 2006.
42. P. Roca, M. Cervera, G. Gariup, and L. Pelà, "Structural Analysis of Masonry Historical Constructions. Classical and Advanced Approaches," *Archives of Computational Methods in Engineering*, vol. 17, pp. 299–325, jul 2010.
43. J. Carvalho, J. Ortega, P. B. Lourenço, L. F. Ramos, and H. Roman, "Safety analysis of modern heritage masonry buildings: Box-buildings in Recife, Brazil," *Engineering Structures*, vol. 80, pp. 222–240, 2014.
44. N. Mendes and P. B. Lourenço, "Sensitivity analysis of the seismic performance of existing masonry buildings," *Engineering Structures*, vol. 80, pp. 137–146, 2014.
45. P. Jäger, P. Steinmann, and E. Kuhl, "On local tracking algorithms for the simulation of three-dimensional discontinuities," *Computational Mechanics*, vol. 42, no. 3, pp. 395–406, 2008.
46. S.-N. Roth, P. Léger, and A. Soulaïmani, "A combined XFEM-damage mechanics approach for concrete crack propagation," *Computer Methods in Applied Mechanics and Engineering*, vol. 283, pp. 923–955, jan 2015.
47. Y. Zhang, R. Lackner, M. Zeiml, and H. a. Mang, "Strong discontinuity embedded approach with standard SOS formulation: Element formulation, energy-based crack-tracking strategy, and validations," *Computer Methods in Applied Mechanics and Engineering*, vol. 287, pp. 335–366, 2015.
48. S. Saloustros, L. Pelà, and M. Cervera, "A crack-tracking technique for localized cohesive-frictional damage," *Engineering Fracture Mechanics*, vol. 150, pp. 96–114, 2015.
49. L. Pelà, M. Cervera, S. Oller, and M. Chiumenti, "A localized mapped damage model for orthotropic materials," *Engineering Fracture Mechanics*, vol. 124-125, pp. 196–216, 2014.
50. C. Linder and A. Raina, "A strong discontinuity approach on multiple levels to model solids at failure," *Computer Methods in Applied Mechanics and Engineering*, vol. 253, pp. 558–583, 2013.
51. M. H. Motamedi, D. A. Weed, and C. D. Foster, "Numerical simulation of mixed mode (I and II) fracture behavior of pre-cracked rock using the strong discontinuity approach," *International Journal of Solids and Structures*, vol. 85-86, pp. 44–56, 2016.
52. J.-b. Li, X.-a. Fu, B.-b. Chen, C. Wu, and G. Lin, "Modeling crack propagation with the extended scaled boundary finite element method based on the level set method," *Computers and Structures*, vol. 167, pp. 50–68, 2016.
53. J. Y. Wu, F. B. Li, and S. L. Xu, "Extended embedded finite elements with continuous displacement jumps for the modeling of localized failure in solids," *Computer Methods in Applied Mechanics and Engineering*, vol. 285, pp. 346–378, 2015.
54. S. Feld-Payet, V. Chiaruttini, J. Besson, and F. Feyel, "A new marching ridges algorithm for crack path tracking in regularized media," *International Journal of Solids and Structures*, vol. 71, pp. 57–69, 2015.
55. C. Comi and U. Perego, "Fracture energy based bi-dissipative damage model for concrete," *International Journal Of Solids And Structures*, vol. 38, no. 36-37, pp. 6427–6454, 2001.
56. L. Pelà, M. Cervera, and P. Roca, "Continuum damage model for orthotropic materials: Application to masonry," *Computer Methods in Applied Mechanics and Engineering*, vol. 200, pp. 917–930, feb 2011.
57. G. Z. Voyiadjis, Z. N. Taqieddin, and P. I. Kattan, "Theoretical Formulation of a Coupled Elastic–Plastic Anisotropic Damage Model for Concrete using the Strain Energy Equivalence Concept," *International Journal of Damage Mechanics*, vol. 18, no. 7, pp. 603–638, 2009.
58. J. Mazars, F. Hamon, and S. Grange, "A new 3D damage model for concrete under monotonic, cyclic and dynamic loadings," *Materials and Structures*, pp. 3779–3793, 2014.
59. W. He, Y. F. Wu, Y. Xu, and T. T. Fu, "A thermodynamically consistent nonlocal damage model for concrete materials with unilateral effects," *Computer Methods in Applied Mechanics and Engineering*, vol. 297, pp. 371–391, 2015.
60. L. F. Pereira, J. Weerheijm, and L. J. Sluys, "A new rate-dependent stress-based nonlocal damage model to simulate dynamic tensile failure of quasi-brittle materials," *International Journal of Impact Engineering*, vol. 94, pp. 83–95, 2016.
61. J. Lemaitre and J. L. Chaboche, "Aspect Phenomenologique de la Rupture par Endommagement," *Journal de Mécanique Appliquée*, vol. 2, no. 3, 1978.
62. J. C. Simo and J. W. Ju, "Strain- and stress-based continuum damage models-I. Formulation," *International Journal of Solids and Structures*, vol. 23, no. 7, pp. 821–840, 1987.
63. J. Oliver, M. Cervera, S. H. Oller Martinez, and J. Lubliner, "Isotropic damage models and smeared crack analysis of concrete," *Proc. SCI-C Computer Aided Analysis and Design of Concrete Structures*, no. February, pp. 945–957, 1990.

64. Z. Bazant and B. Oh, "Crack band theory for fracture of concrete," *Materials and Structures*, vol. 16, pp. 155–177, 1983.
65. M. Cervera, "Viscoelasticity and Rate-dependent Continuum Damage Models, Monography N-79," tech. rep., Barcelona, 2003.
66. J. Oliver, "A consistent characteristic length for smeared cracking models," *International Journal for Numerical Methods in Engineering*, vol. 28, no. 2, pp. 461–474, 1989.
67. J.-Y. Wu and M. Cervera, "On the equivalence between traction- and stress-based approaches for the modeling of localized failure in solids," *Journal of the Mechanics and Physics of Solids*, vol. 82, pp. 137–163, 2015.
68. M. Cervera and J.-Y. Wu, "On the conformity of strong, regularized, embedded and smeared discontinuity approaches for the modeling of localized failure in solids," *International Journal of Solids and Structures*, vol. 71, pp. 19–38, 2015.
69. ASTM:C496/C496M, "Standard Test Method for Splitting Tensile Strength of Cylindrical Concrete Specimens," *ASTM International*, no. 336, pp. 1–5, 2011.
70. ASTM:D3967-08, "Standard Test Method for Splitting Tensile Strength of Intact Rock Core Specimens," *ASTM International*, 2008.
71. COMET, "Coupled Mechanical and Thermal analysis, http://www.cimne.com/comet/," 2013.
72. GiD, "The personal pre and post-processor, http://www.gidhome.com/," 2014.
73. EN 1992 (Eurocode 2), "Design of concrete structures," tech. rep., London, 1992.
74. N. Augenti, F. Parisi, A. Prota, and G. Manfredi, "In-Plane Lateral Response of a Full-Scale Masonry Subassemblage with and without an Inorganic Matrix-Grid Strengthening System," *Journal of Composites for Construction*, vol. 15, no. 4, pp. 578–590, 2011.
75. F. Parisi, G. P. Lignola, N. Augenti, a. Prota, and G. Manfredi, "Nonlinear Behavior of a Masonry Subassemblage Before and After Strengthening with Inorganic Matrix-Grid Composites," *Journal of Composites for Construction*, vol. 15, no. 5, pp. 821–832, 2011.
76. EN 1998-1 (Eurocode 8), "Design of structures for earthquake resistance, Part 1 General rules seismic actions and rules for buildings," 2003.
77. P. Fajfar, "Capacity spectrum method based on inelastic demand spectra," *Earthquake Engineering & Structural Dynamics*, vol. 28, pp. 979–993, sep 1999.

This page is intentionally left blank.

Tracking multi-directional intersecting cracks in numerical modelling of masonry shear walls under cyclic loading

Savvas Saloustros · Luca Pelà · Miguel Cervera

Meccanica, 2017
doi:10.1007/s11012-017-0712-3

Accepted manucript in *Meccanica* - Special Issue of "*New Trends in Masonry Mechanics*"
DOI: 10.1007/s11012-017-0712-3

Tracking multi-directional intersecting cracks in numerical modelling of masonry shear walls under cyclic loading

Savvas Saloustros · Miguel Cervera · Luca Pelà

Received: 16 January 2017
Accepted: 8 June 2017

Abstract In-plane cyclic loading of masonry walls induces a complex failure pattern composed of multiple diagonal shear cracks, as well as flexural cracks. The realistic modelling of such induced localized cracking necessitates the use of costly direct numerical simulations with detailed information on both the properties and geometry of masonry components. On the contrary, computationally efficient macro-models using standard smeared-crack approaches often result in a poor representation of fracture in the simulated material, not properly localized and biased by the finite element mesh orientation. This work proposes a possible remedy to these drawbacks of macro-models through the use of a crack-tracking algorithm. The macro-modelling approach results in an affordable computational cost, while the tracking algorithm aids the mesh-bias independent and localized representation of cracking. A novel methodology is presented that allows the simulation of intersecting and multi-directional cracks using tracking algorithms. This development extends the use of localized crack approaches using tracking algorithms to a wider field of applications exhibiting multiple, arbitrary and interacting cracking. The paper presents also a novel formulation including into an orthotropic damage model the description of irreversible deformations under shear loading. The proposed approach is calibrated through the comparison with an experimental test on a masonry shear wall against in-plane cyclic loading.

Keywords Continuum Damage Mechanics · Crack-Tracking · Cyclic Shear Loading · Intersecting Cracks · Masonry walls

Savvas Saloustros · Miguel Cervera · Luca Pelà

Department of Civil and Environmental Engineering
Universitat Politècnica de Catalunya (UPC-BarcelonaTech)
Jordi Girona 1-3, 08034 Barcelona, Spain.

International Center for Numerical Methods in Engineering (CIMNE)
Gran Capità, S/N, 08034 Barcelona, Spain.

E-mail: savvas.saloustros@upc.edu
E-mail: miguel.cervera@upc.edu
E-mail: luca.pela@upc.edu

1 Introduction

Damage in masonry appears in the form of localized cracks. The propagation of these cracks within the structure determines the development of the collapse mechanism and consequently the capacity of the structure under the given loading conditions. This structural behaviour has been taken into account for the development of both classical and advanced analysis tools for the structural assessment of masonry constructions [1, 2, 3, 4].

Numerical modelling of masonry structures has undergone important developments in the last decades. The inventory of numerical methods today includes simplified techniques such as limit analysis software [5, 6, 7, 8], equivalent frame methods [9, 10, 11] and macro-modelling approaches [12, 13, 14] to sophisticated ones as micro-modelling [15, 16] and multi-scale finite element models [17, 18, 19]. Simplified numerical methods, like the macro-modelling ones, consider masonry as a continuum material with average properties. This simplification allows for the numerical anal-

ysis of large scale structures at an affordable computational cost with however limited accuracy in the damage representation. Reciprocally, the explicit consideration of the masonry micro-structure in micro-modelling techniques results in a more realistic representation of cracking, at the cost of increased computation time and memory requirements that limits up to date their application to small structural elements rather than whole structures.

An affordable alternative to the simulation of localized cracking in large scale structures was proposed by Cervera and co-workers [20, 21, 22]. The method bases on the enhancement of the smeared crack approach with the use of a crack-tracking algorithm. The outcome of this approach is the realistic representation of evolving localized cracks within the analysed structure for a computational cost comparable to that of the classical smeared crack approach [23, 24].

Despite the above recent applications on masonry structures, tracking algorithms have a long history in the simulation of localized failure in quasi-brittle materials. They are used for the enhancement of problems involving the progression of both weak, or smeared (e.g. [25, 26, 22]) and strong, or discrete, discontinuities (e.g. [27, 28, 29, 30]). Independently of the chosen approach, their application aims to circumvent the problem of the mesh-dependency that the irreducible standard finite element formulation presents. An additional feature is the realistic representation of cracking, since the localization of damage occurs within a narrow band of the mesh. Notwithstanding the aforementioned advantages, tracking algorithms are commonly designed with important assumptions regarding the initiation, propagation and completion of the simulated cracks. Such assumptions have limited the use of these approaches to the simulation of propagating cracks under monotonic loading.

This paper presents a methodology to simulate efficiently the localized cracking in masonry structures induced by in-plane cyclic loading using a continuum damage mechanics model enhanced with a crack-tracking algorithm. Cyclic loading of masonry structures may result in complex damage patterns characterized by multiple and intersecting cracks. To appropriately model this, a novel numerical methodology is proposed, on the basis of the tracking algorithm developed in previous works [22, 31, 32], that allows the simulation of intersecting and multi-directional cracking, extending the use of tracking algorithms to a large field of applications. At the constitutive level, the paper presents a novel formulation in the context of a continuum damage model for the description of irreversible deformations under shear loading.

After this introduction, the paper is organized in the following way. Section 2 presents the used constitutive damage model. Following that, the novel tracking algorithm is detailed in Section 3. The proposed approach is calibrated in Section 4 through the simulation of an experimentally tested masonry wall under cyclic shear loading. The same section addresses the issue of mesh objectivity of the tracking algorithm. The paper ends with the concluding Section 5.

2 Constitutive model

The material non-linearity is represented in the numerical simulations through the use of the constitutive model presented in [33]. It is a strain-based continuum damage model with two scalar damage variables for distinguishing between tensile and compressive damage. The decomposition of the effective stress tensor into positive and negative parts, as well as the use of the two damage variables, results in a unilateral effect under tension-compression cyclic loading. The model can account for irreversible deformations through a simple and efficient algorithm, within the context of continuum damage mechanics. The above properties, as well as the limited number of involved material parameters and the simple explicit formulation, make it a suitable model for the seismic analysis of large concrete and masonry structures [34, 35, 36, 37].

For the sake of completeness, this section presents the basic ingredients of the aforementioned *tension-compression damage model*. The shear behaviour of the model is carefully considered through the proper definition of the damage surfaces and the evolution of the irreversible strains. The modelling of the irreversible strains is achieved by improving previous formulations mainly intended for concrete structures in [33, 34, 38]. The section ends with a discussion over the effect of the proposed alterations to the evolution of the irreversible deformations under shear loading.

2.1 Constitutive law

The Cauchy stress tensor (of rank two) $\boldsymbol{\sigma}$ is computed in the tension-compression damage model through the constitutive relation

$$\boldsymbol{\sigma} = (1 - d^+)\,\bar{\boldsymbol{\sigma}}^+ + (1 - d^-)\,\bar{\boldsymbol{\sigma}}^- \tag{1}$$

where d^+ and d^- are scalar variables denoting the compressive and tensile damage affecting the positive $\bar{\boldsymbol{\sigma}}^+$

and negative parts $\bar{\boldsymbol{\sigma}}^-$ of the effective stress tensor respectively. The latter are calculated through the distinguishing stress split according to [38]

$$\bar{\boldsymbol{\sigma}}^+ = \sum_{j=1}^{3} \langle \bar{\sigma}_j \rangle \, \mathbf{p_j} \otimes \mathbf{p_j} \tag{2}$$

$$\bar{\boldsymbol{\sigma}}^- = \bar{\boldsymbol{\sigma}} - \bar{\boldsymbol{\sigma}}^+ \tag{3}$$

In the above equations, σ_j is the principal stress corresponding to the eigenvector $\mathbf{p_j}$ of the effective stress tensor $\bar{\boldsymbol{\sigma}}$ and the symbols $\langle \cdot \rangle$ are the Macaulay brackets ($\langle x \rangle = x$, if $x \geq 0$,$\langle x \rangle = 0$, if $x < 0$).

The model uses two scalar variables τ^+ and τ^- as equivalent stresses, to distinguish between loading-unloading and reloading. The adopted values of τ^+ and τ^- determine the shape of the d^+ and d^- damage surfaces. In this work we have adopted the values proposed in [19, 39]

$$\tau^+ = H\left[\bar{\sigma}_{max}\right] \frac{1}{1-a} \left[\sqrt{3\bar{J}_2} + a\bar{I}_1 + b\langle \bar{\sigma}_{m} \right.$$

$$\tau^- = H\left[-\bar{\sigma}_{min}\right] \frac{1}{1-a} \left[\sqrt{3\bar{J}_2} + a\bar{I}_1 + \kappa_1 l \right.$$

$$a = \frac{\left(f_b^-/f^-\right) - 1}{2\left(f_b^-/f^-\right) - 1}$$

$$b = (1-a)\frac{f^-}{f^+} - (1+a) \tag{7}$$

In the above, f^+ and f^- denote the tensile and compressive uniaxial strengths respectively and f_b^- the biaxial compressive strength. $\bar{I}_1$ is the first invariant of the effective stress tensor and $\bar{J}_2$ the second invariant of the deviatoric effective stress tensor. Finally, $\bar{\sigma}_{max}$ and $\bar{\sigma}_{min}$ stand for the maximum and minimum principal effective stresses respectively. The use of the Heaviside step function ($H[x] = 1$ if $x \geq 0$ and $H[x] = 0$ if $x < 0$) activates the τ^+ for tensile and shear stress states (1st, 2nd and 4th quadrants in Figure 1), and the τ^- for compressive and shear shear stress states (2nd, 3rd and 4th quadrants in Figure 1).

The κ_1 variable controls the shape of the failure surface in the shear quadrants (i.e. 2nd and 4th quadrants in Figure 1). Its value varies between 0 (i.e. the Drucker-Prager criterion) and 1 (i.e. the criterion proposed in [40]). Note that the use of the Macaulay brackets for $\bar{\sigma}_{max}$ in equation (5) makes the function τ^- independent of κ_1 for pure compression. This, in addition to the fact that κ_1 does not appear in equation (4), make the tensile and compressive response in the 1st and 3rd quadrants of Figure 1 independent of κ_1. As shown by Petracca et al. [39, 41], the different choice in the definition of the equivalent stresses from those proposed in [35, 38, 40] results in a better control of the model behaviour under shear monotonic loading. As it will be shown later, the choice of such surfaces in the current model results also in the consideration of the irreversible deformations under shear loading.

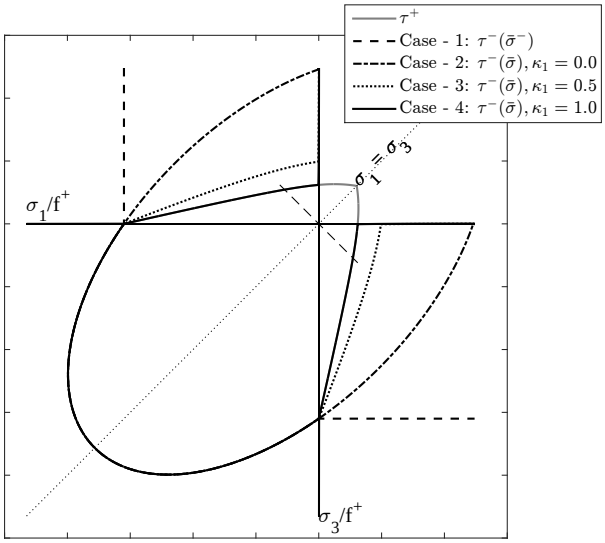

Fig. 1: Effect of the τ^- function to the shape of the d^- failure surface in the shear quadrants for the plane stress case.

Following the above, the damage criteria can be expressed as

$$\Phi^{\pm}(r^{\pm}, \tau^{\pm}) = \tau^{\pm} - r^{\pm} \leq 0 \tag{8}$$

where the internal variables r^+ and r^- represent the current damage thresholds and the respective expansion of the d^+ and d^- damage surfaces. Their initial values are defined to be equal to the uniaxial tensile strength $r_0^+ = f^+$ and the uniaxial compressive strength $r_0^- = f^-$. After damage is triggered, their values are equal to the maximum attained values by the equivalent stresses

$$r_n^{\pm} = max\left[r_0^{\pm}, \max_{i \in (0,n)} \left(\tau_i^{\pm} \right) \right] \tag{9}$$

with n representing the number of the current (load /displacement) increment.

The effect of the irreversible deformations is accounted using the following definition of the effective stress tensor $\bar{\boldsymbol{\sigma}}$

$$\bar{\boldsymbol{\sigma}} = \boldsymbol{C_0} : (\boldsymbol{\epsilon} - \boldsymbol{\epsilon}^i) = \boldsymbol{C_0} : \boldsymbol{\epsilon}^e \tag{10}$$

where $\boldsymbol{C_0}$ denotes the (rank four) elastic constitutive tensor and $\boldsymbol{\epsilon}^i$ the irreversible part of the second order total strain tensor $\boldsymbol{\epsilon}$ and $\boldsymbol{\epsilon}^e$ the elastic one. Contrary to the total strain tensor, which is an external variable of the model, the irreversible strain tensor is an internal variable. The following expression is proposed in this work for the rate of the irreversible strains

$$\dot{\boldsymbol{\epsilon}}^i = \lim_{\Delta t \to \infty} \left(\frac{\beta}{\Delta t} \frac{r^-(\tilde{\bar{\boldsymbol{\sigma}}}) - r_t^-}{r_{t+\Delta t}^-} \boldsymbol{\epsilon}_{t+\Delta t}^e \right) \tag{11}$$

or in incremental form as

$$\Delta \boldsymbol{\epsilon}^i = \beta \frac{r^-(\tilde{\bar{\boldsymbol{\sigma}}}) - r_n^-}{r_{n+1}^-} \boldsymbol{\epsilon}_{n+1}^e \tag{12}$$

In the above equations, n and $n+1$ subscripts refer to subsequent time steps. The symbol "Δ" denotes the increment of a specific quantity from step n to n+1. The variables $\tilde{\bar{\boldsymbol{\sigma}}}$ and $r^-(\tilde{\bar{\boldsymbol{\sigma}}})$ represent, respectively, the effective stress and the stress threshold in the absence of increment of irreversible strains at time step $n+1$

$$\tilde{\bar{\boldsymbol{\sigma}}} = (\bar{\boldsymbol{\sigma}}|_{\Delta \boldsymbol{\epsilon}^i = 0})_{n+1} = \bar{\boldsymbol{\sigma}}_n + \boldsymbol{C_0} : \Delta \boldsymbol{\epsilon}_{n+1} \tag{13}$$

$$r(\tilde{\bar{\boldsymbol{\sigma}}}) = max\left[r_n^-, \tau^-(\tilde{\bar{\boldsymbol{\sigma}}})\right] \tag{14}$$

Note that the quantity $r^-(\tilde{\bar{\boldsymbol{\sigma}}}) - r_n^-$ is always non-negative due to equation (14), an essential thermodynamic requirement for ensuring non-negative dissipation. Finally, the material parameter β, with values between 0 and 1, defines the rate of the irreversible deformation by scaling the current increment of the equivalent stresses, and consequently the stress thresholds, through the following equation

$$\Delta r_{n+1}^- = r_{n+1}^- - r_n^- \tag{15a}$$

$$= (1-\beta)\left(r^-(\tilde{\bar{\boldsymbol{\sigma}}}) - r_n^-\right) \tag{15b}$$

It is convenient to consider the effect of the irreversible strains through the definition of the effective stresses, since the Cauchy stresses are computed using the values of the effective stresses $\bar{\boldsymbol{\sigma}}^{\pm}$ and the two damage variables $d^{\pm}$. This can be performed through the update of the effective stresses using equations (10) and (11) in a similar way to [33]

$$\bar{\boldsymbol{\sigma}}_{n+1} = \lambda \tilde{\bar{\boldsymbol{\sigma}}} \tag{16}$$

$$\lambda = 1 - \beta \left(1 - \frac{r_n^-}{r^-(\tilde{\bar{\boldsymbol{\sigma}}})}\right) \tag{17}$$

The computation of the effective stresses at each increment of the analysis is presented in the flowchart of Table 1.

(i) Compute $\tilde{\bar{\boldsymbol{\sigma}}}$ using equation (13).
(ii) Is $\beta > 0$?
YES: Continue to step (iii)
NO: No evolution of irreversible strains is considered. Set $\bar{\boldsymbol{\sigma}}_{n+1} = \tilde{\bar{\boldsymbol{\sigma}}}$ and EXIT.
(iii) Calculate $\tau^-(\tilde{\bar{\boldsymbol{\sigma}}})$ using equation (5) and $r^-(\tilde{\bar{\boldsymbol{\sigma}}})$ using equation (14).
(iv) Compute λ using equation (17). Set $\bar{\boldsymbol{\sigma}}_{n+1} = \lambda \tilde{\bar{\boldsymbol{\sigma}}}$ and EXIT.

Table 1: Flowchart for the calculation of the effective stresses.

Following the above, the evolution of the damage variables are defined, which in this work follow the exponential relationship proposed in [42].

$$d^{\pm} = 1 - \frac{r_0^{\pm}}{r^{\pm}} \exp\left\{ 2H_d^{\pm} \left(\frac{r_0^{\pm} - r^{\pm}}{r_0^{\pm}} \right) \right\} \tag{18}$$

Tension and compression evolution laws consider respectively the positive G_f^+ and negative G_f^- fracture energies, as well as the characteristic finite element width l_{dis} through the corresponding discrete softening parameter $H_d^{\pm}$ ensuring mesh-size independent energy dissipation according to the crack-band theory [43]. For the case of tension this is [44]

$$H_d^+ = \frac{l_{dis}}{l_{mat}^+ - l_{dis}} \tag{19}$$

For the case of compressive damage, the discrete softening parameter H_d^- is defined as (see Appendix)

$$H_d^- = \frac{1}{1-\beta} \left(\frac{l_{dis}}{l_{mat}^- - l_{dis}} \right) \tag{20}$$

The above definition is consistent with the crack band-width approach yielding objective results for different values of β by considering the contributions to

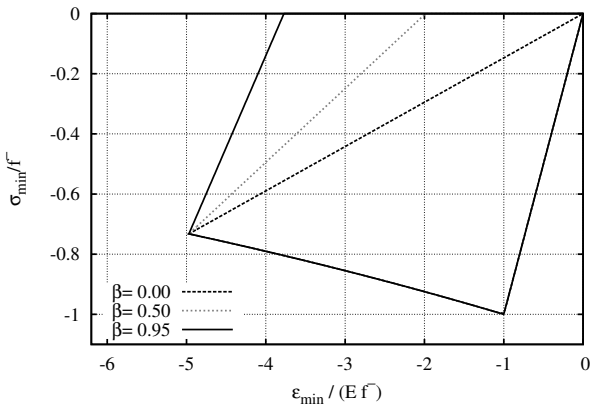

(a)

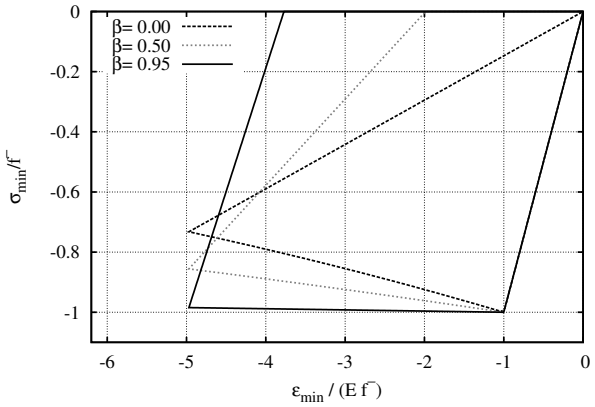

(b)

Fig. 2: Effect of the choice of the discrete softening parameter for compression to the softening behaviour for different values of β: H_d^- (a) using equation (20), (b) using the formulation in [45].

the dissipated energy of the evolution of the irreversible strains and the compressive damage. In the above, the material characteristic length $l_{mat}^{\pm}$ for tension and compression is

$$l_{mat}^{\pm} = \frac{2EG_f^{\pm}}{(f^{\pm})^2} \tag{21}$$

The use of the discrete softening parameter of equation (20) results in an objective representation of the dissipated energy Gf^-. This is illustrated in Figure 2 for the case of a cyclic uniaxial compressive loading using the proposed H_d^- of equation (20) instead of the one adopted in [45], which is the negative counterpart of equation (19). The use of the new softening modulus (Figure 2a) results in a consistent energy dissipation according to the input value of Gf^- independently of the choice of β.

The effect of β can now be visualised using equations (11) and (15) for the two limit cases of $\beta \to 0; 1$

$$\beta = 0 \;\Rightarrow\; \Delta r^- = r^-(\tilde{\bar{\boldsymbol{\sigma}}}) - r_n^- \tag{22}$$
$$\Rightarrow \Delta \boldsymbol{\epsilon}_{n+1}^i = 0 \tag{23}$$
$$\beta \to 1 \;\Rightarrow\; \Delta r^- = 0 \tag{24}$$
$$\Rightarrow \Delta d_{n+1}^- = 0 \tag{25}$$

The first case, with $\beta = 0$, recovers the standard continuum damage mechanics model without any evolution of irreversible strains. Contrariwise, for $\beta \to 1$ the effective stresses are updated such that there is no evolution of the equivalent stress τ^- and correspondingly r^-. For this case, there is no compressive damage evolution and the total incremental strains at this step will be irreversible. A value of β within 0 and 1, gives a proportional evolution of both irreversible strains and compressive damage. The above effect is illustrated in Figure 2a.

2.2 Irreversible strains under shear loading

As implied by their definition in equation (11), irreversible strains $\boldsymbol{\epsilon}^i$ are influenced by the selection of the compressive damage criterion and thus of the compressive equivalent stress τ^-. This means that the evolution of the irreversible strains is possible only when the compressive damage is increasing. The effect of this choice is investigated here locally under pure shear. The assumed material parameters for this demonstrative example are presented in Table 2.

For comparison purposes, four cases have been considered with different definitions of τ^-. In the first one, referred hereafter as Case-1, the τ^- is calculated using only the negative effective stress tensor ($\bar{J}_2{}^-$, $\bar{I}_1{}^-$, σ_{max}^-, σ_{min}^-) as

$$\tau^- = H\left[-\bar{\sigma}_{min}^-\right] \frac{1}{1-a}\left[\sqrt{3\bar{J}_2{}^-} + a\bar{I}_1{}^- + b\langle\bar{\sigma}_{max}^-\rangle\right] \tag{26}$$

The above definition using the negative part of the effective stress tensor, results in an "open" d^- damage surface in the shear quadrants, as shown in Figure 1 for the plane-stress case. This means that in this local test, compressive damage under pure shear is triggered only when the minimum principal stress reaches the uniaxial compressive strength of the material. For the other three cases, the equivalent stress of Eq. (5) is used that is a function of the total effective stress tensor ($\bar{\boldsymbol{\sigma}}$) with κ_1=0.0; 0.5; 1.0 for Case-2, Case-3 and Case-4,

f^+ $[MPa]$	f^- $[MPa]$	G_f^+ $[J/m^2]$	G_f^- $[J/m^2]$	E $[MPa]$	v $[-]$	β $[-]$
0.2	5.0	50.0	10000	3500	0.2	0.50

Table 2: Material parameters used in the elemental shear tests.

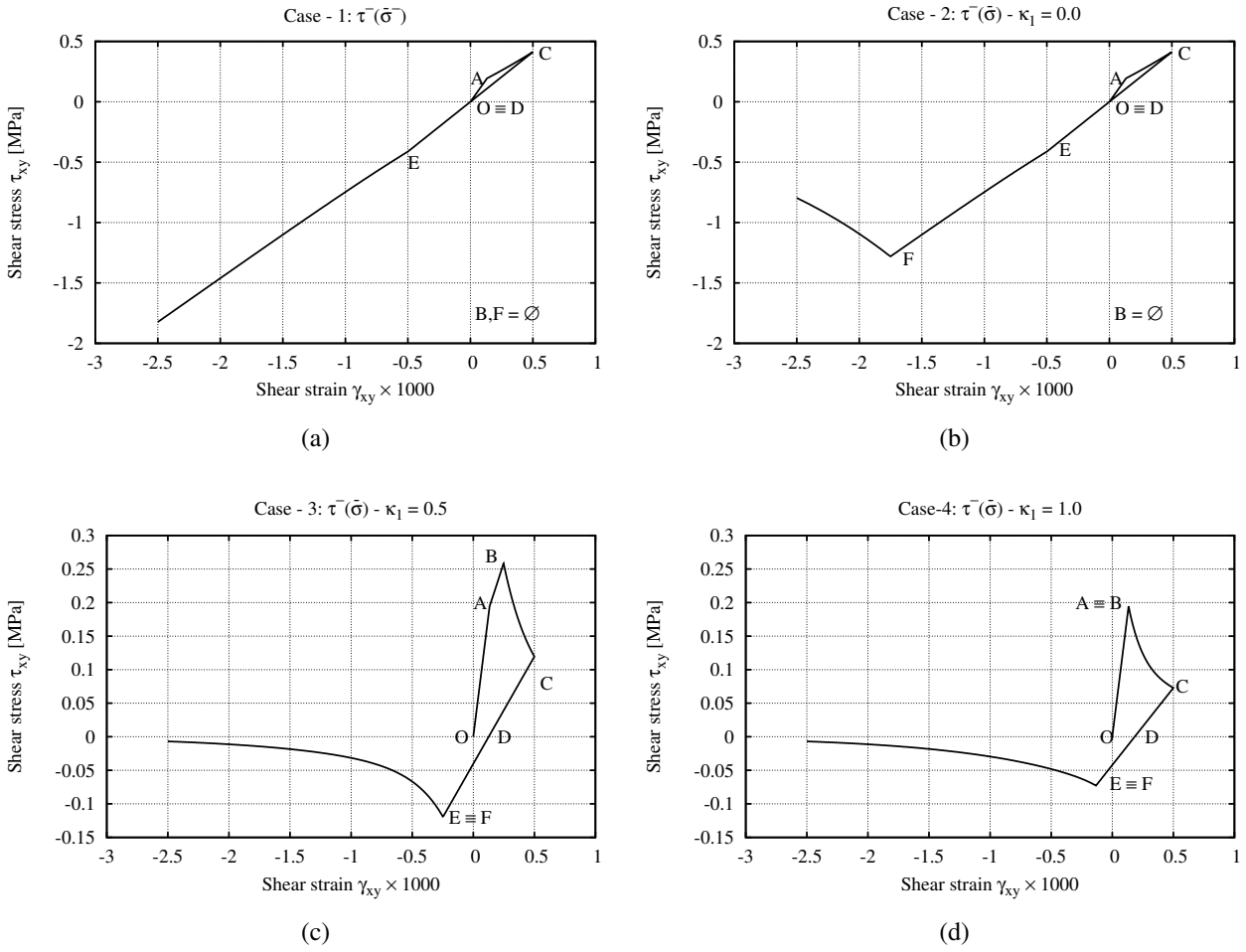

Fig. 3: Response under shear reverse loading for different assumptions about the compressive damage criterion. (a) Case -1 ($\tau^- = \tau^-(\bar{\boldsymbol{\sigma}}^-)$), (b) Case - 2 ($\tau^- = \tau^-(\bar{\boldsymbol{\sigma}})$ and $\kappa_1 = 0.0$), (c) Case - 3 ($\tau^- = \tau^-(\bar{\boldsymbol{\sigma}})$ and $\kappa_1 = 0.5$), (d) Case - 4 ($\tau^- = \tau^-(\bar{\boldsymbol{\sigma}})$ and $\kappa_1 = 1.0$). Point A: Triggering of tensile damage, Point B: Triggering of the compressive damage, Point C: Maximum shear deformation for the first stage of the loading, Point D: Irreversible deformation for $\tau_{xy} = 0$, Point E: Activation of the tensile damage, Point F: Activation of the compressive damage.

respectively. The shapes of the four damage surfaces are presented qualitatively in Figure 1. Each case has been subjected to a shear deformation composed of two stages: (a) loading up to a shear strain of $\gamma_{xy} = 0.5 \times 10^{-3}$ and unloading to zero, (b) loading up to a shear strain of $\gamma_{xy} = -2.5 \times 10^{-3}$.

Figure 3 presents the response under shear for the four different cases. The letters appearing in the graphs refer to the following conditions occurring during the two loading stages: Point "A" triggering of tensile damage, Point "B" triggering of compressive damage, Point "C' maximum shear deformation for the first stage of loading, Point "D" Irreversible deformation for $\tau_{xy} = 0$, Point "E" activation of the tensile damage during the second stage of loading, Point "F" activation of the compressive damage during the second stage of loading.

The part O-A in all graphs is the same and it represents the linear behaviour until reaching the d^+ damage

surface. After this point, the response in the four models depends on the specific assumption of the negative equivalent stress τ^-, i.e. to the specific shape of the d^- failure surface in the the second and fourth quadrants of Figure 1. For Case-1 and Case-2, the compressive failure criterion Φ^- is not reached for the given maximum shear strain of $\gamma_{xy} = 0.5 \times 10^{-3}$. This results in the increase of the shear capacity during the loading path A-C (see Figures 3a-b). An additional consequence of this is that there is no evolution of irreversible strains since the d^- failure surface is not reached (paths C-D in Figures 3a-b). On the contrary, evolution of irreversible strains occurs for both Case-3 and Case-4, since there is evolution of the compressive damage d^- within the loading path A-C (Figures 3c-d). In Case-4, the overlapping of the tensile d^+ and compressive d^- failure surfaces results in the triggering of the tensile and compressive damage at the same time (B $\equiv$ C) and in the earlier evolution of the irreversible strains. For this reason, the unloading path (C-D, Figures 3c-d) is less sharp than the one in Case-3, resulting in larger irreversible strains.

The damage occurring during the first stage of a cyclic static loading analysis (O-D path) has an important effect during the reverse loading at the second stage. The stiffness during the reverse loading depends on the d^+ and d^- values attained during the first stage of the cyclic loading analysis. Damage increases once again when the effective stresses $\tau^\pm$ overcome again the attained thresholds $r^\pm$ (Point E for d^+ and Point F for d^-). For Case-3 and Case-4, this happens at the same increment for both $\tau^\pm$ (E $\equiv$ F in Figures 3c-d). The capacity of Case 2 keeps increasing up to the satisfaction of the failure criterion Φ^- (Point F, Figure 3b). However, this does not happen for Case-1, resulting in an increasing shear capacity.

The above analyses show that the description of the unilateral effect under shear cyclic loading, and thus the definition of the unloading stiffness, requires the careful calibration of the equivalent stresses $\tau^\pm$ as well as the magnitude of the irreversible strains through the β parameter.

3 A tracking algorithm for intersecting and multi-directional cracks

The simulation of localized cracks within the macro-modelling approach is achieved through the use of a local crack-tracking algorithm. The aim of the algorithm is to identify the elements crossed by propagating cracks at each time/load increment. The crack is then simulated through the use of a nonlinear stress-strain relationship for the elements within the crack path, while the ones outside maintain a linear elastic response.

Tracking algorithms are used in different numerical approaches developed for the simulation of localized cracks in quasi-brittle materials (see [46]). Despite the diversity of the applied fields, their function is always the same, i.e. localization of strains in a limited part of the structure, where cracks are expected to propagate. The methodology used here is based on the algorithm presented in [20, 21, 22, 32]. The local nature of this crack-tracking technique enables the identification of the crack trajectories from information already available at each step of a finite element analysis, i.e. the stress state of each finite element. In this way, computational cost, in terms of time and memory resources, is kept to values comparable to the classical smeared crack approach (see [32]). This strategy aims to a good balance between accuracy and efficiency, which is of primary importance in problems involving multiple and intersecting cracks, as is the case of cyclic loads in masonry structures.

This section presents the novel developments making possible the simulation of intersecting and multi-directional cracks using a local crack-tracking algorithm. The new algorithm is a further development of the one presented in [32], allowing the modelling of arbitrary cracking, starting from the boundary or the interior of the analysed structure and propagating towards one or two directions. The latter enhancement is fundamental to simulate the response of structures experiencing multiple and diverse cracking due to flexural, tensile or shear stress states.

The following of this section focuses on the details of the novel algorithm. Firstly, a general introduction on the tasks of the tracking algorithm is presented. This is followed by the up to date assumptions regarding the modelling of crack initiation under monotonic loading. Modelling of crack propagation and intersection is presented in section 3.3. Finally, the section closes with the novel approach to simulate multi-directional cracking.

3.1 Structure of the tracking algorithm

The crack-tracking algorithm presented here is called at the beginning of each numerical increment before the calculation of the stress-state and has two tasks: (a) to identify the origin of new cracks and (b) to recognize the crack path and the finite elements pertaining to it. The output of the crack-tracking subroutine is a flag system used to distinguish elements within a crack-path from those outside. In this way, the two groups of elements follow different constitutive behaviour. Here, the continuum damage model presented in Section 2 is

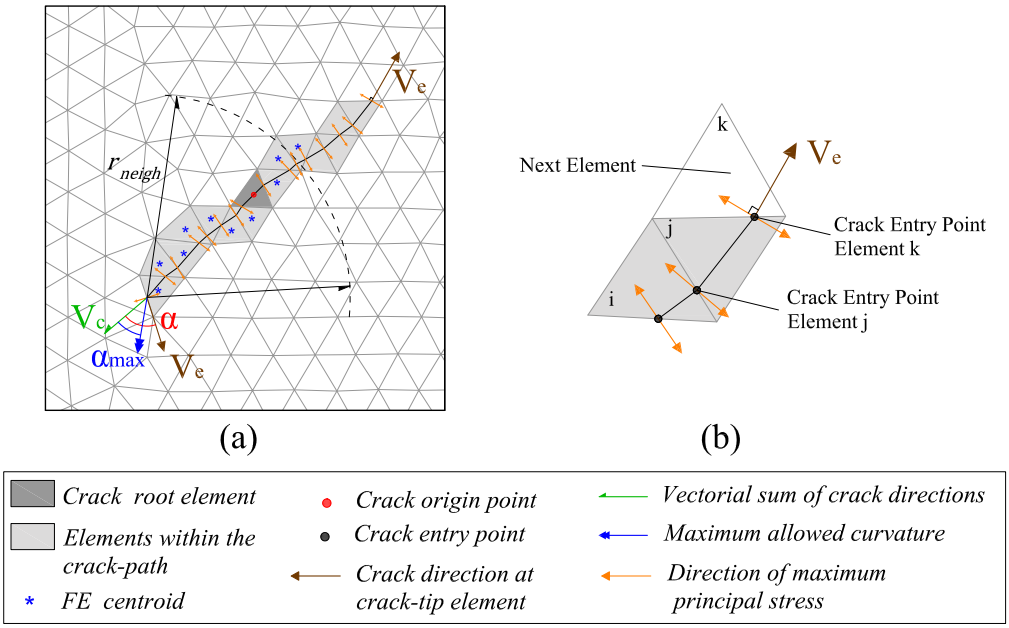

Fig. 4: Illustration of the crack propagation and use of the maximum curvature criterion for a new internal crack.

used for the elements within a crack, while for the rest a linear stress-strain relationship is maintained.

3.2 Crack initiation I - Monotonic Loading

New cracks originate from elements that satisfy the failure condition as defined by Eq. (8). No restrictions are posed to the location of the crack origins in the used mesh as presented in [32]. For cracks initiating at corner or at internal elements, the centroid of the triangular element is selected as the crack origin. For the case of a crack starting at an element with one side on the boundary, the crack origin is located at the midpoint of the boundary edge. A minimum distance is defined between existing and new cracks, referred hereafter as *exclusion radius* r_{excl} [22]. If two finite elements satisfy the failure criterion at the same time/load increment and the distance between them is less than the exclusion radius, the one with the highest value of the tensile equivalent stress τ^+ (see Eq. (4)) is selected as a crack origin. The value of the exclusion radius can be defined according to the structural problem or the fabric of the material analysed as shown in [22, 23, 32]. Apart from this functionality, the definition of an exclusion radius averts the initiation of secondary spurious cracking surrounding the crack-tip [27, 47], a pathology that may spoil the correct damage localization.

3.3 Crack propagation and Crack intersection

The propagation direction is defined as orthogonal to the direction of the maximum principal effective stresses. This direction is calculated for each element at the crack front (crack tip element) using a stress tensor constructed from the average values of the stresses at the nodes of each element. Starting from the crack entry point, and using a vector with the aforementioned direction (V_e in Figure 4), the next potential element of the crack is identified and the crack entry coordinates are saved. Figure 4a presents an example with the propagation of an internal crack, while in Figure 4b shows a detail of the crack propagation and the crack entry coordinates on the wake of a crack tip. If the crack origin is an element lying on the boundary of the structure, the crack propagates in a single direction. This is the case of the flexural cracks at the corner of openings or at the base of piers. On the contrary, shear cracks can initiate from the interior of a masonry wall or a spandrel. To allow this, when the tracking algorithm recognizes that the crack origin is an element at the interior of the structure, the propagation of the crack is monitored towards two opposite orientations, as shown in Figure 4a. In this way, both shear and flexural cracks can be adequately modelled, as in the masonry frame wall presented in Figure 5.

In structures experiencing multiple cracking, it is unavoidable that cracks will meet other cracks during

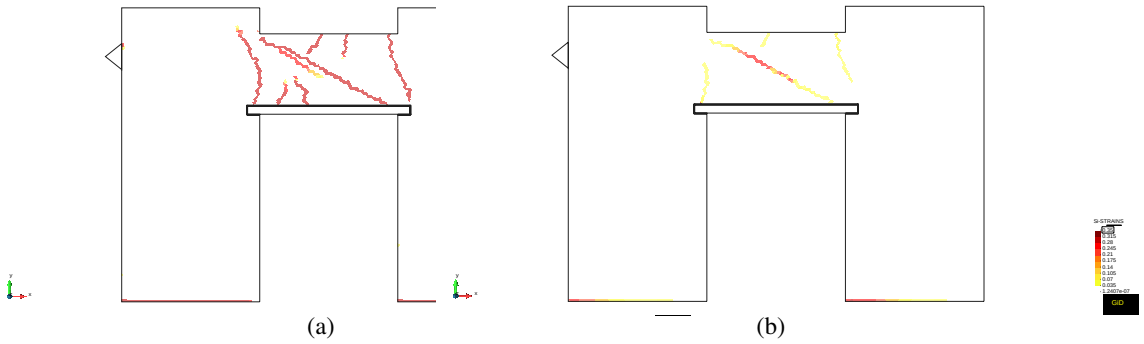

Fig. 5: Example of flexural and shear localized cracks in a masonry frame simulated under in-plane horizontal loading using the crack-tracking algorithm in [32]: (a) Tensile damage contour, and (b) Maximum principal strains at the end of the analysis.

their propagation. The assumption used in [22, 32] that a crack is complete when meeting another crack at its propagation front is reconsidered in this work in order to provide a realist simulation of intersecting cracks in cyclic in-plane loading of shear walls. In the proposed algorithm, a crack continues unimpeded its evolution following the same procedure as if the crack-tip was not a part of another crack. The crack direction is identified as orthogonal to the direction of the maximum principal effective stresses of each finite element and the next elements of the crack are sought. An example of such case is presented in the following section.

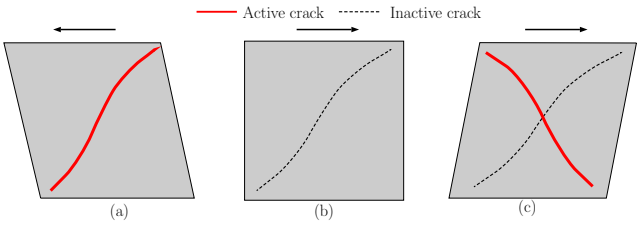

Fig. 6: Example of cracking under the shear loading of a wall: (a) Opening of one crack during the loading towards the left, (b) closing of the crack when returning to the initial configuration and (c) opening of a second crack, diagonal to the first during the reverse loading.

In order to avoid sudden changes in the crack direction due to the poor estimation of the stresses arising from the use of standard finite elements, a correction of the crack propagation can be opportunely applied through the use of a maximum curvature criterion [20, 21, 22]. This criterion compares the crack propagation direction of the crack-tip element V_e with the average crack direction V_c (Figure 4a). The latter is obtained as the average sum of the propagation directions of the elements in the crack path lying within a distance lower than r_{neigh} from the crack-tip. If the propagation direction diverges with an angle α larger than α_{max}, then the next element of the crack is sought using the average crack direction V_c instead of V_e. This correction is illustrated in Figure 4. The value of the r_{neigh} defines the length of the crack behind the crack tip that will be considered in the computation of the vector V_c (see Figure 4a). The maximum curvature angle α_{max} determines the margins of the allowed crack rotation. The effect of these numerical parameters, as well as the criteria for their determination, are detailed in [22, 32].

3.4 Crack initiation II - Multi-directional cracks

The criteria for crack initiation, presented in section 3.2, define that new cracks can start from a certain distance from existing ones, which is determined by the exclusion radius r_{excl}. This procedure is robust for structural cases with monotonic loading, where the crack directions do not show sudden changes during the loading history (see previous works [22, 23, 31, 32]). However, cyclic loading, such in earthquakes or wind loads, may induce *multi-directional cracking* to the structure, referring to cracks initiating in the same region of existing cracks but with a different direction. To illustrate this, consider the simplified case of a shear wall (Figure 6) subjected to cyclic shear loading at its top (restraining the rotation). The top displacement towards the left produces a shear crack, starting from the middle of the wall and propagating towards its two ends (Figure 6a). The reversal of the loading cycle finds the wall at its initial configuration with the crack closed (Figure 6b). The loading in the opposite direction results in the opening of a new crack that propagates diagonally

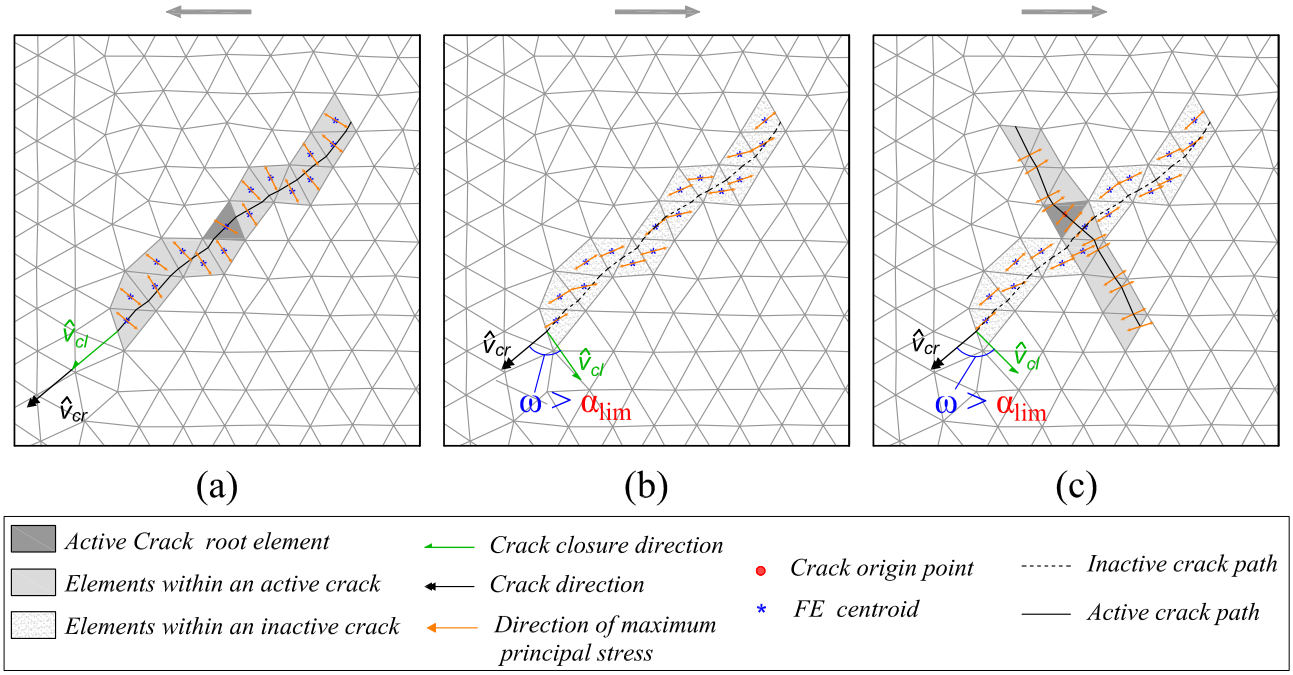

Fig. 7: Crack propagation in the middle of a shear wall: (a) propagation of a shear crack for the loading towards the left, (b) deactivation of the crack due to the change in the stress state, (c) initiation and propagation of a second crack next to the inactive one.

towards the other two corners (Figure 6c). If the first crack is completely closed, the structural condition before the opening of the two cracks will very be similar resulting to the possible origin of the second crack very close to the origin of the first one.

The accurate simulation of such cases needs a different approach regarding crack initiation from the one presented in Section 3.2. For the specific case of the shear wall in Figure 6, this approach must allow the initiation of the second crack at the finite element that satisfies the failure criterion after the reversal of the loading cycle, independently of its distance to the closed crack.

The modelling of cases involving the initiation of cracks due to different stress-states at a region of existing cracks is possible through the categorization of cracks into "*active*" and "*inactive*". Prior to the definition of these two categories, two new versors are introduced:

- **Crack direction** $\hat{v}_{cr}$**:** a versor denoting the average direction of a consolidated crack. The crack direction of a crack is calculated using the crack entry coordinates at each element within the total length of the crack.
- **Crack closure direction** $\hat{v}_{cl}$: a versor denoting the average direction orthogonal to the maximum principal effective stress of all the elements within the crack. This versor shows the average crack propagation direction of all the elements within a crack at each time/load increment of the analysis.

These two versors are updated at the end of each time/load increment for each of the consolidated cracks. A crack i is defined as "*active*" if the angle between its crack direction versor $\hat{v}^i_{cr}$ and its crack closure direction versor $\hat{v}^i_{cl}$ is lower than a predefined limit angle a_{lim}. The crack status is alternatively expressed through the use of the following function

$$H^i[|\hat{v}^i_{cr}\cdot\hat{v}^i_{cl}|-cos(a_{lim})] = \begin{cases} 0 & \text{Inactive crack} \\ 1 & \text{Active crack} \end{cases} \qquad i = 1, N_{cr} \tag{27}$$

where $(\cdot)$ is the dot product, the subscript $i = 1, N_{cr}$ is used to denote the versor values for each crack of the total existing cracks N_{cr} and $H[\bullet]$ is the Heaviside step function.

Following the above, an element will be the crack origin when all of the following criteria are satisfied:

(i) The failure condition, as defined by the constitutive model (Eq. 8), is reached.

(ii) There is no "*active*" crack within a distance defined by the exclusion radius r_{excl}.

This means that new cracks can initiate at locations where the current stress-state has resulted in the closing of the pre-existing cracks. To illustrate this, Figure 7 illustrates how the algorithm models the two shear cracks at the middle of the wall for the example of Figure 6. Figure 7a shows the stress-state within the crack at the moment of the opening of the crack during the movement towards the left. The two versors of the crack ($\hat{v}_{cr}$ and $\hat{v}_{cl}$, shown in one of the two crack-tips of the crack) coincide, as the crack direction has been defined according to the crack-propagation direction of each element within it. The crack is active and can continue its propagation. Figure 7b presents the stress state for a step during the reversal of the cycle. The wall is now deforming towards the right and the existing crack is closed. This can be seen by the direction of the principal effective stresses which have rotated comparing to when the crack was open. The crack closure ($\hat{v}_{cr}$) and crack direction versors ($\hat{v}_{cl}$) form an angle which is greater than the limit angle α_{lim}. The existing crack is therefore identified as inactive, and new cracks are allowed to open. This happens at a later instance, shown in Figure 7c, when a crack initiates very close to the existing crack and propagates thereafter.

The use of a limit angle as a way to identify the closure of existing cracks and the possibility of new ones to open resembles the concept used to model multiple cracks at constitutive level in the smeared crack models by de Borst and Nauta [48]. A similar concept was used also by Song & Belytschko aiming to model crack branching for propagating cracks [47] under dynamic fracture. Likewise, the limit angle introduced in this work (α_{lim}) is a numerical parameter aiming to deactivate the use of the exclusion radius when the strain state of the crack has exceeded the margins set by equation (27) and thus to allow new cracks to emerge close to existing ones.

4 Numerical simulation of a shear wall under cyclic loading

4.1 Experimental and numerical set-up

In this section, the proposed numerical model is calibrated through the comparison with an experimental case study. The test was performed by Antoine et al. [49] and considers the in-plane response of a masonry wall under quasi-static shear loading. The wall has a width of 1.00 m and a height of 1.35 m, while its thickness is 0.25 m. The masonry is constructed using an English bond pattern with unit dimensions of $55 \times 120 \times 250$ mm^3 and 10 mm mortar joint thickness. A vertical load of 150 kN was distributed at the top part of the wall and was maintained constant during the whole experiment, aiming to represent gravitational loading acting on the top of the masonry wall during a seismic event. The seismic action was reproduced by applying an horizontal displacement at the top of the wall. Proper boundary conditions were applied to avoid its top and bottom rotation. Figure 8a shows a sketch of the experimental set-up adopted during the execution of the cyclical shear tests.

The experimentally obtained shear load against displacement graph is presented in Figure 8b. The wall presents the typical behaviour for shear dominating failure. This is characterised by an overall drop in the capacity with increasing load cycles and appreciable energy dissipation throughout the whole loading history, as represented by the area of the hysteretic cycles of the load-displacement curve. The quasi-brittle character of the shear failure is due to the decrease of strength produced by the formation of two systems of crossing diagonal cracks in the wall [49, 50].

In this work, the experiment is reproduced by using the continuum damage model and the crack-tracking algorithm presented in Sections 2 and 3. The wall has been discretized using 3-noded constant-strain triangles (2836 nodes). The material parameters are presented in Table 3. The compressive strength, the density and the Young's modulus are equal to the values obtained through experimental tests on stack bond prisms reported in [51, 50]. The rest of the mechanical properties of the materials, and the parameters of the constitutive model have been chosen in order to calibrate correctly the shear response of the material, on the basis on the discussion presented in Section 2.2. To this aim, a value of $\kappa_1 = 0.15$ has been chosen which is similar to the value used in other available studies on masonry shear walls [19, 39, 41]. Regarding the crack-tracking parameters, the exclusion radius has been set equal to $r_{excl} = 0.20$ m, which is a value between the length and the width of the masonry units. The limit angle used for the activation-deactivation of the cracks under the cyclic loading is $\alpha_{lim} = 40°$. This value means that three additional cracks with an orientation varying by 40° can initiate next to an existing crack. To visualize this, and considering that the exclusion radius has been defined equivalent to the units size, the above value implies that a total of four cracks with different orientations can initiate from the same unit. For the investigated case of a shear wall under cyclic loading, this value seems reasonable as it can allow

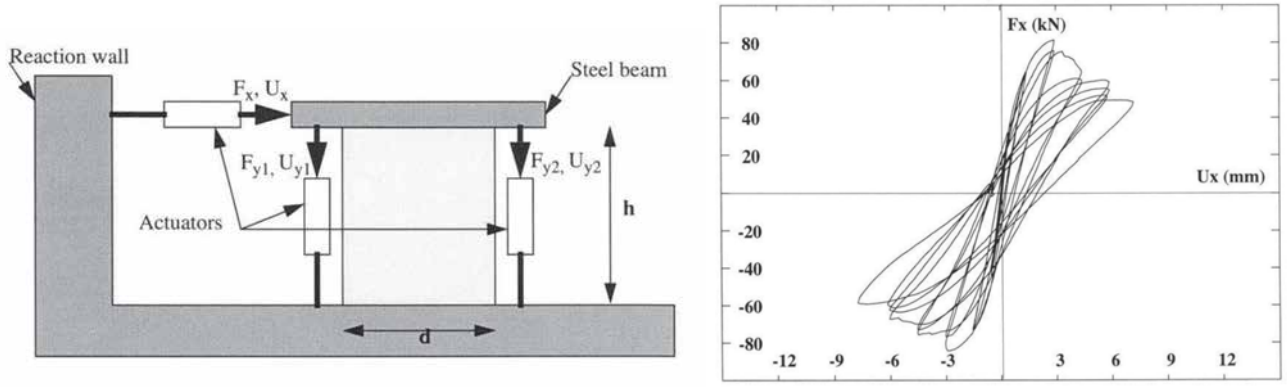

(a) (b)

Fig. 8: (a) Experimental set-up and (b) experimentally obtained force against displacement graph of the tested masonry wall. Pictures adapted from [49].

f^+ $[MPa]$	f^- $[MPa]$	G_f^+ $[J/m^2]$	G_f^- $[J/m^2]$	E $[MPa]$	ρ $[kg/m^3]$	v $[-]$	β $[-]$	κ_1 $[-]$
0.15	6.2	80.0	14000	1490	1750	0.2	0.95	0.15

Table 3: Material parameters for the masonry shear wall.

the formation of diagonal cracking due to shear failure. The parameters for the maximum curvature criterion are $\alpha_{max} = 25°$, $r_{neigh} = 0.60\ \ m$. These values of the parameters showed to be adequate to avoid sudden changes in the crack direction as reported in previous works of the authors [22].

The wall has been analysed under plane stress conditions and the simulation has been performed in two stages. The first one includes the application of the self-weight and the vertical compressive load at the top of the wall. In the second stage, a cyclic horizontal displacement is applied at the top of the wall with increasing magnitude, as in the experiment. Vertical displacement at the top is restrained, precluding the rotation of the wall. The numerical solution is performed in an incremental manner. At each time/load increment, the nonlinear equations are solved with the use of a modified Newton-Raphson (using the secant stiffness matrix). Convergence is achieved when the ratio between the norm of the iterative residual forces and the norm of the total external forces is lower than 10^{-2}. Calculations are performed using an enhanced version of the finite element software COMET [52], while pre- and post-processing with GiD [53], both developed in CIMNE, Barcelona.

4.2 Numerical results

Figure 9 presents the contours of the tensile d^+ and compressive d^- damage indices, as well as that of the maximum principal strains at the end of the analysis. The wall is dominated by diagonal shear cracking, which is in agreement with the reported experimental damage pattern [49, 50]. There is evidence of flexural cracking at the lower and bottom parts of the wall, as well as at the two sides. Despite the opened cracks during the loading history, the main degradation of the wall is concentrated at the two diagonal cracks that have opened in the middle of the wall, as shown by the contour of the maximum principal strains. The use of the crack-tracking algorithm results in a very clear representation of the localized cracks, aiding the identification of the occurring collapse mechanism at the wall.

Figure 10a presents the damage evolution and Figure 10b the state of the cracks for the opposite top displacements of the first cycle. For demonstration purposes, the contour value 1 (red) is used for the active cracks and -1 (white) for the inactive ones, while the elements outside of the crack maintain value equal to 0 (orange) (Figure (10b)). It is visible that all cracks are active for the maximum displacement of the first cycle with a loading direction towards the right. Two flexural cracks at the two corners of the wall consist the

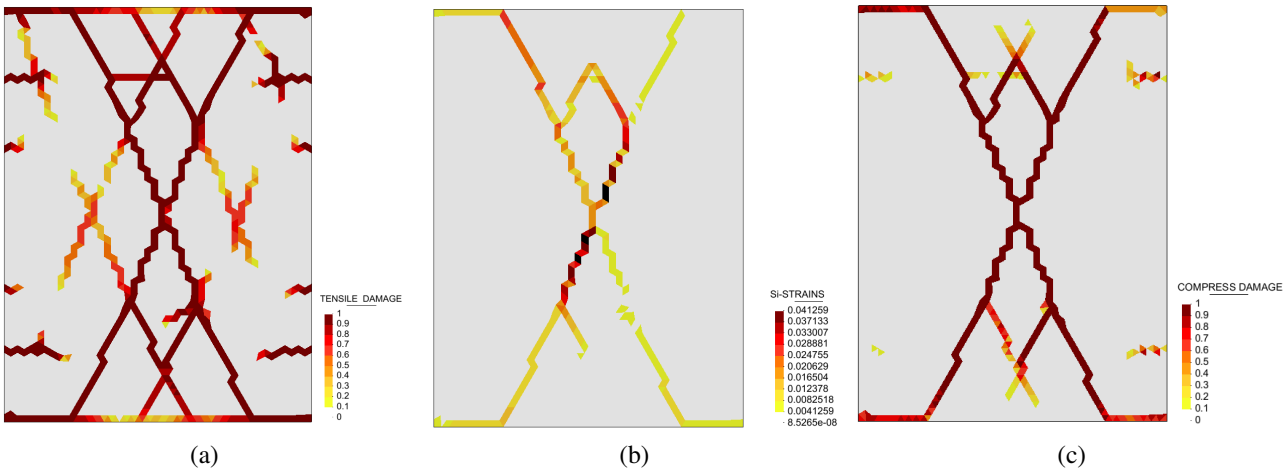

Fig. 9: Contours of: (a) the d^+ damage index, (b) the maximum principal strains at the end of the analysis, (c) the d^- damage index at the end of the analysis.

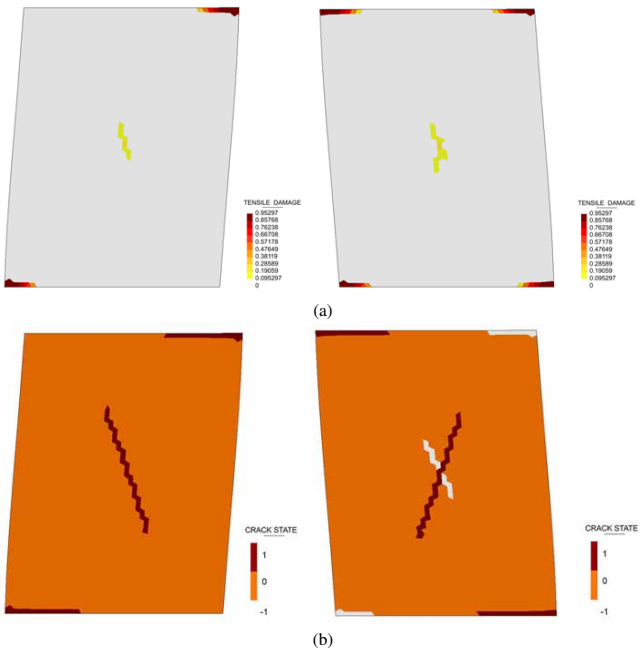

Fig. 10: (a) Tensile damage contour d^+ and (b) crack state during the first loading cycle for the maximum displacement towards the right (left column) and the maximum displacement towards the left (right column) (deformed mesh $\times 100$).

first occurring damage. After those, a shear crack initiated at the middle of the wall (left column of Figure 10). The results with the same top displacement but opposite direction are presented in the right column of Figure 10. All the previously opened cracks have now closed and are correctly identified as inactive. New horizontal cracks appear at the two opposite corners, as well as a diagonal shear crack at the middle of the wall, intersecting the existing crack. The proposed approach is capable to simulate both the correct initiation of new cracks close to the existing ones, as well as their intersection.

Figure 11 presents the damage pattern during the loading cycle with a maximum displacement at the top equal to $\delta = \pm 3.0\,mm$. After the initial damage shown in Figure 10, additional shear cracks have opened, with the deformation, however, localizing at the initial diagonal crack at the middle of the wall (see center column

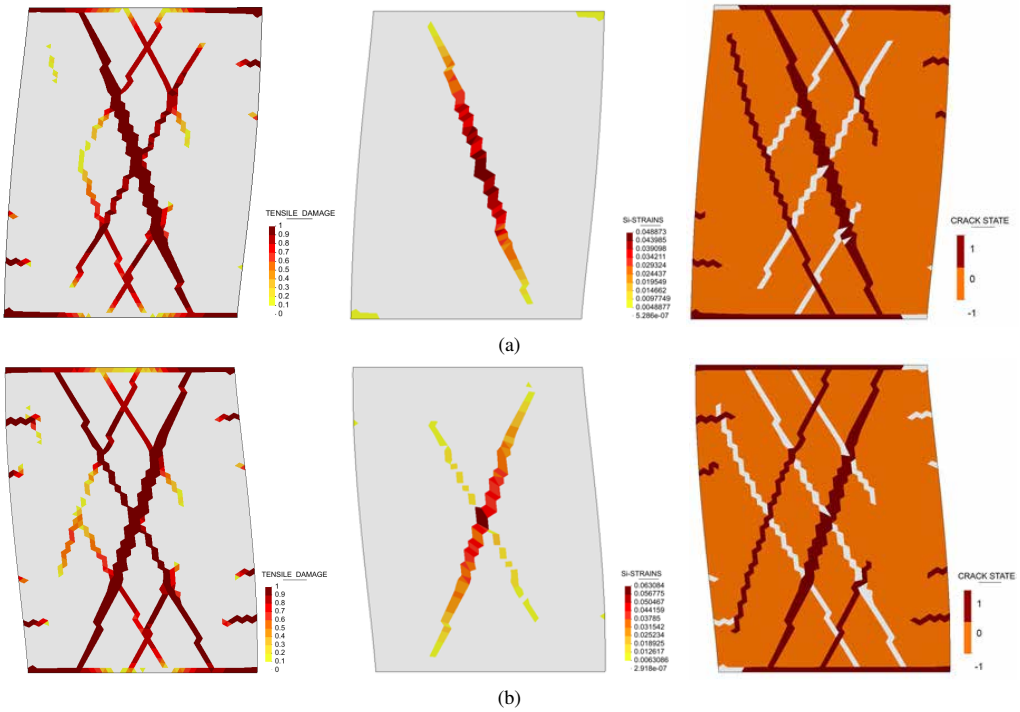

Fig. 11: Contours of tensile d^+ damage (left), maximum principal strains (center) and crack state (right) for a top displacement of 3.0 mm towards the right (a) and left (b), (deformed mesh $\times 50$).

of Figure 11). Some flexural cracks initiate at the two lateral sides of the wall and propagate horizontally towards the interior. Note that the cracks opened during an opposite loading direction have been correctly identified as closed (right column in Figure 11).

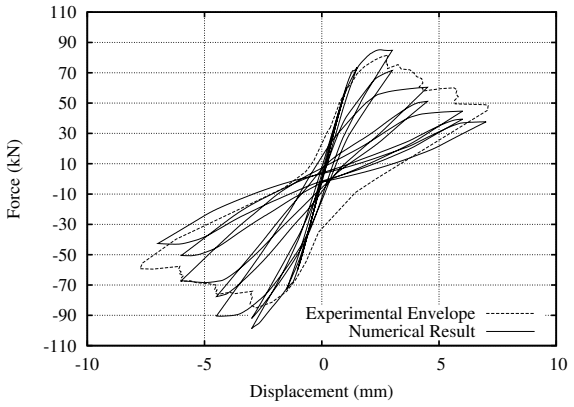

Fig. 12: Force against horizontal displacement graphs for the masonry shear wall obtained through the numerical analysis.

The response of the simulated wall in terms of horizontal load against horizontal displacement is presented in Figure 12. The numerical simulation captures the shear failure of the wall, which is characterized by an overall softening branch and stiffness degradation after exceeding the maximum capacity. The first cycles of the loading are characterized by an almost linear behaviour, due to the small amount of damage as shown in Figure 10. A significant drop in the capacity occurs after the complete degradation of the diagonal cracks at the middle of the wall, which occurs during the loading cycles with the maximum displacement of 3.0 mm, as in the experiment. After that, the increase of the displacement results in the drop of the stiffness due to the degradation of the additional shear cracks, yielding the final damage pattern and strain state of Figure 9.

The used constitutive model is able to represent satisfactorily the cyclic damaging behaviour of the wall. The slight underestimation of the magnitude of the experimental envelope of the hysteretic loops is due to the specific nature of the used damage model, with the association of the evolution of the irreversible strains to only that of the compressive damage variable d^-. In fact, as can be seen in Figure 9c, compressive damage d^- appears only at the two diagonal cracks at the middle of the wall, making them the only source of the irreversible deformations.

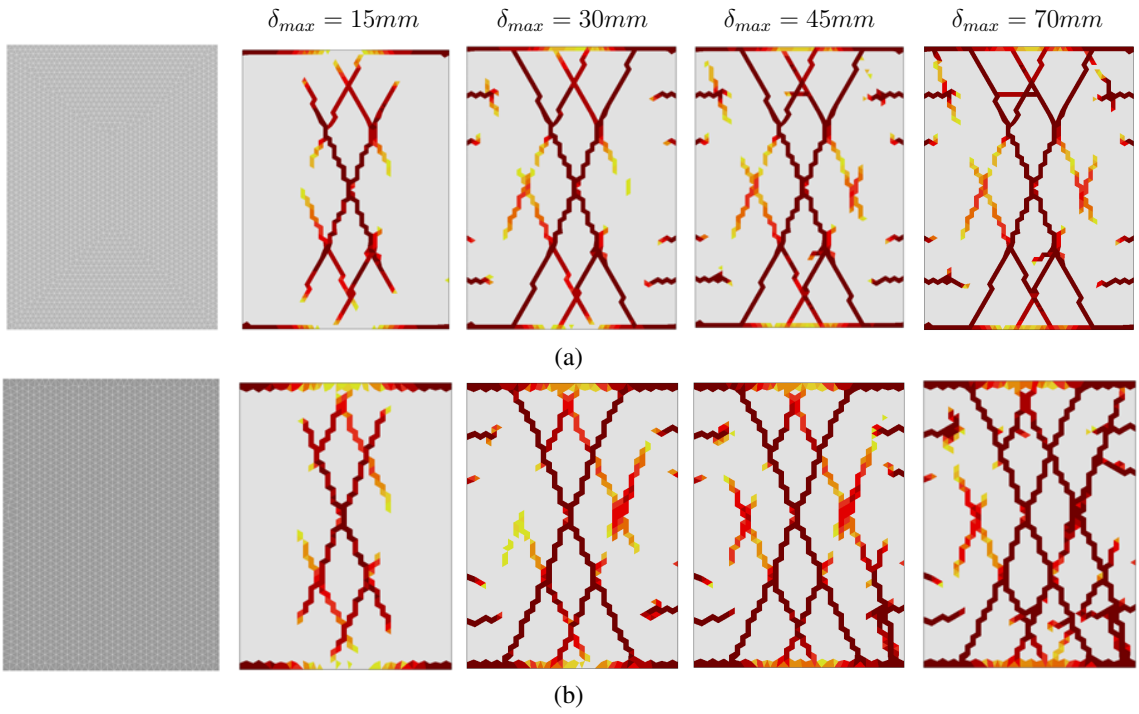

Fig. 13: The used discretization (first column) and the contours of the tensile damage at the end of the various cycles with increasing maximum displacement δ_{max}: (a) Mesh-A, (b) Mesh-B

4.3 Mesh-dependency study

The tracking algorithm has shown to improve the mesh objectivity in structural analyses of small [22, 31, 32] and large scale structures [54] with monotonically propagating cracks. In this section, the shear wall is analysed with an additional mesh aiming to study the mesh dependency of the presented approach for the more demanding case of cyclic loading. The first column of Figure 13 shows the different discretization used in the mesh dependency analyses. The first mesh, denoted hereafter as Mesh-A, is mesh used for the aforementioned results with 5470 elements. The second mesh, Mesh-B, presents a constant structured pattern in the greatest part of the wall with equilateral triangles making angles of 30°, 90° and 150° with the horizontal axis and has a lower number of elements (3704) compared to Mesh-A.

The different columns of Figure 13 present the damage pattern at the end of the different cycles during the loading history. Diagonal shear cracking dominates the main part of the wall in both cases, while flexural cracks appear at the boundaries. The damage pattern is very similar for the greatest loading history of the wall, with some differences occurring in the last cycles, during which the coarser mesh (Mesh-B) presents some additional shear cracking.

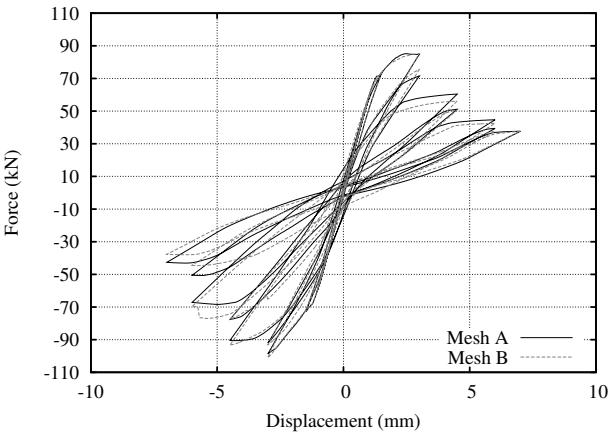

Fig. 14: Horizontal force against displacement at the top of the wall for Mesh-A and Mesh-B

Figure 14 illustrates the force against the applied displacement graphs for the two meshes overlapped. The two analyses bare important similarities. The predicted capacity of the wall shows a variation of less than 3% and is attained at the second loading cycle for a displacement of 3.0 mm. Following that, the structure presents a softening response with dropping capacity and energy dissipation due to the further opening of the cracks. As presented in Figure 13, after the first two

loading cycles most of the cracks have already formed, and the diagonal cracks at the middle of the wall as well as the boundary cracks at the top and bottom ends of the wall have completely opened. Upon this point, the numerical responses reflect the small differences regarding the positions of the cracks and the appearance of more cracks at the coarser mesh (Mesh-B), slightly alternating the residual response of the wall.

5 Conclusions

This paper has presented the enhancement of the macro-modelling finite element method with a crack-tracking algorithm for the simulation of the behaviour of masonry structures under in-plane cyclic loading. A novel methodology has been proposed to simulate intersecting and multi-directional cracks that occur in masonry under cyclic actions with a local crack-tracking technique. This has been achieved by setting suitable crack opening/closure criteria in the numerical algorithm. Cracking is represented at a local level using a continuum damage model with distinct representation of tensile and compressive damage. The constitutive model has been formulated to include the description of the evolution of irreversible deformations in a simplified way.

The enhanced macro-model has been used to simulate an experimentally tested shear masonry wall under cyclic quasi-static loading. The tracking algorithm has shown to be capable to simulate shear and flexural cracks propagating in multiple directions and intersecting among them. The results show that the used constitutive model can represent correctly the gradual decrease of the structural capacity during the cyclic loading process. The proposed approach can therefore properly account for complex damage typologies when cracks appear and propagate under shear cyclic condition.

The paper includes a discussion at constitutive level regarding the evolution of the irreversible strains under shear loading. A simple and explicit algorithmic formulation, together with a proper definition of the compressive damage surface, allow to consider the effect of irreversible strains both under shear and compression stress states.

Compliance with ethical standards

Conflict of interest The authors declare that they have no conflict of interest.

Funding This research has received the financial support from the MINECO (Ministerio de Economia y Competitividad of the Spanish Government) and the ERDF (European Regional Development Fund) through the MULTIMAS project (Multiscale techniques for the experimental and numerical analysis of the reliability of masonry structures, ref. num. BIA2015-63882-P).

References

1. S. Huerta, "The Analysis of Masonry Architecture: A Historical Approach," *Architectural Science Review*, vol. 51, no. 4, pp. 297–328, 2008.
2. P. Roca, M. Cervera, G. Gariup, and L. Pelà, "Structural Analysis of Masonry Historical Constructions. Classical and Advanced Approaches," *Archives of Computational Methods in Engineering*, vol. 17, pp. 299–325, jul 2010.
3. D. Theodossopoulos and B. Sinha, "A review of analytical methods in the current design processes and assessment of performance of masonry structures," *Construction and Building Materials*, vol. 41, pp. 990–1001, 2013.
4. D. Addessi, S. Marfia, E. Sacco, and J. Toti, "Modeling Approaches for Masonry Structures," *The Open Civil Engineering Journal*, no. 2, pp. 288–300, 2014.
5. A. Orduña and P. B. Lourenço, "Cap Model for Limit Analysis and Strengthening of Masonry Structures," *Journal of Structural Engineering*, vol. 129, no. 10, pp. 1367–1375, 2003.
6. P. Block, T. Ciblac, and J. Ochsendorf, "Real-time limit analysis of vaulted masonry buildings," *Computers & Structures*, vol. 84, pp. 1841–1852, nov 2006.
7. M. Gilbert, C. Casapulla, and H. Ahmed, "Limit analysis of masonry block structures with non-associative frictional joints using linear programming," *Computers & Structures*, vol. 84, pp. 873–887, may 2006.
8. G. Milani, P. Lourenço, and A. Tralli, "Homogenised limit analysis of masonry walls, Part I: Failure surfaces," *Computers & Structures*, vol. 84, pp. 166–180, jan 2006.
9. P. Roca, C. Molins, and A. R. Marí, "Strength Capacity of Masonry Wall Structures by the Equivalent Frame Method," *Journal of Structural Engineering*, vol. 131, no. 10, pp. 1601–1610, 2005.
10. S. Lagomarsino, A. Penna, A. Galasco, and S. Cattari, "TREMURI program: An equivalent frame model for the nonlinear seismic analysis of ma-

sonry buildings," *Engineering Structures*, vol. 56, pp. 1787–1799, 2013.
11. R. Siano, V. Sepe, G. Camata, E. Spacone, P. Roca, and L. Pelà, "Analysis of the performance in the linear field of Equivalent-Frame Models for Regular and Irregular Masonry Walls," *Engineering Structures*, vol. In Press, 2017.
12. Y. Endo, L. Pelà, P. Roca, F. Porto, and C. Modena, "Comparison of seismic analysis methods applied to a historical church struck by 2009 L ' Aquila earthquake," *Bulletin of Earthquake Engineering*, 2015.
13. S. Saloustros, L. Pelà, P. Roca, and J. Portal, "Numerical analysis of structural damage in the church of the Poblet monastery," *Engineering Failure Analysis*, vol. 48, pp. 41–61, 2014.
14. L. Pelà, M. Cervera, and P. Roca, "An orthotropic damage model for the analysis of masonry structures," *Construction and Building Materials*, vol. 41, pp. 957–967, 2013.
15. P. B. Lourenço and J. G. Rots, "Multisurface Interface Model for Analysis of Masonry Structures," *Journal of Engineering Mechanics*, vol. 123, no. 7, pp. 660–668, 1997.
16. L. Macorini and B. A. Izzuddin, "A non-linear interface element for 3D mesoscale analysis of brick-masonry structures," *International Journal for Numerical Methods in Engineering*, vol. 85, pp. 1584–1608, mar 2011.
17. T. J. Massart, R. H. J. Peerlings, and M. G. D. Geers, "An enhanced multi-scale approach for masonry wall computations with localization of damage," *International Journal for Numerical Methods in Engineering*, vol. 69, pp. 1022–1059, jan 2007.
18. D. Addessi and E. Sacco, "A multi-scale enriched model for the analysis of masonry panels," *International Journal of Solids and Structures*, vol. 49, no. 6, pp. 865–880, 2012.
19. M. Petracca, L. Pelà, R. Rossi, S. Oller, G. Camata, and E. Spacone, "Multiscale computational first order homogenization of thick shells for the analysis of out-of-plane loaded masonry walls," *Computer Methods in Applied Mechanics and Engineering*, vol. 315, pp. 273–301, 2017.
20. R. Clemente, *Análysis estructural de edificios históricos mediante modelos localizados de fisuración*. Ph.d. thesis, Universitat Politècnica de Catalunya, 2006.
21. L. Pelà, *Continuum Damage Model for Nonlinear Analysis of Masonry Structures*. Ph.d. thesis, Universitat Politècnica de Catalunya, 2009.
22. M. Cervera, L. Pelà, R. Clemente, and P. Roca, "A crack-tracking technique for localized damage in quasi-brittle materials," *Engineering Fracture Mechanics*, vol. 77, no. 13, pp. 2431–2450, 2010.
23. P. Roca, M. Cervera, L. Pelà, R. Clemente, and M. Chiumenti, "Continuum FE models for the analysis of Mallorca Cathedral," *Engineering Structures*, vol. 46, pp. 653–670, 2013.
24. L. Pelà, M. Cervera, S. Oller, and M. Chiumenti, "A localized mapped damage model for orthotropic materials," *Engineering Fracture Mechanics*, vol. 124-125, pp. 196–216, 2014.
25. M. Cervera and M. Chiumenti, "Smeared crack approach: back to the original track," *International Journal for Numerical and Analytical Methods in Geomechanics*, vol. 30, no. 12, pp. 1173–1199, 2006.
26. A. Slobbe, M. Hendriks, and J. Rots, "Smoothing the propagation of smeared cracks," *Engineering Fracture Mechanics*, vol. 132, pp. 147–168, dec 2014.
27. J. Oliver and A. E. Huespe, "Continuum approach to material failure in strong discontinuity settings," *Computer Methods in Applied Mechanics and Engineering*, vol. 193, no. 30-32, pp. 3195–3220, 2004.
28. G. Meschke and P. Dumstorff, "Energy-based modeling of cohesive and cohesionless cracks via X-FEM," *Computer Methods in Applied Mechanics and Engineering*, vol. 196, no. 21-24, pp. 2338–2357, 2007.
29. D. Dias-Da-Costa, J. Alfaiate, L. J. Sluys, and E. Júlio, "A comparative study on the modelling of discontinuous fracture by means of enriched nodal and element techniques and interface elements," *International Journal of Fracture*, vol. 161, no. 1, pp. 97–119, 2010.
30. Y. Zhang, R. Lackner, M. Zeiml, and H. a. Mang, "Strong discontinuity embedded approach with standard SOS formulation: Element formulation, energy-based crack-tracking strategy, and validations," *Computer Methods in Applied Mechanics and Engineering*, vol. 287, pp. 335–366, 2015.
31. S. Saloustros, L. Pelà, and M. Cervera, "A crack-tracking technique for localized cohesive-frictional damage," *Engineering Fracture Mechanics*, vol. 150, pp. 96–114, 2015.
32. S. Saloustros, L. Pelà, M. Cervera, and P. Roca, "Finite element modelling of internal and multiple localized cracks," *Computational Mechanics*, vol. 59, no. 2, pp. 299–316, 2016.
33. R. Faria and J. Oliver, *A Rate Dependent Plastic-Damage Constitutive Model for Large Scale Computations in Concrete Structures*. CIMNE, 1993.
34. M. Cervera, J. Oliver, and R. Faria, "Seismic evaluation of concrete dams via continuum damage models," *Earthquake Engineering & Structural Dynam-*

ics, vol. 24, no. 9, pp. 1225–1245, 1995.
35. R. Faria, J. Oliver, and M. Cervera, "Modeling material failure in concrete structures under cyclic actions," *Journal of Structural Engineering*, no. December, pp. 1997–2005, 2004.
36. P. Roca, M. Cervera, L. Pelà, R. Clemente, and M. Chiumenti, "Viscoelasticity and Damage Model for Creep Behavior of Historical Masonry Structures," pp. 188–198, 2012.
37. L. Pelà, J. Bourgeois, P. Roca, M. Cervera, and M. Chiumenti, "Analysis of the Effect of Provisional Ties on the Construction and Current Deformation of Mallorca Cathedral," *International Journal of Architectural Heritage*, vol. in press, no. doi: 10.1080/15583058.2014.996920, 2014.
38. R. Faria, J. Oliver, and M. Cervera, "A strain-based plastic viscous-damage model for massive concrete structures," *International Journal of Solids and Structures*, vol. 35, pp. 1533–1558, may 1998.
39. M. Petracca, L. Pelà, R. Rossi, S. Oller, G. Camata, and E. Spacone, "Regularization of first order computational homogenization for multiscale analysis of masonry structures," *Computational Mechanics*, vol. 57, pp. 257–276, dec 2016.
40. J. Lubliner, J. Oliver, S. Oller, and E. Oñate, "A plastic-damage model for concrete," *International Journal of Solids and Structures*, vol. 25, no. 3, pp. 299–326, 1989.
41. M. Petracca, L. Pelà, R. Rossi, S. Zaghi, G. Camata, and E. Spacone, "Micro-scale continuous and discrete numerical models for nonlinear analysis of masonry shear walls," *Construction and Building Materials*, vol. In Press, 2017.
42. J. Oliver, M. Cervera, S. Oller, and J. Lubliner, "Isotropic damage models and smeared crack analysis of concrete," *Proc. SCI-C Computer Aided Analysis and Design of Concrete Structures*, no. February, pp. 945–957, 1990.
43. Z. Bazant and B. Oh, "Crack band theory for fracture of concrete," *Materials and Structures*, vol. 16, pp. 155–177, 1983.
44. M. Cervera and M. Chiumenti, "Mesh objective tensile cracking via a local continuum damage model and a crack tracking technique," *Computer Methods in Applied Mechanics and Engineering*, vol. 196, no. 1-3, pp. 304–320, 2006.
45. M. Cervera, "Viscoelasticity and Rate-dependent Continuum Damage Models, Monography N-79," tech. rep., Barcelona, 2003.
46. T. Rabczuk, S. Bordas, and G. Zi, "On three-dimensional modelling of crack growth using partition of unity methods," *Computers and Structures*, vol. 88, no. 23-24, pp. 1391–1411, 2010.
47. J.-H. Song and T. Belytschko, "Cracking node method for dynamic fracture with finite elements," *International Journal for Numerical Methods in Engineering*, vol. 77, pp. 360–385, jan 2009.
48. R. de Borst and P. Nauta, "Non-orthogonal cracks in a smeared finite element model," *Engineering Computations*, vol. 2, no. 1, pp. 35–46, 1985.
49. A. Anthoine, G. Magenes, and G. Magonette, "Shear compression tensting and analysis of brick masonry walls," in *10th European Conference on Earthquake Engineering*, (Vienna), pp. 1657–1662, 1994.
50. G. Magenes and G. M. Calvi, "In-plane seismic response of brick masonry walls," 1997.
51. L. Binda, G. Mirabella Roberti, C. Tiraboschi, and S. Abbaneo, "Measuring Masonry Material Properties," *U.S.-Italy Workshop on Guidelines for Seismic Evaluation and Rehabilitation of Unreinforced Masonry Buildings*, pp. 326–347, 1994.
52. COMET, "Coupled Mechanical and Thermal analysis, http://www.cimne.com/comet/," 2016.
53. GiD, "The personal pre and post-processor, http://www.gidhome.com/," 2016.
54. S. Saloustros, L. Pelà, M. Cervera, and P. Roca, "An enhanced finite element macro-model for the realistic simulation of localized cracks in masonry structures: A large-scale application," *International Journal of Architectural Heritage*, vol. In press, no. doi: 10.1080/15583058.2017.1323245, 2017.

Appendix

The rate of the mechanical dissipation γ of the continuum damage model presented in Section 2 is [33]

$$\dot{\gamma} = -\frac{\partial \psi}{\partial \boldsymbol{\epsilon}^i} : \dot{\boldsymbol{\epsilon}}^i - \frac{\partial \psi}{\partial d^+}\dot{d}^+ - \frac{\partial \psi}{\partial d^-}\dot{d}^- = \dot{\gamma}^i + \dot{\gamma}^d \geq 0 \quad (28)$$

where ψ is the Helmholtz free energy and $\psi_0^{\pm}$ elastic free energies which have the following form [33]

$$\psi = (1 - d^+)\,\psi_0^+ + (1 - d^-)\,\psi_0^- \quad (29)$$

$$\psi_0^+ = \frac{1}{2}\,\bar{\boldsymbol{\sigma}}^+ : \boldsymbol{C_0}^{-1} : \bar{\boldsymbol{\sigma}} \quad (30)$$

$$\psi_0^- = \frac{1}{2}\,\bar{\boldsymbol{\sigma}}^- : \boldsymbol{C_0}^{-1} : \bar{\boldsymbol{\sigma}} \quad (31)$$

It is visible from equation (28) that the evolutions of both damage $\dot{\gamma}^d$ and irreversible strains $\dot{\gamma}^i$ contribute to the total dissipation energy of the solid, with each part being

$$\dot{\gamma}^i = -\frac{\partial \psi}{\partial \boldsymbol{\epsilon}^i} : \dot{\boldsymbol{\epsilon}}^i \geq 0 \tag{32}$$

$$\dot{\gamma}^d = -\frac{\partial \psi}{\partial d^+}\,\dot{d}^+ - \frac{\partial \psi}{\partial d^-}\,\dot{d}^- \geq 0 \tag{33}$$

The total dissipated energy per unit volume g_f is obtained as

$$g_f = \int_0^t \dot{\gamma}^i\,dt + \int_0^t \dot{\gamma}^d\,dt \tag{34}$$

The discrete softening parameter can be defined similarly to [44] considering an ideal uniaxial 1D compressive experiment, with a monotonic increment of the compressive strain (denoted hereafter as ϵ^e) from an initial unstressed state to full degradation. During the loading, and considering equations (5) and (9) the stress threshold will be

$$r^- = E\,\epsilon^e \tag{35}$$

In such case the dissipation due to the damage evolution is (see [44])

$$\gamma^d = \int_0^t \dot{\gamma}^d\,dt \tag{36}$$

$$= \frac{1}{2E}\int_{r0}^{t} (r^-)^2\,d'\,dr \tag{37}$$

$$= \left(1 + \frac{1}{H_d^-}\right)\frac{(f^-)^2}{2E} \tag{38}$$

The contribution of the irreversible strains to the total dissipated energy can be computed considering

$$\dot{\epsilon}^i = \beta\,\frac{E\dot{\epsilon}}{E\,\epsilon^e}\epsilon^e \tag{39a}$$

$$= \beta\,\dot{\epsilon} \tag{39b}$$

$$= \frac{\beta}{(1-\beta)}\dot{\epsilon}^e \tag{39c}$$

and

$$-\frac{\partial \psi}{\partial \epsilon^i} = (1-d^-)\,r^- \tag{40}$$

Using the above equations (39c) and (40), the dissipated energy due to the evolution of the irreversible strains is

$$\gamma^i = \int_{r0}^{t} (1-d^-)\,r^-\,\frac{\beta}{(1-\beta)}\,\dot{\epsilon}^e dt \tag{41}$$

$$= \int_{r0}^{r} (1-d^-)\,r^-\,\frac{\beta}{(1-\beta)}\,\frac{1}{E}\,dr \tag{42}$$

$$= \frac{\beta}{1-\beta}\,\frac{(f^-)^2}{E}\,\frac{1}{2H_d^-} \tag{43}$$

By virtue of equations (36) as well as (41) and considering that the total dissipation should be equal to Gf^-, the updated softening modulus is derived as

$$H_d^- = \frac{1}{1-\beta}\left(\frac{l_{dis}}{l_{mat}^- - l_{dis}}\right) \tag{44}$$

Note that for the limit case of $\beta = 1$, equation (39b) limits to $\dot{\epsilon}^i = \dot{\epsilon}$ and consequently $\dot{\epsilon}^e = 0$. This results in $\Delta r = 0$, which means that there is no damage evolution and hence no softening. In that case, energy is dissipated only due to the evolution of the irreversible strains, which using equations (32), (35) and (40) will be

$$\gamma^i = E\,\epsilon_0^e \int_0^t \dot{\epsilon}\,dt \tag{45a}$$

$$= E\,\epsilon_0^e \int_{\epsilon_0}^{e} d\epsilon \tag{45b}$$

$$= E\,\epsilon_0^e\,[\epsilon - \epsilon_0^e] \tag{45c}$$

with ϵ_0^e being the elastic strain at the peak strength. According to the above, the dissipation will keep increasing linearly with the increase of the strains, resembling the behaviour of a perfectly plastic material.

An Enhanced Finite Element Macro-Model for the Realistic Simulation of Localized Cracks in Masonry Structures: A Large-Scale Application

Savvas Saloustros · Luca Pelà · Miguel Cervera · Pere Roca

International Journal of Architectural Heritage, 2017
doi:10.1080/15583058.2017.1323245

Accepted Manuscript in *International Journal of Architectural Heritage*
DOI: 10.1016/j.engfracmech.2015.10.039

An Enhanced Finite Element Macro-model for the Realistic Simulation of Localized Cracks in Masonry Structures: A Large-Scale Application

Savvas Saloustros · Luca Pelà · Miguel Cervera · Pere Roca

Submitted: 20 December 2017
Revised: 27 February 2017
Accepted 15 March 2017

Abstract Finite element macro-modelling approaches are widely used for the analysis of large-scale masonry structures. Despite their efficiency, they still face two important challenges: the realistic representation of damage and a reasonable independency of the numerical results to the used discretization. In this work, the classical smeared crack approach is enhanced with a crack-tracking algorithm, originating from the analysis of localized cracking in qua-si-brittle materials. The proposed algorithm is for the first time applied to a large-scale wall exhibiting multiple shear and flexural cracking. Discussion covers structural aspects, as the response of the structure under different assumptions regarding the floor rigidity, but also numerical issues, commonly overlooked in the simulation of large structures, such the mesh-dependency of the numerical results.

Keywords Continuum Damage Model · Finite Element Analysis · Façades · Macro-modelling · Masonry · Mesh-independency · Pushover Analysis · Shear/Flexural Cracks · Strain Localization · Tracking Algorithm

Savvas Saloustros · Luca Pelà · Miguel Cervera · Pere Roca

Department of Civil and Environmental Engineering
Universitat Politècnica de Catalunya (UPC-BarcelonaTech)
Jordi Girona 1-3, 08034 Barcelona, Spain.

International Center for Numerical Methods in Engineering (CIMNE)
Gran Capità, S/N, 08034 Barcelona, Spain.

E-mail: savvas.saloustros@upc.edu
E-mail: luca.pela@upc.edu
E-mail: miguel.cervera@upc.edu
E-mail: pere.roca.fabregat@upc.edu

1 Introduction

The important advances of the last decades in the field of computational solid mechanics, as well as the increasing capabilities of modern computers have resulted to an ample inventory of numerical methods used for the analysis of masonry structures. Nevertheless, there is no unified approach adhering all the aspects relative to the realistic simulation of masonry, namely damage localization, geometry representation, material description, and computational efficiency. The choice of the numerical approach depends on the purpose of the structural analysis (e.g. capacity, ductility, damage origin/propagation, collapse mechanism), the complexity and scale of the structure (e.g. single structural member or whole building) and the available resources (e.g. computational cost, knowledge of geometry and material properties).

A common categorization of the various approaches is performed in terms of the detail of the material description within the numerical strategy. Under this scope, we can recognize direct numerical simulations that consider the geometry and the properties of the composite masonry material and simplified approaches that consider masonry as a homogenous material with average properties.

Direct numerical simulations of masonry originate in the pioneering work of Page [29, 30]. Micro-modelling [21, 14, 23] and discrete element methods [31, 19, 25] are today among the most used approaches accounting

for the geometry of the composite material at the scale of its constituents, i.e. mortar joints and units (brick or blocks). Corollary of this detailed modelling are realistic numerical simulations that are in very good agreement with experimental results. Nevertheless, important challenges of direct numerical simulations are the acquisition of a large number of material properties, the calibration of the numerical properties [44] and, most importantly, the high computational cost [39]. Due to these reasons, micro-modelling and discrete element approaches are up-to-date restricted to the analysis of small-scale structural elements or structures.

Numerical simulations of large masonry structures are based on a different philosophy. For large-scale computations, the direct simulation of the masonry components becomes unaffordable both in terms of model preparation and computation times. The alternative is to idealize the masonry as a homogenous material with averaged properties depending on its components. This is the assumption of a wide and diverse family of computational approaches, including equivalent frame methods [24, 28, 32, 18, 1], numerical limit analysis [4, 26] and continuum mechanics (or macro-modelling) finite element methods (FEM) [6, 34, 7].

The macro-modelling approach has been widely used for the analysis of large masonry structures during the last decades [20, 39, 46]. Their popularity bases mostly on the facility to simulate large and complex geometries at a reasonable computational cost. FEM macro-modelling approaches can capture the structural response during the whole loading history, providing important in-formation on the damage evolution and the subsequent collapse mechanism.

Notwithstanding the aforementioned advantages, macro-models have two important limitations. The first one concerns the representation of damage. Failure of masonry under tension, bending or shear, is characterized by localized discrete cracks. Contrary to that, the representation of damage in macro-modelling approaches is often smeared over large areas or volumes of the structure. This inconsistency with the real behaviour hampers the association of existing damage with the simulated one and may result to an inaccurate interpretation of the emerging collapse mechanism. Apart from this, the smeared crack approach in the standard irreducible formulation of the finite element method results to the erroneous damage localization that depends on the alignment of the used mesh. The problem of mesh-bias independent crack localization is an open topic within the research field of computational failure mechanics (see [9, 38]), with, however, limited contributions to the issues related to the analysis of large masonry structures.

To overcome the above limitations of the macro-modelling approach the authors have proposed the enhancement of the classical smeared crack approach with a local crack-tracking algorithm. This approach was introduced in [10] with the aim of simulating localized cracks under tension or bending stress-states in quasi-brittle materials. The algorithm has been validated through comparison with experimental and analytical results on concrete and masonry structural elements [10, 41]. Aiming to account for the linear and non-linear properties of orthotropic materials, PelÃă et al. [35] coupled the algorithm with an orthotropic damage model resulting to the realistic simulation of damage experienced by timber and masonry elements. Large-scale applications include the analysis of representative bays of the Mallorca cathedral [40, 34] and the Poblet monastery [37].

Despite the differences of the materials and the scale of the simulated structures, the above applications bear a common characteristic; the structural collapse is defined by cracks starting from the boundaries of the structure (e.g. wall sides, door/window openings) and propagating along one direction. Apart from these, another common failure mechanism of masonry piers and spandrels is due to diagonal shear cracking emerging from the interior and propagating along two opposite directions. Existing tracking algorithms, however, have been developed for the simulation of cracks with a single propagation direction and starting only from the boundary of the structure or predefined material perturbations. This important simplification inhibits the use of these localization approaches to the analysis of large-scale problems with diverse cracking. Aiming to extend the application field of tracking algorithms, the authors have recently proposed a novel tracking algorithm with capacity to simulate both shear and flexural cracks [43, 42]. The algorithm has been validated through comparison with an experimental result on a full-scale masonry frame.

This work investigates the applicability of the macro-model presented in [43, 42] to the analysis of large masonry structures with failure mechanism defined by a large number of diverse cracks. To this aim, the seismic capacity of a large masonry wall is investigated by using the equivalent non-linear static analysis. To the best of the authors' knowledge, the presented analyses are the first application of tracking algorithms to the simulation of large-scale structures with multiple internal and boundary cracks. Discussion includes both the structural response of the wall under different assumptions regarding the floors' rigidity and the numerical performance of classical smeared crack approach with and without the proposed crack-tracking

algorithm. Special focus is given on the effect of the size and alignment of the mesh used in the numerical simulations, a topic that is rarely addressed in the existing studies about the analysis of large structures exhibiting multiple cracking.

The paper is structured as follows. Section 2 outlines the underlying continuum damage model. The enhancement of the classical smeared crack approach with the tracking algorithm is presented in Section 3. Section 4 constitutes the core of this paper, i.e. the application of the proposed approach to the case study of a large masonry wall of an existing building. The same section covers the important issue of the mesh-dependency of the numerical simulations. The paper closes with some concluding remarks in Section 5.

2 Continuum Damage Macro-model

In a continuum damage model, the actual stresses of a damaged material are associated to the equivalent stresses of the intact material (i.e. the effective stresses [11]) with the use of a scalar variable representing the magnitude of the damage experienced by the material. In this work, the Cauchy stress tensor $\boldsymbol{\sigma}$ is a function of the positive and negative effective stress tensors, $\bar{\boldsymbol{\sigma}}^+$ and $\bar{\boldsymbol{\sigma}}^-$ respectively, through the following constitutive equation

$$\boldsymbol{\sigma} = (1-d^+)\,\bar{\boldsymbol{\sigma}}^+ + (1-d^-)\,\bar{\boldsymbol{\sigma}}^-. \tag{1}$$

This is a model with damage induced rotating orthotropic behaviour. The scalar damage indices d^+ and d^- represent the damage of the material due to tensile and compressive stress states. Their value varies from 0 for intact material to 1 for a completely damaged material. The positive and negative parts of the effective stress tensor are obtained through the following expressions [13]

$$\bar{\boldsymbol{\sigma}}^+ = \sum_{j=1}^{3} \langle \bar{\sigma}_j \rangle \, \mathbf{p_j} \otimes \mathbf{p_j} \tag{2}$$

$$\bar{\boldsymbol{\sigma}}^- = \bar{\boldsymbol{\sigma}} - \bar{\boldsymbol{\sigma}}^+ \tag{3}$$

$$\bar{\boldsymbol{\sigma}} = \boldsymbol{C_0} : \boldsymbol{\epsilon} \tag{4}$$

In the above equations, σ_j is the effective principal stress corresponding to the normalized eigenvector $\mathbf{p_j}$, $\boldsymbol{C_0}$ is the classical elastic constitutive tensor and $\boldsymbol{\epsilon}$ the strain tensor. Symbols $\otimes$ and $\langle\cdot\rangle$ stand for the tensor product and the Macaulay brackets ($\langle\bar{\sigma}_j\rangle = x$ if $x \geq 0, \langle\bar{\sigma}_j\rangle = 0$ if $x < 0$) respectively.

2.1 Damage Criteria

The failure surfaces that determine the triggering of the d^+ and d^- indices are defined through two scalar functions respectively $\tau^\pm$ termed as the equivalent stresses

$$\tau^+ = H_0\left[\bar{\sigma}_{max}\right] \frac{1}{1-a}\left[a\,\bar{I}_1 + \sqrt{3\,\bar{J}_2} + b\,\langle\bar{\sigma}_{max}\rangle\right]\frac{f^+}{f^-} \tag{5}$$

$$\tau^- = H_0\left[-\bar{\sigma}_{min}\right] \frac{1}{1-a}\left[a\,\bar{I}_1 + \sqrt{3\,\bar{J}_2} + \kappa_1\,b\,\langle\bar{\sigma}_{max}\rangle\right] \tag{6}$$

$$a = \frac{\left(f_b^-/f^-\right)-1}{2\left(f_b^-/f^-\right)-1} \tag{7}$$

$$b = (1-a)\,\frac{f^-}{f^+} - (1+a)\,. \tag{8}$$

The above definitions show the dependence of the failure surfaces on the uniaxial tensile f^+ and compressive f^- strengths, as well as on the biaxial f_b^- compressive strength. $\bar{I}_1$ denotes the first invariant of the effective stress tensor and $\bar{J}_2$ the second invariant of the effective deviatoric stress tensor and $\bar{\sigma}_{max}$ and $\bar{\sigma}_{min}$ stand for the maximum and minimum effective principal stresses respectively. The κ_1 variable in Equation (6) has been introduced in [36] to control the shape of the compressive failure surface in the shear quadrants. Its value ranges from 0 (leading to the Drucker-Prager criterion) to 1 (leading to the criterion proposed by Lubliner et al. [22], see Fig. 1. Finally, $H[\cdot]$ is the Heaviside step function ($H[x] = 1$,if $x \geq 0$ and $H[x] = 0$,if $x < 0$).

The damage criteria for tensile Φ^+ and compressive damage Φ^- are simply

$$\Phi^\pm(r^\pm, \tau^\pm) = \tau^\pm - r^\pm \leq 0 \tag{9}$$

The scalars $r^\pm$ represent the loading history of the material and are necessary to distinguish between loading and unloading conditions. Their initial values are equal to the tensile and compressive strength ($r_0^+ = f^+, r_0^- = f^-$) of the material and then vary according to

$$r^\pm = \max\left[r_0^\pm, \max_{i\in(0,n)}\left(\tau_i^\pm\right)\right] \tag{10}$$

with n representing the number of the current (load/displacement) increment.

Finally, an exponential softening law is selected for the evolution of the damage variables

$$d^\pm = 1 - \frac{r_0^\pm}{r^\pm}\exp\left\{2H_d^\pm\left(\frac{r_0^\pm - r^\pm}{r_0^\pm}\right)\right\} \qquad r^\pm \geq r_0^\pm.$$

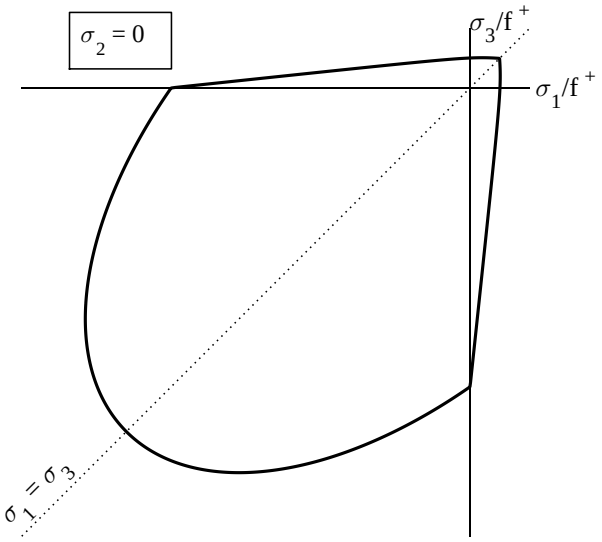

Fig. 1: The damage surface as proposed in [22].

(11)

where $H_d \geq 0$ is the discrete softening parameter taking into account the compressive and tensile fracture energy of the material $G_f^{\pm}$ and the characteristic finite element width l_{dis}, ensuring mesh-size objective results according to the crack-band theory [2]. Its value is defined with the following equations

$$H_d^{\pm} = \frac{l_{dis}}{l_{mat}^{\pm} - l_{dis}} \tag{12}$$

$$l_{mat}^{\pm} = 2\,E\,G_f^{\pm}/(f^{\pm})^2 \tag{13}$$

The value of the characteristic element width is considered as $l_{dis} = \sqrt{2A_e}$, where A_e is the surface of the triangular element.

3 The local crack-tracking algorithm

The crack-tracking algorithm serves as an enhancement of the classical smeared crack approach. Its aim is to the ensure mesh-bias independency of the numerical results and the realistic representation of propagating cracks in the numerical simulation of fracture in quasi-brittle materials. The presented approach has been implemented in the finite element software COMET [12] developed in the International Centre of Numerical Methods in Engineering (CIMNE) at the Technical University of Catalonia, Barcelona.

subroutines that are executed before the computation of the stresses at the first iteration of each (load or displacement) increment of the numerical analysis. The purpose of the algorithm is to identify the propagation path of all new and existing cracks for the current increment. A flag system is used to distinguish between (a) damaged elements, (b) non-damaged elements within a crack-path and (c) non-damaged elements outside a crack-path. The stress-strain state of the elements within the aforementioned (a) and (b) groups is defined according to the constitutive law presented in Section 2. For the elements in group (c) a linear-elastic relationship is maintained. The basic elements of the tracking algorithm are presented in Fig. 2.

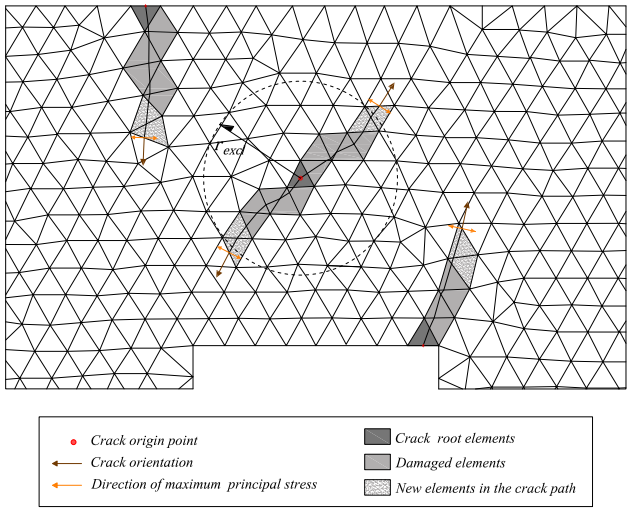

Fig. 2: The basic elements of the crack-tracking algorithm.

The first step of the crack-tracking algorithm consists in identifying new cracks. These originate at elements satisfying the damage criterion as defined in Equation (9). Since the damage condition can be satisfied for more than one element at the same increment, an "exclusion radius criterion" is used to identify the origin of a crack. This defines that the "crack root" element is the one with the highest ratio between the tensile effective stress and tensile strength of the material (i.e. τ^+/f^+) within an area defined by an "exclusion radius" r_{excl}. The latter value represents the minimum distance between existing and new cracks and is determined by the user. The purpose of the exclusion radius criterion is two-fold. The first one is to avoid the non-realistic spreading of damage over large areas, which typically occurs in smeared cracking problems with standard finite elements. This is a numerical pathology, not associated with the nature of the simulated material, leading in the later steps of the analysis to the erroneous and mesh-dependent localization of damage. The problem

of the mesh-independent strain localization is an ongoing challenging topic in the field of computational failure mechanics, with tracking algorithms being one of the current efficient alternatives [8, 17, 45, 41]. The second purpose of the exclusion radius is to account of the composite nature of the simulated material in a simplified and implicit way, when continuum finite element models are used for the numerical analysis. To illustrate this, consider the case of a historical masonry where cracking is mainly localized within the more vulnerable mortar joints, either due to the damage of the mortar or the debonding between the mortar and the (brick or stone) units. In such cases, the exclusion radius can be associated to the size of the units. A value of the exclusion radius less or equal to the finite element size recovers the classical smeared crack approach. The effect of this parameter on the simulation of masonry structures has been presented in [10, 40, 43, 42].

After recognising the new cracks for the current increment, the crack-tracking algorithm proceeds to the identification of the propagation path for each crack. The crack propagation direction is defined to be orthogonal to the direction of the maximum principal stresses as calculated either at the crack origin for new cracks or at the crack-tip element for existing ones. The crack-tip is the last element at the propagation front of a consolidated (at a previous increment) crack. For the case of internal crack origins, the crack path is sought along the two opposite orientations defined by the crack propagation vector. For crack origins lying on the boundary of the numerical domain or for crack-tips, the crack propagates to the single direction defined by the same vector.

the crack propagation direction. This situation occurs for high stress gradients at the propagating front of flexural cracks. To alleviate this pathology a maximum curvature criterion is used [10] that identifies sudden changes in the crack propagation direction at the crack-tip comparing to the last part of the crack with length r_{neigh} and corrects it according to a minimum deviation angle (α_{max}) defined by the user. For further details, the interested reader is referred to [10, 43].

4 Numerical Simulation of a Large-Scale Wall

In this section, the enhanced macro-model with the crack-tracking algorithm is applied for the first time to the analysis of a large-scale structure with multiple cracking. The case study concerns the analysis of a five floor structural wall at the interior of a masonry building situated in Via Martoglio, Catania Italy. The wall has regular openings symmetrically distributed along its central axis. Two irregularities exist in the structure. The first one concerns an opening at the right corner of the top floor and the second is a large door opening at the middle of the base floor. Clay brick vaults supported on concrete girders comprise the floor structural system, while the roof is a timber structure. The masonry is of regular units with dimensions $250 \times 120 \times 55\, mm^3$ (brick UNI5628/65). All the lintels are made of masonry but that of the central door at the base, which is made of reinforced concrete. Figure 3a presents the geometry and dimensions of the analysed structure.

The numerical simulation aims to investigate the structural response of the wall against seismic actions by means of a non-linear equivalent static analysis. Two stages of loading are considered. The first one corresponds to the application of the self-weight of the walls and floors and the live load as defined in [5]. In the second stage, the seismic actions are simulated as horizontal forces applied at the level of each floor. The loading pattern is proportional to the height and the vertical loading of each floor as suggested by the Italian Code [16].

As no information is available regarding the rigidity of the floors, two different models have been considered. In the first one (denoted hereafter as Model A), the same material parameters are used for both the masonry walls and floors assuming the existence of a flexible diaphragm (Material A in Table 1). In the second model (denoted hereafter as Model B), the floors are simulated as linear elastic with the double stiffness of the masonry aiming to consider the effect of a stiff diaphragm (Material B in Table 1). The latter material has been used in both models for modelling the lintel above the central opening at the ground floor. The material properties have been taken from previous analyses on the same building [5, 27]. The κ_1 parameter is taken equal to 0.45 which is equivalent to assume a shear strength of 0.15 MPa, which is the value used in the previous reference studies [5, 27]. The ratio between biaxial and uniaxial compression is equal to 1.15. As presented in [43, 42], the exclusion radius can be associated to the size of units of the simulated masonry. This is because cracking usually localizes in the interface between the units and the mortar. For this reason, an exclusion radius of 0.25 m is used in this case, which is equal to the bricks length, while the rest of the tracking parameters are $\alpha_{max} = 45^\circ$ and $r_{neigh}= 0.5$ m. The last two are minimum values that prevent the overturning of cracks. For a detailed discussion of the effect of the tracking parameters, the reader is referred to [43, 42].

The structure is discretized using an unstructured mesh with two-dimensional constant strain triangles under plane stress conditions. The average size of the

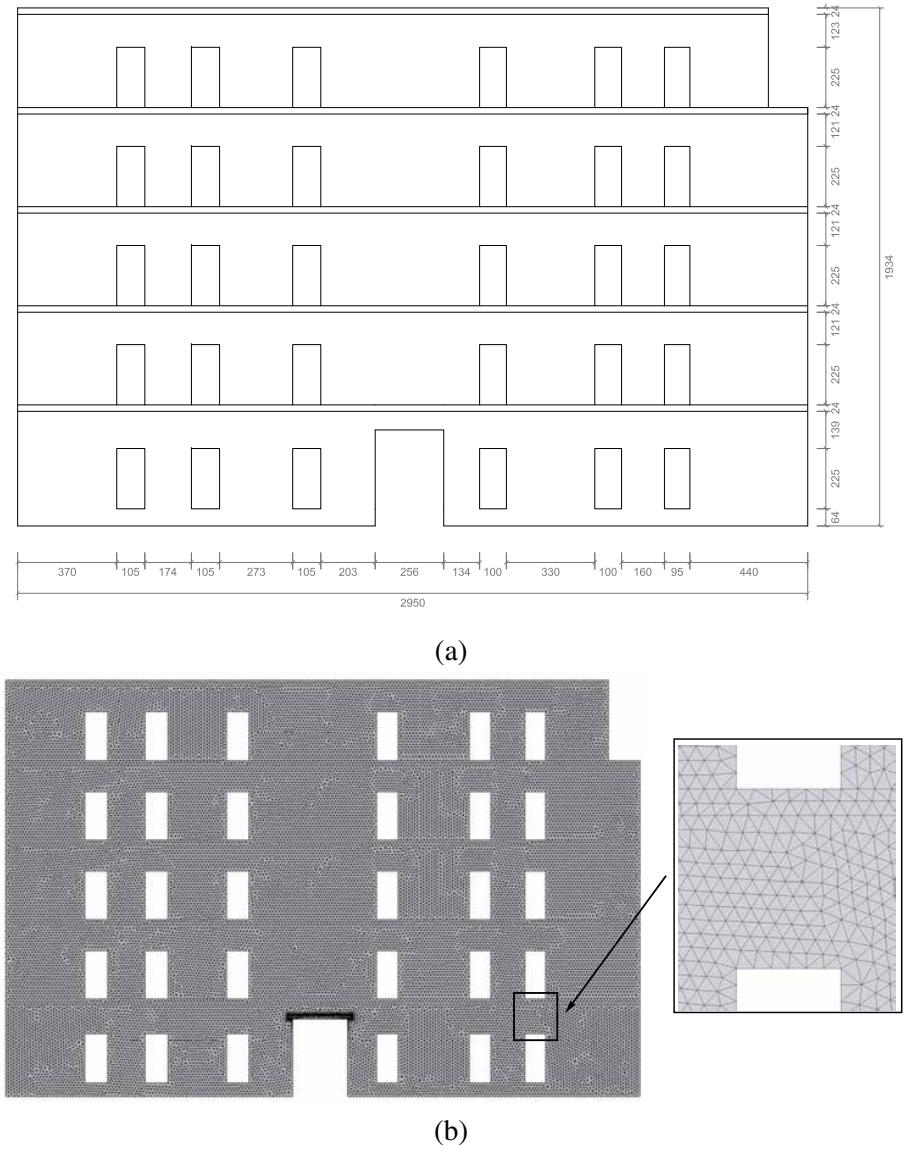

Fig. 3: (a) Geometry of the analysed wall (in mm) and (b) the used unstructured mesh.

finite elements is 0.15 m resulting in a total number of 51052 elements (Fig. 3b). The analysis is performed using an arc-length method along with a line-search procedure. Convergence is achieved for a ratio between the norm of residual forces against the norm of the total external forces less than 0.01. Calculations are performed

Material	γ $[kg/m^3]$	E $[MPa]$	v [-]	f^+ $[MPa]$	f^- $[MPa]$	G_f^+ $[J/m^2]$	G_f^- $[J/m^2]$	Model A	Model B
A	1700	2500	0.2	0.1	3.00	100	50000	Wall & Floors	Walls
B	1700	5000	0.2	-	-	-	-	Lintel	Lintel & Floors

Table 1: Material parameters adopted in the numerical simulations.

using the finite element soft-ware COMET [12], while pre- and post-processing with GiD, developed also in CIMNE, Barcelona [15].

4.1 Model A - Flexible Diaphragm

The structural response of the Model A with flexible floors is presented in terms of base shear against top horizontal displacement in Figure 4. The structure has a maximum capacity of 635 kN. The post-peak response is characterized by a softening part leading to a residual strength of around 530 kN.

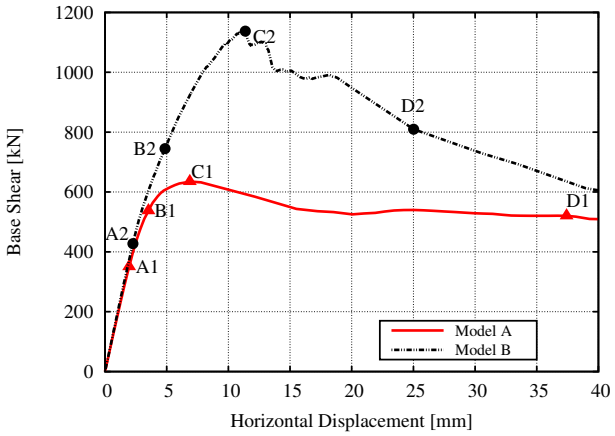

Fig. 4: Base shear versus horizontal displacement at the top right corner of the structure for the flexible diaphragm case (Model A) and for the stiff diaphragm case (Model B).

The first drop in the stiffness occurs for a base shear of around 350 kN. This coincides with the occurrence of shear and flexural cracking at the spandrels of the second and third floor as shown in Figure 5a. The increase in the horizontal load results to the extension of damage to the great majority of the spandrels, see Figure 5b. Flexural cracks initiate from the corner of the openings and propagate vertically within the spandrels. Contrarily, shear cracks emerge from the interior of the spandrels, at their middle height, and continue their propagation diagonally in two directions. Figure 6 presents the evolution of this damage pattern for the spandrel at the 4th floor and second column of openings (counting from the right side). Cracking due to bending initiates at the two ends of the spandrel and propagates towards the interior (Figure 6a). At a later stage, shear cracks emerge at the interior (Figure 6b) of the spandrel and evolve diagonally towards the two ends of the spandrel (Figure 6c). This cracking is characteristic of a strong-pier weak spandrel configuration [3, 33]. The presented tracking algorithm can successfully simulate this common damage typology of masonry because it allows cracks to initiate at any location of the mesh and to propagate in one or two directions.

Figure 5c shows the tensile damage distribution just after the maximum capacity of the structure. The vertical piers of the right side start to behave as cantilevers owing to the extensive damage of the weak spandrels. The collapse mechanism is determined by the rotation of the right corner after the progression of damage at the spandrels of all floors of the extreme right side at levels sufficient to allow its detachment from the rest of the structure. The rest of the analysis finds the right corner rotating around its base, resulting to important shear cracking at the base wall (Figure 5d). The analysis stops when the flexural cracks at the spandrels are entirely opened, resulting to their complete partition from their adjacent piers.

4.2 Model B - Stiff Diaphragm

The assumption of a stiff and elastic diaphragm has an important effect in the response of the structure. The capacity increases around 80%, reaching a horizontal load of 1139 kN (Figure 4). The displacement of the structure for the capacity load increases in the same order, being of 11 mm instead of 6.6 mm for Model A.

The initiation of damage is similar to that of Model A, affecting the spandrels of the second and third floor at the fourth column of openings (counting from the left side) for a base shear of around 425 kN, see Figure 7a. Contrary to Model A, the increase of the horizontal force results in a more uniform distribution of damage at the spandrels. This can be observed in Figure 7b, showing the tensile damage contour for a base shear of around 750 kN. After the spreading of damage at the spandrels, shear cracks start affecting the piers of the base floor. Important cracking seems to affect the pier next to the base door, which is probably due to a hammering effect of the rigid lintel above it. The tensile damage distribution after reaching the maximum capacity is shown in Figure 7c. The stiffer floors have restrained the rotation of the vertical piers despite the severe damage at the spandrels and mobilized the shear response of the piers. Flexural cracks start appearing at the lower left corner, while shear cracks are now evident in many piers of the structure mostly at the right side and the base. The shear failure of these piers determines the capacity of the structure, which can be seen as the drop of the base shear after the peak in the graph of Figure 4. The shear capacity of the rest piers results to a residual strength of the structure as shown by the

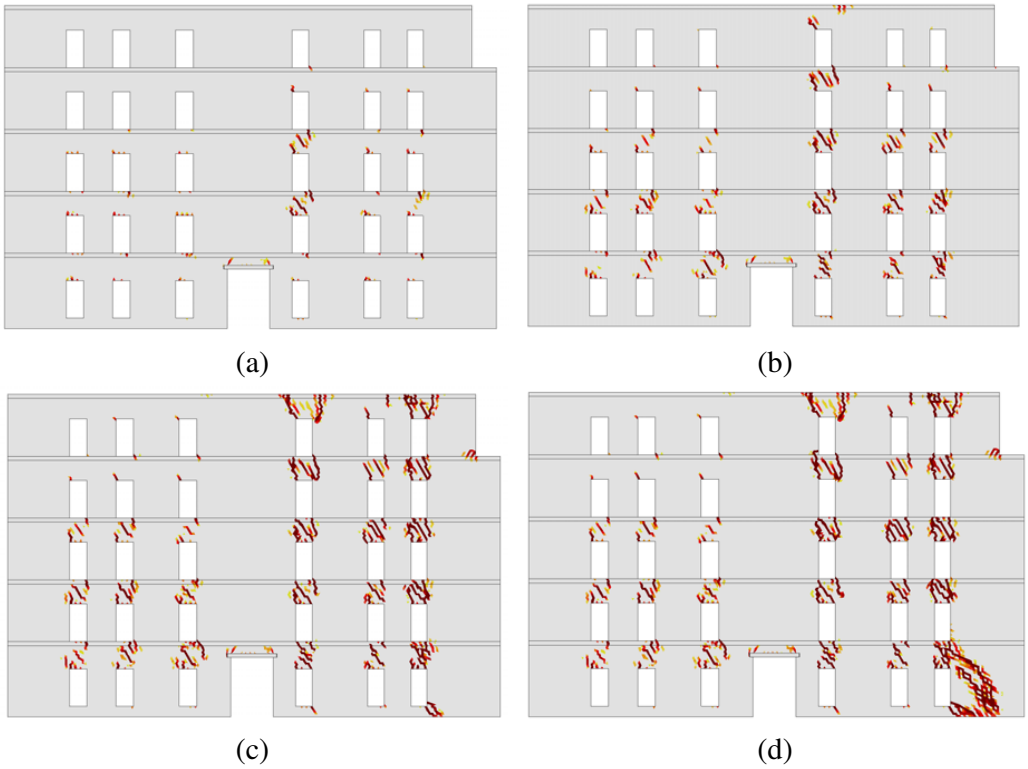

Fig. 5: Tensile damage contour of Model A for a horizontal displacement at the right top of: (a) 2 mm (point A1 in Figure 4), (b) 3.5 mm (point B1 in Figure 4), (c) 6.9 mm (point C1 in Figure 4) and (d) 37 mm (point D1 in Figure 4).

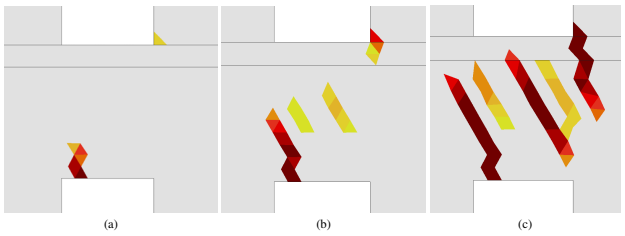

Fig. 6: Flexural and shear cracking evolution at the spandrel of the 4th floor, second column of openings (counting from the right side) for a displacement at the top of: (a) $u = 2.9\ mm$ (b) $u = 4.0\ mm$ (c) $u = 11.9\ mm$.

horizontal plateau in the post-peak response. This is followed by another sudden drop in the residual strength of the structure due to the shear failure of the rest of the piers at the left part of the structure as shown in Figure 7d. The analysis stops when the shear capacity of all the base piers is exhausted.

4.3 Discussion of the diaphragm effect on the structural response

The different assumptions regarding the rigidity and strength of the floors lead to substantial changes of the structural response. Stiff floors increase the integrity of the structure and the collaboration among the vertical piers even after the damage at the spandrels.

The collapse mechanism in Model A is triggered by the flexural cracking at the spandrels. This induces the cantilever behaviour of the last three vertical piers of the right side, which rotate around their base with almost no interaction among them. Failure of the structure is eventually determined by the collapse of the right side, as shown in Figure 8a. Contrarily, the stiff floor in Model B results in the mobilisation of the shear response of the piers, the strength of which determines the global capacity of the structure. Collapse in this case is due to the shear failure of the piers at the base of the structure Figure 8b. The capacity of the tracking algorithm to model internal cracks with two orientations, i.e. shear cracks, is crucial for the realistic simulation of the current case study.

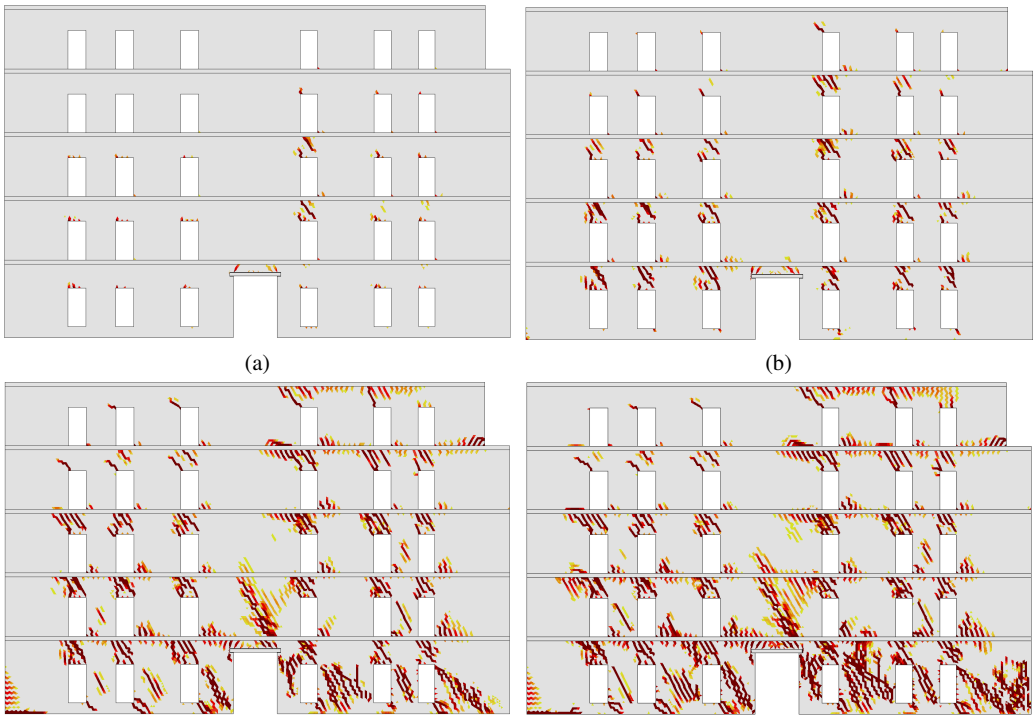

Fig. 7: Tensile damage contour of Model B for a horizontal displacement at the right top of: (a) 2.2 *mm* (point A2 in Figure 4), (b) 4.8 *mm* (point B2 in Figure 4), (c) 11.4 *mm* (point C2 in Figure 4) and (d) 25.1 *mm* (point D2 in Figure 4).

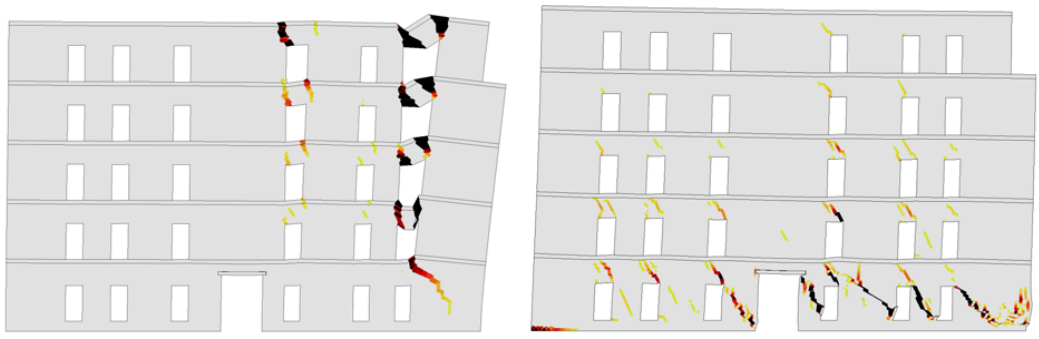

Fig. 8: Contour of the maximum principal strains on a deformed ($\times$ 30) mesh for (a) Model A and (b) Model B.

The different non-linear response between the shear failure and the flexural one can be appreciated through a comparison of the base shear versus displacement graphs in Figure 4. Flexural failure in Model A and rocking of the vertical piers is characterized by a smooth post-peak response. Differently, in Model B the shear failure of the piers at the base results to sudden drops in the load-caring capacity of the structure after the peak-strength.

A common characteristic of both models is the weakness of the spandrels. The most prone of them to fail are those with massive piers at their both sides. This is the case of the spandrels at the fourth column (counting from the left side), which are the first to experience damage during the loading history (see Figs 5a and 7a) for both models. Nevertheless, the damage pattern at the spandrels seems to change from mainly vertical flexural cracks to diagonal shear cracking when

the floor has an increased stiffness compared to that of the masonry walls.

4.4 Comparison with other approaches

Figure 9 presents a comparison between the results obtained with the macro-model proposed in this work and three alternatives from the literature: a finite element model with inserted discontinuities [5], a limit analysis software [27] and an equivalent frame approach [1].

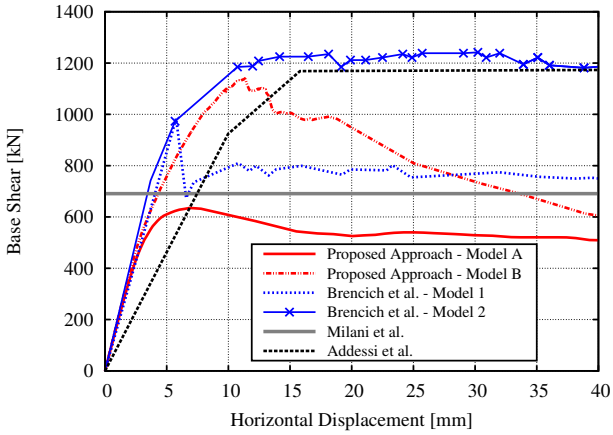

Fig. 9: Comparison of the global response of the Via Martoglio masonry wall as obtained by different numerical approaches.

The capacity obtained using Model A (635 kN) is very similar to the one calculated using the lower bound approach (691 kN) in Milani et al. [27] considering the case with flexible diaphragms. The small difference may be attributed to the different application pattern of the masonry's self-weight, which was concentrated at the floor levels in [27], while here the self-weight of the walls is applied at the masonry surfaces. This difference could explain the lower capacity of the present model since more load is actually located at higher levels of the structure.

Two models are reported from the work of Brencich et al. [5]. In the Model 1 the concrete floors were assumed to have the same properties as the masonry (as in Model A here), while in Model 2 they were modelled as elastic with an elastic modulus of 5 GPa (as in Model B here). In these models, damage could localize only along discontinuities distributed within the structure at horizontal layers and separated by quadrilateral finite elements. Vertical interfaces were positioned only at the location of the masonry lintels at each floor and for a single element height. The different treatment of damage and the above restrains in the propagation of vertical cracks resulted in an increased capacity comparing to the one estimated here for both models. This difference is more important for the case of Model 1 and Model A, where the analyses show that failure is characterized by vertical cracking due to bending at the spandrels. Nevertheless, the damage distribution within the structure is equivalent in both approaches and for both models. In Models 1 and A, damage is mainly localized at the spandrels, while in Models 2 and B significant damage affects the piers of the structure, and especially those of the lower floor.

Finally, the maximum capacity obtained using Model B is very close to the one predicted in [1] for a model with the assumption of elastic diaphragms and using an equivalent frame approach with force-based beam finite elements. The differences existing in the linear response are due to the use of a different value of elastic modulus for the walls of the structure.

The obtained results using the proposed approach are in overall agreement with those existing in the literature. The enhanced capacity of the crack-tracking algorithm to simulate the propagation of damage within the structure results to a more detailed representation of the post-peak response, as shown especially for the case of Model B. The presented approach can be an efficient alternative for the analysis of large structures, especially when the analyst necessitates information regarding the behaviour of the different structural members and the local collapse mechanisms occurring within the structure.

5 Mesh Dependency

This section investigates the dependency of the proposed approach to the discretization size and structure of the mesh. The performed analyses consider the properties of Model A using two additional meshes, and the obtained results are compared with the reference mesh of Figure 3b.

5.1 Mesh-size Dependency

The mesh-size dependency is investigated using a refined unstructured mesh with average element size equal to 75 mm. This increased refinement results in a total number of 204729 elements, i.e. 4 times more than in the reference model. The difference of the refinement level is illustrated in Figure 10.

Figure 11 shows the global response of the structure for the two unstructured meshes with the different element sizes. The two graphs almost coincide providing

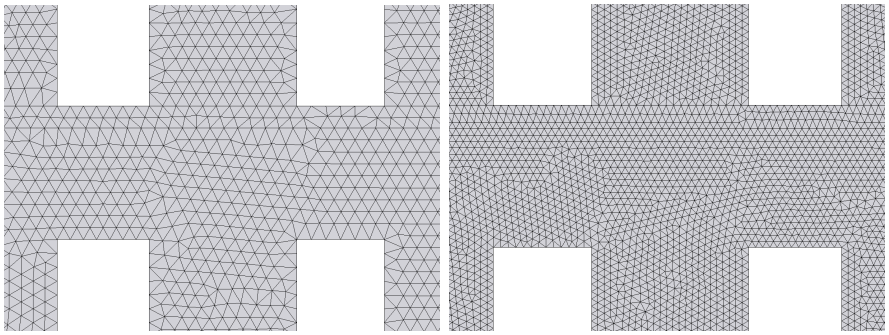

(a) (b)

Fig. 10: Part of the mesh used with average element size of (a) $h_e = 150\,mm$, (b) $h_e = 75\,mm$.

identical capacity for both cases and a very similar post-peak response. As illustrated in Figure 12a, the damage pattern is comparable for both cases. The same occurs for the obtained collapse mechanism, shown with the contour of the maximum principal strains in Figure 12b. The proposed enhanced macro-model gives results that are mesh-size independent. This is due to both the correct localization of the damage and the regularization of the constitutive law according to the finite element's characteristic length as shown from Equations (11) - (13).

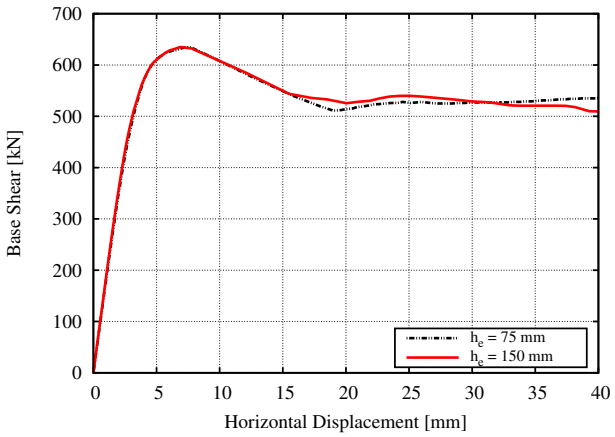

Fig. 11: Base shear versus horizontal displacement at the top right corner of the structure using a mesh with different element size.

5.2 Mesh-bias dependency

The mesh-bias dependency is investigated by comparing the results obtained with the mesh of Figure 3b, with a structured mesh presented in Figure 13. The sides of the orthogonal triangles make angles of 0°, 45°, 90° and 135° with the horizontal direction and have a mean length of 150 mm (44852 elements). Analyses with this mesh are carried-out with both the classical smeared crack approach and the crack-tracking algorithm.

The damage distribution as well as the localized strains for a horizontal displacement of approximately 21 mm using the two different meshes and the enhanced macro-model are presented in Figure 14. The obtained results are in good agreement. The damage typology at the spandrels is similar in both cases, with flexural cracks being present at the two corners of the openings and shear cracks at the middle of the spandrels. Good agreement is found also for the localized cracks and the occurring collapse mechanism, determined by the overturning of the right corner as shown in Figure 14b and Figure 14d.

The effectiveness of the crack-tracking technique to address the mesh-bias dependency is better demonstrated when compared with the numerical simulations carried-out without using the algorithm. To this aim, both meshes of Figure 3b and Figure 13 are analysed using the classical smeared crack approach. Figure 15a presents the contours of tensile damage using the unstructured mesh of Figure 3b, for a horizontal displacement at the top of the structure equal to 15.4 mm. Severe damage affects the spandrel walls resulting to their separation from the adjacent piers and the rotation of the vertical walls at the right side of the structure. Note the direction of the cracks that have opened during the loading history, but also the open cracks after reaching the capacity of the structure (Figure 15b); they are mostly diagonal, referring to a prevailing shear failure at the spandrels. Consider now the results of the numerical analysis using the structured mesh of Figure 13. Figure 15c presents the contour of the tensile damage for a displacement of 15.5 mm at the top of

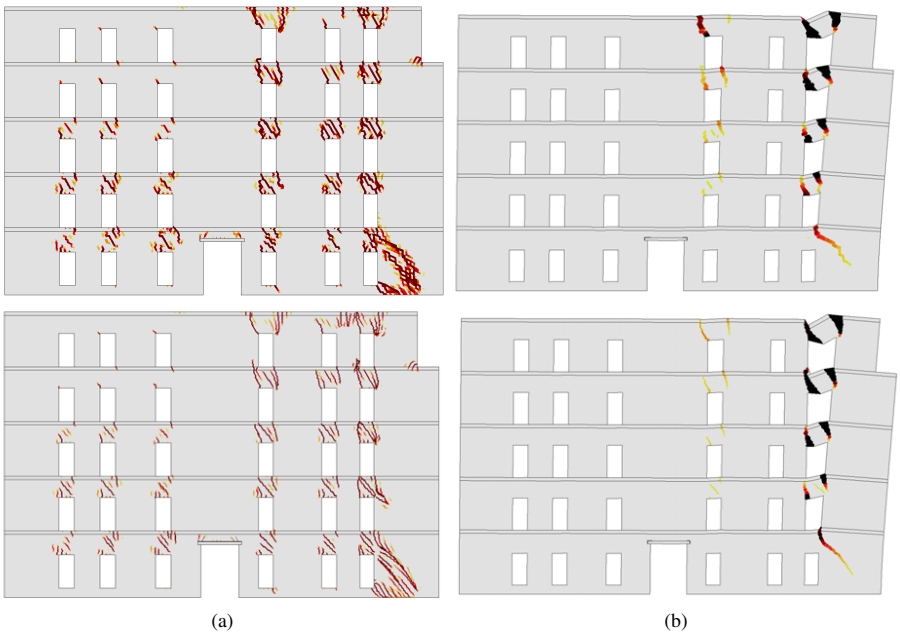

Fig. 12: Contours of (a) tensile damage, (b) maximum principal strains on a de-formed ($\times 40$) mesh for a displacement at the top right corner of 37 mm. Top row: unstructured mesh with average element size of 150 mm, Bottom row: unstructured mesh with average element size of 75 mm.

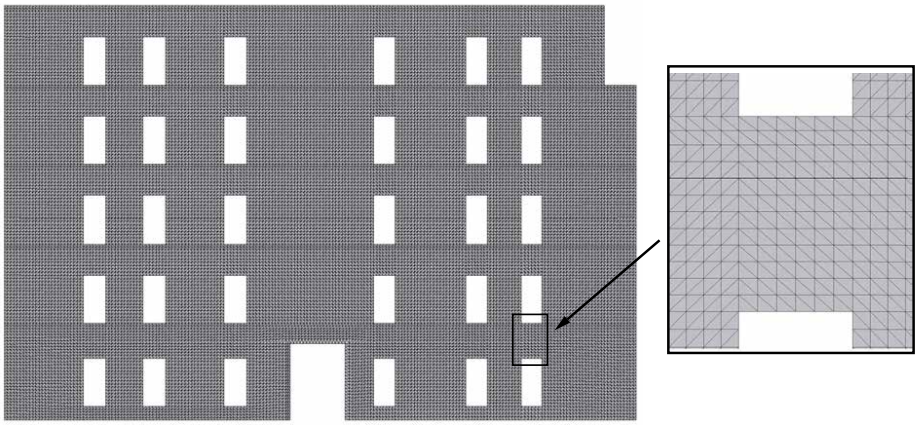

Fig. 13: Structured mesh used in the mesh-bias sensitivity analysis.

the structure. Cracking once again prevails at the spandrels, but this time the crack orientation is vertical in the great majority of the existing cracks. This is better observed with the contour of the maximum principal strains showing the localized cracks in Figure 15d.

It is obvious that the numerical solution is mesh-bias dependent for both the used discretizations when the proposed enhanced macro-model is not used. This numerical pathology inhibits the assessment of the actual local collapse mechanisms. On the contrary, the proposed algorithm shows to be robust, even for the structured mesh with orientations that facilitate the opening of vertical cracks, as the case of the classical smeared crack approach has demonstrated.

The different response of the structure for the two meshes is clear in the base shear against horizontal displacement graphs of Figure 16. The capacity of the structure without the use of the crack-tracking algorithm is lower by around 14% when the structured mesh is used, compared to the result with the structured one. This is due to the mesh-biased cracking at the spandrels, being vertical at the case of the structured mesh and diagonal for the unstructured one. Quite different response is also observed in the post-peak range with

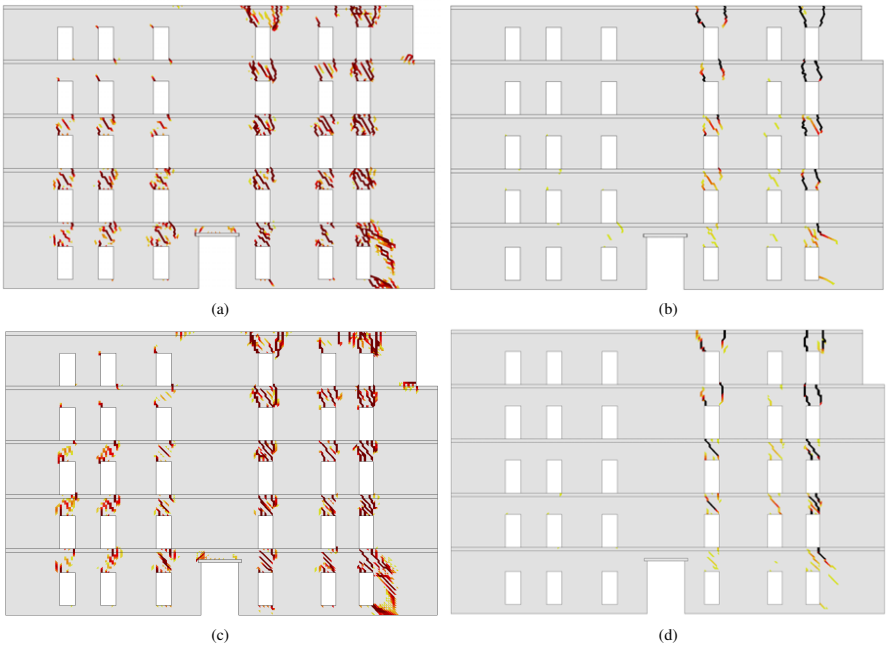

Fig. 14: Simulation of Model A using the proposed crack-tracking algorithm. (a) Tensile damage and (b) maximum principal strains using the unstructured mesh for a horizontal displacement of 20.9 mm (Point 1 in Figure 16). (c) Tensile damage and (d) maximum principal strains using the structured mesh for a horizontal displacement of 21.2 mm (Point 2 in Figure 16).

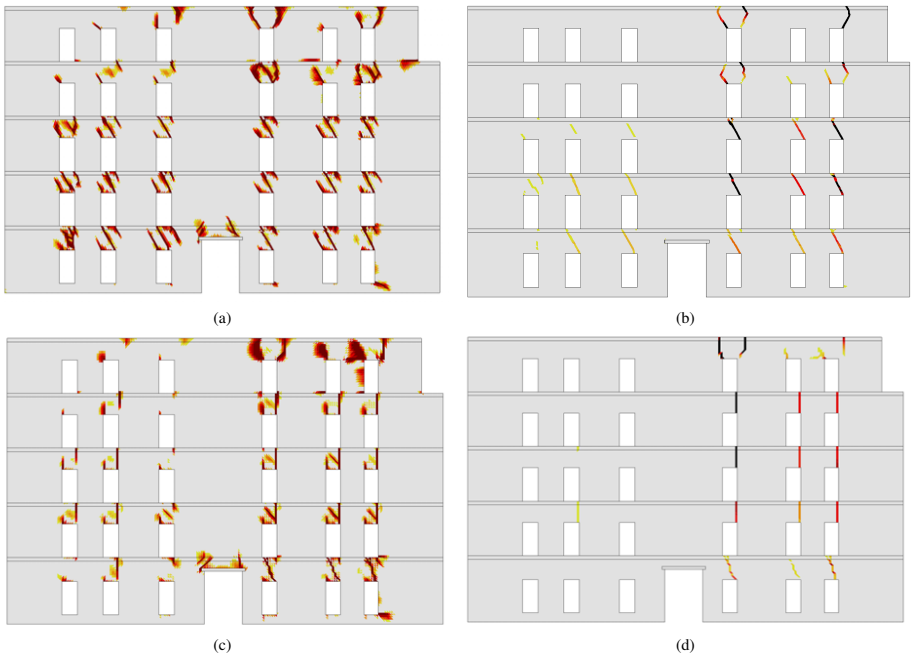

Fig. 15: Simulation of Model A using the classical smeared crack approach. (a) Tensile damage and (b) maximum principal strains using the unstructured mesh for a horizontal displacement of 15.4 mm (Point 3 in Figure 16). (c) Tensile damage and (d) maximum principal strains using the structured mesh for a horizontal displacement of 15.5 mm (Point 4 in Figure 16).

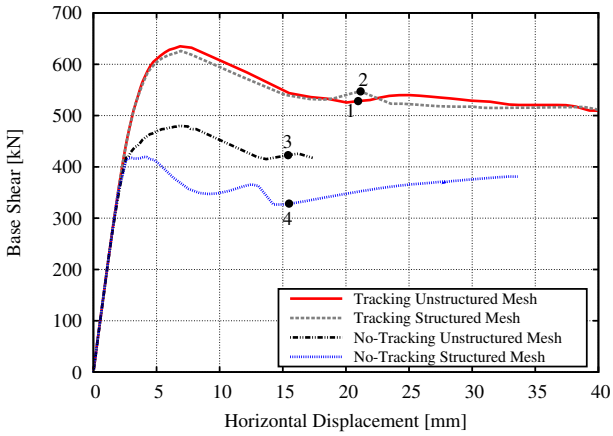

Fig. 16: Base shear versus horizontal displacement at the top right corner of the structure using two different meshes (structured and unstructured), with and without the proposed crack tracking algorithm.

a sharper decrease of the residual capacity. Contrarily, the results using the crack-tracking algorithm are in good agreement among them for both used meshes (Figure 16). The capacity is lower by around 2% for the case with the structured mesh. Despite this, the structural response is clearly similar for both cases, even in the post-peak response. A comparison between the graphs obtained with and without the tracking algorithm reveals the impact of the erroneous localization of damage with the smeared crack approach.

6 Conclusions

In this work, an enhanced continuum finite element model has been applied to the analysis of a large masonry structure. The model bases in the use of standard finite elements, a crack-tracking algorithm and a continuum damage model.

The proposed enhanced continuum finite element model has been used for the non-linear analysis of a real case study consisting of a large masonry faÃğade of an existing building, for the combined gravitational loads and (earthquake equivalent) monotonically increasing horizontal forces. The use of the proposed algorithm has given an important insight on the alteration of the structural response of the simulated wall for the two different assumptions regarding the rigidity of the floor system. A flexible diaphragm results to a reduced capacity and to a collapse mechanism characterized by the cantilever response of the vertical continuous piers after flexural and shear damage in the weak spandrels. The horizontal loading finally evokes the complete separation of the right side of the structure. On contrary, a floor system with increased stiffness and strength (compared to the vertical walls) preserves the integrity of the structure after the shear damage of the spandrels. Failure in this case is characterized by shear cracking at the piers of the base floor.

Numerical analyses carried out using various discretizations with different sizes and orientations demonstrate the mesh-size and mesh-bias independency of the proposed approach. For the mesh-bias dependency study, the enhanced model with the tracking method has been compared with the traditional smeared crack approach. The obtained crack pattern using the classical smeared crack approach has shown to depend notably on the orientation of the mesh, affecting considerably the structural response and the predicted capacity of the analysed wall. On the contrary, the results obtained with the crack-tracking algorithm have been very consistent for both meshes. The proposed approach has shown to be robust and suitable for the realistic simulation of multiple cracking in large structures.

7 Acknowledgements

This research has received the financial support from the MINECO (Ministerio de Economia y Competitividad of the Spanish Government) and the ERDF (European Regional Development Fund) through the MULTIMAS project (Multiscale techniques for the experimental and numerical analysis of the reliability of masonry structures, ref. num. BIA2015-63882-P) and the EACY project (Enhanced accuracy computational and experimental framework for strain localization and failure mechanisms, ref. num MAT 2013-48624-C2-1-P).

References

1. Addessi, D., Liberatore, D., and Masiani, R. Force-Based Beam Finite Element (FE) for the Pushover Analysis of Masonry Buildings. *International Journal of Architectural Heritage 9*, 3 (2015), 231–243.
2. Bažant, Z. P., and Oh, B. Crack band theory for fracture of concrete. *Materials and Structures 16* (1983), 155–177.
3. Beyer, K., and Dazio, A. Quasi-Static Cyclic Tests on Masonry Spandrels. *Earthquake Spectra 28*, 3 (aug 2012), 907–929.
4. Block, P., and Lachauer, L. Three-Dimensional (3D) Equilibrium Analysis of Gothic Masonry Vaults. *International Journal of Architectural Heritage 8*, 3 (2013), 312–335.
5. Brencich, A., Gambarotta, L., and Lagomarsino, S. Catania Project: Research on the seismic response of two masonry buildings. Chapter 6: Analysis of a masonry building in Via Martoglio. *CNR Gruppo Nazionale per la Difesa dei Terremoti* (2000), 107–143.

6. Carvalho, J., Ortega, J., Lourenço, P. B., Ramos, L. F., and Roman, H. Safety analysis of modern heritage masonry buildings: Box-buildings in Recife, Brazil. *Engineering Structures 80* (2014), 222–240.
7. Castellazzi, G., D'Altri, A. M., de Miranda, S., and Ubertini, F. An innovative numerical modeling strategy for the structural analysis of historical monumental buildings. *Engineering Structures 132* (2017), 229–248.
8. Cervera, M., and Chiumenti, M. Mesh objective tensile cracking via a local continuum damage model and a crack tracking technique. *Computer Methods in Applied Mechanics and Engineering 196*, 1-3 (2006), 304–320.
9. Cervera, M., Chiumenti, M., and Codina, R. Mixed stabilized finite element methods in nonlinear solid mechanics. Part I: Formulation. *Computer Methods in Applied Mechanics and Engineering 199*, 37-40 (2010), 2559–2570.
10. Cervera, M., Pelà, L., Clemente, R., and Roca, P. A crack-tracking technique for localized damage in quasi-brittle materials. *Engineering Fracture Mechanics 77*, 13 (2010), 2431–2450.
11. Chaboche, J. L. Continuum Damage Mechanics: Part IIâĂŤDamage Growth, Crack Initiation, and Crack Growth. *Journal of Applied Mechanics 55*, 1 (1988), 65.
12. COMET. Coupled Mechanical and Thermal analysis, http://www.cimne.com/comet/, 2016.
13. Faria, R., Oliver, J., and Cervera, M. A strain-based plastic viscous-damage model for massive concrete structures. *International Journal of Solids and Structures 35*, 14 (1998), 1533–1558.
14. Gambarotta, L., and Lagomarsino, S. Damage models for the seismic response of brick masonry shear walls. Part I: The mortar joint model and its applications. *Earthquake Engineering & Structural Dynamics 26*, 4 (apr 1997), 423–439.
15. GiD. The personal pre and post-processor, http://www.gidhome.com/, 2014.
16. Italian Ministry of Infrastructure and Transport. *Circolare 2 febbraio 2009, n. 617, Istruzioni per l'applicazione delle âĂIJNuove norme tecniche per le costruzioniâĂİ di cui al decreto ministeriale 14 gennaio 2008*. Rome, Italy, 2009.
17. Jäger, P., Steinmann, P., and Kuhl, E. On local tracking algorithms for the simulation of three-dimensional discontinuities. *Computational Mechanics 42*, 3 (2008), 395–406.
18. Lagomarsino, S., Penna, A., Galasco, A., and Cattari, S. TREMURI program: An equivalent frame model for the nonlinear seismic analysis of masonry buildings. *Engineering Structures 56* (2013), 1787–1799.
19. Lemos, J. V. Discrete Element Modeling of Masonry Structures. *International Journal of Architectural Heritage 1*, 2 (may 2007), 190–213.
20. Lourenço, P. B. Computations on historic masonry structures. *Progress in Structural Engineering and Materials 4*, 3 (jul 2002), 301–319.
21. Lourenço, P. B., and Rots, J. G. Multisurface Interface Model for Analysis of Masonry Structures. *Journal of Engineering Mechanics 123*, 7 (1997), 660–668.
22. Lubliner, J., Oliver, J., Oller, S., and Oñate, E. A plastic-damage model for concrete. *International Journal of Solids and Structures 25*, 3 (1989), 299–326.
23. Macorini, L., and Izzuddin, B. A. A non-linear interface element for 3D mesoscale analysis of brick-masonry structures. *International Journal for Numerical Methods in Engineering 85*, 12 (2011), 1584–1608.
24. Magenes, G., and Calvi, G. Prospettive per la calibrazione di metodi semplificati per l'analisi sismica di pareti murarie. In *Atti del Convegno Nazionale âĂIJLa Meccanica delle Murature tra Teoria e ProgettoâĂİ* (Messina, Italy, 1996), P. Ed., Ed.
25. McInerney, J., and DeJong, M. Discrete Element Modeling of Groin Vault Displacement Capacity. *International Journal of Architectural Heritage 9*, 8 (2015), 1037–1049.
26. Milani, G., Esquivel, Y. W., Lourenço, P. B., Riveiro, B., and Oliveira, D. V. Characterization of the response of quasi-periodic masonry: Geometrical investigation, homogenization and application to the Guimarães castle, Portugal. *Engineering Structures 56* (nov 2013), 621–641.
27. Milani, G., Lourenço, P., and Tralli, A. Homogenised limit analysis of masonry walls, Part II: Structural examples. *Computers & Structures 84*, 3-4 (2006), 181–195.
28. Molins, C., and Roca, P. Capacity of Masonry Arches and Spatial Frames. *Journal of Structural Engineering 124*, 6 (1998), 653–663.
29. Page, A. W. Finite element model for masonry. *Journal of the Structural Division 104*, 8 (1978), 1267–1285.
30. Page, A. W. A Model for the In-Plane Behaviour of Masonry and a Sensitivity Analysis of its CriticaI Parameters. In *5th International Brick Masonry Conference* (1979), pp. 262–267.
31. Papastamatiou, D., and Psycharis, I. N. Seismic response of classical monuments-a numerical perspective developed at the Temple of Apollo in Bassae, Greece. *Terra Nova 5*, 6 (1993), 591–601.
32. Parisi, F., and Augenti, N. Assessment of unreinforced masonry cross sections under eccentric compression accounting for strain softening. *Construction and Building Materials 41* (apr 2013), 654–664.
33. Parisi, F., Augenti, N., and Prota, A. Implications of the spandrel type on the lateral behavior of unreinforced masonry walls. *Earthquake Engineering & Structural Dynamics 43*, 12 (2014), 1867–1887.
34. Pelà, L., Bourgeois, J., Roca, P., Cervera, M., and Chiumenti, M. Analysis of the Effect of Provisional Ties on the Construction and Current Deformation of Mallorca Cathedral. *International Journal of Architectural Heritage 10*, 4 (2016), 418–437.
35. Pelà, L., Cervera, M., Oller, S., and Chiumenti, M. A localized mapped damage model for orthotropic materials. *Engineering Fracture Mechanics 124-125*, July (2014), 196–216.
36. Petracca, M., Pelà, L., Rossi, R., Oller, S., Camata, G., and Spacone, E. Regularization of first order computational homogenization for multiscale analysis of masonry structures. *Computational Mechanics 57*, 2 (2016), 257–276.
37. Petromichelakis, Y., Saloustros, S., and Pelà, L. Seismic assessment of historical masonry construction including uncertainty. In *9th International Conference on Structural Dynamics, EURODYN 2014* (2014), Á. Cunha, E. Caetano, P. Ribeiro, C. Papadimitriou, C. Moutinho, and F. Magalhães, Eds., pp. 297–304.
38. Rabczuk, T. Computational Methods for Fracture in Brittle and Quasi-Brittle Solids : State-of-the-art Review and Future Perspectives. *ISRN Applied Mathematics 2013* (2012), 1–61.
39. Roca, P., Cervera, M., Gariup, G., and Pelà, L.

Structural Analysis of Masonry Historical Constructions. Classical and Advanced Approaches. *Archives of Computational Methods in Engineering 17*, 3 (2010), 299–325.
40. Roca, P., Cervera, M., Pelà, L., Clemente, R., and Chiumenti, M. Continuum FE models for the analysis of Mallorca Cathedral. *Engineering Structures 46* (2013), 653–670.
41. Saloustros, S., Pelà, L., and Cervera, M. A crack-tracking technique for localized cohesive-frictional damage. *Engineering Fracture Mechanics 150* (2015), 96–114.
42. Saloustros, S., Pelà, L., Cervera, M., and Roca, P. A macro-modelling finite element technique for the realistic simulation of cracking in masonry structures. *Structural Analysis of Historical Constructions - Anamnesis, diagnosis, therapy, controls*, 2010 (2016), 284–290.
43. Saloustros, S., Pelà, L., Cervera, M., and Roca, P. Finite element modelling of internal and multiple localized cracks. *Computational Mechanics 59*, 2 (2016), 299–316.
44. Sarhosis, V., and Sheng, Y. Identification of material parameters for low bond strength masonry. *Engineering Structures 60* (2014), 100–110.
45. Slobbe, A. T., Hendriks, M. A. N., and Rots, J. G. Smoothing the propagation of smeared cracks. *Engineering Fracture Mechanics 132* (2014), 147–168.
46. Theodossopoulos, D., and Sinha, B. A review of analytical methods in the current design processes and assessment of performance of masonry structures. *Construction and Building Materials 41* (2013), 990–1001.

This page is intentionally left blank.